

ΔE -Effect Magnetic Field Sensors

Dissertation
submitted to the Faculty of Engineering
of Kiel University
for the degree of
Doctor of Engineering

presented by
Benjamin Spetzler, M. Sc.
Kiel

October 21, 2021

1. Referee: Prof. Dr. rer. nat. Franz Faupel
2. Referee: Prof. Dr.-Ing. Jeffrey McCord
3. Referee: Prof. Dr. Nian X. Sun

Date of oral examination: December 21, 2021

ΔE -Effect Magnetic Field Sensors

Many conceivable biomedical and diagnostic applications require the detection of small-amplitude and low-frequency magnetic fields. Against this background, a magnetometer concept is investigated in this work based on the magnetoelastic ΔE effect. The ΔE effect causes the resonance frequency of a magnetoelastic resonator to detune in the presence of a magnetic field, which can be read-out electrically with an additional piezoelectric phase. Various microelectromechanical resonators are experimentally analyzed in terms of the ΔE effect and signal-and-noise response. This response is highly complex because of the anisotropic and nonlinear coupled magnetic, mechanical, and electrical properties. Models are developed and extended where necessary to gain insights into the potentials and limits accompanying sensor design and operating parameters. Beyond the material and geometry parameters, we analyze the effect of different resonance modes, spatial property variations, and operating frequencies on sensitivity. Although a large ΔE effect is confirmed in the shear modulus, the sensitivity of classical cantilever resonators does not benefit from this effect. An approach utilizing surface acoustic shear-waves provides a solution and can detect small signals over a large bandwidth. Comprehensive analyses of the quality factor and piezoelectric material parameters indicate methods to increase sensitivity and signal-to-noise ratio significantly. The latter is currently limited by the loss of the magnetic material. First exchange-biased ΔE -effect sensors pave the way for compact setups and arrays with a large number of sensor elements. With a signal-and-noise model extended to sensor arrays, specific requirements are identified that could improve the signal-to-noise ratio. The insights gained lead to a new resonator and processing concept that can circumvent several previous limitations. With the obtained results and developed models, important contributions are made to the understanding and development of ΔE -effect magnetometers with prospects for sensor improvements in the future.

ΔE -Effekt Magnetfeldsensoren

Viele erdenkbare biomedizinische und diagnostische Anwendungen erfordern die Detektion von Magnetfeldern niedriger Amplitude und Frequenz. Vor diesem Hintergrund wird in dieser Arbeit ein Magnetometerkonzept untersucht, das auf dem magnetoelastischen ΔE Effekt basiert. Ein Magnetfeld kann einen magnetoelastischen Resonator über den ΔE Effekt verstimmen, was über eine zusätzliche piezoelektrische Phase ausgelesen wird. Verschiedene mikroelektromechanische Resonatoren werden experimentell bezüglich des ΔE Effekts und des Signal-Rausch Verhaltens untersucht. Dieses Verhalten ist aufgrund seiner anisotropen und nichtlinear gekoppelten magnetischen, mechanischen und elektrischen Eigenschaften hochgradig komplex. Modelle werden entwickelt und erweitert wo nötig, um Einblicke in die Limitierungen und das Potenzial zu gewinnen, das mit den Design- und Betriebsparametern einhergeht. Dabei wird über die Material- und Geometrieparameter hinausgegangen um den Einfluss von unterschiedlichen Resonanzmoden, räumlichen Eigenschaftsänderungen und Anregungsfrequenzen auf die Sensitivität zu untersuchen. Obwohl der Schermodul einen hohen ΔE Effekt aufweist, ist dessen Nutzung mit Torsionsmoden in klassischen Balkengeometrien schwer umsetzbar. Eine Lösung wird mit einem Sensoransatz gefunden der Oberflächenscherswellen nutzt und damit in der Lage ist Magnetfelder niedriger Amplitude über ein breites Frequenzband zu detektieren. Umfassende Analysen zum Einfluss des Qualitätsfaktors und der piezoelektrischen Eigenschaften demonstrieren, dass die Sensitivität und das Signal-zu-Rausch-Verhältnis signifikant verbessert werden können. Letzteres ist derzeit durch Verluste im magnetischen Material limitiert. Erste Exchange-Bias ΔE -Effekt Sensoren bereiten den Weg für kompakte Versuchsaufbauten und Sensoranordnungen mit einer hohen Anzahl von Sensorelementen. Mit einem erweiterten Signal-Rausch Modell werden konkrete Anforderungen an die Sensoranordnungen identifiziert, die das Signal-zu-Rausch Verhältnis verbessern können. Die gewonnen Erkenntnisse münden in einem neuen Resonator- und Prozesskonzept, das einige vorherige Limitierungen umgehen könnte. Die Ergebnisse und Modelle stellen einen wichtigen Beitrag zu dem Verständnis und der Entwicklung von ΔE -Effekt Magnetometern dar und zeigen vielversprechende Perspektiven für zukünftige Verbesserungen auf.

List of Publications

First authored/equally contributed

First and equally contributing authors are underlined.

- 1 B. Spetzler, P. Wiegand, P. Durdaut, M. Höft, A. Bahr, R. Rieger, and F. Faupel, "Modeling and parallel operation of exchange-biased delta-E effect magnetometers for sensor arrays", *Sensors*, vol. 21, no. 22, 2021, doi: [10.3390/s21227594](https://doi.org/10.3390/s21227594).
- 2 A. D. Matyushov, B. Spetzler, M. Zaeimbashi, J. Zhou, Z. Qian, E. V. Golubeva, C. Tu, Y. Guo, B. F. Chen, D. Wang, A. Will-Cole, H. Chen, M. Rinaldi, J. McCord, F. Faupel, and N. X. Sun, "Curvature and stress effects on the performance of contour-mode resonant ΔE effect magnetometers", *Advanced Materials Technologies*, vol. 6, no. 9, 2021, doi: [10.1002/admt.202100294](https://doi.org/10.1002/admt.202100294).
- 3 B. Spetzler, C. Bald, P. Durdaut, J. Reermann, C. Kirchhof, A. Teplyuk, D. Meyners, E. Quandt, M. Höft, G. Schmidt, and F. Faupel, "Exchange biased delta-E effect enables the detection of low frequency pT magnetic fields with simultaneous localization", *Scientific Reports*, vol. 11, 2021, doi: [10.1038/s41598-021-84415-2](https://doi.org/10.1038/s41598-021-84415-2).
- 4 B. Spetzler, J. Su, R.-M. Friedrich, F. Niekietel, S. Fichtner, F. Lofink, and F. Faupel, "Influence of the piezoelectric material on the signal and noise of magnetoelectric magnetic field sensors based on the delta-E effect", *Applied Physics Letters Materials*, vol. 9, no. 3, 2021, doi: [10.1063/5.0042448](https://doi.org/10.1063/5.0042448).
- 5 B. Spetzler, E. V. Golubeva, R.-M. Friedrich, S. Zabel, C. Kirchhof, D. Meyners, J. McCord, and F. Faupel, "Magnetoelastic coupling and delta-E effect in magnetoelectric torsion mode resonators", *Sensors*, vol. 21, no. 6, 2021, doi: [10.3390/s21062022](https://doi.org/10.3390/s21062022).
- 6 B. Spetzler, C. Kirchhof, E. Quandt, J. McCord, and F. Faupel, "Magnetic sensitivity of bending-mode delta-E-effect sensors", *Physical Review Applied*, vol. 12, no. 16, 2019, doi: [10.1103/PhysRevApplied.12.064036](https://doi.org/10.1103/PhysRevApplied.12.064036).
- 7 B. Spetzler, E. V. Golubeva, C. Müller, J. McCord, and F. Faupel, "Frequency dependency of the delta-E effect and the sensitivity of delta-E effect magnetic field sensors", *Sensors*, vol. 19, no. 21, 2019, doi: [10.3390/s19214769](https://doi.org/10.3390/s19214769).
- 8 B. Spetzler, C. Kirchhof, J. Reermann, P. Durdaut, M. Höft, G. Schmidt, E. Quandt, and F. Faupel, "Influence of the quality factor on the signal to noise ratio of magnetoelectric sensors based on the delta-E effect", *Applied Physics Letters*, vol. 114, no. 18, 2019, doi: [10.1063/1.5096001](https://doi.org/10.1063/1.5096001). Editor's Pick.
- 9 A. Kittmann, P. Durdaut, S. Zabel, J. Reermann, J. Schmalz, B. Spetzler, D. Meyners, N. X. Sun, J. McCord, M. Gerken, G. Schmidt, M. Höft, R. Knöchel, F. Faupel, and E. Quandt, "Wide band low noise Love wave magnetic field sensor system", *Scientific Reports*, vol. 8, 2018, doi: [10.1038/s41598-017-18441-4](https://doi.org/10.1038/s41598-017-18441-4). Top 100 Articles 2018.

Co-Authored Publications

Additional publications related to the ΔE effect and ΔE -effect magnetometers are listed in the following. First and equally contributing authors are underlined.

- 1 J. Schmalz, A. Kittmann, P. Durdaut, **B. Spetzler**, F. Faupel, M. Höft, E. Quandt, and M. Gerken, "Multi-mode Love-wave SAW magnetic-field sensors", *Sensors*, vol. 20, no. 12, 2020, doi: [10.3390/s20123421](https://doi.org/10.3390/s20123421).
- 2 P. Durdaut, E. Rubiola, J.-M. Friedt, C. Müller, **B. Spetzler**, C. Kirchhof, D. Meyners, E. Quandt, F. Faupel, J. McCord, R. Knöchel, and M. Höft, "Fundamental noise limits and sensitivity of piezoelectrically driven magnetoelastic cantilevers", *Journal of Microelectromechanical Systems*, vol. 29, no. 5, 2020, doi: [10.1109/JMEMS.2020.3014402](https://doi.org/10.1109/JMEMS.2020.3014402).
- 3 N. Lukat, R.-M. Friedrich, **B. Spetzler**, C. Kirchhof, C. Arndt, L. Thormählen, F. Faupel, and C. Selhuber-Unkel, "Mapping of magnetic nanoparticles and cells using thin film magnetoelectric sensors based on the delta-E effect", *Sensors and Actuators A: Physical*, vol. 309, 2020, doi: [10.1016/j.sna.2020.112023](https://doi.org/10.1016/j.sna.2020.112023).
- 4 C. Tu, Z.-Q. Chu, **B. Spetzler**, P. Hayes, C.-Z. Dong, X.-F. Liang, H.-H. Chen, Y.-F. He, Y.-Y. Wei, I. Lisenkov, H. Lin, Y.-H. Lin, J. McCord, F. Faupel, E. Quandt, and N. X. Sun, "Mechanical-resonance-enhanced thin-film magnetoelectric heterostructures for magnetometers, mechanical antennas, tunable RF inductors, and filters", *Materials*, vol. 12, no. 14, 2019, doi: [10.3390/ma12142259](https://doi.org/10.3390/ma12142259).
- 5 J. Schmalz, **B. Spetzler**, F. Faupel, and M. Gerken, "Love wave magnetic field sensor modeling - from 1D to 3D model", *Proceedings of the International Conference on Electromagnetics in Advanced Applications (ICEAA)*; IEEE: Granada, Spain, 2019, doi: [10.1109/ICEAA.2019.8879389](https://doi.org/10.1109/ICEAA.2019.8879389).

Contents

Introduction and Objective	3
I Fundamentals	3
1 ΔE Effect	5
1.1 Overview of Previous Work	5
1.2 Introduction to the ΔE Effect	6
1.2.1 Illustration of the ΔE Effect with a Model	7
1.3 Distinction from Similar Effects	10
1.3.1 Magnetostrictive Elongation	10
1.3.2 Stress Stiffening	11
1.3.3 Pole Effect	11
1.3.4 Discussion and Conclusion	12
2 Sensor Concept	13
2.1 Overview of ΔE -Effect Sensors	13
2.1.1 Surface Acoustic Wave ΔE -Effect Sensors	13
2.1.2 ΔE -Effect Sensors Based on Free-Standing Thin-Film Resonators	13
2.1.3 Other ΔE -Effect Sensors	15
2.2 Sensor Operation	16
2.2.1 Open-Loop vs. Closed-Loop Operation	16
2.2.2 Sensor Operation in an Open-Loop System	17
2.2.3 Admittance of Electromechanical Resonators	18
2.2.4 Sensitivities and Operating Point	19
2.2.5 Signal-and-Noise Characterization	22
3 Magneto-Mechanical Theory	25
3.1 Thermodynamic Potentials of a Magnetoelastic System	28
3.2 Contributions to Gibbs Free Energy Density	30
3.2.1 Zeeman Energy	30
3.2.2 Exchange Stiffness Energy	30
3.2.3 Intrinsic Anisotropy Energy	31
3.2.4 Internal Magnetostatic Stray Field	32
3.2.5 Magnetoelastic Coupling	34
3.2.6 Complete Magneto-Mechanical Term	35
3.3 Dynamic Magneto-Mechanical System	37
3.3.1 Mechanical Equation of Motion	37
3.3.2 Magnetic Equation of Motion	39

II	Results	43
4	Magnetic Sensitivity	45
4.1	Magnetic Sensitivity of Bending Modes	46
4.2	Frequency Dependency of the ΔE Effect	60
4.3	Stress Effects in Contour-Mode Resonators	76
4.4	Towards a General Description of Magnetic Sensitivity	98
5	Surface Acoustic Wave Magnetometer	117
5.1	Love Wave Magnetic Field Sensor System	118
6	Signal and Noise	129
6.1	Influence of Quality factor	130
6.2	Influence of Piezoelectric Material	136
6.3	Influence of Magnetic Material	148
7	First Steps Towards Sensor Arrays	163
7.1	Exchange Biased ΔE -Effect Sensors for Localization	164
7.2	Parallel Operation of Sensor Elements	180
III	Outlook	199
8	Compact Sensor Arrays	201
8.1	PiezoMUMPs Technology Platform	201
8.2	First Array Design	202
8.2.1	Electromechanical Properties	202
8.2.2	Magnetic Layer Deposition	204
8.2.3	Scanning Electron Microscopy Measurements	205
8.3	Revised Resonator Design	206
8.4	Summary and Conclusion	208
	Conclusion	214
	Bibliography	243
	Acknowledgments	246
	Appendices	251
A	Additional Calculations	253
A.1	Simplified Mean-Field Model	253
A.2	Resonance Detuning Effects	254
A.2.1	Magnetostrictive Elongation	254
A.2.2	Stress Stiffening and Geometric Nonlinearity	254
A.2.3	Pole Effect	256
A.3	Note on Cauchy's Equation of Motion	258
B	Additional Publications	259
B.1	Love-Wave Magnetic-Field Sensor Modeling	260
B.2	Multimode Love-Wave SAW Magnetic-Field Sensors	266
B.3	Mapping of Magnetic Particles with ΔE -Effect Sensors	283
B.4	Mechanical-Resonance-Enhanced Thin-Film Magnetoelectric Heterostructures	292

Introduction and Objective

The detection of small-amplitude and low-frequency magnetic fields is considerably interesting for many biomedical and diagnostic applications [1]. For example, magnetocardiography (MCG) [2–6] and magnetoencephalography (MEG) [7, 8] for the investigation of brain and heart activities; and the imaging of magnetic particles [9, 10] for growth tracking in tissue engineering; and magnetomyography [11] for the diagnosis and monitoring of movement disorder or robotics control [12]. Such applications are often connected with inverse solution problems [13–15]. An accurate solution for such problems can benefit from large sensor arrays with many sensor elements that facilitate simultaneous high spatial resolution measurements. A profound advantage can arise for a large number of sensor elements by measuring the magnetic field instead of its electrical counterpart: measurements can be performed contactless without the need for attaching electrodes; further additional information is gained [5, 6]. This advantage comes at the cost of small signal amplitudes in the sub-picotesla regime and low-frequency components at which $1/f$ (f : frequency) noise [16, 17] dominates the noise floor. The small signal amplitudes pose a major challenge although the low frequency $1/f$ noise can be avoided by using modulation techniques.

Traditionally used sensor systems based on superconducting quantum interference devices (SQUIDs) can detect signal amplitudes in the sub-femtotesla regime at low frequencies [1, 18]. However, they require extensive magnetic shielding and liquid nitrogen or helium cooling, which makes them extensive and expensive to operate and limits the flexibility of arrays and the number of sensor elements. Therefore, their application is limited to a few research facilities and it has not found its way into clinical practice. Since then, various other sensor approaches have been pursued for biomedical applications [19]. A major step in this direction was achieved with the development of optically pumped magnetometers [1, 20]. These sensors can detect magnetic fields in the femtotesla regime for signal frequencies from ≈ 1 -100 Hz [21] via the change in the transmission of a LASER through a gas cell. Although their handling is significantly improved compared to SQUID magnetometers, they require external temperature control and magnetic shielding. Further, additional coils are required for signal modulation and DC field compensation to avoid the magnetic saturation of the sensor in the earth magnetic field. This limits the minimum size and number of sensor elements that can be used in practical sensor arrays.

Magnetolectric magnetic field sensors have been investigated as an alternative approach for biomedical and diagnostic applications [22–25]. The single-phase magnetolectric effect is very small [26, 27], and therefore, such sensors are based on magnetolectric composites where large magnetolectric coupling coefficients have been measured [28]. These composites comprise mechanically coupled magnetostrictive and piezoelectric materials. They can be processed on a large scale by microelectromechanical system (MEMS) technology with the dimensions of a few millimeters [29] down to the micrometer range [30–32], and they are compatible with complementary metal-oxide-semiconductor (CMOS) electronics [33, 34]. In addition, they can be operated at room temperature and without magnetic shielding because of their large dynamic range [35]. The direct magnetolectric effect [26, 36] has been utilized in centimeter-sized composite resonators, for detecting magnetic flux densities in the low picotesla regime [35, 37]. For detecting such small magnetic fields, it was necessary to amplify the effective magnetolectric

coefficient via the mechanical resonance. This limits the measurement to a narrow frequency band of typically only a few hertz around the mechanical resonance frequency. The resonance frequency scales inversely with the spatial dimensions of the resonator, and therefore, it is usually in the kilohertz or megahertz regime for sizes in the millimeter or micrometer range. Such narrow signal bandwidths at high frequencies are undesirable for most applications, and they outweigh the advantages of utilizing the direct magnetoelectric effect.

In recent years, ΔE -effect magnetic field sensors based on magnetoelectric thin-film composites have been investigated to overcome these limitations [31, 33]. These sensors employ a modulation scheme which makes them robust against acoustic noise and permits signal detection at low frequencies over a larger bandwidth. The modulation scheme is based on the magnetoelastic ΔE effect [38–40] of the magnetic material. This causes a change in the effective mechanical stiffness tensor with magnetization, and hence, with the applied magnetic field or stress. During sensor operation, a magnetoelectric resonator is actively excited at or close to its mechanical resonance frequency. An alternating magnetic field changes the resonance frequency via the ΔE effect and modulates the current through the sensor. Besides such resonator-based ΔE -effect sensors, surface acoustic wave devices were investigated [41], wherein the mechanical surface wave is delayed by a change in the effective mechanical properties caused by the ΔE effect. Although many aspects of the underlying theoretical framework in continuum mechanics and electromagnetism are well developed, the complicated interplay of magnetic, mechanical, and electrical properties make it challenging to provide a complete device description. Strong simplifications were used previously in the description of the ΔE effect, e.g., by omitting the tensor characteristic of stress and strain, magnetic nonlinearity, and spatial inhomogeneity. The influence of such effects on the resonator and sensor properties is highly nontrivial and poses fundamental questions that are further clarified in this thesis. Most previous studies focused either on the ΔE effect or on sensor characterization and fabrication. The relationship between material and design parameters with sensor properties such as sensitivity, signal, and noise remains largely unknown although it is essential for systematic device development.

This cumulative dissertation is intended to contribute to a deeper understanding of the ΔE effect, and the limits and inherent consequences of using the ΔE effect for magnetic field detection. Experimental and theoretical investigations are presented using different sensor designs and materials. This includes a variety of different magnetoelectric MEMS cantilevers, plate resonators, and surface acoustic wave devices. The thin-film composites are based on sputter-deposited soft-magnetic amorphous materials such as FeCoSiB and FeGaB and polycrystalline piezoelectric AlN and AlScN. The experimental investigations of the ΔE effect and relevant sensor properties such as sensitivity, signal, and noise are assessed with analytical and numerical models. The models are based on the combinations of different techniques and theories such as micromagnetics and magnetomechanical macrospin simulations and continuous electromechanical finite-element simulations, and equivalent circuit descriptions of the sensor system and semi-analytical signal-and-noise models. A thorough understanding of the ΔE effect and ΔE -effect sensors can be obtained with this multimethod approach, which provides new perspectives for sensor improvements.

All work reported in this thesis was conducted within the collaborative research center CRC 1261 - *Magnetoelectric Sensors: From Composite Materials to Biomagnetic Diagnostics*. This thesis is structured as follows. In Part I, an introduction to the concept of ΔE -effect sensors and the fundamental theory is introduced. In Part II, the published results and related investigations are presented. Finally, in Part III, an outlook on yet unpublished results with a possible way to achieve noise reduction is discussed, and we conclude with a summary.

Part I

Fundamentals

Chapter 1

ΔE Effect

The magnetoelastic ΔE effect is the underlying physical phenomenon of all sensors investigated in this thesis. The effect is attributed to the coupling of stress and magnetization, and it causes a resonance frequency detuning of magnetoelastic resonators in a magnetic field. After reviewing the previous work on the ΔE effect, it is illustrated in a simplified and qualitative manner to introduce the fundamentals required for the detailed discussion of ΔE -effect magnetic field sensors in Part II. This chapter concludes with a discussion of other mechanisms that can affect magnetoelastic resonators similar to the ΔE effect.

1.1 Overview of Previous Work

In the late 19th and early 20th century [42, 43], measurements were performed in the context of investigations on the Wiedemann effect [44], i.e., the magnetic-field-induced twisting of a ferromagnetic rod through which current flows. They observed changes in the mechanical torsion stiffness and Young's modulus [38, 45] as a function of an applied magnetic field and stress in iron and nickel rods. This phenomenon was later referred to as the ΔE effect [46], with "E" for *Elastizitätsmodul* (eng.: Young's modulus). Simultaneously, early theoretical attempts based on thermodynamic considerations were presented [38, 47] to connect the change in Young's modulus with magnetic susceptibility. The increasing understanding of ferromagnetism [48] and magnetostriction [49–52] in the beginning of the 1930s eventually led to the first explanations of the ΔE effect in terms of magnetostriction [46, 53, 54]. Experimentally, an intrinsic stress-strain nonlinearity [55, 56] was revealed in addition to an increased resonator damping below the magnetically saturated state [56]. In the following years, the dependency on temperature and different annealing conditions were investigated [57–61], considering only the shear and Young's modulus in isotropic magnetic models. Further, this holds for the first investigations and models of the frequency dependency of the ΔE effect and domain wall relaxation effects [62–64] in bulk magnetic materials in the early 1950s. Owing to the lack of magnetic hysteresis models, only small deviations from the demagnetized state and initial magnetization curve were treated [39]. This did not change before the concept of magnetic anisotropy [65] was well established and a first macrospin magnetization model was presented by Stoner and Wohlfarth [66]. Then, the currently used anisotropic description of magnetostriction by Callen and Callen [67, 68] paved the way for a deeper understanding of magnetoelasticity and the ΔE effect in the 1960s.

In the following years, magnon-phonon coupling [69, 70] in surface acoustic waves was studied around the ferromagnetic resonance frequency. Besides simple phenomenological models [71], more elaborate descriptions were developed for the dispersion relation in magnetoelastic media [72] for magnetoelastic bulk waves [73], Love waves [74, 75], and Rayleigh waves [76]. The magnetization induced change in wave velocity was investigated with surface acoustic wave (SAW) devices [41, 77–80] for tunable phase shifters [71, 77], oscillators [78], filters and envisioning magnetic field sensors [41]. Various magnetoelastic thin-films were used for the delay line of

SAWs based on materials such as amorphous Fe-based alloys (FeB, FeSiB) [71, 81], rare-earth alloys [79], garnet [41, 74], and nickel [77, 78].

A considerable amount of work from the 80s to the early 2000s focused on different materials. A large ΔE effect was observed in rare-earth compounds [82, 83] because of the high saturation magnetostriction; however, most of the work focused on soft-magnetic amorphous ribbons [40, 84–97] and wires [94, 98–100]. They were analyzed for anisotropy distributions, magnetomechanical damping, and the maximum Young’s modulus change induced by the magnetic field. The experiments were mostly performed on amorphous ribbon-based cantilever structures and delay lines utilized as first shear-wave magnetometers [101, 102]. In these materials and structures, changes of the Young’s modulus of more than 50% relative to the magnetically saturated state are reported [91, 103].

In the early 2000s, the ΔE effect in soft-magnetic amorphous ribbons found wide-spread application in electronic article surveillance labels as a low-cost mass product [104]. Besides amorphous ribbons, the ΔE effect was measured in amorphous thin-film materials, such as Terfenol-D [105]. Other magnetostrictive thin-films were developed [106]; e.g, for tunable MEMS resonators (FeCo/Ag multilayer) [107] and pressure sensors [108] based on the ΔE effect. At the time, fundamental dependencies of the ΔE effect on the magnetic material parameters were understood using macrospin models for the Young’s modulus [40, 109]. In addition, the first experimental studies on the ΔE effect of torsion resonance modes in thin-film cantilevers were performed and described qualitatively with a macrospin model for the shear modulus [110, 111]. Yet, the models were limited to specific magnetic configurations and did not fully consider the tensor characteristics of stress and strain. Further, initial measurements of the ΔE effect of the C_{44} stiffness tensor component and the shear modulus were performed in Galfenol single-crystals [112].

In the last 20 years, the ΔE effect in Terfenol-D [113] rods and Galfenol rods [114] was investigated as a function of stress, and in FeCoSiB [115, 116] and FeGaB [117] amorphous thin films as a function of the applied magnetic field. The magnetic thin films were used in the following years for detecting small amplitude magnetic fields in thin-film magnetoelectric ΔE -effect sensor [31, 118, 119] and they were investigated for such applications in surface acoustic wave devices [120–125]. A short review on the ΔE -effect magnetometers is provided in Chapter 2.

1.2 Introduction to the ΔE Effect

The interdependency of stress, strain, and magnetization is referred to as magnetoelastic coupling, and it is the origin of the ΔE effect. Although this effect has been known for a long time, the literature on the same is mostly scattered or focused on very specific magnetic configurations or materials. This section provides a short, qualitative introduction to the ΔE effect and its connection to magnetostriction and the underlying magnetoelastic effect. The discussion is simplified by considering uniaxial stress and strain to illustrate the fundamentals and motivate the major points addressed in Part II of this work. A detailed tensor-based discussion of the magneto-mechanical theory is provided in Chapter 3.

The magnetization of magnetoelastic materials is accompanied by a strain λ , commonly referred to as magnetostrictive strain. The maximum value of λ depends on the saturation magnetostriction λ_s , which is typically of the order of 10^{-6} for soft-magnetic amorphous materials [115, 126–128] and 10^{-3} for rare-earth alloys [82, 128, 129]. An overview of values for λ_s of the materials of various classes can be found in [130]. External stress σ applied to the magnetic material can change the magnetization, and thereby λ . In addition, σ induces a mechanical strain e , which obeys Hook’s law ($\sigma = E_m e$) and is proportional to Young’s modulus E_m . Both

strain contributions superpose and constitute a total strain

$$\varepsilon^0 = e + \lambda \quad (1.1)$$

that can be measured as an expansion or contraction of the material. That is, ε^0 is related to the gradient of the displacement field. With Equation 1.1 and Hook's law, an "effective" Young's modulus E can be defined

$$\frac{1}{E} := \frac{\partial \varepsilon^0}{\partial \sigma} = \frac{\partial(e + \lambda)}{\partial \sigma} := \frac{1}{E_m} + \frac{1}{\Delta E}, \quad (1.2)$$

to describe the apparent change in the materials stiffness caused by the additional stress induced magnetostriction. The proportion of the stress-induced λ depends on the magnetization configuration and on the magnetic field H . Consequently, H can change E . Estimating $E(H)$ is challenging because many other factors can affect the magnetostrictive response of the material. Beyond the magnetic and mechanical material parameters, the sample geometry, magnetization, and fabrication history are relevant. The next section illustrates the stress and magnetic field dependent ΔE effect with a magnetoelastic mean-field model.

1.2.1 Illustration of the ΔE Effect with a Model

For illustrating the qualitative connection of the ΔE effect with magnetoelasticity, a mean-field model, which is a strongly simplified version of the model presented in Section 4.1, is used. The simplified model can approximate the quasi-static magnetization process at zero temperature, and it omits the detailed domain structure. As a representative example, we consider a soft-magnetic material with a uniaxial magnetic anisotropy and isotropic, positive magnetoelastic coupling ($\lambda > 0$). Inhomogeneous magnetic properties are introduced and the mean magnetic easy axis is slightly misaligned to obtain a more realistic representation of the magnetization process. A uniaxial stress σ is applied along the direction of an external magnetic field \bar{H} with a component H in this direction and a magnetic vacuum flux density of $\mu_0 H$. Both \bar{H} and σ are applied along the same axis and approximately perpendicular to the mean magnetic easy axis. The volume averaged magnetic configuration of the sample is represented by the mean magnetization vector \bar{M} with saturation magnetization M_s . Using the projection M of \bar{M} on the axis of \bar{H} , we define $m := M/M_s$ and refer to it as *reduced magnetization* to adapt a succinct terminology. The details regarding the model and simulation parameters are listed in Appendix A.1.

The simulated magnetization curve in Fig. 1.1a follows the behavior expected from a hard-axis magnetization process in soft-magnetic samples with uniaxial anisotropy [131, 132]. The small hysteresis and rounding off of the curve around the anisotropy field are attributed to the inhomogeneity and slight tilt of the magnetic easy axis. At each point indicated in Fig. 1.1a, an increasing uniaxial stress σ is applied until m approximately reaches its saturation value. Then, σ is decreased into the compressive regime $\sigma < 0$. As shown in Fig. 1.1b, the resulting $m(\sigma)$ -curves are highly nonlinear with significantly varying slopes around $\sigma = 0$. The smallest slope occurs under positive ($m = 1$) and negative ($m = -1$) magnetic saturation values, where m is pinned by the magnetic field. At $H = 0$, the slope is similarly small and can be explained with symmetry arguments. In the given configuration, the energy density functional of the uniaxial stress σ is symmetric around the magnetic easy axis. Therefore, both orientations of m ($m > 0$, $m < 0$) are energetically almost equally favorable, and the slope is very small. The slope is nonzero because the slight tilt of the easy axis introduces a small asymmetry, which also causes the magnetic hysteresis. An applied magnetic field $H \neq 0$ increases the asymmetry, and therefore, the $m(\sigma)$ -curves saturate either with $m = 1$ or with $m = -1$ depending on the sign of H .

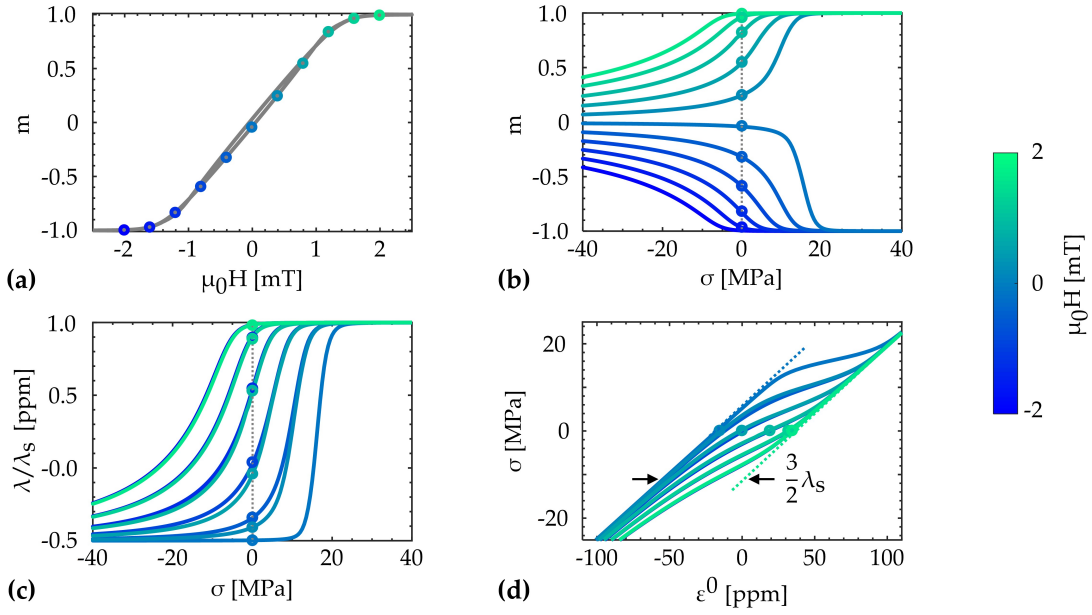


Figure 1.1: (a) Simulated reduced magnetization $m := M/M_s$, defined by the magnetization M and saturation magnetization M_s , and plotted as a function of the applied magnetic flux density $\mu_0 H$. (b) Simulated reduced magnetization m as a function of uniaxial stress σ , which starts at the magnetization states marked in (a). (c) Corresponding magnetostriction λ calculated from the data in (b) via a quadratic approximation and normalized to the saturation magnetostriction λ_s . (d) Stress σ as a function of the total strain ϵ^0 calculated from λ in (c) and the mechanical strain e with Equation 1.1.

According to Equation 1.2, λ must be known as a function of σ to calculate the derivative $\partial\lambda/\partial\sigma$ and estimate the ΔE effect. The magnetostrictive strain $\lambda(m)$ can be described via a quadratic approximation [133]

$$\lambda(m) = \frac{3}{2}\lambda_s \left(m^2 - \frac{1}{3} \right), \quad (1.3)$$

with the saturation magnetostriction λ_s . The magnetostriction $\lambda(\sigma)$ is obtained as a function of stress using Equation 1.3 and the simulated $m(\sigma)$ -curves (Fig. 1.1b). The results are plotted in Fig. 1.1c, normalized to λ_s . The factor of $-1/3$ in Equation 1.3 ensures that $\lambda = 0$ in a hypothetical reference state with an isotropic distribution of the magnetization orientation ($m = 1/3$). Therefore, the normalized magnetostriction λ/λ_s approaches negative values of $\lambda/\lambda_s = -0.5$ for compressive stress and $\lambda/\lambda_s = 1$ for tensile stress. Further, the $\lambda(\sigma)$ -curves are almost identical for $H < 0$ and $H > 0$ because λ is an even function of m , and $|m|$ is almost symmetric around H . The $\lambda(\sigma)$ -curves at $H < 0$ are only partially hidden by those at $H > 0$ because of the slight hysteresis. The displacement-related strain ϵ^0 must be known to estimate the effective Young's modulus. This strain is obtained from the magnetostriction curves in Fig. 1.1c by adding the mechanical strain $e = E_m^{-1}\sigma$ calculated with Hook's law (Equation 1.1). The resulting stress-strain curves in Fig. 1.1d are highly nonlinear and exhibit the same symmetries as described before. Correspondingly, the total strain $\epsilon^0(\sigma)$ shows the largest slope at intermediate magnetic field magnitudes, wherein the magnetization is most susceptible to the applied stress. At a large and small H , the contribution of λ to ϵ^0 is small, and therefore the slope of $\epsilon^0(\sigma)$ is $\partial\epsilon^0/\partial\sigma \approx E_m$.

Following Equation 1.2, the effective Young's modulus $E(\sigma)$ is calculated from the derivative of the stress-strain curves shown in Fig 1.1d. The resulting $E(\sigma)$ -curves are normalized to

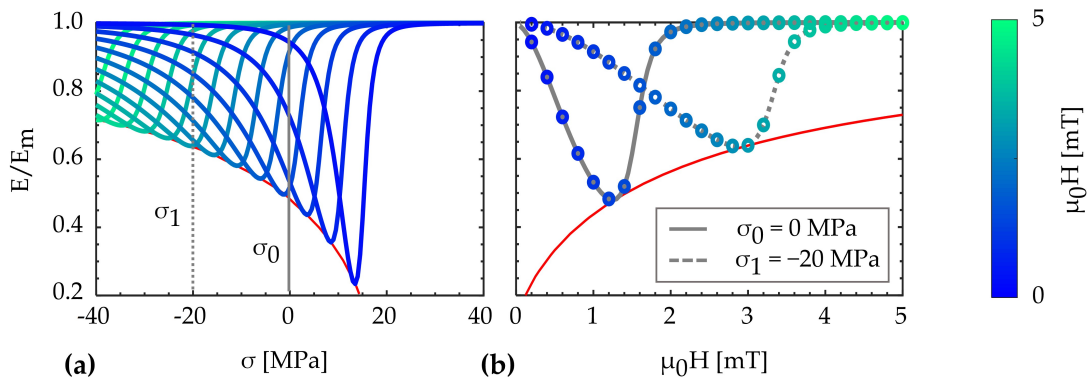


Figure 1.2: (a) Effective Young's modulus E , as a function of stress σ for various magnetic flux densities $\mu_0 H$, with the magnetic field H and vacuum permeability μ_0 . The E -curves are obtained from the derivatives of the stress-strain curves in Fig. 1.1d, and they are normalized to the Young's modulus E_m at fixed magnetization. (b) Young's modulus $E(\mu_0 H)$ for two different stress values, σ_0 and σ_1 . The red, bold lines in both plots indicate the minimum of E .

the Young's modulus E_m at fixed magnetization and are shown in Fig. 1.2a. Each $E(\sigma)$ -curve corresponds to a certain magnitude H of the magnetic field. Only calculations for curves at $H > 0$ are shown to improve the clarity of the plots. All arguments apply similarly for the regime $H < 0$ because the symmetry of $\lambda(H)$ around $H = 0$ results in a correspondingly symmetric effective Young's modulus $E(H)$ according to Equation 1.2. The effective Young's modulus $E(H)$ as a function of the magnetic field is extracted from the $E(\sigma)$ -curves in Fig. 1.2a at fixed stress values $\sigma = 0$ (bold line) and $\sigma = -20$ MPa (dashed line). In Fig. 1.2b the two $E(H)$ curves are shown and the minimum of $E(H)$ is indicated as a function of σ (red, bold line). The example emphasizes that compressive stress ($\sigma < 0$) increases the minimum Young's modulus and shifts it to larger values of the magnetic field, compared to the stress-free state. This stress dependency of $E(H)$ can be understood as a stress-induced change in the effective magnetic anisotropy. Compressive stress $\sigma < 0$ supports the intrinsic magnetic easy axis perpendicular to the stress axis. Therefore, a larger H is required to move the magnetization to the orientation where λ is most susceptible to σ and the minimum of $E(H)$ occurs. Vice versa, $\sigma > 0$ partially compensates the intrinsic magnetic easy axis. This increases the susceptibility of λ to σ , moves the minimum of $E(H)$ to smaller H , and leads to a larger change in $E(H)$.

Discussion

The example simulations illustrate some fundamental aspects of the stress and magnetic field dependency of the effective Young's modulus and its relation to magnetostriction. It was shown qualitatively that the nonlinear stress-strain relationship is intrinsic to the ΔE effect and magnetoelastic materials. Nonlinearity has been demonstrated experimentally in early studies on amorphous wires [55, 56], and it was recently reported in amorphous ribbons [134]. This is expected because magnetostriction as per the definition [135], is a nonlinear effect (in contrast to piezomagnetism). Therefore, defining a Young's modulus and linearizing the stress-strain relationship is a simplification. It is unclear whether this is relevant for thin-film sensors with a small volume fraction of magnetic materials. Another major simplification is related to the uniaxial character of the stress and the strain. Although it is a wide-spread assumption, it will be shown to be highly insufficient in many cases. Stress and strain are tensor fields of the second order that are (in linear approximation) related by the fourth-order stiffness tensor. The ΔE effect occurs in several tensor components of the stiffness tensor; however, their dependencies on

the applied magnetic field and influence on the respective resonance mode utilized is nontrivial. Even if uniaxial approximation is sufficiently valid from an entirely mechanical point of view, the extend to which it still holds in the presence of the ΔE effect remains unclear. Most mean-field approximations and constitutive models consider only spatially homogeneous magnetic properties. However, the effective magnetic properties are inhomogeneous because of the internal magnetic stray fields, residual stress from the deposition process, and other effects. Combined with the dynamic stress field of the respective resonance mode, the inhomogeneity is expected to influence the performance of the ΔE -effect magnetometers. Additional dynamic effects omitted by a quasi-static approximation can become relevant depending on the resonance frequency of the mode. All of these above mentioned points pose compelling questions relevant for the design of ΔE -effect magnetometers; all of them are addressed in Part II. A rigorous analysis requires the magneto-mechanical theory summarized in Chapter 3 to extend discussions beyond standard approximations.

1.3 Distinction from Similar Effects

The ΔE effect is described in the previous section as an apparent change in the stiffness of the magnetic material, caused by an additional, stress-induced magnetostrictive strain that adds to the linear Hookian strain. This definition explicitly states the mechanism of the stiffness change, and distinguishes the ΔE effect from other effects that can cause an apparent change in stiffness upon the application of a magnetic field. Such effects can be caused by magnetic fields that exert an additional force on the resonator (pole effect) or stress stiffening via magnetostriction-induced stress and a change in the geometry of the resonator. These effects are briefly elaborated in the subsections below; further, their contributions to the detuning of the resonator are discussed with various models. The discussed effects are mostly negligible and become relevant only in some boundary cases. Additional details on the calculations are provided in Appendix A.2.

Example Parameters

As a representative example of the geometry [136], a model cantilever is considered with a length $L = 3$ mm, a width $B = 1$ mm, a magnetic layer of thickness $t_f = 2$ μm on the top of a nonmagnetic substrate with a thickness of $t_s = 50$ μm . Young's moduli of the substrate and magnetic film at a fixed magnetization are $E_s = E_f = 150$ GPa. For the magnetic material, we consider a saturation magnetostriction $\lambda_s = 35$ ppm and a saturation flux density of $\mu_0 M_s = 1.5$ T as an example for soft-magnetic FeCoSiB [115]. The sign of λ_s does not affect the magnitude of the resonance detuning for the effects discussed.

1.3.1 Magnetostrictive Elongation

The resonance frequencies of a resonator depend on its geometry. Upon magnetization, magnetostrictive strain changes the geometry, which correspondingly alters the resonance frequency. As a representative example, we consider a cantilever beam composed of a magnetostrictive material that is magnetized along its long axis. For a sufficiently slender beam, lateral contraction is neglected and an approximation of the resonance frequency f_r is obtained from the Euler-Bernoulli beam equation [137]. In this case, the resonance frequency $f_r \propto L^{-2}$ depends strongly on the total length L of the cantilever. The elongation of the cantilever by a magnetostrictive strain λ causes a reduction of f_r with the applied magnetic field. The relative change in the resonance frequency is independent of the mechanical material parameters or the cantilever length and can be derived to $\Delta f/f_r \approx -3\lambda$ considering $\lambda_s \ll 1$ (c.f. Appendix A.2) and assuming that the change in the length of the cantilever equals the magnetostrictive elongation. With this equation, we obtain a relative resonance frequency change of $\Delta f/f_r \approx -0.01\%$ for example

parameters stated at the beginning of this section. This calculation poses a strong overestimation for thin-film resonators, wherein the magnetostrictive strain is partially confined by the mechanical coupling to the substrate. In this case, a bending and curving of the cantilever is expected to occur rather than a simple elongation.

1.3.2 Stress Stiffening

The magnetostrictive strain is partially confined if the magnetic layer is mechanically coupled to a substrate. Mechanical stress and strain develop upon magnetization, which cause a curvature of the resonator and thereby affect the resonance frequency. The framework of linear elasticity is not sufficient and a geometric nonlinearity must be considered in the calculation to capture these effects. The change in the stiffness caused by geometric nonlinearities is often referred to as stress stiffening [138, 139] and it is well known for, e.g., changing the resonance frequency of turbine blades upon rotation [140] and guitar strings during the tuning of the instrument.

In a magnetoelastic cantilever, stress develops because of the partial confinement of the magnetostrictive strain as a response to the mechanical backaction of the nonmagnetic substrate. This stress is referred to as magnetostrictive self-stress and formally described in the theory in Chapter 3. The maximum magnetization induced stress occurs if magnetostrictive strain is entirely confined and is proportional to the saturation magnetostriction λ_s . The influence of residual stress on the bending stiffness of cantilever resonators can be estimated with analytical and numerical models [141]. With the example parameters we can obtain a relative resonance frequency shift of $\Delta f/f_r \approx 5 \cdot 10^{-6} \%$.

Transverse curvature in thin cantilever sheets significantly increased the bending stiffness along the longitudinal axis [142]. In our case, the curvature is induced by the change in the magnetostrictive strain upon magnetization, and it is not explicitly included in the previous estimation. The magnitude of magnetization induced curvature depends on saturation magnetostriction, initial magnetic state, and geometry. For a magnetic thin-film plate, the magnetization induced curvature can be estimated analytically [143] and used to approximate the stiffness change [142]. For the example parameters, the resonance frequency detuning connected with the transverse curvature is of the order of $\Delta f/f_r \approx 10^{-6} \%$. Detailed descriptions of the combination of models, all equations used, and further details are provided in Appendix A.2.

1.3.3 Pole Effect

The pole effect describes the stiffening of a magnetic resonator because of a torque acting on the magnetic moments in an applied magnetic field. This phenomenon has been addressed in the context of cantilever and nanowire magnetometry [144, 145]. It can be estimated analytically with an energy-based macrospin approach [145]. We consider the example cantilever defined at the beginning of this section. A magnetic field with magnitude H is applied along the long axis of the cantilever, sufficiently high to magnetically saturate the film along this direction. When the cantilever oscillates, the magnetization vector is assumed to follow its motion because of the high shape anisotropy. The vector moves at an angle to the applied magnetic field, which creates an additional torque on the magnetization and increases the effective stiffness of the resonator. For small tip deflections in the first bending mode, the resonance frequency change Δf normalized to the initial resonance frequency f_r can be derived as (Appendix A.2)

$$\frac{\Delta f}{f_r} \approx \frac{4\mu_0 M_s^2 L^2 t_f}{E_s t_s} \left(\frac{H}{H + M_s} \right) \quad \text{for } t_f \ll t_s. \quad (1.4)$$

In this equation, $\mu_0 \approx 4\pi \cdot 10^{-7}$ represents the magnetic vacuum permeability, M_s represents the saturation magnetization, and E_s denotes the Young's modulus of the substrate. For the example parameters, we obtain a relative resonance detuning of $\Delta f/f_r \approx 10^{-6}$ at an applied magnetic flux density of $\mu_0 H = 1 \text{ mT}$. With an increasing magnetic field, the shape anisotropy

is successively overcome and the magnetization follows the magnetic field. This reduces the increase in torque and results in maximum detuning at $H \rightarrow \infty$. For the considered parameters, the maximum resonance detuning is approached slowly at several tesla and is approximately equal to $6 \cdot 10^{-3}$. All derivations and equations used are summarized in Appendix A.2.

1.3.4 Discussion and Conclusion

The maximum relative resonance frequency change of reported ΔE -effect magnetometers is in the range of $\Delta f/f_r \approx 0.5 - 1\%$ [31, 136, 146, 147]. This change is about two orders of magnitude larger than the relative resonance frequency change $\Delta f/f_r \approx -0.01\%$ estimated with the magnetostrictive expansion model (Section 1.3.1) despite the strong overestimation expected from the free-layer assumption. As expected, a more realistic estimation that considers the mechanical confinement of the magnetostrictive layer to a non magnetic substrate leads to even smaller values (Section 1.3.2). Both the magnetization-induced curvature and stress are discussed in this context and are expected to contribute $\Delta f/f_r \approx 10^{-6}\%$ to the overall resonance frequency change. The pole effect (Section 1.3.3) causes a resonance detuning of the same order of magnitude and reaches $\Delta f/f_r \approx 10^{-3}\%$ only at extremely large flux densities of several tesla, where typical ΔE -effect magnetometers cannot be operated. Although the discussed effects depend on the geometry and material parameters, the deviations from the example parameters must exceed several orders of magnitude to increase the resonance detuning to a relevant level. In conclusion, such resonance detuning effects can be omitted in all of the following discussions without introducing any significant error.

Chapter 2

Sensor Concept

The ΔE -effect sensor concept is based on standing or traveling mechanical waves in a magnetoelastic structure. Upon the application of a magnetic field, the wave velocity and the resonance frequency change because of the ΔE effect. Various sensor designs have been employed to utilize and read-out this change to detect magnetic fields. After providing an overview of past sensor developments and the state-of-the-art ΔE -effect sensors and systems, the operation and read-out is discussed, and a more detailed definition of important sensor characteristics is finally stated.

2.1 Overview of ΔE -Effect Sensors

In this overview, magnetoelastic structures operated or characterized as a magnetic field sensor are discussed. Such sensors consist of a sensor element, which is sensitive to a magnetic field, and operation and read-out electronics that is required to measure signal and noise. Studies where only the ΔE effect or resonance frequency detuning were measured are therefore excluded. The limit of detection (LOD), also referred to as detectivity, is provided as a measure for the minimum detectable magnetic flux density.

2.1.1 Surface Acoustic Wave ΔE -Effect Sensors

The first magnetic field sensor based on the ΔE effect was suggested in 1987 by Hanna [41]. In their work, a pair of interdigital transducers was used to excite surface-acoustic waves in a piezoelectric material. A magnetic garnet film was deposited on a delay line between the transducers. In a magnetic field, the change in the wave velocity caused by the ΔE effect in the magnetic layer was measured by a phase shift in the output signal relative to the excitation signal. An example of a SAW sensor element is provided in Fig. 2.1a. Although magnetic SAW devices (mSAW) have been investigated frequently for magnetic field sensing within the last ten years [120–125], the analysis is focused on magnetic sensitivity and frequency detuning, and it rarely covers actual operation as a magnetic field sensor in terms of the signal and noise of the sensor element or system. This includes the work of Hanna [41]. A considerable amount of work was conducted earlier on the velocity change of the surface and the bulk acoustic waves in the magnetic materials as described in the overview of the ΔE effect in Section 1.1, without mentioning the potential application as a magnetic field sensor.

2.1.2 ΔE -Effect Sensors Based on Free-Standing Thin-Film Resonators

The first free-standing thin-film resonator operated as a ΔE -effect magnetic field sensor was presented by Osiander et al. in 1996 [118]. It comprises a commercial microcantilever, coated with an amorphous Terfenol-D thin-film. An external alternating magnetic field was used to drive

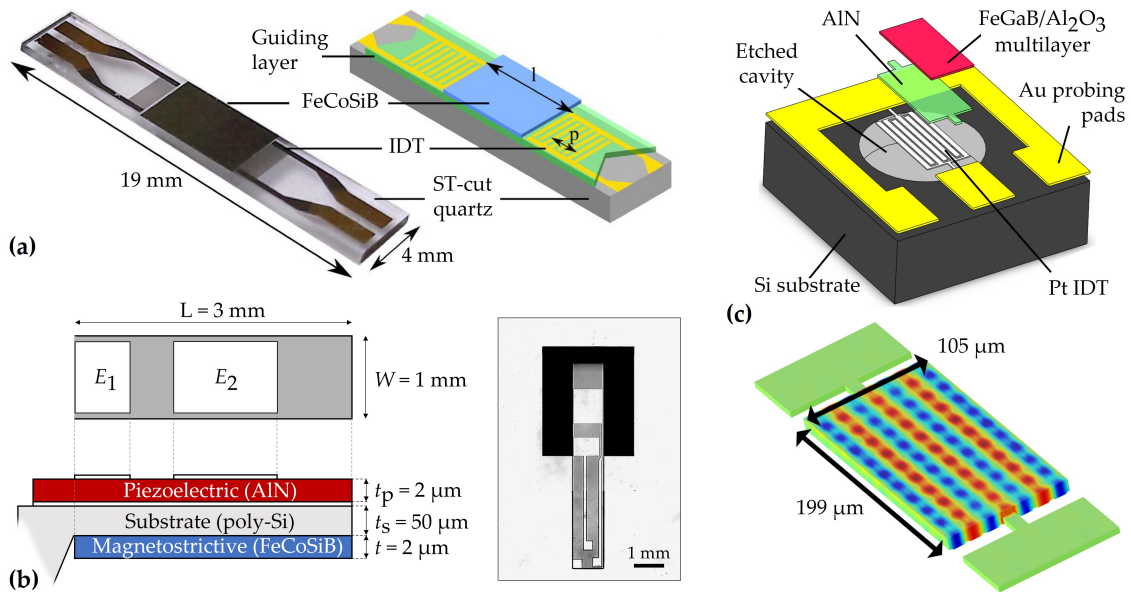


Figure 2.1: (a) Photograph (left) and illustration (right) of a surface acoustic wave (SAW) sensor element based on a quartz-crystal structure with a soft-magnetic FeCoSiB thin-film deposited on the delay line in between a pair of interdigital transducers. Image adapted from Ref. [148]. (b) Schematic structure (left) and top view (right) of a typical sensor element comprising a MEMS-fabricated, free-standing magnetoelastic composite cantilever. The piezoelectric layer is sandwiched by a rear-side electrode and two top electrodes that are as visible as white squares in the photograph. Image adapted from Ref. [132]; copyright 2019 by the American Physical Society. (c) Example of a free-standing magnetoelastic plate-resonator that is fabricated with standard MEMS technology. Interdigital electrodes shown in the schematic (top) are used to excite a higher-order bulk mode (bottom). Image adapted from Ref. [149].

the cantilever in the mechanical resonance. The tip deflection was monitored optically with a position sensitive device (PSD) and used to detect a static magnetic field. Although only DC magnetic fields were measured and the noise of the system was not addressed, this work already comprised the main sensor concept. However, the method employed to excite and read-out using external coils and optical fibers is inconvenient for miniaturization and sensor integration. Another resonator-based ΔE -effect DC magnetometer was presented in 2005 by Yoshizawa et al. [119]. Soft-magnetic amorphous ribbons were pasted on both sides of a lithium niobate and quartz-crystal resonator. In this design, the amorphous ribbons served as electrodes to excite and read-out the sensor element electrically via the piezoelectric material. The electrical excitation was adapted by Gojdka et al. [150] who measured low-frequency, and small-amplitude magnetic fields in 2011. An optically read-out microcantilever was coated with a soft-magnetic amorphous thin-film and piezoelectrically excited at $\approx 320 \text{ kHz}$. The detection of magnetic fields with frequencies up to 1 kHz and amplitudes in the nanotesla regime was demonstrated. Fully integrable ΔE -effect sensors were achieved in the next years by transferring the electrical read-out principle to MEMS technology compatible materials using magnetoelastic thin-film composites.

A ΔE -effect sensor based on magnetoelastic plate-resonators was presented in 2013 for DC magnetic field sensing [33]. It comprises a rectangular thin-film composite plate (width $100 \text{ }\mu\text{m}$, length $200 \text{ }\mu\text{m}$) with a 250-nm -thick AlN piezoelectric layer, and a 250-nm -thick (FeGaB/Al₂O₃) magnetic multilayer. Interdigital transducers (IDTs) electrodes of 50-nm -thick platinum were

used to operate the sensor in a higher order bulk-mode at approximately 250 MHz. A schematic of the sensor element and resonance mode is shown in Fig. 2.1c. Other rectangular plate resonators were presented in the following years, with similar dimensions and structures [151–153] and LODs of $800 \text{ pT}/\sqrt{\text{Hz}}$ [152]. Although such sensor elements were also shown in array configurations [153], only single elements were analyzed. The arrays were not operated as a sensor system with a full signal and noise characterization.

The cantilever approach by Gojdka was further developed by Jahns et al. in 2014 [31]. The sensor element is vacuum encapsulated and comprises MEMS-fabricated magnetoelectric multicomponent cantilevers with a $2\text{-}\mu\text{m}$ -thick AlN layer as a piezoelectric material and a field-annealed $3\text{-}\mu\text{m}$ -thick amorphous FeCoSiB layer as a magnetic material on a $0.65 \mu\text{m}$ SiO₂ substrate. The cantilevers have a width of $200 \mu\text{m}$ and lengths from $300\text{--}900 \mu\text{m}$. An LOD of $12 \text{ nT}/\sqrt{\text{Hz}}$ was measured at 10 Hz in a resonance mode at approximately 6.5 kHz . A significant improvement in the LOD was achieved by Zabel et al. in 2015 [146], who reached $140 \text{ pT}/\sqrt{\text{Hz}}$ at 20 Hz in the first bending mode with millimeter-sized resonators. The 3-mm -long and 1-mm -wide MEMS cantilevers comprises a $2\text{-}\mu\text{m}$ -thick AlN layer and a $\approx 2\text{-}\mu\text{m}$ -thick FeCoSiB-Cr multilayer on a $\approx 53.5\text{-}\mu\text{m}$ -thick Si/SiO₂ substrate. A typical example is shown in Fig. 2.1b. In contrast to the previous sensor system, a charge amplifier was used for the read-out. A more comprehensive measurement of signal and noise was performed as a function of frequency and for the first two bending modes. A low-pass behavior was identified, with a significantly higher -3 dB bandwidth in the second bending mode ($\approx 47 \text{ kHz}$) due to the higher resonance frequency. Despite a lower noise level in the second bending mode, the LOD was superior in the first bending mode. This correlated with the electrical excitation and electrode design. Subsequently, an adapted electrode design optimized for the second bending mode resulted in an LOD of $< 100 \text{ pT}/\sqrt{\text{Hz}}$ in the frequency range between 10 Hz and 100 Hz [147].

The sensor system has been analyzed from a signal-processing perspective, including adaptive and multicarrier read-out schemes for signal-to-noise optimization [154]. The sensor element was described in a signal model as a magnetic-field-dependent impedance. An alternating magnetic field modulates the amplitude and phase of the current passing through the sensor. The low-pass characteristic of the sensor was well described by a first-order Bessel filter in this model. An LOD of $240 \text{ pT}/\sqrt{\text{Hz}}$ was measured at 10 Hz . Soon after, an equivalent-circuit noise model was devised for a sensor system with a single sensor element [155]. It was shown that the noise floor around the resonance frequency of the sensor is dominated by thermal-electrical noise at low excitation frequencies. Away from the resonance frequency, the noise floor is dominated by the thermal-electrical noise of the charge amplifier or the excitation source. At large amplitudes of the excitation voltage, the measurements increasingly deviate from the model owing to the additional noise around the resonance frequency of the sensor. It was interpreted as sensor-intrinsic magnetic noise, and is not included in the model.

2.1.3 Other ΔE -Effect Sensors

In recent years, ΔE -effect sensors based on macroscopic laminar composites [156, 157] or completely free-standing magnetic thin-films [158] have been presented. The magnetoelectric laminate presented by Zhuang et al. in 2015 [156] has dimensions ($8 \text{ cm} \times 1 \text{ cm} \times 0.035 \text{ cm}$) in the centimeter range. This comprises two rectangular Metglas sheets pasted to piezoelectric macrofibers. Neither the materials nor the mounting conditions are specified. The sensor is actively excited via interdigital electrodes and read-out with a charge amplifier. LODs close to $100 \text{ pT}/\sqrt{\text{Hz}}$ were measured at 10 Hz . A similar macroscopic composite ΔE -effect sensor was demonstrated by Staruch et al. in 2017 [157], based on a Metglas-PZT composite beam. The beam was clamped on both ends, which permitted the application of static stress for tuning the effective anisotropy. It was excited electrically in a longitudinal resonance mode, and it achieved

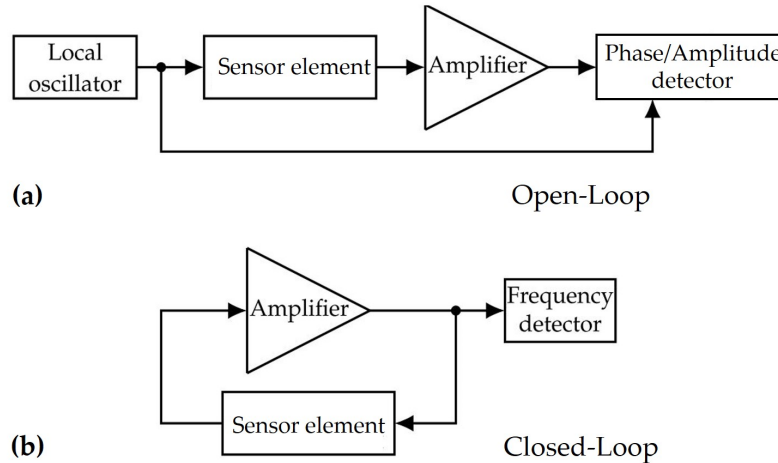


Figure 2.2: (a) Schematic setup of an open-loop and a (b) closed-loop operation and read-out system. The sketch is adapted from [164].

an LOD of approximately 2 nT at 10 Hz. A doubly clamped free-standing CoFe thin-film of 300 nm thickness was operated in a torsion mode by Staruch et al. in 2020 [158]. It was excited with a magnetic AC field, and read out optically, which resulted in an LOD of approximately $200 \text{ nT}/\sqrt{\text{Hz}}$. Shear-wave magnetometers suggested by Squire et al. in 1987 [101, 159] with double-clamped magnetic ribbons achieved an LOD of $100 \text{ pT}/\sqrt{\text{Hz}}$ at 1 Hz [102]. This sensor comprises a 25- μm -thick amorphous ribbon with a length of about 2 cm. The transducer electrodes made of PZT fibers were glued to both ends and they enabled the excitation and detection of bulk-shear waves. Similar to delay-line SAW sensors, the magnetic field was detected by the magnetic field induced phase shift of the input signal. These sensors can be considered the first-reported magnetic field sensors that utilize the ΔE effect.

2.2 Sensor Operation

2.2.1 Open-Loop vs. Closed-Loop Operation

Two read-out structures are most commonly used for ΔE -effect sensors: open-loop [160] or closed-loop configuration [161–163]. In the open-loop sensor system (Fig. 2.2a), the sensor element is excited with a signal from a local oscillator that is subsequently amplified and compared with the original signal. Thus, changes in amplitude and phase can be detected. A magnetic field that changes the amplitude or phase response of the sensor element modulates the oscillating signal. This modulating signal can be reconstructed by amplitude and phase demodulation. In addition, the frequency response can be characterized with such a setup. In the context of ΔE -effect sensors, a local oscillator has been used for bulk-shear-wave magnetometers [101, 102] as well as for cantilever sensors [146, 147, 154]. The other commonly used read-out system avoids using a local oscillator. Instead, the sensor element is inserted into the feedback loop of an amplifier as shown in Fig. 2.2b. Here, it forms a closed-loop system that starts to oscillate when the Barkhausen stability criterion [165] is fulfilled. A sufficiently large gain of the amplifier is required to compensate for the loss of the sensor, and a constructive superposition of the signal at a certain frequency. The latter condition is often only fulfilled for one frequency, or a small range of frequencies depending on the resonator bandwidth of the sensor element. If the phase response of the sensor changes because of an external magnetic field, the stability

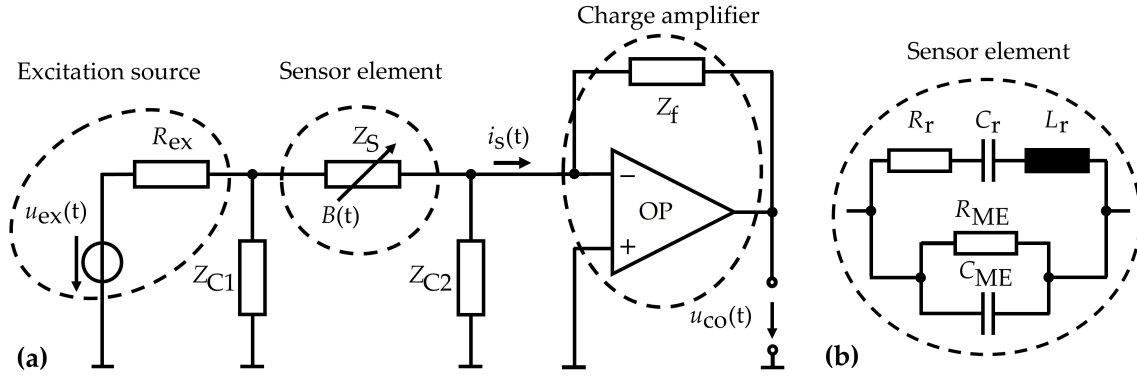


Figure 2.3: (a) Simplified equivalent-circuit representation of an open-loop operation and read-out system adapted from [155]. It comprises an excitation source with output resistance R_{ex} , a sensor element with an impedance $Z_s = 1/Y_s$ that depends on the applied magnetic flux density $\vec{B}(t) = \mu_0 \vec{H}(t)$ (t : time, μ_0 : magnetic vacuum permeability, \vec{H} : magnetic field), and a charge amplifier with an operational amplifier (OP) and a feedback impedance Z_f . The impedance of the two cables is denoted with Z_{C1} and Z_{C2} , respectively. (b) The example of a typical modified Butterworth-Van Dyke (mBvD) equivalent circuit as used in [146] to describe the electrical behavior of the sensor element.

criterion is no longer fulfilled and the oscillating signal is forced to change its frequency. Hence, the oscillating signal is frequency modulated, and a frequency detector, such as a phase-locked loop (PLL), can be used to reconstruct the modulating signal [166]. This read-out structure is the most common for SAW devices [161–163]; however, has been used for ΔE -effect sensors based on high-frequency plate resonators [151]. Compared to an open-loop system, a closed-loop system appears to be simpler [167, 168]. However, it requires a reference oscillator for frequency detection and is only suitable for detecting the phase response of the sensor [164]. A change in the oscillator’s signal amplitude is usually suppressed by the saturation of the amplifier.

The detailed discussion of the two read-out and operation systems including a comparison of the signal, noise, and LOD can be found in [164]. In that study, the equivalence of both configurations with respect to the limit of detection was demonstrated. However, the description of the sensing process and definition of sensitivities differ. The sensors used throughout this thesis are operated in an open-loop system, and therefore, the corresponding sensitivities and details on the operation are provided in the following section.

2.2.2 Sensor Operation in an Open-Loop System

We consider the open-loop system illustrated in Fig. 2.3a, which has been used in several previous studies [147, 155, 169]. During sensor operation, a sinusoidal voltage $u_{ex} = \hat{u}_{ex} \sin(2\pi f_{ex} t)$ with time t , amplitude \hat{u}_{ex} , and frequency f_{ex} is applied to the piezoelectric layer of the sensor element to excite the resonator at or close to its mechanical resonance frequency f_r . An alternating magnetic field results in an alternating change in the frequency characteristic of the admittance $Y_s(f_{ex}) = 1/Z_s$ via the ΔE effect, and modulates the current i_s through the sensor element in amplitude and in phase. This current is measured as a voltage u_{co} at the output of a charge amplifier. The output voltage is analog-digital converted and demodulated to reconstruct the alternating magnetic field. From a signal processing point-of-view, the sensor element can be described by its electrical admittance $Y_s(f_{ex}, \vec{B})$, which depends on the operating frequency f_{ex} , and the magnetic flux density $\vec{B} = \mu_0 \vec{H}$ with magnetic field \vec{H} and magnetic vacuum permeability μ_0 . The leakage current through the cable with impedance Z_{C1} is negligible and the output resistance is small compared to the impedance Z_s of the sensor element. The output

voltage $u_{\text{co}}(t)$ of the charge amplifier can then be described [155]

$$u_{\text{co}}(t) \approx -Z_{\text{f}}(f_{\text{ex}}) \cdot \hat{u}_{\text{ex}} \cdot |Y_{\text{s}}(f_{\text{ex}}, \bar{B})| \cdot \cos\left(2\pi f_{\text{ex}}t + \arg\{Y_{\text{s}}(f_{\text{ex}}, \bar{B})\} + \phi\right), \quad (2.1)$$

where ϕ represents a constant, magnetic-field-independent phase shift between the excitation signal and the output signal. The output signal $u_{\text{co}}(t)$ is fed into a quadrature detector with amplitude or phase demodulation. With components $I = u_{\text{co}} \cdot \cos(2\pi f_{\text{ex}}t)$ and $Q = u_{\text{co}} \cdot \sin(2\pi f_{\text{ex}}t)$, the amplitude demodulated signal $u_{\text{A}}(t)$ and phase demodulated signal $u_{\Phi}(t)$ are given by

$$u_{\text{A}}(t) = \sqrt{I^2 + Q^2}, \quad (2.2)$$

$$u_{\Phi}(t) = \arctan(Q/I), \quad (2.3)$$

which are low-pass filtered to remove the undesired frequency components. The sensor itself exhibits a band-pass behavior around the resonance frequencies of the resonator. To the best of our knowledge, its physical origin has never been discussed in detail. As will be confirmed in Part II, Section 7.2, this behavior can be understood intuitively as being caused by a delayed response of the resonator to the magnetic-field-induced stiffness change owing to its mass inertia. Equation 2.1 is only approximately valid for small magnetic field frequencies f_{ac} well within the pass-band of the filter, because this equation does not consider the band-pass filter of the sensor. The filter behavior has been considered previously entirely phenomenologically by applying a first-order Bessel filter to the demodulated signal [154] with a -3 dB cut-off frequency that equals half the bandwidth BW of the resonator [170]. Yet, this is only valid if the sensor is excited to its mechanical resonance $f_{\text{ex}} = f_{\text{r}}$ and a more general expression must be derived for arbitrary f_{ex} . This is important if the resonance frequency is not identical with the optimum excitation frequency and if several sensor elements are operated in parallel with the same excitation source. In the latter case, slight variations always cause a distribution of the resonance frequency, and $f_{\text{ex}} = f_{\text{r}}$ can never be fulfilled for all sensor elements. An extension of this model is developed in Part II, Section 7.2.

2.2.3 Admittance of Electromechanical Resonators

The sensor element enters the equivalent circuit of the sensor system as a magnetic-flux-dependent electrical admittance $Y_{\text{s}} = 1/Z_{\text{s}}$ (Fig. 2.3a). At a fixed magnetic flux density, Y_{s} is mostly determined by the electrical and effective mechanical properties of the resonator. The electrical properties of such electromechanical resonators can be described by an equivalent circuit representation shown in Fig. 2.3b. This method was first introduced by Van Dyke in 1928 [171] and is frequently employed for the characterization and simulation of piezoelectric resonators [172–174]; further, it has been used for ΔE -effect magnetometers [31, 33, 146]. The original model [171] is often referred to as Butterworth-Van Dyke (BvD) model and it comprises an LCR-series resonance circuit with inductance L_{r} , resistance R_{r} , and capacitance C_{r} , in parallel to a capacitance C_{ME} . While the LCR-circuit represents the electrical response of the mechanical resonator, C_{ME} describes the capacitance of the piezoelectric layer. Modifications of this equivalent circuit are referred to as modified Butterworth-Van Dyke (mBvD) models [175–178]. Often, resistance R_{ME} is added as shown in the mBvD equivalent circuit in Fig. 2.3b to include the piezoelectric loss. Although this loss contribution depends on frequency, it is well approximated as a constant within the bandwidth of the resonator [146, 155]. Other extensions introduce nonlinear elements (Part II, Section 6.2) and additional parallel circuits to include superposed resonance modes and several parallel connected sensor elements (Part II, Sections 7.1 and 7.2).

The equivalent circuit parameters can be obtained by fitting the model to measurements with a nonlinear optimization procedure. An example fit of the mBvD model presented in Fig. 2.3b to an electromechanical resonance curve of a ΔE -effect sensor is shown in Fig. 2.4. The magnitude $|Y_{\text{s}}|$ of the electrical admittance Y_{s} of the sensor element is shown in Fig. 2.4a (top) and the

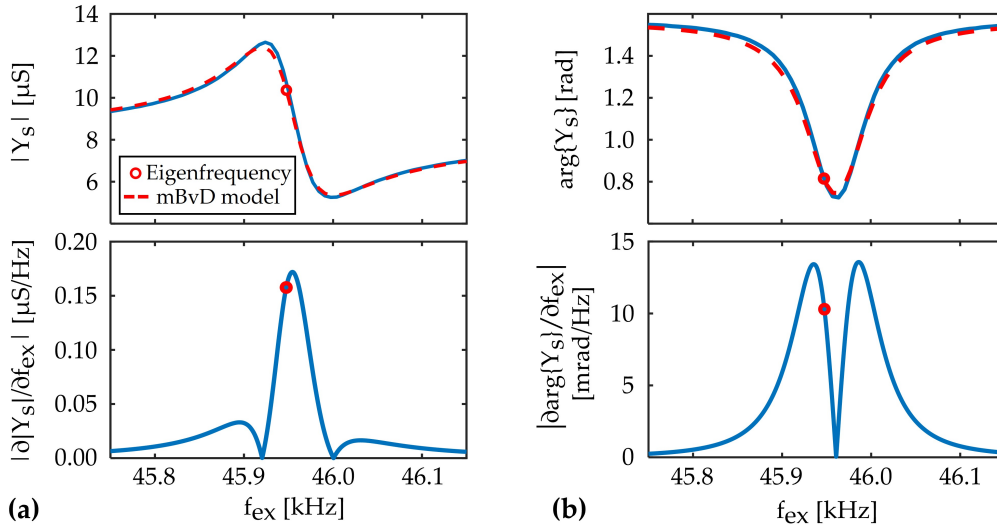


Figure 2.4: Example of measured sensor admittance Y_s as a function of excitation frequency f_{ex} compared with a Butterworth-van Dyke equivalent circuit fit. The mechanical eigenfrequency f_r obtained from the model is indicated. **(a)** Magnitude $|Y_s|$ of the electrical sensor admittance Y_s and magnitude $|\partial|Y_s|/\partial f_{\text{ex}}|$ of the derivative with respect to the excitation frequency f_{ex} . **(b)** Phase angle $\arg\{Y_s\}$ of Y_s and magnitude $|\partial\arg\{Y_s\}/\partial f_{\text{ex}}|$ of the derivative of the phase angle.

corresponding phase angle $\arg\{Y_s\}$ in Fig. 2.4b (top). A local minimum is visible in both: the magnitude and the phase angle; this is because of the contribution of the parallel capacitance C_{ME} to the admittance, and it masks the typical behavior of the magnitude and phase angle of the linear oscillator described by the LCR-circuit. As a consequence, the mechanical resonance frequency f_r is located somewhere between the local maximum and the local minimum in the $|Y_s(f_{\text{ex}})|$ curve, as illustrated in Fig. 2.4. A larger contribution of the LCR-circuit (e.g., by a larger quality factor) shifts the local maximum towards f_r on the frequency axis. The resonance frequency f_r and the quality factor Q of the mechanical resonator can be extracted from the LCR-circuit parameters. With [174]

$$f_r = \frac{1}{2\pi\sqrt{L_r C_r}}, \quad (2.4)$$

and

$$Q = \frac{1}{R_r} \sqrt{\frac{L_r}{C_r}}, \quad (2.5)$$

the bandwidth

$$BW \approx f_r/Q, \quad (2.6)$$

of the resonator can be estimated [179]. The mBvD parameters of the ΔE -effect magnetometers depend on the operating parameters like the applied magnetic flux density or the amplitude \hat{u}_{ex} of the excitation voltage because of the magnetoelastic layer. The mBvD models that have been used previously for ΔE -effect sensors are limited to linear electromechanical resonance. Further details on linear mBvD models for piezoelectric resonators can be found in [180].

2.2.4 Sensitivities and Operating Point

All sensor properties enter Equation 2.1 via the electrical admittance $Y_s(f_{\text{ex}}, \bar{B})$ of the sensor element. We omit the full vector characteristic of \bar{B} and consider only the magnetic flux density

B along one axis to simplify Y_s . Then, the magnitude $|Y_s|$ and phase angle $\arg\{Y_s\}$ of Y_s are described as functions of B developing a Taylor series around a certain value B_0 of B . Previously, only the first two terms were kept in linear approximation [154, 155]. It is given as

$$|Y_s(f_{\text{ex}}, B)| \approx |Y_s(f_{\text{ex}}, B_0)| + \left. \frac{\partial |Y_s(f_{\text{ex}}, B)|}{\partial B} \right|_{B=B_0} \cdot (B - B_0), \quad (2.7)$$

and

$$\arg\{Y_s(f_{\text{ex}}, B)\} \approx \arg\{Y_s(f_{\text{ex}}, B_0)\} + \left. \frac{\partial \arg\{Y_s(f_{\text{ex}}, B)\}}{\partial B} \right|_{B=B_0} \cdot (B - B_0). \quad (2.8)$$

Now, we consider a magnetic flux density $B = B_0 + B_{\text{ac}}(t)$ that is a superposition of the static magnetic flux density B_0 with a small alternating magnetic flux density $B_{\text{ac}}(t)$. We simplify the notation by defining $Y_0 := |Y_s(f_{\text{ex}}, B_0)|$ and $\phi_0 := \arg\{Y_s(f_{\text{ex}}, B_0)\}$. With Equations 2.7-2.11 the signal equation (Equation 2.1) can be written as

$$u_{\text{co}}(t) \approx -Z_f(f_{\text{ex}}) \cdot \hat{u}_{\text{ex}} \cdot [Y_0 + S_{\text{am}} B_{\text{ac}}] \cdot \cos(2\pi f_{\text{ex}} t + S_{\text{pm}} B_{\text{ac}} + \phi_0 + \phi). \quad (2.9)$$

The partial derivatives in Equations 2.7 and 2.8 are referred to as amplitude sensitivity S_{am} and phase sensitivity S_{pm} , respectively. If the sensor is excited in its mechanical resonance ($f_{\text{ex}} = f_r$), S_{am} and S_{pm} can be further decomposed into two differentials

$$S_{\text{am}} := \left. \frac{\partial |Y_s(f_{\text{ex}}, B)|}{\partial B} \right|_{B=B_0, f_{\text{ex}}=f_r} = \left. \frac{\partial |Y_s(f_{\text{ex}}, B)|}{\partial f_{\text{ex}}} \right|_{B=B_0, f_{\text{ex}}=f_r} \left. \frac{\partial f_r(B)}{\partial B} \right|_{B=B_0}, \quad (2.10)$$

$$S_{\text{pm}} := \left. \frac{\partial \arg\{Y_s(f_{\text{ex}}, B)\}}{\partial B} \right|_{B=B_0, f_{\text{ex}}=f_r} = \left. \frac{\partial \arg\{Y_s(f_{\text{ex}}, B)\}}{\partial f_{\text{ex}}} \right|_{B=B_0, f_{\text{ex}}=f_r} \left. \frac{\partial f_r(B)}{\partial B} \right|_{B=B_0}. \quad (2.11)$$

The first partial derivatives with respect to the excitation frequency f_{ex} are referred to as electrical sensitivities $S_{\text{el,am}}$ and $S_{\text{el,pm}}$, because they contain the electrical response of the sensor element. The partial derivative of the resonance frequency f_r with respect to the magnetic flux density B is called magnetic sensitivity and denoted as S_m . It includes the ΔE effect, and describes the effective mechanical response to the magnetic flux density. In summary, the three derivative are defined as

$$S_{\text{el,am}} := \left. \frac{\partial |Y_s(f_{\text{ex}}, B)|}{\partial f_{\text{ex}}} \right|_{B=B_0, f_{\text{ex}}}, S_{\text{el,pm}} := \left. \frac{\partial \arg\{Y_s(f_{\text{ex}}, B)\}}{\partial f_{\text{ex}}} \right|_{B=B_0, f_{\text{ex}}}, \quad (2.12)$$

and

$$S_m := \left. \frac{\partial f_r(B)}{\partial B} \right|_{B=B_0}. \quad (2.13)$$

Several approximations made in the signal model need to be mentioned. Linearization is a good approximation for small magnetic field amplitudes, but it cannot describe harmonic distortions at larger magnetic fields. Because the vector characteristics of the magnetic field and magnetic sensitivity are not considered, all values obtained for the sensitivities are only valid for a specific measurement configuration. In addition, Equation 2.12 does not consider the filter characteristic of the sensor, and the previously used solutions to this problem are only valid if the sensor is excited at its mechanical resonance frequency.

Operating Point and Magnetic Sensitivity

A large amplitude sensitivity S_{am} or phase sensitivity S_{pm} can be beneficial for sensor operation. This requires optimizing the product of electrical sensitivities ($S_{\text{el,am}}$, $S_{\text{el,pm}}$) and magnetic sensitivity S_m according to Equations 2.10 and 2.11. The electrical sensitivities are illustrated at the example of the measured admittance curve shown in Fig. 2.4a (magnitude) and Fig. 2.4b (phase

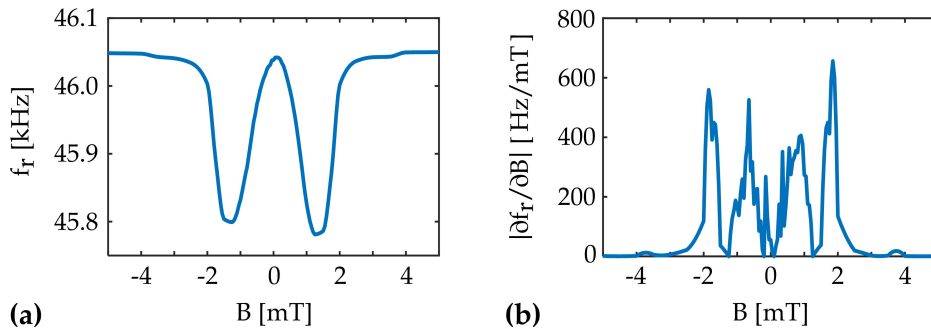


Figure 2.5: (a) Mechanical resonance frequency f_r as a function of the magnetic flux density B obtained from a series of admittance measurements and BvD fits as shown in Fig. 2.4. The measurement was started close to magnetic saturation at -5 mT. (b) The magnitude $|\partial f_r / \partial B|$ of the derivative of f_r with respect to the magnetic flux density B ; We refer to this derivative as the magnetic sensitivity S_m .

angle). The BvD model is fitted to the admittance data to extract the resonance frequency f_r and form the derivatives of the magnitude and phase angle with respect to the frequency. The resulting electrical sensitivities $S_{el,am}$ and $S_{el,pm}$ are plotted in Fig. 2.4 (bottom) and are indicated at f_r with red dots. Whether amplitude modulation or phase modulation dominates the signal depends on the selected f_{ex} because the maxima of the two different derivatives are at different frequencies. In the case shown here, the maxima are both close to f_r , so we expect a significant contribution of phase and amplitude modulation to u_{co} for $f_{ex} = f_r$. Using $f_{ex} = f_r$ as an excitation frequency is not a necessary condition for sensor operation, e.g., it has been shown that several carriers can be used to improve signal-to-noise ratio [154]. However, operating at $f_{ex} = f_r$ is convenient because it simplifies the theoretical treatment, and often it does not significantly impair the sensitivity.

To determine the magnetic sensitivity S_m and the optimum magnetic bias field B_0 , admittance measurements are performed for a set of magnetic flux densities B , and f_r is extracted from the BvD fits. The resulting $f_r(B)$ -curve is plotted in Fig. 2.5a, and it follows qualitatively the simulations of the Young's modulus of a hard axis magnetization process (Section 1.2.1). The absolute of the derivative, i.e., $|S_m|$, is plotted in Fig. 2.5b. It exhibits four local extrema at $|B| > 0$, and a minimum around $B = 0$. Therefore, a bias flux density $B_0 > 0$ is typically applied when operating a ΔE -effect sensor. Exceptions are discussed in Part II, Section 7.1. However, not only S_m changes with B but also the electrical sensitivities; this causes the local maxima in $|S_{am}|$ and $|S_{pm}|$ to be slightly off the local maxima in $|S_m|$. Approximating the response of the sensor with the three sensitivities $S_{el,am}$, $S_{el,pm}$, and S_m is in particular useful for analyzing the different magnetic, mechanical, or electrical contributions to the output signal. Additional normalization is required to compare electrical and magnetic sensitivities of different sensors reasonably (c.f. Part II, Sections 4.1 and 4.4).

Besides B_0 and f_{ex} , the third major operating parameter is the amplitude \hat{u}_{ex} of the excitation voltage. According to Equation 2.12, the output signal depends linearly on \hat{u}_{ex} . However, also the ΔE effect and sensor admittance depend on \hat{u}_{ex} because of the nonlinearity of the magnetoelastic effect (c.f. Section 3.2.5), and the dependency of the quality factor on \hat{u}_{ex} [146]. Consequently, the three operating parameters depend highly non-linearly on each other, which makes describing the sensor behavior challenging. In general, large parameter sweeps have to be performed to find the optimum operating parameters of a specific sensor device.

2.2.5 Signal-and-Noise Characterization

For a signal characterization of the sensor, a sinusoidal magnetic test signal $B_{ac} = \hat{B}_{ac} \sin(2\pi f_{ac}t)$ is applied with amplitude \hat{B}_{ac} and frequency f_{ac} . The output signal $u_{co}(t)$ of the charge amplified is fed into a quadrature demodulator to obtain the amplitude demodulated output signal $u_A(t)$ in volt, or the phase demodulated output signal $u_\Phi(t)$ in radians. The amplitude spectrum $\hat{A}(f)$ of $u_A(t)$ and the phase spectrum $\hat{\Phi}(f)$ of $u_\Phi(t)$ can then be used to define a normalized measure for the response of the sensor to a magnetic field. We define

$$S_V(f_{ac}) := \frac{\hat{A}(f_{ac})}{\hat{B}_{ac}}, \quad S_\Phi(f_{ac}) := \frac{\hat{\Phi}(f_{ac})}{\hat{B}_{ac}}. \quad (2.14)$$

The two quantities S_V and S_Φ relate the amplitude \hat{B}_{ac} of the alternating magnetic flux density to the output signal in volt or radians at the frequency f_{ac} of the magnetic test signal. Sometimes, S_V is referred to as voltage sensitivity [181, 182] and correspondingly, S_Φ is called phase sensitivity here. In contrast to the electrical and magnetic sensitivities, S_V and S_Φ depend directly on the excitation voltage amplitude \hat{u}_{ex} via Equation 2.12 and they include the filter characteristic of the sensor. A reasonable measure for the noise must be normalized to the data acquisition time and is therefore called noise density. The noise density can be obtained from the power spectral density (PSD) with units of V^2/Hz . We refer to the square root of the PSD of the charge amplifiers output signal $u_{co}(t)$ as the voltage noise density $U_{co}(f)$ with units of $V/\sqrt{\text{Hz}}$. Similarly, the square root of the PSD of the amplitude demodulated signal $u_A(t)$ is referred to as amplitude noise density $A(f)$ and of the phase demodulated signal $u_\Phi(t)$ as the phase noise density $\Phi(f)$. The measurement must be performed without an applied magnetic test signal.

Typical measurements of an example sensor are shown in Fig. 2.6. The sensor is excited in mechanical resonance at $f_{ex} = f_r = 9070 \text{ Hz}$ and two measurements are performed. First with a magnetic test signal with $f_{ac} = 10 \text{ Hz}$ and subsequently without. Accordingly, in Fig. 2.6a, two peaks are visible in the voltage spectrum \hat{U}_{co} at $f_{ex} \pm 10 \text{ Hz}$ around the carrier, and no peaks in the corresponding voltage density spectrum U_{co} , measured without a magnetic test signal. In this example, the signal is amplitude demodulated and the resulting amplitude spectrum \hat{A} and amplitude noise density spectrum A are plotted in Fig. 2.6b as functions of frequency f . Following Equation 2.15, the value of \hat{A} at $f = f_{ac}$ can be used to calculate the voltage sensitivity S_V as the amplitude \hat{B}_{ac} of the magnetic test signal is known. Similarly, the noise level at $f = f_{ac}$ can be obtained from the amplitude noise density A . Both, the noise density and sensitivities S_V and S_Φ are functions of the magnetic field frequency $f = f_{ac}$, as illustrated in Fig. 2.6c at the example of the first and second bending mode (BM 1 and BM 2) of a cantilever resonator operated at $f_{ex} = f_r$ [146]. In this particular example, the sensor intrinsic noise causes an increased noise floor around f_r , which is also present in the spectra shown in Fig. 2.6a and b. The voltage sensitivity S_V in this case follows the magnitude-frequency response of a first-order Bessel filter [154] as mentioned in Section 2.2.2. Because the quality factor Q is of the same order for BM1 and BM2 in this case, the increased resonance frequency of BM2 results in a larger bandwidth according to Equation 2.6. The corresponding -3 dB cut-off frequencies f_{-3dB} of the low-pass filter are shown in Fig. 2.6c.

The sensitivities (S_V , S_Φ) and noise densities (A , Φ) can be used to define a measure for the smallest magnetic field amplitude that can be detected. Various terminologies have been used for this measure, such as equivalent magnetic noise [183], field equivalent noise [184], equivalent magnetic noise limit [185], detectivity [186] or limit of detection (LOD) [154, 187]. This measure can be defined for amplitude demodulation (LOD_{am}) and phase demodulation (LOD_{pm}) as

$$\text{LOD}_{am}(f_{ac}) := \frac{A(f_{ac})}{S_V(f_{ac})}, \quad \text{LOD}_{pm}(f_{ac}) := \frac{\Phi(f_{ac})}{S_\Phi(f_{ac})}. \quad (2.15)$$

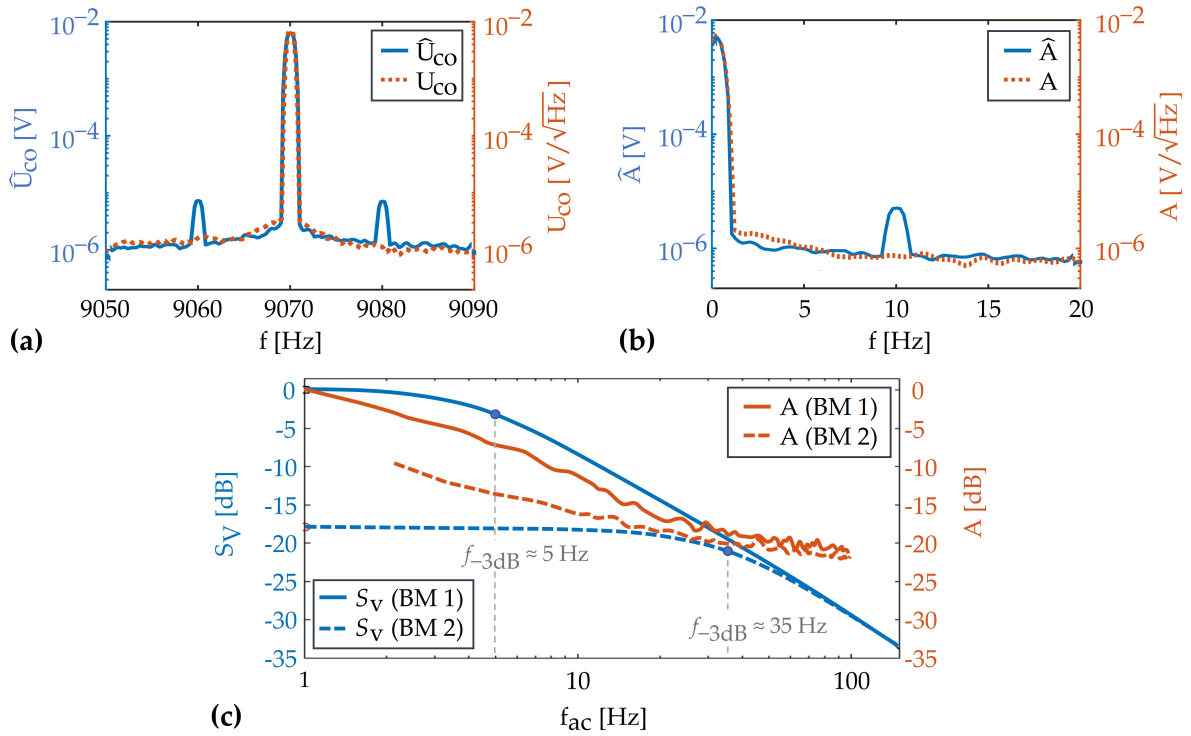


Figure 2.6: Example spectra from measurements with a typical cantilever-based ΔE -effect magnetic field sensor around the resonance frequency $f_r = 9070$ Hz. (a) Voltage spectrum $\hat{U}_{co}(f)$ (f :frequency) of the output signal $u_{co}(t)$ of the charge amplifier with the applied magnetic test signal with a frequency of $f_{ac} = 10$ Hz, and voltage noise density spectrum $U_{co}(f)$ without the applied test signal; (b) amplitude spectrum $\hat{A}(f)$ of the amplitude demodulated signal $u_A(t)$ with the applied magnetic test signal and amplitude noise density spectrum $A(f)$ without the applied test signal. (c) Illustration of the voltage sensitivity S_V and the amplitude noise density A as a function of f_{ac} of an example sensor operated in the first and second bending mode (BM 1 and BM 2), where the sensor-intrinsic noise sources dominate the noise floor around f_r . The data in (c) are obtained from [146].

Although S_V and S_Φ at f_{ac} must be measured with the applied magnetic test signal, A and Φ must be obtained from a measurement without the test signal being applied. The qualitative and quantitative behaviors of signal and noise are complex because they depend not only on the sensor system, but also on the operating parameters. Signal, noise, and LOD as functions of different parameters are analyzed in detail in Part II, Chapter 6.

Chapter 3

Magneto-Mechanical Theory

This chapter provides a short overview of the most important theoretical foundations of magnetoelastic and mechanical systems within the framework of continuum mechanics and the phenomenological theory of micromagnetism. After providing the general form of the thermodynamic potential of the magneto-mechanical system in Section 3.1, the individual energy density contributions are discussed in Section 3.2 with a focus on the magnetoelastic coupling term. The thermodynamic potential is used to describe the dynamic behavior with the coupled mechanical and magnetic equations of motion in Section 3.3. In this chapter, the summation convention is used for italic indices to simplify the sum notations if not stated differently. Summations are always performed over all three spatial dimensions. Energies and energy densities are denoted by uppercase symbols and lowercase symbols, respectively.

Overview of Modeling Methods

The first attempts at describing the magnetization process used entirely mathematical models without an underlying physical basis. An early well-known example is the Rayleigh model from 1887 [188] that used a second-order power expansion in the flux density to approximate the magnetization curve for small, applied magnetic fields. Many other mathematical models based on step functions [189–193] and piece-wise linear approximations [194–197], power-series [198–204] or exponential fits [205,206], and similar mathematical approximations [207–209] have been used since then for hysteretic or anhysteretic parts of the magnetization curve. In 1935, Preisach [210] presented the first scalar model that describes the complete ferromagnetic hysteresis curve by an ensemble of minor hysteresis loops characterized by a distribution of their coercive fields and offsets from the zero field. Considerable effort was invested into the various extensions [211–213]; for example, to include dynamic behavior [214,215], stress [216,217], and to reflect the vector characteristics of the magnetization [218,219]. Similar properties were captured by the Chua model [220,221] from 1970 and its various extensions [222–224]. The relationships between the Preisach and Chua models have been derived [225,226]. Both models describe minor hysteresis loops and other generic properties of magnetic hysteresis. These and other mathematical models of hysteresis have proved useful for embedding magnetic hysteresis into lumped parameter models [223,227] and electromagnetic finite element calculations [190,191,196,228–230], where microscopic and mesoscopic behaviors are not of primary interest. Yet, these mathematical models have a limited connection to the underlying physical mechanisms that impedes the predictions and complicates the physical interpretations of the results.

Physically, the state of the magnetization of a ferromagnetic material can be defined by a set of all atomic magnetic moments that assemble the magnetic domain structure. The occurrence of the magnetic moment is in itself a relativistic quantum mechanical phenomenon [231] and its interactions pose a complicated multibody problem [232]. Hence, this field unifies major aspects of modern theoretical physics. Solutions are traditionally approximated by *ab-initio*

methods such as the Hartree-Fock method and density-functional theory [233], or by using the more recent relativistic density functional theory (rDFT) or Korringa-Kohn-Rostoker (KKR) method [234]. Such calculations are computationally extensive, and this restricts the range of applications to atomic dimensions [233].

Atomistic spin-dynamics models [235, 236] represent a discrete modeling approach, wherein each atom is ascribed a localized effective magnetic moment treated as a classical spin of fixed length [237]. Although there are arguments and studies that support the localization approximation well [237, 238], even for itinerant ferromagnetic materials, its validity is often considered a "topic of historical debate" [239]. The short-range interactions of the localized atomic spins are modeled by some type of exchange interaction that leads to a long-range magnetic order and macroscopic magnetic properties. Spin-dynamics obeys a phenomenological equation of motion [237] inherited and adapted from the continuous micromagnetic approach, which is introduced in the paragraph below. A detailed introduction to the underlying theory of atomistic spin-dynamics has been reported in [240]. Advanced atomistic spin models that include the correct crystal structure and more realistic descriptions of the interatomic magnetic interaction have emerged within the last twenty years [241] and contributed significantly to the fundamental understanding of magnetic phenomena in different materials such as Fe_3O_4 [242], IrMn [243, 244], or YIG [245] among many other examples [246–249]. Besides the rather fundamental investigations, a fairly recent trend is the massive parallelization of atomistic spin-dynamics simulations with software packages such as VAMPIRE [235, 250] and UPPASD [251]. This has enabled large-scale simulations of nanogranular materials with dimensions on the length scale of > 100 nm [235] for heat-assisted magnetic recording [252, 253], where discrete magnetic properties of spin-ensembles and temperature fluctuations on atomic scale [254] become relevant. These models can consider a realistic atomistic configuration obtained from previous molecular dynamics simulations. Recently, atomistic spin-dynamics simulations have been combined with molecular dynamics in a single model [236, 255, 256] that permits a more realistic description of magnetic defect and lattice interactions and thermal fluctuations of the magnetic and mechanical sub-systems. A comprehensive overview of the recent progress is summarized in [257].

Micromagnetic models approximate magnetization as a continuous vector field that obeys a phenomenological equation of motion (c.f. Section 3.3). Forces that enter the equation of motion are derived from the thermodynamic potential of the system. The origin of this approach can be traced back to the well-known magnetic domain calculations of Landau and Lifshitz [258] in 1935, which is in conjunction with the variational formulation of Brown in 1940 [259], and the work of Gilbert in 1955 [260], who introduced the equation of motion that is commonly applied today. The work of many other authors in the early and mid twentieth century contributed to the theoretical framework, which was laid out in detail by Brown [261] in the first unified description of micromagnetism in 1963. Non-local energy density terms make the micromagnetic equation of motion an integro-differential equation that can be solved only with numerical methods in its general form. Therefore, the early applications were limited to strongly simplified problems such as one-dimensional domain wall calculations [258, 261] or linearizations at large magnetic field values [259]. An increase in the computational power in the late 20th century and the implementation of numerical schemes such as the finite difference [262] and finite element method [263, 264] permitted the handling of increasingly extensive problems [265]. This led to deeper insights into many fields, e.g., the magnetization reversal process and interaction of ferromagnetic nano-particles [266, 267], properties of thin-film recording media [268, 269], and sintered permanent magnets [270, 271]. Currently, micromagnetic modeling is a well established research tool for investigating magnetic microstructures and their magnetization dynamics [272]. A variety of codes have been presented with advanced functions, e.g., to include eddy currents [273], spin-transfer torque [274, 275], or stochastic formulations to consider finite temperatures [276–278]. The wide-spread application and transition from a purely research-based topic to an engineering tool is reflected by the large number of commercial and

open source software packages such as OOMMF [279], magnum.fe [280], MuMax³ [281], and many others. A comprehensive overview of the available micromagnetic software is provided in [282]. Graphical processor unit accelerated implementations improved the performance in recent years significantly and extended the accessible length scales to several micrometers with desktop workstations [282–284]. Relative to the more traditional finite difference methods, finite element implementations simplify the simulation of complex sample geometries, e.g., for spintronic devices [275] or sample structures in the emerging field of curvilinear magnetism [285,286]. An overview of some other recent advances and trends in micromagnetism and its applications have been presented elsewhere [283]. In very few recent studies, micromagnetics has been combined with phase-field approaches [287–290] to consider the effect of the mechanical subsystem on the domain evolution of highly magnetostrictive materials. Such multiphysics approaches are still an exception in the field of micromagnetic modeling, and only as recent as this year, simplified mechanical equations of motion were included into the available micromagnetic software [291]. Magnetomechanics is of central importance in this thesis, and most relevant effects can be fully captured by a continuous, micromagnetic description of magnetism. Therefore, micromagnetism represents a major part of the underlying theoretical framework of this work and is the basis for further simplifications that must be imposed to reduce the computational costs for simulating structures with dimensions beyond the micrometer regime. The typical strategies for upscaling the simulation volume are described below.

Multiscale models combine the approximations made on different length scales to improve the performance and cover larger spatial or temporal domains while keeping a sufficient level of detail [292,293]. *Concurrent* multiscale models combine the scales in one simulation, which is often a discrete atomistic region with continuous micromagnetic areas. This permits, e.g., resolving magnetic interfaces [294] or domain walls with high accuracy [295] or treating singularities such as Bloch points to be more physical [296]. *Sequential* models pass on the results obtained from simulations on a small scale to a larger scale over an extended spatial or temporal domain. A classical example is calculating the effective material parameters with ab-initio methods for subsequently treating a larger problem with atomistic or micromagnetic models [297–299]. Combining micromagnetic and macroscopic models is challenging because of the global characteristic of energy contributions that determine the magnetic domain structure within the micromagnetic framework. Thus, the magnetic microstructure is to a large degree determined by the sample geometry on a macroscopic scale. This physical coupling of the mesoscopic micromagnetic scale with the macroscopic scale makes separating the two scales with a hierarchical multiscale approach difficult. The few multiscale models that combine the micromagnetic scale with macro-scale simulations are mainly concurrent models wherein a small volume is modeled micromagnetically and coupled to a larger region described with magnetic constitutive relations, e.g., to simulate magnetic recording heads with storage media [300,301].

Macroscopic magnetic material models strongly simplify the micromagnetic description to approximate the magnetization behavior of magnetic materials on a macroscopic scale. The Stoner-Wohlfarth model [66] provides a simple phenomenological, but physics-based description that can approximate reversible and irreversible ferromagnetic magnetization processes. Within this approximation, the magnetization field is represented by a single macroscopic magnetic moment, which neglects the specific magnetic microstructure and assumes homogeneous magnetic properties. Instead of solving the micromagnetic equation of motion, the quasi-static equilibrium orientation is found by minimizing the Gibbs free energy density. Hence, it can be understood as a quasi-static simplification of the continuous micromagnetic description. Modifications and extensions based on this macrospin approach have been used to approximate the static and dynamic magnetization behaviors of extended ferromagnetic samples with different properties [40,93,302–305].

Macroscopic mean-field models provide an extension of the macrospin approximation by considering an ensemble of macrospins, sometimes coupled with an effective mean field that

depends on the mean magnetization of the ensemble. Mathematically, this concept is identical to the Weiss molecular field [306], originally introduced to provide a microscopic interpretation of ferromagnetism. Such a mean field is used in the originally isotropic Jiles-Atherton model [307] and its extensions to anisotropic media [308, 309] and a vectorized formulation [310]. Models of the Jiles-Atherton type have been used for various device simulations wherein bulk magnetic properties were of major interest, including magnetostrictive transducers [311–313] and fluxgate sensors [314]. In addition to the mean-field approximation, the model is based on a modified Langevin function for anhysteretic bulk magnetization with another term weighted by a fitting factor for the hysteretic part of the magnetization. Although the reasoning for the model is based on physical arguments, the method for including hysteretic effects is not directly derived from the micromagnetic theory of magnetism and to some degree, it is mathematically arbitrary. Consequently, such models can be considered as semi-physical wherein the transition to entirely mathematical models is continuous and depends on the additional assumptions made and the specific application.

Armstrong’s model [315, 316] and modifications [317, 318] do not include a mean interaction field or an ensemble of macro spins. Instead, they assume an inverse exponential distribution of magnetization energy states to modify the energy density function of a single macro spin, and they obtain a fully differentiable magnetization curve that can be used as a smooth constitutive relation. The distribution is quantified with a fit parameter. A brief overview of other mean-field models is provided in [319]. In contrast, the mean-field models that are more directly based on ensembles of the Stoner-Wohlfarth-like macro spins are intrinsically anisotropic, and they have a closer connection to the continuous micromagnetic theory of magnetism [320]. Examples include mean-field coupled macrospin ensembles with prescribed anisotropy distribution [320] or uncoupled macrospin ensembles with energy densities based on the Boltzmann distribution approximating thermally activated switching [321]. A macrospin model that considers the distributions of specific domain configurations was presented by Squire [109, 322]. In this model, pairs of macro spins represent magnetic domains coupled by their respective volume fraction via a movable magnetic domain wall.

Although some models include magnetoelastic interaction, most do not explicitly address the ΔE effect or are limited to the Young’s modulus and omit the influence of the geometry of the device in terms of local stray fields or stress distributions. Most ΔE effect models omit the effective mechanical anisotropy introduced by anisotropic magnetic properties because it requires a complete tensor description of the effective mechanical properties. In this work, energy-based magnetoelastic models are developed, implemented, or extended where necessary to analyze and approximate the magnetization and magnetoelastic properties of thin film ΔE -effect sensors. The most important theoretical fundamentals are introduced and summarized in this chapter, with a focus on the magnetoelastic interaction within the micromagnetic theory.

3.1 Thermodynamic Potentials of a Magnetoelastic System

The basis for most physical magnetic models is a thermodynamic potential that represents the state of the considered system. From the first law of thermodynamics, the exact differential $dU = \delta Q + \delta W$ of the internal energy U can be expressed by the heat transfer Q into the system and the work W performed *on* the system. From the second law of thermodynamics and considering a reversible process, the differential heat $\delta Q = TdS$ is given by the change dS of entropy S and the temperature T . It is

$$dU = \delta Q + \delta W = TdS + \sum_i P_g^{(i)} dV_g^{(i)}. \quad (3.1)$$

As shown in the second part of this equation, the differential work δW added to the system can be described by the sum of all generalized forces $P_g^{(i)}$ (intensive) that act on the system over corresponding generalized displacements $dV_g^{(i)}$ (extensive). Writing the entirely mechanical part of δW as $P_{\text{mech}}dV_{\text{mech}}$ and summarizing all nonmechanical contributions as $\sum_i P_{\text{mag}}^{(i)}dV_{\text{mag}}^{(i)}$,

$$dU = \delta Q + \delta W = TdS + \sum_i P_{\text{mag}}^{(i)}dV_{\text{mag}}^{(i)} + P_{\text{mech}}dV_{\text{mech}}. \quad (3.2)$$

The differential enthalpy dH can be obtained from dU by the Legendre transformation of the mechanical quantity $dV_{\text{mech}} \rightarrow dP_{\text{mech}}$ to obtain

$$dH := dU - p_{\text{mech}}dV_{\text{mech}} - V_{\text{mech}}dp_{\text{mech}} = TdS + \sum_i P_{\text{mag}}^{(i)}dV_{\text{mag}}^{(i)} - V_{\text{mech}}dp_{\text{mech}}. \quad (3.3)$$

The Legendre transformation $dS \rightarrow dT$ of dH is used to eliminate the entropy term ($-TdS$) and the differential Gibbs free energy dG is obtained. Further, considering that the temperature is constant ($dT = 0$),

$$dG := dH - TdS - SdT = \sum_i P_{\text{mag}}^{(i)}dV_{\text{mag}}^{(i)} - V_{\text{mech}}dp_{\text{mech}} \quad \text{for } dT = 0. \quad (3.4)$$

The Gibbs free energy is often discussed for chemical reactions occurring at constant temperature and constant pressure. Then, the mechanical term ($V_{\text{mech}}dp_{\text{mech}}$) vanishes and dG equals the nonmechanical work performed on the system. This holds if the pressure is the only component of the mechanical work. In magneto-mechanical systems, the mechanical term does not vanish because of the potentially present internal and external stresses. For computations, it is convenient to normalize dG to volume V and obtain an energy density. The mechanical energy density $V_{\text{mech}}dp_{\text{mech}}/V = \sigma_{ij}d\varepsilon_{ij}$ can be expressed with the components of the stress tensor σ_{ij} and strain tensor ε_{ij} . Thus, the differential Gibbs free energy density dg becomes

$$dg = \frac{1}{V} \sum_i P_{\text{mag}}^{(i)}dV_{\text{mag}}^{(i)} - \frac{1}{V} V_{\text{mech}}dp_{\text{mech}} = du_{\text{mag}} - \varepsilon_{ij}d\sigma_{ij}. \quad (3.5)$$

Here, du_{mag} is defined as the nonmechanical contributions of the differential internal energy density. Equation 3.5 is integrated to obtain the Gibbs free energy density g . For the integration, the stress-strain relationship is linearized ($\sigma_{ij} = C_{ijkl}\varepsilon_{kl}$) using the components C_{ijkl} of the mechanical stiffness tensor. Defining u_{mag} as the magnetic contribution to the internal energy it is

$$g = \int du_{\text{mag}} - \int \varepsilon_{ij}d\sigma_{ij} = u_{\text{mag}} - \frac{1}{2}\varepsilon_{ij}\sigma_{kl} = u_{\text{mag}} + \frac{1}{2}\varepsilon_{ij}C_{ijkl}\varepsilon_{kl} - \varepsilon_{ij}\sigma_{ij}, \quad (3.6)$$

which is consistent with the results of other authors [323, 324]. Depending on the model, the system is often described in quasi-static approximation by minimizing the thermodynamic potential or via the generalized forces in the equations of motion (c.f. Section 3.3). This is demonstrated at the end of this chapter for the magneto-dynamic and coupled elasto-dynamic system. In the magneto-dynamic context, the generalized forces are referred to as "effective fields" and the volume normalized generalized differential displacement is the differential magnetization vector $d\vec{M}$. In a mechanical context, the generalized force (per area) is referred to as stress with a differential strain $d\varepsilon_{ij}$ being the generalized displacement (per length) shown above. This is further discussed in Section 3.3.

3.2 Contributions to Gibbs Free Energy Density

Most physical models are based on the Gibbs free energy density g of the magneto-mechanical system. Dating back to 1935, the basic contributions to the internal energy part of g were described by Landau and Lifshitz [258] and later formulated in a continuous (micromagnetic) form by Brown [259, 261]. One can distinguish local and nonlocal terms in these formulations. The local terms are computationally inexpensive because they only depend on the local orientation of the magnetization vector. These terms include the Zeeman energy density u_z , crystalline or intrinsic anisotropy energy density u_K , magnetoelastic u_{me} energy density, and in good approximation the exchange energy density u_{ex} . In contrast, the nonlocal terms are functions of the whole magnetization field. These global contributions to the internal energy density arise from the internal magnetostatic stray field (magnetostatic self-energy density) and internal magnetization induced stress field (magnetostrictive self-energy density). Surface anisotropy is not considered here because it becomes relevant only for film thicknesses of less than a few nanometers [325].

3.2.1 Zeeman Energy

A magnetic field \bar{H}_{app} exerts torque $\bar{\tau} = \bar{\mu}_m \times \mu_0 \bar{H}_{app}$ on a magnetic moment $\bar{\mu}_m$, and energy U_μ can be assigned to every angular orientation of $\bar{\mu}_m$ to \bar{H}_{app} . To obtain a macroscopic and continuous representation of this energy, it is summed over all N magnetic moments within a small volume V . If this volume is sufficiently small, \bar{H}_{app} can be assumed to be approximately constant and the energy can be written as [326]

$$U_z := \sum_{n=1}^N U_{\mu,n} \approx -\mu_0 \bar{H}_{app} \cdot \sum_{n=1}^N \bar{\mu}_{m,n}, \quad (3.7)$$

with the magnetic vacuum permeability $\mu_0 \approx 4\pi \cdot 10^{-7}$ H/m [327]. If the magnetic field is applied externally and does not arise from the magnetic stray field of the magnetic moments, the energy contribution is called Zeeman energy. The corresponding energy density u_z can be obtained from normalizing U_z to V by defining the magnetization $\bar{M} := \sum_{n=1}^N \bar{\mu}_{m,n}/V$. From Equation 3.7,

$$u_z = -\mu_0 \bar{H}_{app} \bar{M} = -\mu_0 M_s H_{app,i} m_i, \quad (3.8)$$

with the components $H_{app,i}$ of \bar{H}_{app} , the magnitude $M_s := |\bar{M}|$ and the components m_i of the reduced magnetization vector $\bar{m} := \bar{M}/M_s$.

3.2.2 Exchange Stiffness Energy

The spins of magnetic materials feature a spontaneous small-range order below a certain temperature. In ferromagnetic materials, they tend to align parallel below the Curie temperature, and in anti-ferromagnetic materials, they align anti-parallel below the Néel temperature. This phenomenon is of a quantum mechanical nature and can be attributed to various mechanisms, depending on the material and structure [328]. A continuous representation of the energy penalty received by adjacent magnetic moments from being misoriented is derived with a Taylor series from the short-range Heisenberg interaction between adjacent, localized spins to [65, 258]

$$U_{ex} = \int A(\bar{r}) \left(|\bar{\nabla} m_1(\bar{r})|^2 + |\bar{\nabla} m_2(\bar{r})|^2 + |\bar{\nabla} m_3(\bar{r})|^2 \right) dV, \quad (3.9)$$

with the gradient $\bar{\nabla} m_i$ of the components m_i ($i = 1, 2, 3$) of the reduced magnetization vector $\bar{m} := \bar{M}/M_s$ defined by the magnetization vector \bar{M} and its magnitude M_s . Other equivalent expressions can be found elsewhere [328, 329]. The energy is scaled by the exchange stiffness constant $A(\bar{r})$, and it favors a parallel magnetization alignment for $A > 0$, with typical values of

the order of $A = 1 \cdot 10^{-11}$ J/m [330] for ferromagnetic materials. Further, Equation 3.9 is used if the Heisenberg interaction model is not strictly applicable, e.g., because the magnetic moment is carried by delocalized electrons. In this context, Equation 3.9 and the exchange constant can be considered an entirely phenomenological first-order approximation [328]. Within this approximation, the exchange stiffness energy is a local energy contribution. A major contributor to U_{ex} includes domain walls caused by the large magnetization gradients in the walls. In mean-field modeling and other macroscopic modeling techniques that do not attempt to describe the domain structure of the sample or where the gradient is zero per definition, the volume exchange energy density is usually omitted.

3.2.3 Intrinsic Anisotropy Energy

Magnetic materials can exhibit anisotropic magnetic properties intrinsic to the material and structure. Intrinsic magnetic anisotropy can have different origins. It can arise from the structural and crystalline anisotropy of the material via spin-orbit-lattice coupling (magneto-crystalline anisotropy) and be induced by annealing and sputter deposition in the presence of a magnetic field (magnetization-induced magnetic anisotropy). Magnetization-induced magnetic anisotropy is relevant for amorphous materials where the crystalline anisotropy cannot be present. The anisotropy of magnetic properties can be described by a corresponding energy density functional that is anisotropic with respect to the magnetization orientation. An expression for this energy density term can be found by expanding spherical harmonics with respect to the orientation of the magnetization vector, and removing all terms that do not meet the required symmetry restrictions. These boundary conditions are not known *a priori* for a certain material because they depend on its structure and the sample history. Prefactors K_0 and K_n that occur in the expansion are also not known. They are called magnetic anisotropy constants and must be determined from experiments or simulations, together with the symmetry. Hence, this energy density term is of a completely phenomenological origin. Expressions for various symmetry conditions can be found elsewhere [331, 332]. In this thesis, the magnetic anisotropy energy density with uniaxial symmetry is most relevant, and it can be described as [332]

$$u_K = K_0 + \sum_{n=1}^N K_n \sin^{2n}(\phi), \quad (3.10)$$

where ϕ represents the angle between the axis of symmetry and magnetization vector \bar{M} . The specific characteristic of the uniaxial symmetry depends on the signs and values of the prefactors K_n ; further, the order N of expansion significantly influences the resulting magnetization behavior. Typically, only the first two terms ($N = 1$) have to be considered because the thermal agitation of spins at room temperature tends to average out higher order terms [333]. The energy density can be expressed in the first-order approximation ($N = 1$) as

$$u_K = K_0 + K_1 \sin^2(\phi) = K_0 + K_1(1 - \cos^2 \phi) = K_0 + K_1 - K_1 (m_i EA_i)^2, \quad (3.11)$$

using the components m_i of the reduced magnetization vector $\bar{m} := \bar{M}/M_s$ with $M_s := |\bar{M}|$ and the components EA_i of the easy axis orientation vector \bar{EA} with magnitude $|\bar{EA}| = 1$. For Equation 3.11, u_K is rotational symmetric around a minimum at $\phi = 0$, if $K_1 > 0$. Hence, an easy axis of magnetization is described with a hard magnetic basal plane perpendicular to it. Vice versa, $K_1 < 0$ results in a hard axis of magnetization and an easy basal plane. Because this expansion approach uses symmetry arguments only, it can be used to describe magnetic anisotropy independent of its specific origin, only characterized by its symmetry. The expansion can be used to describe the energy density of a sample if the specific origin is not relevant, and no additional information are provided or available. Then it is usually referred to as effective anisotropy energy density with corresponding effective anisotropy constants $K_{n,\text{eff}}$. Because the zero-order anisotropy term K_0 is independent of magnetization, this term does not contribute to the forces that act on the magnetization and is usually omitted.

Unidirectional Anisotropy in Multilayers

Exchange coupling can occur across the interface between two magnetic materials and cause ferromagnetic or anti-ferromagnetic ordering. Such interface effects are very complex and the materials, microstructure, interface, and interlayer topology are relevant [334, 335]. The exchange interaction in ferromagnetic-antiferromagnetic multilayers [336] has found applications in various types of magnetic field sensors [337–339]. The magnetization of a ferromagnetic layer can be pinned by the layer exchange interaction with an antiferromagnetic material using appropriate processing steps during the fabrication. This pinning has the overall effect of a unidirectional anisotropy that provides a preferred orientation of the magnetization in the ferromagnetic layer [340]. It can be used to avoid unwanted domain walls and tune the magnetic properties of the device without applying external magnetic fields. The exchange anisotropy can be described phenomenologically by a term identical to the Zeeman energy, but by replacing \bar{H}_{app} in Equation 3.8 by the effective exchange field \bar{H}_{ex} . The magnitude H_{ex} of the exchange field can be estimated as a function of the material and film thicknesses [341] and be tuned to achieve the desired multilayer properties. Details about the exchange bias in magnetoelectric composites can be found elsewhere [342–344]. In Section 7.1, this effect is used to provide an internal effective bias field for ΔE -effect sensors and operate them at the optimum working point without the need for applying an external magnetic field.

3.2.4 Internal Magnetostatic Stray Field

If a sample is magnetized with an externally applied magnetic field \bar{H}_{app} , the magnetic field inside and outside the magnetic body differs from this applied field. This difference arises from the magnetic field of the magnetization \bar{M} itself, which is called the magnetic stray field \bar{H}_{d} . The effective field H_{eff} present results from a superposition

$$\bar{H}_{\text{eff}} = \bar{H}_{\text{app}} + \bar{H}_{\text{d}}. \quad (3.12)$$

From Maxwell's equation $\bar{\nabla} \cdot \bar{B} := \bar{\nabla} \cdot (\mu_0 \bar{H} + \mu_0 \bar{M}) = 0$, we define \bar{H}_{d} as the field generated by the divergence $\bar{\nabla} \cdot \bar{M}$ of magnetization

$$\bar{\nabla} \cdot \bar{H}_{\text{d}} = -\bar{\nabla} \cdot \bar{M}. \quad (3.13)$$

From that definition, \bar{H}_{d} represents a static magnetic field, and it does not include dynamic components that can occur, e.g., from electrical eddy currents. This magnetostatic stray field can be expressed by the gradient of an arbitrary potential ϕ_{d} , which is a function of the location vector \bar{r}

$$\bar{H}_{\text{d}} = -\bar{\nabla} \phi_{\text{d}}(\bar{r}). \quad (3.14)$$

Substituting \bar{H}_{d} into Equation 3.13 yields a differential equation for the potential. It can be solved with a unique solution as a direct consequence of Maxwell's equations. A detailed discussion and different approximation methods for ϕ_{d} have been reported in [345] and a review of Maxwell's equations including various simplifications has been presented in [346]. An exact solution yields the magnetic scalar potential ϕ_{d} as a function of the location vector \bar{r}

$$\phi_{\text{d}}(\bar{r}) = M_{\text{s}} \left(\int \frac{\lambda_{\text{v}}(\bar{r}')}{|\bar{r} - \bar{r}'|} dV' + \int \frac{\sigma_{\text{s}}(\bar{r}')}{|\bar{r} - \bar{r}'|} dS' \right). \quad (3.15)$$

Thus, calculating the scalar potential requires solving a six-fold integral in three dimensions because Equation 3.15 includes the sum of a volume and surface integral over the ferromagnetic body. Parameters λ_{v} and σ_{s} represent the reduced volume and surface charge densities, respectively. They are defined by the divergence $\bar{\nabla} \cdot \bar{m}$ of the reduced magnetization vector $\bar{m} := \bar{M}/M_{\text{s}}$, and its component along the surface normal vector \bar{n} of the body. It is

$$\lambda_{\text{v}} = -\bar{\nabla} \cdot \bar{m}, \quad \sigma_{\text{s}} = \bar{m} \cdot \bar{n}. \quad (3.16)$$

The magnetostatic stray field can be described by the gradient of the magnetic scalar potential function (Equation 3.15), which is obtained by integrating the charge densities over volume and surface, respectively. This nonlocal characteristic of the stray field equation requires substantial computational effort that results in a bottleneck in the numerical micromagnetic simulations [347]. The magnetostatic stray field within the magnetic material is often called an internal magnetostatic stray field.

Magnetostatic Self-Energy Density

The direction of the magnetization does not necessarily coincide locally with the direction of \bar{H}_d because the internal magnetostatic stray field of a magnetic material is the superposition of the magnetic dipole fields from all magnetic charges. Hence, a torque may act locally on the magnetization and result in a contribution to its internal energy density similar to the Zeeman energy. This magnetostatic energy density contribution u_d tends to reduce the macroscopic magnetization of the sample via the formation of magnetic domains. It is also referred to as demagnetizing energy density, and \bar{H}_d is frequently called the demagnetizing field. A continuous representation of u_d can be obtained similar to the Zeemann energy by summing up the energy from the dipole interactions of all magnetic moments over the volume. In contrast to the Zeemann energy density, \bar{H}_d is not externally applied, but it results from the magnetization field of the material itself. Therefore, u_d is also called the magnetostatic self-energy, and a factor of 1/2 enters to avoid counting the contributions of magnetic moments twice. It is

$$u_d = -\frac{1}{2}\mu_0\bar{H}_d\bar{M} = -\frac{1}{2}\mu_0M_sH_{d,i}m_i, \quad (3.17)$$

with the components $H_{d,i}$ of \bar{H}_d . The internal magnetostatic stray field \bar{H}_d at a specific location cannot be obtained from the magnetization field at this location alone because the integration in Equation 3.15 must be performed over the entire volume and surface of the sample. Hence, u_d is a global energy contribution.

Demagnetizing Factor

If the magnetization field within a body is homogeneous, \bar{H}_d in Equation 3.17 can be expressed by a simple proportionality relationship, with the proportional constant \mathbf{D} . Because the demagnetizing field and magnetization are both vector fields, \mathbf{D} it is a second-order tensor with nonzero elements along the main diagonal. The components D_{ij} of \mathbf{D} are sometimes called demagnetizing factors and can be used to express $H_{d,i}$ as

$$H_{d,i} = -D_{ij}M_j \quad \text{with} \quad \sum_{i=1}^3 \sum_{j=1}^3 D_{ij} = 1. \quad (3.18)$$

As a homogeneous, single domain ferromagnetic material does not carry volume charges as per the definition, the demagnetizing field depends only on the integral over the surface charge density in Equation 3.15. The integrated surface charge density is larger, the larger the cross-section area in the direction of magnetization. Therefore, D_{ij} are functions of aspect ratios of the sample, which yield the largest demagnetizing field for the magnetization oriented along the shortest axis. If D_{ij} are functions of aspect ratios only, the above equation is only valid for saturated ellipsoidal samples because they provide a homogeneous stray field. The analytic expressions for this case are well known [332, 348].

For samples of other geometries, the demagnetizing field is a function of the location, even if no volume charges are present. This has been handled analytically using various averaging procedures of magnetization and demagnetizing fields for the definition of D_{ij} presented in Equation 3.18. The *magnetometric* demagnetizing factor is obtained by averaging the magnetization

and demagnetizing fields over the entire sample volume [349]. The averaged magnetization can be obtained easily from measurements, but it incurs a complete loss of spatial information. The *ballistic* (also *fluxmetric*) demagnetization factor represents a compromise; it relates the area cross-section averaged demagnetizing field and magnetization as a function of location in the third free dimension. Therefore, the demagnetizing factors become spatial functions. Analytic expressions for such ballistic demagnetizing factors have been derived for general rectangular prisms of arbitrary aspect ratios [350]. Although such expressions are only strictly valid in magnetic saturation, they have been proved to be capable of characterizing aspects of the global magnetic behavior of rectangular samples [351]. This approximation is used, e.g., in Section 4.1, to include the spatial dependence of the demagnetizing field in a mean-field model of the sensor.

3.2.5 Magnetoelastic Coupling

The underlying physical effect of ΔE -effect sensors is most fundamentally based on magnetoelastic coupling. Magnetoelastic coupling describes the mutual dependence (coupling) of the magnetization field with elastic fields such as stress and strain. The origin of this effect is a nonspherical charge density distribution of the atoms, which is coupled to the magnetic spin (spin-orbit coupling) and alters the atomic equilibrium distance (orbit-lattice coupling). As a consequence, stress and strain become functions of the magnetic moment orientation. Phenomenologically, the coupling can be described by an energy density term that depends on the orientation of the magnetization vector and the strain of the sample. The energy density contribution is called magnetoelastic energy density u_{me} . It can be expressed using a power expansion of the magnetization, while keeping only the even powers to describe the uniaxial nature of this energy density term [133]

$$u_{\text{me}} = A + B_{ijkl}m_i m_j \varepsilon_{kl} + C_{ijklmn}m_i m_j m_k m_l \varepsilon_{mn} + \dots \quad (3.19)$$

In Equation 3.19, A , B_{ijkl} , and C_{ijklmn} are proportionality constants between the reduced magnetization vector $\bar{m} := M/M_s$ with components m_i and the linear strain tensor ε with components ε_{ij} . These proportionality constants are referred to as zero-, first-, and second-order magnetoelastic coupling coefficients. The coupling constants are tensors of fourth and higher order in the most general case because the strain is a tensor of second order. Keeping only the first-order term and defining $b_{kl} := B_{ijkl}m_i m_j$, the widely used quadratic approximation of u_{me} is [133]

$$u_{\text{me}} = B_{ijkl}m_i m_j \varepsilon_{kl} := b_{kl}\varepsilon_{kl}. \quad (3.20)$$

The quadratic dependency of the energy density term on the magnetization orientation in Equation 3.20 is included in the components b_{kl} of \mathbf{b} . Physically, \mathbf{b} can be interpreted as stress accompanied with magnetization. Hence, \mathbf{b} is referred to as the magnetoelastic stress tensor. Using symmetry conditions of the respective magnetic system, \mathbf{b} can be simplified and reduced to, e.g., two independent components for cubic symmetry and one for isotropic symmetry. A collection of formulations for various symmetries can be found in [352]. All materials used in this thesis are magnetoelastically isotropic and can be described by [323]

$$\mathbf{b} = B_1 \begin{pmatrix} m_1^2 - \frac{1}{3} & m_1 m_2 & m_1 m_3 \\ m_2 m_1 & m_2^2 - \frac{1}{3} & m_2 m_3 \\ m_3 m_1 & m_3 m_2 & m_3^2 - \frac{1}{3} \end{pmatrix}. \quad (3.21)$$

The proportionality factor B_1 that connects all components b_{ij} with the components m_i of the reduced magnetization is referred to as the first magnetoelastic coupling coefficient, and it is redefined as $B_1 := B_{1111}$. It describes the maximum magnetoelastic stress that can occur along any coordinate axis. In the general case, more than one component of \mathbf{B} is necessary, e.g., at least two in the cubic case [133]. The equilibrium strain can be obtained from the minimum of

the Gibbs free energy density g as a function of strain ε [323, 353]. Here, the mechanical energy density $u_{\text{el}} = \frac{1}{2}\varepsilon_{ij}C_{ijkl}\varepsilon_{kl}$ and magnetoelastic energy density u_{me} (Equation 3.20) constitute the strain-dependent part of g in Equation 3.6. The factor $-1/3$ results from providing a strain relative to a hypothetical reference configuration in which the magnetization is isotropically distributed. Dropping all strain independent terms,

$$\frac{\partial g}{\partial \varepsilon_{ij}} = \frac{\partial}{\partial \varepsilon_{ij}} \left(\frac{1}{2}\varepsilon_{ij}C_{ijkl}\varepsilon_{kl} + b_{ij}\varepsilon_{ij} - \sigma_{ij}\varepsilon_{ij} \right) = 0, \quad (3.22)$$

which yields the components ε_{ij}^0 of the total *equilibrium* strain $\boldsymbol{\varepsilon}^0$

$$\varepsilon_{ij}^0 = C_{ijkl}^{-1}\sigma_{kl} - C_{ijkl}^{-1}b_{kl} := e_{ij} + \lambda_{ij}, \quad (3.23)$$

at which the magnetoelastic and mechanical energy densities balance each other. According to this relation, equilibrium strain $\boldsymbol{\varepsilon}^0$ can be described by the superposition of two strain contributions $\boldsymbol{\lambda}$ and \boldsymbol{e} . The contribution \boldsymbol{e} is connected to the mechanical stress $\boldsymbol{\sigma}$ by Hooks law, and therefore, it is referred to as Hookian or mechanical strain. The same form is valid for the second strain contribution $\boldsymbol{\lambda}$, except that the origin of the stress is not a mechanical load, but magnetization. It is called a magnetostrictive strain $\boldsymbol{\lambda}$ or simply magnetostriction. As $\boldsymbol{\varepsilon}^0$ is the sum of both strain tensors in equilibrium, we call it the *total* strain or *equilibrium* strain. According to Equation 3.23, the magnetoelastic stress components b_{ij} and strain components λ_{ij} are related by $b_{ij} = -C_{ijkl}\lambda_{kl}$ for isotropic magnetoelastic coupling, and this allows us to obtain an expression for the magnetostrictive strain tensor in a form similar to Equation 3.21. For an isotropic ferromagnetic material, the magnetotriuctive strain can be written in terms of one constant (Equation 3.24), namely the saturation magnetostriction λ_s , and the components m_i of the reduced magnetization vector. The magnetostrictive strain tensor is given as

$$\boldsymbol{\lambda} = \frac{3}{2}\lambda_s \begin{pmatrix} m_1^2 - \frac{1}{3} & m_1m_2 & m_1m_3 \\ m_2m_1 & m_2^2 - \frac{1}{3} & m_2m_3 \\ m_3m_1 & m_3m_2 & m_3^2 - \frac{1}{3} \end{pmatrix}, \quad \text{with} \quad \lambda_s = -\frac{2B_1}{3(C_{1111} - C_{1122})}. \quad (3.24)$$

According to Equation 3.24 magnetostrictive strain is anisotropic¹, essentially because of the vector characteristics of the magnetization. Such anisotropic magnetostriction is often called Joule magnetostriction, named after J. P. Joule, who discovered the effect in iron rods in 1842 [354]. In addition to anisotropic Joule magnetostriction, there is an isotropic strain accompanying the magnetization. It is called volume magnetostriction or isotropic forced magnetostriction if a magnetic field is applied [68]. At room temperature and under moderate magnetic fields, it is orders of magnitude smaller than Joule magnetostriction [355] and therefore not relevant in the context of this work.

3.2.6 Complete Magneto-Mechanical Term

A general equation for the Gibbs free energy density function that governs the behavior of the magneto-mechanical system was provided in Section 3.1. For clarity, we summarize all terms that are usually in good approximation independent of strain or stress in $u' := u_K + u_{\text{ex}} + u_z + u_d$. The Gibbs free energy density as a function of $\boldsymbol{\varepsilon}$ is

$$g = u' + u_{\text{el}} + u_{\text{me}} - \varepsilon_{ij}\sigma_{ij} = u' + \frac{1}{2}\varepsilon_{ij}C_{ijkl}\varepsilon_{kl} + b_{ij}\varepsilon_{ij} - \varepsilon_{ij}\sigma_{ij}. \quad (3.25)$$

¹The symmetry of the magnetostrictive strain is not to be confused with the symmetry of the magnetoelastic coupling, which is isotropic here.

With Equation 3.23, ε_{ij} can be substituted by the equilibrium strain ε_{ij}^0 . After rearranging we get

$$g = u' - \lambda_{ij}\sigma_{ij} - \frac{1}{2}\sigma_{ij}C_{ijkl}^{-1}\sigma_{kl} + \frac{1}{2}\lambda_{ij}C_{ijkl}\lambda_{kl}. \quad (3.26)$$

This equation represents the Gibbs free energy density for a magneto-mechanical system where the mechanical and magnetostrictive strains are in equilibrium. Experiments and ab-initio simulations indicate that this equilibrium is reached on a timescale of picoseconds [356], and therefore, Equation 3.26 is expected to be a good approximation for most dynamic processes. The last term ($1/2 \cdot \lambda_{ij}C_{ijkl}\lambda_{kl}$) depends only on the magnetization orientation, but not on the stress and can be integrated into the effective anisotropy term [353]. The third term ($1/2 \cdot \sigma_{ij}C_{ijkl}^{-1}\sigma_{kl}$) is only a function of mechanical quantities and depend only indirectly on the magnetization. This term merely shifts the energy density landscape by a constant value and is often omitted. The remaining expression

$$g = u' - \lambda_{ij}\sigma_{ij}, \quad (3.27)$$

is the frequently used Gibbs free energy density term that describes a magnetoelastic system. For an isotropic magnetostrictive material, the components λ_{ij} are given by Equation 3.24. The factor $1/3$ in the magnetostrictive strain results in a purely mechanical energy density contribution and can be omitted to obtain the final expression for the magnetoelastic energy density

$$\begin{aligned} g_{me} &:= -\lambda_{ij}\sigma_{ij} \\ &= -\frac{3}{2}\lambda_s \left(\sigma_{11}m_1^2 + \sigma_{22}m_2^2 + \sigma_{33}m_3^2 + 2\sigma_{23}m_2m_3 + 2\sigma_{13}m_1m_3 + 2\sigma_{12}m_1m_2 \right). \end{aligned} \quad (3.28)$$

Magnetostrictive Self Energy

Magnetostrictive thin films are often notably constrained by their substrate. If a magnetostrictive strain is induced by magnetization, the mechanical response of the film-substrate system can cause additional stress that affects the magnetization. The stress in Equation 3.28 can then be considered as the total mechanical stress $\sigma_{ij} = \sigma_{ij}^{\text{ex}} + \sigma_{ij}^{\text{in}}$, which is a superposition of an externally applied stress σ^{ex} with an internal stress σ^{in} . Then, the Gibbs free energy density (Equation 3.27) becomes

$$g_{me} = -\lambda_{ij}\sigma_{ij}^{\text{ex}} - \lambda_{ij}\sigma_{ij}^{\text{in}} := u' + u_{\text{me,ex}} + u_{\text{me,in}}. \quad (3.29)$$

Whereas $u_{\text{me,ex}}$ is caused by external stress, the second term $u_{\text{me,in}}$ is caused by stress induced indirectly by the magnetization. Thus, it is similar to the magnetostatic self-energy but with stress fields instead of magnetic fields. Correspondingly, $u_{\text{me,in}}$ is called *magnetostrictive self-energy density* with the components σ_{ij}^{in} of the self-stress. Such self-stress does not only occur in film-substrate systems, but also in free films to fulfill the compatibility of the deformation² in the presence of magnetic domains. Whereas σ^{ex} is given, σ^{in} can only be obtained indirectly from $\sigma_{ij}^{\text{in}} = \sigma_{ij} - \sigma_{ij}^{\text{ex}}$ if the total stress σ_{ij} is known. The total stress can be calculated by solving the mechanical equation of motion or the simplified elastostatic equation (c.f. Section 3.3.1). Like magnetostatic energy density, the magnetostrictive self-energy density is a nonlocal energy density term. Hence, its local value is a function of the complete magnetization field.

²Compatibility condition $\bar{\nabla} \times \mathbf{F} = \mathbf{0}$ (\mathbf{F} : deformation gradient tensor) must be fulfilled for a continuous displacement field without gaps or overlaps in the deformed body.

3.3 Dynamic Magneto-Mechanical System

We discussed the thermodynamic potentials and relevant contributions to the internal energy of the magneto-mechanical system in the previous sections. The gradient of the potential is required by the equations of motion as a driving force of the time evolution of the system. The magneto-mechanical system can be described by two coupled equations of motion. The mechanical (Section 3.3.1) and the magnetic equations of motion (Section 3.3.2) are coupled via the magnetostrictive strain tensor λ . Together they provide a full dynamic description of the magneto-mechanical system in the underlying continuum approximation.

3.3.1 Mechanical Equation of Motion

The equation of motion of the displacement field can be derived directly from Newton's second law (Appendix A.3). In the following form, it is referred to as Cauchy's equation of motion [357–359]

$$\rho(\bar{r}) \frac{\partial^2 \bar{u}(\bar{r}, t)}{\partial t^2} = \bar{\nabla} \sigma(\bar{r}, t), \quad (3.30)$$

where body forces such as gravity are omitted. In the equation, $\bar{u}(\bar{r}, t)$ represents the displacement vector field as a function of time t and the location vector \bar{r} . The parameter $\rho(\bar{r})$ represents the mass density, and the force $\bar{f} = \bar{\nabla} \sigma$ on the right-hand side of Equation 3.30 is given by the divergence $\bar{\nabla} \sigma$ of the stress tensor field $\sigma(\bar{r}, t)$. To keep the notation succinct, dependencies on \bar{r} and t are not explicitly written in the following equations. If only the static equilibrium configuration is of interest, the left-hand side of Equation 3.30 vanishes, and we obtain the condition for static equilibrium referred to as the elastostatic equation [358, 359]

$$\bar{\nabla} \sigma = \mathbf{0}. \quad (3.31)$$

Including Magnetostriction

The equation of motion as given in Equation 3.30 is a different formulation of Newton's second law. Besides the mass density, material properties are indirectly included in the equation of motion via the constitutive equations that relate the stress to the components u_i of displacement. Throughout this work, we consider linear-elastic materials where Hook's law holds in good approximation, and the mechanical strain e_{ij} (Equation 3.23) is connected with σ_{ij}

$$\sigma_{ij} = C_{ijkl} e_{kl} = C_{ijkl} (\varepsilon_{kl}^0 - \lambda_{kl}) \quad \text{with} \quad \varepsilon_{kl}^0 = \frac{1}{2} \left(\frac{\partial u_k}{\partial r_l} + \frac{\partial u_l}{\partial r_k} \right). \quad (3.32)$$

The mechanical strain e_{ij} is not directly related to the displacement in a magnetostrictive material. According to this equation, only the total strain ε_{ij}^0 can be obtained from the displacement. A part of this total strain is attributed to magnetostriction and does not induce mechanical stress. Hence, according to Equation 3.32, magnetostrictive strain λ_{ij} must be subtracted from ε_{ij}^0 to obtain the mechanical strain $e_{ij} = \varepsilon_{ij}^0 - \lambda_{ij}$ that induces stress σ_{ij} . This is thermodynamically consistent as shown with Equation 3.23 derived earlier. For a small stress, the magnetoelastic behavior can be linearized to include Equation 3.32 in the stiffness tensor, which is shown in Part II, Chapter 4. This approach has an advantage in that linear, lower computational cost methods such as frequency domain calculations can still be used.

Including Loss

ΔE -effect sensors are based on forced resonators. All forces in Equation 3.30 are covered by the stress gradient $\bar{\nabla} \sigma$, including the external driving force. The formulation in Equation 3.30 does not include the dissipation of energy, which can cause diverging displacement amplitudes. The dissipation of energy can occur through different physical mechanisms such as air and

viscous damping [360–365], thermoelastic damping [366–368], anchor loss [369–371], acoustic loss [365, 372, 373], and surface loss [374, 375]. Summaries of some mechanisms and physical loss models are provided in [376–378]. The large variety of different superposed loss mechanisms and the fundamental stochastic nature of loss makes the quantitative description challenging. Whereas analytical models are restricted to specific geometries and boundary conditions, numerical simulations can be very time consuming and prone to numerical errors and side effects that must be carefully examined [370]. For these reasons, the physical loss mechanisms are often not directly included in the mathematical description of the resonator. Instead, mathematical (structural) loss models can be used that consider energy dissipation via a generic parameter, which can be obtained from measurements or previous calculations. Rayleigh damping [379, 380], loss factor damping, and viscous damping are three common structural damping models [381]. The latter two models are the most relevant here and are elaborated in the following paragraphs.

Viscous damping can be introduced into the equation of motion as an additional force $\bar{f} = c \cdot \partial \bar{u} / \partial t$ proportional to the local velocity $\partial \bar{u} / \partial t$ via the damping coefficient c . Hence, the damping term is frequency dependent and cannot represent stress-strain hysteresis. For $c > 0$, the force term counteracts the driving force and reduces the displacement magnitude compared to the undamped case. With the external driving force \bar{F} , the damped equation of motion can be written as [382]

$$\rho \frac{\partial^2 \bar{u}}{\partial t^2} + c \frac{\partial \bar{u}}{\partial t} = \bar{\nabla} \sigma + \bar{F} \quad \text{with} \quad c \geq 0. \quad (3.33)$$

Loss factor damping (or complex modulus damping) represents a method to introduce hysteresis loss into the equation of motion [383]. In this method, the response of the displacement vector lags behind the driving force, which can be included by defining a complex modulus [383], or a more general complex stiffness tensor \mathbf{C}^* in the constitutive equations. The stress-strain relationship is then represented as [381, 382]

$$\sigma^* = \mathbf{C}^* e^* \quad \text{with} \quad \mathbf{C}^* = \mathbf{C}' + i\mathbf{C}'' = \mathbf{C}(1 + i\eta), \quad (3.34)$$

and $i := \sqrt{-1}$, the complex strain tensor e^* , and complex stress tensor σ^* . The complex stiffness tensor \mathbf{C}^* is represented by its real part \mathbf{C}' , and imaginary part \mathbf{C}'' [383]. According to Equation 3.34, \mathbf{C}^* can be rewritten as a function of the loss factor tensor $\eta_{ij} = \tan \delta_{ij}$ or the loss tangent ($\tan \delta_{ij}$) with the loss angle δ_{ij} [383]. The loss factor tensor is a direct measure for energy loss relative to the energy stored per oscillation period. For isotropic damping, η is a scalar (η) and the inverse of the quality factor $Q = 1/\eta$. Both loss measures (η , c) can only be approximately related to each other, which implies the loss model used to extract the quality factor from measurements must be specified. Owing to the complex representation, all time-dependent quantities in the equation of motion, such as stress, strain, and displacement become complex. The complex formulation of loss factor damping prevents using a time-domain formulation of the equation of motion and requires using equivalent viscous damping models [384, 385] or solving the equation of motion in a linearized form in the frequency domain. Loss factor damping is used for all finite element method simulations in this thesis, where the specific loss mechanism is not of interest. Similar formulations for the two loss mechanisms described above can be found elsewhere [381].

Formulation in the Frequency Domain

Often, the major parameters of interest include the amplitude and phase angle of the resonator as functions of the driving frequency. In such cases, the equation of motion can be further simplified and solved directly in the frequency domain. The loss of generality of such a frequency-domain formulation is often outweighed by a substantial reduction in the computational effort. A frequency domain representation of the equation of motion is described below; this representation

is used later in Part II. First, we consider a harmonic oscillating force \bar{F}^* that drives the system with an amplitude \hat{F} , a frequency f , and a phase angle ϕ_F relative to an arbitrary reference. The response of displacement \bar{u}^* is assumed to be linear, and hence, of equal frequency, but with a magnitude \hat{u} and a phase difference of ϕ_u relative to \bar{F}^* . The driving force and displacement are then expressed as

$$\bar{F}^* = \hat{F}e^{i(2\pi f + \phi_F)}, \quad (3.35)$$

$$\bar{u}^* = \hat{u}e^{i(2\pi f + \phi_u)}. \quad (3.36)$$

From Equation 3.34, it follows that the stress can be expressed in the form

$$\boldsymbol{\sigma}^* = \mathbf{C}^* \mathbf{e}^* = \hat{\boldsymbol{\sigma}} e^{i(2\pi f + \phi_u)}, \quad (3.37)$$

noting that it is connected with the displacement (now \bar{u}^*) via Equation 3.32. Substituting Equations 3.35-3.37 into the equation of motion (Equation 3.30), and dividing by $\exp(i(2\pi f + \phi_u))$ leads to the frequency domain expression

$$-\rho\omega^2\hat{u} = \bar{\nabla}\hat{\boldsymbol{\sigma}} + \hat{F}e^{i\Delta\phi} \quad \text{with} \quad \Delta\phi = \phi_F - \phi_u, \quad (3.38)$$

with a circular frequency $\omega = 2\pi f$, gradient $\bar{\nabla}\hat{\boldsymbol{\sigma}}$ of the stress amplitude $\hat{\boldsymbol{\sigma}}$, and phase shift $\Delta\phi$ between the excitation force and displacement and stress response. Although analytic solutions exist for very few degrees of freedoms, numerical methods are required for the solution in general.

3.3.2 Magnetic Equation of Motion

An equation of motion of the magnetization field was derived by Landau and Lifshitz in 1935 [258]. With the gyromagnetic ratio γ and effective magnetic field \bar{H}_{eff} , the Landau-Lifshitz (LL) equation [258]

$$\frac{d\bar{M}}{dt} = -\gamma(\bar{M} \times \bar{H}_{\text{eff}}) - \gamma \frac{\lambda}{M_s} \left[\bar{M} \times (\bar{M} \times \bar{H}_{\text{eff}}) \right], \quad (3.39)$$

describes the precession of the magnetization vector \bar{M} and eventual relaxation along the orientation of \bar{H}_{eff} . The second term on the right-hand side with the double vector product introduces energy dissipation with the damping factor λ , and is based entirely on phenomenological arguments. While conserving the magnitude M_s of \bar{M} , the dissipation term drives \bar{M} towards its minimum energy orientation along \bar{H}_{eff} . As indicated by the authors in their original publication [258], Equation 3.39 is applicable only in a precession dominated regime where the damping factor $\lambda \ll 1$. For moderate and large λ , the damping term on the right-hand side dominates the magnetization dynamics and predicts a faster change in the magnetization ($d\bar{M}/dt$) for a larger λ . This is not in line with the phenomenology and shows that λ cannot be assumed to be proportional to the dissipation of energy [277]. In 1955, Gilbert suggested a different equation of motion [260, 386],

$$\frac{d\bar{M}}{dt} = -\gamma \left[\bar{M} \times \left(\bar{H}_{\text{eff}} - \frac{\alpha}{M_s} \cdot \frac{d\bar{M}}{dt} \right) \right], \quad (3.40)$$

with the Gilbert damping factor α . Gilbert damping can be understood as equivalent to mechanical viscous damping described in Section 3.3.1. It slows down the precession of \bar{M} proportional to the speed of relaxation. In contrast to mechanical viscous damping, the Gilbert damping term additionally conserves the magnitude of \bar{M} . The time-implicit form of Equation 3.40 is often inconvenient for computation, and it can be rearranged to a time-explicit expression to obtain a form similar to the LL-equation. This form of the equation is often called the Landau-Lifshitz-Gilbert (LLG) equation [387]

$$\frac{d\bar{M}}{dt} = -\frac{\gamma}{1 + \alpha^2} (\bar{M} \times \bar{H}_{\text{eff}}) - \frac{\alpha\gamma}{(1 + \alpha^2)M_s} \left[\bar{M} \times (\bar{M} \times \bar{H}_{\text{eff}}) \right]. \quad (3.41)$$

In contrast to the LL-equation, the LLG-equation is valid for the full range of the damping factor. For small damping $\alpha \rightarrow 0$ and $\alpha = \gamma$, Equations 3.41 and 3.39 are identical, which is further discussed elsewhere [277, 388]. A detailed overview of the physics and mathematics of the LLG equation can be found in [387]. Several modifications of the LLG equation have been suggested to extend the validity of the equation, e.g., the Landau–Lifshitz–Gilbert–Slonczewski equation [389, 390] that includes spin-transfer torque, and the Landau-Lifshitz-Bloch equation [276, 391] to consider thermal fluctuations at nonzero temperatures. All of these equations require the effective field \bar{H}_{eff} as an input.

Effective Field

Constitutive equations relate the generalized displacement dV_g to the generalized force P_g , and are derived from the thermodynamic potential of the considered system (Section 3.1). In the context of a magnetic system, the generalized magnetic force $P_{\text{mag}} = \mu_0 \bar{H}_{\text{eff}}$ is expressed as an effective flux density $\mu_0 \bar{H}_{\text{eff}}$, with the effective field \bar{H}_{eff} , and the magnetic vacuum permeability μ_0 . The generalized magnetic displacement $dV_{\text{mag}} = d\bar{M}V$ is given by the differential magnetization $d\bar{M}$ and the volume V , and has units of magnetic moment. From Equation 3.5 we obtain for the magnetic part dg_{mag} of the differential Gibbs free energy density dg

$$dg_{\text{mag}} := \frac{1}{V} P_{\text{mag}} dV_{\text{mag}} = -\mu_0 \bar{H}_{\text{eff}} d\bar{M}. \quad (3.42)$$

This equation is rearranged to obtain \bar{H}_{eff} as a function of the Gibbs free energy density g

$$\bar{H}_{\text{eff}} = -\frac{1}{\mu_0 M_s} \frac{\partial g}{\partial \bar{m}} = -\frac{1}{\mu_0 M_s} \frac{\partial g_{\text{mag}}}{\partial \bar{m}} = \bar{H}_z + \bar{H}_d + \bar{H}_K + \bar{H}_{\text{ex}} + \bar{H}_{\text{me}}, \quad (3.43)$$

with the reduced magnetization vector $\bar{m} = \bar{M}/M_s$, and $M_s := |\bar{M}|$. Because the mostly phenomenological expressions for the internal energy density are given as functions of \bar{m} , $g(\bar{m})$ is known and \bar{H}_{eff} can be calculated. In Equation 3.43, \bar{H}_{eff} is expressed as a superposition of effective fields that correspond to the different magnetic contributions to the Gibbs free energy density. The resulting effective fields are given as follows. The effective Zeemann field \bar{H}_z is obtained from the derivative of Equation 3.8. It is identical with the external magnetic field \bar{H}_{app}

$$\bar{H}_z := -\frac{\partial u_z}{\partial \mu_0 \bar{M}} = \bar{H}_{\text{app}}. \quad (3.44)$$

Consistently, also the effective demagnetizing field is already introduced. Using the demagnetizing energy density u_d from Equation 3.17, and considering that \bar{H}_d is a function of magnetization, the factor 1/2 is canceled out when forming the derivative, and it is

$$\bar{H}_d := -\frac{\partial u_d}{\partial \mu_0 \bar{M}} = \bar{H}_d. \quad (3.45)$$

The effective field of the uniaxial anisotropy \bar{H}_K is calculated using Equation 3.11 of u_K , and it results to

$$\bar{H}_K := -\frac{\partial u_K}{\partial \mu_0 \bar{M}} = H_K \bar{E}A \cos \phi = H_K \bar{E}A (m_i E A_i). \quad (3.46)$$

Here, $H_K := 2K_1/(\mu_0 M_s)$ is the anisotropy field defined within the Stoner-Wohlfarth model [66], and $E A_i$ represents the components of the normalized orientation vector of the easy axis with magnitude $|\bar{E}A| = 1$. With Equation 3.9, the effective exchange field \bar{H}_{ex} is

$$\bar{H}_{\text{ex}} := -\frac{\partial u_{\text{ex}}}{\partial \mu_0 \bar{M}} = \frac{2A}{\mu_0 M_s} (\bar{\nabla}^2 \bar{m}). \quad (3.47)$$

The components $H_{\text{me},i}$ of the magnetoelastic field \bar{H}_{me} can be calculated from the magnetoelastic Gibbs free energy density term in Equation 3.28

$$H_{\text{me},i} := -\frac{1}{\mu_0 M_s} \frac{\partial g_{\text{me}}}{\partial m_i} = -\frac{3\lambda_s}{\mu_0 M_s} (\sigma_{ii} m_i + \sigma_{ik} m_k + \sigma_{ij} m_j). \quad (3.48)$$

The summation convention is not employed in Equation 3.48. Instead, the first component of \bar{H}_{me} is obtained from $i, j, k = 1, 2, 3$ and the other two from the cyclic permutations $i, j, k = 2, 3, 1$ and $i, j, k = 3, 1, 2$.

Part II
Results

Chapter 4

Magnetic Sensitivity

4.1 Magnetic Sensitivity of Bending Modes

The magnetic sensitivity connects the output signal of the sensor with the magnetic properties of the magnetoelastic layer and the mechanical and structural properties of the resonator. Therefore, understanding the complex interaction of geometry, mechanics, and magnetoelasticity is a prerequisite for obtaining the desired sensor characteristics by making deliberate design decisions. Despite the central role of magnetic sensitivity, no attempts have been reported to derive and analyze how it can be tuned by altering the typical design parameters.

The internal magnetic stray field contributes to the effective magnetic anisotropy of the magnetic material. It is decisive for the formation of magnetic domains, and it depends on the geometry of the magnetic layer. Therefore, the resonator and magnetic properties cannot be varied entirely independently. Further, purely mechanical or geometric material parameters (e.g., mass density or layer thickness) can affect the magnetic sensitivity by changing the contribution of the magnetic material to the resonance frequency. Many other factors could influence the magnetic sensitivity; for example, the spatial inhomogeneities of the magnetic and mechanical properties or the type of resonance mode. Previously, cantilever ΔE -effect sensors that operated in the first and second bending modes were presented [147]. They were characterized electrically and showed a superior LOD in the second bending mode. Therefore, there is a need to determine whether there are fundamental differences in the magnetic sensitivities of the first and second bending mode, how they can be explained, and if one of them is advantageous over the other.

The above mentioned questions are addressed in this section. The ΔE effect and magnetic sensitivity are experimentally and theoretically analyzed for the first and second bending modes of the magnetoelectric cantilever sensors. The magnetic sensitivity is explicitly formulated as a function of the magnetic and mechanical material parameters and discussed as a function of the geometry that includes the layer thicknesses and aspect ratios. Spatially distributed magnetic properties are considered with a numerical model.

Contribution

- Conceptualization
- Writing of original manuscript
- Modeling and simulations
- Measurements (shared)
- Data analysis and interpretation

The following material in this chapter is reproduced from: B. Spetzler, C. Kirchhof, E. Quandt, J. McCord, F. Faupel, *Physical Review Applied*, 23, 064036, 2019. "Copyright 2019 by the American Physical Society."


Magnetic Sensitivity of Bending-Mode Delta-E-Effect Sensors

Benjamin Spetzler¹,[✉] Christine Kirchhof,² Eckhard Quandt,² Jeffrey McCord,³ and Franz Faupel^{1,*}

¹Chair for Multicomponent Materials, Faculty of Engineering, Kiel University, Kiel, Germany

²Chair for Inorganic Functional Materials, Faculty of Engineering, Kiel University, Kiel, Germany

³Chair for Nanoscale Magnetic Materials, Faculty of Engineering, Kiel University, Kiel, Germany

 (Received 29 July 2019; revised manuscript received 21 October 2019; published 13 December 2019)

In recent years, magnetoelectric Delta-E-effect sensors have proven the potential to detect low-frequency and low-amplitude magnetic fields, while being fully integrable. The magnetic field sensors use the magnetization-induced change of the effective Young's modulus, referred to as the Delta-E effect. Although several sensor types have been demonstrated, little is reported about the dependence of the design parameters and the resulting sensor characteristics, such as sensitivity and noise. In this Paper, we comprehensively analyze and discuss theoretically and experimentally the magnetic sensitivity and the Delta-E effect of bending-mode Delta-E-effect sensors. Analytical expressions are derived for the magnetic sensitivity and compared with the results of a more elaborate numerical mean-field model. The mean-field model additionally considers spatial variations of the magnetic properties, including the internal stray field of the real shape. Measurements are performed on state-of-the-art bending-mode Delta-E-effect sensors. We find that the Delta-E effect significantly depends on the resonance mode and, moreover, second-order bending modes increase the magnetic sensitivity compared to first-order modes. This can be explained well by the spatial variation of the internal stray field in agreement with the numerical simulations and magneto-optical measurements. Overall, we provide a comprehensive description of the magnetic sensitivity for the improvement of bending-mode Delta-E-effect sensors. We show that the weighting of local properties by the mode shape is not only key for modeling and understanding the Delta-E effect of different bending modes, but also an important factor for improving magnetic sensitivities.

DOI: [10.1103/PhysRevApplied.12.064036](https://doi.org/10.1103/PhysRevApplied.12.064036)

I. INTRODUCTION

The change of the effective elastic properties with magnetization due to inverse magnetostriction is referred to as the Delta-E effect. Early experiments in the beginning of the 20th century on the change of Young's modulus were first explained in terms of domain theory and magnetostriction [1–6]. Many simplifying assumptions were used due to a lack of proper magnetic hysteresis models. The first specific features of Young's modulus $E(H)$ as a function of the magnetic field H were explained using a stress-extended Stoner-Wohlfarth model for a hard-axis magnetization case [7]. Adding another phenomenological energy term permitted the inclusion of domain-wall motion and the description of the dependency of $E(H)$ on the orientation of the magnetic easy axis [8,9] within certain limits. Besides $E(H)$, the magnetic field dependency of other elastic constants [10] and components of the mechanical stiffness tensor [11–13] have been investigated experimentally and theoretically using single-spin models. These works focus mainly on hard magnetic

plane thin films in specific configurations of the magnetic system.

For soft-magnetic amorphous ribbons [9,14], normal distributions of the effective anisotropy are required to match Delta-E-effect models with measurements on amorphous ribbons. Such distributions are used as a purely phenomenological fit parameter without assigning a physical origin. Spatial distributions of magnetic properties and the influence of higher-order modes on the Delta-E effect have always been ignored.

Early studies on the Delta-E effect in cantilever resonators used an external magnetic field for excitation. Replacing the magnetic excitation by an electrical one opened the possibility of an integrated sensor device [15]. Several designs for magnetic field sensing have been presented: magnetic films on the delay line of surface acoustic wave resonators [16–18], magnetoelectric nanoplate resonators with higher-order bulk modes [19,20] and cantilever sensors with first- and second-order bending modes [21,22]. Various Delta-E-effect sensors have shown the potential to detect low-frequency (<100 Hz) and low-amplitude (<1 nT) magnetic fields [16,19,21,23]. Cantilever sensors with an adapted electrode design operating

*ff@tf.uni-kiel.de

in the second bending mode reached noise levels below $100 \text{ pT}/\sqrt{\text{Hz}}$ at frequencies from about 10–100 Hz [22]. Details about the operation employed, read-out [24], and noise level [25,26] of this sensor design have been discussed.

In particular, for medical diagnostic and biomedical applications, the detection of low-amplitude and low-frequency magnetic fields is of great interest [27–29]. Because small amplitudes well below the picotesla regime and low-frequency components are required, mainly superconducting quantum interference devices (SQUID) [30] are used, and recently atomic magnetometers [31,32] as well. In such instruments, the advantage of very small noise levels comes at the expense of high operational costs, limited dynamic range, and difficulties in integrating sensors into array applications. Here Delta-E-effect sensors could be an alternative for some specific applications in the future [33].

Despite the promising properties of bending-mode Delta-E-effect sensors, there is little connection in the literature between the sensor-design parameters, investigations of the Delta-E effect and the resulting sensitivity. In fact, none of the studies mentioned includes an explicit theoretical treatment or a comprehensive discussion of the magnetic sensitivity.

This Paper is structured as follows: first, we present the cantilever sensors used in this work (Sec. I A), before the read-out methods and the definitions for the sensitivity are discussed (Sec. I B). After that the magnetic sensitivity is analyzed with an analytical model (Sec. II). The consequences and limitations of the model are outlined. To overcome the limitations, a numerical model is presented (Sec. III) that considers spatial inhomogeneities. The numerical model is discussed and validated with measurements (Sec. IV), before it is applied in an example. We summarize and give a conclusion in Sec. V.

A. Bending-mode Delta-E-effect sensors

Magnetolectric composite cantilevers, used for magnetic field sensing can be fabricated with dimensions from

the centimeter range [34] down to the millimeter [35] and micrometer range [23,36]. In this study all measurements and models are made for a MEMS design cantilever that had shown the lowest detection limit for the Delta-E-effect read-out previously [22]. A sketch including dimensions and layer structure and a top-view photograph of the design are shown in Fig. 1.

The $3 \times 1 \text{ mm}^2$ cantilever sensor consists of a $2\text{-}\mu\text{m}$ piezoelectric layer of AlN [37] on a $50\text{-}\mu\text{m}$ -thick poly-Si substrate. A $2\text{-}\mu\text{m}$ -thick amorphous magnetostrictive layer [38] is deposited on the backside. A magnetic field is applied during the deposition to induce a magnetic easy axis along the short cantilever axis. For actuation and read-out, two electrodes contact the AlN layer on the top. The counter electrode covers the whole beam area and is located between the AlN layer and the substrate. As magnetostrictive material we use a $2\text{-}\mu\text{m}$ multilayer with $20 \times [100 \text{ nm } (\text{Fe}_{90}\text{Co}_{10})_{78}\text{Si}_{12}\text{B}_{10} \text{ and } 6 \text{ nm Cr}]$. The magnetic layers are deposited in a magnetic field to induce an easy axis perpendicular to the cantilever's long axis. More information about the layer structures and process details can be found in Ref. [21]. For operating the sensor's first bending mode, it is excited and read-out at approximately 7.4 kHz using the short electrode E_1 close to the clamping. The second bending mode is analyzed with electrode E_2 at frequencies around 46 kHz. All discussions and measurements are carried out for this design and on the same sensor.

B. Sensitivity: definition and frequency dependency

The sensors are operated either in a closed-loop (CL) configuration [20] or in an open-loop configuration (OL) [16,24]. For the CL read-out, the sensor is inserted into the feedback loop of an amplifier in which the oscillating signal is frequency modulated by the ac magnetic field via the Delta-E effect [39]. The sensitivity S_H for CL can be defined as the change of resonance frequency f_r with the applied magnetic flux density $\mu_0 H$ at a chosen magnetic bias field H_0 . In OL operation, the resonator is actively excited with a local oscillator. The ac magnetic field to

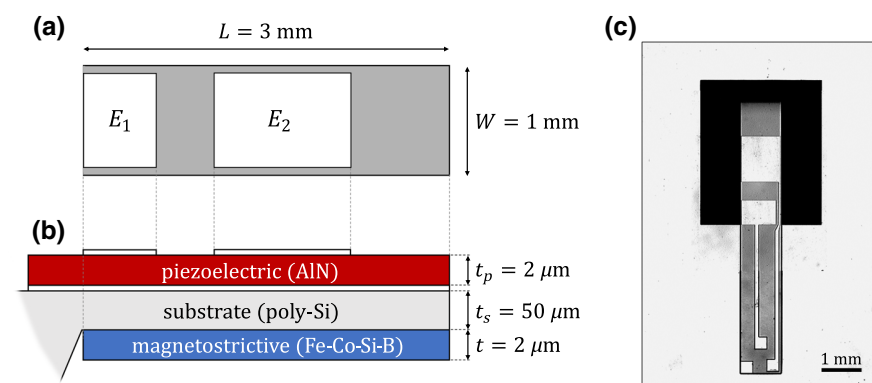


FIG. 1. Cantilever design analyzed in this study: (a) sketch of the top view with top electrodes E_1 and E_2 and the in-plane dimensions of the beam. The counter electrode is located between the AlN layer and the poly-Si substrate; (b) illustration of the layer structures including the respective thicknesses; (c) photograph of the MEMS sensor from above. More information and process details can be found in Ref. [21].

be measured modulates the excitation current in amplitude and in phase. This is caused by a dependency of the magnitude $|Y| = \text{abs}\{Y\}$ and phase angle $\phi = \text{arg}\{Y\}$ of the sensor admittance Y on the magnetization due to the Delta-E effect. Consequently, two sensitivities S_{AM} and S_{PM} can be defined for OL operation, corresponding respectively to amplitude modulation (AM) and phase modulation (PM) [26]. Both include the sensitivity S_H for the CL operation:

$$S_{AM} = \left. \frac{\partial |Y|}{\partial \mu_0 H} \right|_{f_r, H_0} = \left. \frac{\partial |Y|}{\partial f} \right|_{f_r} \left. \frac{\partial f_r}{\partial \mu_0 H} \right|_{H_0} := S_{el, Y} S_H, \quad (1)$$

$$S_{PM} = \left. \frac{\partial \phi}{\partial \mu_0 H} \right|_{f_r, H_0} = \left. \frac{\partial \phi}{\partial f} \right|_{f_r} \left. \frac{\partial f_r}{\partial \mu_0 H} \right|_{H_0} := S_{el, \phi} S_H. \quad (2)$$

In Eqs. (1) and (2), $S_{el, Y}$ is referred to as electrical magnitude sensitivity and $S_{el, \phi}$ as electrical phase sensitivity. They can be obtained with the derivative of $|Y|$ or ϕ with respect to frequency f at the chosen operation frequency, which is here the resonance frequency f_r of the oscillator.

To find the frequency dependence of the OL sensitivities, S_{el} and S_H are treated separately. For S_{el} it is $S_{el} \propto 1/f_{BW}$, with the bandwidth f_{BW} of the electromechanical resonator. Because $f_{BW} = f_r/(2Q)$, it is $S_{el} \propto 1/f_r$ for a constant quality factor Q . Because the CL sensitivity $S_H \propto f_r$ [20] from basic mechanics, the dependency of S_{AM} and S_{PM} on f_r cancels out. This presumes that frequency dependencies of the magnetic properties can be neglected.

Because the OL and CL sensitivities have different units, they are not directly comparable, so the noise level must be considered. For phase modulation, the detection limit as a function of frequency for both modes of operation is equivalent [39]. To eventually compare S_{el} or S_H of sensors operated at different f_r or in different operation modes, it is convenient to define relative quantities $S_{el, r}$ and $S_{H, r}$ normalized to f_r :

$$\begin{aligned} S_{el, r} &= \left. \frac{\partial |Y|}{\partial f} \right|_{f_r} f_r; & S_{el, \phi, r} &= \left. \frac{\partial \phi}{\partial f} \right|_{f_r} f_r; \\ S_{H, r} &= \left. \frac{\partial f_r}{\partial \mu_0 H} \right|_{H_0} \frac{1}{f_r}. \end{aligned} \quad (3)$$

Details about the operation employed, read-out [24], and noise level [25,26] of the sensors discussed here can be found elsewhere. In this work, we focus on S_H and $S_{H, r}$ because they include the magnetic properties of the device.

II. ANALYTICAL MODEL: TREATMENT OF THE DELTA-E EFFECT AND SENSITIVITY

In this section, analytical equations are derived for the magnetic sensitivities S_H and $S_{H, r}$ as functions of material parameters and geometry. The model is based on a single-spin approach for the Delta-E effect and a Euler-Bernoulli cantilever for the mechanical response.

A. Extended Stoner-Wohlfarth model

For hard-axis magnetization processes, the change in Young's modulus can be calculated analytically. We consider the Stoner-Wohlfarth energy density function and extend it by a uniaxial magnetoelastic and a demagnetizing term. After dropping constants, it is

$$\begin{aligned} u &= K_u \sin^2(\varphi - \varphi_{EA}) + K_s \cos^2 \varphi + K_\sigma \cos^2 \varphi \\ &\quad - \mu_0 M_s H \cos \varphi, \end{aligned} \quad (4)$$

with the angle φ and φ_{EA} of the magnetization vector and the magnetic easy axis, defined relative to the orientation of the applied external field \vec{H} with magnitude H . The effective uniaxial anisotropy energy density of first order is given by K_u . Besides a magnetization-induced uniaxial energy density, it may include other uniaxial contributions from various origins that are not distinguished here. The magnetoelastic anisotropy energy density $K_\sigma = -(3/2)\lambda_s \sigma$ includes the external applied stress σ along \vec{H} and the saturation magnetostriction λ_s . The shape-anisotropy energy-density constant $K_s = \mu_0 M_s^2 (D_{11} - D_{22})/2$ is expressed with the 11-component D_{11} and the 22-component D_{22} of the demagnetizing tensor \mathbf{D} . The magnetic vacuum permeability is given by μ_0 and the saturation magnetization by M_s . For a hard-axis magnetization process with $\varphi_{EA} = 90^\circ$, the solution for the component M of the magnetization vector along \vec{H} is well known as [40–43]

$$\begin{aligned} M(H, \sigma) &= \begin{cases} \frac{H}{H_a} M_s & \text{for } H \leq H_a \\ M_s & \text{for } H > H_a \end{cases} \\ \text{with } H_a &= \frac{2(K_u + K_\sigma + K_s)}{\mu_0 M_s} := \frac{2K_a}{\mu_0 M_s}, \end{aligned} \quad (5)$$

where H_a and K_a are the effective field and the effective energy density that must be overcome to reach magnetic saturation along the magnetically hard axis.

B. Analytical calculation of the ΔE effect and the magnetic sensitivity S_H

To calculate Young's modulus as a function of magnetization and stress, its inverse $E(H, \sigma)^{-1} = \partial(e + \lambda)/\partial \sigma$ can be expressed as the sum of mechanical strain e and magnetostrictive strain $\lambda = (3/2)\lambda_s (\cos^2 \varphi - 1/3)$ along the \vec{H} axis. Using Eq. (5) for the hard-axis magnetization case and Young's modulus E_m at fixed magnetization, the

result is [7]

$$E(H, \sigma) = \begin{cases} \left(\frac{1}{\Delta E} + \frac{1}{E_m} \right)^{-1}, & H \leq H_a \\ E_m & H > H_a \end{cases} \quad (6)$$

with $\Delta E = \frac{\mu_0 M_s H_a^3}{9\lambda_s^2 H^2}$.

The normalized, minimum Young's modulus $E_{r,\min} := E(H = H_a)/E_m$ can be used as a measure for the Delta-E effect. It is obtained from Eq. (6) as

$$E_{r,\min} = \left(1 + \frac{9\lambda_s^2 E_m}{2K_a} \right)^{-1}. \quad (7)$$

For Delta-E effect sensors, not the absolute value of $E(H, \sigma)$ but instead the derivative with respect to the magnetic field is required to calculate the S_H part of the sensitivities. The first derivative of Eq. (6) results in

$$\begin{aligned} \partial_{E,H} &:= \frac{\partial E(H, \sigma)}{\partial H} \\ &= \begin{cases} -\frac{18\lambda_s^2 E_m^2 \mu_0 M_s H_a^3 H}{(9\lambda_s^2 H^2 E_m + \mu_0 M_s H_a^3)^2} & H \leq H_a \\ 0 & H > H_a \end{cases}. \end{aligned} \quad (8)$$

The sensors are usually operated at a dc bias field where the slope is maximum. This maximum slope is obtained at

the point of inflection of Eq. (6),

$$\begin{aligned} \partial_{E,H}^{\max} &:= \left. \frac{\partial E(H, \sigma)}{\partial H} \right|_{H_{1,2}} = \pm \frac{3^{5/2}}{8} \sqrt{\frac{\lambda_s^2 E_m^3}{\mu_0 M_s H_a^3}} \quad \text{with} \\ H_{1,2} &= \pm \sqrt{\frac{\mu_0 M_s H_a^3}{27 E_m \lambda_s^2}}, \end{aligned} \quad (9)$$

at the corresponding optimum dc bias fields H_1 and H_2 . The following Fig. 2(a) shows $E(H, \sigma)$ from Eq. (6) and the slope $\partial_{E,H}$ of $E(H)$ as calculated from Eq. (8). Using the material parameters of the sensors discussed here (Sec. III A) we obtain $E_{r,\min} \approx 0.54$ and $|\partial_{E,H}^{\max}| \approx 68 \text{ GPa/mT}$.

C. The magnetic sensitivity S_H

The magnetic sensitivity S_H can be obtained via Eq. (10) from two different derivatives, where the first is given by the magnetic properties and the second by the mechanical properties of the resonance mode:

$$\begin{aligned} S_H &= \frac{1}{\mu_0} \left. \frac{\partial f_r}{\partial H} \right|_{H_{1,2}} = \frac{1}{\mu_0} \left. \frac{\partial E}{\partial H} \right|_{H_{1,2}} \left. \frac{\partial f_r}{\partial E} \right|_{E(H_{1,2})} \quad \text{with} \\ [S_H] &= \text{Hz/T}. \end{aligned} \quad (10)$$

Considering a Euler-Bernoulli beam, the second part of S_H can be obtained from the eigenfrequency equations [21] with mode number i , in approximation of large quality factors:

$$f_{r,i} = \frac{\lambda_i^2}{2\pi L^2} \sqrt{\frac{\sum_k E_k I_k}{m_L}} \Rightarrow \frac{\partial f_{r,i}}{\partial E} = \frac{\lambda_i^2}{4\pi L^2} \frac{I}{\sqrt{m_L \sum_k E_k I_k}}, \quad (11)$$

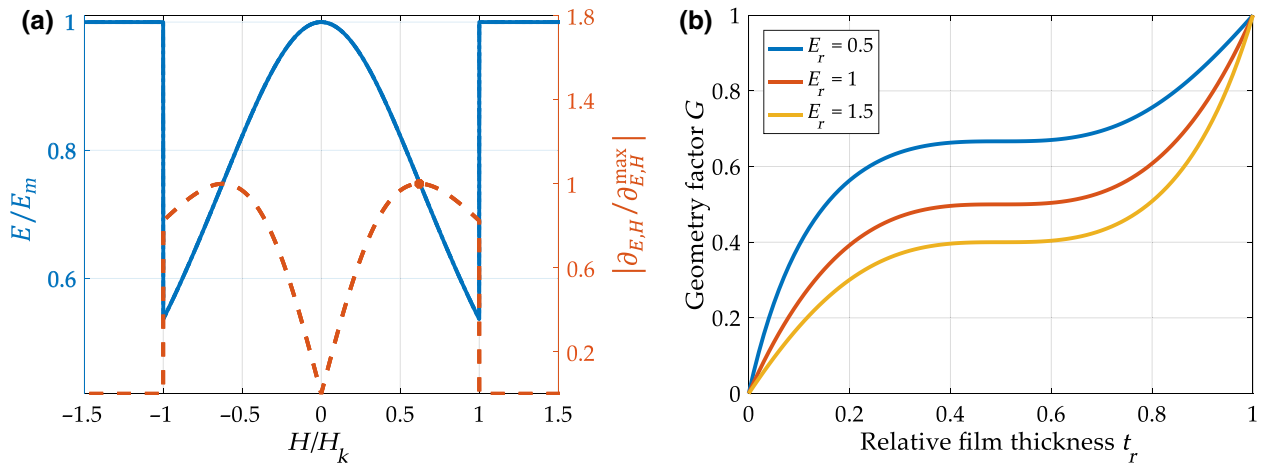


FIG. 2. Results from the analytical calculations for a hard-axis magnetization process. (a) Young's modulus $E(H)$ [Eq. (6)] normalized to its value E_m at fixed magnetization and its derivative $|\partial_{E,H}| := |dE/dH|$ [Eq. (8)] normalized to its maximum $\partial_{E,H}^{\max} \approx 68 \text{ GPa/mT}$. (b) Geometry factor G of the magnetic sensitivity S_H [Eq. (16)] as a function of the ratio $t_r = t/h$ of film thickness t to total thickness h of the cantilever beam for different ratios $E_r = E_s/E$ of the two Young's moduli E of the film and E_s of the substrate.

with the mode factor λ_i of the i th bending mode, the cantilever length L the mass per length m_L , the Young's modulus E_k and the second moment of area I_k both of the k th layer. In the following, we consider a magnetic layer, with E and I , on top of a nonferromagnetic substrate with E_s and I_s . Here E_s and I_s can be approximated as average Young's modulus and average second moment of area of all other nonmagnetostrictive layers. For our system it comprises the piezoelectric AlN layer and the poly-Si. Using Eq. (11) and $\frac{\partial E}{\partial H}^{\max}$ from Eq. (9), the expression for the magnetic sensitivity in bending modes becomes

$$S_H = \pm \frac{3^{5/2}}{8\sqrt{8}} \cdot \frac{M_s \lambda_s E_m^{3/2}}{K_a^{3/2}} \cdot \frac{\lambda_i^2}{4\pi L^2} \frac{I}{\sqrt{m_L(EI + E_s I_s)}}. \quad (12)$$

For small changes of E due to the Delta-E effect, one can further simplify Eq. (12) by setting $E \approx E_m$.

D. Relative magnetic sensitivity $S_{H,r}$

The relative magnetic sensitivity $S_{H,r}$ is defined in Eq. (3) as a frequency-independent measure of the magnetic sensitivity. From that definition it can be expressed as

$$S_{H,r} := S_H f_{r,i}^{-1} = \frac{1}{\mu_0} \frac{\partial E}{\partial H} \bigg|_{H_{1,2}} \frac{\partial f_r}{\partial E} \bigg|_{E(H_{1,2})} \frac{1}{f_r}. \quad (13)$$

With Eq. (11) for f_r and $\partial f_r / \partial E$ the latter product in Eq. (13) simplifies to

$$\frac{1}{f_r} \frac{\partial f_r}{\partial E} \bigg|_{E(H_{1,2})} = \frac{1}{2} \frac{I}{\sum_k E_k I_k}. \quad (14)$$

Now we again consider a two-layer structure with a magnetic film on top of a substrate. With the thicknesses t of the magnetic layer, a relative thickness can be defined as $t_r := t/h$, with the total thickness h of the composite beam. Further we define the relative Young's modulus $E_r := E_s/E$. Calculating the two second moments of area [44] I and I_s with the parallel-axis theorem and substituting the defined quantities, it is directly

$$\frac{1}{f_r} \frac{\partial f_r}{\partial E} \bigg|_{E(H_{1,2})} = \frac{1}{2E} \frac{g}{g + E_r(1-g)} := \frac{G}{2E} \quad \text{with} \quad g := 3t_r - 6t_r^2 + 4t_r^3. \quad (15)$$

The factor G as defined in Eq. (15) includes only the geometry of the layer system and the relative Young's modulus E_r , which is typically $E_r \approx 1$. This permits a separate treatment of the geometric and the material's influence on the magnetic sensitivity. To obtain a final equation for $S_{H,r}$, we substitute Eq. (15) into S_H from Eq. (13) and use Eq. (9)

for $\partial E / \partial H$. With the approximation $E \approx E_m$ the relative magnetic sensitivity becomes

$$S_{H,r} = \pm \frac{3^{5/2}}{16\sqrt{8}} \frac{M_s \lambda_s E_m^{1/2}}{K_a^{3/2}} G \quad \text{with} \quad [S_{H,r}] = \frac{1}{\text{T}}. \quad (16)$$

Typically, $E_r \approx 1$ is a good approximation, which simplifies the geometric factor to $G \approx g$. For the sensors discussed here, it is $G \approx 0.1$, with $E_r \approx 1$ and $t_r \approx 0.04$, which results in $S_{H,r} \approx 0.02 \text{ T}^{-1}$. The material parameters used are given in Sec. III A.

E. Discussion of the analytical model

An analytical model for the Delta-E effect is used to calculate its slope and the magnetic sensitivities. Expressions are calculated for the derivative $\partial_{E,H}$ and maximum derivative $\frac{\partial E}{\partial H}^{\max}$ of Young's modulus $E(H)$. With the eigenfrequency of a Euler-Bernoulli beam, an equation for the magnetic sensitivity S_H is found. Simple expressions for the minimum Young's modulus $E_{r,\min}$ and the relative magnetic sensitivity $S_{H,r}$ are derived and calculated with material and geometry parameters of a typical cantilever sensor. In comparison to measurements [45], the model overestimates $E_{r,\min}$ by a factor of about 2, whereas the modeled $S_{H,r} \approx 0.02 \text{ T}^{-1}$ is slightly closer to reported values [22] and our measurements (Sec. IV C). The mismatch between model and measurement is expected to be caused mainly by the single-spin assumption within the magnetic model [46].

The influence of the layer structure on $S_{H,r}$ is described by the geometry factor G . It is plotted in Fig. 2(b) as a function of the relative film thickness t_r for different E_r . An improvement is predicted in the sensitivity by a factor of about 5 for a decrease in the substrate thickness to achieve $t_r = 0.3$. A further increase in t_r is expected to be less efficient due to the plateau of G around $t_r = 0.5$. This prediction holds only if changing the geometry does not alter K_a or φ_{EA} , e.g., by an additional impact of anisotropic stress.

The absolute dimension of the magnetic film contributes to the relative magnetic sensitivity $S_{H,r}$ via the demagnetizing field. The shape-anisotropy energy-density K_s results in a reduction of K_a [Eq. (5)] with increasing film thickness. Consequently, it follows from Eq. (16) that $S_{H,r} \rightarrow \infty$, if $t \rightarrow t_c$. Exceeding the critical film thickness t_c , it is $K_a < 0$ which switches the easy axis to 0° . Because $M = \pm M_s$ for a single-spin easy axis case, it follows directly that $E(H, \sigma) = E_m$ and $S_{H,r} = 0$. With the ballistic demagnetizing factors in the center of a rectangular prism [47] and $K_u = 1.6 \text{ kJ/m}^3$ (Sec. IV), the critical film thickness for the given geometry results in $t_c = 2.8 \mu\text{m}$. This behavior is a result of the single-spin assumption and not expected for a real sample.

In summary, the analytical model is successfully used to estimate and describe Young's modulus and the magnetic

sensitivity of typical cantilever sensors. In particular, for a realistic description around $t = t_c$ and $H = H_a$, a refined model is required.

III. NUMERICAL MEAN-FIELD MODEL

In this part, a numerical model for Young's modulus is presented to avoid the main assumptions and limits of a homogeneous system. Spatial distributions of different K_u and φ_{EA} are introduced before a spatially varying internal stray field is used. For the mechanical part of the sensitivity, an analytical and a finite-element (FE) model are used.

A. Model geometry and material parameters

Corresponding to the geometry in Fig. 1, we consider a cantilever geometry with in-plane dimensions of $3 \times 1 \text{ mm}^2$, for all models. For simplicity we neglect the piezoelectric layer and add its $2\text{-}\mu\text{m}$ thickness to the $50\text{-}\mu\text{m}$ substrate thickness. This approximation is justified, because the AlN layer is thin and only the resonance frequencies and not the electrical properties are of interest here. The final geometry consists of one $2\text{-}\mu\text{m}$ -thick

magnetostrictive layer on top of a $52\text{-}\mu\text{m}$ -thick poly-silicon substrate (poly-Si). Thin supporting layers and the electrodes are neglected. The mechanical model parameters, which are used for the two layers, are summarized in Table I. For the magnetic material (Fe-Co-Si-B) a saturation flux density of $\mu_0 M_s = 1.5 \text{ T}$ and a saturation magnetostriction of $\lambda_s = 32 \text{ ppm}$ is used [45]. For the single-spin model and the calculations in Secs. IV A and IV B, $K_a = 800 \text{ J/m}^3$ is used, if not stated otherwise.

B. Calculation of Young's modulus E

To calculate Young's modulus as a function of stress and external magnetic field, ΔE is expressed more general in terms of the first derivative u_φ of the energy-density function u [Eq. (4)]. From the equilibrium condition $u_\varphi := \partial u / \partial \varphi = 0$ it is

$$\frac{1}{\Delta E} = \frac{\partial \lambda}{\partial \sigma} = \frac{\partial \lambda}{\partial \varphi} \frac{\partial \varphi}{\partial \sigma} = \frac{\partial \lambda}{\partial \varphi} \left(-\frac{\partial u_\varphi}{\partial \sigma} / \frac{\partial u_\varphi}{\partial \varphi} \right). \quad (17)$$

Assuming in-plane magnetization only, for the soft magnetic material, Eq. (17) directly results in

$$\frac{1}{\Delta E} = \frac{9\lambda_s^2 \cos^2(\varphi) \sin^2(\varphi)}{2K_u \cos[2(\varphi - \varphi_{\text{EA}})] + \mu_0 M_s H \cos \varphi - 2K_s \cos[2\varphi] - 2K_\sigma \cos[2\varphi]}. \quad (18)$$

With $\varphi_{\text{EA}} = 90^\circ$, this expression for ΔE is equivalent to ΔE in Eq. (6). The advantage of Eq. (18) is that only the equilibrium magnetization angle φ must be known to obtain the linearized Young's modulus as a function of magnetic field and applied stress. The magnetization angle is obtained by solving Eq. (4) numerically for φ , always starting with $H \gg H_a$.

C. Anisotropy distributions and local internal stray fields

A major advantage of treating Eq. (4) numerically is the possibility of modeling arbitrary easy-axis orientations and including spatial inhomogeneities of the internal stray field. An ensemble of single-domain regions, each described by Eq. (4), is considered with a distribution of K_u around its mean (\bar{K}_u) with standard deviation δ_K . For the easy-axis angles, a Van Mises distribution is used with standard deviation δ_{EA} around the mean easy-axis angle $\bar{\varphi}_{\text{EA}}$. The local stray field is modeled analytically using the ballistic demagnetizing tensor $\tilde{\mathbf{D}}$ [47–49] of a rectangular prism. This is a rough approximation, as it is only fully valid in magnetic saturation. The resulting distribution of the demagnetizing anisotropy constant K_s for

our film geometry is shown in Fig. 3(b). For each single-domain region the angle φ of magnetization is calculated as a function of the external magnetic field H by solving Eq. (4). Then φ is used to calculate the local Young's modulus $E_n(H)$ with Eq. (18).

D. Calculation of resonance frequencies

To calculate the resonance frequencies, the magnetostrictive layer is separated along the x axis into six equally sized spatial regions ($R1 - R6$). This number is found to be the minimum required for a sufficient discretization. The local Young's modulus $E_n(H)$ is averaged within each spatial region R to obtain the mean Young's moduli $\bar{E}_i(H)$ of that region.

TABLE I. Saturation Young's modulus E_m , Poisson's ratio ν , density ρ , and thickness of the films used in the cantilever models.

Composition	E_m	ν	ρ	Thickness
Fe-Co-Si-B	150 GPa	0.35	7870 kg/m ³	2 μm
Poly-Si	160 GPa	0.22	2330 g/m ³	52 μm

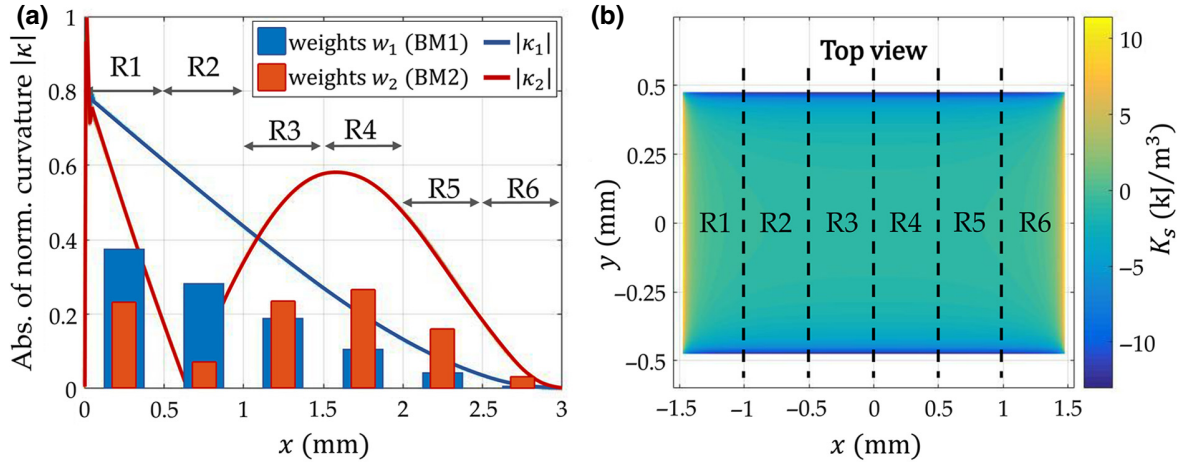


FIG. 3. (a) Absolutes $|\kappa_1|$ and $|\kappa_2|$ of the normalized curvature κ for the first bending mode (BM1) and the second bending mode (BM2) of a cantilever beam. The effective mechanical properties are locally weighted by the weighting factors w_1 (BM1) and w_2 (BM2) indicated as bar diagrams. (b) Top view of the magnetic layer, with local shape-anisotropy energy-density constant $K_s \propto D_{11} - D_{22}$ calculated from the ballistic demagnetizing factors in x and y direction. The six regions (R1–R6) of spatial discretization for the mechanical calculations are indicated.

For the analytical approximation, the six mean Young's moduli $\bar{E}_i(H)$ are weighted by the absolutes of the six normalized mean curvatures w_i of the respective bending mode (Fig. 3) of a Euler-Bernoulli beam. The resulting Young's moduli $E = \sum_{i=1}^6 w_i \bar{E}_i(H)$ are used in Eq. (11) to calculate the eigenfrequency of the beam.

The analytical results are compared with eigenfrequency calculations from a FE model using an eigenfrequency study in COMSOL Multiphysics 5.3a with the mean $\bar{E}_i(H)$ as input.

IV. RESULTS AND DISCUSSION

In the following results from the numerical model are presented and compared with measurements. In the first part (IV A), the Delta-E effect of a single-domain particle is calculated at different easy-axis angles using Eq. (18). No distributions are used. In the second part (IV B), Young's modulus and its maximum slope are calculated as a function of the magnetic easy-axis tilt to quantify how it affects the magnetic sensitivity. Normal distributions of the magnetic easy-axis angle and the anisotropy energy density are used to quantify their influence on the magnetic sensitivity. In the third part (IV C), the numerical model is used with the inhomogeneous internal stray field. The results are compared with magnetization and resonance frequency measurements on the cantilever sensors. For those calculations no fitted normal distributions are used, only the local stray fields defined by the shape of the magnetic film. Finally, in part (IV D) the numerical model is applied to calculate the dependency of the magnetic layer thickness on the sensitivity.

A. Results for a single-domain region

Results for Young's modulus from Eq. (18) of one single-domain region are shown in Fig. 4 for different easy-axis orientations φ_{EA} . At $\varphi_{EA} = 90^\circ$, the result resembles the analytical hard-axis curve perfectly. With increasing tilt of the easy axis from this position, the minimum Young's modulus increases and the curve rounds around the anisotropy field. The maximum located at $\mu_0 H = 0$ mT at $\varphi_{EA} = 90^\circ$ shifts to the left and its peak becomes narrower until it vanishes for angles $\varphi_{EA} > 45^\circ$. At this angle, the curve has a v-shaped form. For smaller φ_{EA} the minimum shifts further to the left and the overall effect reduces until it is zero at $\varphi_{EA} = 0^\circ$. For all angles $\varphi_{EA} \neq 90^\circ$, a singularity occurs at the switching field, where $E = 0$. Here, the magnetization can be tilted with an infinitely small stress along the magnetic field axis. In experiments, Young's modulus at the switching field is expected to be >0 due to damping of the magnetization dynamics [50–52], which is not included here.

B. Influence of distributions on $E(H)$ and the sensitivity

In Fig. 5(a), $E(H)$ is shown for different mean tilt angles $\bar{\varphi}_{EA}$ and the fixed distribution $\delta_K = 15\%$ around $K_u = K_a = 800$ J/m³ and $\delta_{EA} = 0.6\%$ of the easy-axis angle. We define two maximum slopes $\partial_{E,H}^1$ and $\partial_{E,H}^2$, which are indicated with a red bold line in Fig. 5(a). Their absolute is plotted over the mean easy-axis angle $\bar{\varphi}_{EA}$ for different δ_K in Fig. 5(b). The influence of a distribution around $\bar{\varphi}_{EA}$ is not explicitly shown here because it has a similar influence on the sensitivity as a tilt of $\bar{\varphi}_{EA}$.

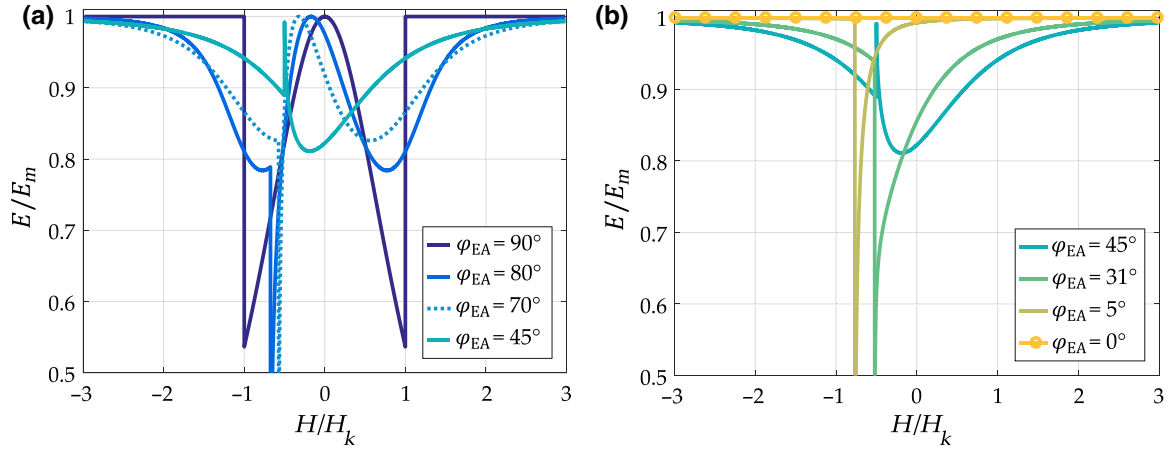


FIG. 4. Delta-E effect calculated for a single-domain region: (a) for different angles φ_{EA} of the easy axis between 90° and 45° and (b) between 45° and 0° to the magnetic field direction. The calculations are started at positive magnetic fields close to magnetic saturation.

For mean angles between $\bar{\varphi}_{EA} = 90^\circ$ and $\bar{\varphi}_{EA} \approx 80^\circ$, δ_K influences the outer slope $\partial_{E,H}^1$ strongly because $\partial_{E,H}^1 (\delta_K = 0) = \infty$ for only one single-domain region. For $\bar{\varphi}_{EA} < 80^\circ$, the tilt of $\bar{\varphi}_{EA}$ dominates $\partial_{E,H}^1$ and the influence of δ_K becomes negligible. Overall, $\partial_{E,H}^1$ decreases by about 50–80% at a tilt of only 10° from the ideal $\bar{\varphi}_{EA} = 90^\circ$ orientation for the δ_K considered. In contrast, $\partial_{E,H}^2$ is approximately constant with δ_K for all $\bar{\varphi}_{EA} > 60^\circ$ and is close to the analytical solution [Eq. (9)] at $\bar{\varphi}_{EA} = 90^\circ$. For smaller $\bar{\varphi}_{EA}$, δ_K dominates $\partial_{E,H}^2$ because a larger δ_K results in a stronger outaveraging of the center peak with increasing $\bar{\varphi}_{EA}$. In Fig. 5(b) the slope $\partial_{E,H}^0$ of $E(H)$ at $H = 0$ A/m is also plotted over $\bar{\varphi}_{EA}$. It exhibits a maximum at about $\bar{\varphi}_{EA} = 72^\circ$ with almost the same value as the minimum of $\partial_{E,H}^2$.

C. Comparison of the model with measurements

In the following, measurements on the bending-mode resonators with amorphous Fe-Co-Si-B multilayers are compared with the full numerical model from Sec. III that includes the spatially varying effective Young's modulus.

Magneto-optical Kerr effect (MOKE) microscopy [53, 54] is used to obtain data on the local magnetic properties of the magnetic multilayer. Images are taken in three parts (P1, P2, P3) along the cantilever for different magnetic fields starting close to magnetic saturation at about 10 mT. The optical sensitive axis is set along the intended easy axis, perpendicular to the cantilever's long axis.

The resulting magnetization curves are shown in Fig. 6(a) together with an illustration of the measurement configuration. Compared with region P2 in the center, the

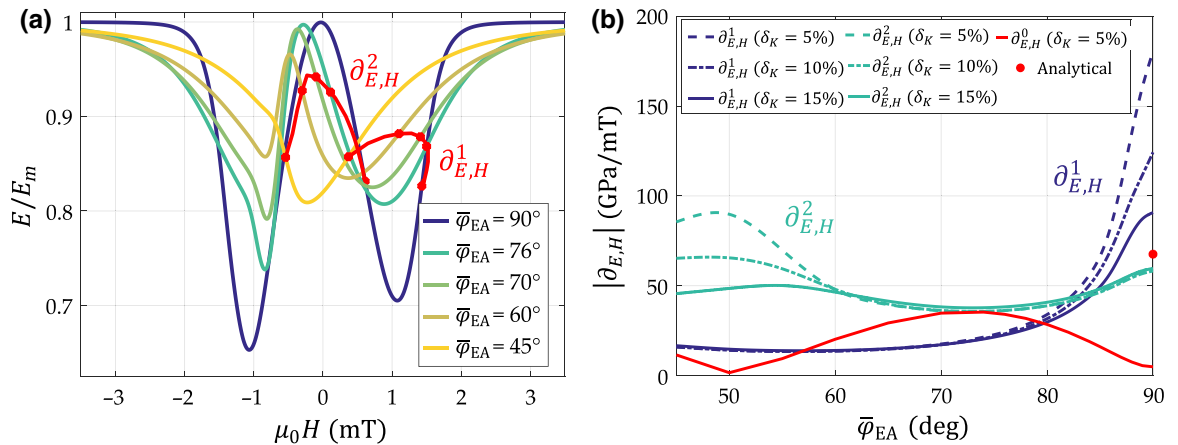


FIG. 5. (a) Influence of the tilt of the mean easy $\bar{\varphi}_{EA}$ from its ideal 90° orientation, with fixed dispersion parameters $\delta_K = 15\%$ and $\delta_{EA} = 0.6\%$. The two maximum slopes $\partial_{E,H}^1$ and $\partial_{E,H}^2$ of the magnetic field (H) dependent Young's modulus $E(H)$ are plotted with a red line. (b) Absolute of the slopes $\partial_{E,H}^1$ and $\partial_{E,H}^2$ for different δ_K and fixed $\delta_{EA} = 0.6\%$ plotted over the tilt angle $\bar{\varphi}_{EA}$ of the magnetic easy axis. The slope $\partial_{E,H}^0$ of $E(H)$ at $H = 0$ is indicated with a red line. The analytical solution from Eq. (9) is shown for comparison with a red dot.

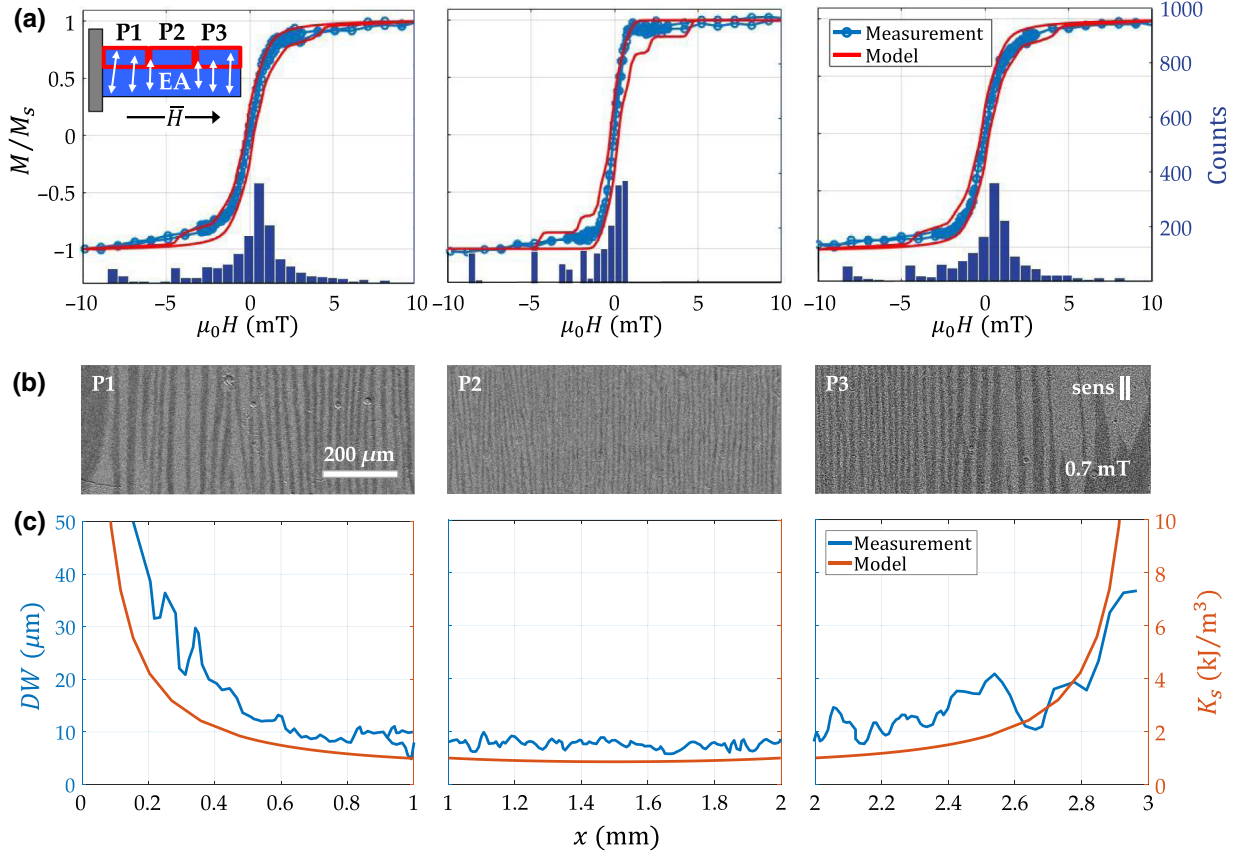


FIG. 6. Measurements and models of the cantilever sensor in three different regions (P1, P2, P3). The magnetic easy axis (EA) is induced perpendicular to the short axis. (a) Hysteresis curves for three regions along the beam compared with the results from the numerical model (red). The resulting distribution that entered the simulation via the spatial shape anisotropy is shown as a histogram of all H_a values [Eq. (5)]. (b) Example of magneto-optical Kerr effect measurements along the cantilever at 0.7 mT and (c) the domain width (DW) extracted from (b) and plotted over the cantilever length, compared with the calculated demagnetizing anisotropy energy density K_s .

magnetization curves from P1 and P3 exhibit smaller susceptibility and are more rounded. This is consistent with the magneto-optical measurements. They show that the domain formation starts at the left and right edges of the magnetic film. From there they move towards the center and reduce in width. An example is shown in Fig. 6(b) for an external field of 0.7 mT. Whereas small domain widths (DW) of about $10 \mu\text{m}$ are present in the center region P2, the domain width increases towards the left and the right edge of the sample in P1 and P3. This correlates with the distribution of the demagnetizing field, which increases towards the sample edges. Figure 6(c) illustrates this relation. Here, the mean domain widths extracted from the images are plotted over the cantilever length together with the shape-anisotropy constant K_s . The increase of K_s in P1 and P3 is consistent with the smaller susceptibility of the measured hysteresis curves in these regions. A discussion of magnetic domain width in the structures is not straightforward, but the overall inhomogeneity of the local demagnetization field distribution

[see also Fig. 3(b)] might play an additional role in the resulting magnetic domain distribution [55,56]. In addition to the internal stray field, other effects like stress anisotropies and material inhomogeneities can influence the local magnetic properties. Such effects may result in fluctuations of the domain width, visible in Fig. 6(c) on a smaller length scale. The measurements indicate that such influences play a minor role compared to the inhomogeneity of the internal stray field.

Simulations are made with a homogeneous intrinsic anisotropy energy density of $K_u = 1.6 \text{ kJ/m}^3$ and perfectly aligned magnetic easy axis $\bar{\varphi}_{\text{EA}} = 90^\circ$ in all regions. Neither distributions of K_u nor of $\bar{\varphi}_{\text{EA}}$ are used in the calculations. The only inhomogeneity used for the simulations is the spatially varying demagnetizing anisotropy energy density K_s from Fig. 3(b) to obtain its influence on the magnetization. The modeled hysteresis curves in Fig. 6(a) match overall with the measurements and resemble the tendency of a steeper curve in the center (P2) of the sample and rounder at the sample ends (P1 and P3). This, in

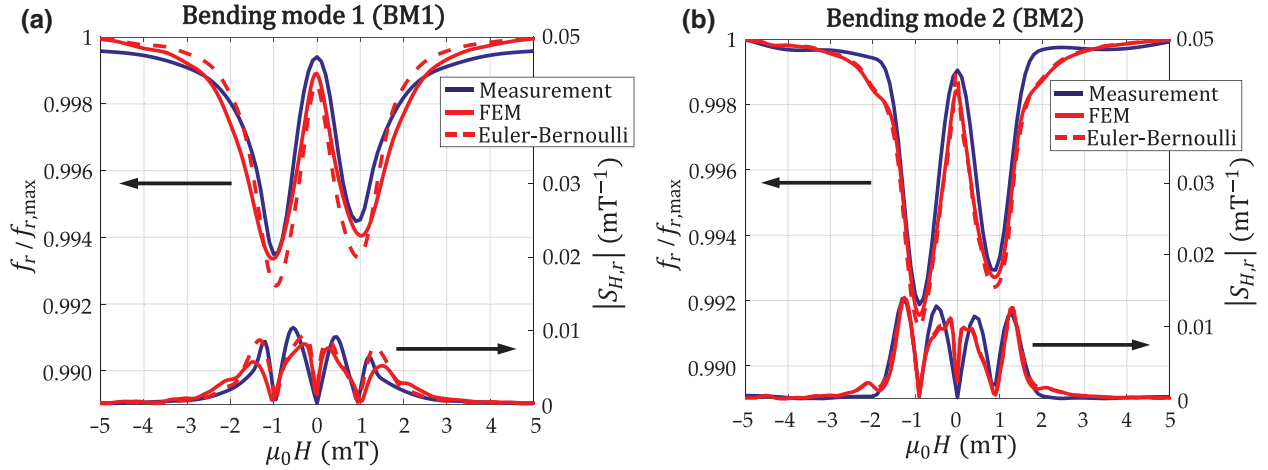


FIG. 7. Comparison of measured resonance frequency and relative magnetic sensitivity $S_{H,r}$ with results from the combined mean-field FE model and mean-field Euler-Bernoulli approximation for (a) the first bending mode (BM1) and (b) the second bending mode (BM2). Apart from the local stray field, no additional distributions are used for these calculations.

addition to the MOKE images, shows that the inhomogeneous demagnetizing field is the dominant reason for the spatially different magnetization response of the sample.

Discrepancies between model and measurements arise from a larger coercive field and steps in the modeled hysteresis curves. This is a direct consequence of averaging hysteresis loops of single-domain regions, which cannot resemble the domain formation that occurs in the real sample. As soon as the internal field is not 90° to the effective easy axis or if the effective easy axis switches, rotational hysteresis occurs. The local nonalignment and easy-axis magnetization process reduce the mean Delta-E effect in the model, as demonstrated in Fig. 4 for one single-domain region.

Impedance measurements are performed with an Agilent impedance analyzer in a Helmholtz coil setup with an excitation amplitude of 10 mV. The resonance frequencies are extracted from the impedance data using an mBVD fit as done previously [21]. Simulations for the resonance frequency $f_{r,1}$ of BM1 and $f_{r,2}$ of BM2 are compared with the measurements and the calculated $S_{H,r}$ in Fig. 7. Overall, the model matches and resembles the trend visible in the measurements. Compared to BM1, the resonance frequency $f_{r,2}$ shows a larger Delta-E effect with lower minima and a steeper curve. As expected, the larger impact of the distributions from region P1 in BM1 mainly affects the outer slope of $f_{r,1}$. It is worth mentioning that the model predicts the asymmetry in $f_{r,1}$ and $f_{r,2}$ well. It results from the averaging of the zero Young's modulus at the switching field. Such good agreement with the literature [45] emphasizes the importance of the spatial character of the effective anisotropy.

Deviations between model and measurements are visible for both resonance modes, especially around the center maximum, which is narrower and slightly lower in the

simulations. In this magnetic field regime, the demagnetizing field of the sample along the short axis is lower than the modeled one, due to the multilayer structure of the samples. In BM2 a mismatch is apparent at about ± 2 mT, which can result from the rough spatial discretization only along the long-beam axis. Also, local distributions, e.g., from anisotropic stress, can contribute to K_a [57] and result in partial mismatches with the measured $f_r(H)$. The good agreement between measurements and simulations indicates that the internal stray field strongly dominates and sufficiently describes the major differences between the two bending modes.

D. Optimum film thickness

In contrast to the single-domain model, increasing the magnetic layer thickness t does not result in $S_H \rightarrow \infty$ when approaching a critical thickness. Instead a maximum of S_H results, which is shown in Fig. 8 for the second bending mode of the current beam geometry. The origin of the maximum is the dependency of S_H on the spatial distribution of the internal stray field, which changes with the magnetic layer thickness t . At large t , the internal stray field overcomes K_u in most regions of the film. Consequently, the Delta-E effect is strongly reduced and a v-shaped curve results as shown in Fig. 8(b) with the example of $t = 6 \mu\text{m}$. Decreasing t results in more magnetoelastically active regions and a narrower distribution, which enhances the Delta-E effect. Simultaneously, the mean energy density \bar{K}_a increases with decreasing t , which counteracts the beneficial effects. The interplay of both effects yields a maximum of $S_{H,r}$ at about $t = 3.3 \mu\text{m}$. At this thickness, the $f_r(H)$ curve exhibits a maximum with a steep slope at around $H = 0$ [Fig. 8(b), $t = 3.3 \mu\text{m}$]. With $t \rightarrow 0$, the geometric factor G [Fig. 2(b)] increasingly

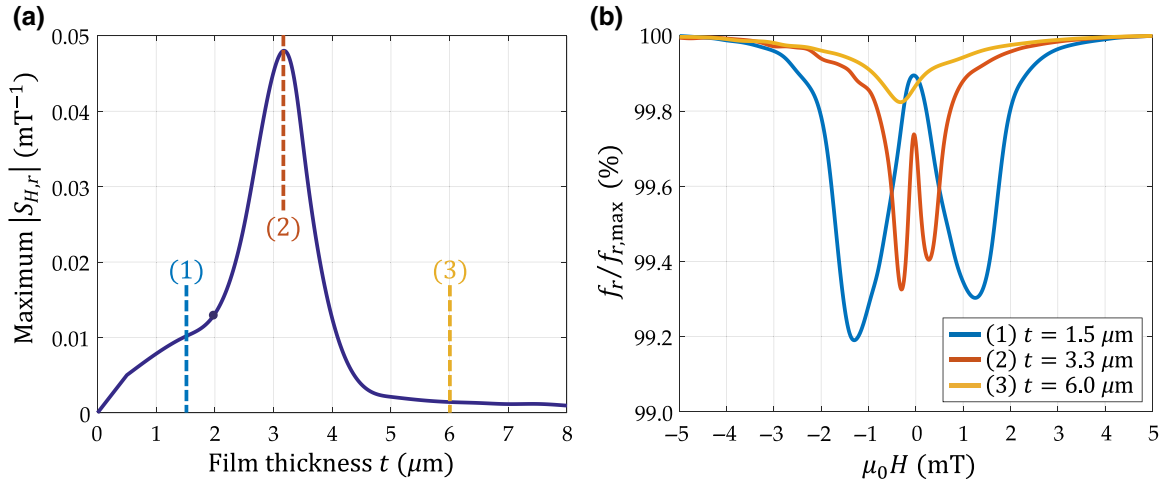


FIG. 8. (a) Maximum of the relative magnetic sensitivity $S_{H,r}$ calculated as a function of the magnetic layer thickness t for the second bending mode. (b) Examples of resonance frequency curves calculated for the three different layer thicknesses indicated in (a).

dominates $S_{H,r}$ and results in a decrease of the magnetic sensitivity until $S_{H,r} = 0$, although $\partial_{E,H} \gg 0$ [Fig. 8(b), $t = 1.5 \mu\text{m}$]. The maximum $S_{H,r}(t = 3.3 \mu\text{m})$ is about three times larger compared to $S_{H,r}$ of the current sensor geometry ($t = 2 \mu\text{m}$).

V. SUMMARY AND CONCLUSION

In this Paper, we analyze and discuss the Delta-E effect and the magnetic sensitivity of the first and second bending mode for cantilever Delta-E-effect sensors. Analytical expressions are derived and compared with the results of a numerical mean-field model. The numerical model additionally treats normal distributions of the effective anisotropy energy density and includes the spatially inhomogeneous internal stray field of the real specimen geometry. Magneto-optical imaging and resonance frequency measurements are analyzed and used for model validation.

As pointed out, the sensitivity is constant with the operating frequency if the magnetic properties are constant as well. With an analytical single-spin model, we describe the magnetic sensitivity as a function of material parameters and the geometry. From the model, the sensitivity can benefit strongly from a decrease in the substrate thickness to achieve a film-substrate thickness ratio of $t_r \approx 0.3$. Although the analytical simulations roughly match the measurements within a factor of 2, qualitative limitations arise from the single-spin approximation. Major limitations occur when describing the magnetic sensitivity as a function of the magnetic layer thickness or easy-axis angle. As a first-order improvement, a numerical mean-field model is analyzed that includes normal distributions of the effective anisotropy energy and easy-axis orientation. We quantify how small deviations from an ideal 90° easy-axis orientation can dramatically decrease the

maximum magnetic sensitivity. In our example, the sensitivity decreased by a factor of 2–6 for an easy-axis misalignment of only 5° . This effect reduces with increasing initial distributions present in the magnetic layer. For mean energy densities $\bar{K}_a \gg 0$ with distributions $\delta_a \ll \bar{K}_a$, the sensitivity approximately equals the analytical single-spin result.

Next, the internal stray field of the sample is included in the model as a physical origin for spatial variations in the magnetization behavior. The model is validated with resonance frequency measurements. It is shown that second-order bending modes are advantageous over first-order modes for the magnetic sensitivity of our sensors. This can be explained well by the internal stray field within the mean-field model and is confirmed with magneto-optical measurements. Because the internal stray field dominates the distributions, the numerical model can predict the influence of different bending modes on the Delta-E effect.

Finally, the magnetic sensitivity is calculated for the second bending mode as a function of the magnetic layer thickness t using the internal stray field of the real shape. In contrast to the analytical single-spin model, a maximum occurs at about $t = 3.3 \mu\text{m}$. The magnetic sensitivity approaches zero for thicker magnetic films, as expected.

In conclusion, we present a detailed and comprehensive analysis of the magnetic sensitivity for cantilever sensors. It is shown that spatial inhomogeneities must be considered for the design but also for the simulation of highly sensitive Delta-E-effect sensors. Because the magnetic properties are locally weighted by the curvature of the resonance mode, the Delta-E effect and the magnetic sensitivity can significantly differ depending on the mode shape. We show that the second bending mode can reduce the impact of the inhomogeneous internal stray fields and thereby increase the magnetic sensitivity. Consequently,

the weighting of local properties by the mode shape is not only key to understanding the Delta-E effect and the sensitivity of different resonance modes, but also an important factor in improving future sensitivities.

ACKNOWLEDGMENTS

This research is funded by the German Research Foundation (DFG) via the collaborative research center CRC 1261.

The authors declare no conflict of interest. The funders had no role in the design of the study; in the collection, analyses, or interpretation of data; in the writing of the manuscript, and in the decision to publish the results.

-
- [1] N. Akulov and E. Kondorsky, Über einen magnetomechanischen Effekt, *Zeitschrift Für Phys.* **78**, 801 (1932).
- [2] N. Akulov and E. Kondorsky, Über Mechanostriktion und δ E-Effekt, *Zeitschrift Für Phys.* **85**, 661 (1933).
- [3] M. Kersten, Über den Temperaturkoeffizienten des Elastizitätsmoduls ferromagnetischer Stoffe, *Zeitschrift Für Phys.* **85**, 708 (1933).
- [4] E. W. Lee, Magnetostriction and magnetomechanical effects, *Rep. Prog. Phys.* **18**, 184 (1955).
- [5] R. Becker and W. Döring, *Ferromagnetismus* (Verlag von Julius Springer, Berlin, 1939).
- [6] K. Honda and T. Terada, II, On the change of elastic constants of ferromagnetic substances by magnetization, *Philos. Mag. Ser. 6*, 36 (1907).
- [7] J. D. Livingston, Magnetomechanical properties of amorphous metals, *Phys. Status Solidi A* **70**, 591 (1982).
- [8] P. T. Squire, Phenomenological model for magnetization, magnetostriction and delta-E effect in field-annealed amorphous ribbons, *J. Magn. Magn. Mater.* **87**, 299 (1990).
- [9] P. T. Squire, Domain model for magnetoelastic behaviour of uniaxial ferromagnets, *J. Magn. Magn. Mater.* **140**, 1829 (1995).
- [10] Z. Sárközi, K. Mackay, and J. C. Peuzin, Elastic properties of magnetostrictive thin films using bending and torsion resonances of a bimorph, *J. Appl. Phys.* **88**, 5827 (2000).
- [11] O. Bou Matar, J. F. Robillard, J. O. Vasseur, A. C. Hladky-Hennion, P. A. Deymier, P. Pernod, and V. Preobrazhensky, Band gap tunability of magneto-elastic phononic crystal, *J. Appl. Phys.* **111**, 054901 (2012).
- [12] H. Zhou, A. Talbi, N. Tiercelin, and O. Bou Matar, Multilayer magnetostrictive structure based surface acoustic wave devices, *Appl. Phys. Lett.* **104**, 114101 (2014).
- [13] S. Datta, J. Atulasimha, C. Mudivarthi, and A. B. Flatau, Stress and magnetic field-dependent Young's modulus in single crystal iron-gallium alloys, *J. Magn. Magn. Mater.* **322**, 2135 (2010).
- [14] J. Gutiérrez, V. Muto, and P. T. Squire, Induced anisotropy and magnetoelastic properties in Fe-rich metallic glasses, *J. Non. Cryst. Solids* **287**, 417 (2001).
- [15] B. Gojdka, R. Jahns, K. Meurisch, H. Greve, R. Adelung, E. Quandt, R. Knöchel, and F. Faupel, Fully integrable magnetic field sensor based on delta-E effect, *Appl. Phys. Lett.* **99**, 1 (2011).
- [16] A. Kittmann, P. Durdaut, S. Zabel, J. Reermann, J. Schmalz, B. Spetzler, D. Meyners, N. X. Sun, J. McCord, M. Gerken, G. Schmidt, M. Höft, R. Knöchel, F. Faupel, and E. Quandt, Wide band low noise love wave magnetic field sensor system, *Sci. Rep.* **8**, 1 (2018).
- [17] F. Charles, Ph.D. thesis, University of Bath, 1992.
- [18] V. Polewczyk, K. Dumesnil, D. Lacour, M. Moutaouekkil, H. Mjahed, N. Tiercelin, S. Petit Watelot, H. Mishra, Y. Dusch, S. Hage-Ali, O. Elmazria, F. Montaigne, A. Talbi, O. Bou Matar, and M. Hehn, Unipolar and Bipolar High-Magnetic-Field Sensors Based on Surface Acoustic Wave Resonators, *Phys. Rev. Appl.* **8**, 1 (2017).
- [19] M. Li, A. Matyushov, C. Dong, H. Chen, H. Lin, T. Nan, Z. Qian, M. Rinaldi, Y. Lin, and N. X. Sun, Ultra-sensitive NEMS magnetoelectric sensor for picotesla DC magnetic field detection, *Appl. Phys. Lett.* **110**, 143510 (2017).
- [20] Y. Hui, T. Nan, N. X. Sun, and M. Rinaldi, High resolution magnetometer based on a high frequency magnetoelectric MEMS-CMOS oscillator, *J. Microelectromech. Syst.* **24**, 134 (2015).
- [21] S. Zabel, C. Kirchhof, E. Yarar, D. Meyners, E. Quandt, and F. Faupel, Phase modulated magnetoelectric delta-E effect sensor for sub-nano tesla magnetic fields, *Appl. Phys. Lett.* **107**, 152402 (2015).
- [22] S. Zabel, J. Reermann, S. Fichtner, C. Kirchhof, E. Quandt, B. Wagner, G. Schmidt, and F. Faupel, Multimode delta-E effect magnetic field sensors with adapted electrodes, *Appl. Phys. Lett.* **108**, 222401 (2016).
- [23] T. Nan, Y. Hui, M. Rinaldi, and N. X. Sun, Self-biased 215 MHz magnetoelectric NEMS resonator for ultra-sensitive DC magnetic field detection, *Sci Rep.* **3**, 1985 (2013).
- [24] J. Reermann, S. Zabel, C. Kirchhof, E. Quandt, F. Faupel, and G. Schmidt, Adaptive readout schemes for thin-film magnetoelectric sensors based on the delta-E effect, *IEEE Sens. J.* **16**, 4891 (2016).
- [25] P. Durdaut, J. Reermann, S. Zabel, C. Kirchhof, E. Quandt, F. Faupel, G. Schmidt, R. Knöchel, and M. Höft, Modeling and analysis of noise sources for thin-film magnetoelectric sensors based on the delta-E effect, *IEEE Trans. Instrum. Meas.* **66**, 2771 (2017).
- [26] B. Spetzler, C. Kirchhof, J. Reermann, P. Durdaut, M. Höft, G. Schmidt, E. Quandt, and F. Faupel, Influence of the quality factor on the signal to noise ratio of magnetoelectric sensors based on the delta-E effect, *Appl. Phys. Lett.* **114**, 183504 (2019).
- [27] L. Duez, S. Beniczky, H. Tankisi, P. O. Hansen, P. Sidenius, A. Sabers, and A. Fuglsang-Frederiksen, Added diagnostic value of magnetoencephalography (MEG) in patients suspected for epilepsy, where previous, extensive EEG workup was unrevealing, *Clin. Neurophysiol.* **127**, 3301 (2016).
- [28] J. S. W. Kwong, B. Leithäuser, J. W. Park, and C. M. Yu, Diagnostic value of magnetocardiography in coronary artery disease and cardiac arrhythmias: A review of clinical data, *Int. J. Cardiol.* **167**, 1835 (2013).
- [29] V. Sakkalis, Review of advanced techniques for the estimation of brain connectivity measured with EEG/MEG, *Comput. Biol. Med.* **41**, 1110 (2011).

- [30] R. Kleiner, D. Koelle, F. Ludwig, and J. Clarke, Superconducting quantum interference devices: State of the art and applications, *Proc. IEEE* **92**, 1534 (2004).
- [31] C. N. Johnson, P. D. D. Schwindt, and M. Weisend, Multi-sensor magnetoencephalography with atomic magnetometers, *Phys. Med. Biol.* **58**, 6065 (2013).
- [32] W. C. Griffith, S. Knappe, and J. Kitching, Femtotesla atomic magnetometry in a microfabricated vapor cell, *Opt. Express* **18**, 27167 (2010).
- [33] J. Reermann, P. Durdaut, S. Salzer, T. Demming, A. Piorra, E. Quandt, N. Frey, M. Höft, and G. Schmidt, Evaluation of magnetoelectric sensor systems for cardiological applications, *Meas. J. Int. Meas. Confed.* **116**, 230 (2018).
- [34] C. W. Nan, M. I. Bichurin, S. Dong, D. Viehland, and G. Srinivasan, Multiferroic magnetoelectric composites: Historical perspective, status, and future directions, *J. Appl. Phys.* **103**, 031101 (2008).
- [35] V. Röbisch, E. Yarar, N. O. Urs, I. Teliban, R. Knöchel, J. McCord, E. Quandt, and D. Meyners, Exchange biased magnetoelectric composites for magnetic field sensor application by frequency conversion, *J. Appl. Phys.* **117**, 1 (2015).
- [36] S. Marauska, R. Jahns, C. Kirchhof, M. Claus, E. Quandt, R. Knöchel, and B. Wagner, Highly sensitive wafer-level packaged MEMS magnetic field sensor based on magnetoelectric composites, *Sens. Actuators, A* **189**, 321 (2013).
- [37] E. Yarar, V. Hrkac, C. Zamponi, A. Piorra, L. Kienle, and E. Quandt, Low temperature aluminum nitride thin films for sensory applications, *AIP Adv.* **6**, 075115 (2016).
- [38] V. Hrkac, E. Lage, G. Köppel, J. Strobel, J. McCord, E. Quandt, D. Meyners, and L. Kienle, Amorphous FeCoSiB for exchange bias coupled and decoupled magnetoelectric multilayer systems: Real-structure and magnetic properties, *J. Appl. Phys.* **116**, 134302 (2014).
- [39] P. Durdaut, M. Höft, J.-M. Friedt, and E. Rubiola, Equivalence of open-loop and closed-loop operation of SAW resonators and delay lines, *Sensors* **19**, 185 (2018).
- [40] R. C. O'Handley, *Modern Magnetic Materials Principles and Applications* (John Wiley & Sons, Hoboken, 2000).
- [41] E. C. Stoner and E. P. Wohlfarth, A mechanism of magnetic hysteresis in heterogeneous alloys, *Philos. Trans. R. Soc. London* **240**, 599 (1948).
- [42] D. L. Atherton and J. R. Beattie, A mean field stoner-wohlfarth hysteresis model, *IEEE Trans. Magn.* **26**, 3059 (1990).
- [43] S. J. Collocott, Application of the StonerWohlfarth model with interaction for the determination of the saturation magnetisation, anisotropy field, and mean field interaction in bulk amorphous ferromagnets, *J. Magn. Magn. Mater.* **323**, 2023 (2011).
- [44] S. Schmid, L. G. Villanueva, and M. L. Roukes, *Fundamentals of Nanomechanical Resonators* (Springer International Publishing, Switzerland, 2016).
- [45] A. Ludwig and E. Quandt, Optimization of the delta E effect in thin films and multilayers by magnetic field annealing, *IEEE Trans. Magn.* **38**, 2829 (2002).
- [46] J. Gutiérrez, A. García-Arribas, J. S. Garitaonandia, J. M. Barandiarán, and P. T. Squire, ΔE effect and anisotropy distribution in metallic glasses with oblique easy axis induced by field annealing, *J. Magn. Magn. Mater.* **157**, 543 (1996).
- [47] A. Aharoni, Demagnetizing factors for rectangular ferromagnetic prisms, *J. Appl. Phys.* **83**, 3432 (1998).
- [48] A. Aharoni, L. Pust, and M. Kief, Comparing theoretical demagnetizing factors with the observed saturation process in rectangular shields, *J. Appl. Phys.* **87**, 6564 (2000).
- [49] A. Aharoni, "Local" demagnetization in a rectangular ferromagnetic prism, *Phys. Status Solidi Basic Res.* **229**, 1413 (2002).
- [50] G. Herzer, Magnetomechanical damping in amorphous ribbons with uniaxial anisotropy, *Mater. Sci. Eng. A* **226**, 631 (1997).
- [51] G. Herzer, Effect of domain size on the magneto-elastic damping in amorphous ferromagnetic metals, *Zeitschrift Für Met.* **93**, 978 (2002).
- [52] S. Azzawi, A. T. Hindmarch, and D. Atkinson, Magnetic damping phenomena in ferromagnetic thin-films and multilayers, *J. Phys. D: Appl. Phys.* **50**, 473001 (2017).
- [53] J. McCord, Progress in magnetic domain observation by advanced magneto-optical microscopy, *J. Phys. D: Appl. Phys.* **48**, 333001 (2015).
- [54] T. Von Hofe, N. Onur Urs, B. Mozooni, T. Jansen, C. Kirchhof, D. E. Bürgler, E. Quandt, and J. McCord, Dual wavelength magneto-optical imaging of magnetic thin films, *Appl. Phys. Lett.* **103**, 142410 (2013).
- [55] H. A. M. Van Den Berg and D. K. Vatvani, Wall clusters and domain structure conversions, *IEEE Trans. Magn.* **18**, 880 (1982).
- [56] J. McCord, A. Hubert, and A. Chizhik, Domains and hysteresis in patterned soft magnetic elements, *IEEE Trans. Magn.* **33**, 3981 (1997).
- [57] J. McCord, Irregular domain patterns in structured magnetic thick films, *J. Appl. Phys.* **95**, 6855 (2004).

4.2 Frequency Dependency of the ΔE Effect

The ΔE effect and magnetic sensitivity were analyzed in different bending modes with resonance frequencies of the order of several kilohertz in the previous section. A larger resonance frequency f_r can be advantageous for several reasons. First, the signal bandwidth BW of the sensor increases linearly with f_r . In the bending mode resonators analyzed in the previous section, BW is between 5 Hz and 100 Hz. Second, thermal electrical $1/f$ (f: frequency) noise can reduce the LOD at low frequencies. A small size of the resonator is potentially accompanied by a high spatial resolution and low power consumption, and it can permit the design of compact devices and sensor arrays with many sensor elements. Yet, the resonance frequency is inversely proportional to the dimensions of the resonator and typically in the megahertz regime for micrometer-sized sensor elements. Such high resonance frequencies can also occur in cm-sized devices, e.g., because of specific resonance modes selected for other reasons. One example is the surface acoustic wave device demonstrated in Section 5.1 that operates at ≈ 150 MHz.


In this section, the frequency dependency of the ΔE effect is discussed and used to estimate the magnetic sensitivity as a function of the resonance frequency. In contrast to previous quasi-static approaches appropriate for comparatively low frequencies, the calculations presented here are based on the linearization of the Landau-Liftshitz-Gilbert equation that remains valid for high frequencies around the ferromagnetic resonance.

Contribution

- Conceptualization
- Writing of original manuscript (shared)
- Modeling and simulations (shared)
- Data analysis and interpretation (shared)

Article

Frequency Dependency of the Delta-E Effect and the Sensitivity of Delta-E Effect Magnetic Field Sensors

Benjamin Spetzler, Elizaveta V. Golubeva, Cai Müller, Jeffrey McCord and Franz Faupel * 

Kiel University, 24118 Kiel, Germany; besp@tf.uni-kiel.de (B.S.); elgo@tf.uni-kiel.de (E.V.G.);
camu@tf.uni-kiel.de (C.M.); jmc@tf.uni-kiel.de (J.M.)

* Correspondence: ff@tf.uni-kiel.de; Tel.: +49-431-880-6229

Received: 16 October 2019; Accepted: 31 October 2019; Published: 2 November 2019



Abstract: In recent years the delta-E effect has been used for detecting low frequency and low amplitude magnetic fields. Delta-E effect sensors utilize a forced mechanical resonator that is detuned by the delta-E effect upon application of a magnetic field. Typical frequencies of operation are from several kHz to the upper MHz regime. Different models have been used to describe the delta-E effect in those devices, but the frequency dependency has mainly been neglected. With this work we present a simple description of the delta-E effect as a function of the differential magnetic susceptibility χ of the magnetic material. We derive an analytical expression for χ that permits describing the frequency dependency of the delta-E effect of the Young's modulus and the magnetic sensitivity. Calculations are compared with measurements on soft-magnetic $(\text{Fe}_{90}\text{Co}_{10})_{78}\text{Si}_{12}\text{B}_{10}$ thin films. We show that the frequency of operation can have a strong influence on the delta-E effect and the magnetic sensitivity of delta-E effect sensors. Overall, the delta-E effect reduces with increasing frequency and results in a stiffening of the Young's modulus above the ferromagnetic resonance frequency. The details depend on the Gilbert damping. Whereas for large Gilbert damping the sensitivity continuously decreases with frequency, typical damping values result in an amplification close to the ferromagnetic resonance frequency.

Keywords: delta-E effect; magnetoelasticity; resonators; magnetic field sensing; dynamic susceptibility; surface acoustic wave (SAW)

1. Introduction

The change of the effective elastic properties with magnetization is referred to as the delta-E effect. It results from inverse magnetostriction that adds an additional strain to the purely elastic Hookean strain [1–3]. The delta-E effect has been used to build various types of magnetic field sensors for the detection of low frequency and low amplitude magnetic fields. The first integrable devices [4] were achieved using magnetoelectric MEMS (Micro-Electro-Mechanical Systems) cantilevers [5–7] and nano-plate resonators [8–10] with thin soft-magnetic layers from 100 nm–2 μm . These structures are excited electrically via a piezoelectric layer to oscillate at their respective resonance frequencies. Typical operation frequencies are from several kHz up to several hundred MHz [11]. Upon application of a magnetic field, the Young's modulus of the magnetostrictive layer changes, which detunes the resonance frequency. Similar kinds of delta-E effect sensors are based on surface acoustic wave (SAW) devices [12–17]. Rayleigh or Love waves are excited with interdigital electrodes at MHz frequencies up to the low GHz regime. The surface waves propagate through a magnetic thin film which is deposited on top of the delay line. Upon application of a magnetic field, the delta-E effect of the magnetic material results in a delay of the surface wave which can be detected as a phase change at the output electrodes. Both kinds of delta-E effect sensors require an external or internal magnetic bias field to be operated at

their optimum sensitivities. Besides sensor applications, the delta-E effect has been used for tunable SAW devices operating up to the GHz range [18–24].

Early experiments and models on the frequency dependency of the delta-E effect focused mainly on polycrystalline nickel rods. In these structures, a strong decrease (from 20% down to 3%) of the delta-E effect was found by an increase of the frequency from a few kHz up to 10 MHz [25,26]. The good agreement with calculations showed that this phenomenon can be assigned to eddy current damping: at low frequencies, micro eddy currents increasingly impede domain wall motion until also the moment rotation is being damped [27]. These calculations are made for bulk structures and are limited to the demagnetized state. The models are based on a quasi-static approach and are only valid for frequencies well below the ferromagnetic resonance frequency.

Despite the first theoretical attempts and the interest in high frequency devices, the existing delta-E effect models [2,28–35] are mainly quasi-static single-spin approaches. Dynamic magnetoelastic models treat the wave velocity [36–38] of Rayleigh waves and the electrically driven ferromagnetic resonance [39,40]. Neither calculations for the dynamic delta-E effect nor for the sensitivity for delta-E effect sensors are available.

Here we present a simple but general approach to include the frequency dependency in calculations of the delta-E effect of the Young's modulus. It is applied to the example of the high frequency regime using a linearization of the magnetization dynamics. Calculations of the dynamic susceptibility are compared with measurements on soft-magnetic material, which has been used for magnetic field sensing before. The resulting parameters are used to calculate the Young's modulus $E(H, f)$ as a function of magnetic field H and operation frequency f . From $E(H, f)$ the magnetic part $\partial_{E,H} := \partial E / \partial H$ of the sensitivity $S \propto \partial_{E,H}$ is calculated for resonators dominated by the Young's modulus. Finally, the results are compared with measurements from the literature.

2. The Delta-E Effect

In the following section, a simple equation for the delta-E effect as a function of the differential susceptibility and the magnetoelastic properties is derived and illustrated. Next, an expression for the dynamic differential susceptibility is presented that permits us to describe the frequency and magnetic field dependency of the Young's modulus.

2.1. The ΔE -Effect

The change of Young's modulus E with the magnetic field results from a change of the magnetoelastic response upon magnetization. Applying a stress σ to the magnetic material results in a purely mechanical strain $e = E_m^{-1}\sigma$, inversely proportional to Young's modulus E_m at fixed magnetization. The mechanical strain e is superposed by a stress induced magnetostrictive strain λ that depends on the magnetization M . The total Young's modulus can be described by [3]

$$\frac{1}{E} = \frac{\partial(e + \lambda)}{\partial\sigma} := \frac{1}{E_m} + \frac{1}{\Delta E} \text{ with } \frac{1}{\Delta E} := \frac{\partial\lambda}{\partial\sigma} = \frac{\partial\lambda}{\partial H} \frac{\partial H}{\partial M} \frac{\partial M}{\partial\sigma}. \quad (1)$$

This expression is rearranged to describe the delta-E effect as a function of easy to measure magnetic properties. Using the relation $\partial M / \partial\sigma = (1/\mu_0)\partial\lambda / \partial H$ [41] to replace $\partial M / \partial\sigma$, the equation becomes

$$\frac{1}{\Delta E} = \frac{(\partial\lambda/\partial H)^2}{\mu_0\partial M/\partial H} := \frac{\chi_{me}^2}{\mu_0\chi}, \quad (2)$$

which is consistent with [3]. Consequently, the change of Young's modulus is inversely proportional to the square of the differential magnetoelastic susceptibility $\chi_{me} := \partial\lambda/\partial H$, with the differential magnetic susceptibility $\chi := \partial M/\partial H$ as a proportionality factor.

The relation between $M(H)$, $\lambda(H)$ and $E(H)$ is illustrated in Figure 1 in the example of a soft magnetic amorphous FeCoSiB thin film with uniaxial magnetic anisotropy, typical for cantilever delta-E

effect sensors [7]. A mean-field model based on a single-spin ensemble is used to describe $\lambda(H)$ and $M(H)$, required for Equation (2). Details of the model and the material parameters are given in the Appendix A. A slight hysteresis occurs in $M(H)$, $\lambda(H)$ and $E(H)$ due to a dispersion of the magnetic easy axis introduced in the model. Note that the minimum of $E(H)$ is at slightly larger fields than the maximum of χ_{me}^2 . This occurs because χ_{me}^2 is divided in Equation (2) by $\mu_0\chi$, which is maximum around $H = 0$. The calculation in Figure 1 is consistent the measurements [42] and the trend reported in the literature [29,43].

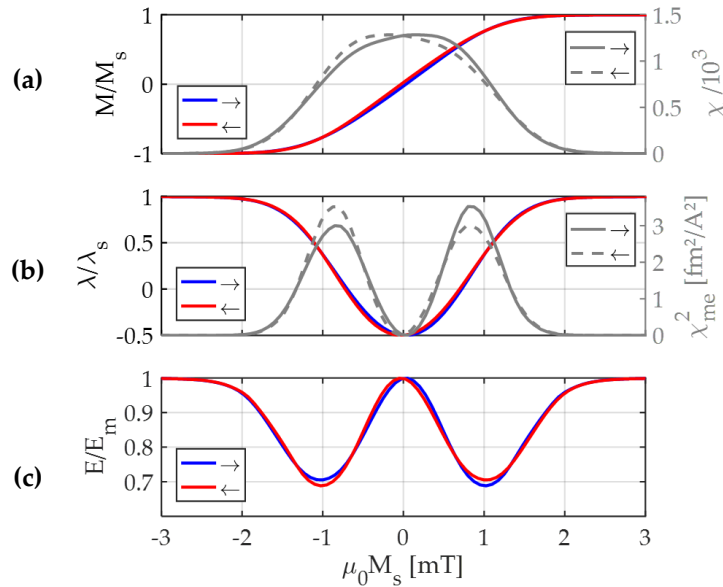


Figure 1. Illustration of the proportionality of the delta-E effect to the squared magnetoelastic susceptibility $\chi_{\text{me}}^2 := (\partial\lambda/\partial H)^2$ in Equation (2) using a mean-field model based on a single-spin ensemble (Appendix A). (a) Modelled magnetic hysteresis curve normalized to the saturation magnetization M_s and the differential magnetic susceptibility χ ; (b) modelled magnetostriction curve, normalized to the magnetostriction λ_s at magnetic saturation and its squared derivative χ_{me}^2 ; (c) resulting Young's modulus E as function of the applied magnetic field H , normalized to its value E_m at fixed magnetization. The mean-field model and the parameters used for the simulation are given in the Appendix A.

2.2. Frequency Dependency of the Young's Modulus

To describe the frequency dependency of the delta-E effect, Equation (2) cannot be used directly, because both χ_{me} and χ are functions of the magnetization. Instead, the magnetic field and magnetization dependency of χ_{me} are separated to describe E as function of χ only. For that, we first use the common quadratic approximation of λ [44] to form the derivative of the magnetostrictive strain to the magnetization

$$\lambda = \frac{3}{2}\lambda_s\left(m_0^2 - \frac{1}{3}\right) \rightarrow \frac{\partial\lambda}{\partial M} = \frac{1}{M_s} \frac{\partial\lambda}{\partial m_0} = \frac{3\lambda_s m_0}{M_s}. \quad (3)$$

In this equation, m_0 is the projection of the normalized quasi-static magnetization vector \bar{m}_0 on the axis of the applied static bias field \bar{H} . The expression $\chi_{\text{me}} := \partial\lambda/\partial H = \partial\lambda/\partial M \cdot \partial M/\partial H$ is substituted into Equation (2) with $\partial\lambda/\partial M$ from Equation (3), which results in

$$\frac{1}{\Delta E} = \frac{\chi}{\mu_0} \left(\frac{\partial\lambda}{\partial M}\right)^2 = \frac{9\lambda_s^2 m_0^2}{\mu_0 M_s^2} \chi. \quad (4)$$

Then the Young's modulus $E(H, f)$ finally is

$$E(H, f) = \left(\frac{1}{E_m} + \frac{1}{\Delta E(H, f)} \right)^{-1} \text{ with } \frac{1}{\Delta E} = \frac{9\lambda_s^2 m_0^2}{\mu_0 M_s^2} \chi. \quad (5)$$

The magnetostrictive strain $\lambda(M)$ results from the strain response of the mechanical structure to the magnetization induced magnetoelastic stress. Measurements and simulations on FePt nanoparticles indicate that this local structural response occurs on the timescale of a few pico-seconds [45]. Hence, we assume $\lambda(M)$ to be constant in the GHz regime which is of interest here. With this the differential dynamic susceptibility χ can be used to describe the frequency dependency of the delta-E effect. For the specific situation of a hard axis magnetization process the projection $m_0(H)$ can be eliminated from Equation (5) with the Stoner–Wohlfarth model [46]. The solution for a hard axis magnetization process is [44,46]

$$m_0(H) = \left\{ \begin{array}{ll} H/H_K & |H| < H_K \\ 1 & |H| > H_K \end{array} \right\}. \quad (6)$$

The effective anisotropy field $H_K = 2K/(\mu_0 M_s)$ is expressed via the first order anisotropy constant K . The final solution for the Young's modulus $E(H, f)$ as a function of the differential susceptibility for this specific case is

$$E(H, f) = \left\{ \begin{array}{ll} 1/E_m + 1/\Delta E & |H| < H_K \\ E_m & |H| > H_K \end{array} \right\} \text{ with } \frac{1}{\Delta E} = \frac{9}{4} \frac{\mu_0 \lambda_s^2 H^2}{K^2} \chi. \quad (7)$$

2.3. Dynamic Differential Susceptibility

For the differential dynamic susceptibility, a single spin model is used. The motion of the magnetic moments is described by the Landau–Lifshitz–Gilbert equation [47]:

$$\frac{\partial \bar{M}}{\partial t} = \gamma \bar{M} \times \bar{H}_{\text{eff}} + \frac{\alpha}{M_s} \bar{M} \times \frac{\partial \bar{M}}{\partial t}. \quad (8)$$

In the equation, γ is the gyromagnetic ratio, α is the Gilbert damping parameter, \bar{H}_{eff} is the effective field vector and \bar{M} is the magnetization vector. The components of the effective field result from the energy density function u , which is given in the Appendix A. For u we consider an effective uniaxial energy density, a Zeeman term and a demagnetizing energy density. The components $H_{\text{eff},i}$ of the effective field are then given by

$$H_{\text{eff},i} = H_K (m_{0,1}ea_1 + m_{0,2}ea_2 + m_{0,3}ea_3)ea_i + H_i + H_{d,i} \text{ with } i = 1, 2, 3. \quad (9)$$

The components $H_{d,i} = D_{ii}M_s m_{0,i}$ of the demagnetizing field are given by the product of the respective component $m_{0,i}$ of the normalized magnetization and the component D_{ii} of the diagonal demagnetizing tensor \mathbf{D} . The direction cosines of the easy axis vector are given by ea_i . H_i are the components of the applied static magnetic field vector.

The spin dynamic is linearized using a procedure similar to the one commonly used for ferromagnetic resonance (FMR) calculations [48,49]. In our case, the effective AC driving field is aligned with the magnetic bias field. The fact that the AC effective field originates from an external stress and not from an external magnetic field does not change the calculation procedure. \bar{m}_0 can be obtained from minimizing the energy density u numerically or from Equation (6) in the ideal hard axis

case. The following expression is the result for the component $\chi_{11} := \chi$ of the dynamic differential magnetic susceptibility along the magnetic bias field

$$\chi = \frac{\gamma M_s m_{0,2}^2}{\gamma(H_{\text{eff}} + M_s \tilde{D} - H_K \tilde{e}a^2 - \alpha i\omega/\gamma) - \frac{\omega^2}{\gamma(H_{\text{eff}} + M_s D_{33} - \frac{\alpha i\omega}{\gamma})}}, \quad (10)$$

with $\tilde{D} := D_{11}m_{0,2}^2 + D_{22}m_{0,1}^2$, $\tilde{e}a := ea_1m_{0,2} + ea_2m_{0,1}$ and the angular frequency $\omega = 2\pi f$ of the driving field. The magnitude H_{eff} of the effective field is given by $H_{\text{eff}} = (H_{\text{eff},1}^2 + H_{\text{eff},2}^2 + H_{\text{eff},3}^2)^{1/2}$ with $H_{\text{eff},i}$ from Equation (9). The full tensor of the differential susceptibility and more details on the calculation procedure are given in the Appendix A. Together with Equation (5) or Equation (7), Equation (10) can be used to describe the frequency and magnetic field dependency of the Young's modulus. Results are shown and discussed in the following section.

3. Results and Discussion

In this section, we first present results of the dynamic susceptibility and the Young's modulus $E(H, f)$ from an ideal single-spin. Afterwards, a mean-field model is used to compare the modeled magnetization $M(H)$ and the ferromagnetic resonance frequency f_{FMR} with measurements. The extracted parameters are used to calculate the magnetic part $\partial_{E,H} := \partial E / \partial H$ of the sensitivity of delta-E effect sensors as a function of damping parameter α and operation frequency f .

For all calculations in this section, we consider a thin film for which the approximation $D_{11} \approx 0$, $D_{22} \approx 0$ and $D_{33} \approx 1$ holds well. For the material parameters we consider the gyromagnetic ratio $\gamma = 2.21 \times 10^{-5}$ Hz/(A/m) [50] of the free electron, a saturation magnetostriction of $\lambda_s = 35$ ppm [42] and a saturation Young's modulus of $E_m = 150$ GPa [42]. We use $K = 1400$ J/m³ and a saturation flux density of $\mu_0 M_s = 1.48$ T, obtained from the measurements in Section 3.2.

3.1. Frequency Dependency of the Young's Modulus and Dynamic Susceptibility

In the following section, we illustrate the frequency and magnetic bias field dependency of the differential dynamic susceptibility χ and the Young's modulus E . Calculations are made with the example of an ideal hard-axis magnetization process of a single-spin. For the Young's modulus Equation (7) is used with the dynamic differential susceptibility χ from Equation (10). A damping parameter of $\alpha = 0.02$ is used.

In Figure 2a the results for the normalized quasi-static magnetization M/M_s and the normalized magnetostrictive strain λ/λ_s are illustrated. They resemble the well-known Stoner–Wohlfarth behavior of a uniaxial anisotropy material. Because $M(H)$ is a linear function for $-H_K < H < H_K$, the static differential susceptibility χ_0 is constant in this magnetic field regime. The real part $Re\{\chi\}$ of the differential dynamic susceptibility χ (Figure 2b) is consistent with the quasi-static solution at low frequencies. With increasing frequency, the discontinuity around $H = H_K$ is rounded off and $Re\{\chi\}$ develops two minima. The minima occur due to the continuous shift of the ferromagnetic resonance frequency from $f_{\text{FMR}} = 0$ Hz at $H = \pm H_K$ (due to the simple single-spin model) up to about $f_{\text{FMR}} = 1.65$ GHz at $H = 0$. The result at $H = 0$ is equal to the result from the equation of Kittel [51].

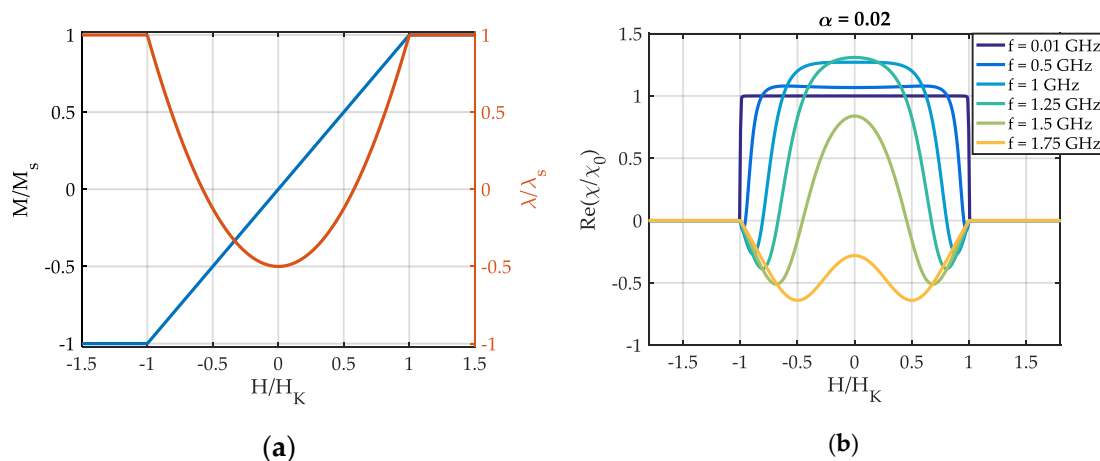


Figure 2. (a) Modelled magnetization component M along the magnetically hard axis, normalized to the value M_s at magnetic saturation and the magnetostrictive strain λ normalized to its value λ_s at magnetic saturation. (b) Modelled real part $Re(\chi)$ of the dynamic differential susceptibility χ (Equation (10)), normalized to the static susceptibility $\chi_0 \approx 639$ of its quasi-static magnetization value at a magnetic bias field $H = 0$.

In Figure 3a the real part $Re\{E\}$ of the Young's modulus is plotted, normalized to its value E_m at magnetic saturation. At low frequencies ($f = 0.01$ GHz), $Re\{E(H)\}$ is consistent with the results from quasi-static single-spin models [2,28]. With increasing excitation frequency f , the curve rounds out and develops two maxima E_{max} in addition to the minima E_{min} present at quasi static f . These maxima have been observed experimentally in a previous study [22]. The change of the maxima E_{max} and minima E_{min} with frequency depends strongly on the damping factor α as shown in Figure 3b. For $\alpha = 0.03$, E_{min} continuously increases with f . For smaller α , a minimum occurs in $E_{min}(f)$ that is more pronounced for lower damping and shifted to higher f . The maximum of E_{max} increases for smaller α and shifts to lower frequencies.

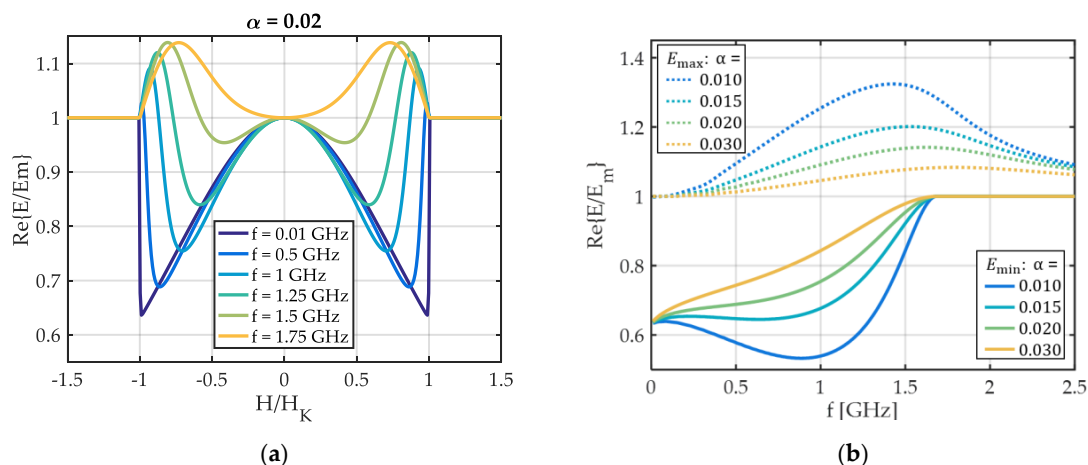


Figure 3. Results for the real part $Re(E)$ of the Young's modulus E , normalized to its value E_m at magnetic saturation. (a) As a function of the magnetic bias field for different excitation frequencies f and (b) the evolution of maxima and minima visible in (a) with the excitation frequency f .

The complete dependency of the complex $E(H, f)$ and $\chi(H, f)$ are shown in Figure 4. The behavior of the Young's modulus with frequency can be understood by considering the ferromagnetic resonance frequency f_{FMR} . The f_{FMR} is obtained from the maximum of the imaginary part $Im\{\chi(f)\}$ of the dynamic differential susceptibility χ (Figure 4a, bottom) in frequency f . A dashed red line in Figure 4a(bottom) shows how the f_{FMR} changes with the magnetic bias field H and f . Starting at $H = 0$, f_{FMR} continuously

decreases until $|H| = H_K$. The decrease occurs, because the AC magnetization always oscillates in a plane perpendicular to \bar{m}_0 . Hence, it oscillates along the hard axis initially at $H = 0$. With rotation of \bar{m}_0 , the AC magnetization increasingly oscillates along the easy axis. Consequently, the restoring force reduces and f_{FMR} decreases. For $|H| > H_K$, $\text{Im}\{\chi\}$ and $\text{Re}\{\chi\}$ are zero because $m_{0,2} = 0$ in Equation (10). At the ferromagnetic resonance frequency f_{FMR} , the sign of the real part $\text{Re}\{\chi\}$ of χ changes and becomes negative above it (Figure 4a, top). Consequently, the change of sign occurs also at f_{FMR} in $\text{Re}\{\Delta E\}$ as defined in Equation (4). Though, because of the inversion, the frequency at which $\text{Re}\{E/E_m\} = 1$ is at frequencies $f > f_{\text{FMR}}$ in Figure 4b (top). The same applies for the maximum of $\text{Im}\{E/E_m\}$ in Figure 4b (bottom).

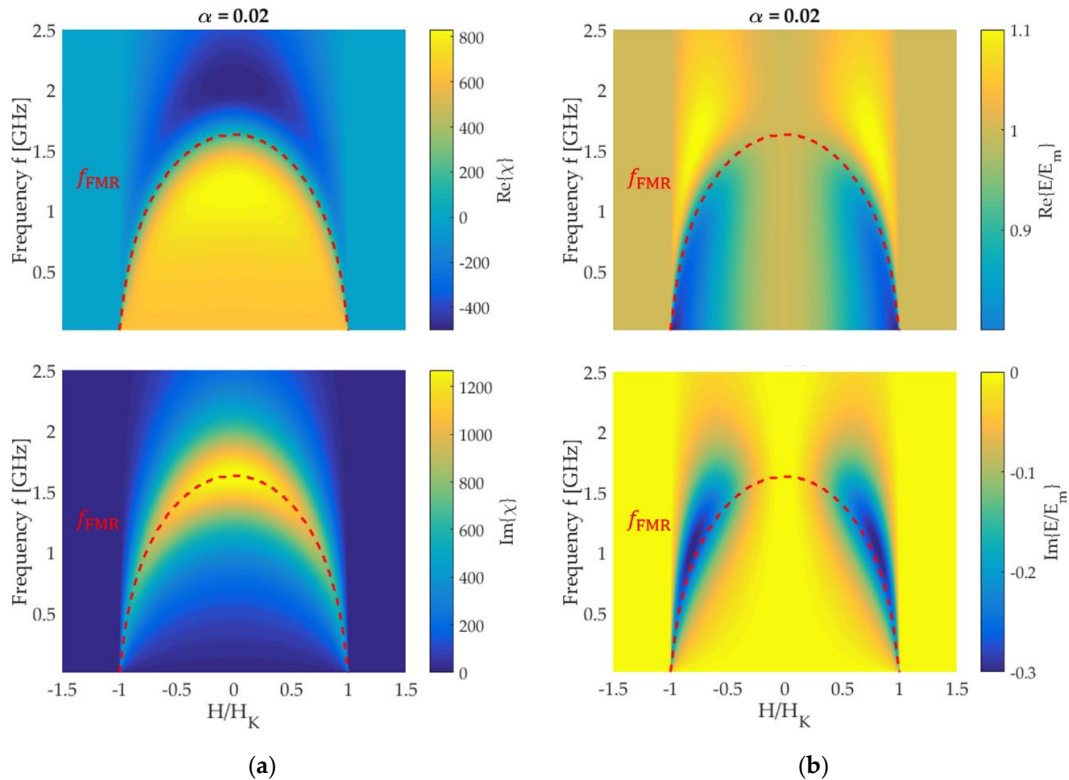


Figure 4. Model results for an ideal hard axis magnetization process: (a) real part $\text{Re}\{\chi\}$ (top) and imaginary part $\text{Im}\{\chi\}$ (bottom) of the differential dynamic susceptibility χ . (b) The real part $\text{Re}\{E/E_m\}$ (top) and the imaginary part $\text{Im}\{E/E_m\}$ of the normalized Young's modulus E/E_m as a function of the external magnetic field and the frequency. A damping factor of $\alpha = 0.02$ is used. The ferromagnetic resonance frequency f_{FMR} defined by the maximum of $\text{Im}\{\chi\}$ is denoted by a red dashed line. Because $\text{Im}\{\chi\} = 0$ for $H > |H_K|$, f_{FMR} is not shown in this field regime.

3.2. Mean-Field Calculations and Measurements

At $|H| = H_K$ the discontinuity in $M(H)$ results in a discontinuity in $\text{Re}\{E\}$ as well. Hence, the sensitivity $S \propto \partial \text{Re}\{E\} / \partial H$ is not defined at H_K within the single-spin model. In real magnetic films, distributions of the magnetization may occur due to inhomogeneities in material, structure or geometry and the resulting variations in the demagnetizing field. By the distributions, the discontinuity in $M(H)$ and $E(H)$ vanishes, which makes these functions fully differentiable. For the mean-field model, we use normal distributions δ_{EA} and δ_K of the easy axis (EA) angle and the effective anisotropy energy density K in a single-spin ensemble (Appendix A).

To obtain meaningful model parameters, measurements are performed on a 5×5 mm sample of 200 nm thick $(\text{Fe}_{90}\text{Co}_{10})_{78}\text{Si}_{12}\text{B}_{10}$ with an induced easy axis of anisotropy (Appendix A). The magnetic mean-field model is fitted to quasi-static magnetization measurements performed with a BH-loop tracer. An excellent fit is obtained with $\delta_{\text{EA}} \approx 1\%$, $\delta_K = 15\%$ and $K = 1400 \text{ J/m}^3$ (Figure 5a). The

other material parameters required are obtained from PIMM measurements. As a result, we obtain a saturation flux density of $\mu_0 M_s = 1.48$ T, a damping constant of $\alpha = 0.01$ and a dynamic anisotropy energy density of $K = 1.6$ kJ/m³. A discrepancy between the static K and the dynamic K has been observed before [52,53] and was explained with magnetic dispersion [54,55]. This dispersion might also be reflected in the deviation of measured and modelled f_{FMR} (Figure 5b), which occurs with increasing magnetic field magnitude. The domain structure of the sample is not represented by the single-spin based mean-field model. Additionally, sample misalignment of a few degrees can result in errors. With increasing $|H|$ the component $m_{0,2}$ decreases, until it is too small for a meaningful measurement at large H . For a tilted magnetic easy axis, magnetic saturation along the applied field can never be reached within the Stoner–Wohlfarth model. For such a case it follows that $m_{0,2} > 0$, while $H \rightarrow \infty$. From Equation (10) it is $\chi \rightarrow 0$ because $m_{0,2} \rightarrow 0$ with $H \rightarrow \infty$. Consequently, f_{FMR} increases due to the stiffening of the magnetic resonator by the increase of the effective field as shown in Figure 5b.

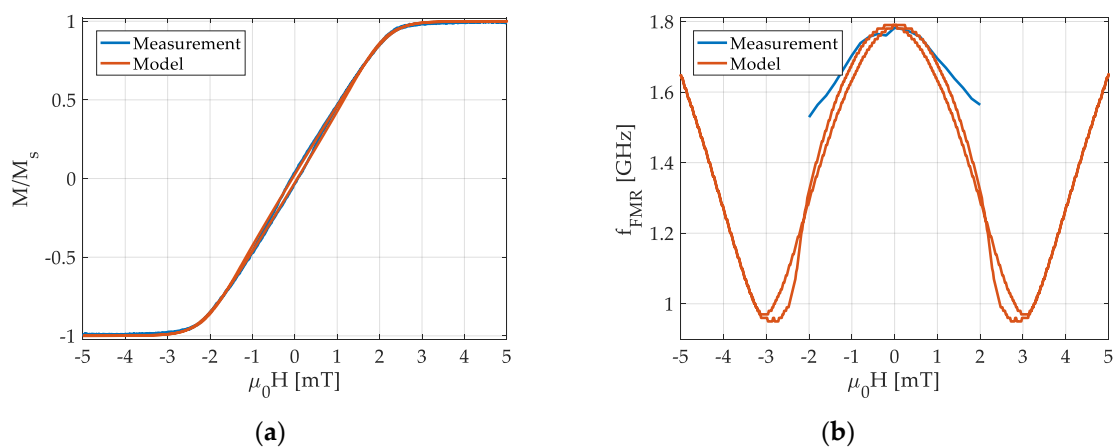


Figure 5. Comparison of measurement and model for (a) the normalized magnetization M/M_s along the magnetically hard axis and (b) the ferromagnetic resonance frequency f_{FMR} , defined as the maximum of the imaginary part $\text{Im}\{\chi\}$ of the dynamic susceptibility in the model.

3.3. The Magnetic Sensitivity of Delta-E Effect Sensors

Delta-E effect sensors utilize the change of their mechanical resonance frequency f_r upon application of a magnetic field for magnetic field sensing. If the Young's modulus' contribution to f_r dominates, the magnetic part of the sensitivity S results from the derivative $\partial_{E,H} := \partial E / \partial H$, with $S \propto \partial_{E,H}$. The derivative $\partial_{E,H}$ is calculated using the mean-field model. Due to the distributions introduced, $E(H, f)$ smooths out and the extrema reduce but it does not fundamentally differ from the single-spin result in Figure 4b (top). The absolute $|\partial_{E,H}|$ of the derivative is shown in Figure 6a for $\alpha = 0.01$, together with f_{FMR} . A global maximum is apparent at frequencies just below $f_{\text{FMR}}(H = 0)$. In Figure 6b the absolute $|\partial_{E,H}^{\text{max}}|$ of the maximum slope is plotted over the operation frequency f for different damping parameters α . Overall, $|\partial_{E,H}^{\text{max}}|$ decreases with increasing f , shown, e.g., for $\alpha = 0.03$. For lower α , a local maximum evolves and increases with decreasing damping. At sufficiently low α , the local maximum becomes a global one and exceeds the maximum at quasi-static frequencies.

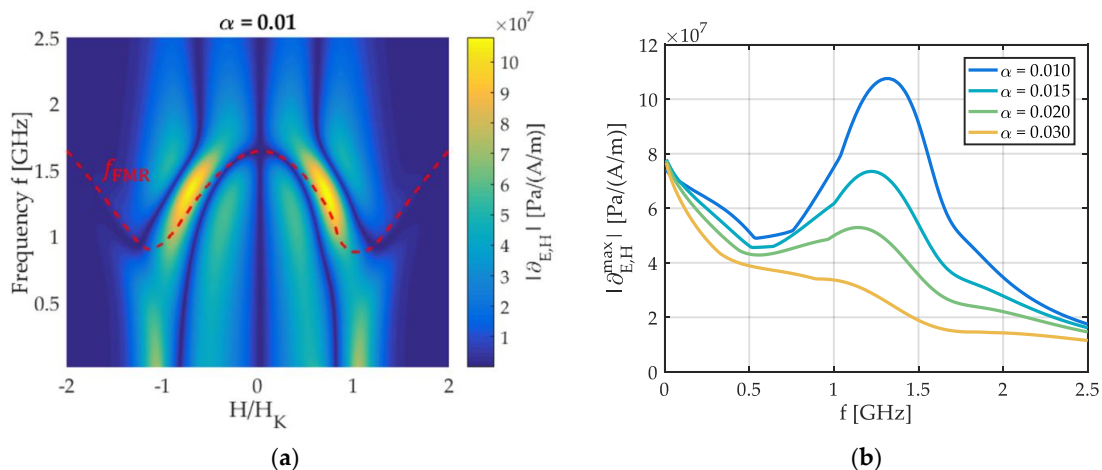


Figure 6. (a) Absolute of the derivative $|\partial_{E,H}|$ of the real part $Re\{E\}$ of Young's modulus E with magnetic field H and (b) the absolute $|\partial_{E,H}^{\max}|$ of the maximum of $|\partial_{E,H}(H)|$ plotted for various damping parameters α .

4. Summary and Conclusions

We described the delta-E effect as a function of the dynamic differential susceptibility χ of the magnetization. It can be used to estimate the delta-E effect from static magnetization and magnetostriction measurements if χ is known. A linearization of the Landau–Lifshitz–Gilbert equation was used to describe χ as a function of the magnetization in a single-spin model. χ includes the complete diagonal demagnetizing tensor for a film with uniaxial magnetic anisotropy and an external magnetic field applied in an arbitrary direction. Hence, the model is not restricted to an infinite-plane assumption. The susceptibility calculations match the measurements performed on a typical soft-magnetic FeCoSiB thin film frequently used for magnetic field sensing.

With the extracted material parameters, the Young's modulus is calculated and discussed as a function of the magnetic field and the operation frequency. A stiffening of the material is observed above the ferromagnetic resonance frequency, which matches with measurements in the literature. The stiffening results from the large phase shift between the oscillating stress and the alternating magnetostrictive strain response. Depending on the damping factors α , the magnitude of the delta-E effect either decreases continuously or exhibits a maximum just below the ferromagnetic resonance frequency.

The model is used to discuss the delta-E effect for magnetic field sensor applications by calculating the magnetic sensitivity of delta-E effect sensors. Like the magnitude of the delta-E effect, a maximum in magnetic sensitivity is visible close to the ferromagnetic resonance frequency for sufficiently small damping factors α . For larger damping factors, the sensitivity continuously decreases with frequency. The results indicate strong influence of the operating frequency on the delta-E effect and the sensitivity, even below the ferromagnetic resonance frequency. Especially for high sensitivity devices, very soft magnetic properties are required that result in a low ferromagnetic resonance frequency. Consequently, the delta-E effect's frequency dependence should be considered during the design of high sensitivity and high frequency sensors. As the delta-E effect occurs in several components of the mechanical stiffness tensor, we expect a similar dependency on the frequency in those components.

Author Contributions: Conceptualization, B.S.; validation, B.S., E.G.V., C.M.; investigation, B.S., E.V.G., C.M.; methodology, B.S., E.V.G.; writing—original draft preparation, B.S., E.V.G., C.M.; writing—review and editing, B.S., E.V.G., C.M., J.M., F.F.; visualization, B.S.; supervision, J.M., F.F.; project administration, J.M., F.F.; funding acquisition, J.M., F.F.

Funding: This research was funded by the German Research Foundation (DFG) via the collaborative research center CRC 1261.

Acknowledgments: The authors give many thanks to Lars Thormählen for the preparation and deposition of the magnetic film.

Conflicts of Interest: The authors declare no conflict of interest. The funders had no role in the design of the study; in the collection, analyses, or interpretation of data; in the writing of the manuscript, and in the decision to publish the results.

Appendix A

Appendix A.1. Calculation of the Dynamic Susceptibility

For the calculation of the dynamic susceptibility we used two coordinate systems: a global one (x_1, x_2, x_3) and a rotated one (x'_1, x'_2, x'_3) as it is illustrated in Figure A1. The rotation angle φ is defined as the angle between the static equilibrium vector \vec{M} of magnetization \vec{M}^* and the x_1 -axis. Along the x_1 -axis an external magnetic field $\vec{H}_{\text{app}}^* = \vec{H} + \vec{h}$ is applied with a static part \vec{H} and a dynamic part \vec{h} .

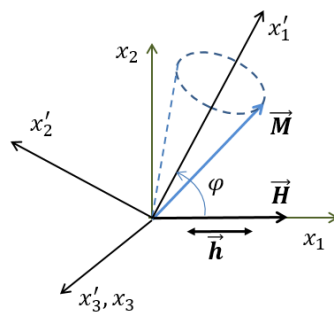


Figure A1. Coordinate system used in the analytical dynamic susceptibility calculation.

The effective field \vec{H}_{eff}^* and the rotation angle φ are obtained from the energy density u :

$$u = K - \frac{1}{M_s^2} K (\vec{M}^* \vec{e}_a)^2 + \frac{1}{2} \mu_0 \vec{M}^* \mathbf{D} \vec{M}^* - \mu_0 \vec{H}_{\text{app}}^* \vec{M}^*. \quad (\text{A1})$$

For the following calculations we separate the magnetization vector $\vec{M}^* = \vec{M} + \vec{m}$ into a static part \vec{M} and a dynamic part \vec{m} . Correspondingly, the effective field vector $\vec{H}^* = \vec{H}_{\text{eff}} + \vec{h}_{\text{eff}}$ is expressed as a sum of a static effective field \vec{H}_{eff} and a dynamic one \vec{h}_{eff} . In equilibrium, \vec{M} lies along the static part \vec{H}_{eff} of the effective field vector. Hence, in the rotated coordinate system (x') the only non-zero component of \vec{H}_{eff} is $H'_{\text{eff},1} = H_{\text{eff}}$ and of \vec{M} is $M'_1 = M_s$. The dynamic vectors \vec{m} and \vec{h}_{eff} can be described with harmonic oscillations, presuming that the amplitude of the precession is small. In rotated coordinates the complete vectors are

$$\vec{H}^{*'} = \begin{pmatrix} H_{\text{eff}} \\ 0 \\ 0 \end{pmatrix} + \begin{pmatrix} h'_{\text{eff},1} \\ h'_{\text{eff},2} \\ h'_{\text{eff},3} \end{pmatrix} e^{i\omega t}, \quad \vec{M}^{*'} = \begin{pmatrix} M_s \\ 0 \\ 0 \end{pmatrix} + \begin{pmatrix} 0 \\ m'_2 \\ m'_3 \end{pmatrix} e^{i\omega t}, \quad (\text{A2})$$

with the dynamic components $h'_{\text{eff},i} e^{i\omega t}$ of the effective field vector and the corresponding dynamic magnetization components, both in rotated coordinates.

Substituting $\vec{H}^{*'}$ and $\vec{M}^{*'}$ into Equation (8) the LLG equation is rearranged to obtain the components $\chi'_{ij} := m'_i / h'_j$ of the dynamic susceptibility tensor χ' in the rotated coordinate system. The harmonic approximation only holds for small oscillations ($m'_i \ll M_s$, $h'_{\text{eff},i} \ll H_{\text{eff}}$) of the magnetization and the effective field. As a consequence, all terms $m'_i h'_{\text{eff},i} \approx 0$ in the cross product of the LLG equation (Equation (8)), which results in all $\chi'_{i1} = 0$. Furthermore, the plane of magnetization precession is

perpendicular to \bar{M} and the driving field \bar{h} is perpendicular to the x'_3 axis. Hence, all components χ'_{1j} and χ'_{i3} vanish as well. The residual rotated non-zero components are:

$$\chi'_{22} = \frac{\gamma M_s / [\gamma H_{\text{eff}} + \gamma M_s D' - \gamma H_K e a \nu^2 - \alpha i \omega]}{1 - \frac{\omega^2}{[\gamma H_{\text{eff}} + \gamma M_s \bar{D} - \gamma H_K \bar{e} a^2 - \alpha i \omega](\gamma M_s D_{33} + \gamma H_{\text{eff}} - \alpha i \omega)}}, \quad (\text{A3})$$

$$\chi'_{32} = \frac{i \omega \gamma M_s}{[\gamma H_{\text{eff}} + \gamma M_s \bar{D} - \gamma H_K \bar{e} a^2 - \alpha i \omega](\gamma M_s D_{33} + \gamma H_{\text{eff}} - \alpha i \omega) - \omega^2}, \quad (\text{A4})$$

with $\bar{D} := D_{11} m_{0,2}^2 + D_{22} m_{0,1}^2$ and $\bar{e} a := e a_1 m_{0,2} + e a_2 m_{0,1}$. By rotating χ' back to the x -coordinate system, we get the final tensor χ of the dynamic magnetic susceptibility:

$$\chi = \begin{pmatrix} \chi'_{22} \sin^2 \varphi & \chi'_{22} \cos \varphi \sin \varphi & 0 \\ \chi'_{22} \cos \varphi \sin \varphi & \chi'_{22} \cos^2 \varphi & 0 \\ \chi'_{32} \sin \varphi & \chi'_{32} \cos \varphi & 0 \end{pmatrix}. \quad (\text{A5})$$

In this paper, only uniaxial stress is considered. Therefore, only the χ_{11} component is used for the Young's modulus calculations.

Appendix A.2. Magnetic Mean-Field Model

For the simulation, we consider an ensemble of single-domain particles. Each particle has a different orientation of its easy axis vector $\bar{e} a$ to the external magnetic field \bar{H} and an anisotropy energy density K . The orientations of $\bar{e} a$ and values of K are taken to be normally distributed with a standard deviation δ_{EA} of the easy axis and a standard deviation δ_K of K . The global magnetization curve is obtained by averaging the magnetization over all particles. For the delta-E effect, the Young's modulus is calculated for each particle and then averaged over all particles to obtain the global Young's modulus. The normalized static magnetization vector \bar{m}_0 is obtained for each particle by minimizing its energy density function u (Equation (A1)), setting the dynamic components of \bar{h}' and \bar{m}' in Equation (A2) to zero.

Appendix A.3. Model Parameters for Figure 1

For the calculations shown in Figure 1 (Section 2.1) we used a standard deviation $\delta_K = 30\%$ around a mean of $K = 1.9 \text{ kJ/m}^3$ and a standard deviation $\delta_{\text{EA}} = 1\%$ of the easy axis. A size of $(3 \times 1 \times 0.002) \text{ mm}^3$ is used for the magnetic layer, corresponding to the dimensions given in [7]. These dimensions result in $D_{11} = 2.4223 \cdot 10^{-4}$, $D_{22} = 15 \cdot 10^{-4}$ and $D_{33} = 0.9983$ for the ballistic demagnetizing factors in the center of a rectangular prism [56]. Except of K , we used the same material parameters as given in Section 3.

Appendix A.4. Measurements

Experiments are performed on a $5 \times 5 \text{ mm}$ sample of 200 nm thick $(\text{Fe}_{90}\text{Co}_{10})_{78}\text{Si}_{12}\text{B}_{10}$ on a Si substrate. A uniaxial anisotropy is induced by magnetization during the deposition. Quasi static magnetization curves are measured by a BH-loop tracer at 10 Hz . FMR frequencies are measured by pulsed inductive microwave magnetometry (PIMM) [57] in flip chip geometry on a coplanar waveguide (CPW). The hard axis of the sample is aligned parallel to the Oersted field of the CPW and magnetic bias fields are also applied parallel to the Oersted field of the CPW. Each bias field is reached starting from positive saturation of the sample and lowering it to the desired field strength to perform the PIMM measurement. The magnetic field strength of the Oersted field is ca. 3 A/m . The FMR frequency for each bias field is extracted by the maximum of the magnitude of the Fourier transformed time signal.

References

1. Kneller, E. *Ferromagnetismus*; Springer-Verlag OHG: Berlin/Göttingen/Heidelberg, 1962; ISBN 978-3-642-86695-1.
2. Livingston, J.D. Magnetomechanical properties of amorphous metals. *Phys. Status Solidi A* **1982**, *70*, 591–596. [[CrossRef](#)]
3. Lee, E.W. Magnetostriction and Magnetomechanical Effects. *Reports Prog. Phys.* **1955**, *18*, 184–229. [[CrossRef](#)]
4. Gojdka, B.; Jahns, R.; Meurisch, K.; Greve, H.; Adlung, R.; Quandt, E.; Knöchel, R.; Faupel, F. Fully integrable magnetic field sensor based on delta-E effect. *Appl. Phys. Lett.* **2011**, *99*, 1–4. [[CrossRef](#)]
5. Jahns, R.; Zabel, S.; Marauska, S.; Gojdka, B.; Wagner, B.; Knöchel, R.; Adlung, R.; Faupel, F. Microelectromechanical magnetic field sensor based on the delta-E effect. *Appl. Phys. Lett.* **2014**, *105*, 2012–2015. [[CrossRef](#)]
6. Zabel, S.; Kirchof, C.; Yasar, E.; Meyners, D.; Quandt, E.; Faupel, F. Phase modulated magnetoelectric delta-E effect sensor for sub-nano tesla magnetic fields. *Appl. Phys. Lett.* **2015**, *107*. [[CrossRef](#)]
7. Zabel, S.; Reermann, J.; Fichtner, S.; Kirchof, C.; Quandt, E.; Wagner, B.; Schmidt, G.; Faupel, F. Multimode delta-E effect magnetic field sensors with adapted electrodes. *Appl. Phys. Lett.* **2016**, *108*, 222401. [[CrossRef](#)]
8. Nan, T.; Hui, Y.; Rinaldi, M.; Sun, N.X. Self-biased 215 MHz magnetoelectric NEMS resonator for ultra-sensitive DC magnetic field detection. *Sci Rep* **2013**, *3*, 1985. [[CrossRef](#)]
9. Hui, Y.; Nan, T.; Sun, N.X.; Rinaldi, M. High resolution magnetometer based on a high frequency magnetoelectric MEMS-CMOS oscillator. *J. Microelectromechanical Syst.* **2015**, *24*, 134–143. [[CrossRef](#)]
10. Li, M.; Matyushov, A.; Dong, C.; Chen, H.; Lin, H.; Nan, T.; Qian, Z.; Rinaldi, M.; Lin, Y.; Sun, N.X. Ultra-sensitive NEMS magnetoelectric sensor for picotesla DC magnetic field detection. *Appl. Phys. Lett.* **2017**, *110*, 143510. [[CrossRef](#)]
11. Tu, C.; Chu, Z.-Q.; Spetzler, B.; Hayes, P.; Dong, C.-Z.; Liang, X.-F.; Chen, H.-H.; He, Y.-F.; Wei, Y.-Y.; Lisenkov, I.; et al. Mechanical-Resonance-Enhanced Thin-Film Magnetoelectric Heterostructures for Magnetometers, Mechanical Antennas, Tunable RF Inductors, and Filters. *Materials* **2019**, *12*, 2259. [[CrossRef](#)] [[PubMed](#)]
12. Hanna, S.M. Magnetic Field Sensors Based on SAW Propagation in Magnetic Films. *IEEE Trans. Ultrason. Ferroelectr. Freq. Control* **1987**, *34*, 191–194. [[CrossRef](#)] [[PubMed](#)]
13. Liur, X. Enhanced sensitivity of temperature- compensated SAW-based current sensor using the magnetostrictive effect. *Smart Mater. Struct.* **2016**, *26*, 025008.
14. Polewczyk, V.; Dumesnil, K.; Lacour, D.; Moutaouekkil, M.; Mjahed, H.; Tiercelin, N.; Petit Watelot, S.; Mishra, H.; Dusch, Y.; Hage-Ali, S.; et al. Unipolar and bipolar high-magnetic-field sensors based on surface acoustic wave resonators. *Phys. Rev. Appl.* **2017**, *8*, 1–11. [[CrossRef](#)]
15. Kittmann, A.; Durdaut, P.; Zabel, S.; Reermann, J.; Schmalz, J.; Spetzler, B.; Meyners, D.; Sun, N.X.; McCord, J.; Gerken, M.; et al. Wide Band Low Noise Love Wave Magnetic Field Sensor System. *Sci. Rep.* **2018**, *8*, 1–10. [[CrossRef](#)] [[PubMed](#)]
16. Liu, X.; Tong, B.; Ou-Yang, J.; Yang, X.; Chen, S.; Zhang, Y.; Zhu, B. Self-biased vector magnetic sensor based on a Love-type surface acoustic wave resonator. *Appl. Phys. Lett.* **2018**, *113*. [[CrossRef](#)]
17. Mazzamurro, A.; Talbi, A.; Dusch, Y.; Elmazria, O.; Pernod, P.; Matar, O.B.; Tiercelin, N. Highly Sensitive Surface Acoustic Wave Magnetic Field Sensor Using Multilayered TbCo₂/FeCo Thin Film. *Proceedings* **2018**, *2*, 902. [[CrossRef](#)]
18. Webb, D.C.; Forester, D.W.; Ganguly, A.K.; Vittoria, C. Applications of amorphous magnetic-layers in surface-acoustic-wave devices. *IEEE Trans. Magn.* **1979**, *15*, 1410–1415. [[CrossRef](#)]
19. Robbins, W.P.; Hietala, A. A Simple Phenomenological Model of Tunable SAW Devices Using Magnetostrictive Thin Films. *IEEE Trans. Ultrason. Ferroelectr. Freq. Control* **1988**, *35*, 718–722. [[CrossRef](#)]
20. Wiegert, R.F.; Levy, M. Enhanced magnetically tunable attenuation and relative velocity of 0.6 GHz Rayleigh waves in nickel thin films. *Appl. Phys. Lett.* **1989**, *54*, 995–997. [[CrossRef](#)]
21. Wiegert, R.F. Magnetoelastic surface acoustic wave attenuation and anisotropic magnetoresistance in Ni[sub 3]Fe thin films. *J. Appl. Phys.* **2002**, *91*, 8231. [[CrossRef](#)]
22. Smole, P.; Ruile, W.; Korden, C.; Ludwig, A.; Quandt, E.; Krassnitzer, S.; Pongratz, P. Magnetically tunable SAW-resonator. In Proceedings of the IEEE International Frequency Control Symposium and PDA Exhibition Jointly with the 17th European Frequency and Time Forum, Tampa, FL, USA, 4–8 May 2003; pp. 4–7.

23. Sun, N.X.; Srinivasan, G. Voltage Control of Magnetism in Multiferroic Heterostructures and Devices. *Spin* **2012**, *2*, 1240004. [[CrossRef](#)]
24. Liu, X.; Ou-Yang, J.; Tong, B.; Chen, S.; Zhang, Y.; Zhu, B.; Yang, X. Influence of the delta-E effect on a surface acoustic wave resonator. *Appl. Phys. Lett.* **2019**, *114*, 062903. [[CrossRef](#)]
25. Mason, W.P. Domain Wall Relaxation in Nickel. *Phys. Rev.* **1949**, *83*, 683. [[CrossRef](#)]
26. Johnson, S.J.; Rogers, T.F. Magnetically induced ultrasonic velocity changes in polycrystalline nickel. *J. Appl. Phys.* **1952**, *23*, 574–577. [[CrossRef](#)]
27. Mason, W.P. Rotational Relaxation in Nickel at High Frequencies. *Rev. Mod. Phys.* **1953**, *25*. [[CrossRef](#)]
28. Squire, P.T. Phenomenological model for magnetization, magnetostriction and delta-E effect in field-annealed amorphous ribbons. *J. Magn. Magn. Mater.* **1990**, *87*, 299–310. [[CrossRef](#)]
29. Squire, P.T. Domain model for magnetoelastic behaviour of uniaxial ferromagnets. *J. Magn. Magn. Mater.* **1995**, *140–144*, 1829–1830. [[CrossRef](#)]
30. Datta, S.; Atulasimha, J.; Mudivarathi, C.; Flatau, A.B. Stress and magnetic field-dependent Young's modulus in single crystal iron-gallium alloys. *J. Magn. Magn. Mater.* **2010**, *322*, 2135–2144. [[CrossRef](#)]
31. Bou Matar, O.; Robillard, J.F.; Vasseur, J.O.; Hladky-Hennion, A.C.; Deymier, P.A.; Pernod, P.; Preobrazhensky, V. Band gap tunability of magneto-elastic phononic crystal. *J. Appl. Phys.* **2012**, *111*. [[CrossRef](#)]
32. Zhou, H.; Talbi, A.; Tiercelin, N.; Bou Matar, O. Multilayer magnetostrictive structure based surface acoustic wave devices. *Appl. Phys. Lett.* **2014**, *104*, 114101. [[CrossRef](#)]
33. Daniel, L.; Hubert, O. An analytical model for the ΔE effect in magnetic materials. *Eur. Phys. J. Appl. Phys.* **2009**, *45*, 31101. [[CrossRef](#)]
34. Hubert, O.; Daniel, L. Measurement and Analytical Modeling of the delta-E Effect in a Bulk Iron-Cobalt Alloy. *IEEE Trans. Magn.* **2010**, *46*, 401–404. [[CrossRef](#)]
35. Zhang, D.G.; Li, M.H.; Zhou, H.M. A general one-dimension nonlinear magneto-elastic coupled constitutive model for magnetostrictive. *AIP Adv.* **2015**, *5*. [[CrossRef](#)]
36. Ganguly, A.K.; Davis, K.L.; Webb, D.C.; Vittoria, C. Magnetoelastic surface waves in a magnetic film-piezoelectric substrate configuration. *J. Appl. Phys.* **1976**, *47*, 2696–2704. [[CrossRef](#)]
37. Ganguly, A.K.; Davis, K.L.; Webb, D.C. Magnetoelastic surface waves on the (110) plane of highly magnetostrictive cubic crystals. *J. Appl. Phys.* **1978**, *49*, 759–767. [[CrossRef](#)]
38. Walikainen, D.; Wiegert, R.F.; Levy, M. Magnetic Field Dependency of 600 MHz SAW Velocity Changes For Thin Ni Films. In Proceedings of the Ultrasonics Symposium, Chicago, IL, USA, 2–5 October 1988; Volume 192, pp. 173–180.
39. Weiler, M.; Dreher, L.; Heeg, C.; Huebl, H.; Gross, R.; Brandt, M.S.; Goennenwein, S.T.B. Elastically driven ferromagnetic resonance in nickel thin films. *Phys. Rev. Lett.* **2011**, *106*, 1–4. [[CrossRef](#)] [[PubMed](#)]
40. Dreher, L.; Weiler, M.; Pernpeintner, M.; Huebl, H.; Gross, R.; Brandt, M.S.; Goennenwein, S.T.B. Surface Acoustic Wave-Driven Ferromagnetic Resonance in Nickel Thin Films: Theory and Experiment. *Phys. Rev. B* **2012**, *134415*, 1–13. [[CrossRef](#)]
41. Becker, R.; Döring, W. *Ferromagnetismus*; Verlag von Julius Springer: Berlin, 1939; ISBN 9783642471124.
42. Ludwig, A.; Quandt, E. Optimization of the delta E effect in thin films and multilayers by magnetic field annealing. *IEEE Trans. Magn.* **2002**, *38*, 2829–2831. [[CrossRef](#)]
43. Sárközi, Z.; Mackay, K.; Peuzin, J.C. Elastic properties of magnetostrictive thin films using bending and torsion resonances of a bimorph. *J. Appl. Phys.* **2000**, *88*, 5827–5832. [[CrossRef](#)]
44. O'handley, R.C. *Modern Magnetic Materials Principles and Applications*; John Wiley & Sons, Ltd.: Hoboken, NJ, USA, 2000; ISBN 978-0-471-15566-9.
45. Reid, A.H.; Shen, X.; Maldonado, P.; Chase, T.; Granitzka, P.W.; Carva, K.; Li, R.K.; Li, J.; Wu, L.; Vecchione, T.; et al. Beyond a phenomenological description of magnetostriction. *Nat. Commun.* **2018**, *9*. [[CrossRef](#)]
46. Stoner, E.C.; Wohlfarth, E.P. A Mechanism of Magnetic Hysteresis in Heterogeneous Alloys. *Philos. Trans. R. Soc. Lond. Ser. A Math. Phys. Sci.* **1948**, *240*, 599–642. [[CrossRef](#)]
47. Gilbert, T.L. A phenomenological theory of damping in ferromagnetic materials. *IEEE Trans. Magn.* **2004**, *40*, 3443–3449. [[CrossRef](#)]
48. Gurevich, A.G.; Melkov, G.A. *Magnetization Oscillation and Waves*; CRC Press: Boca Raton, FL, USA, 1996; ISBN 978-0849394607.

49. Panina, L.V.; Mohri, K.; Uchiyama, T.; Noda, M. Giant Magneto-Impedance in Co-Rich Amorphous Wires and Films. *IEEE Trans. Magn.* **1995**, *31*, 1249–1260. [[CrossRef](#)]
50. Kraus, L. GMI modeling and material optimization. *Sens. Actuators A Phys.* **2003**, *106*, 187–194. [[CrossRef](#)]
51. Kittel, C. On the theory of ferromagnetic resonance absorption. *Phys. Rev.* **1948**, *73*, 155–161. [[CrossRef](#)]
52. Gebert, A.; McCord, J.; Schmutz, C.; Quandt, E. Permeability and Magnetic Properties of Ferromagnetic NiFe/FeCoBSi Bilayers for High-Frequency Applications. *IEEE Trans. Magn.* **2007**, *43*, 2624–2626.
53. Neudert, A.; McCord, J.; Schäfer, R.; Schultz, L. Dynamic anisotropy in amorphous CoZrTa films. *J. Appl. Phys.* **2004**, *95*, 6595–6597. [[CrossRef](#)]
54. Hoffmann, H. Theory of magnetization ripple. *IEEE Trans. Magn.* **1968**, *4*, 32–38. [[CrossRef](#)]
55. Rantschler, J.O.; Alexander, C. Ripple field effect on high-frequency measurements of FeTiN films. *J. Appl. Phys.* **2003**, *93*, 6665–6667. [[CrossRef](#)]
56. Aharoni, A. Demagnetizing factors for rectangular ferromagnetic prisms. *J. Appl. Phys.* **1998**, *83*, 3432–3434. [[CrossRef](#)]
57. Silva, T.J.; Lee, C.S.; Crawford, T.M.; Rogers, C.T. Inductive measurement of ultrafast magnetization dynamics in thin-film Permalloy. *J. Appl. Phys.* **1999**, *85*, 7849–7862. [[CrossRef](#)]



© 2019 by the authors. Licensee MDPI, Basel, Switzerland. This article is an open access article distributed under the terms and conditions of the Creative Commons Attribution (CC BY) license (<http://creativecommons.org/licenses/by/4.0/>).

4.3 Stress Effects in Contour-Mode Resonators

In the previous sections, the material, geometry, and operating parameters were analyzed to determine how they influence the ΔE effect and magnetic sensitivity. Ensuring the technological feasibility of the sensor concept including reproducibility of the devices, is as important as optimizing such parameters. As described in Section 4.1, a key parameter for large magnetic sensitivity is a small and spatially homogeneous effective anisotropy energy density K_{eff} . Owing to the magnetoelastic interaction, K_{eff} is affected by anisotropic stress that can build up during the fabrication process. Although magnetoelastic coupling is a well-understood phenomenon, the relationship between the geometric parameters and spatially inhomogeneous stress and magnetization fields is nontrivial and can cause a variation of the device parameters. Therefore, understanding the influence of stress effects on the performance is key for optimizing sensing characteristics and improving reproducibility.

In this section, the effects of stress on the performance of the ΔE -effect sensor elements are investigated in detail using double-clamped plate resonators with a large ratio of magnetic film-thickness to non-magnetic film thickness of ≈ 1 -1.5. A large sample of sensor elements is analyzed with two different multilayer systems based on soft-magnetic amorphous FeGaB and FeGaC thin-films. The results shed light on major technological challenges and restate the importance of the magnetic material parameters in sensor development.

Contribution

The contribution to this work is shared equally with Alexei D. Matyushov.

- Conceptualization (shared)
- Writing of original manuscript (shared)
- Modeling and simulations
- Data analysis and interpretation (shared)

Curvature and Stress Effects on the Performance of Contour-Mode Resonant ΔE Effect Magnetometers

Alexei D. Matyushov, Benjamin Spetzler, Mohsen Zaeimbashi, James Zhou, Zhenyun Qian, Elizaveta V. Golubeva, Cheng Tu, Yingxue Guo, Brian F. Chen, Damo Wang, Alexandria Will-Cole, Huaihao Chen, Matteo Rinaldi, Jeffrey McCord, Franz Faupel, and Nian X. Sun*

Miniaturized piezoelectric/magnetostrictive contour-mode resonators are effective magnetometers by exploiting the ΔE effect. With dimensions of $\approx 100\text{--}200\ \mu\text{m}$ across and $< 1\ \mu\text{m}$ thick, they offer high spatial resolution, portability, low power consumption, and low cost. However, a thorough understanding of the magnetic material behavior in these devices is lacking, hindering performance optimization. This manuscript reports on the strong, nonlinear correlation observed between the frequency response of these sensors and the stress-induced curvature of the resonator plate. The resonance frequency shift caused by DC magnetic fields drops off rapidly with increasing curvature: about two orders of magnitude separate the highest and lowest frequency shift in otherwise identical devices. Similarly, an inverse correlation with the quality factor is found, suggesting a magnetic loss mechanism. The mechanical and magnetic properties are theoretically analyzed using magnetoelastic finite-element and magnetic domain-phase models. The resulting model fits the measurements well and is generally consistent with additional results from magneto-optical domain imaging. Thus, the origin of the observed behavior is identified and broader implications for the design of nanomagnetoelastic devices are derived. By fabricating a magnetoelastic nanoplate resonator with low curvature, a record-high DC magnetic field sensitivity of $5\ \text{Hz nT}^{-1}$ is achieved.

1. Introduction

Small magnetic sensors have played a tremendously important role in modern times, perhaps most obviously as the integral components of read and write heads in magnetic storage technology and, by extension, in the digital revolution that this technology facilitated. Other far-reaching applications for magnetic sensors abound. These include functions like miniature integrated compasses, contact-less sensing of mechanical parts in automotive^[1] and other industries, contact-less switching, optimization of electric motors,^[2] and a range of biomedical applications.

Ongoing research on magnetic sensors is focused on improving the smallest detectable magnetic field, while minimizing the other critical parameters of (especially) size, power consumption, and cost. Specifically, one research and development challenge is in magnetic biodetection; relevant magnetic fields in this context range from about 25 pT for the human heart, down to 1 pT or less

Dr. A. D. Matyushov, Prof. Z. Qian, Y. Guo, D. Wang, A. Will-Cole, H. Chen, Prof. M. Rinaldi, Prof. N. X. Sun
Department of Electrical and Computer Engineering
Northeastern University
Boston, MA 02115, USA
E-mail: n.sun@northeastern.edu

Dr. A. D. Matyushov
Department of Physics
Northeastern University
Boston, MA 02115, USA


B. Spetzler, E. V. Golubeva, Prof. J. McCord, Prof. F. Faupel
Institute of Material Science
Kiel University
24118 Kiel, Germany

Dr. M. Zaeimbashi
Wellman Center for Photomedicine
Massachusetts General Hospital
Harvard Medical School
Boston, MA 02114, USA

J. Zhou
Department of Mathematics
University of California, Davis
Davis, CA 95616, USA

Dr. C. Tu
School of Electronic Science and Engineering
University of Electronic Science and Technology of China
Chengdu, China

B. F. Chen
Department of Electrical and Computer Engineering
University of Illinois at Urbana-Champaign
Urbana, IL 61801, USA

 The ORCID identification number(s) for the author(s) of this article can be found under <https://doi.org/10.1002/admt.202100294>.

DOI: 10.1002/admt.202100294

for the brain, and in-between magnitudes for other areas of the body.^[3] In addition, magnetometers for this task must attain such resolution at static or quasistatic (low frequency) fields. Generally, the best detection limits can be achieved by SQUID (superconducting quantum interference device) magnetometers.^[4–6] However, the cryogenic cooling necessary for SQUIDS leads to a host of associated problems such as high cost and complexity, high power consumption, large size of the overall instrument package and, as a consequence, essentially nonexistent portability.

In this work, we studied a type of magnetometer that can potentially satisfy demand for small size and room temperature operation: sensors featuring a nanoelectromechanical system (NEMS) contour-mode resonator, made up of thin-film magneto-electric (ME) composites, and operating on the ΔE effect. Laminated ME composites were pioneered in 2001^[7] and consist of distinct layers of magnetic and piezoelectric phases, which are coupled by strain. To fashion a sensor out of these materials, ME magnetometers typically feature a mechanically resonant element (e.g., a cantilever or resonator plate),^[8–13] in contrast to many previously developed sensor classes such as magnetoresistive (MR) sensors, fluxgates, etc.^[14]

Magnetometers made up of laminated ME composites can generally be divided into two types: passive sensors based on the ME effect and those based on the ΔE effect. A passive ME resonator can produce an output voltage in response to an AC magnetic field, a process that is amplified by a few orders of magnitude when the field frequency matches the mechanical resonance frequency of the composite structure.^[15] Due to this amplification, the detection limit of such sensors can be impressive, down to $400 \text{ fT Hz}^{-1/2}$,^[16,17] but only within a small frequency range around the sensor's resonance frequency. For many applications, however, good detection capability over a wider range of magnetic field frequencies, including—and especially—at low frequencies and DC, is desired. But due to the inverse relationship between resonance frequency and size, these ME sensors are difficult to optimize for low field frequencies, where they show strongly degraded detection limits.^[16,17]

On the other hand, the ΔE effect^[18,19] is the property of magnetic materials in which the Young's modulus changes nonlinearly as a function of magnetic field, which may be DC or AC. This can be utilized as a sensing mechanism by monitoring the magnetic field-induced change in output signal from a driven resonator, caused by a shift in resonance frequency. An early example of a magnetometer operating on this principle is the microcantilever developed by Osiander et al.,^[20] and numerous other devices have been put forward since then.^[8,21–24] Such a detection scheme does not require matching the frequencies of the magnetic field and the resonator, giving the freedom to scale down the sensor dimensions; thus, the NEMS magnetometers in this work feature a resonator plate typically hundreds of nanometers thick and on the order of $200 \times 100 \text{ }\mu\text{m}$ across. Such a small form factor brings advantages of high spatial resolution if used in a sensor array, low power consumption, and low cost as a result of the fabrication process. In addition, these high frequency, ΔE -effect magnetometers demonstrate higher signal bandwidths than larger cantilever-based sensors operating at lower frequencies.^[25] Depending on the design, the sensors we have developed resonate within the range of roughly

100–250 MHz; yet they have proved capable of detecting weak DC magnetic fields.^[11,12]

Here we present an investigation of the mechanical and magnetic properties of the thin-film ME resonator plate, which is the main functional element of our ΔE effect-based NEMS magnetometer, and how those properties affect the frequency response to DC magnetic fields and quality factor Q of the sensor. In the course of fabricating and testing these magnetic sensors, significant variation in performance was observed when comparing ostensibly identical devices. After systematic testing, about two orders of magnitude difference in normalized frequency response was found in devices that were fabricated with the same materials, same layer thicknesses, deposited under the same sputtering conditions, and having similar or identical sensor geometry. Better understanding of the phenomena behind these discrepancies could lead to further advancements in the detection limit of these magnetometers.

First, we implemented an optical method to quantify the curvature of the resonator plate and studied the correlation between this parameter and the achievable frequency shift, in response to DC magnetic fields, in an ensemble of sensors with eight different designs. The laminated ME composites in these sensors were made up of piezoelectric AlN and amorphous FeGaB as the magnetic material. We repeated a similar investigation but introduced varying thicknesses of the magnetic material and also switched to FeGaC in some cases. Q was measured in all the sensors in both batches. To study the physics connecting resonator curvature to sensor performance, we performed magneto-optical Kerr effect (MOKE) imaging of magnetic domains and conducted simulations and modeling of the stress distribution and its influence on the magnetic easy axis orientation and on the effective magnetic anisotropy energy density. The modeling results predict a nonlinear variation of magnetization orientation as a function of depth within the magnetic layer. Based on the distribution of resonator plate curvature among the sensors, we identified trends in the calculated averages of magnetic anisotropy orientation and energy. These trends were then used to inform the application of a simple magnetic domain-phase model of the ΔE effect to the ensemble of experimental data. A good fit was obtained from the model, and the experimentally observed behavior is explained.

2. Results and Discussion

ΔE effect-based NEMS magnetic field sensors, microfabricated on $4''$ Si wafers, were characterized in this study. There were eight sensor design variations, all consisting of rectangular nanoplate resonators—on the order of $200 \times 100 \text{ }\mu\text{m}$ across—suspended in air by two anchors and made up of ME thin films, with interdigital electrodes (IDE) on the bottom of the plate (**Figure 1**). The variations on this core arrangement included different numbers of IDE “fingers,” resulting in different resonance frequencies f_r , and different dimensions of resonator plate and anchors (**Table 1**). The eight designs were subdivided into four pairs so that only the width of anchors was different between the two members of each pair, with everything else the same.

The microfabrication process consisted of photolithography for patterning the device structures and sputtering for

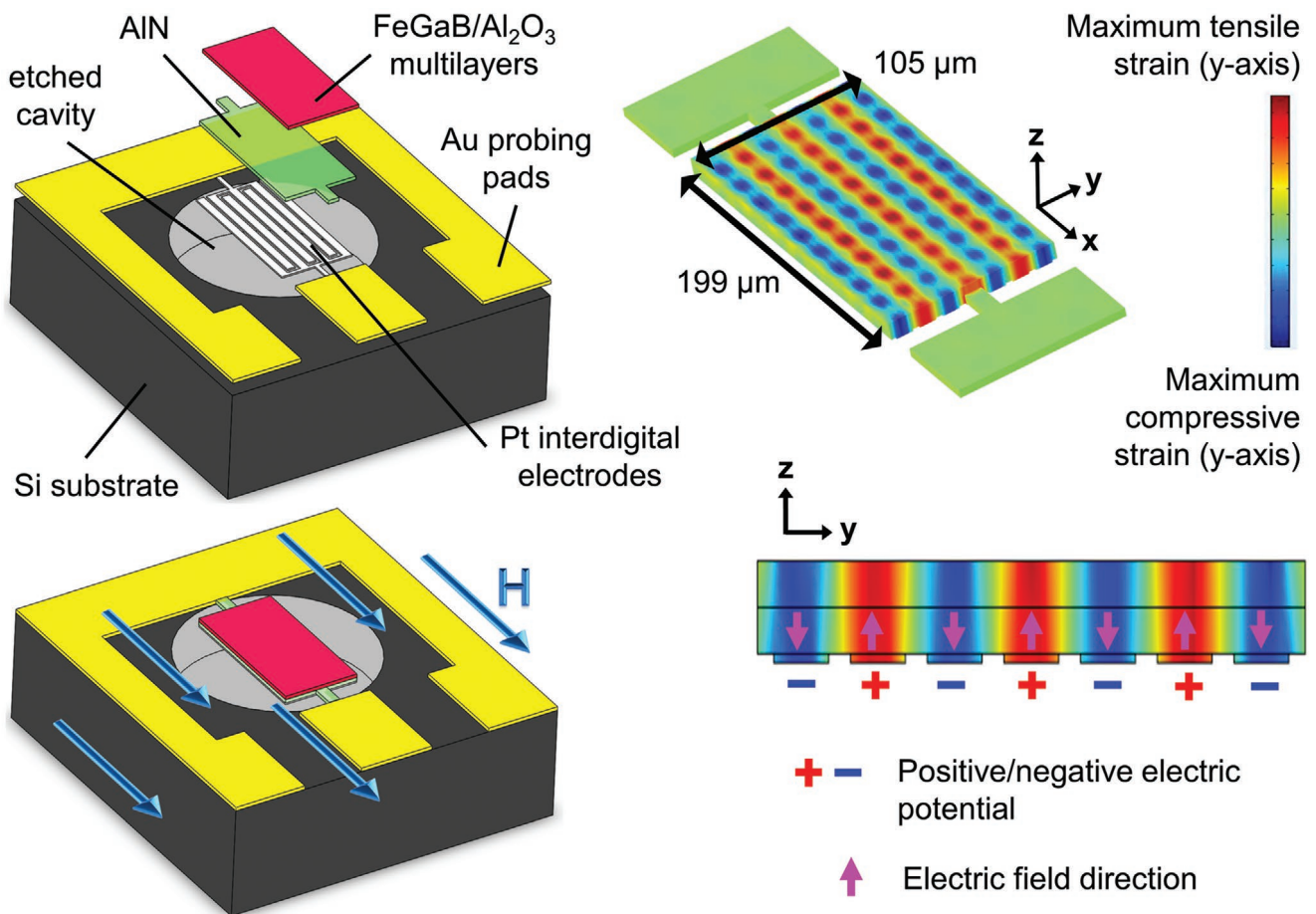


Figure 1. Left: schematic of the magnetoelastic sensor components (top) and of a completed sensor with magnetic DC field applied during testing (bottom). Right: qualitative illustration of the electromechanical standing wave that is induced by an AC voltage driving signal, as simulated in COMSOL Multiphysics. A simplified construction of the sensor is used in both the component schematic and the simulation, in which the materials overlying the interdigital electrodes are made flat; in reality, these materials are sputter-deposited both on top of, and in between, the electrodes, resulting in an undulating shape that follows the electrode contours. Piezoelectric AlN is excited into its d_{31} mode by the AC voltage applied through the interdigital electrodes, causing contour-mode vibrations of the resonator plate. The model structure used for the simulation represents the design of sensor ID 1 in Table 1.

depositing all constituent materials. In Investigation 1, the thin film layers were kept constant (same thickness and composition) for all devices, with three major components: a 50 nm thick IDE made of Pt on the bottom, followed by a 250 nm piezoelectric layer of AlN, and ≈ 300 nm of magnetic FeGaB/Al₂O₃ multilayers on top. Thin spacer layers of Al₂O₃ were deposited between magnetic layers in order to limit losses that would arise

from eddy currents. The magnetic layers added up to 250 nm of the total thickness, and were composed of (Fe₈₀Ga₂₀)₈₈B₁₂ at%, which has been shown to give amorphous films with small coercivity and FMR linewidth^[26] (<0.1 , 2 mT, respectively). The specific FeGaB/Al₂O₃ multilayer stack used here has been recently demonstrated to exhibit a high saturation magnetostriction constant of 75 ppm and a ΔE of 130 GPa^[27] in as-deposited

Table 1. NEMS magnetoelastic sensor design parameters, Investigation 1.

Sensor ID	Lateral dimensions (μm)	Number of fingers	Anchor length (μm)	Anchor width (μm)	Avg. f_r (MHz)	AlN thickness (nm)	FeGaB thickness (nm)	IDE thickness (nm)
1	199 × 105	7	25	15	224.4	250	250	50
2				30	224.4			
3	145 × 70	5	20	7	245.8			
4				14	245.6			
5	200 × 60	3	10	10	172.4			
6				17	171.9			
7	200 × 75	3	20	10	136.8			
8				25	137.1			

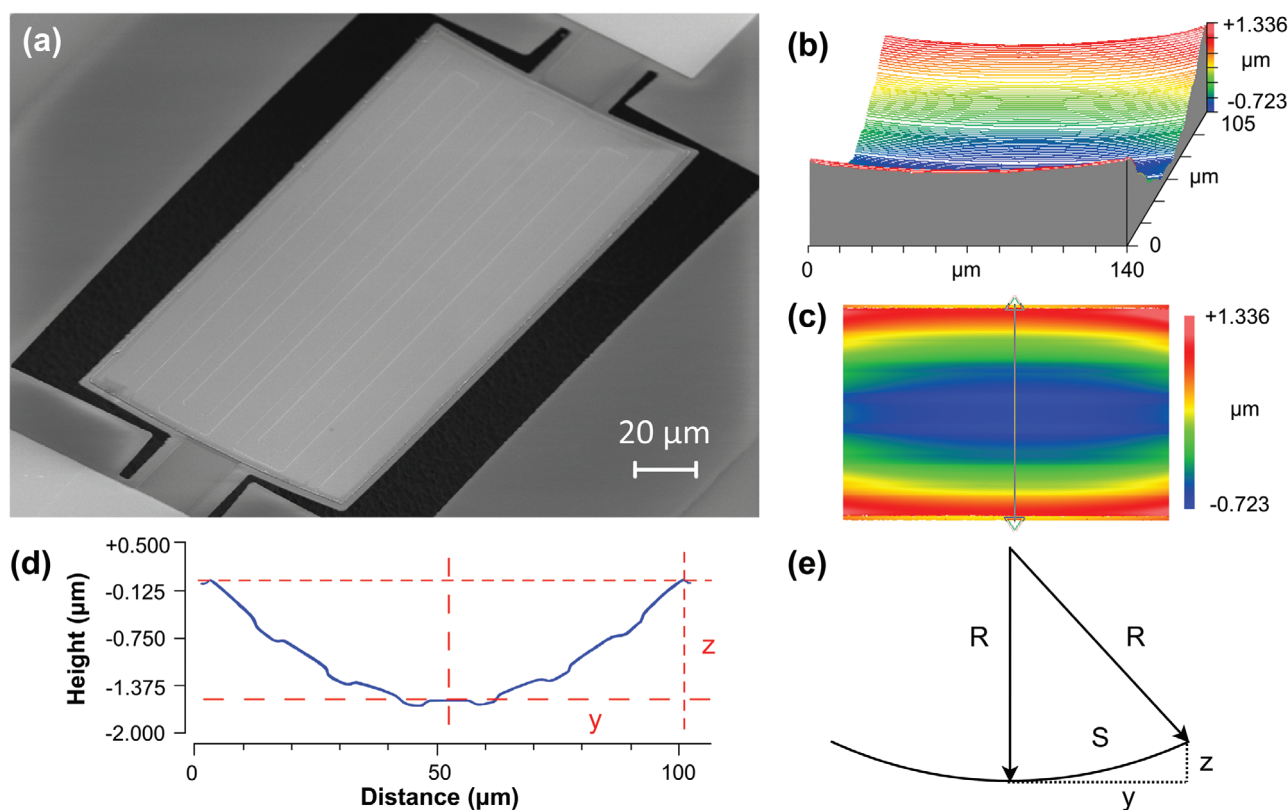


Figure 2. Example of a magnetolectric nanoplate resonator and analysis of its curvature using an optical profilometer. The vertical scale in the profilometer output is exaggerated. a) Scanning electron micrograph of a resonator (ID 2 in Table 1) suspended above a chemically etched trench. The outline of the interdigital electrode fingers is faintly visible. b) A 3D profile of the resonator surface obtained by an optical profilometer. The field of view was too small to capture the full resonator in that magnification, so only 140 μm of length is visible, with the view window approximately centered on the resonator. c) A top-down view of the same image, with a line drawn across it to generate a cross-section slice of the surface profile. d) The cross-section slice spans the width of the resonator plate. The surface topography is more evident, and the outlines of seven electrode fingers, forming the bottom layer, are visible. Parameters y and z are obtained from this measurement, and z in this particular case is 1.56 μm . e) The cross-section of the resonator plate surface is modeled as a circular arc, and R is calculated numerically using the known value of S and the obtained value of z .

state (no annealing). In Investigation 2, the magnetic material was varied both in thickness and in composition: 250, 500, and 1000 nm of total thickness was used, with FeGaC used for some sensors and FeGaB for others. FeGaC ((Fe₈₀Ga₂₀)₈₉C₁₁ at%) was introduced because recent results showed a potentially improved ΔE effect^[28] compared to FeGaB. Each batch of sensors used in Investigation 1 and Investigation 2 was fabricated on a separate Si wafer.

By virtue of the piezoelectricity of AlN, and the particulars of the IDE layout, the sensors can be driven in contour-mode vibrations by supplying an AC electric signal through the IDE, thereby activating the d_{31} vibrational mode^[29] in the AlN. Figure 1 (right) provides a qualitative illustration of the induced electromechanical wave, obtained from COMSOL Multiphysics for a sensor of design ID 1. The mechanical resonance frequency of the resonator can be approximated by^[30]

$$f_0 = \frac{1}{2w_0} \sqrt{\frac{E_{\text{eq}}}{\rho_{\text{eq}}}} \quad (1)$$

where w_0 is the pitch (separation) of the IDE fingers, E_{eq} is the equivalent Young's modulus, and ρ_{eq} is the equivalent density of the composite resonator. This expression was accurate

to within $\approx 8\%$ of the resonance frequency measured, with no magnetic field applied. (Modulus and density values for the constituent materials are listed in the Experimental section.)

In the course of fabrication, every device (for both Investigation 1 and Investigation 2) was subjected to a widthwise in situ magnetic field during sputter-deposition of the magnetic material with the objective of setting the material's magnetic easy axis along the width of the resonator (perpendicular to the IDE fingers). During testing, a DC magnetic field was applied along the length of the resonator, or parallel to the IDE fingers (Figure 1, bottom left). This causes the average magnetization to change and the magnetostrictive layers to undergo a change in Young's modulus (ΔE effect); consequently, a change in resonance frequency can be observed in the sensor as a whole.

2.1. Resonator Plate Curvature and Sensor Frequency Response

At the end of fabrication, but before performance testing, the suspended resonator plates were imaged by an optical profilometer (Figure 2b–d), whereby quantitative, 3D profiles of the resonator surfaces could be obtained thanks to the metallic and reflective top material layer. To quantify the resonator plate

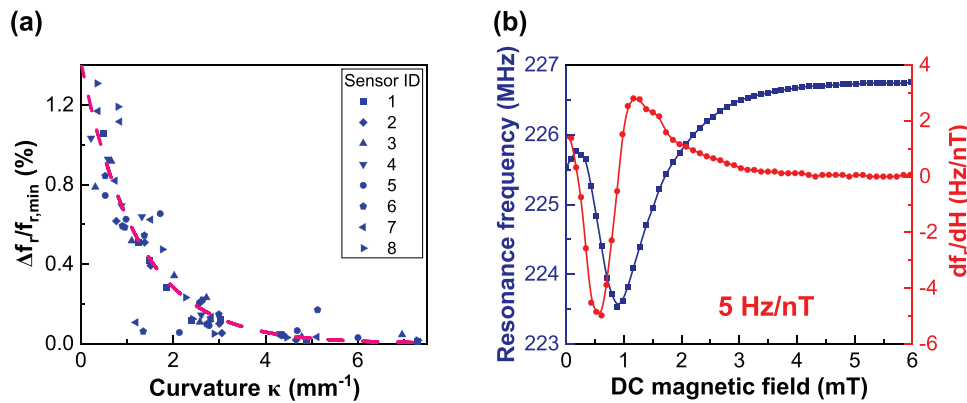


Figure 3. a) Compilation of performance results for all the magnetoelectric sensors that were microfabricated and characterized from a single 4" Si wafer in Investigation 1. Each sensor device is one of eight possible designs but with identical material layers, as summarized in Table 1, and designated by data point shape. Multiple copies of each design were made and characterized, with strongly varying outcomes in resonator plate curvature and response to magnetic fields. The total frequency response of each sensor to DC magnetic fields ranging from 0 to ≈ 14 mT is quantified as $\Delta f_r / f_{r,\min}$. It is plotted against the resonator plate curvature determined by optical profilometer measurements. A strong correlation is evident, with a decaying exponential function fit included to highlight the trend. b) The frequency response curve of the best performing sensor. A difference of 3.22 MHz between maximum and minimum frequencies was observed, giving $\Delta f_r / f_{r,\min}$ of 1.4%. Maximum sensitivity, $|df_r/dH|$, was about 5 Hz nT^{-1} at 0.6 mT DC bias field.

deformation, we performed line scans of each resonator surface across its width, approximately centered midway between the anchors (Figure 2c,d). We then modeled this surface cross-section as a circular arc (Figure 2e) and calculated the curvature κ ($= 1/R$) so as to normalize the deformation between devices of different widths. Concave-shaped resonators (such as in Figure 2) were assigned $\kappa > 0$, while any convex resonator plates were given $\kappa < 0$.

The sensor performance was tested by sweeping the frequency of the driving AC electric signal while applying a DC magnetic field lengthwise to the sensor. The DC magnetic field was incrementally increased from zero to over 10 mT, with frequency sweeps performed at each DC field value. The resonance frequency f_r for each DC field was recorded, and a total frequency response for a given sensor was quantified by

$$\Delta f_r / f_{r,\min} (\%) = \frac{f_{r,\max} - f_{r,\min}}{f_{r,\min}} \times 100 \quad (2)$$

Often, f_r initially decreased with applied magnetic field and then increased again, which is consistent with trends observed in studies on the ΔE effect.^[31–35] But this was not always the case, as many sensors did not really exhibit an initial dip in frequency. Reasons for this will be presented in Section 2.3. In all cases, however, the maximum observed frequency ($f_{r,\max}$) was higher than f_r at zero field. (A sample of $f_r(H)$ curves is available in Supporting Information).

2.1.1. Investigation 1: Material Layers Kept Constant in All Sensors

It was found that significant variation in resonator plate curvature κ occurred between the sensor devices. This was the case even though, in the first investigation, all the sensors had the same layer composition and were fabricated on the same Si wafer, and the geometry of resonator plate and IDE were either identical or similar. It became apparent that this curvature—which is a manifestation of residual stress—was a dominant

predictor of sensor performance, superseding the effects of the eight design variations that are listed in Table 1. Illustrated in Figure 3a, lower $\Delta f_r / f_{r,\min}$ is strongly correlated with higher κ (less flat resonator plate). The trend declines rapidly and nonlinearly and results in large variation in sensor performance: two orders of magnitude separate devices with the highest and lowest $\Delta f_r / f_{r,\min}$. An exponential decay curve was fitted here (details available in Experimental section) simply to highlight the trend, but a fit based on modeled magnetic behavior will be shown later in this work (Figure 10). As detailed further in Section 2.3., the curvature is an outward indicator, but the underlying influence on magnetic behavior of the sensors is ultimately caused by stress.

One of the devices with design 1 (see Table 1) had the best performance, and its $f_r(H)$ curve is illustrated in Figure 3b. From $f_{r,\min}$, occurring at 0.88 mT, to $f_{r,\max}$, the Δf_r was 3.22 MHz, with $\Delta f_r / f_{r,\min}$ of 1.4%. For applications, the more important parameter is sensitivity, and maximum sensitivity occurs at 0.6 mT, with $|df_r/dH|$ of about 5 Hz nT^{-1} . As far as we know, this is the highest sensitivity achieved in any magnetometer that involves a frequency shift in its working principle.

Furthermore, we quantified the degree to which the resonator plate curvature—and with it, sensor performance—could be modified by two processes after fabrication was complete. One procedure, which produced very substantial changes in the resonator attributes, was magnetic annealing (Figure 4a). A set of eight sensors, after initial performance tests, was subsequently annealed in vacuum at $280 \text{ }^\circ\text{C}$, with ≈ 150 mT applied along the width of the resonator (same orientation as when the magnetic films were deposited). Annealing has been shown to elicit improved magnetostrictive properties in FeGaB multilayer films,^[27] which could help to improve the frequency response of the sensors. However, when the devices were characterized again, they showed significantly increased κ (factor of 2 or more), and $\Delta f_r / f_{r,\min}$ was also reduced in all sensors—over an order of magnitude in some cases.

A secondary way to affect the resonator's initial physical state, with less drastic outcomes, was also found: using an elevated voltage amplitude of the AC electric signal that drives

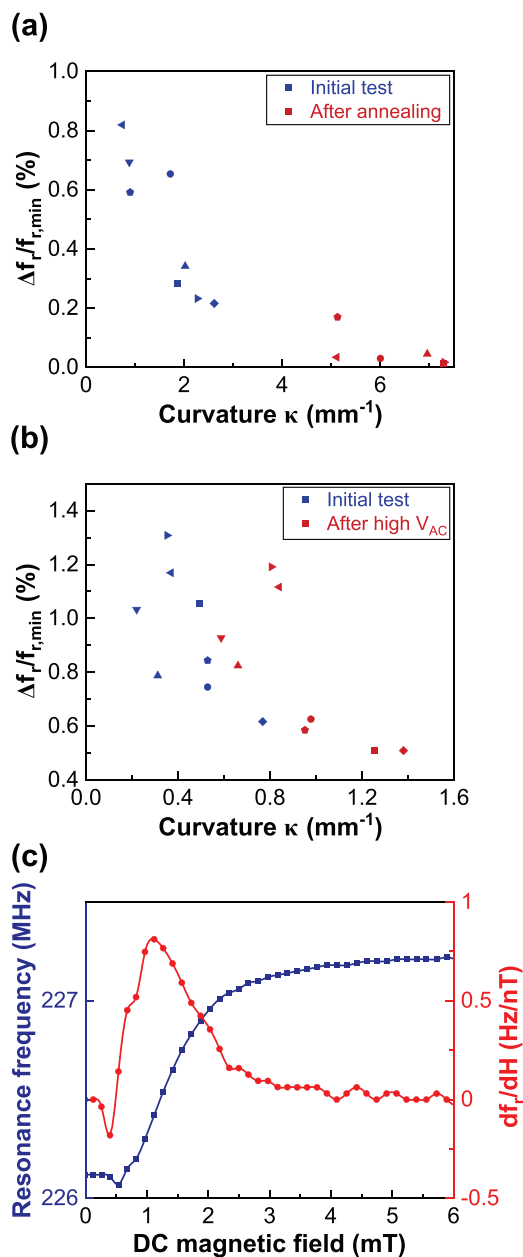


Figure 4. It was found that the resonator curvature and sensor performance could be affected after fabrication had been completed. a) One set of sensors was characterized and then annealed with a strong magnetic field applied in the same way as during original fabrication. After annealing, the sensors featured considerably more curved resonators than before, with a much-reduced $\Delta f_i/f_{r,\min}$. b) A similar but much smaller effect was also demonstrated by using an elevated amplitude of the driving AC electric signal. After testing a set of eight sensors with a driving signal of 150 mV amplitude, the degree of resonator warping was remeasured and the sensor performance retested, with results indicating increased curvature and decreased total frequency response. c) In addition to changes in $\Delta f_i/f_{r,\min}$, the shape of the response curve $f_i(H)$ was also affected. Performance of the same device as in Figure 3b is shown here, at a later time, after it was tested for the fourth time at 150 mV driving AC voltage.

the resonator's contour-mode vibrations. After initial testing of another set of eight sensors (not the same as the annealed set), these devices were subjected to multiple rounds of testing at

150 mV of AC amplitude. Figure 4b compares the early state of devices to their later state, after approximately 2–5 trials of such testing (some devices were tested more than others), and reveals an increased κ for all eight devices—with a corresponding drop in $\Delta f_i/f_{r,\min}$.

In addition, the characteristics of the $f_i(H)$ curve were also modified when the shape of the resonator plate changed. Figure 4c illustrates the same device as in Figure 3b after being tested for the fourth time at 150 mV driving voltage. The $f_i(H)$ no longer exhibits a large, steep drop to a local minimum; instead, there is just a slight dip, and the rise to saturation also covers a smaller range of only ≈ 1 MHz. Hence, we observe a reduced maximum sensitivity of $|df_i/dH| < 1$ Hz nT⁻¹, as well as a different combination of parameters (DC bias field and excitation frequency) corresponding to this sensitivity maximum. We have since found that a driving voltage of < 70 mV under this setup appears to be safe for avoiding this phenomenon (data not shown).

In both of the outlined processes, either annealing or use of high driving voltage, increased κ correlated directly with a reduced frequency response of the sensors. This reinforces the evidence that the physical effects associated with the curvature parameter have a deterministic influence on the ΔE -effect behavior of the magnetic material. Clearly, the curvature is a manifestation of residual stresses that accumulate in the thin films during fabrication and equilibrate after the release of the resonator from the substrate. Furthermore, it is unsurprising that residual stress may vary across a wafer in sputtered films, as evidenced by studies that have quantified stress variations in AlN across wafers.^[36–38] We do not know the degree to which such wafer location-based stress nonuniformity in the AlN film, compared to the subsequent chip-by-chip deposition of the magnetic multilayer, contributes to causing residual stress differences between the completed sensor devices. One way or another, the stress nonuniformities evidently led to significant variation in the performance of these magnetometers.

Of the two mechanisms, annealing caused a much stronger change in the relative stress between the layers. Specifically, the significant increase in κ after annealing implies that the stress on the magnetic film became more tensile.^[33,39,40] Hence, annealing with the parameters used here could be utilized to relax the stress in the magnetic layers if the resonator plates have $\kappa < 0$ after fabrication, and thereby improve the sensor frequency response. But there is an opportunity to study the annealing method further to see if different process parameters can tune the stress in the other direction^[41] so as to achieve performance improvement for sensors with $\kappa > 0$ as well. Further investigation is also necessary to fully understand the effect generated by high-voltage driving amplitude.

2.1.2. Investigation 2: Varying Thickness and Composition of Magnetic Layer

In the second investigation, another batch of magnetometers was fabricated on a new Si wafer using the same lithographic masks, so the produced ME sensors had the same layouts in the lateral dimensions. However, new parameters were introduced

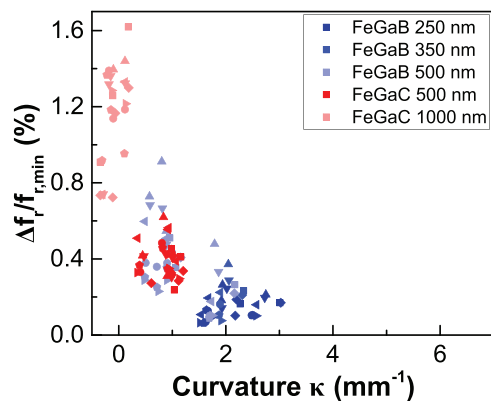


Figure 5. Another investigation of frequency response was conducted with a second batch of magnetometers. For comparison, the span of the x-axis was scaled to match that of Figure 3a, and the same data point shapes are retained to indicate the eight sensor designs from Table 1. These sensors were made with a varying total thickness of magnetic films, and the composition of the magnetic material was also varied: FeGaC was tested in addition to FeGaB.

by varying the total thickness of the magnetic material—from 250 nm up to 1 μm —and also its composition: in addition to the same FeGaB films, FeGaC ((Fe₈₀Ga₂₀)₈₉C₁₁ at%) was also used to test for an improved ΔE effect.^[28] The sensors were analyzed and tested in the same way as previously.

Several aspects of the results, presented in **Figure 5**, stand out. In aggregate, flatter resonators had greater total frequency response, $\Delta f_r/f_{r,\min}$, as before, and again the frequency response decreases very rapidly as the curvature κ increases. Because the material thickness and composition are no longer kept constant, however, curve fitting was not done here. Inspecting the subsets of the data, it can be seen that thicker films generally result in a less-curved resonator plate. Also, there is reduced scatter in κ in the thickest sensors (1 μm FeGaC). At the same time, the scatter along the y -axis of the plot seems to increase as the magnetic film thickness increases. These aspects of the data subsets may be interconnected. Intuitively, greater flexural forces are required to attain the same curvature in a thicker plate, all else being equal. Therefore, κ being a proxy for stress, a given distribution in residual stress should translate to a narrower distribution in κ in the thicker resonators compared to the thinner ones. However, it is the stress that influences the magnetic properties, not κ directly; so, thicker magnetic films should result in greater change in magnetic properties (here $\Delta f_r/f_{r,\min}$) for every unit of change in κ . There may also be other effects at play in adding to the scatter in $\Delta f_r/f_{r,\min}$ performance. Also of note is that there seems to be no significant difference in the potency of the ΔE effect between FeGaB and FeGaC, since the cluster of points at around 1 mm^{-1} of κ , with 500 nm of magnetic layer thickness, have similar $\Delta f_r/f_{r,\min}$ for either material. A recent study^[28] suggested that FeGaC has superior ΔE effect at higher thickness, but these results do not support that.

Based on Equation 1, it may be expected that thicker magnetic material—that is, larger magnetic volume fraction—would produce a bigger change in equivalent Young's

modulus (E_{eq}) of the resonator and in turn a larger frequency response, $\Delta f_r/f_{r,\min}$. Qualitatively, this is somewhat supported by the results, as the highest $\Delta f_r/f_{r,\min}$ performance from a sensor with 1 μm thick magnetic layer is higher than that of any sensor in Figure 3a. However, this improvement is smaller than Equation 1 predicts: given some $\Delta f_r/f_{r,\min}$ for a sensor with 250 nm of magnetic material, and then assuming the same ΔE effect for 1000 nm of magnetic films, the expected $\Delta f_r/f_{r,\min}$ would be $\approx 80\%$ higher than for 250 nm. That is, $\Delta f_r/f_{r,\min}$ should reach to $>2\%$. With a larger magnetic volume fraction, changes in the magnetic properties may appear that Equation 1 does not account for, such as changes in domain configurations and demagnetizing field.

2.2. Quality Factor

Another property of the magnetometers that was examined is the resonator quality factor. **Figure 6a,b** shows a compilation of quality factor data for the same sets of sensors that were evaluated for frequency response in Investigation 1 and Investigation 2. These measurements were performed separately, following the completion of the $\Delta f_r/f_{r,\min}$ tests. No magnetic field was applied, and a network analyzer was used to collect the data. We can conclude that, generally, there appears to be a tradeoff between larger $\Delta f_r/f_{r,\min}$ and Q . On the other hand, there can be a high amount of inconsistency in Q results, with the 500 nm FeGaC category showing especially high scatter. On a basic level, the trend of declining Q can be understood as a consequence of greater energy loss (damping) in the magnetic material than in the nonmagnetic part of the resonator. When $\Delta f_r/f_{r,\min}$ is large (large ΔE effect), the magnetization is more susceptible to the oscillating stress induced by the driving voltage. The magnetization and magnetic domains then undergo larger oscillations that lead to greater energy dissipation.^[42,43] The total Q can therefore be expected to asymptotically approach a minimum at which this magnetic damping is maximized and corresponds to the highest achievable $\Delta f_r/f_{r,\min}$ in these magnetometers.

From its basic definition, Q can be written as

$$Q = \frac{2\pi f_r}{\gamma} \quad (3)$$

where γ , the damping constant, contains the terms for total energy and power loss. As a rudimentary model, we can split the damping into a sum of two parts: the contribution from the nonmagnetic portion of the resonator (IDE and AlN), and the contribution from the magnetic layers. As an idealization, we assume that the variations in damping between the same type of sensors are entirely due to differences in magnetic behavior, so the nonmagnetic properties are constant. This assumes that the microfabrication can be performed with consistent outcomes. The magnetic contribution would need to go to zero in the case of a sensor where the ΔE effect is very low and should have an upper limit when the highest frequency response is achieved. The simplest way to represent this may be the following:

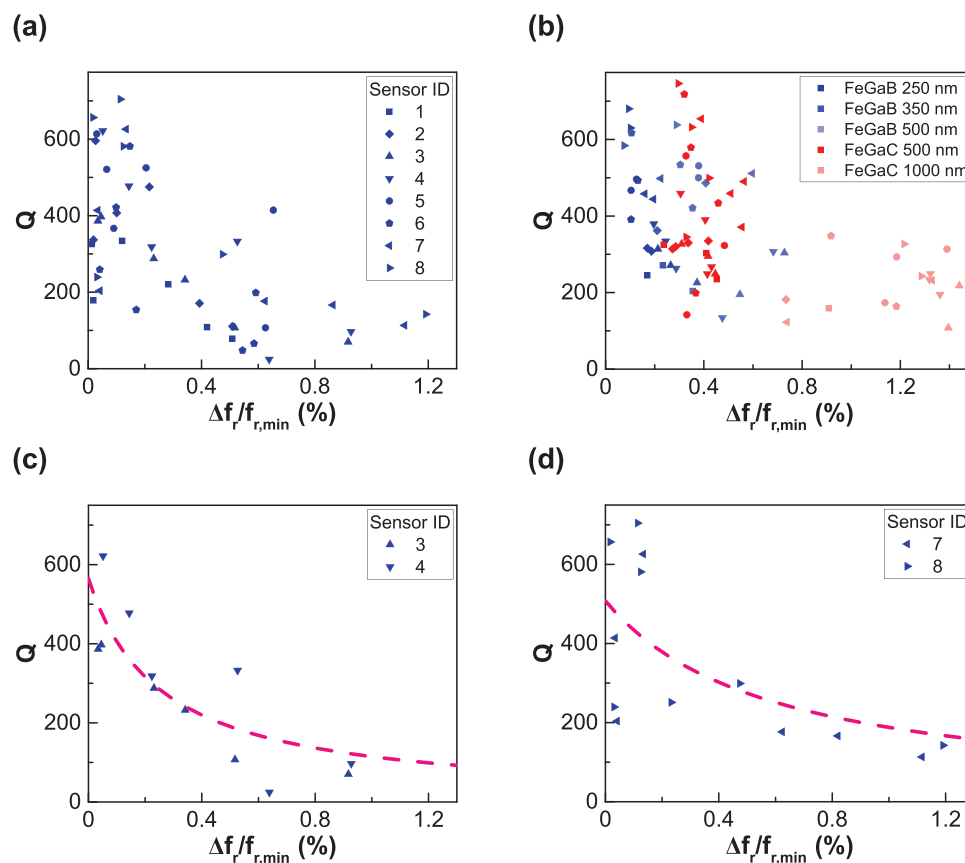


Figure 6. Q measured (no magnetic field applied) on the same sensors that were tested in Investigation 1 and Investigation 2 and presented in Figures 3a and 5, respectively. Stronger frequency response appears to be correlated with a lower Q . a) Q of the set of sensors from Investigation 1, with the multilayer structure kept constant. b) Set of sensors from Investigation 2, with varying magnetic material and thickness. c,d) Subsets of the data in a) with a simple model used for curve fitting (Equation 4). The model requires a fixed resonance frequency f_r , so the full dataset in a) could not be used due to different sensors operating at different f_r . Instead, two of the four pairs of sensor designs were selected. Within each pair, the sensors are identical except for the anchor width (See Table 1), and f_r is constant to within 6%. Sensor designs 3 and 4 are presented in c) with average f_r of 246 MHz, and designs 7 and 8 are shown in (d), with average f_r of 138 MHz.

$$Q = \frac{2\pi f_r}{\gamma_{NM} + \gamma_M \frac{x}{x_{max}}} \quad (4)$$

Here $x = \Delta f_r / f_{r,min}$, x_{max} is the highest $\Delta f_r / f_{r,min}$ that was achieved for that type of sensor, and γ_{NM} and γ_M are the damping constants for the nonmagnetic and magnetic parts of the sensor, respectively, which can be obtained as fitting parameters. The f_r is known, but this value varies between the different sensor designs, so this simple model cannot be fitted to the full ensemble of sensor data in Figure 6a,b.

Two subsets of data from the full dataset of Figure 6a are presented in Figure 6c,d: sensor design pairs 3 and 4, and 7 and 8 (see Table 1). Within each pair, the only difference between the two sensor types is different anchor width, which generally had minimal impact on performance characteristics, and the f_r (at zero field) in each subset of sensors was constant to within 6%. The expression from Equation 4 was fitted to each subset, and the results are given in Table 2, showing that the magnetic damping constant thus derived is larger than the nonmagnetic constant by at least a factor of two.

2.3. Magnetic Properties and the ΔE Effect

The possibility of observing changes in the output signal from a ΔE effect-based magnetoelectric sensor, in response to changing DC magnetic fields, is fundamentally made possible by the magnetostrictive property of ferromagnetic materials (FeGaB and FeGaC have positive magnetostriction^[26–28]). When the sensor is under test, the resonator plate (including the magnetic layer) is in a state of forced, contour-mode electromechanical vibrations actuated by the driving AC voltage. The antinode regions of the resonator are undergoing compressive/tensile cycles that are superposed on whatever preexisting level of residual (static) stress exists within the films.^[34] As the sensor is exposed to magnetic fields, any magnetization rotation in the

Table 2. Damping constants obtained from Equation 4.

Sensor ID	γ_{NM} (10^8 Hz)	γ_M (10^8 Hz)
3 & 4	0.027	0.15
7 & 8	0.017	0.041

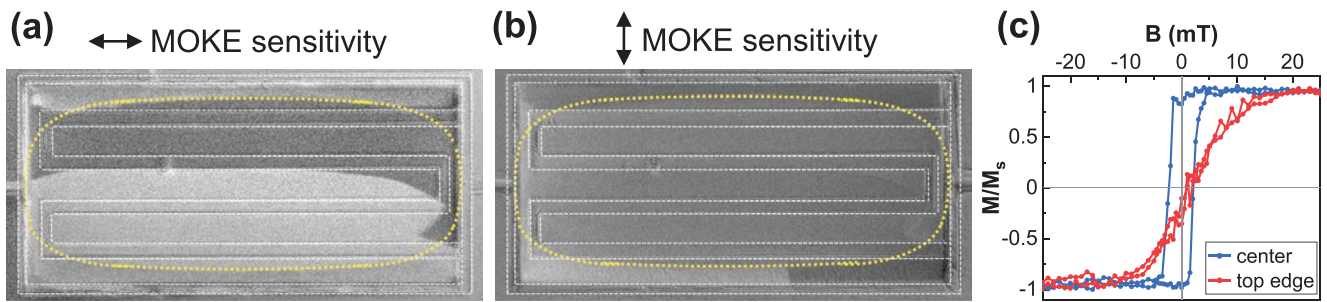


Figure 7. a,b) Magnetic domain images obtained using the magneto-optical Kerr effect (MOKE), measured on a sensor of type ID 3 (see Table 1) from Investigation 2, with 500 nm of total FeGaB thickness. The images show the magnetic state after demagnetizing along the x -axis, and the same magnetic state is shown in both but with different orientations of the MOKE sensitivity axis. The contours of the IDE are highlighted with the white dotted lines. The yellow dotted lines denote an approximate boundary between regions with differently aligned magnetic anisotropy. c) Corresponding magnetization curves for a region inside the yellow boundary and a region on the outside, at the top edge of the resonator plate. Magnetic domain images were obtained after degaussing along the x -axis.

magnetic film induces a magnetostrictive strain λ that adds up to the mechanical strain ϵ . This causes an apparent change of the elastic modulus— ΔE effect—which in turn affects a shift in resonance frequency.^[18,44]

During sputter-deposition of the magnetic thin films, an in situ magnetic field was applied along every sensor's width (defined as the y -axis) to induce an in plane uniaxial magnetic anisotropy. In the analysis to follow, we define this field-induced anisotropy together with the film's shape anisotropy as the effective field-induced anisotropy K_{eff} . However, residual stress accumulates in sputtered films, and through magnetoelastic interactions the stress anisotropy may dominate the magnetic anisotropy landscape and the magnetization behavior. This is of high relevance, as upon release of the structure, a strain develops until a static-equilibrium stress σ and strain ϵ remain. The out-of-plane component u_z of the corresponding equilibrium displacement vector \mathbf{u} is then visible as a curvature, and the remaining stress will influence the magnetic properties, if it is anisotropic. But the exact behavior and coupling of magnetic properties with the observed curvature in such devices are not trivial to predict.

2.3.1. MOKE Analysis

The domain state of one of the sensors (a device from Investigation 2, with 500 nm total FeGaB thickness, and design ID 3) was imaged using magneto-optical Kerr effect (MOKE) microscopy.^[45] Example images of the demagnetized state of magnetization are displayed in **Figure 7a,b** together with magnetic hysteresis curves in **Figure 7c** representing the center region—inside the yellow dashed oval in **Figure 7a,b**—as well as an area at the top edge of the sensor that is outside the oval. Noticeable are the irregular shape of the domains and the absence of closure domains at the edges. The absence of closure domains is an indication of a weakly coupled magnetic multilayer structure.^[46,47]

In **Figure 7a,b**, the dashed oval identifies an approximate center area where coarse domains have formed with magnetization oriented lengthwise (defined as the x -axis), indicating that the effective easy axis of magnetization is also aligned mostly along x . This is further supported by the magnetization loop

that was recorded in the center region (blue curve in **Figure 7c**), showing typical easy axis behavior. In contrast, the edges and corners of the sample (outside the yellow dashed oval) behave differently. There the magnetization is not aligned with x ; rather, the effective magnetic easy axis is aligned mainly along y . From the magnetization loop in **Figure 7c**, the strength of the effective anisotropy density in the edge region is estimated to be approximately $K_{\text{eff}} = 4 \text{ kJ m}^{-3}$ (assuming $\mu_0 M_s = 1.4 \text{ T}$), which is much higher in magnitude than the estimated $K_{\text{eff}} \approx 0.8 \text{ kJ m}^{-3}$. (The estimation process for K_{eff} is described in Experimental section.) Given the local scope of the hysteresis loop measurement, magnetic stray field interactions from other regions of the magnetic layer could be contributing to field offsets in the hard axis loop. In addition, these stray field interactions could also be a result of magnetic layers of a different configuration underneath. In summary, the MOKE analysis proves the dominance of spatially varying magnetoelastic anisotropy contributions. Considering the surface sensitivity of the MOKE signal and the evidence of magnetic multilayer behavior in the layer stack, the magnetization and anisotropy distribution in the buried magnetic layers cannot be easily determined. Modeling can give more insight on this and help explain the magnetoelastic influence on the sensor response.

2.3.2. Magnetomechanical Model

For that, we have performed mechanical finite-element-method (FEM) simulations to explain the observed correlation between the sensors' frequency response and curvature κ of the resonator plates. The sensors were simulated in COMSOL Multiphysics (v. 5.4) using a simplified geometry with flat material layers (without the undulations visible in **Figure 2d**) and without the thin nonmagnetic spacer layers in the magnetic multilayer. The release process is modeled by setting an initial homogeneous plane stress σ_0 for the FeGaB layer and zero stress for the AlN layer while the simulated resonator plate is flat. In this case, the deformation of the resonator after release is determined mainly by the difference in stress between the layers before release, so these initial values represent that difference of mean stresses between the two layers. A linear static study is then performed (allowing the plate to deform) to

obtain the static equilibrium displacement \mathbf{u} , the corresponding strain ϵ , and stress σ . Details about the FEM model are given in the Experimental section.

With the equilibrium stress tensor field from the FEM model, the magnetoelastic enthalpy density of a given magnetization field can be obtained by^[48] (using tensor notation)

$$h_{me} = \frac{1}{2} b_{ij} C_{ijkl}^{-1} b_{kl} - b_{ij} C_{ijkl}^{-1} \sigma_{kl} - \frac{1}{2} \sigma_{ij} C_{ijkl}^{-1} \sigma_{kl} \quad (5)$$

In this expression C_{ijkl}^{-1} are the components of the isotropic inverse mechanical stiffness tensor, σ_{ij} are the components of the mechanical stress tensor, and b_{ij} are the components of the magnetoelastic stress tensor. In the case of isotropic magnetoelastic coupling, b_{ij} is given in quadratic approximation by^[49]

$$b_{kl} = B_{ijkl} m_i m_j \text{ with } B_{ijkl} = B_1 = -\frac{3}{2} \lambda_s (C_{1111} - C_{1122}) \quad (6)$$

Given that $\lambda_s = 75$ ppm, $C_{1111} = 289.4$ GPa, and $C_{1122} = 124$ GPa (from $E_m = 215$ GPa and Poisson's ratio $\nu = 0.3$), the magnetoelastic coupling constant of FeGaB is approximately $B_1 = -18.6$ MPa. The components of the reduced magnetization vector \bar{m} are given by $m_i = \cos(\alpha_i)$, with the magnetization orientation angle α_i relative to the i^{th} coordinate axis. Due to the assumption of a large out-of-plane demagnetization factor that keeps the magnetization in-plane, we assume $m_3 = 0$. By this, we are neglecting any domain wall and edge effects. The magnetoelastic anisotropy energy density $K_\sigma = \max(h_{me}) - \min(h_{me})$ is obtained from the minimum and maximum of h_{me} as a function of α_i , and the stress-induced easy axis angle ϕ_σ corresponds to the α_1 that minimized h_{me} .

2.3.3. Magnetomechanical Model Results

The mechanical model constructed in COMSOL was fitted to the profilometer-obtained surface profile of the sensor that

was also imaged by MOKE (Figure 7), from Investigation 2, and to the surface profiles of six other sensors from Investigation 1 (250 nm total FeGaB), all having designs 3 or 4 from Table 1. Together, this subset of seven sensors spans essentially the same range of κ values as the full ensemble of sensors in Figure 3a. For the MOKE-imaged device, initial stress components were tuned until a good match was obtained with $\sigma_{0,11} = 45$ MPa, $\sigma_{0,22} = 75$ MPa, and $\sigma_{0,12} = 5$ MPa, which is in the range of stress that may be expected for sputtered films.^[36,38,50] The z-component of the displacement vector field, after letting the initial stress go to equilibrium, is shown in comparison with the measured profile in Figure 8a, and it can be seen that measurement and simulation match very well. The displacement is asymmetric relative to the xy -coordinate axes, which is caused by the nonzero in-plane shear component σ_{12} of the equilibrium stress. The nonzero equilibrium stress components are plotted as a function of the z -position for the center of the plate in Figure 8b, and they show a clear stress anisotropy that varies linearly with z , except for the abrupt change at the material interface. Because of the large ratio of magnetic layer thickness to AlN layer thickness, an approximate neutral axis is present at $z \approx 300$ nm in the FeGaB layer, where the signs of the three stress components change (although the components do not cross zero at precisely the same location). This pattern of the stress components as a function of z is qualitatively in line with expectations based on analytical calculations of a similar case.^[51] Hence, at the surface $\Delta\sigma \equiv \sigma_{11} - \sigma_{22} > 0$, whereas $\Delta\sigma < 0$ in the rest of the FeGaB layer, with values up to $|\Delta\sigma| \approx 30$ MPa and shear components $\sigma_{12} < 6$ MPa. Compared to σ_{11} and σ_{22} , the value of σ_{12} is small, but its effect can still be clearly seen as a twist of the plate.

Whether this stress distribution significantly influences the magnetization behavior or not depends on whether the magnetoelastic anisotropy energy density K_σ is greater than K_u , which includes the effects of the y -directional in situ magnetic field during film growth as well as the film's shape anisotropy. Indeed, we find this to be the case for most sensors, as we demonstrate below. First, however, we present the magnetoelastic

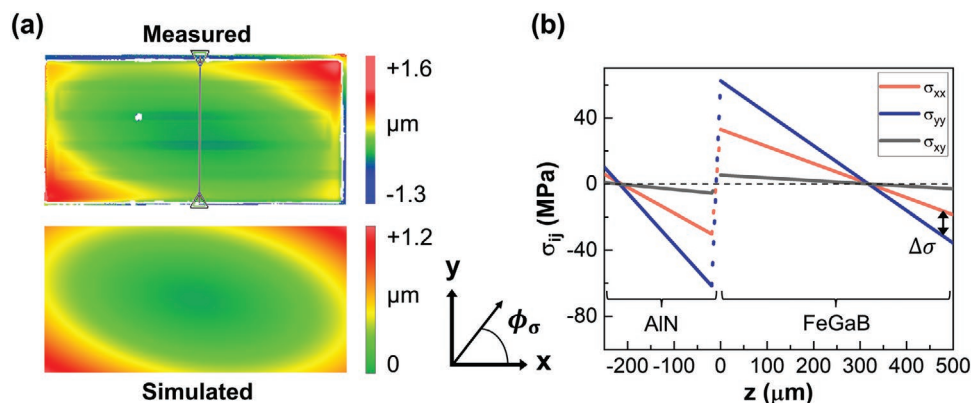


Figure 8. a) Comparison of measured and simulated z -displacement of the same sensor that was imaged by MOKE (Figure 7): design ID 3, with 500 nm of total FeGaB thickness. The simulation featured flat layers in the material stack, so the electrodes on the underside of the resonator are not visible in the simulated result. The z -displacement scale in the measured result covers a wider range because the profilometer is detecting the edge of the underlying AlN layer, and due to automatic scale settings in the profilometer software, whereas the scale for the simulated result spans only the range of the surface topography. Coordinate axes relative to the resonator plate are defined by the schematic with the xy -axes. All angles are defined as relative to the x -axis, as indicated by the stress-induced easy axis angle ϕ_σ . b) In-plane stress components of the simulated resonator plate along a z -cutline through the center of the xy -plane.

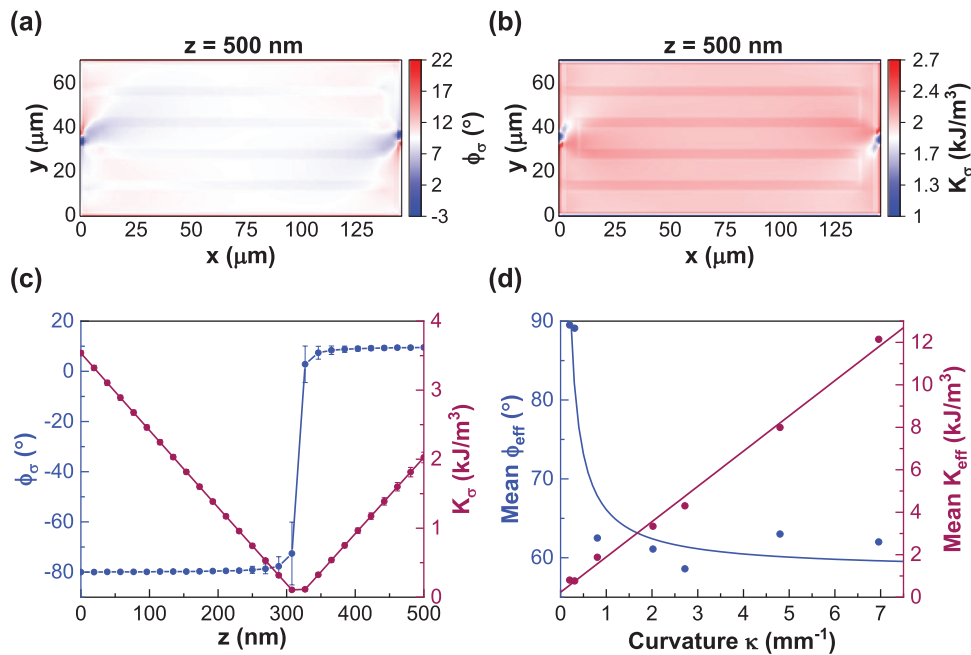


Figure 9. a–c) Magnetomechanical model results for the same sensor that was analyzed by MOKE (Figure 7). a) Stress-induced magnetic easy axis angle at the surface layer ($z = 500$ nm) of the magnetic film. b) Magnetoelastic anisotropy energy density at the surface layer. c) Mean stress-induced easy axis angle and magnetoelastic anisotropy energy density, averaged over the xy -plane, as a function of z -position and the standard deviation of each. d) The effective easy axis angle and effective anisotropy energy density are averaged over each xy -plane; these plane averages are then averaged to obtain a single volume-averaged ϕ_{eff} and K_{eff} for each sensor. This simulation and modeling process is repeated for six additional sensors with different curvatures κ : ϕ_{eff} is fitted with a power function and K_{eff} with a linear function, both given in the Experimental section.

effects alone. In **Figure 9a**, the stress-induced magnetic easy axis angle ϕ_{σ} at the surface of the resonator ($z = 500$ nm) is plotted over the xy -plane. Over the whole plate surface, ϕ_{σ} varies mainly around approximately 9° , whereas larger values of up to 16° occur in narrow strips at the very top and bottom edges. Close to the anchors, high-stress gradients are present that result in local maxima and minima of around 22° and -3° . Overall, the average angle ϕ_{σ} across this plane is nearly perpendicular to the y -direction that was intended with the in situ magnetic field.

A similar pattern is visible in the magnetoelastic anisotropy energy density K_{σ} (Figure 9b): again, the extreme values are found near the anchors and at the top and bottom plate edges. A variation of approximately 1.5 kJ m^{-3} from highest to lowest is confined to a small space around the anchors, and minimum values of $K_{\sigma} \approx 1 \text{ kJ m}^{-3}$ exist at the edges. Although the electrodes are on the other side of the plate, they are clearly visible in both the ϕ_{σ} and K_{σ} fields due to their impact on the equilibrium stress balance within the material stack.

The values of ϕ_{σ} and K_{σ} , averaged over the xy -plane, are plotted as a function of z in Figure 9c together with the corresponding standard deviations. In accordance with the stress anisotropy changing with z in Figure 8b, the average angle ϕ_{σ} rotates continuously from -80° to about 10° relative to the x -axis, with a rapid transition around the neutral axis. Around the neutral axis, K_{σ} necessarily has a minimum, but it is not exactly zero because the zero transitions of σ_{ij} components are at slightly different z -positions. The thickness dependency of the stress results in a volume-mean magnetoelastic anisotropy that differs markedly from the properties of the top layer, which

is the only layer that can be directly compared with the MOKE observations.

Crucially, K_{σ} reaches almost 3.5 kJ m^{-3} , and is as high as 18 kJ m^{-3} in other sensors (not shown). Such large K_{σ} values occur—despite the small stress anisotropy—due to the large saturation magnetostriction λ_s . By comparison, we estimated K_u of just $\approx 0.8 \text{ kJ m}^{-3}$ (detailed in Experimental section). Thus, we conclude that the effective anisotropy energy density K_{eff} is expected to be dominated by the internal stress field in most cases.

The influence of the shear component, σ_{12} , should also be noted. Assuming that the bias field-induced uniaxial magnetic anisotropy K_u is well aligned to the y -axis, the effective magnetic energy minima/maxima would coincide with the xy -axes. The principal stress components can then only flip the energetically favorable orientation between x and y but cannot rotate these energy axes. Shear stress, however, acts to rotate the magnetic easy axis to 45° . Hence, despite the small values of σ_{12} compared to σ_{11} and σ_{22} , there is still notable rotation, about 10° , of the stress-induced magnetic easy axis: ϕ_{σ} switches between roughly -80° to 10° instead of -90° to 0° .

The process of fitting the mechanical model to the measured sensor profile (exemplified in Figure 8a) and finding the stress distribution (like Figure 8b) was repeated with another six sensors that form a representative subset. (These stress distribution results are available in Supporting Information.) Likewise, the calculations of ϕ_{σ} and K_{σ} for the remaining sensors were carried out as above (via Equations 5 and 6), and K_{eff} and effective easy axis angle ϕ_{eff} were calculated using K_{σ} , ϕ_{σ} , and a superposed K_u of 0.8 kJ m^{-3} with angle ϕ_u . In Figure 9d,

the volume-averaged ϕ_{eff} and K_{eff} for each of the seven sensors are plotted as a function of the curvature κ . Whereas the mean K_{eff} increases linearly with κ up to approximately 12 kJ m^{-3} at $\kappa = 7 \text{ mm}^{-1}$, the mean ϕ_{eff} decreases from approximately 90° to around 60° relative to x , as soon as the stress anisotropy K_σ is large enough to dominate the effective anisotropy K_{eff} . The orientation of around 60° results from the neutral axis being at approximately $1/3$ of the magnetic layer thickness in the thicker sensor (500 nm of FeGaB) from Investigation 2 (Figure 8b) and at around $1/4$ of the magnetic layer thickness in the other six sensors from Investigation 1 (Supporting Information). Because the location of the neutral axis is a direct consequence of the layer thickness ratios, this condition remains mostly constant no matter the value of curvature. However, varying amounts of shear stress in the sensors can result in slight variations in the mean ϕ_{eff} even with constant magnetic layer thickness. To approximate the trends found as a function of κ , the mean ϕ_{eff} is fitted with a power function and K_{eff} with a linear function (given in the Experimental section). These will be used in the domain-phase model in Section 2.3.4.

2.3.4. Magnetoelastic Domain-Phase Model of the ΔE Effect

To describe the sensors' resonance frequency shift, we consider that only a certain magnetic volume fraction ν contributes to the ΔE effect.^[52] The total Young's modulus $E^*(H) = \nu E(H) + (1 - \nu)E_m$ is obtained from modeled $E(H)$ and the value E_m at fixed magnetization; the resonance frequency can then be calculated using Equation 1, with $f_r(H) = f_r(E^*(H))$. The magnetic-field-dependent Young's modulus $E(H)$ therefore represents only the magnetoelastically active volume fraction.

To calculate $E(H)$, we describe the magnetoelastic properties of the active volume fraction ν with a domain-phase model based on work by Squire.^[53] This model considers two adjacent magnetic domain regions that represent the average magnetic domain configuration of ν . The domains have an effective uniaxial magnetic anisotropy with energy density K_{eff} and an easy axis angle of ϕ_{eff} relative to the axis of applied magnetic field

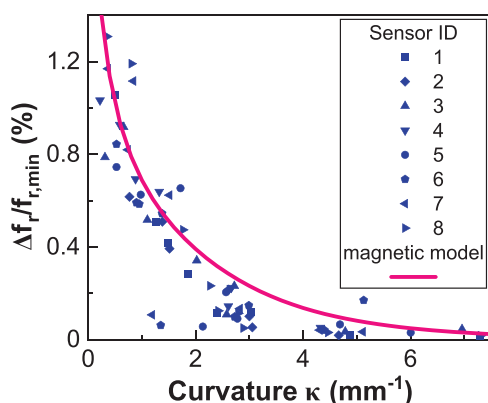


Figure 10. Two-domain magnetic model fitted to the experimental results shown previously in Figure 3a. The model relied on the fitted functions $\phi_{\text{eff}}(\kappa)$ for the mean easy axis rotation, $K_{\text{eff}}(\kappa)$ for the effective anisotropy energy density, and a fixed volume fraction $\nu = 8\%$ to convert predicted Young's modulus $E(H)$ to $\Delta f_r/f_{r,\text{min}}$.

and are separated by a movable magnetic domain wall. We find the equilibrium configuration of the system by minimizing its total enthalpy density numerically. For the calculation, we use the fitted functions from Figure 9d for $K_{\text{eff}}(\kappa)$ and $\phi_{\text{eff}}(\kappa)$. The model matches the measurements very well, for $\nu = 8\%$ as shown in Figure 10. The small value of ν might be caused by additional effects that reduce the overall ΔE effect and the frequency shift, leading to an apparent reduction in ν . Such effects could include damping of moment rotation and wall motion due to the high resonance frequency^[54,55] as well as stress-induced relaxation or recrystallization.^[56] Especially at the edges of the IDEs, the topography of the magnetic layer (which is not included in the FEM simulation) influences the magnetostatic fields. Furthermore, local non-zero out-of-plane magnetization components at the domain walls and edges of the magnetic multilayer structure are not considered in the model.

3. Discussion

The results from our magnetomechanical model are largely in agreement with the general trends observed in the sensors' $f_r(H)$ curves as well as the magnetization behavior observed via MOKE (Figure 7). Many of the sensors exhibited $f_r(H)$ curves that looked similar to Figure 4c, without an obvious drop to a local minimum as in Figure 3b (sample set available in Supporting Information). This aligns moderately well with ΔE -effect behavior modeled by Squire^[53] for when magnetization is at 60° relative to the applied field.

In the MOKE results, the magnetic domain images in the center of the sample correlate with the model's predictions for the stress-induced magnetic easy axis orientation at the sensor's surface (Figure 9a). In both model and measurements, the easy axis is close to the x -axis, confirming the dominant role of stress-induced anisotropy in the overall magnetization behavior. That is to say, the effective magnetic anisotropy K_{eff} is dominated by the internal stress field. Despite similar trends in how the modeled and MOKE-observed magnetic anisotropy varies across the xy -plane, discrepancies exist in the easy axis alignment within the edge regions. This might be due to stray field effects that are not included in the magnetoelastic model. Other reasons could include inaccuracies in matching the mechanical model to the shape of the resonator plate and the assumption of homogeneous initial plane stress values in the films, which are known to vary inhomogeneously with thickness in sputtered films.^[57] Yet, the variation of magnetic anisotropy with thickness, not accessible by other means, as well as the general behavior, can be identified from the modeling.

Despite simplifications, the overall trend of $\Delta f_r/f_{r,\text{min}}(\kappa)$ is reproduced very well by the domain-phase model. Accordingly, we conclude that the rapid decay of $\Delta f_r/f_{r,\text{min}}$ is caused by stress-induced magnetic anisotropy that dominates the magnetic behavior for not-too-small κ . The mechanical model shows that a strong inhomogeneity of stress, as a function of z , is present in the magnetic layer after the resonator is released. As a result, the neutral axis is found to be within the magnetic layer, which is a direct consequence of the large magnetic volume fraction. This causes a significant change of $\Delta\sigma$ ($\equiv \sigma_{11} - \sigma_{22}$) within the

magnetic material: the deeper fraction of the layer has $\Delta\sigma < 0$, where the tensile stress along y is stronger than along x , but in the upper fraction of the material, $\Delta\sigma > 0$, with a stronger compressive stress along y . Thus, the stress anisotropy tends to align the magnetic easy axis along y in the deeper portion of the magnetic material but along x in the upper portion. (This would be reversed for negatively magnetostrictive materials.) For very small curvature κ , the stress is small enough that the field-induced anisotropy K_u is larger than the stress anisotropy K_σ . In that case, mostly uniform magnetization along the y -axis of the sensor can still be achieved, as exemplified by the two outliers in Figure 9d, with nearly 90° ϕ_{eff} orientation. In most of the sensors, however, the mean easy axis rotates over the magnetic film thickness in accordance with the $\Delta\sigma$ sign change, thereby reducing the achievable ΔE effect. It also explains how, after a certain κ , the volume-mean easy axis orientation remains largely stable even as κ increases, since the location of the neutral axis stays essentially constant. Consequently, the magnetic material volume is always divided into parts with mostly lengthwise and mostly widthwise easy axis alignment, and the volume ratio of these parts is largely invariant.

If the thickness ratio of magnetic to nonmagnetic materials were reduced, the neutral axis would move closer to the surface and at some point disappear. This can be seen in how this axis is closer to the surface in the six sensors with 250 nm of FeGaB (Supporting Information) compared to the one sensor with 500 nm of FeGaB in Figure 8b. The smaller the fraction of the magnetic material with $\Delta\sigma > 0$, the less material there is with the ϕ_{eff} flipped to align lengthwise along the resonator instead of the intended widthwise alignment. With further simulations (not shown), in which the FeGaB thickness was varied, we have determined that the neutral axis within the magnetic layer disappears when the ratio of FeGaB-to-AlN thicknesses is about 0.6. Thus, if there is enough residual stress that $K_\sigma > K_u$, any FeGaB that takes the thickness ratio above 0.6 is essentially wasted, since the magnetization orientation there is not aligned as intended and does not meaningfully contribute to the ΔE effect. But, if $K_\sigma < K_u$ (residual stress is very low), all of the magnetic material contributes to the ΔE effect at any thickness. However, magnetization alignment is not the only issue; the mean K_{eff} increases with increasing stress and κ (Figure 9d), and this trend also has a strong negative influence on the ΔE effect and, in turn, the sensors' $\Delta f_i/f_{r,\text{min}}$ performance. Thus, keeping the magnitude of residual stress very small would still be the best solution, assuming it is technologically achievable, if maximized ΔE effect is desired.

In summary, we show that a large ratio of magnetic layer thickness to nonmagnetic layer thickness is not necessarily beneficial as it can lead to magnetic inhomogeneity, even if only small residual stress is present. This suggests an upper limit for the magnetic layer thickness—depending on the combination of materials used, and their properties—in magnetoelastic device applications for which magnetic uniformity is the highest priority. Stress effects become increasingly important for soft magnetic materials with small induced magnetic anisotropy energy density and large magnetoelastic coupling, properties which have usually been considered to be desirable for high-sensitivity magnetoelastic sensors and devices.^[16,58,59] For sensors in particular, other than maximizing sensitivity,

another critical consideration is how to minimize the overall intrinsic noise. This invites questions about how the magnetic noise depends on the magnetic layer thickness and on the other parameters examined in this work, including the stress anisotropy and uniformity (or lack thereof) of magnetization. These questions are beyond the scope of this manuscript, but do suggest a path forward for further study.

4. Conclusion

Though the fundamentals of the magnetoelastic relationship between stress and magnetization are well known, this work provides a quantitative overview of the significance of these magnetoelastic interactions in the context of a sensor composed of ME thin films, while also carrying implications for the design of other magnetoelastic devices. By attaining an adequately large sample size of sensor test results to show reliable trends in the data, it was established that just a small increase in the residual stress in the magnetic film results in a sharp decline in the total frequency response and, indirectly, the sensitivity of these contour-mode resonant magnetometers. The residual stress manifested outwardly as a slight deformation in the resonator plate: the edges were typically curled in the z -direction by a few % relative to the width dimension of the plate, but caused a drop in the frequency response by factors of 2 or more. In conjunction with the simulations that we used to obtain the stress distribution within the resonators, we applied a magnetomechanical model to show that the magnetization orientation changes throughout the thickness of the magnetic films as a result of the stress distribution and the large magnetostrictive coefficient λ_s of the magnetic material. This has important ramifications for the design and fabrication of such magnetic sensors or other magnetoelastic devices. It shows that simply maximizing the characteristics that may appear to be desirable—high magnetostriction, high magnetic volume fraction, and low induced magnetic anisotropy—come at a price. Namely, the magnetic material in such a device becomes highly sensitive to small amounts of residual stress, resulting in reduced uniformity of magnetization. Good uniformity of magnetization orientation across the entire thickness of the magnetic films is challenging to achieve in the laminated devices studied here because of the neutral axis located within the magnetic film and the resulting variation of stress around it. Thus, more careful considerations for how to balance the various magnetic properties need to be made. One strategy may be to actually reduce the magnetic layer thickness relative to the piezoelectric phase to achieve better stress uniformity, and in turn, better magnetization uniformity.

However, some important details were beyond the scope of this study. First and foremost is probably the issue of the origin of the in-plane stress anisotropy in these resonator structures, which was necessary to achieve a good match between the simulated resonator plates and the optical measurements. Beyond that, there are structural simplifications in the simulated resonator, and not all aspects of the magnetic behavior are captured by the magnetic model, such as the effect of domain walls, the high resonance frequency, and perhaps other factors. More

detailed modeling may be necessary to elucidate the full details of the magnetization behavior in these devices.

5. Experimental Section

Production of the RF (radio frequency) contour-mode resonator sensors was carried out via a 5 mask photolithography and microfabrication process on high-resistivity, undoped 4" Si wafers. This fabrication process generally followed the steps reported previously.^[11,13] Initially, a pattern for the IDE was formed in positive photoresist, and a 50 nm Pt film was deposited by sputtering; lift-off was used to remove the excess film, leaving the completed Pt IDE. A layer of piezoelectric AlN, 250 nm thick, was then sputter-deposited by OEM Group, Inc. To establish electrical contact with the IDE underneath, vias were wet-etched in the AlN with phosphoric acid while the second photoresist pattern was in place, and Au probing pads were then sputter-deposited onto the third lithographic pattern, and again finalized by lift-off. At the sites of the etched vias, the Au was deposited directly onto the bottom Pt, thereby electrically linking the probing pads and the IDEs. The fourth lithography process outlined the resonator plate and anchors, and the AlN was etched in an anisotropic dry etch process to give the resonator vertical sidewalls. Lithography was performed a fifth time before sputter-depositing—in the presence of an in situ bias field—a multilayer stack of either FeGaB or FeGaC, Al₂O₃ spacer layers, and an Al capping layer onto the resonator plate. The total thickness of magnetic material varied from 250 nm to 1 μm, and the Al₂O₃ spacer layers were approximately 5 nm thick, interspersed between every 25 nm of magnetic film. The capping layer of roughly 10 nm Al served to protect the magnetic material. Typical base pressure was around 2×10^{-7} Torr, and an in-plane bias field was maintained using hard magnets, with a magnitude of at least 20 mT and orientated widthwise relative to the resonator plates. As before, lift-off was used afterward. Lastly, the Si substrate was isotropically dry-etched to release the sensor by removing the Si underneath the resonator plate, leaving it suspended in air by the two anchors.

One of the sensor chips was subjected to magnetic annealing. The temperature was ramped up to 280 °C over approximately 30 min in a Futek F-3103 furnace. This was maintained for 1 h with 150 mT applied along the width of the resonators at a vacuum of 1×10^{-5} Torr.

The fabricated sensors were imaged in several ways. The curvature of the resonator plate of every sensor was quantified using a Zygo NewView 6200 optical profilometer. To find curvature κ , we numerically solved the below expression for R :

$$\frac{z}{R} + \cos\left(\frac{S}{R}\right) - 1 = 0 \quad (7)$$

S is known from the width of the resonator specified in the photolithography mask, while parameters y and z in Figure 2e were obtained from the profilometer. Scanning electron microscopy (SEM) images were also obtained (Figure 2a) using a Supra 25 SEM. Magnetic domain observations in varying magnetic fields were carried out by high-resolution magneto-optical Kerr effect (MOKE) microscopy in longitudinal mode.^[45]

Sensor $\Delta f_r/f_{r,\min}$ performance was tested as follows. Each chip with sensor devices was positioned on a sample holder in a customized probe station. A nonmagnetic ground-signal-ground (GSG) probe, made by GGB Industries, was used to probe the Au probing pads of the desired sensor and to establish an electrical connection to a high-frequency lock-in amplifier from Zurich Instruments (model UHFLL). As reported in greater detail previously,^[13] the lock-in amplifier and a ZDC-10-1+ MiniCircuits coupler were used to drive the resonator in a frequency sweep and measure the demodulated voltage output so as to find the resonance frequency, while the sensor was subjected to a DC magnetic field oriented lengthwise, parallel to the IDE. The DC magnetic field was provided by an in house-made electromagnet, shaped similar to a horseshoe magnet, which was positioned underneath the sample

holder such that the sensor chip was between the magnet poles in a region with good uniformity of magnetic field. A LakeShore Model 425 Gaussmeter was used to measure the bias DC field, with the Gaussmeter probe positioned directly adjacent to the device chip. This DC field was typically varied from zero up to roughly 10–15 mT. The fitting function applied in Figure 3a is the following: $\gamma = A_1 e^{-x/t_1} + \gamma_0$. The fitting parameters obtained were: $A_1 = 1.4135$; $t_1 = 0.00124$; and $\gamma_0 = 0.00157$.

Quality factor results were collected for all the sensors using an Agilent E8364A PNA network analyzer after the $\Delta f_r/f_{r,\min}$ tests were complete. The same customized probe station was used as for $\Delta f_r/f_{r,\min}$ measurements, with the electromagnet removed and replaced by a nonmagnetic platform, and the same GSG probe was utilized for electrical contact with the sensor. Prior to measurements, the network analyzer was calibrated using a calibration kit provided by the manufacturer of the probes.

Finite element method simulations (FEM) of the sensors, both static and dynamic, were done in COMSOL Multiphysics v. 5.4.^[60] In the static simulations, for investigating stress, designs 3 and 4 from Table 1 were used for the final analysis presented in this manuscript; this is because these were the only sensors that fit entirely within the field of view of the Zygo NewView 6200 optical profilometer at the magnification (50×) that was used to obtain accurate measures of the resonator plate curvatures, while the other six designs were too long. Using devices of designs 3 and 4 from multiple chips allowed a full comparison between the imaged surfaces and the virtual resonators from the simulations as illustrated in Figure 8a. The simulated sensors did not include the surrounding substrate and probing electrodes, and the Al₂O₃ spacer layers and Al capping layer were also omitted. The undulating form of all the materials above the Pt IDE was simplified as flat. Out of the seven sensors thusly simulated, all were from Investigation 1, with one exception: the sensor analyzed by MOKE from Figure 7, from Investigation 2, was also included in order to compare simulation and MOKE results. Thus, the layers in the simulated resonators were 50 nm of Pt, 250 nm of AlN, and 250 nm of FeGaB, with one having 500 nm of FeGaB instead (Figure 8). The numbers for Young's moduli used for the layers were 168, 350,^[61] and 215 GPa,^[13] respectively, and for density we used 21.45, 3.20, and 7.33 g cm⁻³, respectively.

To simulate the release of the resonator plate from the substrate and the subsequent deformation due to internal stress, zero initial stress was entered for the AlN and Pt layers, but constant initial stress values of $\sigma_{0,xx}$, $\sigma_{0,yy}$ and $\sigma_{0,xy}$ were set for the volume of FeGaB, with all other stress tensor components being zero. Under static equilibrium condition, the mechanical equation of motion is solved to obtain the corresponding equilibrium stress $\sigma = \sigma_0 + C:(\epsilon - \epsilon_0)$ and the equilibrium strain ϵ assuming zero initial strain ($\epsilon_0 = 0$).^[60] The mechanical stiffness tensor is given by C .

A dynamic simulation was also performed in COMSOL on a structure representing Sensor ID 1 in Table 1 to show the electromechanical standing wave in the resonator. This was accomplished by a frequency domain analysis solving the linear mechanical equation of motion, coupled to the electrostatic equations via the piezoelectric constitutive relations. For the geometry the same simplifications were used as above, but in addition, the Pt IDE was further simplified by not being connected to the probing pads through the anchor of the resonator. Boundary conditions were established by fixing the rectangular pads connected to the resonator by the anchors (Figure 1, top right). These pads represent regions of AlN situated directly above the Pt pads, which are an extension of the IDE, and these rectangular AlN areas are therefore part of the substrate surrounding the resonator.

A rough estimate for K_u was derived from the $f_r(H)$ curve in Figure 3b. In that sample, the curvature, and hence also K_σ , was very small and could therefore be neglected. K_u can then be estimated from the anisotropy field magnitude that is approximately at the minimum of $f_r(H)$: $H_k = 2 \frac{K_u}{\mu_0 M_s}$, where $\mu_0 M_s = 1.4$ T. The functions found from fitting the mean effective easy axis angle and the mean effective anisotropy energy density in Figure 9d are $\phi_{\text{eff,fit}} = (a \cdot x^b + c)$ rad ($a = 0.1242$; $b = -0.9817$; $c = 1.021$) and $K_{\text{eff,fit}} = (p_1 \cdot x + p_2)$ J m⁻³ ($p_1 = 1692$; $p_2 = 54.73$) with $[x] = \kappa \cdot \text{mm}$ and $[x] = 1 \text{ mm}^{-1}$.

Supporting Information

Supporting Information is available from the Wiley Online Library or from the author.

Acknowledgements

A.D.M. and B.S. contributed equally to this work. The authors gratefully acknowledge Daniel Schiwietz for contributing to the acquisition of MOKE images, Prof. Carol Livermore and Dr. Ivan Lisenkov for helpful discussions, and Dr. Sivasubramanian Somu and Scott McNamara for assistance and training related to the usage of the cleanroom facility at Northeastern University, the George J. Kostas Nanoscale Technology and Manufacturing Research Center. This work was supported by the National Science Foundation TANMS ERC Award 1160504, by the National Institutes of Health Award U01NS107694, and by the German Research Foundation through the Collaborative Research Center CRC 1261.

Conflict of Interest

The authors declare no conflict of interest.

Data Availability Statement

The data that support the findings of this study are available from the corresponding author upon reasonable request.

Keywords

delta-E effect, magnetic field sensor, magnetoelastic, magnetoelectric, MEMS, residual stress, resonator

Received: March 15, 2021

Revised: May 4, 2021

Published online:

-
- [1] C. P. O. Treutler, *Sens. Actuators, A* **2001**, *91*, 2.
- [2] L. Jogschies, D. Klaas, R. Kruppe, J. Rittinger, P. Taptimthong, A. Wienecke, L. Rissing, M. Wurz, *Sensors* **2015**, *15*, 28665.
- [3] L. Panina, *Recent Application in Biometrics*, IntechOpen, London **2011**.
- [4] A. Edelstein, *J. Phys.: Condens. Matter* **2007**, *19*, 165217.
- [5] K. Sternickel, A. I. Braginski, *Supercond. Sci. Technol.* **2006**, *19*, S160.
- [6] M. Xie, J. F. Schneiderman, M. L. Chukharkin, A. Kalabukhov, S. Whitmarsh, D. Lundqvist, D. Winkler, *IEEE Trans. Appl. Supercond.* **2015**, *25*, 1.
- [7] J. Ryu, A. V. Carazo, K. Uchino, H.-E. Kim, *Jpn. J. Appl. Phys.* **2001**, *40*, 4948.
- [8] N. Yoshizawa, I. Yamamoto, Y. Shimada, *IEEE Trans. Magn.* **2005**, *41*, 4359.
- [9] B. Gojdka, R. Jahns, K. Meurisch, H. Greve, R. Adelung, E. Quandt, R. Knöchel, F. Faupel, *Appl. Phys. Lett.* **2011**, *99*, 223502.
- [10] S. Marauska, R. Jahns, H. Greve, E. Quandt, R. Knöchel, B. Wagner, *J. Micromech. Microeng.* **2012**, *22*, 065024.
- [11] T. Nan, Y. Hui, M. Rinaldi, N. X. Sun, *Sci. Rep.* **2013**, *3*.
- [12] Y. Hui, T. Nan, N. X. Sun, M. Rinaldi, *J. Microelectromech. Syst.* **2015**, *24*, 134.
- [13] M. Li, A. Matyushov, C. Dong, H. Chen, H. Lin, T. Nan, Z. Qian, M. Rinaldi, Y. Lin, N. X. Sun, *Appl. Phys. Lett.* **2017**, *110*, 143510.
- [14] P. Ripka, M. Janosek, *IEEE Sens. J.* **2010**, *10*, 1108.
- [15] M. Fiebig, *J. Phys. D: Appl. Phys.* **2005**, *38*, R123.
- [16] A. Piorra, R. Jahns, I. Teliban, J. L. Gugat, M. Gerken, R. Knöchel, E. Quandt, *Appl. Phys. Lett.* **2013**, *103*, 032902.
- [17] E. Yarar, S. Salzer, V. Hrkac, A. Piorra, M. Höft, R. Knöchel, L. Kienle, E. Quandt, *Appl. Phys. Lett.* **2016**, *109*, 022901.
- [18] J. D. Livingston, *Phys. Status Solidi A* **1982**, *70*, 591.
- [19] B. Spetzler, E. V. Golubeva, R.-M. Friedrich, S. Zabel, C. Kirchhof, D. Meyners, J. McCord, F. Faupel, *Sensors* **2021**, *21*, 2022.
- [20] R. Osiander, S. A. Ecelberger, R. B. Givens, D. K. Wickenden, J. C. Murphy, T. J. Kistenmacher, *Appl. Phys. Lett.* **1996**, *69*, 2930.
- [21] R. Jahns, S. Zabel, S. Marauska, B. Gojdka, B. Wagner, R. Knöchel, R. Adelung, F. Faupel, *Appl. Phys. Lett.* **2014**, *105*, 052414.
- [22] M. Staruch, B. R. Matis, J. W. Baldwin, S. P. Bennett, O. van 't Erve, S. Lofland, K. Bussmann, P. Finkel, *Appl. Phys. Lett.* **2020**, *116*, 232407.
- [23] B. Spetzler, C. Bald, P. Durdaut, J. Reermann, C. Kirchhof, A. Teplyuk, D. Meyners, E. Quandt, M. Höft, G. Schmidt, F. Faupel, *Sci. Rep.* **2021**, *11*, 5269.
- [24] B. Spetzler, J. Su, R.-M. Friedrich, F. Niekiel, S. Fichtner, F. Lofink, F. Faupel, *APL Mater.* **2021**, *9*, 031108.
- [25] B. Spetzler, C. Kirchhof, J. Reermann, P. Durdaut, M. Höft, G. Schmidt, E. Quandt, F. Faupel, *Appl. Phys. Lett.* **2019**, *114*, 183504.
- [26] J. Lou, R. E. Insignares, Z. Cai, K. S. Ziemer, M. Liu, N. X. Sun, *Appl. Phys. Lett.* **2007**, *91*, 182504.
- [27] C. Dong, M. Li, X. Liang, H. Chen, H. Zhou, X. Wang, Y. Gao, M. E. McConney, J. G. Jones, G. J. Brown, B. M. Howe, N. X. Sun, *Appl. Phys. Lett.* **2018**, *113*, 262401.
- [28] X. Liang, B. M. Howe, N. X. Sun, C. Dong, S. J. Celestin, X. Wang, H. Chen, K. S. Ziemer, M. Page, M. E. McConney, J. G. Jones, *IEEE Magn. Lett.* **2019**, *10*, 1.
- [29] G. Piazza, in *Advanced Microand Nanosystems* (Eds: O. Brand, I. Dufour, S. M. Heinrich, F. Josse), Wiley-VCH, Weinheim, Germany **2015**, p. 147.
- [30] S. Timoshenko, *Vibration Problems in Engineering*, 2nd ed., D. Van Nostrand Company, Inc., New York **1937**.
- [31] D. Atkinson, P. T. Squire, S. Atalay, *J. Appl. Phys.* **1996**, *79*, 1664.
- [32] J. Gutiérrez, V. Muto, P. T. Squire, *J. Non-Cryst. Solids* **2001**, *287*, 417.
- [33] A. Ludwig, E. Quandt, *IEEE Trans. Magn.* **2002**, *38*, 2829.
- [34] R. Kellogg, A. Flatau, *J. Intell. Mater. Syst. Struct.* **2008**, *19*, 583.
- [35] S. Datta, J. Atulasimha, C. Mudivarthi, A. B. Flatau, *J. Magn. Magn. Mater.* **2010**, *322*, 2135.
- [36] S. Choi, B. A. Griffin, *J. Micromech. Microeng.* **2016**, *26*, 025009.
- [37] S. Shelton, M.-L. Chan, H. Park, D. Horsley, B. Boser, I. Izyumin, R. Przybyla, T. Frey, M. Judy, K. Nunan, F. Sammoura, K. Yang, in *IEEE Int. Ultrasonics Symp.*, IEEE, Piscataway, NJ **2009**, p. 402.
- [38] J. Jung, J.-C. Bastien, A. Lefevre, K. Benedetto, R. Dejaeger, F. Bland, B. Fain, *Eng. Res. Express* **2020**, *2*, 045013.
- [39] S. M. Na, S. J. Suh, H. J. Kim, S. H. Lim, *J. Magn. Magn. Mater.* **2002**, *239*, 570.
- [40] C. W. Kim, K. H. Cho, H. G. Suk, *Phys. Met. Metallogr.* **2014**, *115*, 1338.
- [41] N. X. Sun, S. Mehdizadeh, C. Bonhote, Q. F. Xiao, B. York, *J. Appl. Phys.* **2005**, *97*, 10N904.
- [42] G. Herzer, *Mater. Sci. Eng., A* **1997**, *226–228*, 631.
- [43] G. Herzer, *Z. Metallkd.* **2002**, *93*, 978.
- [44] , *Handbook of Magnetism and Advanced Magnetic Materials*, (Eds: H. Kronmüller, S. S. P. Parkin), John Wiley & Sons, Hoboken, NJ **2007**.
- [45] J. McCord, *J. Phys. D: Appl. Phys.* **2015**, *48*, 333001.
- [46] J. C. Slonczewski, B. Petek, B. E. Argyle, *IEEE Trans. Magn.* **1988**, *24*, 2045.

- [47] J. McCord, J. Westwood, *IEEE Trans. Magn.* **2001**, *37*, 1755.
- [48] C. Mudivarthi, S. Datta, J. Atulasimha, P. G. Evans, M. J. Dapino, A. B. Flatau, *J. Magn. Magn. Mater.* **2010**, *322*, 3028.
- [49] R. C. O'Handley, *Modern Magnetic Materials: Principles and Applications*, Wiley, New York **2000**.
- [50] H. Mehner, S. Leopold, M. Hoffmann, *J. Micromech. Microeng.* **2013**, *23*, 095030.
- [51] S. Timoshenko, *J. Opt. Soc. Am.* **1925**, *11*, 233.
- [52] D. Y. Kim, C. G. Kim, H. C. Kim, U. H. Sung, *J. Appl. Phys.* **1997**, *81*, 5811.
- [53] P. T. Squire, *J. Magn. Magn. Mater.* **1990**, *87*, 299.
- [54] B. Spetzler, E. V. Golubeva, C. Müller, J. McCord, F. Faupel, *Sensors* **2019**, *19*, 4769.
- [55] W. P. Mason, *Rev. Mod. Phys.* **1953**, *25*, 136.
- [56] B.-J. Lee, C. S. Lee, J. C. Lee, *Acta Mater.* **2003**, *51*, 6233.
- [57] S. Dieter, A. Pyzalla, A. Bauer, N. Schell, J. McCord, K. Seemann, N. Wanderka, W. Reimers, *Z. Metallkd.* **2004**, *95*, 164.
- [58] C.-W. Nan, M. I. Bichurin, S. Dong, D. Viehland, G. Srinivasan, *J. Appl. Phys.* **2008**, *103*, 031101.
- [59] J. Kiser, P. Finkel, J. Gao, C. Dolabdjian, J. Li, D. Viehland, *Appl. Phys. Lett.* **2013**, *102*, 042909.
- [60] *Structural Mechanics Module User's Guide, COMSOL Multiphysics v. 5.4*, COMSOL AB, Stockholm, Sweden **2018**, <https://doc.comsol.com/5.4/doc/com.comsol.help.sme/StructuralMechanicsModuleUsersGuide.pdf> (accessed: February 2021).
- [61] P. J. Stephanou, A. P. Pisano, in *IEEE Ultrasonics Symp.*, IEEE, Piscataway, NJ **2006**, p. 2401.

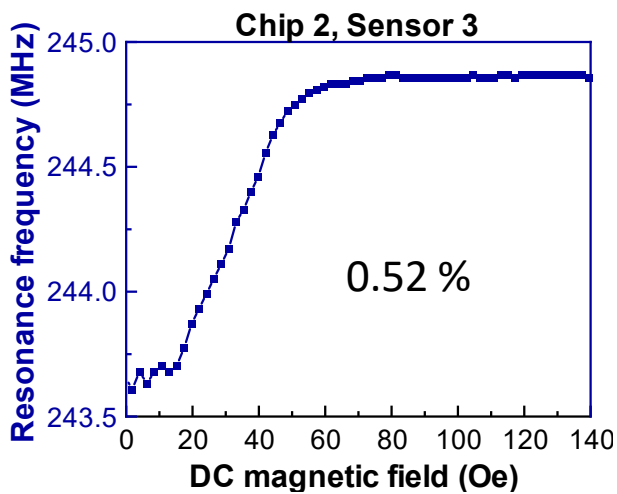
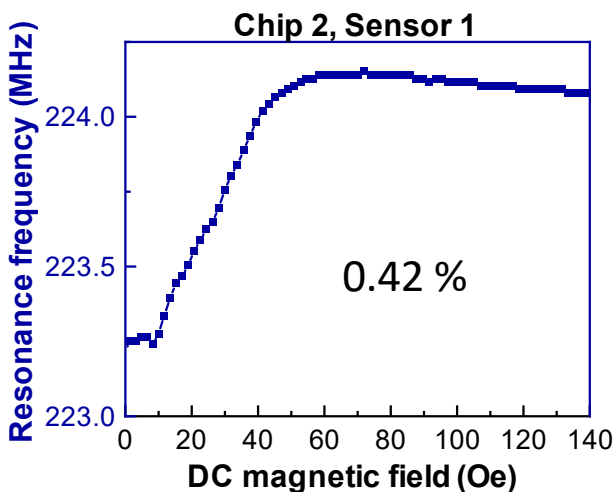
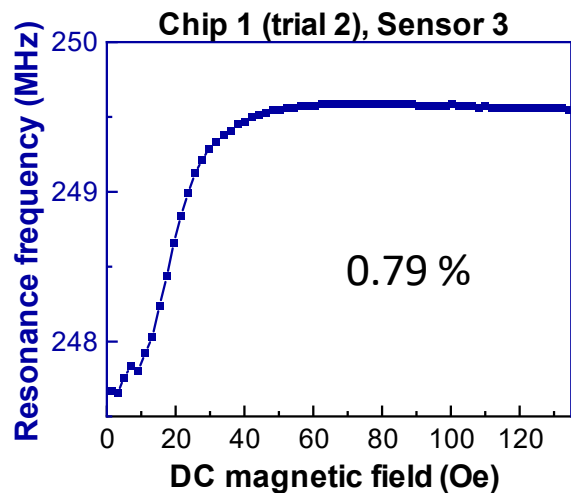
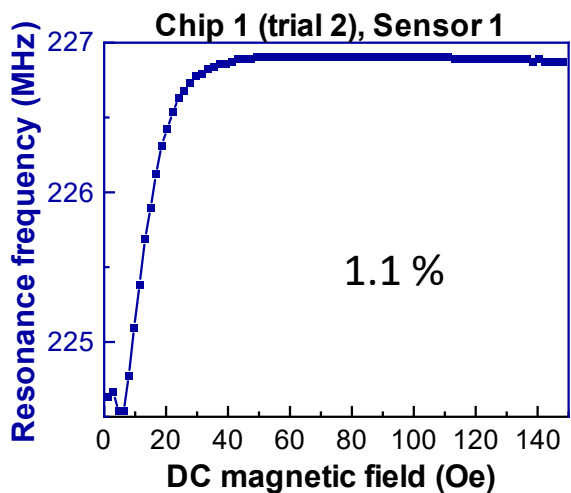
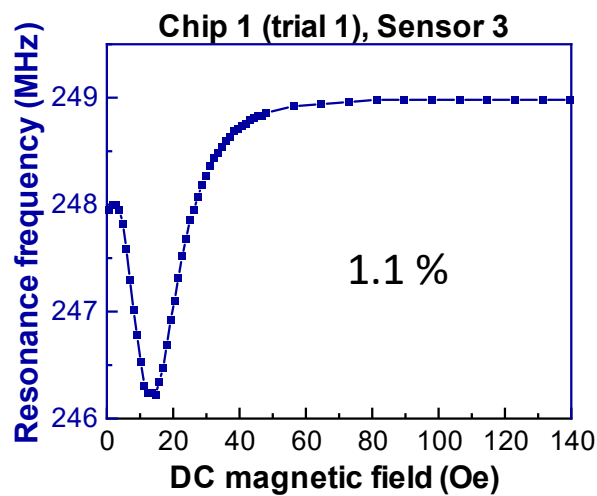
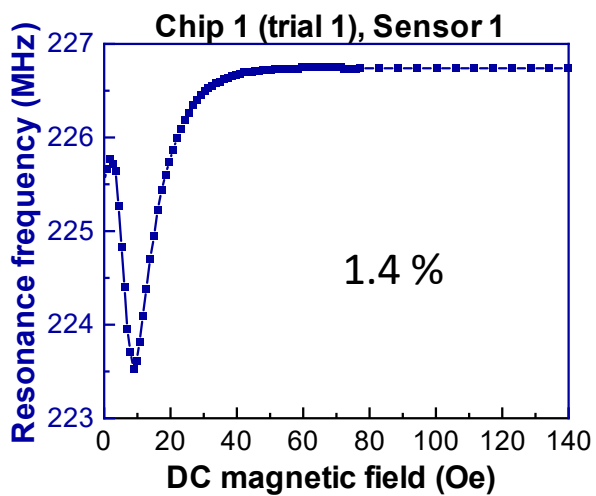
Supporting Information

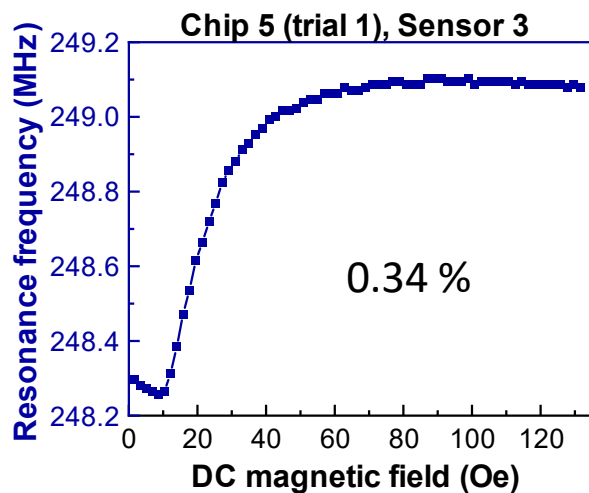
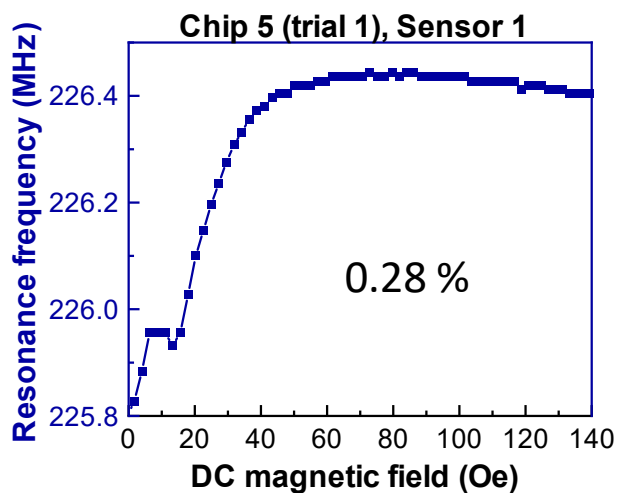
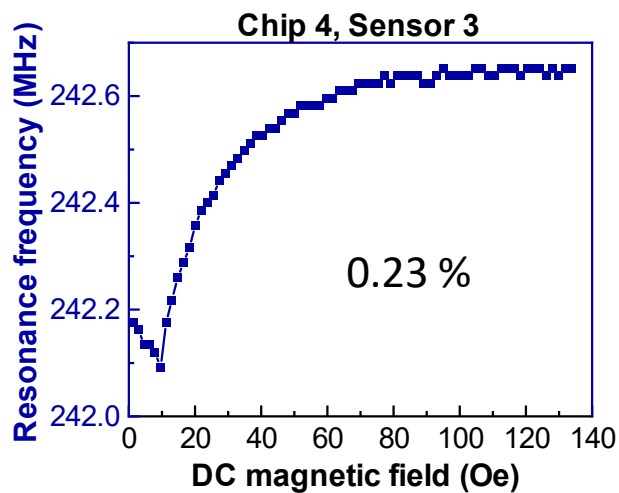
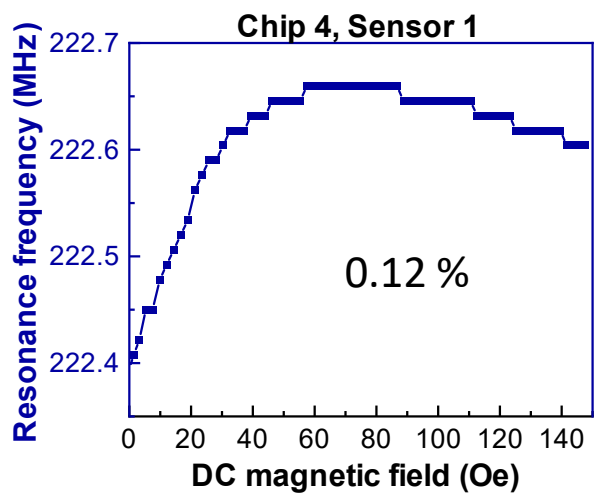
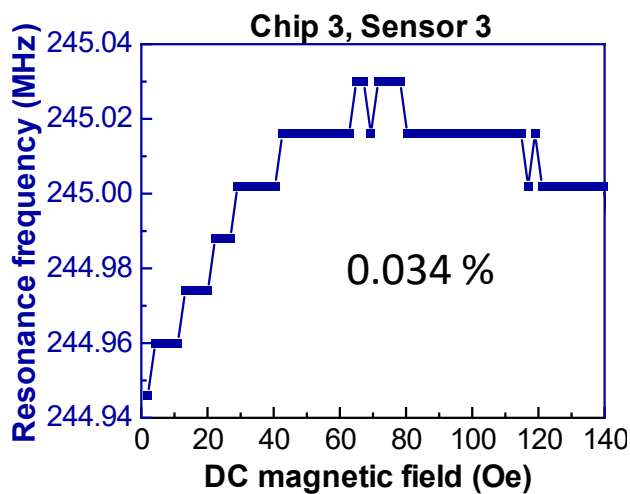
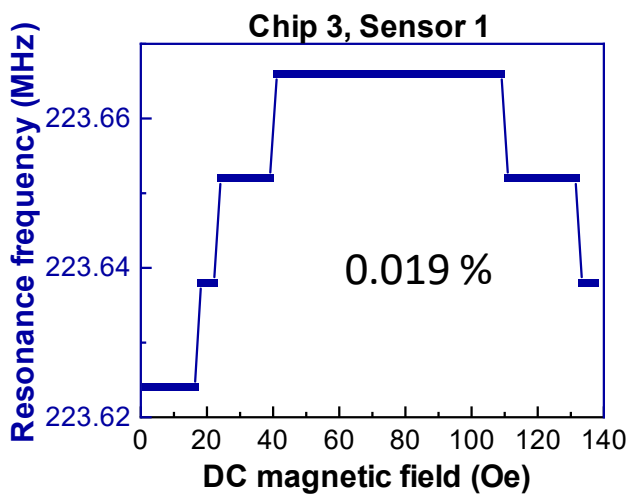
Curvature and Stress Effects on the Performance of Contour-Mode Resonant ΔE Effect Magnetometers

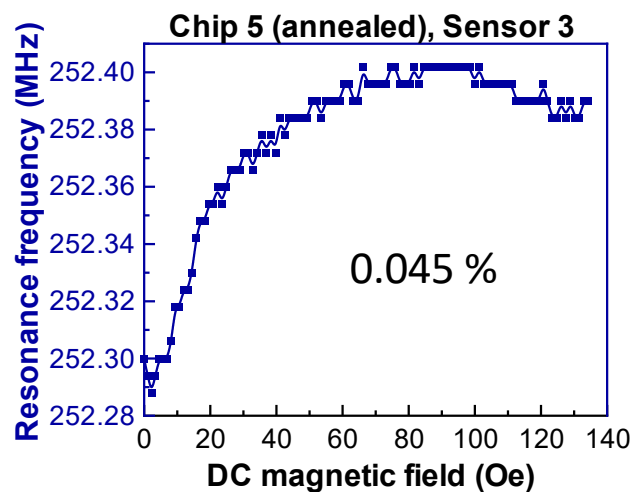
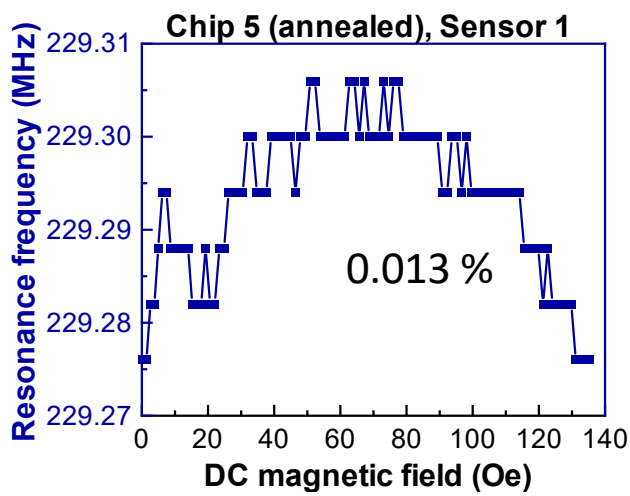
*Alexei D. Matyushov, Benjamin Spetzler, Mohsen Zaeimbashi, James Zhou, Zhenyun Qian, Elizaveta V. Golubeva, Cheng Tu, Yingxue Guo, Brian F. Chen, Damo Wang, Alexandria Will-Cole, Huaihao Chen, Matteo Rinaldi, Jeffrey McCord, Franz Faupel, Nian X. Sun**

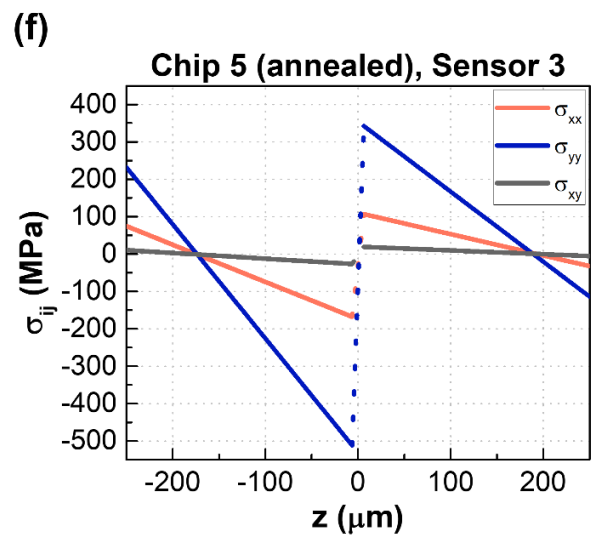
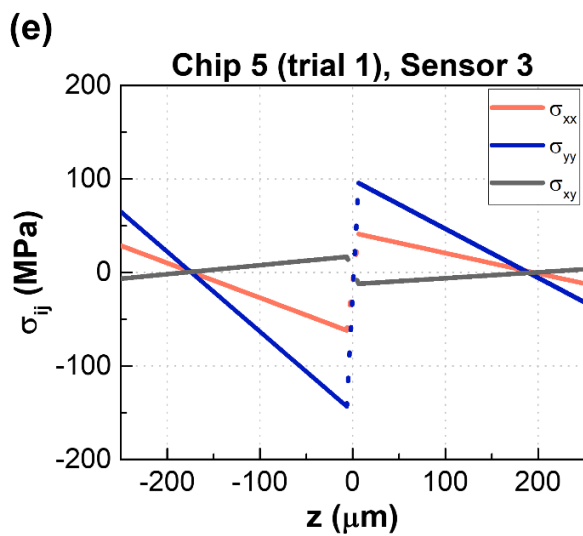
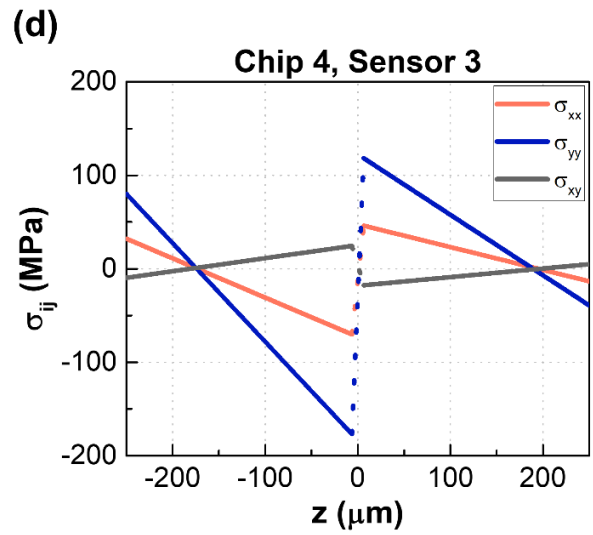
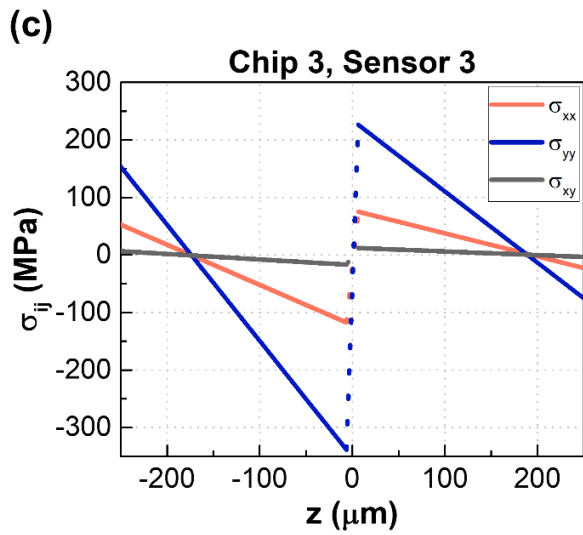
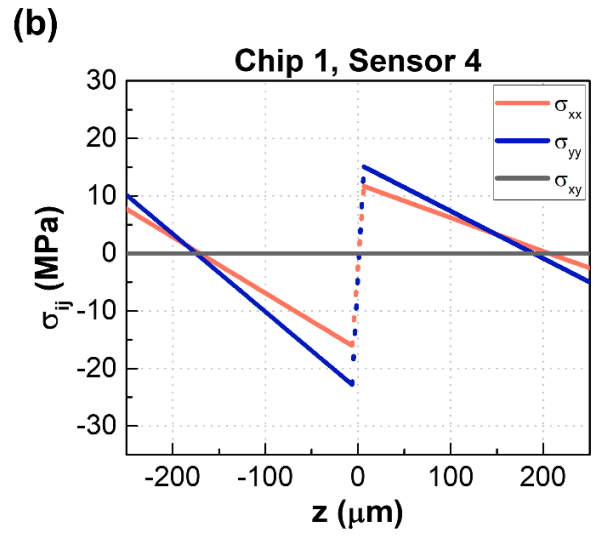
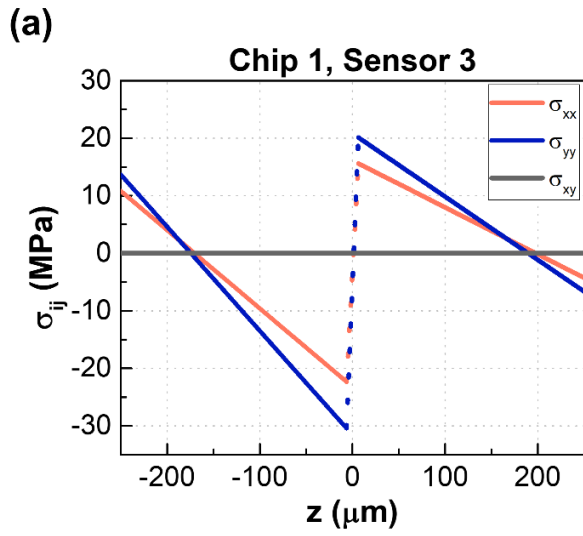
Below we include a representative sample of resonance frequency $f_r(H)$ results from individual sensors that are a subset of the data presented in Fig. 3a. Included are sensors of design ID 1 and 3 (see Table 1). The $\Delta f_r/f_{r,min}$ value for each device is written inside each plot. In some cases, results for the same sensor are shown more than once if the $f_r(H)$ performance changed substantially between trials (e.g. after annealing).

Further, we also include the stress distribution results from the other six sensors that were simulated in COMSOL Multiphysics © via a mechanical model that was allowed to relax (simulating release of the plate from the substrate), with initial stress conditions tuned until the equilibrium shape was qualitatively similar to the measured optical sensor profiles. Including the stress distribution given in Fig. 8b, these together comprise the seven sensors featured in Fig. 9d.









4.4 Towards a General Description of Magnetic Sensitivity

The ΔE effect and magnetic sensitivity were discussed in the previous sections for examples of bending and contour-mode resonators. The analysis focused on the ΔE effect of the Young's modulus, which was assumed to be an acceptable approximation for resonance modes where the alternating stress is mainly uniaxial. This uniaxial approximation has been used frequently in the last decades [40, 86, 92, 95, 322] to describe the ΔE effect in cantilever resonators based on amorphous ribbons. Discrepancies between macro-spin simulations and measurements occur around the anisotropy or switching field, wherein a discontinuity is visible in the simulation and the ΔE effect is overestimated. In previous studies, this was avoided by introducing distributions of the effective anisotropy as fitting parameters [92, 95, 322]. If the distributions are not interpreted as an entirely mathematical feature, they are assumed to reflect the non-ideal magnetization behavior and inhomogeneous magnetic properties, which is qualitatively supported by measurements [91, 392–394]. Yet, the uniaxial approximation has never been tested against a more complete description of the ΔE effect, wherein all components of the effective mechanical stiffness tensor are considered. Therefore, there is no clarity on the extent to which the distribution parameters reflect physical inhomogeneity or artifacts introduced by the uniaxial approximation.

Additionally, a more complete description of the ΔE effect is of general importance for understanding and estimating the response of resonance modes and geometries where several components of the stiffness tensor need to be considered. Such cases have rarely been investigated for ΔE -effect sensors; however, they could provide new perspectives for tuning the sensing characteristics. Torsion modes in cantilever resonators are such an example. A large ΔE effect has been observed in these resonance modes [110], and this makes them potentially interesting for increasing magnetic sensitivity.

This section attempts to take a step towards providing a general description of the ΔE effect and magnetic sensitivity of ΔE -effect magnetometers. Fully tensor-based models of the magnetic and electric sensitivities are developed and compared with the measurements of bending and torsion modes to assess the potential of torsion modes for magnetic field sensing.

Contribution

- Conceptualization
- Writing of original manuscript
- Modeling and simulations (shared)
- Measurements (shared)
- Data analysis and interpretation (shared)

Article

Magnetoelastic Coupling and Delta-E Effect in Magnetolectric Torsion Mode Resonators

Benjamin Spetzler, Elizaveta V. Golubeva, Ron-Marco Friedrich, Sebastian Zabel, Christine Kirchhof, Dirk Meyners, Jeffrey McCord and Franz Faupel *

Institute of Materials Science, Faculty of Engineering, Kiel University, 24143 Kiel, Germany; besp@tf.uni-kiel.de (B.S.); elgo@tf.uni-kiel.de (E.V.G.); rmfr@tf.uni-kiel.de (R.-M.F.); seza@tf.uni-kiel.de (S.Z.); cki@tf.uni-kiel.de (C.K.); dm@tf.uni-kiel.de (D.M.); jmc@tf.uni-kiel.de (J.M.)
* Correspondence: ff@tf.uni-kiel.de; Tel.: +49-431-880-6229

Abstract: Magnetolectric resonators have been studied for the detection of small amplitude and low frequency magnetic fields via the delta-E effect, mainly in fundamental bending or bulk resonance modes. Here, we present an experimental and theoretical investigation of magnetolectric thin-film cantilevers that can be operated in bending modes (BMs) and torsion modes (TMs) as a magnetic field sensor. A magnetoelastic macrospin model is combined with an electromechanical finite element model and a general description of the delta-E effect of all stiffness tensor components C_{ij} is derived. Simulations confirm quantitatively that the delta-E effect of the C_{66} component has the promising potential of significantly increasing the magnetic sensitivity and the maximum normalized frequency change Δf_r . However, the electrical excitation of TMs remains challenging and is found to significantly diminish the gain in sensitivity. Experiments reveal the dependency of the sensitivity and Δf_r of TMs on the mode number, which differs fundamentally from BMs and is well explained by our model. Because the contribution of C_{11} to the TMs increases with the mode number, the first-order TM yields the highest magnetic sensitivity. Overall, general insights are gained for the design of high-sensitivity delta-E effect sensors, as well as for frequency tunable devices based on the delta-E effect.

Keywords: delta-E effect; magnetolectric; magnetoelastic; resonator; torsion mode; bending mode; magnetic modeling; MEMS; FEM

Citation: Spetzler, B.; Golubeva, E.V.; Friedrich, R.-M.; Zabel, S.; Kirchhof, C.; Meyners, D.; McCord, J.; Faupel, F. Magnetoelastic Coupling and Delta-E Effect in Magnetolectric Torsion Mode Resonators. *Sensors* **2021**, *21*, 2022. <https://doi.org/10.3390/s21062022>

Academic Editor: Nicolò Marconato

Received: 10 February 2021
Accepted: 9 March 2021
Published: 12 March 2021

Publisher's Note: MDPI stays neutral with regard to jurisdictional claims in published maps and institutional affiliations.



Copyright: © 2021 by the author. Licensee MDPI, Basel, Switzerland. This article is an open access article distributed under the terms and conditions of the Creative Commons Attribution (CC BY) license (<http://creativecommons.org/licenses/by/4.0/>).

1. Introduction

In recent years, thin-film magnetolectric sensors have been studied, frequently envisioning biomedical applications in the future [1,2]. Such applications often require the measurement of small amplitude and low frequency magnetic fields [1–3]. With the direct magnetolectric effect, such small detection limits are only obtained at high frequencies and in small-signal bandwidths of a few Hz [2,4]. One way to overcome these limitations is by using a modulation scheme based on the delta-E effect. The delta-E effect is the change of the effective elastic properties with magnetization due to magnetoelastic coupling [5–8]. It results from inverse magnetostriction that adds additional stress-induced magnetostrictive strain to the purely elastic Hookean strain. The delta-E effect can occur generally in various elastic moduli and several components of the elastic stiffness tensor C [9,10]. Hence, it is sometimes referred to as the delta-C effect [11]. Typically, delta-E effect sensors are based on magnetolectric resonators that are electrically excited via the piezoelectric layer at or close to the resonance frequency f_r . Upon the application of a magnetic field, the magnetization changes and the delta-E effect alters the mechanical stiffness tensor of the magnetostrictive layer. If the altered stiffness tensor components contribute to the resonance frequency of the excited mode, the resonance frequency changes, which can be read-out electrically. The delta-E effect of the Young's modulus has

especially been studied thoroughly in soft magnetic amorphous materials [12–18]. It was used for magnetic field sensing with magnetoelectric plate resonators [19–22] and beam structures [23–32]. Such resonators are operated in bending or bulk modes and some have achieved limits of detection down to the sub-nT regime at low frequencies. Microelectromechanical systems (MEMS) cantilever sensors based on the delta-E effect were recently used for the mapping of magnetically labeled cells [33], and have shown promising properties for sensor array applications [34].

In contrast to the delta-E effect of the Young's modulus, the delta-E effect of the shear modulus has been studied less extensively [35] and mainly in amorphous wires [36,37]. It has been used for a different kind of delta-E effect sensors where shear waves, traveling through the magnetoelastic material, are influenced by the delta-E effect. This concept was realized with bulk acoustic shear waves in amorphous ribbons [38] and recently with surface acoustic shear waves in magnetic thin film devices [10,39–42]. Only very few studies investigate torsion modes in beam structures [43,44], either with electrostatically actuated cantilevers [43] or double-clamped beams [44]. Both studies are limited to specific configurations of the magnetic system and consider neither the full tensor relations of the mechanics and the delta-E effect nor higher resonance modes. Until now, a comprehensive experimental and theoretical analysis has been missing as well as a discussion of implications for the design of delta-E effect-based devices.

2. MEMS Torsion Mode Sensors

In this study, all measurements and models are made for a microelectromechanical system (MEMS) technology-fabricated cantilever with an electrode design that permits the excitation of torsion modes. A sketch including dimensions and layer structure and a top-view photograph of the design are shown in Figure 1. The approximately 3.1 mm-long and 2.15 mm-wide cantilever consists of a $\approx 2 \mu\text{m}$ -thick piezoelectric layer of AlN [45] on a $50 \mu\text{m}$ -thick poly-Si substrate. A $2 \mu\text{m}$ -thick amorphous magnetostrictive multilayer is deposited on the rear side. A magnetic field is applied during the deposition to induce a magnetic easy axis along the short cantilever axis. For actuation and read-out, three top electrodes (E_1 , E_2 and E_3) of 100 nm -thick Au with lengths $L_1 = L_2 \approx 1 \text{ mm}$ and $L_3 \approx 0.6 \text{ mm}$ and widths $W_1 = W_2 \approx 0.5 \text{ mm}$ and $W_3 \approx 1 \text{ mm}$ contact the AlN layer on the top. The counter electrode (150 nm Pt) covers the whole beam area and is located between the AlN layer and the substrate. All measurements are performed with electrode E_1 . As a magnetostrictive material, we use a $2 \mu\text{m}$ multilayer of $20 \times (100 \text{ nm } (\text{Fe}_{90}\text{Co}_{10})_{78}\text{Si}_{12}\text{B}_{10} \text{ and } 6 \text{ nm Cr})$. It is covered by a top Cr-layer that serves as a protection against corrosion. More information about the layer structures and the fabrication process can be found elsewhere [27]. In contrast to the sensors in Ref. [27], the sensor presented here is significantly wider and the adapted electrode design additionally permits the excitation of torsion modes. Details on the geometry are given in the appendix.

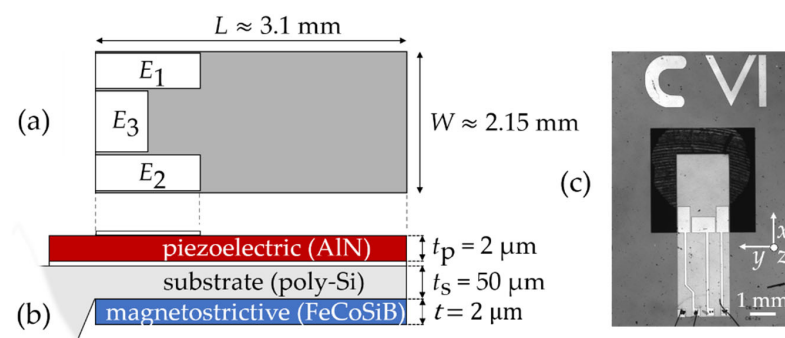


Figure 1. Delta-E effect sensor analyzed in this study: (a) schematic top view of the cantilever, with three different electrodes E_1 , E_2 and E_3 of lengths $L_1 = L_2 \approx 1 \text{ mm}$, $L_3 \approx 0.6 \text{ mm}$ and widths

$W_1 = W_2 \approx 0.5$ mm and $W_3 \approx 1$ mm; (b) schematic side-view of the cantilever with the thickness of the functional layers and the poly-Si substrate; (c) top-view photograph of the fabricated structure.

3. Sensitivity

3.1. Definition of the Sensitivity

An important parameter that characterizes a magnetic field sensor is its sensitivity. During sensor operation, an alternating voltage is applied to excite the cantilever at its mechanical resonance frequency f_r . Applying a magnetic field, shifts f_r via the delta-E effect and correspondingly the sensor's admittance characteristic on its frequency axis f . Hence, the magnitude $|Y| = \text{abs}\{Y\}$ and phase angle $\phi = \text{arg}\{Y\}$ of the sensor admittance Y depend on the magnetic field. Consequently, the ac magnetic field to be measured causes an amplitude modulation (am) and phase modulation (pm) of the current through the sensor. Detailed information on the operation and read-out can be found elsewhere [46–48]. The linearized change of $|Y|$ and ϕ with the magnetic field can be described by the amplitude sensitivity $S_{\text{am}} = S_{Y,r} \cdot S_{H,r}$ and the phase sensitivity $S_{\text{pm}} = S_{\phi,r} \cdot S_{H,r}$ [49], respectively. Both sensitivities have a magnetic part $S_{H,r}$ that includes the delta-E effect and an electric part $S_{Y,r}$ or $S_{\phi,r}$, which can be determined from the admittance. We refer to the three sensitivities as relative sensitivities, because they are normalized to the excitation frequency $f_{\text{ex}} = f_r$. The normalization is required to eventually compare the electrical and magnetic sensitivities of sensors with different geometries operated at different f_r or in different resonance modes. Usually a magnetic bias field H_0 is applied to operate the sensor at optimum conditions. The relative sensitivities are then defined in linear approximation as derivatives [49]:

$$S_{Y,r} := \left. \frac{\partial |Y|}{\partial f} \right|_{f=f_r, H=H_0} \cdot f_r; \quad S_{\phi,r} := \left. \frac{\partial \phi}{\partial f} \right|_{f=f_r, H=H_0} \cdot f_r; \quad S_{H,r} := \left. \frac{1}{f_r} \frac{\partial f_r}{\partial \mu_0 H} \right|_{H=H_0}, \quad (1)$$

with the magnetic vacuum permeability $\mu_0 \approx 4\pi \cdot 10^{-7}$ N/A². From Equation (1), the relative magnetic sensitivity $S_{H,r}$ is the linearized and normalized change of the resonance frequency f_r with the applied magnetic flux density $\mu_0 H$.

3.2. Magnetic Sensitivity of Arbitrary Resonance Modes

The delta-E effect is included in the relative magnetic sensitivity $S_{H,r}$ because the resonance frequency $f_r = f_r(C_{ij})$ is a function of the stiffness tensor components C_{ij} . Depending on the respective resonance mode, different C_{ij} dominate f_r and depending on the magnetoelastic properties they might result in non-zero $S_{H,r}$. To describe $S_{H,r}$ for arbitrary resonance modes, it can be separated into a purely mechanical part $f_r^{-1} \partial f_r / \partial C_{ij}$ that contains the resonance properties of the structure and a purely magnetoelastic part $\partial C_{ij} / \partial \mu_0 H$:

$$S_{H,r} := \left. \frac{1}{f_r} \frac{\partial f_r}{\partial \mu_0 H} \right|_{H=H_0} = \sum_{i=1}^3 \sum_{j=1}^3 \frac{1}{f_r} \frac{\partial f_r}{\partial C_{ij}} \left. \frac{\partial C_{ij}}{\partial \mu_0 H} \right|_{H=H_0} := \sum_{i=1}^3 \sum_{j=1}^3 \partial_C f_{r,ij} \partial_H C_{ij}. \quad (2)$$

If treated separately, the factors $\partial f_r / \partial C_{ij}$ and $\partial C_{ij} / \partial \mu_0 H$ must be normalized to remove the dependency on the absolute value of C_{ij} that cancels out in $S_{H,r}$. We define:

$$\partial_C f_{r,ij} := \left. \frac{C_{ij}}{f_r} \frac{\partial f_r}{\partial C_{ij}} \right|_{H=H_0}; \quad \partial_H C_{ij} := \left. \frac{1}{C_{ij}} \frac{\partial C_{ij}}{\partial \mu_0 H} \right|_{H=H_0}. \quad (3)$$

From Equation (3), the factor $\partial_C f_{r,ij}$ represents a normalized measure for the influence of the stiffness tensor component C_{ij} on the resonance frequency f_r of the considered resonance mode. It is a purely mechanical quantity and hence determined by the geometry, the resonance mode, and the effective mechanical properties of the resonator. The second factor $\partial_H C_{ij}$, includes the delta-E effect and describes the normalized influ-

ence of the applied flux density $\mu_0 H$ on C_{ij} . Hence, the two factors quantify the mechanical and the magnetoelastic parts of the relative magnetic sensitivity $S_{H,r}$. They will be used later to analyze the sensitivity and the frequency detuning of higher bending and torsion modes of the cantilever.

4. Sensor Modelling

The model used to describe and analyze the sensor consists of two parts. With a semi-analytical magnetoelastic macrospin model, the delta-E effect is obtained, i.e., the effective mechanical stiffness tensor $C(H)$ as a function of the applied field H . It is used as an input for an electromechanical finite element mechanics (FEM) model that describes the resonance frequency and the sensor's impedance response. In addition to a macrospin approximation, we assume a quasi-static magnetization behavior. Consequently, it is only valid for operation frequencies and magnetic field frequencies far below the ferromagnetic resonance frequency (FMR). The FMR generally depends on the geometry and the magnetic properties of the thin-film [50] and can cause a frequency dependency of the delta-E effect [51]. For the soft-magnetic material and thin-film geometry used here, it is in the GHz regime [51,52]. Because the operation frequencies are of the order of several kHz, magnetodynamic effects and the frequency dependency of the delta-E effect are neglected [51]. Due to the low frequencies, we assume that also electrodynamic effects can be omitted in the electromechanical model. In the following, both parts of the model are discussed in detail.

4.1. Electromechanical Model

In the electromechanical part of the model, we consider a simplified cantilever geometry, reduced to the poly-Si substrate, the piezoelectric AlN layer, and the magnetic FeCoSiB layer. Details on the geometry used are given in Appendix C. We assume all materials to be mechanically linear, which is a good approximation at sufficiently small excitation voltages. The material parameters used are given in the appendix. The cantilever is oriented in a cartesian coordinate system as illustrated in Figure 2, used throughout this paper. The mechanical equation of motion is given by (e.g., [53])

$$\rho \frac{\partial^2 \bar{u}}{\partial t^2} = \bar{\nabla} \cdot \boldsymbol{\sigma}, \quad (1)$$

if no external forces are present. It includes the displacement vector \bar{u} , the time t , the mass density ρ , and the divergence $\bar{\nabla} \cdot \boldsymbol{\sigma}$ of the mechanical stress tensor $\boldsymbol{\sigma}$. For sufficiently small excitation frequencies, eddy current effects can be neglected and the electrostatic equations [54]:

$$\begin{aligned} \bar{E} &= -\bar{\nabla} U, \\ \bar{\nabla} \cdot \bar{D} &= \rho_c, \end{aligned} \quad (2)$$

are valid in good approximation. They include the electrical vector field \bar{E} , the gradient $\bar{\nabla} U$ of the electrical potential U and the divergence $\bar{\nabla} \cdot \bar{D}$ of the electric flux density \bar{D} with the free charge density ρ_c . The electrostatic equations are coupled to the mechanical equation of motion via the constitutive piezoelectric equations, here in the stress-charge form [54,55]:

$$\begin{aligned} \boldsymbol{\sigma} &= \mathbf{C}^* \boldsymbol{\varepsilon} - \mathbf{e}_c^T \bar{E} \\ \bar{D} &= \mathbf{e}_c \boldsymbol{\varepsilon} - \boldsymbol{\varepsilon}_{el} \bar{E}, \end{aligned} \quad (3)$$

with the linear strain tensor $\boldsymbol{\varepsilon}$ and the complex mechanical stiffness tensor $\mathbf{C}^* = \mathbf{C}(1 + i\eta)$. Its real part is the material's stiffness tensor \mathbf{C} and its imaginary part $\mathbf{C}\eta$ includes the isotropic loss factor η , which is used to consider damping in the materials [56]. The electromechanical coupling tensor is denoted as \mathbf{e}_c and the electrical permittivity tensor as $\boldsymbol{\varepsilon}_{el}$. For the calculation, we set fixed boundary conditions ($\bar{u} = 0$) at the left face of the

beam. For the piezoelectric material, we assumed at the boundaries $\bar{n}\bar{D} = 0$ (with surface normal vector \bar{n}), and an initial value for the electric potential of $U = 0$, except for the area covered by the electrodes. The electrodes are modeled with a fixed potential boundary condition, where an alternating voltage $U_{\text{app}} = U_0 \cdot \exp(i[\omega t + \varphi_v])$ is applied, with amplitude U_0 , the angular frequency ω and phase angle φ_v . To calculate the electrical admittance $Y = I/U$ the current I is obtained from integrating the surface charge density over the electrode areas. For the solution, a linear response of the system is assumed, with a displacement of the form $\bar{u} = \hat{u} \cdot \exp(i[\omega t + \varphi_u])$ and a solution for the electrical potential of $U = \hat{U} \cdot \exp(i[\omega t + \varphi_v])$. The equations are solved within a frequency domain study in COMSOL® Multiphysics v. 5.3a (COMSOL AB, Stockholm, Sweden) [56]. All material parameters used are given in the appendix.

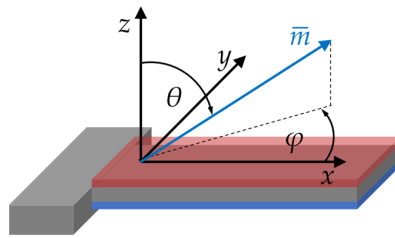


Figure 2. Coordinate system used for the electromechanical and the magnetic model. All three components m_i of the reduced magnetization vector \bar{m} are described by the polar angle θ and the azimuthal angle φ .

4.2. Magnetoelastic Model

For the magnetic model, we consider the enthalpy density function of a macrospring with a uniaxial anisotropy energy density, an external magnetic field, a demagnetizing term, and magnetoelastic energy density. Using Einstein's summation convention, the enthalpy density term we use is:

$$u = K(1 - (m_i EA_i)^2) - \mu_0 M_s m_i H_i - \frac{1}{2} \mu_0 M_s m_i H_{d,i} - \sigma_j \lambda_j \quad \text{with} \quad i = 1,2,3 \quad j = 1, \dots, 6 . \quad (4)$$

In this equation, the components of the reduced magnetization vector are denoted by m_i , the magnitude of the magnetization vector by M_s and the magnetic vacuum permeability by μ_0 . The effective easy axis of magnetization is characterized by its orientation vector EA_i and the effective first-order uniaxial anisotropy energy density constant K . The components of the external magnetic field vector are given by H_i and the components of the mean demagnetizing field by $H_{d,i} = -D_{ii} m_i M_s$, with the main diagonal components D_{ii} of the demagnetizing tensor. For the magnetoelastic energy density, we use the coupling term $-\sigma_i \lambda_i$ with the stress tensor components σ_i and the components λ_i of the isotropic magnetostrictive strain tensor. Both are given in Voigt's notation. The coupling term results from omitting magnetostrictive self-energy and incorporating the term constant with stress into K [57]. In the following, the polar angle θ and the azimuthal angle φ of \bar{m} in the spherical coordinate system (Figure 2) are used to define its components m_i . The exact definition of all vector and tensor components is given in the appendix. The linearized change of the elastic compliance components S_{ij} with the magnetic field and stress is derived from the expression

$$S_{ij}(H, \sigma) = \frac{\partial \varepsilon_i}{\partial \sigma_j} = \frac{\partial (e_i + \lambda_i)}{\partial \sigma_j} := S_{m,ij} + \Delta S_{ij} . \quad (5)$$

where the first summand $S_{m,ij}$ is the constant, fixed magnetization elastic compliance tensor component. The magnetization dependent part ΔS_{ij} can be obtained from the equilibrium conditions that are given by the first-order derivatives of u :

$$u_\varphi := \frac{\partial u}{\partial \varphi} = 0 \quad \text{and} \quad u_\theta := \frac{\partial u}{\partial \theta} = 0. \quad (6)$$

From these equilibrium conditions a general expression for the linearized change ΔS_{ij} of the compliance tensor can be derived (Appendix A). Denoting the second-order derivatives as $u_{\varphi\varphi}$ and $u_{\theta\theta}$ it is:

$$\Delta S_{ij} := \frac{\partial \lambda_i}{\partial \sigma_j} = -\frac{\partial \lambda_i}{\partial \varphi} \frac{\partial u_\varphi}{\partial \sigma_j} \frac{1}{u_{\varphi\varphi}} - \frac{\partial \lambda_i}{\partial \theta} \frac{\partial u_\theta}{\partial \sigma_j} \frac{1}{u_{\theta\theta}}. \quad (7)$$

This expression permits a quick calculation of the compliance tensor for different magnetic systems described by an enthalpy density u . From Equation (10), the non-zero components of $\Delta \mathbf{S}$ for in-plane magnetization ($\theta = \pi/2$) are:

$$\Delta S_{11} = \Delta S_{22} = -\Delta S_{12} = \frac{9\lambda_s^2 \cos[\varphi]^2 \sin[\varphi]^2}{u_{\varphi\varphi}}, \quad (8)$$

$$\Delta S_{16} = -\Delta S_{26} = -\frac{9\lambda_s^2 \cos[\varphi] \cos[2\varphi] \sin[\varphi]}{u_{\varphi\varphi}}, \quad (9)$$

$$\Delta S_{44} = \frac{9\lambda_s^2 \sin[\varphi]^2}{u_{\theta\theta}}, \quad (10)$$

$$\Delta S_{45} = \frac{9\lambda_s^2 \cos[\varphi] \sin[\varphi]}{u_{\theta\theta}}, \quad (11)$$

$$\Delta S_{55} = \frac{9\lambda_s^2 \cos[\varphi]^2}{u_{\theta\theta}}, \quad (12)$$

$$\Delta S_{66} = \frac{9\lambda_s^2 \cos[2\varphi]^2}{u_{\varphi\varphi}}. \quad (13)$$

The final compliance tensor for in-plane magnetization as a function of magnetic field and stress is:

$$\mathbf{S}(H, \sigma) = \begin{bmatrix} S_{11} & S_{12} & S_{m,13} & 0 & 0 & \Delta S_{16} \\ S_{12} & S_{22} & S_{m,23} & 0 & 0 & \Delta S_{26} \\ S_{m,13} & S_{m,23} & S_{m,33} & 0 & 0 & 0 \\ 0 & 0 & 0 & S_{44} & \Delta S_{45} & 0 \\ 0 & 0 & 0 & \Delta S_{45} & S_{55} & 0 \\ \Delta S_{16} & \Delta S_{26} & 0 & 0 & 0 & S_{66} \end{bmatrix} \quad \text{with} \quad S_{ij}(H, \sigma) = S_{m,ij} + \Delta S_{ij}. \quad (14)$$

Because in our case both, \mathbf{S}_m and $\Delta \mathbf{S}$ are symmetric, and \mathbf{S} is also symmetric. Note that $S_{m,16} = S_{m,26} = S_{m,45} = 0$ in our isotropic magnetic material and consequently $S_{16} = \Delta S_{16}$, $S_{26} = \Delta S_{26}$ and $S_{45} = \Delta S_{45}$. Finally, the stiffness tensor \mathbf{C} is obtained by numerically calculating the inverse $\mathbf{C}(H, \sigma) = \mathbf{S}(H, \sigma)^{-1}$. It has the same non-zero components and symmetry. All equations (Equations (11)–(17)) are obtained from Equation (10) assuming in-plane magnetization ($\theta = \pi/2$) and are valid for the isotropic magnetoelastic coupling used in the enthalpy density function (Equation (7)). For all the following simulations, we additionally assume in-plane magnetic fields ($\theta_H = \pi/2$) and an in-plane easy axis ($\theta_{EA} = \pi/2$). These two assumptions influence and simplify u and its derivatives, which are given in the appendix.

5. Implications of the Magnetic Model

In the following, results for the C_{ij} of the magnetoelastic model are discussed at the example of a thin-film geometry. For the calculations, we assumed zero static stress ($\sigma_i = 0$) and $D_{33} = 1$. The large shape anisotropy results in $C_{44} \approx C_{m,44}$ and $C_{55} \approx C_{m,55}$. We

limit the discussion to the C_{11} , C_{12} and C_{66} components as they are most relevant for torsion and bending modes.

In Figure 3a, the normalized C_{11} , C_{12} and C_{66} components are plotted for a macrospin and $\varphi_{EA} = 90^\circ$. Because $u_{\varphi\varphi}(H = H_K) = 0$ and so $\Delta S_{66}(H \rightarrow H_K) \rightarrow \infty$ (Equation (13)) it is $C_{66}(H = H_K) = 0$. At $|H| > |H_K|$, it is $C_{66} < C_{m,66}$ with $C_{66} = C_{m,66}$ only for $H \rightarrow \infty$. Hence, for finite H even a small shear stress σ_6 can always tilt the magnetization vector out of the applied magnetic field direction. It occurs, because the magnetoelastic energy density contribution $-\sigma_6\lambda_6$ of the shear stress σ_6 is asymmetric around $\varphi = 0^\circ$. Its minimum is shifted by 45° compared to the minimum of the one-component at $\varphi = 0^\circ$. Consequently, at the two local maxima it is $C_{66}(\varphi = 45^\circ, 135^\circ) = C_{m,66}$. The C_{11} component shows two distinct minima but unlike the delta-E effect in the Young's modulus (e.g., [6,14,49]) no discontinuities at $|H| = |H_K|$. Although the discontinuities are present in S_{11} (not shown), they vanish during the inversion due to contributions of other S_{ij} components to C_{11} . In contrast to C_{11} , C_{12} stiffens with applied magnetic bias field because $\Delta S_{12} = -\Delta S_{11}$. The signs are a direct consequence of the positive isotropic magnetoelastic coupling. As the macrospin rotates towards the x axis, magnetostrictive expansion occurs along the x axis, but contraction occurs along the y axis. Compared with C_{11} , the maximum relative change of C_{12} is larger because $S_{m,12} < S_{m,11}$, which results in a different weighting in Equation (5). In Figure 3b, C_{66} is shown for three different angles of the easy axis $\varphi_{EA} = 90^\circ, 85^\circ$, and 75° . It is apparent that a change of φ_{EA} strongly influences C_{66} . Relative to $\varphi_{EA} = 90^\circ$, the two minima at $H = \pm H_K$ shift to a larger $|H|$ and the minimum value increases strongly by more than 85% at $\varphi_{EA} = 85^\circ$ and about 95% at $\varphi_{EA} = 75^\circ$. The center minimum shifts due to the single domain hysteresis and decreases slightly with decreasing φ_{EA} . A singularity occurs at $\varphi_{EA} = 85^\circ$ due to the magnetic discontinuity at the switching field of the single-spin model. Due to the strong impact of small deviations from $\varphi_{EA} = 90^\circ$ on $C_{66}(H)$, the magnetic sensitivity is expected to change notably with φ_{EA} .

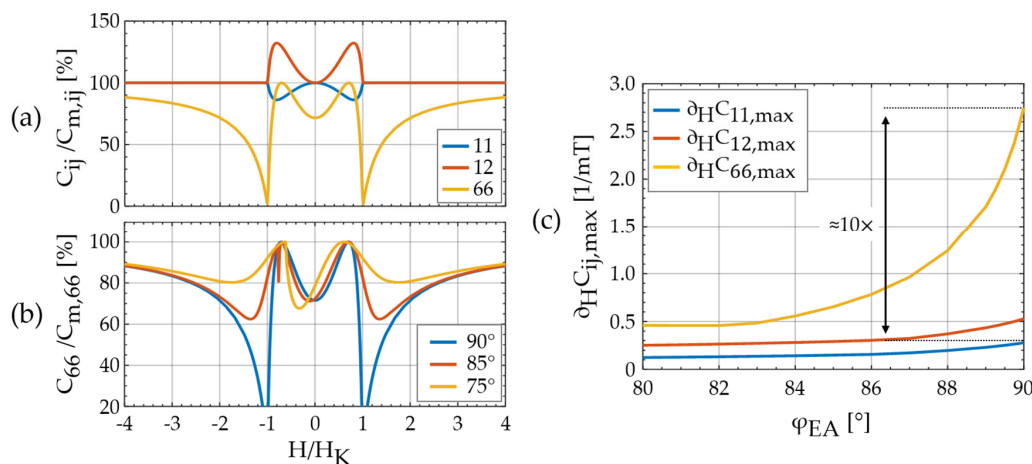


Figure 3. (a) Magnetic field dependent components C_{ij} of the effective stiffness tensor for an ideal hard axis magnetization process of a macrospin. The external magnetic field with magnitude H is applied along the x axis and normalized the anisotropy field H_K ; (b) component C_{66} for different angles φ_{EA} of the magnetic easy axis to the x axis; (c) maximum value $\partial_H C_{ij,max}$ of $\partial_H C_{ij}(H)$ (Equation (3)) for the C_{11} and C_{66} components as functions of the easy axis angle φ_{EA} . For the calculations in (c), a distribution of effective anisotropy energy density is used as in Ref. [49] with a standard deviation of $\delta_K = 15\%$ for a more quantitative estimation and to prevent singularities.

In the following, we quantify the influence of the C_{ij} components on the relative magnetic sensitivity $S_{H,r}$ using $\partial_H C_{ij}$ as defined in Equation (3). Calculating $\partial_H C_{ij}$ requires forming the derivate $\partial C_{ij}/\partial H$, which results in singularities for the 66-component

at $\varphi_{EA} = 90^\circ$ and $|H| = |H_K|$. A finite derivative can be estimated by including the distribution of the effective anisotropy energy density K in a mean-field approach [15,49,58]. With such a distribution, inhomogeneities in the magnetization response are considered that can occur, e.g., from spatially varying stress or internal stray fields. We use a normal distribution of K with a standard deviation $\delta_K = 15\%$ as a representative example value that has been used previously for a similar device [49]. We calculate $\partial_H C_{ij}(H)$ numerically from $C_{ij}(H)$ and extract the maximum $\partial_H C_{ij,max}(H)$ for $H > 0$, at various angles φ_{EA} of the easy axis. They are plotted in Figure 3c. As a result of the distribution, both $\partial_H C_{ij,max}$ are finite at $\varphi_{EA} = 90^\circ$ with $\partial_H C_{66,max} \approx 10 \times \partial_H C_{11,max} \approx 4.5 \times \partial_H C_{12,max}$. This is reduced to $\partial_H C_{66,max} \approx 4 \times \partial_H C_{11,max} \approx 2 \times \partial_H C_{12,max}$ at $\varphi_{EA} = 80^\circ$. In conclusion, the C_{66} component potentially offers a significantly larger magnetic sensitivity than the C_{11} and C_{12} components.

6. Results

6.1. Magnetization Measurements

Magneto-optical Kerr effect (MOKE) microscopy [59] was used to analyze the magnetic multilayer. The picture in Figure 4a shows the rear side of the cantilever and is composed of a series of images. For each image, the magnetic multilayer was demagnetized along the x axis and the MOKE sensitivity axis was set along the y axis. The region of the magnetic multilayer is marked with a white frame and the estimated easy axis orientation is indicated with white arrows. In a large region around the left, top, and bottom edge, no magnetic response is visible. A comparison with light microscopy images reveals possibly corroded regions. They might have formed due to incomplete Cr-coverage at the edges. At the time, a particularly thin Cr-layer was deposited to ensure good magneto-optical contrast. Close to the clamping region (blue rectangle in Figure 4a), the layer is partially delaminated. Despite these nonidealities, the overall magnetic response in the magnetically active region is quite homogeneous. The average easy axis orientation is approximately $\varphi_{EA} = -75^\circ \pm 5^\circ$ relative to the x axis. An effective uniaxial anisotropy energy density of $K = (1.2 \pm 0.1) \text{ kJ/m}^3$ is estimated with the magnetoelastic model. We used the ballistic demagnetizing tensor [60] in the center of the film and assumed $\sigma_j = 0$. A representative magnetization curve of the center region, recorded along the x axis, is shown in Figure 4b, and compared with one recorded at the clamping region. The difference between these curves indicates a different alignment of the effective anisotropy. However, due to the magnetic multilayer structure and the partial delamination additional effects cannot be excluded. From previous investigations [49], we expect that the deteriorated magnetic properties at the clamping especially reduce the resonance frequency detuning and the magnetic sensitivity of the first bending mode.

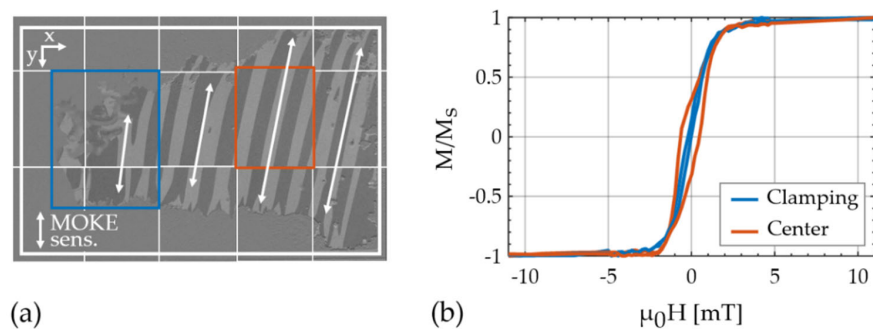


Figure 4. (a) Magneto-optical Kerr effect microscopy image of the analyzed structure, demagnetized along the x axis and composed of a series of different images. The region of the magnetic layer is marked by a white square and the approximated orientation of the magnetic easy axis is indicated with arrows at approximately $-75^\circ \pm 5^\circ$ relative to the x axis; (b) magnetization curve

close to the clamping and in the center of the magnetic film. The two evaluated regions are indicated with squares in (a).

6.2. Electromechanical Properties

To analyze the electromechanical properties of the sensor, the sensor admittance $Y(f_{\text{ex}})$ is measured over a large range of excitation frequencies f_{ex} . Six resonance modes are characterized in detail by fitting a modified Butterworth van Dyke (mBvD) model (e.g., [61]) with the equivalent circuit configuration from [47] to the measurements. The resonance frequencies f_r and quality factors are calculated from the mBvD parameters of each admittance curve and compared with the eigenfrequencies obtained from the finite element method (FEM) model. With this comparison, the eigenmodes are identified to be the first three bending modes (BM1–3) and the first three torsion modes (TM1–3). The FEM model was fitted to admittance measurements of the first torsion mode (TM1) close to magnetic saturation at $\mu_0 H = -10$ mT. It matches the measurements very well as shown in Figure 5a. The material parameters match excellently with literature values. Details on the material parameters and on the geometry are given in Appendix C. A comparison of the measured resonance frequencies in magnetic saturation with the FEM simulations results in extremely small deviations $< 2\%$ for all six modes (Appendix B).

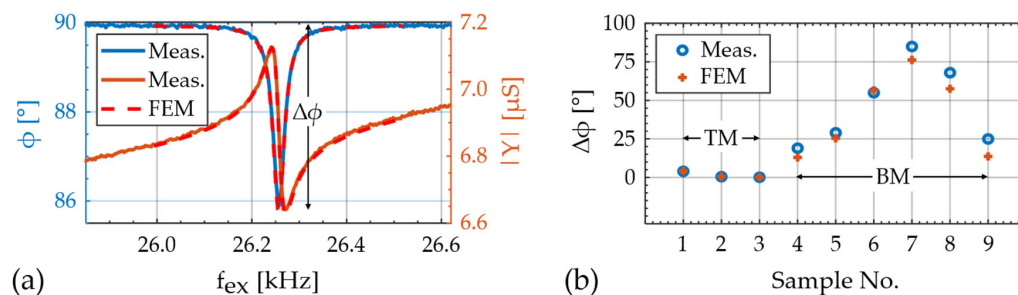


Figure 5. (a) Example comparison of measurement and FEM simulation of the sensor admittance around the first torsion mode (TM1), close to magnetic saturation at -10 mT; (b) comparison of measured and modeled maximum phase shift of the first three torsion modes (TM, samples 1–3) and the first and second bending modes (BMs, samples 4–9) with various electrode configurations. The BM measurements are published in Ref. [28].

The set of material parameters found is used to predict, and compare the impedance characteristic of other cantilever delta-E effect sensors published previously [28]. The sensors differ in their geometry from our torsion mode sensor. They were designed to excite the first and second bending mode with various electrode geometries. For the simulations, we used the same material parameters found for the torsion mode sensors but adjusted the geometry.

As a figure of merit for the electromechanical model, we compared the absolute difference $\Delta\phi = \phi_{\text{max}} - \phi_{\text{min}}$ of the phase angle ϕ of the electrical admittance Y . The simulation results are plotted in Figure 5b and compared with values of the torsion modes (Appendix B) measured here, and the bending mode from Ref. [28]. The TMs were measured close to magnetic saturation at $\mu_0 H = -10$ mT to reduce the influence of the delta-E effect. Slight deviations between the measurement and simulation might result from effectively different magnetolectric coupling factors, e.g., due to the slightly different material parameters, geometric inaccuracies, or stress [62]. In conclusion, the model can estimate the electromechanical properties of the device and the effect of different electrode configurations well. For the application of magnetoelastic resonators as delta-E effect sensors, a high $\Delta\phi$ and hence a high electrical sensitivity is desirable. In comparison to the bending modes, the $\Delta\phi$ of the torsion modes is systematically smaller, which is also reflected in the electrical sensitivities. With $S_{Y,r} \approx 0.85$ mS of TM1, the maximum relative

electrical amplitude sensitivity $S_{Y,r} \approx 5.8$ mS of sample No. 7 (BM2) [28] is almost a factor of seven larger, despite a similar quality factor. Hence, the large factor potentially gained in the magnetic sensitivity from utilizing the C_{66} component can be diminished by a reduced electrical sensitivity.

Additional simulations show that further optimization of the electrode design and reduction in the parasitic capacity from bond pads and wires could improve $\Delta\phi$ of TM1 to $\Delta\phi = 10^\circ$. Alternatively, the parasitic effect of the sensor capacitance could be neutralized with additional electronics to utilize the phase-modulated signal for magnetic field detection [48]. A further improvement by a factor of two could be obtained by exciting both electrodes E_1 and E_2 , phase shifted by 180° . Additionally, alternative piezoelectric materials with larger piezoelectric coefficients, such as AlScN [63–65] could increase the electrical sensitivity significantly and result in $\Delta\phi$ comparable with bending modes.

6.3. Delta-E Effect and Sensitivities

The $f_r(H)$ plots extracted from the modified Butterworth van Dyke (mBvD) fits of the first three bending modes (BM1–3) are shown in Figure 6a (right). They are normalized to $f_{r,\max} := f_r(-10 \text{ mT})$ and have a respective minimum resonance frequency $f_{r,\min}$. As a measure for the maximum resonance frequency detuning, we defined the normalized resonance frequency change $\Delta f_r := (f_{r,\max} - f_{r,\min})/f_{r,\max}$. All three curves are w-shaped and Δf_r increases with increasing mode number. This effect was reported previously and explained with a strong weighting of the magnetic properties at the clamping in BM1 [49]. Here, the difference between the BM1 and BM2 is significantly larger, which is consistent with the deteriorated material around the clamping region, visible in the magneto-optical Kerr effect microscopy (MOKE) images (Figure 4a). Correspondingly, the relative magnetic sensitivity $S_{H,r} \approx 3.5 \text{ T}^{-1}$ is smallest in BM1 and increases up to $S_{H,r} \approx 9 \text{ T}^{-1}$ in BM2.

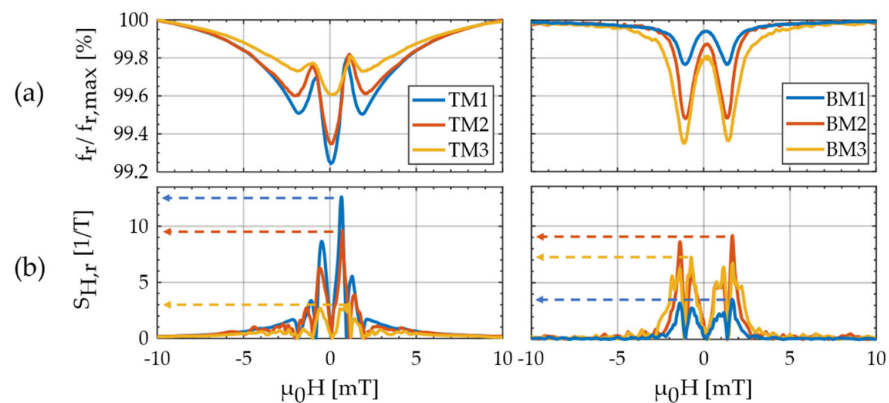


Figure 6. Measurements of the resonance frequency f_r as a function of the applied magnetic flux density $\mu_0 H$ along the long cantilever axis (x axis) starting at $\mu_0 H = -10$ mT: (a) normalized resonance frequency $f_r/f_{r,\max}$ of the first three torsion modes (TMs) (left) and the first three transversal bending modes (BMs) (right). The maximum resonance frequencies $f_{r,\max}$ of the TMs are 26.256, 87.478, 175.150 kHz, and of the BMs: 7.649, 47.182, 121.400 kHz; (b) relative magnetic sensitivities $S_{H,r} = S_H/f_{r,\max}$ calculated from the data in (a) with Equation (1).

The normalized $f_r(H)$ plots of the torsion modes (TMs) and their corresponding $S_{H,r}$ are shown in Figure 6 (left). Although the sample is close to magnetic saturation at $\mu_0 H = -10$ mT, all three $f_r(H)$ curves still exhibit a non-zero slope as expected from the presented theory. The three $f_r(H)$ curves have a global minimum around $H = 0$, two local minima at around ± 2 mT, and two local maxima at about ± 1 mT. With an increasing

mode number, the local maxima are almost unaffected, whereas Δf_r significantly decreases. Consequently, the maximum $S_{H,r}$ also decrease with the increasing mode number, here from $S_{H,r} = 12.6 \text{ T}^{-1}$ in TM1 to $S_{H,r} = 3.0 \text{ T}^{-1}$ in TM3. The trend is notably opposed to the corresponding behavior of the bending modes and will be analyzed and explained in detail in the next section using the magnetoelastic and electromechanical models. Overall, the magnetic sensitivities are in the range of $\approx 10 \text{ T}^{-1}$ also measured with other magnetoelastic resonators in bending and bulk resonance modes [22,49]. At first glance, the similarity of BM and TM in $S_{H,r} \propto \partial_H C_{ij}$, might contradict the magnetoelastic model results in Figure 3c. To resolve this and explain the dependency of the torsion modes on the mode number, the second factor $\partial_C f_{r,ij}$ that contributes to $S_{H,r}$ must be considered.

6.4. Resonance Frequency Simulations

In the following, we use the stiffness tensor components from the magnetic model as input in the finite element method (FEM) model to describe and analyze the frequency detuning and the magnetic sensitivity of the bending and torsion modes measured before. The demagnetizing tensor is approximated with the ballistic demagnetizing tensor in the center of the magnetic layer [60]. Consistently with the measurements the easy axis angle is set to $\varphi_{EA} = -75^\circ$ and the effective anisotropy energy density constant to $K = 1.2 \text{ kJ/m}^3$, assuming $\sigma_j = 0$. Results for the normalized resonance frequencies $f_r(H)$ of the torsion modes are shown in Figure 7a and of the bending modes in Figure 7b. Despite the simplifying assumptions, a striking similarity with the measurements is apparent. All simulated torsion mode (TM) curves in Figure 7a exhibit two local maxima around one global minimum. Due to the single-domain hysteresis, the local minimum is shifted slightly leftwards away from $\mu_0 H = 0$. The frequency difference between the local maxima and the global minimum decreases significantly with increasing mode number, as also observed in the measurements.

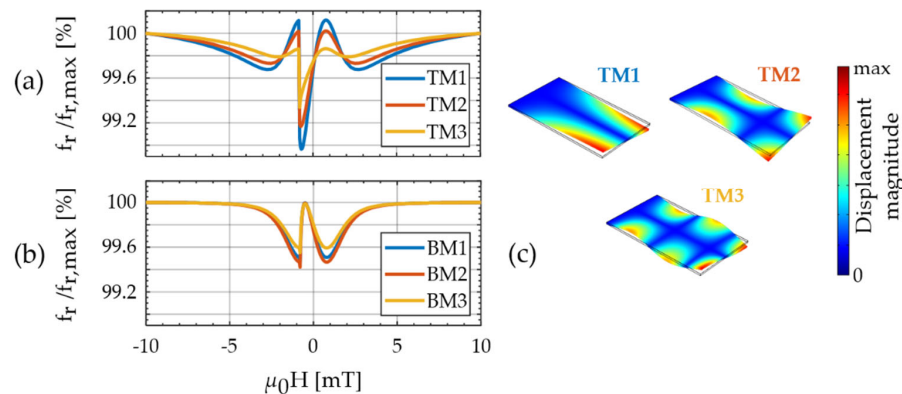


Figure 7. (a) Simulated resonance frequency f_r normalized to its maximum, as a function of the magnetic bias flux density $\mu_0 H$ for the first three torsional modes (TMs); and (b) the first three bending modes (BMs); and (c) the magnitude of the displacement vector of the first three torsion modes plotted and calculated with COMSOL® Multiphysics v. 5.3a (COMSOL AB, Stockholm, Sweden).

Within the model, this phenomenon can be explained with the mode shapes of the higher torsion modes (Figure 7c). Due to the multiple twisting of the cantilever in higher modes, the resonance nodes are closer together. This results in an increasing contribution of the stiffness tensor components C_{11} and C_{22} to f_r relative to the C_{66} component. Quantitatively, we can explain the contribution of C_{ij} to f_r with the 11- and the 66-components of the normalized frequency factors $\partial_C f_{r,ij}$ (Equation (3)). They are estimated with the

FEM model and summarized in Table 1. Whereas $\partial_C f_{r,11}$ increases by almost a factor of three, $\partial_C f_{r,66}$ shows the opposite trend and decreases by a factor of approximately two, from TM1 to TM3. Because the minima and maxima of C_{11} and C_{66} occur at similar magnetic bias fields they increasingly compensate each other in higher torsion modes. This causes similar magnetic sensitivities of TMs and BMs in our sensor, although $\partial_H C_{66, \max} > \partial_H C_{11, \max}$ in Figure 3c. If the delta-E effect of C_{66} is to be utilized, consequently, the first torsion mode is preferable to higher modes.

Table 1. Normalized frequency factors $\partial_C f_{r,11}$ and $\partial_C f_{r,66}$ (Equation (3)) of the first three torsion modes (TMs) and bending modes (BMs), calculated with the electromechanical finite element model.

Resonance Mode	TM1	TM2	TM3	BM1	BM2	BM3
$\partial_C f_{r,11}$	0.010	0.017	0.029	0.060	0.056	0.052
$\partial_C f_{r,66}$	0.034	0.026	0.016	0	0	0
$\partial_C f_{r,12}$	0	0	0	-0.003	-0.006	-0.001

In contrast to the measured bending mode curves (Figure 6), the corresponding modeled curves (Figure 7b) are almost independent of the mode number. Consistently, the $\partial_C f_{r,11}$ of the BMs are approximately constant with the mode number. The other frequency factor $\partial_C f_{r,12}$ is very small and $\partial_C f_{r,66} \approx 0$. A different effect dominates the mode dependency observed in the measured bending modes. This corroborates the hypothesis stated earlier in Section 6.3 that the reduced maximum normalized resonance frequency change Δf_r (as defined in Section 6.3) of BM1 is likely caused by the deteriorated magnetic layer present around the clamping (Figure 4a).

As shown earlier in Figure 3a, the minima of $C_{11}(H)$ occur at the same magnetic bias fields as the maxima of $C_{12}(H)$. Whereas $C_{11}(H)$ softens upon the application of a magnetic bias field, $C_{12}(H)$ increases. However, upon application of a magnetic field, they both reduce the resonance frequency of bending modes. Consequently, their corresponding frequency factors have opposite signs and $\partial_C f_{r,12} < 0$.

7. Summary and Conclusions

In summary, we provide an experimental and theoretical study on the delta-E effect, the normalized resonance frequency change Δf_r (defined in Section 6.3) and the sensitivity of first and higher-order bending modes (BMs) and torsion modes (TMs). The study was conducted on a magnetoelectric thin-film cantilever with a soft magnetic FeCoSiB–Cr multilayer and an electrode design that enables the excitation of various resonance modes. A general expression was developed that permits the detailed analysis of the magnetic sensitivity of arbitrary resonance modes. An electromechanical finite element method model was set up to describe the resonator and the electrical sensitivity. It was combined with a magnetoelastic macrospin model to include the tensor of the linearized delta-E effect for isotropic magnetostriction in the approximation of negligible magnetostrictive self-energy. The models are valid for moderately high-operation frequencies, where electrodynamic and magnetodynamic effects can be omitted.

The delta-E effect model is discussed in detail for here the most relevant components C_{66} , C_{11} , and C_{12} of the magnetic field-dependent stiffness tensor. Simulation results imply that the C_{66} component potentially offers a ten-fold higher contribution to the magnetic sensitivity than the C_{11} component. With an increasing tilt of the magnetic easy axis, this factor reduces to approximately four at an easy axis angle aligned at 80° relative to the long axis of the cantilever. However, the measurements and simulations of the current design confirm that the TMs exhibit a systematically smaller electromechanical response compared to BMs, which can significantly diminish the potential gain in sensitivity. Possible ways of improvement are sketched out. From simulated and measured resonance

frequency curves $f_r(H)$ we found that the maximum normalized resonance frequency change Δf_r and the magnetic sensitivity of TMs reduce with the increasing mode number due to the increasing contribution of C_{11} to the resonance frequency. Hence, the dependency of TMs on the mode number is opposite to the one observed for BMs and caused by a different mechanism.

In conclusion, the delta-E effect of the C_{66} component shows the promising potential of significantly increasing the magnetic sensitivity and the maximum normalized resonance frequency change Δf_r . However, the efficient electrical excitation of TMs remains challenging for achieving high electrical sensitivity. Generally, the results imply that the delta-E effect of different C_{ij} can have opposite effects on Δf_r , depending on the resonance mode. This was demonstrated in the example of torsion modes. Because the contribution of C_{11} increases with the torsion mode number, the first-order torsion mode shows the highest magnetic sensitivity. In addition to fundamental insights on the delta-E effect in higher resonance modes, a model for the electrical and the magnetic sensitivity was presented. The results are not only relevant for the development of magnetoelastic magnetic field sensors, but also for frequency tunable devices based on the delta-E effect.

Author Contributions: Conceptualization, B.S.; methodology, B.S., E.V.G., R.-M.F.; validation, B.S.; formal analysis, B.S., E.V.G.; investigation, B.S., E.V.G., S.Z., C.K.; writing—original draft preparation, B.S.; writing—review and editing, B.S., E.V.G., R.-M.F., S.Z., C.K., D.M., J.M., F.F.; visualization, B.S., E.V.G.; supervision, D.M., J.M., F.F.; project administration, D.M., J.M., F.F.; funding acquisition, D.M., J.M., F.F. All authors have read and agreed to the published version of the manuscript.

Funding: This research was funded by the German Research Foundation (DFG) via the collaborative research center CRC 1261.

Institutional Review Board Statement: Not applicable.

Informed Consent Statement: Not applicable.

Data Availability Statement: Not applicable.

Acknowledgments: The authors thank Christoph Elis for performing the density measurements on FeCoSiB.

Conflicts of Interest: The authors declare no conflict of interest. The funders had no role in the design of the study; in the collection, analyses, or interpretation of data; in the writing of the manuscript, and in the decision to publish the results.

Appendix A. Magnetoelastic Model

A.1. Definition of Vectors

In the following, a detailed definition of all vectors is given in the spherical coordinate system. All polar angles are denoted by θ and all azimuthal angles by φ , with an index if it is not the angles of the reduced magnetization. The reduced magnetization vector is denoted as

$$\vec{m} = [\cos \varphi \sin \theta \quad \sin \varphi \sin \theta \quad \cos \theta]^T, \quad (\text{A1})$$

The easy axis unit vector \vec{EA} is given by

$$\vec{EA} = [\cos \varphi_{EA} \sin \theta_{EA} \quad \sin \varphi_{EA} \sin \theta_{EA} \quad \cos \theta_{EA}]^T. \quad (\text{A2})$$

The vector \vec{H} of the external applied field and \vec{H}_d of the demagnetizing field are given by

$$\vec{H} = H [\cos \varphi_H \sin \theta_H \quad \sin \varphi_H \sin \theta_H \quad \cos \theta_H]^T, \quad (\text{A3})$$

$$\vec{H}_d = -M_S [D_{11} m_1 \quad D_{22} m_2 \quad D_{33} m_3]^T. \quad (\text{A4})$$

For all higher-order tensors, we use the Voigt notation. The magnetostriction tensor is then given by

$$\lambda = \frac{3}{2}\lambda_s \begin{bmatrix} m_1^2 - \frac{1}{3} & m_2^2 - \frac{1}{3} & m_3^2 - \frac{1}{3} & 2m_2m_3 & 2m_1m_3 & 2m_1m_2 \end{bmatrix}^T. \quad (\text{A5})$$

A.2. General Expression for ΔS_{ij}

From the equilibrium conditions, one can write

$$\begin{aligned} \Delta S_{ij} &= \frac{\partial \lambda_i}{\partial \sigma_j} = \frac{\partial \lambda_i}{\partial \varphi} \frac{\partial \varphi}{\partial \sigma_j} + \frac{\partial \lambda_i}{\partial \theta} \frac{\partial \theta}{\partial \sigma_j} = \frac{\partial \lambda_i}{\partial \varphi} \left(-\frac{\partial u_\varphi}{\partial \sigma_j} / \frac{\partial u_\varphi}{\partial \varphi} \right) + \frac{\partial \lambda_i}{\partial \theta} \left(-\frac{\partial u_\theta}{\partial \sigma_j} / \frac{\partial u_\theta}{\partial \theta} \right) \\ &:= -\frac{\partial \lambda_i}{\partial \varphi} \frac{\partial u_\varphi}{\partial \sigma_j} \frac{1}{u_{\varphi\varphi}} - \frac{\partial \lambda_i}{\partial \theta} \frac{\partial u_\theta}{\partial \sigma_j} \frac{1}{u_{\theta\theta}}. \end{aligned} \quad (\text{A6})$$

A.3. Derivatives of the Energy Density Functional

For in-plane magnetization ($\theta = \pi/2$), easy axis ($\theta_{EA} = \pi/2$), and magnetic field ($\theta_H = \pi/2$), the second-order derivatives of u (Equation (7)) are given by

$$\begin{aligned} u_{\varphi\varphi} &:= \frac{\partial^2 u}{\partial \varphi^2} = 3\lambda_s [\sigma_{11} \cos(2\varphi) - \sigma_{22} \cos(2\varphi) + 2\sigma_{12} \sin(2\varphi)] + \mu_0 M_s H \cos(\varphi - \varphi_H) + 2K \cos(2[\varphi - \varphi_{EA}]) \\ &\quad + \mu_0 M_s^2 (D_{22} - D_{11}) \cos(2\varphi) \end{aligned} \quad (\text{A7})$$

$$\begin{aligned} u_{\theta\theta} &:= \frac{\partial^2 u}{\partial \theta^2} = 3\lambda_s [\sigma_{11} \cos^2 \varphi + \sigma_{22} \sin^2 \varphi - \sigma_{33} + \sigma_{12} \sin(2\varphi)] + \mu_0 M_s H \cos(\varphi - \varphi_H) + 2K \cos^2(\varphi - \varphi_{EA}) \\ &\quad - \mu_0 M_s^2 (D_{11} \cos^2 \varphi + D_{22} \sin^2 \varphi - D_{33}) \end{aligned} \quad (\text{A8})$$

Appendix B. Resonance Frequencies and Sensitivities

A summary of the maximum measured resonance frequencies $f_{r,\max}$ at $\mu_0 H = -10$ mT is given in Table A1, together with the corresponding quality factor Q_{\max} and the maximum magnetic sensitivities from Figure 6. The bending modes (BMs) and the torsion modes (TMs) were all measured using only electrode E1. Hence, the electrodes are not optimized for the bending modes. Additionally, the maximum quality factor of the BMs is a factor of three smaller than in TM1. Due to both factors, the electrical sensitivity of BMs is significantly smaller than that of TMs for our cantilever.

Table A1. Measured resonance frequencies $f_{r,\max}$ of the six modes analyzed and the quality factor Q_{\max} , both measured in magnetic saturation at $\mu_0 H = -10$ mT. The maximum magnetic sensitivity S_H and the maximum relative magnetic sensitivity $S_{H,r}$ are obtained from Figure 6b. The maximum relative electrical sensitivities found are given by $S_{\phi,r}$ and $S_{Y,r}$.

Mode	$f_{r,\max}$ (kHz)	$f_{r,model}$ (kHz)	Q_{\max}	S_H (Hz/mT)	$S_{H,r}$ (1/T)	$S_{\phi,r}$ (°)	$S_{Y,r}$ (μS)
TM1	26.26	26.26	900	330	12.6	4780	850
TM2	87.48	88.20	700	837	9.5	59	27.5
TM3	175.15	179.20	280	542	3.0	115	95
BM1	7.65	7.80	300	26.7	3.5	2550	150
BM2	47.18	48.55	300	432	9.2	220	70
BM3	121.40	116.20	300	811	6.7	18	42

Appendix C. Geometry and Material Parameters

C.1. Geometry

The poly-Si cantilever was measured with an optical microscope to be $L = 3.12$ mm long and $W = 2.15$ mm wide. For the simulations, the length in the model was slightly adjusted within the measurement accuracy to 3.116 mm. The magnetostrictive layer was deposited directly at the clamping on the bottom side of the poly-Si cantilever and has a

width of $W_{\text{mag}} = 2$ mm and a length of $L_{\text{mag}} = 3.05$ mm. The AlN layer is of the same geometry but deposited on top of the poly-Si. The electrodes E_1 and E_2 are positioned at the clamping on top of the AlN layer and the left and right edge, respectively. An additional parallel capacitance of $C_0 = 17.7$ pF is used. It is consistent with the area of the bond pads, the conduction lines, and the relative electrical permittivity used for the AlN.

C.2. Substrate (Poly-Si)

For the poly-silicon substrate, we use isotropic material parameters, with Young's modulus $E_{\text{Si}} = 160$ GPa [66,67] a Poisson's ratio of $\nu_{\text{Si}} = 0.22$ [67] and a mass density of $\rho_{\text{Si}} = 2300$ kg/m³ [68].

C.3. Magnetic Material (FeCoSiB)

The mass density of FeCoSiB was experimentally determined by estimating the volume with profilometer measurements and the mass with a microbalance. The measurements were performed on a 6-inch wafer with a mean FeCoSiB layer thickness of approximately 1.5 μm . A density of $\rho_{\text{FeCoSiB}} = (7870 \pm 1350)$ kg/m³ was obtained. For the simulation, a corresponding mass density of $\rho_{\text{FeCoSiB}} = 7700$ kg/m³ was used. For the stiffness tensor of the mechanically isotropic magnetic film, we use:

$$C_{m,ij} = \begin{bmatrix} C_{m,11} & C_{m,12} & C_{m,12} & 0 & 0 & 0 \\ C_{m,12} & C_{m,11} & C_{m,12} & 0 & 0 & 0 \\ C_{m,12} & C_{m,12} & C_{m,11} & 0 & 0 & 0 \\ 0 & 0 & 0 & C_{m,44} & 0 & 0 \\ 0 & 0 & 0 & 0 & C_{m,55} & 0 \\ 0 & 0 & 0 & 0 & 0 & C_{m,66} \end{bmatrix} \quad (\text{A9})$$

Using a Young's modulus of $E = 150$ GPa and a Poisson's ratio of $\nu = 0.3$, both at fixed magnetization, the non-zero components of the fixed magnetization stiffness tensor are:

$$C_{m,11} = C_{m,22} = C_{m,33} = \frac{E(1-\nu)}{(1+\nu)(1-2\nu)} = 201.92 \text{ GPa} \quad (\text{A10})$$

$$C_{m,12} = C_{m,13} = C_{m,23} = \frac{E\nu}{(1+\nu)(1-2\nu)} = 86.54 \text{ GPa} \quad (\text{A11})$$

$$C_{m,66} = C_{m,55} = C_{m,44} = \frac{E}{2(1+\nu)} = 57.69 \text{ GPa} \quad (\text{A12})$$

For the magnetoelastic simulations, we use a saturation magnetic flux density of $\mu_0 M_s = 1.5$ T [17] and saturation magnetostriction of $\lambda_s = 35$ ppm [17].

C.4. Piezoelectric Material (AlN)

For the stiffness matrix \mathbf{C}_{AlN} and the piezoelectric stress-charge coefficient tensor \mathbf{d} we use values based on ab initio calculations [69]. Those tend to overestimate \mathbf{d} and are here slightly adjusted. The stiffness tensor is:

$$\mathbf{C}_{\text{AlN}} = \begin{bmatrix} 410.2 & 142.2 & 110.1 & 0 & 0 & 0 \\ 142.2 & 410.2 & 110.1 & 0 & 0 & 0 \\ 110.1 & 110.1 & 385.0 & 0 & 0 & 0 \\ 0 & 0 & 0 & 122.9 & 0 & 0 \\ 0 & 0 & 0 & 0 & 122.9 & 0 \\ 0 & 0 & 0 & 0 & 0 & 134.0 \end{bmatrix} \text{ GPa}, \quad (\text{A13})$$

The piezoelectric coupling tensor $\mathbf{c}_e = \mathbf{d}\mathbf{C}_{\text{AlN}}$ results as

$$\mathbf{c}_e = \begin{bmatrix} 0 & 0 & 0 & 0 & -0.27828 & 0 \\ 0 & 0 & 0 & -0.27828 & 0 & 0 \\ -0.4496 & -0.4496 & 1.41 & 0 & 0 & 0 \end{bmatrix} \frac{\text{pC}}{\text{m}^2}. \quad (\text{A14})$$

For the density, we use $\rho_{\text{AlN}} = 3300 \text{ kg/m}^3$ and for the electrical permittivity $\epsilon_{\text{el}} = \epsilon_r \epsilon_0$ with the electrical vacuum permittivity ϵ_0 and the relative electrical permittivity ϵ_r , given by

$$\epsilon_r = \begin{bmatrix} 9.2081 & 0 & 0 \\ 0 & 9.2081 & 0 \\ 0 & 0 & 10.1192 \end{bmatrix}. \quad (\text{A15})$$

References

- Reermann, J.; Durdaut, P.; Salzer, S.; Demming, T.; Piorra, A.; Quandt, E.; Frey, N.; Höft, M.; Schmidt, G. Evaluation of magnetoelectric sensor systems for cardiological applications. *Meas. J. Int. Meas. Confed.* **2018**, *116*, 230–238, doi:10.1016/j.measurement.2017.09.047.
- Zuo, S.; Schmalz, J.; Ozden, M.-O.; Gerken, M.; Su, J.; Niekil, F.; Lofink, F.; Nazarpour, K.; Heidari, H. Ultrasensitive Magnetoelectric Sensing System for pico-Tesla MagnetoMyoGraphy. *IEEE Trans. Biomed. Circuits Syst.* **2020**, 1–1, doi:10.1109/tbcas.2020.2998290.
- Kwong, J.S.W.; Leithäuser, B.; Park, J.W.; Yu, C.M. Diagnostic value of magnetocardiography in coronary artery disease and cardiac arrhythmias: A review of clinical data. *Int. J. Cardiol.* **2013**, *167*, 1835–1842, doi:10.1016/j.ijcard.2012.12.056.
- Röbisch, V.; Salzer, S.; Urs, N.O.; Reermann, J.; Yarar, E.; Piorra, A.; Kirchhof, C.; Lage, E.; Höft, M.; Schmidt, G.U.; et al. Pushing the detection limit of thin film magnetoelectric heterostructures. *J. Mater. Res.* **2017**, *32*, 1009–1019, doi:10.1557/jmr.2017.58.
- Kneller, E. *Ferromagnetismus*; Springer: Berlin/Heidelberg, Germany, 1962; ISBN 9783642866951.
- Livingston, J.D. Magnetomechanical properties of amorphous metals. *Phys. Status Solidi A* **1982**, *70*, 591–596, doi:10.1002/pssa.2210700228.
- Lee, E.W. Magnetostriction and Magnetomechanical Effects. *Rep. Prog. Phys.* **1955**, *18*, 184–229, doi:10.1088/0034-4885/18/1/305.
- De Lacheisserie, T. *Theory and Application of Magnetoelasticity*; CRC Press: Boca Raton, FL, USA, 1993; ISBN 9780849369346.
- Bou Matar, O.; Robillard, J.F.; Vasseur, J.O.; Hladky-Hennion, A.C.; Deymier, P.A.; Pernod, P.; Preobrazhensky, V. Band gap tunability of magneto-elastic phononic crystal. *J. Appl. Phys.* **2012**, *111*, doi:10.1063/1.3687928.
- Mazzamuro, A.; Dusch, Y.; Pernod, P.; Matar, O.B.; Addad, A.; Talbi, A.; Tiercelin, N. Giant magnetoelastic coupling in Love acoustic waveguide based on uniaxial multilayered TbCo2/FeCo nanostructured thin film on Quartz ST-cut. *Phys. Rev. Appl.* **2020**, *13*, doi:10.1103/PhysRevApplied.13.044001.
- Del Moral, A. Magnetostriction and magnetoelasticity theory: A modern view. In *Handbook of Magnetism and Advanced Magnetic Materials*; Kronmüller, H., Parkin, S., Eds.; Wiley-Interscience: Hoboken, NJ, USA, 2007; Volume 1, ISBN 9780470022177.
- Atkinson, D.; Squire, P.T.; Gibbs, M.R.J.; Atalay, S.; Lord, D.G. The effect of annealing and crystallization on the magnetoelastic properties of Fe-Si-B amorphous wire. *J. Appl. Phys.* **1993**, *73*, 3411–3417, doi:10.1063/1.352942.
- Barandiarán, J.M.; Gutiérrez, J.; García-Arribas, A.; Squire, P.T.; Hogsdon, S.N.; Atkinson, D. Comparison of magnetoelastic resonance and vibrating reed measurements of the large delta-E effect in amorphous alloys. *J. Magn. Magn. Mater.* **1995**, *140–144*, 273–274, doi:10.1016/0304-8853(94)00613-X.
- Squire, P.T. Domain model for magnetoelastic behaviour of uniaxial ferromagnets. *J. Magn. Magn. Mater.* **1995**, *140–144*, 1829–1830, doi:10.1016/0304-8853(94)00918-X.
- Gutiérrez, J.; García-Arribas, A.; Garitaonandia, J.S.; Barandiarán, J.M.; Squire, P.T. ΔE effect and anisotropy distribution in metallic glasses with oblique easy axis induced by field annealing. *J. Magn. Magn. Mater.* **1996**, *157–158*, 543–544, doi:10.1016/0304-8853(95)01119-6.
- Squire, P.T.; Atalay, S.; Chiriac, H. ΔE effect in amorphous glass covered wires. *IEEE Trans. Magn.* **2000**, *36*, 3433–3435, doi:10.1109/20.908850.
- Ludwig, A.; Quandt, E. Optimization of the delta-E effect in thin films and multilayers by magnetic field annealing. *IEEE Trans. Magn.* **2002**, *38*, 2829–2831, doi:10.1109/TMAG.2002.802467.
- Dong, C.; Li, M.; Liang, X.; Chen, H.; Zhou, H.; Wang, X.; Gao, Y.; McConney, M.E.; Jones, J.G.; Brown, G.J.; et al. Characterization of magnetomechanical properties in FeGaB thin films. *Appl. Phys. Lett.* **2018**, *113*, 262401, doi:10.1063/1.5065486.
- Yoshizawa, N.; Yamamoto, I.; Shimada, Y. Magnetic field sensing by an electrostrictive/magnetostrictive composite resonator. *IEEE Trans. Magn.* **2005**, *41*, 4359–4361, doi:10.1109/TMAG.2005.855168.
- Nan, T.; Hui, Y.; Rinaldi, M.; Sun, N.X. Self-biased 215 MHz magnetoelectric NEMS resonator for ultra-sensitive DC magnetic field detection. *Sci. Rep.* **2013**, *3*, 1985, doi:10.1038/srep01985.
- Hui, Y.; Nan, T.; Sun, N.X.; Rinaldi, M. High resolution magnetometer based on a high frequency magnetoelectric MEMS-CMOS oscillator. *J. Microelectromech. Syst.* **2015**, *24*, 134–143, doi:10.1109/JMEMS.2014.2322012.
- Li, M.; Matyushov, A.; Dong, C.; Chen, H.; Lin, H.; Nan, T.; Qian, Z.; Rinaldi, M.; Lin, Y.; Sun, N.X. Ultra-sensitive NEMS magnetoelectric sensor for picotesla DC magnetic field detection. *Appl. Phys. Lett.* **2017**, *110*, 143510, doi:10.1063/1.4979694.

23. Osiander, R.; Ecelberger, S.A.; Givens, R.B.; Wickenden, D.K.; Murphy, J.C.; Kistenmacher, T.J. A microelectromechanical-based magnetostrictive magnetometer. *Appl. Phys. Lett.* **1996**, *69*, 2930–2931, doi:10.1063/1.117327.
24. Gojdka, B.; Jahns, R.; Meurisch, K.; Greve, H.; Adelong, R.; Quandt, E.; Knöchel, R.; Faupel, F. Fully integrable magnetic field sensor based on delta-E effect. *Appl. Phys. Lett.* **2011**, *99*, 1–4, doi:10.1063/1.3664135.
25. Kiser, J.; Finkel, P.; Gao, J.; Dolabdjian, C.; Li, J.; Viehland, D. Stress reconfigurable tunable magnetoelectric resonators as magnetic sensors. *Appl. Phys. Lett.* **2013**, *102*, doi:10.1063/1.4789500.
26. Jahns, R.; Zabel, S.; Marauska, S.; Gojdka, B.; Wagner, B.; Knöchel, R.; Adelong, R.; Faupel, F. Microelectromechanical magnetic field sensor based on the delta-E effect. *Appl. Phys. Lett.* **2014**, *105*, 2012–2015, doi:10.1063/1.4891540.
27. Zabel, S.; Kirchhof, C.; Yarar, E.; Meyners, D.; Quandt, E.; Faupel, F. Phase modulated magnetoelectric delta-E effect sensor for sub-nano tesla magnetic fields. *Appl. Phys. Lett.* **2015**, *107*, doi:10.1063/1.4932575.
28. Zabel, S.; Reermann, J.; Fichtner, S.; Kirchhof, C.; Quandt, E.; Wagner, B.; Schmidt, G.; Faupel, F. Multimode delta-E effect magnetic field sensors with adapted electrodes. *Appl. Phys. Lett.* **2016**, *108*, 222401, doi:10.1063/1.4952735.
29. Bian, L.; Wen, Y.; Li, P.; Wu, Y.; Zhang, X.; Li, M. Magnetostrictive stress induced frequency shift in resonator for magnetic field sensor. *Sens. Actuators A Phys.* **2016**, *247*, 453–458, doi:10.1016/j.sna.2016.06.041.
30. Bennett, S.P.; Baldwin, J.W.; Staruch, M.; Matis, B.R.; Lacombe, J.; Van 'T Erve, O.M.J.; Busmann, K.; Metzler, M.; Gottron, N.; Zappone, W.; et al. Magnetic field response of doubly clamped magnetoelectric microelectromechanical AlN-FeCo resonators. *Appl. Phys. Lett.* **2017**, *111*, doi:10.1063/1.5011728.
31. Staruch, M.; Yang, M.-T.; Li, J.F.; Dolabdjian, C.; Viehland, D.; Finkel, P. Frequency reconfigurable phase modulated magnetoelectric sensors using ΔE effect. *Appl. Phys. Lett.* **2017**, *111*, 2–6, doi:10.1063/1.4994663.
32. Bian, L.; Wen, Y.; Wu, Y.; Li, P.; Wu, Z.; Jia, Y.; Zhu, Z. A Resonant Magnetic Field Sensor with High Quality Factor Based on Quartz Crystal Resonator and Magnetostrictive Stress Coupling. *IEEE Trans. Electron Devices* **2018**, *65*, 2585–2591, doi:10.1109/TED.2018.2827382.
33. Lukat, N.; Friedrich, R.M.; Spetzler, B.; Kirchhof, C.; Arndt, C.; Thormählen, L.; Faupel, F.; Selhuber-Unkel, C. Mapping of magnetic nanoparticles and cells using thin film magnetoelectric sensors based on the delta-E effect. *Sens. Actuators A Phys.* **2020**, *309*, 1–8, doi:10.1016/j.sna.2020.112023.
34. Spetzler, B.; Bald, C.; Durdaut, P.; Reermann, J.; Kirchhof, C.; Teplyuk, A.; Meyners, D. Exchange biased delta—E effect enables the detection of low frequency pT magnetic fields with simultaneous localization. *Sci. Rep.* **2021**, *11*, 1–14, doi:10.1038/s41598-021-84415-2.
35. Becker, R.; Döring, W. *Ferromagnetismus*; Springer: Berlin/Heidelberg, Germany, 1939; ISBN 9783642471124.
36. Atalay, S.; Squire, P.T. Magnetomechanical damping in FeSiB amorphous wires. *J. Appl. Phys.* **1993**, *73*, 871–875, doi:10.1063/1.353299.
37. Squire, P. Magnetostrictive materials for sensors and actuators. *Ferroelectrics* **1999**, *228*, 305–319, doi:10.1080/00150199908226144.
38. Charles, F.K. *Development of the Shear Wave; Magnetometer*; University of Bath: Bath, UK, 1992.
39. Kittmann, A.; Durdaut, P.; Zabel, S.; Reermann, J.; Schmalz, J.; Spetzler, B.; Meyners, D.; Sun, N.X.; McCord, J.; Gerken, M.; et al. Wide Band Low Noise Love Wave Magnetic Field Sensor System. *Sci. Rep.* **2018**, *8*, 1–10, doi:10.1038/s41598-017-18441-4.
40. Schmalz, J.; Spetzler, B.; Faupel, F.; Gerken, M. Love Wave Magnetic Field Sensor Modeling—From 1D to 3D Model. In Proceedings of the 2019 International Conference on Electromagnetics in Advanced Applications (ICEAA), Granada, Spain, 9–13 September 2019; pp. 765–769.
41. Schell, V.; Müller, C.; Durdaut, P.; Kittmann, A.; Thormählen, L.; Lofink, F.; Meyners, D.; Höft, M.; McCord, J.; Quandt, E. Magnetic anisotropy controlled FeCoSiB thin films for surface acoustic wave magnetic field sensors. *Appl. Phys. Lett.* **2020**, *116*, doi:10.1063/1.5140562.
42. Schmalz, J.; Kittmann, A.; Durdaut, P.; Spetzler, B.; Faupel, F.; Höft, M.; Quandt, E.; Gerken, M. Multi-mode love-wave SAW magnetic-field sensors. *Sensors* **2020**, *20*, 3421, doi:10.3390/s20123421.
43. Sárközi, Z.; Mackay, K.; Peuzin, J.C. Elastic properties of magnetostrictive thin films using bending and torsion resonances of a bimorph. *J. Appl. Phys.* **2000**, *88*, 5827–5832, doi:10.1063/1.1318388.
44. Staruch, M.; Matis, B.R.; Baldwin, J.W.; Bennett, S.P.; van 't Erve, O.; Lofland, S.; Busmann, K.; Finkel, P. Large non-saturating shift of the torsional resonance in a doubly clamped magnetoelastic resonator. *Appl. Phys. Lett.* **2020**, *116*, 232407, doi:10.1063/5.0010975.
45. Yarar, E.; Hrkac, V.; Zamponi, C.; Piorra, A.; Kienle, L.; Quandt, E. Low temperature aluminum nitride thin films for sensory applications. *AIP Adv.* **2016**, *6*, 075115, doi:10.1063/1.4959895.
46. Durdaut, P.; Höft, M.; Friedt, J.-M.; Rubiola, E. Equivalence of Open-Loop and Closed-Loop Operation of SAW Resonators and Delay Lines. *Sensors* **2019**, *19*, 185, doi:10.3390/s19010185.
47. Spetzler, B.; Kirchhof, C.; Reermann, J.; Durdaut, P.; Höft, M.; Schmidt, G.; Quandt, E.; Faupel, F. Influence of the quality factor on the signal to noise ratio of magnetoelectric sensors based on the delta-E effect. *Appl. Phys. Lett.* **2019**, *114*, 183504, doi:10.1063/1.5096001.
48. Durdaut, P.; Rubiola, E.; Friedt, J.; Müller, C.; Spetzler, B.; Kirchhof, C.; Meyners, D.; Quandt, E.; Faupel, F.; McCord, J.; et al. Fundamental Noise Limits and Sensitivity of Piezoelectrically Driven Magnetoelastic Cantilevers. *J. Microelectromech. Syst.* **2020**, 1–15, doi:10.1109/JMEMS.2020.3014402.
49. Spetzler, B.; Kirchhof, C.; Quandt, E.; McCord, J.; Faupel, F. Magnetic Sensitivity of Bending-Mode Delta-E-Effect Sensors. *Phys. Rev. Appl.* **2019**, *12*, 1, doi:10.1103/PhysRevApplied.12.064036.

50. Kittel, C. On the theory of ferromagnetic resonance absorption. *Phys. Rev.* **1948**, *73*, 155–161, doi:10.1103/PhysRev.73.155.
51. Spetzler, B.; Golubeva, E.V.; Müller, C.; McCord, J.; Faupel, F. Frequency Dependency of the Delta-E Effect and the Sensitivity of Delta-E Effect Magnetic Field Sensors. *Sensors* **2019**, *19*, 1–14, doi:10.3390/s19214769.
52. Gebert, A.; McCord, J.; Schmutz, C.; Quandt, E. Permeability and Magnetic Properties of Ferromagnetic NiFe/FeCoBSi Bilayers for High-Frequency Applications. *IEEE Trans. Magn.* **2007**, *43*, 2624–2626.
53. Avdiaj, S.; Setina, J.; Sylá, N. Modeling of the piezoelectric effect using the finite-element method (FEM). *Mater. Technol.* **2009**, *43*, 283–291.
54. Yang, J. An Introduction to the theory of piezoelectricity. In *Advances in Mechanics and Mathematics*, 2nd ed.; Springer International Publishing: Cham, Switzerland, 2018; Volume 9, ISBN 9783030031367.
55. IEEE Standards Board. IEEE Standard on Magnetostrictive Materials: Piezomagnetic Nomenclature. *IEEE Trans. Sonics Ultrason.* **1973**, *20*, 67–77, doi:10.1109/T-SU.1973.29725.
56. COMSOL AB. *Structural Mechanics Module User's Guide, COMSOL Multiphysics (TM) v. 5.4*; COMSOL AB: Stockholm, Sweden, 2018.
57. Mudivarthi, C.; Datta, S.; Atulasimha, J.; Evans, P.G.; Dapino, M.J.; Flatau, A.B. Anisotropy of constrained magnetostrictive materials. *J. Magn. Magn. Mater.* **2010**, *322*, 3028–3034, doi:10.1016/j.jmmm.2010.05.024.
58. Gutiérrez, J.; Muto, V.; Squire, P.T. Induced anisotropy and magnetoelastic properties in Fe-rich metallic glasses. *J. Non. Cryst. Solids* **2001**, *287*, 417–420, doi:10.1016/S0022-3093(01)00599-3.
59. McCord, J. Progress in magnetic domain observation by advanced magneto-optical microscopy. *J. Phys. D. Appl. Phys.* **2015**, *48*, 333001, doi:10.1088/0022-3727/48/33/333001.
60. Aharoni, A. Demagnetizing factors for rectangular ferromagnetic prisms. *J. Appl. Phys.* **1998**, *83*, 3432–3434, doi:10.1063/1.367113.
61. Varadan, V.K.; Vinoy, K.J.; Gopalakrishnan, S. *Smart Material Systems and MEMS: Design and Development Methodologies*; John Wiley & Sons: Hoboken, NJ, USA, 2007; ISBN 0470093617.
62. Krey, M.; Hähnlein, B.; Tonisch, K.; Krischok, S.; Töpfer, H. Automated parameter extraction of ScALN MEMS devices using an extended euler–bernoulli beam theory. *Sensors* **2020**, *20*, 1001, doi:10.3390/s20041001.
63. Akiyama, M.; Umeda, K.; Honda, A.; Nagase, T. Influence of scandium concentration on power generation figure of merit of scandium aluminum nitride thin films. *Appl. Phys. Lett.* **2013**, *102*, doi:10.1063/1.4788728.
64. Fichtner, S.; Wolff, N.; Krishnamurthy, G.; Petraru, A.; Bohse, S.; Lofink, F.; Chemnitz, S.; Kohlstedt, H.; Kienle, L.; Wagner, B. Identifying and overcoming the interface originating c-axis instability in highly Sc enhanced AlN for piezoelectric micro-electromechanical systems. *J. Appl. Phys.* **2017**, *122*, doi:10.1063/1.4993908.
65. Su, J.; Niekil, F.; Fichtner, S.; Thormaehlen, L.; Kirchhof, C.; Meyners, D.; Quandt, E.; Wagner, B.; Lofink, F. AlScN-based MEMS magnetolectric sensor. *Appl. Phys. Lett.* **2020**, *117*, 132903, doi:10.1063/5.0022636.
66. Sharpe, W.N.; Turner, K.T.; Edwards, R.L. Tensile testing of polysilicon. *Exp. Mech.* **1999**, *39*, 162–170, doi:10.1007/BF02323548.
67. Sharpe, W.N.; Yuan, B.; Vaidyanathan, R.; Edwards, R.L. Measurements of Young's modulus, Poisson's ratio, and tensile strength of polysilicon. *Proc. IEEE Micro Electro Mech. Syst.* **1997**, 424–429, doi:10.1109/memsys.1997.581881.
68. Marc, J. *Madou Fundamentals of Microfabrication: The Science of Miniaturization*, 2nd ed.; CRC Press: Boca Raton, FL, USA, 2002; ISBN 0849308267.
69. Caro, M.A.; Zhang, S.; Riekkinen, T.; Ylilampi, M.; Moram, M.A.; Lopez-Acevedo, O.; Molarius, J.; Laurila, T. Piezoelectric coefficients and spontaneous polarization of ScAlN. *J. Phys. Condens. Matter* **2015**, *27*, 245901, doi:10.1088/0953-8984/27/24/245901.

Chapter 5

Surface Acoustic Wave Magnetometer

5.1 Love Wave Magnetic Field Sensor System

The previous section indicated that the ΔE effect of the C_{66} component can be significantly larger than that of the C_{11} component and it could lead to an improved sensitivity of the ΔE -effect sensors. Exploiting this effect with torsion-mode resonators is possible; however, it is not necessarily advantageous over the bending modes for two major reasons: (1) The contributions of other stiffness tensor components can reduce the frequency change in the torsion modes. (2) Exciting torsion modes in cantilever sensors efficiently is challenging, because of the required asymmetry in the excitation around the torsional axis.

An alternative method for utilizing the ΔE effect of the C_{66} component is explored in this section. A sensor system based on surface acoustic shear waves is developed and analyzed for magnetoelastic properties, sensitivity, signal, and noise. In contrast to the torsion modes in cantilever structures, shear stress dominates the magnetoelastic waves. Further the SAW device constitutes an exception in this thesis because it is not based on a released resonator structure. After this publication, a new project was initiated for the further development of these sensors. Two follow-up publications on the modeling and higher modes of Love-wave SAW sensors have been presented in Appendix B.

Contribution

The authorship is shared equally with Anne Kittmann, Phillip Durdaut, Sebastian Zabel, Jens Reerman, and Julius Schmalz.

- Conceptualization (shared)
- Writing of original manuscript (shared)
- Modeling and simulations (shared)
- Data analysis and interpretation (shared)

SCIENTIFIC REPORTS

OPEN

Wide Band Low Noise Love Wave Magnetic Field Sensor System

Anne Kittmann¹, Phillip Durdaut¹, Sebastian Zabel¹, Jens Reermann², Julius Schmalz², Benjamin Spetzler¹, Dirk Meyners¹, Nian X. Sun³, Jeffrey McCord¹, Martina Gerken², Gerhard Schmidt², Michael Höft², Reinhard Knöchel², Franz Faupel¹ & Eckhard Quandt¹

Received: 29 August 2017

Accepted: 11 December 2017

Published online: 10 January 2018

We present a comprehensive study of a magnetic sensor system that benefits from a new technique to substantially increase the magnetoelastic coupling of surface acoustic waves (SAW). The device uses shear horizontal acoustic surface waves that are guided by a fused silica layer with an amorphous magnetostrictive FeCoSiB thin film on top. The velocity of these so-called Love waves follows the magnetoelastically-induced changes of the shear modulus according to the magnetic field present. The SAW sensor is operated in a delay line configuration at approximately 150 MHz and translates the magnetic field to a time delay and a related phase shift. The fundamentals of this sensor concept are motivated by magnetic and mechanical simulations. They are experimentally verified using customized low-noise readout electronics. With an extremely low magnetic noise level of ≈ 100 pT/ $\sqrt{\text{Hz}}$, a bandwidth of 50 kHz and a dynamic range of 120 dB, this magnetic field sensor system shows outstanding characteristics. A range of additional measures to further increase the sensitivity are investigated with simulations.

Magnetic field sensing is an important task for many applications ranging, e.g., from positioning and navigation to electronic stability programs, electrical current sensors to biomagnetic field detection^{1–3}. Naturally, the requirements differ and depend on the specific application. Common demands on sensors include ambient temperature operation without cooling, small dimensions necessary for high spatial resolution and/or limited available installation space as well as low energy consumption. Very demanding specifications arise in terms of the dynamic magnetic field range and the frequency bandwidth in case of a current sensor⁴ as well as in a limit of detection (LOD) in the pT/ $\sqrt{\text{Hz}}$ to fT/ $\sqrt{\text{Hz}}$ range in case of sensors for biomagnetic signals⁵. Furthermore, both applications require the detection of DC or very low frequency magnetic fields, which is especially challenging if $1/f$ (f : frequency) noise is present. Ultra-low LODs for magnetic field sensing in combination with ambient temperature operation and sufficient spatial resolution have been reported for orthogonal fluxgate magnetometers⁶, sensors employing the giant magnetoimpedance effect⁷, atomic magnetometers⁸, magneto-resistive devices⁹, and, most recently, for sensors using the ΔE -effect¹⁰. Table 1 summarizes the main important properties of these sensors.

Magnetoelastic coupling describes the property of materials to have an interdependency between magnetization and elastic strain. It is commonly known in the form of so-called Joule magnetostriction that causes the humming noise in electrical transformer cores, where the core length changes during the magnetization. In an inverse process (also known as Villari Effect) under mechanical stress, these materials exhibit an additional strain caused by a rotation of the magnetic moments. Such extra strain leads to altered elastic properties proportional to the material's piezomagnetic coefficient. For high piezomagnetic coefficients, softmagnetic properties in combination with a high magnetostriction are required: thus, the largest piezomagnetic coefficients have been found in amorphous FeGaB¹² or FeCoSiB¹³ thin films. The phenomenon is commonly known as the ΔE -effect for changes in the Young's modulus E ^{14–16}, but other elastic constants are also affected. Although it is well known that the relative effects of other elastic moduli such as the shear modulus G are generally more pronounced¹⁷, most approaches for magnetic sensing have been made using E . The ΔE -effect has been used to detune either cantilever^{18–20} or bulk resonators²¹ coated with a magnetic material. Also, surface acoustic waves (SAWs) have been utilized in resonator or delay line configurations²². These approaches use a piezoelectric substrate with two interdigital transducer (IDT) electrodes, one to excite and one to receive acoustic waves. If a magnetic film is deposited in-between these

¹Institute for Materials Science, Kiel University, Kiel, 24143, Germany. ²Institute of Electrical Engineering and Information Technology, Kiel University, Kiel, 24143, Germany. ³W.M. Keck Laboratory for Integrated Ferroics, Electrical and Computer Engineering Department, Northeastern University, Boston, Massachusetts, 02115, USA. Anne Kittmann, Phillip Durdaut, Sebastian Zabel, Jens Reermann, Julius Schmalz and Benjamin Spetzler contributed equally to this work. Correspondence and requests for materials should be addressed to E.Q. (email: eq@tf.uni-kiel.de)

	Microwire fluxgate	Giant magnetoimpedance	Atomic magnetometer	Anisotropic magnetoresistive	Resonant ΔE -effect
LOD at 1 Hz	1.5 pT/ $\sqrt{\text{Hz}}$ ⁶	3 pT/ $\sqrt{\text{Hz}}$ ⁷	10 fT/ $\sqrt{\text{Hz}}$ ⁸	1 nT/ $\sqrt{\text{Hz}}$ ⁹	300 pT/ $\sqrt{\text{Hz}}$ ¹⁰
Frequency Bandwidth	400 Hz ⁶	70 kHz ¹¹	100 Hz ⁸	1 MHz ⁹	5 Hz ¹⁰
Range	1000 nT ⁶	$\pm 100 \mu\text{T}$ ¹¹	15 nT ⁸	$\pm 0.5 \text{ mT}$ ⁹	$> 1 \mu\text{T}$ ¹⁰

Table 1. Overview of compact high resolution magnetometers that operate at ambient temperature. A range above 50 μT enables unshielded operation. Biomagnetic applications require a detection limit below at least 10 pT/ $\sqrt{\text{Hz}}$.

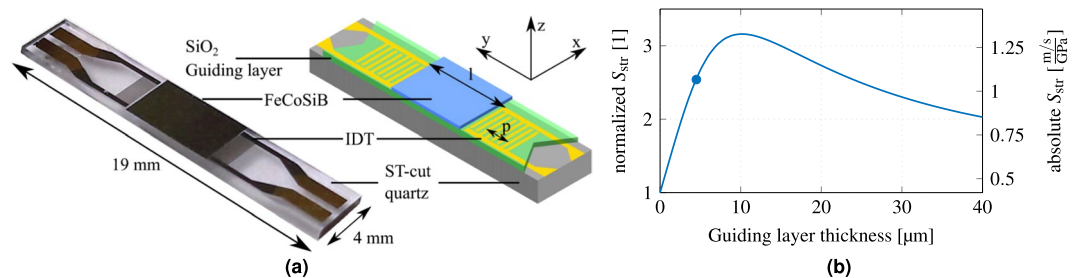


Figure 1. Sensor design and modeled structural sensitivity. (a) A Love wave surface acoustic wave sensor based on ST-cut quartz substrate and a $4.5 \mu\text{m}$ SiO_2 guiding layer. The 200 nm magnetostrictive material FeCoSiB is deposited between the transducers on top of the delay line with a length l of 3.8 mm. The interdigital transducers have a periodicity p of $28 \mu\text{m}$. (b) Simulation of structural sensitivity S_{str} for different guiding layer thicknesses and a 200 nm thick magnetostrictive layer. The sensitivity of the fabricated device (indicated by blue dot) is close to the maximum sensitivity at $10 \mu\text{m}$.

two IDT electrodes, changes in the elastic properties of the film influence the wave velocity and alter the delay of a transmitted signal.

There are various kinds of waves that can be excited, and they differ in the type of deformation and velocity due to the different elastic moduli involved. Rayleigh waves are concentrated at the surface with out-of-plane shear and longitudinal deformation. Their amplitude exponentially decays with a penetration depth of about one wavelength. In amorphous magnetic thin films greater than 50 nm thick, the magnetization is usually confined in-plane, which restricts all changes of elastic components to this plane. Consequently, the propagation of Rayleigh waves is only magnetically sensitive to magnetoelastic alterations of E . Shear horizontal waves perform a bulk shear motion parallel to the magnetic film and are thus sensitive to changes of G . While the wave extends through the whole substrate, the modulus effect occurs only in the magnetic layer on the top and, consequently, has little leverage on the wave velocity. Love waves, in contrast, combine the advantages of both wave types with respect to magnetic field sensing. They are horizontal shear waves that are confined at the surface by a phase velocity gradient towards the surface²³. Despite these advantages, most studies focus on Rayleigh waves^{24,25}, few on shear horizontal waves²⁶ and even fewer on Love waves²⁷. Although numerous devices with strong coupling of surface waves to magnetic properties have been presented, many were intended to be used as magnetically tunable RF-components²², and only a few have been thoroughly analyzed for their potential as magnetic field sensors.

In this paper, the design of a novel Love wave-type magnetic field SAW sensor will be outlined with an emphasis on finite element modeling (FEM) simulations to work out the advantages of using a dedicated guiding layer. Next, the SAW sensor will be characterized electrically and the magnetic properties of the magnetostrictive layer will be investigated and compared with simulations. Then, the sensor will be integrated in a readout circuit, which is tailored to obtain a sensor system, where the intrinsic noise of the sensor dominates. Very promising characteristics of the sensor system in terms of sensitivity, LOD, dynamic range, and bandwidth will be measured and analyzed. Prospects of different measures to further increase the sensitivity and the LOD will be proposed thereafter.

Sensor Design

The presented Love wave sensor is based on a $500 \mu\text{m}$ ST-cut quartz substrate and is shown in Fig. 1a. The two IDT electrode pairs form a delay line of $l = 3.8 \text{ mm}$. They are made of 300 nm Au and structured by ion-beam etching to a doublefinger structure of 25 pairs with a periodicity of $28 \mu\text{m}$ and a finger width of $3.5 \mu\text{m}$. A 12 nm Cr layer above and below the Au serves as an adhesion promoter. The propagation direction of the wave is orthogonal to the X-axis of the ST-cut quartz wafer. In this configuration only shear waves are excited²³. A layer of $4.5 \mu\text{m}$ thick SiO_2 is deposited with a PECVD process and covers the IDTs and the delay line, and is angled at both ends to prevent multiple transient signals. The structure acts as a guiding layer and leads to a concentration of the wave energy in the magnetic material. The magnetostrictive material $(\text{Fe}_{90}\text{Co}_{10})_{78}\text{Si}_{12}\text{B}_{10}$ is deposited with a thickness of 200 nm by magnetron sputtering on the delay line and structured using a lift-off process. During deposition a magnetic field is applied along the Y-axis to saturate the film and introduce an easy axis of magnetization. Below and above the magnetic layer a 10 nm Ta layer is deposited to promote adhesion and prevent oxidation.

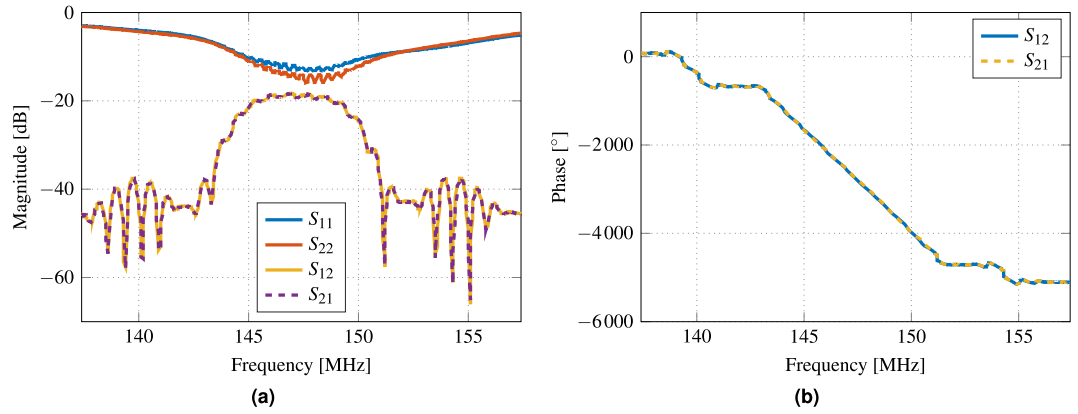


Figure 2. Scattering parameters of the SAW device measured with a vector network analyzer at $B_{\text{bias}} = 0$ T. (a) The passband of the SAW device around the center frequency of 147.2 MHz offers a 3 dB bandwidth of 4.4 MHz, where the insertion loss is approximately -20 dB. (b) The phase decreases virtually linear with a slope of -460 °/MHz.

The overall sensitivity S of the sensor is the product of several major contributions that are introduced here and discussed in detail in the following sections. The sensitivity of the magnetic material

$$S_{\text{mag}} = \frac{\partial G}{\partial H} \quad (1)$$

corresponds to the change in the shear modulus G in the presence of an external magnetic field H . S_{mag} depends on the magnetostrictive properties of the material, the orientation of the magnetic easy axis, the directions of the wave propagation, and external magnetic field, respectively. How much the change in shear modulus affects the velocity v of the surface wave is expressed by a structural sensitivity

$$S_{\text{str}} = \frac{\partial v}{\partial G}. \quad (2)$$

S_{str} is influenced by the vertical structure of the device that influences the confinement of the wave as well as the contribution of each layer. According to the FEM-simulation results shown in Fig. 1b an even higher factor of 3.16 could be achieved by choosing an 10 μm thick guiding layer, but was not carried out because of process limitations. The chosen thickness of 4.5 μm still increases the structural sensitivity S_{str} by a factor of 2.54 to 1.07 $\frac{\text{m/s}}{\text{GPa}}$.

The phase shift per change in wave velocity depends on the geometric sensitivity S_{geo}

$$S_{\text{geo}} = \frac{\partial \varphi}{\partial v} = -\frac{l}{v^2} \cdot f \cdot 2\pi \quad (3)$$

of the device. A change in wave velocity v at the frequency f leads to a change of the phase $\varphi = \frac{l}{v} \cdot f \cdot 2\pi$ at the end of the delay line with a length l . The results of the simulations are a geometric sensitivity of $S_{\text{geo}} = -11.3 \frac{\text{s}}{\text{m}}$. In combination, these three contributions lead to the overall sensitivity

$$S = \frac{\partial \varphi}{\partial H} = \frac{\partial G}{\partial H} \cdot \frac{\partial v}{\partial G} \cdot \frac{\partial \varphi}{\partial v} = S_{\text{mag}} \cdot S_{\text{str}} \cdot S_{\text{geo}}. \quad (4)$$

Electrical Properties

Figure 2 shows the measured scattering parameters of the fabricated Love wave SAW sensor, which were determined with a vector network analyzer at zero bias flux density $B_{\text{bias}} = 0$ T.

Prior to the measurements, the electrical impedance of each port was matched to the system's impedance of 50 Ω . Hence, the return loss was reduced, slightly different for each port due to component tolerances, between -13 dB and -15 dB in the passband around the center frequency of 147.2 MHz. However, in the same frequency band an insertion loss of about -20 dB was obtained, which is typical for Love wave delay line sensors^{28,29}. The total phase angle decreases virtually linear over a frequency range of 7.6 MHz between 143.4 MHz and 151 MHz with a slope of $\partial \varphi / \partial f = -460$ °/MHz corresponding to a time delay of $\tau_{\text{SAW}} = 1 / (2\pi) \cdot \partial \varphi / \partial f = 1.28$ μs . Due to its insertion loss, the SAW device is only usable as a sensor within the 3 dB bandwidth from 145 MHz to 149.4 MHz since the signal-to-noise ratio (SNR) decreases with increasing attenuation³⁰.

Magnetic Properties

The origin of the magnetic field-induced phase shift can be directly attributed to the change of effective stiffness constants of the ferromagnetic film. The effective stiffness constants are functions of magnetization, and therefore depend on the direction and amplitude of the external magnetic field H and the magnetic easy axis (EA)

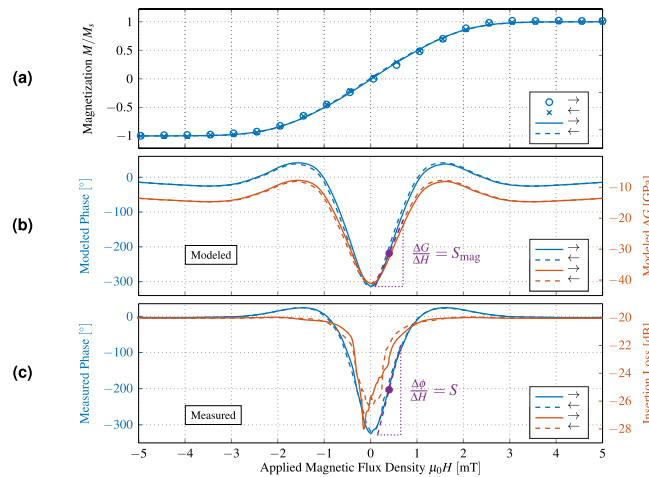


Figure 3. Characterization and modeling of the SAW device. **(a)** Measured magnetization curve of the SAW device using MOKE magnetometry (dot and cross symbols) together with the modeled magnetization curve (solid and dashed lines). **(b)** Modeled ΔG with a minimum of -30 GPa at 0 mT. This corresponds to 55% change relative to the value at fixed magnetisation G_m . With these data, the change of phase is calculated using the mechanical model. **(c)** Measured phase shift of the SAW device per magnetic field and corresponding insertion loss at the center frequency of 147.2 MHz. All arrows in the legends represent the direction of the magnetization process starting from a magnetically saturated state.

orientation. In the following, a magnetomechanical mean field model is used to quantify the magnetic properties of the ferromagnetic film and derive consequences for sensor optimization later on.

The magnetic mean field model is based on an ensemble of simple uncoupled Stoner-Wohlfarth particles. For each particle, the static equilibrium magnetization M_0 is obtained by minimizing the internal energy density. A distribution of the effective anisotropy energy density K_{eff} and of the easy axis orientation γ_i is used to approximate the magnetization distribution. A standard distribution for K_{eff} with standard deviation δ and a van Mises distribution with dispersion parameter κ for the dispersion of the effective easy axis is assumed. Hence, an ideal magnetic film is described by a small δ and a large κ . Distributions may arise from local stray fields, local stresses, or an intrinsic distribution of the easy axis, e.g., from the deposition process. For the simulation of magnetic hysteresis curves, the magnetization of all particles is averaged. Following the approach by Mater³¹, the magnetoelastic wave results in a small dynamic perturbation, which justifies an expansion of the enthalpy density around the static equilibrium. The effective stiffness tensor C can be described by a constant, magnetization-independent part C_m and a superposed magnetization-dependent part ΔC . The stiffness correction tensor ΔC is then obtained from the derivatives of the enthalpy density with respect to the magnetization orientation. These derivatives depend on M_0 and are obtained from the magnetic mean field model. For our specific axis configuration, this approach reduces to the Zhou model as described previously²⁶. Because M_0 is a function of space, the effective stiffness is also considered as a local property and underlies a spatial distribution. As input for the mechanical model, these values are averaged.

To obtain the structural sensitivity S_{str} from the derived magnetic-field-dependent shear modulus, the concentration effect of the wave at the surface due to the changed shear modulus has to be considered. Hence, an FEM model is used to calculate the wave properties. The propagation region depicted in the schematic of Fig. 1a consists of a horizontally layered stack of a quartz substrate, a SiO_2 guiding layer, and a magnetostrictive layer. Assuming isotropic material parameters, the structure may be approximated by only considering the z dependence. The solution to the one-dimensional problem is given by the following differential equation for the displacement $U(k, z, \omega)$ ³²

$$\frac{d}{dz} \left[G(z) \frac{dU}{dz} \right] = [k^2 G(z) - \omega^2 \rho(z)] U(k, z, \omega) \quad (5)$$

with the shear modulus G , the wave vector k , and the density ρ . The anisotropic parameters of the ST-cut quartz substrate and the magnetostrictive layer are reduced to isotropic values for this simulation. The neglected stress components are lower by at least a factor of 10 than the considered component. Therefore, the error made by this simplification does not influence the general behavior as shown by the small deviation between measurement and simulation in Fig. 3. Eq. (5) is solved numerically with the FEM software package Comsol Multiphysics. To obtain the structural sensitivity S_{str} at the operating point, the first derivative of the simulated wave velocity v is calculated at the maximum of the sensitivity S_{mag} of the material. The model results are shown in Fig. 1b for a variation of the guiding layer thickness.

Hard axis magnetization curves of the complete ferromagnetic film were recorded using large-view magneto-optical Kerr effect (MOKE) microscopy³³. The measured data are shown in Fig. 3a as dot and cross symbols. The magnetic model was fitted to the MOKE data to extract the magnetic material parameter (solid and dashed lines). For the fit, an effective distribution of the easy axis of magnetization of $\kappa = 5500$ is used. With

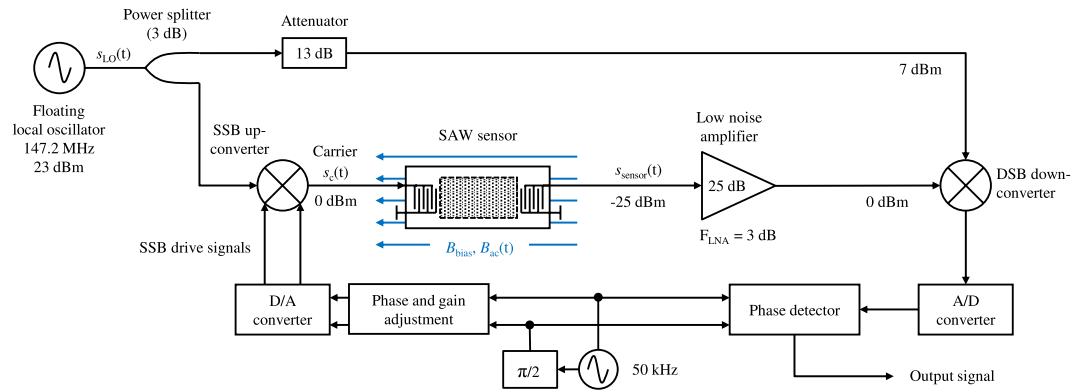


Figure 4. Readout circuit with inherent phase noise suppression. A low phase noise signal of a numerically controlled oscillator (NCO) at 50 kHz is transposed to the operating frequency range of the SAW device and received using a floating local oscillator, which eliminates the phase noise of the local oscillator. To avoid distortions due to an undesired sideband, a signal sideband upconverter is used. Phase detection is achieved in the digital domain after analog-to-digital conversion.

$\delta = 300 \text{ J/m}^3$ a broad effective anisotropy distribution is described around a mean value of $K_{\text{eff}} = 1.3 \text{ kJ/m}^3$. As a result, a magnetoelastic coupling factor of $b^{\gamma,2} = -12.7 \text{ MPa}$ is obtained, corresponding to a positive saturation magnetostriction. This value is slightly larger compared to previously reported results for FeCoSiB thin films¹³.

In Fig. 3b the resulting function of ΔG is shown. It resembles a V-shaped curve, which is consistent with the results of other authors but exceeds the maximum absolute change of G by a factor of about two²⁶. Note that $\Delta G < 0 \text{ MPa}$ for all values of the magnetic field, as a direct consequence of the averaging procedure. From ΔG the maximum slope at a magnetic bias field of $\mu_0 H = 0.4 \text{ mT}$ is directly obtained, resulting in a magnetic sensitivity of $S_{\text{mag}} = 36.8 \text{ GPa/mT}$.

From the variation of shear modulus, the phase is calculated as a function of H using the mechanical model. For Love waves, the dominant component of C is expected to be the shear modulus G . Consequently, the functions of the modeled phase and shear modulus are of similar overall appearance, as shown in the figure. In Fig. 3c the measured phase shift of the SAW is plotted together with the insertion loss. This loss can be attributed to periodic changes of the magnetization by magnetoelastic coupling to the surface wave. The magnetization changes lead to the formation of eddy currents that dissipate the energy by Joule heating. An identical maximum phase shift of 340° is obtained and a similar general behavior for measurement and simulation is confirmed. From the slope of the measured phase we obtain a maximum sensitivity of $S = 504^\circ/\text{mT}$, which is in agreement with S as calculated from the modeled data with an accuracy about 10%. Deviations are expected to arise from local stress anisotropies or stray fields that result in slightly different distribution functions.

Sensor System

The electronic readout circuit is depicted in Fig. 4. A sinusoidal carrier signal $s_c(t)$ is injected into the sensor with a frequency f_c within the SAW device's passband. Through the magnetic field-dependent travelling time and, thus, the phase shift of the carrier, the magnetic flux density $B_{\text{ac}}(t)$ can be measured. The sensor's output signal is given by

$$s_{\text{sensor}}(t) \propto \cos(2\pi f_c t + S \cdot B_{\text{ac}}(t) \cdot \mu_0^{-1} + \phi_c(t) + \phi_{\text{SAW}}(t)), \quad (6)$$

where S is the sensitivity defined in Eq. (4). The measurement results in $S = 264^\circ/\text{mT}$ which is about a factor of two smaller than what was derived from Fig. 3c. However, the deviation is within the variation between the various tested samples. The measurement is impaired by the phase noise $\phi_c(t)$ of the carrier signal and by random phase fluctuations of the SAW device $\phi_{\text{SAW}}(t)$. To minimize the phase noise contribution of the sensor electronics, the carrier $s_c(t)$ is derived from the output of a numerically controlled oscillator (NCO) at 50 kHz (phase noise at -128 dBc/Hz at an offset frequency of 10 Hz, cf. Figure 5b), which is upconverted to the SAW device's passband by means of a single sideband (SSB) upconverter and a local oscillator $s_{\text{LO}}(t)$. The single sideband upconverter suppresses an undesired sideband which would fall into the passband of the SAW device. Otherwise the phase measurement after the downconversion process would be distorted. Sufficient sideband suppression is achieved by adjustment of amplitude and phase of the SSB drive signals in the digital domain. The sensor output signal $s_{\text{sensor}}(t)$ is amplified and downconverted to the original frequency of 50 kHz by means of a double sideband mixer (DSB) using the same local oscillator $s_{\text{LO}}(t)$. Thus, the phase noise $\phi_c(t)$ of the carrier is largely suppressed. The degree of suppression depends on the delay time of the SAW device τ_{SAW} ³⁴. For the Love wave SAW sensor with typical delay times between $1 \mu\text{s}$ and $2 \mu\text{s}$ presented here, LO phase noise is reduced by approximately 80 dB for an offset frequency of 10 Hz and by approximately 60 dB for an offset frequency of 100 Hz, respectively³⁵. The local oscillator utilized here has a phase noise of -80 dBc/Hz and -95 dBc/Hz , respectively, and is therefore — after downconversion — well below the phase noise of the low-frequency 50 kHz signal. Final phase detection is carried out digitally. The bidirectional conversion between the analog and the digital domain is performed by high resolution 24-bit converters at a sample rate of 192 kHz.

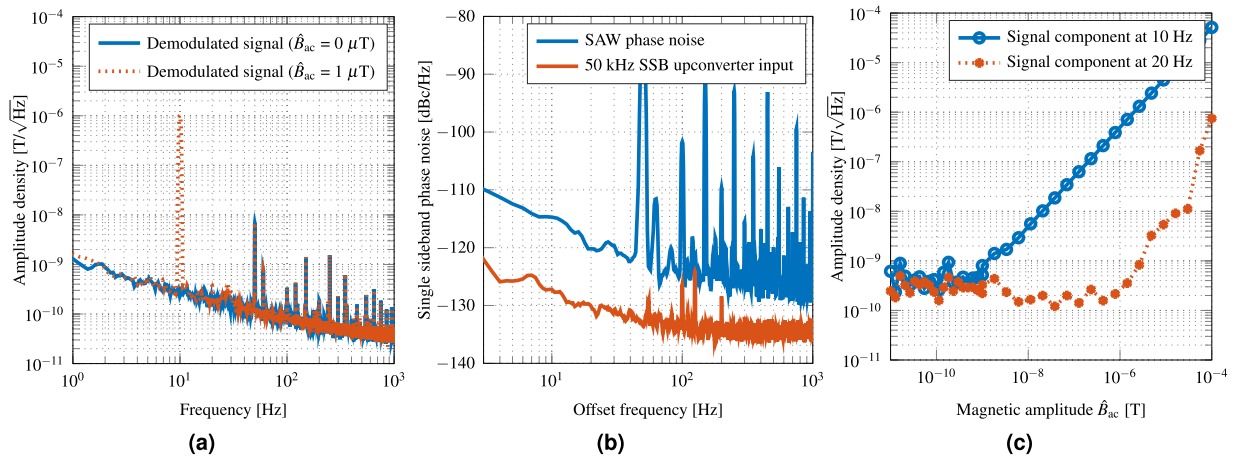


Figure 5. SAW device noise and linearity characteristics. **(a)** Equivalent magnetic noise floor of the demodulated output signal shows the frequency dependent LOD. At 10 Hz an equivalent magnetic noise of 250 pT/√Hz and at 100 Hz a value of 80 pT/√Hz are achieved. The LOD is degraded by $1/f$ noise at low frequencies. **(b)** The measured single sideband phase noise of the 50 kHz SSB upconverter input signal reveals a 10 dB lower phase noise value at 10 Hz than the contribution of the SAW sensor itself. **(c)** The response of the phase demodulated sensor signal increases linearly over a large range of magnetic amplitudes \hat{B}_{ac} . The linearity (at f_{ac}) as well as the nonlinearity represented by the first harmonic (at $2f_{ac}$) is plotted. From amplitudes of 100 μT to approximately 250 pT, a linear response is measured. The interception point of the linearity line and the progression of the first harmonic is not reached for magnetic amplitudes $\hat{B}_{ac} < 100 \mu\text{T}$.

Due to the chosen operating frequency of 50 kHz, the bandwidth of the sensor system is limited to this frequency. In general, the SAW bandwidth permits a system bandwidth up to 2 MHz by using a higher operating frequency. However, other limiting factors can appear. A trade-off between the system noise due to the NCO and the bandwidth must be found for the chosen application.

In Fig. 5a the equivalent magnetic noise floor achieved with the sensor system is shown. It was measured inside a magnetically and mechanically shielded chamber³⁶. At 10 Hz and 100 Hz equivalent magnetic noise levels of 250 pT/√Hz and 80 pT/√Hz, are achieved, respectively. These values are well within the 100 pT/√Hz range of thin-film ΔE -effect sensors²⁰, but the bandwidth is far higher.

Obviously, the measured equivalent magnetic noise density in Fig. 5a is degraded by $1/f$ noise in the low-frequency regime. This contribution originates from the SAW sensor itself, which is a common phenomenon^{37–39}. However, the origin of this noise contribution is presently not well understood³⁹. With the same method as proposed by Baer³⁹ the phase noise of the SAW sensor presented here was measured for $B_{bias} = 0\text{ T}$ after the measurement setup was carefully calibrated⁴⁰. The result is shown in Fig. 5b. Power line spurs and subharmonics can be seen and must be disregarded when analyzing the data. The measurement reveals a single sideband phase noise level of $-115\text{ dBc}/\sqrt{\text{Hz}}$ for an offset frequency of 10 Hz. The value is 10 dB⁴⁰ to 20 dB³⁸ higher than phase noise densities previously reported in the literature. However, these values are not directly comparable due to different structures, delay times, and operating frequencies of the various SAW devices. Further investigation with respect to the phase noise properties of Love wave SAW sensors is required. A lower phase noise would directly result in an improved LOD.

In many applications the dynamic field range is of extreme importance. Biomagnetic measurements without magnetic shielding, which is, e.g., mandatory for any long-term monitoring, would require differential measurements to extract the biomagnetic signals from the million-times higher noise background. Thus, a dynamic range of at least 120 dB is required for these measurements. In the case of current sensors, such as for electro-mobility applications, there is again the need to measure both very small leakage currents and very high currents under full load using the same sensor. Figure 5c shows the linear response of the phase demodulated signal of the Love wave SAW sensor. Across a range of 120 dB (approximately from 100 pT to 100 μT) linear behaviour is achieved. The intercept point of the linear response at $f_{ac} = 10\text{ Hz}$ and the nonlinear response, measured by the first harmonic response at $2f_{ac} = 20\text{ Hz}$, is not reached for magnetic amplitudes $\hat{B}_{ac} < 100 \mu\text{T}$. Hence, the sensor is suitable for unshielded measurements since it would not be saturated by earth's magnetic field.

Sensitivity Improvement

To improve the sensitivity of the Love wave magnetic field sensor described here, various strategies can be followed. Because the readout electronics are not the dominating noise of the sensor system, the sensitivity of the sensor has to be increased or its intrinsic noise level has to be lowered to achieve a higher SNR. A first approach in order to increase the sensitivity is to improve the structural sensitivity S_{str} , which could be achieved either with a thicker magnetic layer, a thicker guiding layer, or a shorter wavelength. According to Fig. 6a the sensitivity can be increased significantly for a magnetostrictive layer thickness of 400 nm by a factor of 3 to 20 by reducing the wavelength to 20 μm or 10 μm, respectively. A second measure to improve the structural sensitivity would be thicker

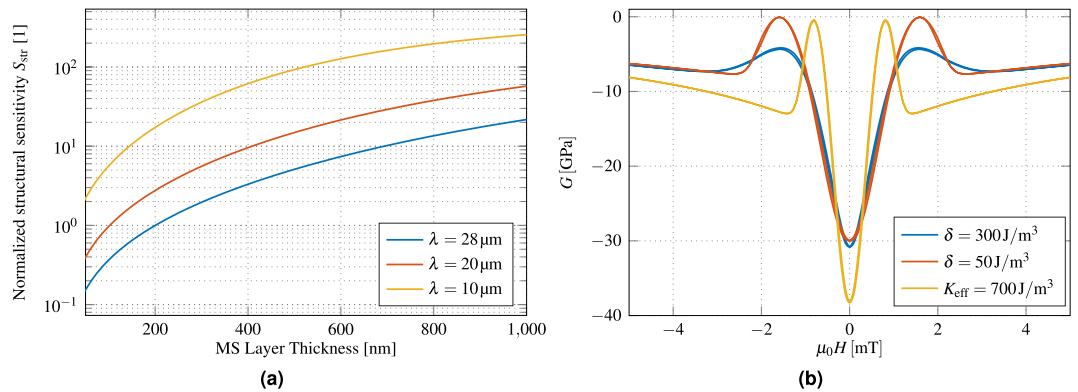


Figure 6. Modeling of potential sensitivity improvements. **(a)** Normalized structural sensitivity S_{sr} for different magnetostrictive (MS) layer thicknesses and different periodicities of the IDTs. For thicker MS layers as well as for lower wavelengths the sensitivity is improved. **(b)** Calculated change of shear modulus ΔG for our sensor ($\delta = 300 \text{ J/m}^3$), a strongly reduced anisotropy dispersion ($\delta = 50 \text{ J/m}^3$), and a reduced anisotropy dispersion with additionally reduced mean anisotropy energy density ($K_{eff} = 700 \text{ J/m}^3$).

magnetostrictive layers, although this might have conflicting influence on the magnetic properties of the film. A reduction of the wavelength by a factor of 2.8 would also multiply the geometric sensitivity by the same factor. However, all these measures might potentially increase the insertion loss of the sensor. A compromise between delay time and insertion loss has to be made. The insertion loss could potentially be reduced by structuring the magnetic film with isolating layers to reduce eddy currents²⁷.

A third approach is to optimize the magnetic properties of the magnetostrictive layer to increase the magnetic sensitivity S_{mag} , especially the key parameters of the mean anisotropy energy density K_{eff} and the effective anisotropy distribution δ . In Fig. 6b the calculated change ΔG of shear modulus is plotted for the current sensor parameters ($\delta = 300 \text{ J/m}^3$), a strongly reduced anisotropy distribution ($\delta = 50 \text{ J/m}^3$) and an additionally reduced mean anisotropy energy density ($K_{eff} = 700 \text{ J/m}^3$). From the first two datasets of Fig. 6b, the influence of δ is evident. A reduced dispersion of K_{eff} results in an increase of the two maxima to $\Delta G \approx 0$ GPa. Additionally, decreasing δ reduces the curvature at about 2.5 mT, which becomes a discontinuity for zero δ . Interestingly, the region around 0 mT between the two maxima is barely influenced by the distribution. The magnetic working point for the sensor is set, where the model predicts identical maximum magnetic sensitivities for both distributions. Because smaller K_{eff} are prone to static stresses and local stray fields, they are expected to be accompanied by larger δ . Hence, the current configuration is advantageous if small mean anisotropy energy densities can be achieved. As an example, the third dataset ($K_{eff} = 700 \text{ J/m}^3$) shows the change of shear modulus with respect to magnetic field for K_{eff} additionally reduced by a factor of about two, which yields a corresponding increase in sensitivity. If K_{eff} cannot be reduced, the easy axis can be tilted by 90 degrees relative to the propagation direction of the wave. In this configuration we expect to approach a singularity instead of a discontinuity for vanishing δ ¹⁷. As a result, the sensitivity is dominated by δ instead of K_{eff} . Initial estimations yield to an improvement of the magnetic sensitivity S_{mag} by a factor between 2 and 7, depending on δ . Consequently, future sensor designs must make a compromise between small K_{eff} and small δ depending on the axis configuration of the magnetic film. Such arguments are similarly valid for an angular distribution of the easy axis. To allow bias field-free operation, the magnetic layer could be biased using exchange coupled multilayers, as has been demonstrated for other magnetostrictive sensors⁴¹.

A fourth method to increase the SNR could be the allocation of several carrier signals within the transmission bandwidth of the sensor, provided that the respective noise signal are uncorrelated. The sensor offers enough bandwidth for approximately 50 carriers, spaced 100 kHz apart. The signals of these carriers could be processed separately and, thus, the noise should be reduced by $\sqrt{50} \approx 7$ according to Reermann *et al.*⁴². Thermal cross sensitivity could be reduced with an uncoated delay line as a reference sensor to improve DC stability. A significant improvement by two orders of magnitude of the overall sensitivity might be achieved by combination of the proposed measures. Nevertheless, a higher sensitivity only increases the signal strength and the goal is always to improve the signal to noise ratio. It is possible, that trade offs will have to be made to respond to potential increase of noise.

Conclusion

Love wave SAW delay lines present an effective means to utilize the magnetoelastic effect in thin films for magnetic field sensing. A comprehensive study of the complete sensor system is presented, including measurements and simulations of the electrical, mechanical, and magnetic properties. With a detection limit of $\approx 100 \text{ pT}/\sqrt{\text{Hz}}$ over a large bandwidth of 50 kHz and a dynamic range larger than 120 dB, the sensor system is a promising addition to existing sensor concepts. Additionally, there is the potential to greatly increase the bandwidth up to the MHz-range. Significant improvements of sensitivity can also be expected by further perusing the Love wave concept of wave confinement with thicker and magnetically softer layers, or higher SAW frequencies.

Methods

Sensor fabrication. The Love wave sensors are based on 500 μm ST-cut quartz wafers ($42^\circ 45'$ Y-cut) for SAW applications. All layers, except the SiO_2 guiding layer, are deposited by magnetron sputtering using a von Ardenne CS730 S sputtering system. Cr and Au are deposited by DC sputtering. The magnetostrictive layer is deposited by RF sputtering with a target composition of $(\text{Fe}_{90}\text{Co}_{10})_{78}\text{Si}_{12}\text{B}_{10}$ while applying a magnetic field of 100 Oe. Lift-off of the magnetostrictive layer is performed with the negative photoresist AZ nLof 2070 from MicroChemicals. For ion-beam etching of the IDT structures, the positive photoresist AZ 1518 also from MicroChemicals is used. The SiO_2 layer is deposited by a PECVD process with a SENTECH SI 500 PPD tool and afterwards structured by an ICP-RIE etching process.

Magnetic measurements. The magnetic measurements of Fig. 3 are performed at a temperature of 21°C in the center of a pair of 10 cm Helmholtz coils. The magnetically induced phase shift is averaged from 25 measurements between 148 and 149 MHz with a lock-in amplifier (Zurich Instruments UHFLI) to compensate for small non-linearities in the device relation of phase and frequency. The non-linearities are attributed to electrical feedthrough and also cause the fine ripple in the scattering parameters.

Model and Material Properties. With regards to the magnetic model, the internal energy density h is minimized for each Stoner-Wohlfarth particle. It can be described using Einstein notation by^{15,43}

$$h = K_{\text{eff}} \sin^2[\arccos(\alpha_i' \gamma_i')] - \mu_0 H M_s \alpha_i' \beta_i' \quad (7)$$

Here α_i', β_i' and γ_i' denote the direction cosines of the equilibrium magnetization, the applied magnetic field with amplitude H , and the easy axis orientation vector with respect to the coordinate axes. K_{eff} is the effective anisotropy energy density constant of first order. All clamping effects and initial stress contributions are taken into account by K_{eff} . For the saturation magnetization M_s , we used $\mu_0 M_s = 1.5 \text{ T}^{44}$. Furthermore, we assume in-plane magnetization. The magnetoelastic coupling coefficient $b^{\gamma,2}$ is defined according to Callen and Callen⁴⁵.

The mechanical model for the Love waves is described by Eq. (5) and is calculated using Comsol Multiphysics with the following boundary conditions: the bottom interface is clamped (displacement $u = 0$) and the top interface is a free surface (stress $\sigma_{12} = 0$). At the layer interfaces, continuity of displacement and stress is required. The anisotropic parameters of the ST-cut quartz substrate are reduced to the isotropic values $G_{\text{Quartz}} = 49.2 \text{ GPa}$, $\rho_{\text{Quartz}} = 2650 \text{ kg/m}^3$ for this simulation. For the mechanically isotropic magnetostrictive layer, we use $E_{\text{MS}} = 150 \text{ GPa}$, $\nu_{\text{MS}} = 0.38$ and $\rho_{\text{MS}} = 7250 \text{ kg/m}^3$, which results in $G_{\text{MS}} = 54.3 \text{ GPa}$ for the shear modulus at fixed magnetization. For the amorphous, isotropic guiding layer, the following parameters are used: $E_{\text{SiO}_2} = 77.6 \text{ GPa}$, $\nu_{\text{SiO}_2} = 0.1638$, and $\rho_{\text{SiO}_2} = 2200 \text{ kg/m}^3$. For the magnetic sensitivity, a value of $S_{\text{mag}} = 36.8 \text{ GPa/mT}$ was determined from the modeled change of G depicted in 3b at the operating point of $\mu_0 H = 0.4 \text{ mT}$. The structural sensitivity is depicted in 1b with a value of $S_{\text{str}} = 1.07 \frac{\text{m/s}}{\text{GPa}}$. For the calculation of S_{geo} the following parameters were used: a delay line length $l = 3.8 \text{ mm}$, a frequency $f = 147.2 \text{ MHz}$ and a wave velocity of $v = 4220 \text{ m/s}$. The overall sensitivity derived from model and simulations is $S = 450^\circ/\text{mT}$.

Electrical properties. To measure the scattering parameters of the Love wave SAW sensor, the vector network analyzer E8361A from Agilent Technologies is used. Prior to the measurements, both ports of the sensor are matched to 50Ω by means of a parallel capacitor of 22 pF and a series inductor of 202 nH (as seen from the 50 Ω ports into the sensor ports).

Readout circuit. The readout circuit is mainly composed of various components from Mini-Circuits. The SSB upconverter consists of a 2-way- 90° power splitter ZMSCQ-2-180+ at the input and a 2-way- 0° combiner ZMSC-2-1W+ at the output. In-between, two level 17 mixers ZAD-1H+ perform the frequency conversion. The downconversion is realized by a level 7 mixer ZP-3+ after the output signal of the SAW is amplified by a low noise amplifier ZFL-1000LN+. For the floating LO an SMBV100A vector signal generator from Rohde & Schwarz is utilized. The bidirectional conversion between the analog and the digital domain is performed by a high resolution 24-bit converter RME Fireface UFX at a sample rate of 192 kHz. The digital signals are processed in the in-house built real-time framework KiRAT (Kiel Real-time Application Toolkit) as well as in MATLAB. The sinusoidal oscillator signals at 50 kHz, ahead referred to as NCO, are calculated in real-time by means of the CORDIC trigonometric computing technique⁴⁶.

Equivalent magnetic noise floor. The equivalent magnetic noise floor is measured with the use of a calibrated solenoid. With the calibration information and the measured transfer function a scaling-based equalization on a scaling is performed in the time domain after the demodulation process with the help of an in-phase and quadrature (IQ) approach. Due to this processing, a signal with the unit Tesla equivalent to the applied magnetic field is generated. The length of the recorded signal is set to 30 s.

To determine the power spectral density (in units of T^2/Hz), Welch's method⁴⁷ is used. Based on the utilized flattop window and the FFT order of 8 times the sample rate, the effective noise bandwidth (ENBW) is set to a value of 0.47 Hz, which is taken into account in the power spectral density estimation. The overlap is set to three quarters of the FFT order. To obtain the amplitude spectral density (in units of $\text{T}/\sqrt{\text{Hz}}$), which represents the magnetic noise floor, the square root is taken.

References

1. Lenz, J. & Edelstein, S. Magnetic sensors and their applications. *IEEE Sensors Journal* **6**, 631–649, <https://doi.org/10.1109/JSEN.2006.874493> (2006).
2. Sternickel, K. & Braginski, A. I. Biomagnetism using SQUIDs: status and perspectives. *Superconductor Science and Technology* **19**, S160 (2006).

3. Pasku, V., de Angelis, A., de Angelis, G., Moschitta, A. & Carbone, P. Magnetic Field Analysis for 3-D Positioning Applications. *IEEE Transactions on Instrumentation and Measurement* **66**, 935–943, <https://doi.org/10.1109/TIM.2017.2682738> (2017).
4. Ripka, P. Electric current sensors: a review. *Measurement Science and Technology* **21**, 112001 (2010).
5. Hämäläinen, M., Hari, R., Ilmoniemi, R. J., Knuutila, J. & Lounasmaa, O. V. Magnetoencephalography - theory, instrumentation, and applications to noninvasive studies of the working human brain. *Rev. Mod. Phys.* **65**, 413–497, <https://doi.org/10.1103/RevModPhys.65.413> (1993).
6. Bazinet, R., Jacas, A., Confalonieri, G. A. B. & Vazquez, M. A low-noise fundamental-mode orthogonal fluxgate magnetometer. *IEEE Transactions on Magnetics* **50**, 1–3 (2014).
7. Uchiyama, T., Nakayama, S., Mohri, K. & Bushida, K. Biomagnetic field detection using very high sensitivity magnetoimpedance sensors for medical applications. *physica status solidi (a)* **206**, 639–643, <https://doi.org/10.1002/pssa.200881251> (2009).
8. Shah, V. K. & Wakai, R. T. A compact, high performance atomic magnetometer for biomedical applications. *Physics in Medicine & Biology* **58**, 8153 (2013).
9. Sensitec GmbH. *MagnetoResistive Field Sensor AFF755B* (2015).
10. Zabel, S. *et al.* Phase modulated magnetoelectric delta-E effect sensor for sub-nano tesla magnetic fields. *Applied Physics Letters* **107**, 152402, <https://doi.org/10.1063/1.4932575> (2015).
11. Dufay, B., Saez, S., Dolabdjian, C., Yelon, A. & Menard, D. Development of a high sensitivity giant magneto-impedance magnetometer: Comparison with a commercial flux-gate. *IEEE Transactions on Magnetics* **49**, 85–88, <https://doi.org/10.1109/TMAG.2012.2219579> (2013).
12. Lou, J. *et al.* Soft magnetism, magnetostriction, and microwave properties of fegab thin films. *Applied Physics Letters* **91**, 182504 (2007).
13. Greve, H., Woltermann, E., Quenzer, H.-J., Wagner, B. & Quandt, E. Giant magnetoelectric coefficients in (fe90co10)78si12b10-aln thin film composites. *Applied Physics Letters* **96**, 182501, <https://doi.org/10.1063/1.3377908> (2010).
14. Livingston, J. D. Magnetomechanical properties of amorphous metals. *Physica Status Solidi A* **70**, 591–596, <https://doi.org/10.1002/pssa.2210700228> (1982).
15. O'Handley, R. C. Modern Magnetic Materials: Principles and Applications, <https://doi.org/10.1109/MEI.2005.1490004> (2000).
16. Atkinson, D., Squire, P. T., Gibbs, M. R. J., Atalay, S. & Lord, D. G. The effect of annealing and crystallization on the magnetoelastic properties of Fe-Si-B amorphous wire. *Journal of Applied Physics* **73**, 3411–3417, <https://doi.org/10.1063/1.352942> (1993).
17. Sárközi, Z., Mackay, K. & Peuzin, J. C. Elastic properties of magnetostrictive thin films using bending and torsion resonances of a bimorph Elastic properties of magnetostrictive thin films using bending and torsion resonances of a bimorph. *Journal of Applied Physics* **5827**, <https://doi.org/10.1063/1.1318388> (2000).
18. Mungle, C. S., Grimes, C. A. & Dreschel, W. R. Magnetic field tuning of the frequency–temperature response of a magnetoelastic sensor. *Sensors and Actuators A: Physical* **101**, 143–149, [https://doi.org/10.1016/S0924-4247\(02\)00179-6](https://doi.org/10.1016/S0924-4247(02)00179-6) (2002).
19. Gojdka, B. *et al.* Fully integrable magnetic field sensor based on delta-E effect. *Appl. Phys. Lett.* **99**, 223502, <https://doi.org/10.1063/1.3664135> (2011).
20. Zabel, S. *et al.* Multimode delta-e effect magnetic field sensors with adapted electrodes. *Applied Physics Letters* **108**, 222401, <https://doi.org/10.1063/1.4952735> (2016).
21. Nan, T., Hui, Y., Rinaldi, M. & Sun, N. X. Self-biased 215 MHz magnetoelectric NEMS resonator for ultra-sensitive DC magnetic field detection. *Sci. Rep.* **3**, 1985, <https://doi.org/10.1038/srep01985> (2013).
22. Webb, D. C., Forester, D. W., Ganguly, A. K. & Vittoria, C. Applications of amorphous magnetic-layers in surface-acoustic-wave devices. *IEEE Transactions on Magnetics* **15**, 1410–1415, <https://doi.org/10.1109/TMAG.1979.1060442> (1979).
23. Jakoby, B. & Vellekoop, M. J. Properties of love waves: applications in sensors. *Smart Materials and Structures* **6**, 668, <https://doi.org/10.1088/0964-1726/6/6/003> (1997).
24. Huang, L. *et al.* Theoretical investigation of magnetoelectric surface acoustic wave characteristics of ZnO/Metglas layered composite. *AIP Advances* **6**, <https://doi.org/10.1063/1.4939846> (2016).
25. Elhosni, M. *et al.* Magnetic field SAW sensors based on magnetostrictive-piezoelectric layered structures: FEM modeling and experimental validation. *Sensors and Actuators, A: Physical* **240**, 41–49, <https://doi.org/10.1016/j.sna.2015.10.031> (2016).
26. Zhou, H., Talbi, A., Tiercelin, N. & Bou Matar, O. Multilayer magnetostrictive structure based surface acoustic wave devices. *Applied Physics Letters* **104**, 0–4, <https://doi.org/10.1063/1.4868530> (2014).
27. Inoue, M., Fujita, N. & Fujii, T. Optimum geometrical structure of highly magnetostrictive multilayer films for horizontally polarized high frequency magneto-surface-acoustic-wave propagation. *Journal of Applied Physics* **73**, 6159–6161, <https://doi.org/10.1063/1.352735> (1993).
28. Hirst, E. R., Xu, W. L., Bronlund, J. E. & Yuan, Y. J. Surface Acoustic Wave Delay Line for Biosensor Application. In *2008 15th International Conference on Mechatronics and Machine Vision in Practice*, <https://doi.org/10.1109/MMVIP.2008.4749504>, 40–44 (2008).
29. Baer, R. L., Flory, C. A., Tom-Moy, M. & Solomon, D. STW chemical sensors. In *IEEE 1992 Ultrasonics Symposium Proceedings*, 293–298 vol. 1, <https://doi.org/10.1109/ULTSYM.1992.275993> (1992).
30. Li, S., Sankaranarayanan, S. K. R. S., Fan, C., Su, Y. & Bhethanabotla, V. R. Achieving Lower Insertion Loss and Higher Sensitivity in a SAW Biosensor via Optimization of Waveguide and Microcavity Structures. *IEEE Sensors Journal* **17**, 1608–1616, <https://doi.org/10.1109/JSEN.2017.2651102> (2017).
31. Bou Matar, O. *et al.* Band gap tunability of magneto-elastic phononic crystal. *Journal of Applied Physics* **111**, <https://doi.org/10.1063/1.3687928> (2012).
32. Keilis-Borok, W. I. *Seismic Surface Waves in a Laterally Inhomogeneous Earth* (Kluwer Academic Publishers, Dordrecht, 1989).
33. McCord, J. Progress in magnetic domain observation by advanced magneto-optical microscopy. *Journal of Physics D: Applied Physics* **48**, 333001, <https://doi.org/10.1088/0022-3727/48/33/333001> (2015).
34. Podesta, J. J. Phase Noise Cancellation in a Mixer Circuit: Analysis using a Random Phase Function. Tech. Rep., US Army Armament Research, Development and Engineering Center (1996).
35. Holtzman, R. Phase Noise Cancellation in RF Transceivers. Tech. Rep., Elisra Electronic Systems Ltd. - Microwave Division (2007).
36. Jahns, R. *et al.* Magnetoelectric sensors for biomagnetic measurements. In *2011 IEEE International Workshop on Medical Measurements and Applications*, 107–110 <https://doi.org/10.1109/MeMeA.2011.5966676> (2011).
37. Baer, R. L., Hoover, D. M., Molinari, D. & Herleikson, E. C. Phase Noise in SAW Filters. In *IEEE 1984 Ultrasonics Symposium* 30–35, <https://doi.org/10.1109/ULTSYM.1984.198258> (1984).
38. Jungerman, R. L., Baer, R. L. & Bray, R. C. Delay Dependence of Phase Noise in SAW Filters. In *IEEE 1985 Ultrasonics Symposium*, 258–261, <https://doi.org/10.1109/ULTSYM.1985.198514> (1985).
39. Baer, R. L. Phase noise in surface-acoustic-wave filters and resonators. *IEEE Transactions on Ultrasonics, Ferroelectrics, and Frequency Control* **35**, 421–425, <https://doi.org/10.1109/58.20463> (1988).
40. Breitbarth, J. & Koebel, J. Additive (Residual) Phase Noise Measurement of Amplifiers, Frequency Dividers and Frequency Multipliers. *Microwave Journal* **51**, 66–82 (2008).
41. Lage, E. *et al.* Exchange biasing of magnetoelectric composites. *Nature Materials* **11**, 523–529, <https://doi.org/10.1038/nmat3306> (2012).
42. Reermann, J. *et al.* Adaptive Readout Schemes for Thin-Film Magnetoelectric Sensors Based on the delta-E Effect. *IEEE Sens. J.* **16**, 4891–4900, <https://doi.org/10.1109/JSEN.2016.2553962> (2016).

43. Mudivarthi, C. *et al.* Anisotropy of constrained magnetostrictive materials. *Journal of Magnetism and Magnetic Materials* **322**, 3028–3034, <https://doi.org/10.1016/j.jmmm.2010.05.024> (2010).
44. Ludwig, A. & Quandt, E. Optimization of the DeltaE effect in thin films and multilayers by magnetic field annealing. *IEEE Transactions on Magnetics* **38**, 2829–2831, <https://doi.org/10.1109/TMAG.2002.802467> (2002).
45. Du, Tremolet de Lacheisserie E. *Magnetostriction: Theory and application of magnetoelasticity*, chap. 2, 62 (CRC Press, 1994).
46. Volder, J. E. The CORDIC Trigonometric Computing Technique. *IRE Transactions on Electronic Computers* EC-8, 330–334, <https://doi.org/10.1109/TEC.1959.5222693> (1959).
47. Welch, P. D. The use of fast fourier transform for the estimation of power spectra: A method based on time averaging over short, modified periodograms. *Audio and Electroacoustics, IEEE Transactions on* **15**, 70–73 (1967).

Acknowledgements

This work was supported by the German Research Foundation (Deutsche Forschungsgemeinschaft, DFG) through the Collaborative Research Centre CRC 1261 *Magnetolectric Sensors: From Composite Materials to Biomagnetic Diagnostics* and by the Defense Advanced Research Projects Agency (DARPA) through the *Materials for Transduction (MATRIX) TE3* program.

Author Contributions

All authors interpreted the data, discussed the results, reviewed, and commented on the manuscript. J.Mc., F.F., M.G., M.H., R.K., E.Q., G.S. and N.S. designed the experiments and supervised the research. A.K. prepared the sensor. A.K., S.Z. and B.S. performed the magnetic characterization. P.D. and S.Z. conducted the electric characterization. B.S. and J.S. performed the simulation. P.D. and J.R. built the readout circuit and measured the sensor system. All authors wrote the paper.

Additional Information

Competing Interests: The authors declare that they have no competing interests.

Publisher's note: Springer Nature remains neutral with regard to jurisdictional claims in published maps and institutional affiliations.



Open Access This article is licensed under a Creative Commons Attribution 4.0 International License, which permits use, sharing, adaptation, distribution and reproduction in any medium or format, as long as you give appropriate credit to the original author(s) and the source, provide a link to the Creative Commons license, and indicate if changes were made. The images or other third party material in this article are included in the article's Creative Commons license, unless indicated otherwise in a credit line to the material. If material is not included in the article's Creative Commons license and your intended use is not permitted by statutory regulation or exceeds the permitted use, you will need to obtain permission directly from the copyright holder. To view a copy of this license, visit <http://creativecommons.org/licenses/by/4.0/>.

© The Author(s) 2017

Chapter 6

Signal and Noise

6.1 Influence of Quality factor

The quality factor Q is a major parameter for the design of any resonator. This factor depends on a multitude of different geometric, material, and operating parameters based on various effects mentioned briefly in Section 3.3. Combined with the resonance frequency, Q determines the bandwidth of the resonator and the displacement amplitude around the resonance frequency. A large Q corresponds to a small bandwidth (c.f. Section 2.2), but a large displacement amplitude in resonance may increase the output signal amplitude of the sensor. A compromise may be achieved between a large signal amplitude and sufficient bandwidth. The dependence of the signal amplitude on Q is nontrivial because the sensitivity and signal amplitude are largely determined by the electromechanical properties rather than the mechanical properties. In addition, sensor-intrinsic noise is connected inherently with Q and can contribute to a complicated dependency of the LOD as a function of Q .

The discussion in this section will confirm that the Q for the beam resonators used is mostly dominated by air damping and can be tuned and increased by operating under vacuum conditions. The behavior of the signal, noise, and the LOD as functions of Q are investigated theoretically and experimentally with several cantilever ΔE -effect sensors. The sensors are operated under different vacuum pressures and analyzed with a signal-and-noise model to assess the quality factor as a potential parameter for tuning the sensing characteristics. General implications for the sensor development are derived.

Contribution

The authorship of this paper is equally shared with Christine Kirchhof.

- Conceptualization (shared)
- Writing of original manuscript
- Modeling and simulations (shared)
- Data analysis and interpretation (shared)

Reproduced from [395], with the permission of AIP Publishing.

Influence of the quality factor on the signal to noise ratio of magnetoelectric sensors based on the delta-E effect

Cite as: Appl. Phys. Lett. **114**, 183504 (2019); doi: [10.1063/1.5096001](https://doi.org/10.1063/1.5096001)

Submitted: 14 March 2019 · Accepted: 9 April 2019 ·

Published Online: 8 May 2019







View Online



Export Citation



CrossMark

Benjamin Spetzler,^{1,a)} Christine Kirchhof,^{1,a)} Jens Reermann,²  Phillip Durdaut,²  Michael Höft,² 
Gerhard Schmidt,² Eckhard Quandt,¹ and Franz Faupel^{1,b)} 

AFFILIATIONS

¹Institute for Materials Science, Faculty of Engineering, Kiel University, Kaiserstraße 2, D-24143 Kiel, Germany

²Institute for Electrical Engineering, Faculty of Engineering, Kiel University, Kaiserstraße 2, 24143 Kiel, Germany

^{a)}Contributions: B. Spetzler and C. Kirchhof contributed equally to this work.

^{b)}Author to whom correspondence should be addressed: ff@tf.uni-kiel.de

ABSTRACT

Recently, there has been much interest in magnetoelectric magnetic field sensors utilizing the delta-E effect. Such sensors are fully integrable and combine the advantages of high sensitivity at low frequencies with broad bandwidth. Here, we report the influence of the quality factor Q on the signal-to-noise ratio of magnetoelectric magnetic field sensors utilizing the delta-E effect. The sensor consists of a silicon cantilever covered by a magnetostrictive and a piezoelectric thin film. The magnetization-dependent elasticity of the magnetostrictive film leads to detuning of the sensor's resonance, which is excited and read out via the piezoelectric layer. The signal-to-noise ratio is experimentally analyzed as a function of the quality factor, the excitation amplitude and the signal frequency. The results are compared with a signal and noise model to describe general tendencies. The model demonstrates that, in contrast to the conventional direct operation of magnetoelectric sensors, an improvement in the limit of detection proportional to $Q^{3/2}$ can be achieved if thermal-mechanical noise is dominant. The relationship still holds for frequencies far away from the resonance frequency. This reveals the potential for improving the limit of detection significantly by increasing the quality factor, if magnetic and electronic noise can be suppressed.

Published under license by AIP Publishing. <https://doi.org/10.1063/1.5096001>

The detection of magnetic fields in the subpicotesla regime for frequencies below 100 Hz is of interest for medical diagnostics and potential therapies.^{1–3} Up to now, mainly SQUID magnetometers⁴ are used. Because they need liquid helium cooling, the equipment costs are huge and they have a limited local resolution, thus creating the demand for alternative technologies for magnetometers. Significant progress has been achieved with atomic magnetometers,^{5,6} which in turn need to be heated and are complicated to fabricate. In the future, another alternative could be magnetoelectric composites,^{7,8} which show limits of detection (LOD) of 20 pT/Hz^{1/2} for 1–10 Hz for centimeter sized sensors.⁹ Magnetoelectric sensors can be processed on a large scale by MEMS technology with dimensions in the range of a few micrometers^{10,11} to a few millimeters,¹² thus reducing equipment costs and improving the local resolution. The magnetic field is detected by using either the magnetoelectric effect in resonance,¹³ frequency conversion techniques,^{14,15} or the magnetoelastic properties of the magnetostrictive part via the delta-E readout scheme.^{11,16,17} With the last, we

have shown recently that resonant magnetoelectric composites made from piezoelectric AlN and magnetostrictive FeCoSiB thin films on thin silicon substrates possess the capability of measuring small magnetic fields on the order of 100 pT/Hz^{-1/2} for frequencies from 10 to 100 Hz.¹⁸ For the magnetoelectric effect in resonance, an increase in the quality factor, e.g., by operation in vacuum (pressures <0.1 mbar), increases the magnetoelectric signal-to-noise ratio (SNR) in resonance by \sqrt{Q} . This is because in resonance the signal increases linearly with Q (Ref. 19) and the dominating thermal-mechanical noise of the cantilever scales in resonance by \sqrt{Q} .²⁰ For the delta-E-operation scheme, the behavior of the signal and the noise is different and discussed here.

In this work, the signal and the noise are analyzed experimentally and theoretically for thin film magnetoelectric sensors with similar designs and properties. The sensitivity is analyzed under both atmospheric and vacuum conditions. These measurements are compared with a signal and noise model in the second part. Finally, the optimum

limit of detection (LOD) is measured and general trends are derived from the model.

All sensors consist of a $50\ \mu\text{m}$ thick, $3\ \text{mm}$ long poly-silicon cantilever, covered by a $2\ \mu\text{m}$ AlN piezoelectric layer and a $2\ \mu\text{m}$ magnetostrictive film of amorphous $(\text{Fe}_{90}\text{Co}_{10})_{78}\text{Si}_{12}\text{B}_{10}$. The process details are published in Ref. 21. During the delta-E operation, the cantilever is electrically excited to oscillate close to the mechanical resonance by applying a sinusoidal voltage u_{ex} to the piezoelectric layer with a frequency f_{ex} . A change in the magnetic field leads to a shift of the resonance frequency f_r , which results in a corresponding frequency shift of the admittance characteristic. Consequently, an alternating magnetic field modulates the current through the sensor. The current is measured as the voltage u by utilizing a charge amplifier. It is equipped with an additional JFET input stage to lower the amplifier's noise contribution.²² In a small signal approximation, the measured voltage is

$$u(t) \propto \hat{u}_{\text{ex}} [\hat{Y}_0 + S_{\text{am}} B_{\text{ac}}] \cdot \cos(2\pi f_{\text{ex}} t + \phi_0 + S_{\text{pm}} B_{\text{ac}}). \quad (1)$$

Here, \hat{u}_{ex} is the amplitude of the excitation voltage. $\hat{Y}_0 := |Y(f_{\text{ex}}, B_{\text{bias}})|$ is the magnitude of the electrical admittance and $\phi_0 := \phi(f_{\text{ex}}, B_{\text{bias}})$ is the zero-phase angle, both at f_{ex} and the magnetic dc bias flux density B_{bias} . The alternating magnetic flux density B_{ac} modulates both the amplitude u via the amplitude sensitivity S_{am} and the phase via the phase sensitivity S_{pm} . They are defined as

$$S_{\text{am}} = S_{\text{mag}} S_{\text{el,am}} := \left. \frac{df_r}{dB} \right|_{B=B_{\text{bias}}} \left. \frac{d|Y|}{df} \right|_{f=f_{\text{ex}}}, \quad (2a)$$

$$S_{\text{pm}} = S_{\text{mag}} S_{\text{el,pm}} := \left. \frac{df_r}{dB} \right|_{B=B_{\text{bias}}} \left. \frac{d\phi}{df} \right|_{f=f_{\text{ex}}}, \quad (2b)$$

with the AM electrical sensitivity $S_{\text{el,am}}$ and the PM electrical sensitivity $S_{\text{el,pm}}$. The phase angle of the electrical admittance Y is denoted ϕ . The magnetic sensitivity S_{mag} for the described sensor is about $60\ \text{Hz/mT}$ under an optimum magnetic bias field $B_{\text{bias}} = 0.65\ \text{mT}$. Further details about the readout and demodulation schemes are described in Ref. 23.

To analyze the influence of the quality factor on the sensitivities, the sensor's admittance is modeled by a modified Butterworth van Dyke (mBvD) equivalent circuit.²¹ It consists of a series resonant circuit (L_r , C_r , R_r) in parallel to the sensor's capacitance C_{me} and resistance R_{me} . The circuit parameters are determined for atmospheric (atm) and vacuum (vac, pressure $\approx 10^{-5}$ mbar) by fitting the model to admittance measurements performed at B_{bias} (Fig. 1). The parameters extracted from the fit are given in Table I.

With those values, the quality factor of the mechanical resonator is calculated via $Q = R_r^{-1}(L_r/C_r)^{1/2}$. By operation in the vacuum, the quality factor of the considered sensor at B_{bias} increases from roughly 1000 by a factor of about 4 to around 4000. The increase can mainly be attributed to the reduction of viscous air damping. It can be deduced from the analysis of the quality factor as a function of pressure p ($Q \sim p^{-1/2}$) and comparison with theoretical calculations.^{24,25} As reported in Ref. 21, the quality factor also depends on the magnetic bias field. For the sensor used, a decrease in the quality factor by 10% can be observed at B_{bias} relative to magnetic saturation. This behavior is independent of the operation pressure and results probably from magnetoelastic loss mechanisms during the oscillation. Due to reduced damping, the resonance frequency shifts from $7597\ \text{Hz}$ (atm) to $7622\ \text{Hz}$ (vac).

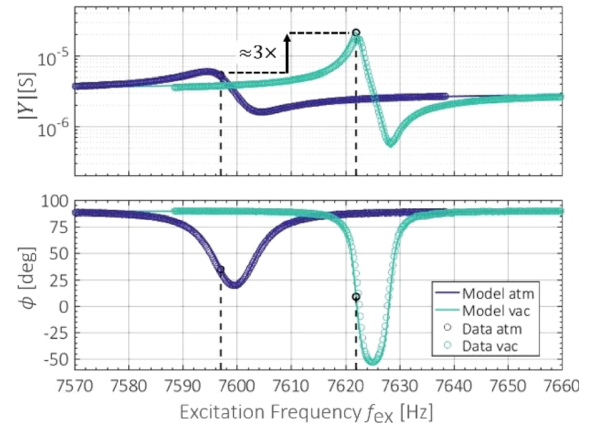


FIG. 1. Measured magnitude $|Y|$ and phase angle ϕ of the electrical admittance of the sensor at B_{bias} under atmospheric (atm) and vacuum (vac) conditions. The dashed vertical lines mark the mechanical resonance frequencies at $7597\ \text{Hz}$ and $7622\ \text{Hz}$.

The increase in Q leads to a steeper and larger sensor admittance magnitude and a steeper phase angle, as shown in Fig. 1, as a direct consequence of reduced losses of the mechanical resonator. A higher Q increases the contribution of the serial RCL circuit to the admittance relative to the contribution of the constant parallel capacitance C_{me} . Hence, at large Q , the excitation in resonance occurs closer to the maximum of $|Y|$ and the inflection point of ϕ . In the vacuum, the maximum $S_{\text{el,am}}$ is increased by a factor of 11 and the maximum $S_{\text{el,pm}}$ by a factor of about 6. At the chosen operation frequency $f_{\text{ex}} = f_r$, these maximum electrical sensitivities are not reached. Here, $S_{\text{el,pm}}$ increases by a factor of about 5.6, whereas $S_{\text{el,am}}$ increases only by a factor of about 5. With absolute values of $S_{\text{el,am}} = 3.3\ \mu\text{S/Hz}$ and $S_{\text{el,pm}} = 0.85\ \text{rad/Hz} = 48.7\ \text{deg/Hz}$ at f_r in the vacuum, the signal is modulated in both the amplitude and the phase.

To analyze the impact on the resulting signal and noise, a sinusoidal magnetic signal with an amplitude of $1\ \text{nT}$ was applied with a frequency of $f_s = 2\ \text{Hz}$. For the excitation in mechanical resonance, an amplitude $\hat{u}_{\text{ex}} = 1\ \text{mV}$ was used. From the amplitude density spectrum in Fig. 2, the noise around the resonance frequency increases by a factor of $\approx \sqrt{Q}$, as expected from the thermal-mechanical noise in the noise model.²⁶ Away from the resonance frequency, the noise under vacuum conditions is slightly lower than at atmospheric pressure. Due to the increased \hat{Y}_0 under vacuum, the corresponding carrier amplitude is also a factor of about 3 times larger.

In Fig. 2, the sidebands in the vacuum increase by a factor of ≈ 8 , which is due to the increased sensitivities under vacuum compared to atmospheric conditions. To fully explain the behavior of the signal

TABLE I. Equivalent circuit parameters under atmospheric (atm) and vacuum (vac) conditions obtained from measurements at $B_{\text{bias}} = 0.65\ \text{mT}$. C_{me} is constant within the accuracy of the fit.

	Q	L_r (H)	C_r (fF)	R_r (k Ω)	R_{me} (M Ω)	C_{me} (pF)
atm	1000	4922.3	89.163	229.81	54.077	63.08
vac	4000	3986.4	109.38	47.675	33.334	66.88

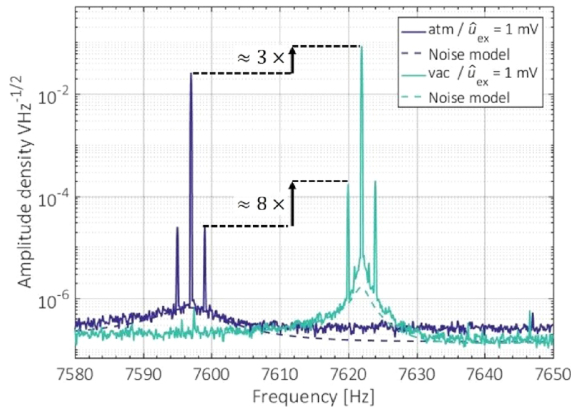


FIG. 2. Amplitude density for a sinusoidal signal with an amplitude of 1 nT and a frequency of $f_s = 2$ Hz under atmospheric (atm) and vacuum (vac) conditions. The excitation amplitude is $\hat{u}_{ex} = 1$ mV. Noise model according to Ref. 26, extended by the low noise charge amplifier from Ref. 22.

amplitude with the quality factor, the limited frequency bandwidth must also be considered. For the sensor employed, the bandwidth decreases from 3.7 Hz under atmospheric pressure to 1 Hz under vacuum. Consequently, the decreasing bandwidth is expected to counteract the advantage of increased sensitivity at large Q . For delta-E effect sensors, this could generally be avoided by choosing larger resonance frequencies.

To gain general insights, a signal and noise model is used. The unfiltered output signal is modeled using Eq. (1). To obtain sensitivities depending on the quality factor, the sensor resistance is calculated via $R_r = Q^{-1}(L_r/C_r)^{1/2}$. The other mBvD parameters are obtained as mean values from impedance measurements of sensors with varying quality factors resulting from the vacuum, atmospheric pressure or changes in the magnetic working point. In this approximation, the resonance frequency stays constant with Q . From the calculated admittances, the sensitivities at the respective excitation frequencies are obtained. The band pass behavior of the sensor around its mechanical resonance frequency is described by a first order Bessel filter²³ with a cut-off frequency $f_{-3dB} = f_r/(2Q)$ after Mertz.²⁷

Calculations are made with an excitation amplitude $\hat{u}_{ex} = 50$ mV and a typical magnetic sensitivity of $S_{mag} = 60$ Hz/mT. In Fig. 3(a), a modeled signal with a frequency of 0.1 Hz is compared with the

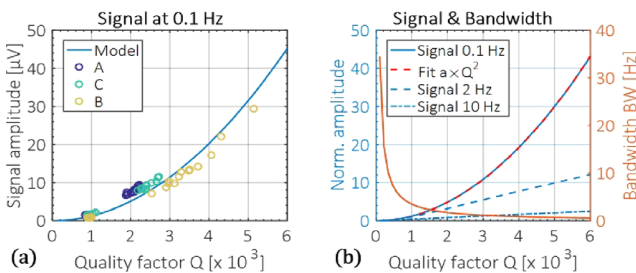


FIG. 3. (a) Modeled signal voltage as a function of Q assuming an excitation amplitude $\hat{u}_{ex} = 50$ mV and a magnetic sensitivity of 60 Hz/mT ($f_s = 0.1$ Hz). (b) Normalized signal amplitude $\hat{u}_{norm} = \hat{u}/\hat{u}$ ($Q = 1000$) as a function of Q and the signal frequency with the lowpass characteristic for $f_s = 1$ Hz and $f_s = 10$ Hz. A function $g = aQ^2$ is fitted to the signal at 0.1 Hz.

data from impedance measurements of three exemplary sensors (A, B, and C). Model and measurements are in good agreement. The main deviations can be attributed to a slightly different electrode geometry of sensor B, but the overall trend is conserved. The sensor's resonance frequency is assumed to be constant because the change due to operation in the vacuum is only 0.3%.

The strongly decreasing bandwidth is shown in Fig. 3(b), together with the signal amplitude normalized to the value at $Q = 1000$ (\hat{u}_{norm}) for signals of various frequencies. At 2 Hz and $Q = 4000$, the signal amplitude is increased by a factor of about 8, consistent with the measurement in Fig. 2. Compared to the case without the lowpass filter (frequencies well below the bandwidth), the signal amplitude is already strongly reduced.

To describe the general trend of the signal amplitude as a function of Q , a function $g = aQ^2$ is fitted to the data obtained from the model. From the fit, the signal voltage increases quadratically for signal frequencies well below the bandwidth, as shown in Fig. 3(b) for the normalized signal amplitude \hat{u}_{norm} . The quadratic increase occurs although the sensitivities are linear functions of Q , because \hat{Y}_0 and ϕ_0 change with Q as well. With increasing signal frequency, the quadratic coefficient decreases due to the filter inset [Fig. 3(b)]. At $f_s = 10$ Hz, \hat{u}_{norm} can be approximated by a linear function. At intermediate frequencies, higher order coefficients are additionally required for a satisfying polynomial description. Within the assumptions, such behavior is independent of the excitation amplitude. The complete signal amplitude is plotted in Fig. 4(a) as a function of the signal frequency and the quality factor.

For comparison, the thermal-mechanical voltage noise density is plotted in Fig. 4(b) for the same parameter space, calculated from the model published in Ref. 26. Other noise sources, such as thermal-electrical and magnetic noise, are not included. Hence, it represents the theoretical minimum noise level for the given geometry and the materials parameters at room temperature.

The measured signal-to-noise ratio (SNR) and the signal amplitude density as functions of the excitation voltage amplitude \hat{u}_{ex} are shown in Fig. 5(a) for a signal frequency of 10 Hz. For small \hat{u}_{ex} , the noise floor is almost constant, independent of the operating pressure. The signal amplitude increases proportionally to \hat{u}_{ex} and is a factor of 4 higher in the vacuum, which matches the model in Fig. 3(b).

At large excitation amplitudes of $\hat{u}_{ex} \approx 48$ mV, the noise level under atmospheric pressure starts to increase roughly linearly. Simultaneously, the slope of the signal amplitude is reduced due to a shift of the magnetic working point. Under vacuum conditions, this behavior sets in at $\hat{u}_{ex} \approx 11$ mV, about 4 times earlier than under

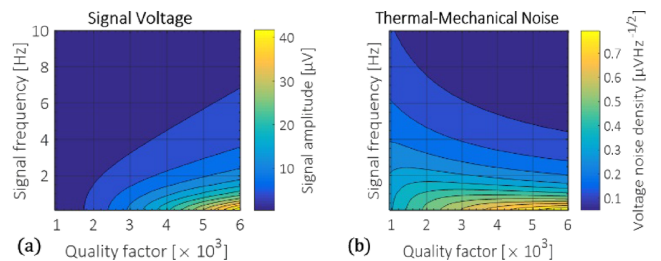


FIG. 4. (a) Amplitude of the signal voltage as a function of the quality factor and the signal frequency. (b) Voltage noise density for the same set of parameters, based on the noise model in Ref. 26 assuming a dominant thermal-mechanical noise.

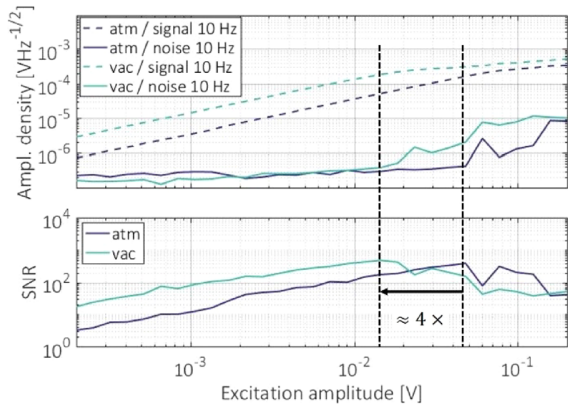


FIG. 5. Signal and noise density of the sidebands for a sinusoidal signal with an amplitude of 1 nT and a frequency of 10 Hz under atmospheric pressure and vacuum conditions as a function of the excitation voltage. The signal amplitude under vacuum is increased by a factor of 4 for small excitation amplitudes.

atmospheric conditions. As discussed in Ref. 26, the increase in noise is of magnetic origin: With increasing excitation amplitude, the cantilever deflection increases and so does the change in magnetization due to inverse magnetostriction. The alternating magnetization is associated with magnetic loss and dissipation scaling in our experiments with the mechanical amplitude. All in all, the inset of magnetic noise shifts the optimum excitation amplitude from about 48 mV under atmospheric pressure to ≈ 11 mV under vacuum [Fig. 5(b)].

In Fig. 6, the measured LOD is shown as a function of frequency for different \hat{u}_{ex} . At small $\hat{u}_{ex} = 0.2$ mV, thermal-mechanical noise dominates up to 10 Hz and the LOD is constant. At frequencies larger than 10 Hz, the constant thermal-electrical noise floor starts to dominate, while the signal is more and more damped by the sensor's low pass behavior. This results in an increasing LOD at large signal frequencies. Operation in the vacuum improves the LOD by a factor of 8. At the optimum excitation amplitudes of $\hat{u}_{ex} \approx 48$ mV and $\hat{u}_{ex} \approx 11$ mV, a minimum LOD of about $160 \text{ pT}/\sqrt{\text{Hz}}$ is measured at

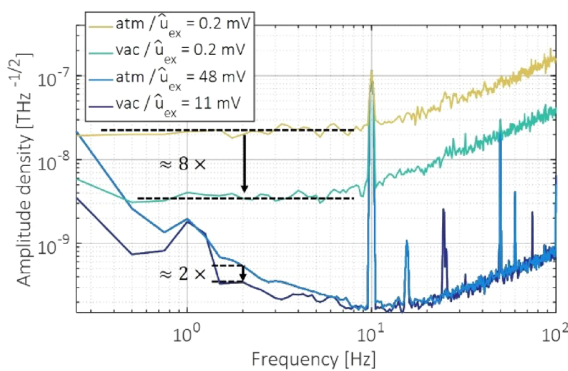


FIG. 6. Resultant limit of detection (LOD) for excitation voltages (48 mV and 11 mV) corresponding to the best signal-to-noise ratio under atmospheric and vacuum conditions and the LOD for small \hat{u}_{ex} (0.2 mV), where thermal-mechanical noise dominates at small frequencies. A signal with a frequency of 10 Hz is applied. Noise artifacts at 1 Hz and above 10 Hz are visible due to incomplete electrical shielding.

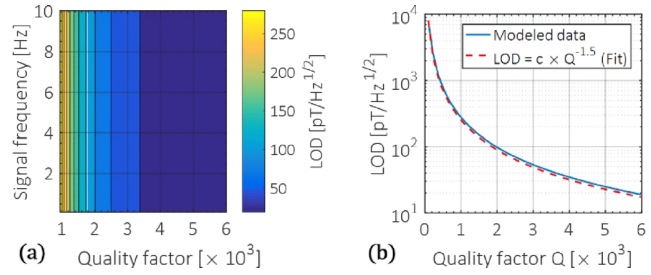


FIG. 7. (a) Estimated LOD as a function of the quality factor and the signal frequency when only the thermal mechanical noise is considered. (b) Fit to modeled data at a signal frequency of 0.1 Hz with the fitting parameter $c = 8.03 \times 10^{-6} \text{ T}/\sqrt{\text{Hz}}$.

10 Hz under both atmospheric and vacuum conditions. At low frequencies (< 10 Hz), the magnetic noise amplified by the resonance dominates the LOD. With increasing frequency, the magnetic noise contribution reduces until the thermal-mechanical noise dominates again. At 2 Hz, the LOD is improved by a factor of about 2. In Fig. 7(a), the estimated LOD is plotted as a function of the quality factor and the signal frequency. The LOD is calculated using the data from Fig. 4, without considering the magnetic and thermal-electrical noise. For Q-factors and \hat{u}_{ex} below the onset of magnetic noise, the model is consistent with the measurements in Fig. 6. From a fit, the LOD is found to be $\propto Q^{-3/2}$. This is to be expected, since the signal amplitude $\propto Q^2$, but the noise $\propto \sqrt{Q}$ in resonance. Note that the resulting LOD is constant with the frequency as long as the thermal-mechanical noise dominates. This behavior results, because the thermal-mechanical noise and the signal amplitude are equally influenced by the cantilever's resonance behavior. The simulation emphasizes the potential of large quality factors if the magnetic noise can be suppressed.

In conclusion, the impact of the quality factor on the signal-to-noise ratio was shown for the delta-E-readout scheme of magnetoelectric cantilever-based sensors. In the interesting range well below the cut-off frequency, the signal amplitude increases quadratically with the quality factor. From the model, the detection limit is $\propto Q^{-3/2}$, independent of the signal's frequency, if thermal-mechanical noise dominates. Thus, the delta-E sensor benefits from an increase in the quality factor Q of the resonator much stronger than conventional magnetoelectric sensors, where the increase is $\propto Q^{1/2}$.

In the present case, the overall limit-of-detection is improved by a factor of about 2 at 2 Hz. The improvement is limited by the earlier onset of magnetic noise with higher Q. However, by improving the magnetic layer, i.e., reduction of magnetic noise by using an exchange bias multilayer as reported in Ref. 12, it should be possible to push the onset of the magnetic noise to higher excitation voltages. For other resonance modes and geometries, the model can be adjusted and will be investigated experimentally and theoretically in future.

We gratefully thank the German Research Foundation (DFG) for funding this work by the Collaborative Research Centre CRC 1261 *Magnetoelectric Sensors: From Composite Materials to Biomagnetic Diagnostics*.

REFERENCES

¹L. Duez, S. Beniczky, H. Tankisi, P. O. Hansen, P. Sidenius, A. Sabers, and A. Fuglsang-Frederiksen, *Clin. Neurophysiol.* **127**, 3301 (2016).

- ²J. S. W. Kwong, B. Leithäuser, J. W. Park, and C. M. Yu, *Int. J. Cardiol.* **167**, 1835 (2013).
- ³V. Sakkalis, *Comput. Biol. Med.* **41**, 1110 (2011).
- ⁴R. Kleiner, D. Koelle, F. Ludwig, and J. Clarke, *Proc. IEEE* **92**, 1534 (2004).
- ⁵C. N. Johnson, P. D. D. Schwindt, and M. Weisend, *Phys. Med. Biol.* **58**, 6065 (2013).
- ⁶W. C. Griffith, S. Knappe, and J. Kitching, *Optics Express*, **18**, 27167 (2010).
- ⁷J. Reermann, P. Durdaut, S. Salzer, T. Demming, A. Piorra, E. Quandt, N. Frey, M. Höft, and G. Schmidt, *Meas., Band 116*, 230 (2018).
- ⁸C.-W. Nan, M. I. Bichurin, S. Dong, D. Viehland, and G. Srinivasan, *J. Appl. Phys.* **103**, 31101 (2008).
- ⁹J. Zhai, Z. Xing, S. Dong, J. Li, and D. Viehland, *Appl. Phys. Lett.* **88**, 62510 (2006).
- ¹⁰S. Marauska, R. Jahns, C. Kirchhof, M. Claus, E. Quandt, R. Knöchel, and B. Wagner, *Sens. Actuators A* **189**, 321 (2013).
- ¹¹T. Nan, Y. Hui, M. Rinaldi, and N. X. Sun, *Sci. Rep.* **3**, 1985 (2013).
- ¹²V. Röbisch, E. Yarar, N. O. Urs, I. Teliban, R. Knöchel, J. McCord, E. Quandt, and D. Meyners, *J. Appl. Phys.* **117**, 17B513 (2015).
- ¹³M. Bichurin, D. Filippov, V. Petrov, V. Laletsin, N. Paddubnaya, and G. Srinivasan, *Phys. Rev. B* **68**, 132408 (2003).
- ¹⁴R. Jahns, R. Knoechel, and E. Quandt, Patent application DPMA No. DE 10 2011 008 866.0 (18 January 2011).
- ¹⁵S. M. Gillette, A. L. Geiler, D. Gray, D. Viehland, C. Vittoria, and V. G. Harris, *IEEE Magn. Lett.* **2**, 1 (2011).
- ¹⁶B. Gojdka, R. Jahns, K. Meurisch, H. Greve, R. Adelung, E. Quandt, R. Knöchel, and F. Faupel, *Appl. Phys. Lett.* **99**, 223502 (2011); *Nature*, **480**, 155 (2011).
- ¹⁷R. Jahns, S. Zabel, S. Marauska, B. Gojdka, B. Wagner, R. Knöchel, R. Adelung, and F. Faupel, *Appl. Phys. Lett.* **105**, 052414 (2014).
- ¹⁸S. Zabel, J. Reermann, S. Fichtner, C. Kirchhof, E. Quandt, B. Wagner, G. Schmidt, and F. Faupel, *Appl. Phys. Lett.* **108**, 222401 (2016).
- ¹⁹C. Kirchhof, M. Krantz, I. Teliban, R. Jahns, S. Marauska, B. Wagner, R. Knöchel, M. Gerken, D. Meyners, and E. Quandt, *Appl. Phys. Lett.* **102**, 232905 (2013).
- ²⁰P. Durdaut, S. Salzer, J. Reermann, P. Hayes, D. Meyners, E. Quandt, G. Schmidt, R. Knöchel, and M. Höft, *IEEE Sens. J.* **17**, 2338 (2017).
- ²¹S. Zabel, C. Kirchhof, E. Yarar, D. Meyners, E. Quandt, and F. Faupel, *Appl. Phys. Lett.* **107**, 152402 (2015).
- ²²P. Durdaut, V. Penner, C. Kirchhof, E. Quandt, R. Knöchel, and M. Höft, *IEEE Sens. J.* **17**, 7364 (2017).
- ²³J. Reermann, S. Zabel, C. Kirchhof, E. Quandt, F. Faupel, and G. Schmidt, *IEEE Sens. J.* **16**, 4891 (2016).
- ²⁴H. Hosaka, K. Itao, and S. Kuroda, *Sens. Actuators A* **49**, 87 (1995).
- ²⁵J. Lübke, M. Temmen, H. Schnieder, and M. Reichling, *Meas. Sci. Technol.* **22**, 55501 (2011).
- ²⁶P. Durdaut, J. Reermann, S. Zabel, C. Kirchhof, E. Quandt, F. Faupel, G. Schmidt, R. Knöchel, and M. Höft, *IEEE Trans. Instrum. Meas.* **66**, 2771 (2017).
- ²⁷J. Mertz, O. Marti, and J. Mlynek, *Appl. Phys. Lett.* **62**, 2344 (1993).

6.2 Influence of Piezoelectric Material

The previous section indicated that Q can significantly improve sensitivity, and under certain conditions, the LOD. Another major aspect that influences the electrical admittance of the sensor (and thereby signal and noise) is the piezoelectric material. All ΔE -effect sensors presented in the previous sections are based on aluminum nitride, which is a well established piezoelectric material in microelectromechanical systems (MEMS) technology owing to its thermal and electrical properties and unique compatibility with complementary metal-oxide-semiconductor (CMOS) technology [396]. The addition of scandium can significantly increase piezoelectric coefficients [397–399] along with changes in other material parameters such as electric permittivity, and mechanical stiffness [400, 401]. Details on the piezoelectric effect in AlN and AlScN and a review of other piezoelectric materials can be found elsewhere [402]. The availability of potential alternatives for AlN opens challenges of selecting an optimum candidate for obtaining desired sensor properties such as signal, noise, and LOD. Yet, the dependencies of these sensor characteristics on the mentioned material parameters remain unknown.

In this section, the influence of piezoelectric material parameters on signal, noise, and LOD is analyzed experimentally and theoretically considering examples of AlN and AlScN.

Contribution

- Conceptualization
- Writing of original manuscript
- Modeling and simulations
- Measurements
- Data analysis and interpretation

Influence of the piezoelectric material on the signal and noise of magnetoelectric magnetic field sensors based on the delta-E effect

Cite as: APL Mater. 9, 031108 (2021); doi: 10.1063/5.0042448

Submitted: 30 December 2020 • Accepted: 1 March 2021 •

Published Online: 15 March 2021



View Online



Export Citation



CrossMark

Benjamin Spetzler,¹  Jingxiang Su,²  Ron-Marco Friedrich,¹  Florian Niekiel,²  Simon Fichtner,² 
Fabian Lofink,² and Franz Faupel^{1,a)} 

AFFILIATIONS

¹Chair for Multicomponent Materials, Faculty of Engineering, Kiel University, Kaiserstraße 2, D-24143 Kiel, Germany

²Fraunhofer Institute for Silicon Technology ISIT, Frauenhoferstr. 1, 25524 Itzehoe, Germany

Note: This paper is part of the Special Topic on Magnetoelectric Materials, Phenomena, and Devices.

^{a)}Author to whom correspondence should be addressed: ff@tf.uni-kiel.de

ABSTRACT

Magnetoelectric thin-film sensors based on the delta-E effect have widely been reported for the detection of low frequency and small amplitude magnetic fields. Such sensors are usually fabricated with microelectromechanical system technology, where aluminum nitride (AlN) is the established piezoelectric material. Here, we present aluminum scandium nitride (AlScN) for delta-E effect sensors instead and compare it with AlN using two sensors of identical design. The sensors are experimentally and theoretically analyzed regarding sensitivity, noise, limit of detection (LOD), and resonator linearity. We identify the influence of the dominating piezoelectric coefficients d_{ij} and other material parameters. Simulations and measurements demonstrate that, in contrast to the conventional direct operation of magnetoelectric sensors, a sensitivity increase $\propto d_{ij}^2$ and a LOD improvement $\propto d_{ij}^{-1}$ can be achieved if thermal-mechanical noise is dominant. In the present case, an $8\times$ improved sensitivity and LOD are measured with AlScN at small excitation amplitudes. This factor decreases with increasing amplitude and resonator nonlinearities. The overall minimum LOD does not change due to an earlier onset of magnetic noise in the AlScN sensor. All in all, this study reveals the influence of the piezoelectric material on the signal and noise of delta-E effect sensors and the potential of AlScN to significantly improve sensitivity.

© 2021 Author(s). All article content, except where otherwise noted, is licensed under a Creative Commons Attribution (CC BY) license (<http://creativecommons.org/licenses/by/4.0/>). <https://doi.org/10.1063/5.0042448>

INTRODUCTION

Detecting small amplitude and low-frequency magnetic fields is of high interest in the field of biomagnetics and opens promising prospects for potential medical diagnostics and therapies.^{1–3} Thin-film magnetoelectric composite sensors have been investigated for such purposes.^{4–7} They can be downscaled with standard microelectromechanical system (MEMS) technology and are compatible with complementary metal-oxide-semiconductor (CMOS) technology. Combining with the possibility of room-temperature operation could make them attractive alternatives^{8,9} to traditionally used sensor types¹⁰ and atomic magnetometers^{11,12} in the future.

Detection limits in the range of few pT/\sqrt{Hz} ¹³ can be achieved with the direct magnetoelectric effect yet only in a small bandwidth of a few Hz around the resonance frequency of the device. One way to overcome this hurdle is the utilization of modulation techniques such as the delta-E effect read-out scheme.¹⁴ It has widely been demonstrated in numerous studies^{15–27} and has shown the potential of detecting low-frequency magnetic fields with typical signal amplitudes in the pT and nT regimes.

MEMS cantilever delta-E effect sensors were experimentally and theoretically analyzed regarding geometry and sensitivity,²⁸ the influence of the electrode design,²⁶ frequency effects,²⁹ signal and noise,^{30,31} and how it is influenced by the quality factor.³² Recently,

they enabled the detection of magnetically labeled cells.³³ Such delta-E effect sensors consist of magneto-electric thin-film composites with a soft-magnetic material and a piezoelectric layer. Whereas macroscopic delta-E effect sensors^{22,27,34} often use PZT as a piezoelectric material, the established material in MEMS technology is aluminum nitride (AlN).

Recently, it was shown that the addition of scandium can increase the piezoelectric coefficient by more than a factor of 2.^{35,36} This caused a corresponding increase in the signal in direct magneto-electric operation³⁷ by a factor of ~2. Because the sensor intrinsic thermal-mechanical noise in resonance increases accordingly, no improvement in the limit of detection (LOD) was achieved.

In contrast to conventional magneto-electric sensors, the signal and noise of delta-E effect sensors behave differently and have not been investigated with respect to the properties of the piezoelectric material, yet.

In this work, we identify and discuss the influence of the piezoelectric material on the sensing characteristics of delta-E effect magnetic field sensors. As an example, two sensors with AlScN and AlN as the respective piezoelectric material are compared. After introducing the sensors in section Sensor Design and Materials, the delta-E effect read-out concept is reviewed to define the quantities that are used throughout this paper. Measurement results are then presented and analyzed using an electromechanical finite element model and a signal-and-noise model. Finally, we focus the analysis on the influence of the piezoelectric coefficients on the signal and noise to identify general trends for the LOD.

SENSOR DESIGN AND MATERIALS

A schematic cross section of the sensors investigated here and a photograph are shown in Fig. 1. The sensors consist of a 5 μm thick poly-silicon cantilever with targeted dimensions of $1000 \times 200 \mu\text{m}^2$. It is sandwiched between two SiO_2 layers with thicknesses of 990 nm (bottom) and 650 nm (top). A 1 μm thick piezoelectric layer (AlN or $\text{Al}_{0.73}\text{Sc}_{0.27}\text{N}$) on top is covered by a 1 μm thick Si_3N_4 passivation layer. The piezoelectric layer is contacted via a 120 nm thin Pt/Ti bottom electrode that extends over the whole cantilever. From the top, through the Si_3N_4 layer, a 4 μm thick Au contact line is

connected to a 150 nm thin Mo top electrode. A 2 μm thick magnetostrictive layer of amorphous $(\text{Fe}_{90}\text{Co}_{10})_{78}\text{Si}_{12}\text{B}_{10}$ (FeCoSiB) is deposited on Si_3N_4 , also covering the Au contact line. A magnetic DC field (≈ 10 mT) was applied during the deposition to induce a magnetic easy axis along the short axis of the cantilever. In a final step, the cantilevers are encapsulated with a wafer-level AuSn transient-liquid-phase (TLP) bonding.³⁸ Except for the deposition process of AlN and $\text{Al}_{0.73}\text{Sc}_{0.27}\text{N}$ layers, the design and the fabrication steps are identical for both sensors. In this work, the piezoelectric layers were grown by a reactive pulsed direct current co-sputter deposition, described in Ref. 35. An overview of the layer dimensions is given in the supplementary material, and a detailed description of the fabrication process can be found in Ref. 39. In all following discussions and simulations, we consider the cantilevers to be oriented lengthwise in the x_1 -direction and widthwise along the x_2 -direction of a right-handed Cartesian coordinate system.

SENSOR OPERATION

During the delta-E operation, the cantilever is electrically excited to oscillate. For that, a sinusoidal voltage u_{ex} with excitation frequency f_{ex} and amplitude \hat{u}_{ex} is applied to the piezoelectric layer. A magnetic field alters the sensor's mechanical resonance frequency f_r via the delta-E effect,^{40,41} which shifts the sensor's admittance characteristic $Y(f_{\text{ex}})$ on its frequency axis. An alternating magnetic field consequently modulates the current through the sensor. It is measured as a voltage $u(t)$ over time t by utilizing a charge amplifier with impedance Z_f . In small signal approximation, it is given by

$$u(t) \approx -Z_f(f_{\text{ex}}) \cdot \hat{u}_{\text{ex}} \cdot [Y_0 + S_{\text{am}}B_{\text{ac}}] \cdot \cos(2\pi f_{\text{ex}}t + \phi_0 + S_{\text{pm}}B_{\text{ac}}). \quad (1)$$

The magnitude and phase angle of the sensor's admittance Y are given by $|Y|$ and ϕ , respectively. In Eq. (1), $Y_0 := |Y(f_{\text{ex}}, \mu_0 H)|$ and $\phi_0 := \phi(f_{\text{ex}}, \mu_0 H)$ at $\mu_0 H = B$ and $f_{\text{ex}} = f_r(B)$. Hence, each sensor is operated at a defined magnetic bias flux density B and excited at the corresponding mechanical resonance frequency $f_r(B)$. An alternating sinusoidal magnetic test signal $B_{\text{ac}}(t)$ with frequency f_{ac} and amplitude \hat{B}_{ac} will later be applied to characterize the sensors. It modulates the amplitude of u via the amplitude sensitivity S_{am} and the phase via the phase sensitivity S_{pm} . They are defined by³²

$$S_{\text{am}} = S_{\text{H}}S_{\text{el,am}} := \left. \frac{df_r}{d\mu_0 H} \right|_B \left. \frac{d|Y|}{df_{\text{ex}}} \right|_{f_r}, \quad (2a)$$

$$S_{\text{pm}} = S_{\text{H}}S_{\text{el,pm}} := \left. \frac{df_r}{d\mu_0 H} \right|_B \left. \frac{d\phi}{df_{\text{ex}}} \right|_{f_r}, \quad (2b)$$

with the electrical magnitude sensitivity $S_{\text{el,am}}$ and the electrical phase sensitivity $S_{\text{el,pm}}$. The dynamic behavior of the sensor can be approximated by using a first-order Bessel filter.¹⁴ The output signal of the charge amplifier is fed into a quadrature amplitude demodulator to obtain the demodulated output signal $u_{\text{co}}(t)$. For small magnetic field amplitudes \hat{B}_{ac} , the voltage amplitude spectrum $\hat{U}_{\text{co}}(f)$ of $u_{\text{co}}(t)$ is used to define a voltage sensitivity S_V ,

$$S_V(f_{\text{ac}}) := \frac{\hat{U}_{\text{co}}(f_{\text{ac}})}{\hat{B}_{\text{ac}}}, \quad (3)$$

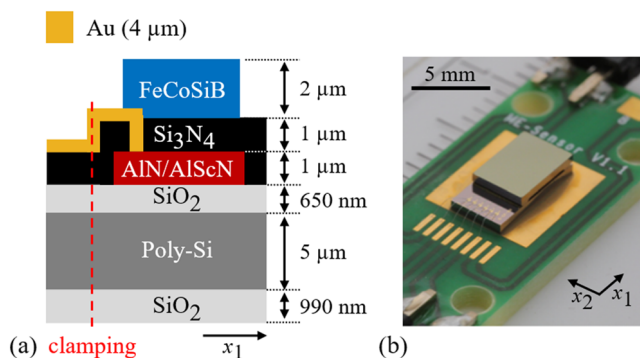


FIG. 1. (a) Schematic cross section of the cantilever's layer structure including all layers thicker than 0.15 μm ; the AlN/AlScN layer is sandwiched by two electrodes (not shown). (b) Photograph of the real device on a printed circuit board; the cantilever is covered by Si-encapsulation.

at the frequency $f = f_{ac}$. The voltage sensitivity can be used to estimate the equivalent magnetic field noise density also referred to as detectivity or limit of detection (LOD),

$$LOD(f_{ac}) := \frac{U_{co}(f_{ac})}{S_V(f_{ac})}, \quad (4)$$

with the voltage noise density U_{co} of $u_{co}(t)$ measured without applying the magnetic test signal B_{ac} .

All signal and noise measurements were performed with a high-resolution A/D and D/A converter *Fireface UFX+* (RME, Germany) in a magnetically shielded setup⁴ with a mu-metal cylinder ZG1 (Aaronia AG, Germany). The AD745-based charge amplifier⁴² has a feedback capacitance of $C_f = 33$ pF and a feedback resistance of $R_f = 5$ G Ω .

RESULTS AND DISCUSSION

To analyze the magnetic properties, i.e., the delta-E effect of the two sensors, admittance measurements were performed at various applied magnetic flux densities $\mu_0 H$ starting close to the negative magnetic saturation at -10 mT. An excitation voltage amplitude of $u_{ex} = 10$ mV was used. With a modified Butterworth Van Dyke (mBvD) equivalent circuit model like in Ref. 32, the resonance frequencies f_r and quality factors Q were extracted. The $f_r(H)$ curves are plotted in Fig. 2(a), normalized to the respective maximum values of $f_{r,max}(AlN) = 9119.5$ kHz and $f_{r,max}(AlScN) = 7546.8$ kHz. Resonance detuning via the delta-E effect has been investigated before²⁸ in similar cantilever sensors and is generally well understood (e.g., Refs. 40 and 41).

In Fig. 2(b), the corresponding derivatives of $f_r(H)$, the magnetic sensitivities S_H are shown. Both sensors show a similar maximum drop in the resonance frequency around 0.75% and maximum magnetic sensitivities of ≈ 55 Hz/mT (AlN) and ≈ 37 Hz/mT (AlScN). These values are within the typical range reported for other delta-E effect sensors (e.g., Refs. 16, 23, 26, 27, and 34).

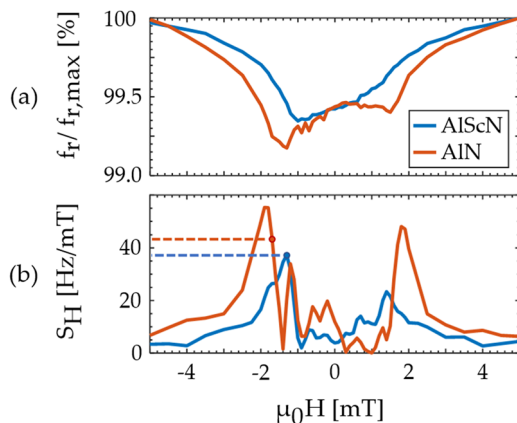


FIG. 2. (a) Normalized resonance frequency of the AlScN and the AlN sensors, extracted from admittance curves measured with an excitation voltage amplitude of $u_{ex} = 10$ mV, and (b) magnetic sensitivity S_H calculated from the data in (a), and the values of S_H at the magnetic bias fields $B_{AIN} = -1.7$ mT and $B_{AlScN} = -1.3$ mT are indicated.

Here, we do not operate both sensors at maximum S_H but chose $B_{AIN} = -1.7$ mT and $B_{AlScN} = -1.3$ mT. At these bias flux densities, $S_H \approx (40 \pm 5)$ Hz/mT for both sensors. The mBvD parameters at B_{AIN} and B_{AlScN} are given in the [supplementary material](#). From these parameters, we obtain resonance frequencies of $f_{r,AIN} = 9045.5$ Hz and $f_{r,AlScN} = 7508.2$ Hz and quality factors of $Q_{AIN} = 570$ and $Q_{AlScN} = 635$. All following measurements are performed at these bias fields.

In Fig. 3(a), the electrical admittance magnitude $|Y|$ of AlN and AlScN at B_{AIN} and B_{AlScN} is plotted as functions of the excitation frequency f_{ex} , shifted by the respective f_r . The AlScN sensor shows a significantly increased admittance magnitude $|Y|$ compared to the AlN sensor. From $|Y|$, the corresponding electrical amplitude sensitivities $S_{el,am}$ are calculated and plotted in Fig. 3(b). In mechanical resonance, $S_{el,am}$ of the AlScN sensor is approximately a factor of 8 times higher than $S_{el,am}$ of the AlN sensor. Averaging over 20 measurements results in mean values and standard deviations of $S_{el,am}(AlN) = -4.6 \pm 0.6$ nS/Hz and $S_{el,am}(AlScN) = -38.9 \pm 2.6$ nS/Hz at f_r . An overview of all mean values is given in the [supplementary material](#).

In Figs. 3(c) and 3(d), the phase angle ϕ and its derivative the electrical phase sensitivity $S_{el,pm}$ are plotted, calculated with the mBvD model. Because the minima of ϕ are close to f_r , $S_{el,pm}$ at f_r is close to 0 for both sensors. Hence, the following discussions are focused on the amplitude sensitivities. The factor of 8 in $S_{el,am}$ might be caused by the different piezoelectric materials. Yet, due to the large difference in the resonance frequencies (≈ 1.5 kHz) of the two sensors, additional geometrical influences cannot be excluded.

To distinguish geometric from material effects, a detailed finite element method (FEM) model is set up (COMSOL MultiphysicsTM, v. 5.4). This model solves the mechanical equations of motion⁴³ with linear strains, coupled to the electrostatic equations⁴⁴ via the piezoelectric constitutive relations.⁴⁵ As we deal with small displacements and rather low frequencies, both major approximations are justified.

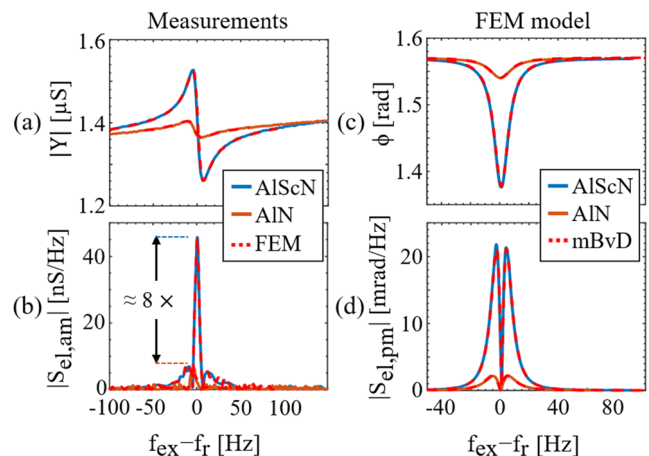


FIG. 3. (a) Measured magnitude $|Y|$ of electrical sensor admittance Y at magnetic bias flux densities B_{AIN} and B_{AlScN} and (b) the electrical magnitude sensitivity $S_{el,am}$. (c) Phase angle ϕ calculated with the mBvD model and (d) its derivative, the electrical phase sensitivity $S_{el,pm}$; all measurements and mBvD results are compared with finite element method calculations, and all frequency axes are shifted by the mechanical resonance frequency f_r of the respective sensor.

The cantilever's geometry is approximated with a stratified structure of thin rectangular cuboids of different lengths and widths that correspond to the dimensions of the mask layout. Details on the model and all material parameters^{59–71} and layer dimensions are given in the [supplementary material](#).

During the wet etching process that releases the cantilever, the three-layer structure of SiO₂ and poly-Si can be underetched at the anchor. The depth of underetching is represented by the parameter L_{etch} in the model. The components of the piezoelectric coupling tensor and the values of L_{etch} are determined from a fit of the model to the data in [Fig. 3\(a\)](#).

With the measured quality factors ($Q_{\text{AlN}} = 570$, $Q_{\text{AlScN}} = 635$), the simulations match the measurements and mBvD simulations in [Fig. 3](#) very well. From the fit, we obtain underetch lengths of $L_{\text{etch}} = 80.7 \mu\text{m}$ for AlN and $L_{\text{etch}} = 275.0 \mu\text{m}$ for AlScN. Other factors such as geometric inaccuracies and stress could contribute to L_{etch} . It is worth mentioning that the difference in resonance frequency cannot be explained by reasonable variations in material parameters or layer thicknesses alone. Hence, they were considered to be fixed parameters during the fit. The other fitting parameters are given in [Table I](#). For the components of the piezoelectric coupling tensor e_{ij} , we obtain values overall close to *ab initio* calculations,⁴⁶ yet slightly smaller.

The admittance measurements in [Fig. 3](#) are repeated for an increase in the excitation voltage amplitude \hat{u}_{ex} . Example measurements of $|Y|$ at three different \hat{u}_{ex} are shown in [Figs. 4\(a\)](#) and [4\(b\)](#). With an increase in \hat{u}_{ex} , the resonance visible in the admittance magnitude incrementally shifts toward lower frequencies. The difference between the maximum and minimum values decreases, and the curvature around the maximum increases. Whereas the linear mBvD model matched the measurements at $\hat{u}_{\text{ex}} = 10 \text{ mV}$ very well, it is not sufficient at higher voltage amplitudes. Instead, a nonlinear equivalent circuit model similar to that of [Ref. 47](#) is implemented ([supplementary material](#)). It extends the previous model by an additional cubic restoring force with capacitance C_3 in the LCR resonator circuit of the mBvD model. The ratio C_3/C_r of the additional capacitance C_3 and the linear capacitance C_r is used as a quantitative measure for the nonlinearity of the resonator. From the nonlinear mBvD fit, the linear resonance frequencies and the quality factors are extracted.

As demonstrated in [Figs. 4\(a\)](#) and [4\(b\)](#), the nonlinear model matches the measurements for both sensors very well. With an increase in the voltage amplitude \hat{u}_{ex} , the admittance magnitude $|Y|$ becomes increasingly asymmetric. The electrical resonance and antiresonance peaks shift to lower frequencies, and the difference in their admittance magnitude decreases. These effects are significantly more distinct in the AlScN sensor. Accordingly, the nonlinearity

TABLE I. Independent components e_{ij} of the hexagonal piezoelectric coupling tensor and the shunt capacitance C_0 found from the fit of the FEM model to the admittance measurements in [Fig. 3\(a\)](#). The cantilevers are oriented lengthwise in the x_1 -direction and widthwise along the x_2 -direction.

	e_{31} (C/m ²)	e_{33} (C/m ²)	e_{24} (C/m ²)	C_0 (pF)
AlN	-0.3703	0.8597	-0.2292	9.58
AlScN	-0.7569	2.1757	-0.2420	0.95

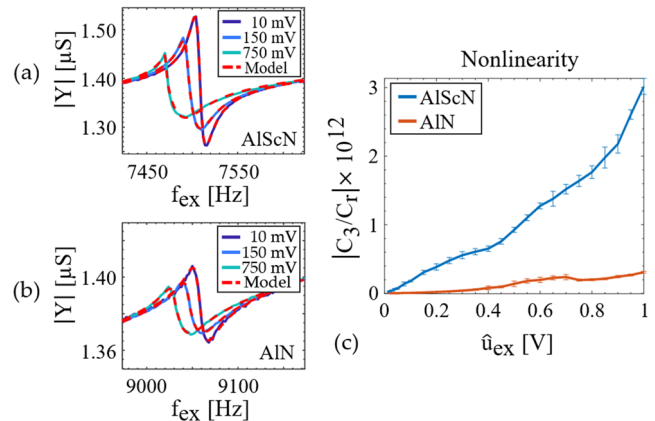


FIG. 4. (a) Example fits of the nonlinear equivalent circuit model to the measured admittance magnitude of the AlScN sample and (b) the AlN sample at three different excitation voltage amplitudes. (c) The absolute ratio of capacitances C_3 and C_r as a measure for the nonlinearity of the resonator as functions of the excitation voltage amplitude \hat{u}_{ex} .

increases with \hat{u}_{ex} and is more than an order of magnitude larger in the AlScN sensor [[Fig. 4\(c\)](#)].

Such resonator nonlinearities are expected to emerge from the nonlinearity of the magnetostrictive stress–strain relation (e.g., [Refs. 48–50](#)). During sensor operation, the oscillating stress in the magnetic layer induces an alternating magnetization, which is accompanied by a magnetostrictive strain. With an increase in \hat{u}_{ex} , the amplitude of stress and induced magnetostriction increases, and the nonlinearity becomes visible for both sensors, as shown in [Fig. 4](#). Yet, the amplitude of the oscillating stress does not only depend on \hat{u}_{ex} but also on the piezoelectric material. AlScN exhibits significantly larger electromechanical coupling factors compared to AlN. The larger coupling causes a larger stress amplitude and results in a larger nonlinearity at the same \hat{u}_{ex} , as visible in [Fig. 4](#). A strong magnetic bias field ($\approx 80 \text{ mT}$) was applied to fix the magnetization and thereby suppress the change in the magnetostrictive strain during the oscillation of the cantilever. As expected, the nonlinearity vanishes, which confirms its magnetic origin ([supplementary material](#)). It is worth noting that the nonlinear stress–strain relation is not only an inherent property of magnetostrictive materials⁴⁵ but also the origin of the magnetic field dependent delta-E effect.^{28,40,51,52} Consequently, the delta-E effect sensor concept is necessarily connected with nonlinearities.

Because the nonlinearity changes the admittance characteristic, it can potentially reduce the electrical sensitivity. How exactly the electrical sensitivity changes with \hat{u}_{ex} depends also on the operation frequency f_{ex} chosen. In the present case, we observe a reduction in $S_{\text{el,am}}$ at $f_{\text{ex}} = f_r$ by more than 99% (AlScN) and 85% (AlN) with \hat{u}_{ex} ([supplementary material](#)). Besides the nonlinearity, the quality factor Q can strongly influence the admittance and the sensitivity of delta-E effect sensors.³² A reduction in Q with an increase in \hat{u}_{ex} was reported previously^{24,31} with similar magnetoelastic resonators and could be explained with loss from stress-induced magnetic domain activity.⁵³ In our case, the quality factors of both sensors decrease by up to $40\% \pm 5\%$ with \hat{u}_{ex} . Consequently, we expect a significant contribution of Q to the reduction in the electrical sensitivity.

In the following, the mean resonance frequency as a function of \hat{u}_{ex} is used as an excitation frequency for operating the sensor at larger voltage amplitudes. Signal and noise are measured 20 times, respectively, at each \hat{u}_{ex} . During the signal measurements, a sinusoidal magnetic test signal with an amplitude of $\hat{B}_{ac} = 1 \mu\text{T}$ and a frequency of $f_{ac} = 10 \text{ Hz}$ is applied. From the measurements, we obtain the voltage sensitivity S_V and the limit of detection (LOD) [Eqs. (3) and (4)] at a frequency of 10 Hz. The resulting mean values and standard deviations are plotted in Fig. 5.

A linear signal model based on Eq. (1) is set up like that in Ref. 32 to calculate the expected voltage sensitivity S_V . As input we use the admittance data obtained from the measurements at $\hat{u}_{ex} = 10 \text{ mV}$. With the same input dataset, we estimate S_V at larger \hat{u}_{ex} . Because the sensitivity changes with \hat{u}_{ex} and nonlinearities are present (Fig. 4), the simulations at larger \hat{u}_{ex} represent rather ideal reference values than predictions.

A comparison of measured and modeled voltage sensitivity is given in Fig. 5(a). At $\hat{u}_{ex} = 10 \text{ mV}$, the modeled $S_V = 0.97 \text{ V/T}$ (AlN) and $S_V = 7.9 \text{ V/T}$ (AlScN) match the measurement of $S_V = (0.84 \pm 0.4) \text{ V/T}$ (AlN) and $S_V = (7.0 \pm 1.9) \text{ V/T}$ (AlScN) very well. The simulations reproduce the factor of ~ 8 between $S_V(\text{AlScN})$ and $S_V(\text{AlN})$ seen in the measurements. As expected from Eq. (1), the modeled S_V increases linearly with \hat{u}_{ex} . In contrast, a deviation from this linearity is present in the measurements. After an initial drop of the measured $S_V(\text{AlN})$ by a factor of 2 at $\hat{u}_{ex} = 20 \text{ mV}$, relative to the simulation, it continues increasing approximately linearly. In contrast, $S_V(\text{AlScN})$ continuously decreases relative to the reference, until deviations of almost a factor of 8 are present at large \hat{u}_{ex} .

Such deviations are expected due to the altered admittance and reduced electrical sensitivity. Additional effects not considered in the model might contribute to the behavior of S_V with \hat{u}_{ex} . The magnetic susceptibility can change with \hat{u}_{ex} ⁵⁴ and potentially alter the magnetic sensitivity.²⁴ Overall, the behavior of S_V and the output signal with \hat{u}_{ex} is complex, and a detailed analysis of all potential contributions is beyond the scope of this paper.

The measured voltage noise density U_{co} at $f_{ac} = 10 \text{ Hz}$ is plotted in Fig. 5(b). At small \hat{u}_{ex} , it is approximately

constant and similar for both sensors. At around $\hat{u}_{ex} = 100 \text{ mV}$, $U_{co}(\text{AlScN})$ increases significantly with \hat{u}_{ex} . Notably, larger amplitudes are required to reach this regime with the AlN sensor. In this regime, $U_{co}(\text{AlN})$ is approximately a factor of 8 times smaller than $U_{co}(\text{AlScN})$.

Comparing the data with results from a previously developed noise model³⁰ suggests that thermal–electrical noise of the charge amplifier dominates the noise floor at small \hat{u}_{ex} . The slightly different noise densities of the two sensors in this regime are expected from the different sensor capacities that alter the amplification factor of the charge amplifier. The increase in noise at larger \hat{u}_{ex} was previously explained with magnetic noise, induced by alternating stress during the oscillation of the cantilever.^{30,31} In magnetically modulated cantilevers, the noise has been linked directly to magnetic domain activity,⁵³ which might similarly apply here.

In Fig. 5(c), the LOD estimated with S_V and U_{co} is plotted as a function of the excitation voltage amplitude \hat{u}_{ex} . Overall, a factor of 8 in LOD is gained with the AlScN sensor, but only at small \hat{u}_{ex} where the thermal–electrical noise is dominant. Both LOD curves reach a minimum roughly at the voltage amplitudes where the magnetic noise starts to dominate the noise floor. With approximately $(40 \pm 5)n\text{T}/\sqrt{\text{Hz}}$, the minimum LOD at 10 Hz of both sensors is identical.

It might be possible to reduce the thermal–electrical noise level using optimized amplifiers^{32,42} and suppress the magnetic noise with advanced magnetic multilayers.^{55,56} If magnetic noise can be sufficiently reduced, the thermal–mechanical noise of the resonator represents the limiting sensor intrinsic noise source at room temperature.^{31,57} It depends on the geometry and the electromechanical properties of the resonator and, therefore, also on the piezoelectric material.^{30,58} In the following, we extend our discussion to this fundamental noise limit to gain more general insights into the signal, noise, and minimum LOD as functions of the piezoelectric material properties.

With the FEM model, we calculate the sensor admittance as a function of the piezoelectric charge–stress coefficient tensor $d = x \cdot d_{\text{AlScN}}$. Here, $d_{\text{AlScN}} = e_{\text{AlScN}} C_{\text{AlScN}}^{-1}$ is the piezoelectric charge–stress coefficient tensor of AlScN. It is given by the double-dot product of the inverse stiffness tensor C_{AlScN}^{-1} and the piezoelectric coupling tensor e_{AlScN} . In the simulation, we use the geometry and all other material properties of the AlScN sensor and vary only the scaling factor x . The resulting amplitude sensitivity $S_{am}(x)$ satisfies a quadratic fit very well [Fig. 6(a)]. Because S_{am} is the dominating sensitivity at our excitation frequency $f_{ex} = f_r$, also $S_V(x)$ is approximately quadratic [Fig. 6(b)]. In Fig. 6(c), the modeled voltage noise density $U_{co}(x)$ is plotted, considering only thermal–mechanical noise. It is calculated with a previously developed model^{32,57} from the simulated admittance curves. Consistent with analytical estimations,³⁷ the thermal–mechanical noise increases linearly with x . Consequently, the LOD estimate [Eq. (4)] improves $\text{LOD} \propto 1/x$ if thermal–mechanical noise is dominant. In contrast to the direct ME detection, we excite the resonator electrically in the delta-E operation scheme. Hence, the deflection magnitude of the resonator increases linearly with d and contributes to the quadratic behavior observed in the sensitivities and the output signal amplitude. For the given geometry and resonance mode, the quadratic response is dominated by components d_{31} and d_{33} of d . Details are given in the supplementary material.

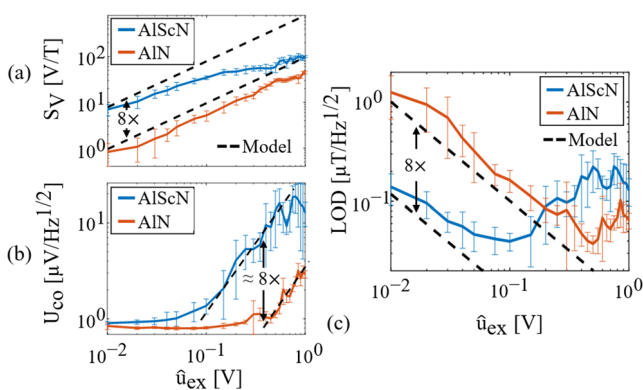


FIG. 5. (a) Measured voltage sensitivity S_V with standard deviation and modeled reference, calculated using the data at $\hat{u}_{ex} = 10 \text{ mV}$, and (b) voltage noise density U_{co} with standard deviation, and black dotted lines are to guide the eye. (c) Limit of detection (LOD) at 10 Hz estimated with the data from (a) and (b) and model results as a reference.

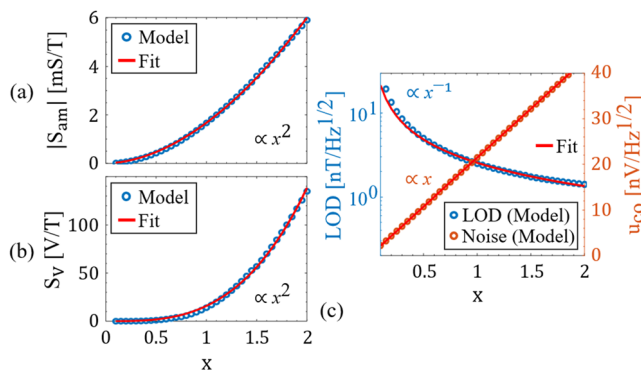


FIG. 6. Modeled sensitivities, noise, and LOD at 10 Hz and $\hat{u}_{ex} = 10$ mV as a function of the piezoelectric stress–charge coefficient tensor $\mathbf{d} = x \cdot \mathbf{d}_{\text{AIScN}}$. (a) Numerically calculated amplitude sensitivity S_{am} . (b) Voltage sensitivity S_V using $S_{mag} = 40$ kHz/T and (c) the theoretical minimum LOD estimated using the voltage noise density u_{co} , considering only thermal–mechanical noise.

Because $S_V(x) \propto x^2$, we expect $\text{LOD} \propto 1/x^2$ for constant thermal–electrical noise. At first glance, this seems to be contradictory to the factor of 8 found experimentally. Additional FEM simulations reveal that this is mainly caused by the differences in the quality factor, stiffness tensor, and geometry of the sensors. Whereas the reduced underetching of the AlN sensor increases S_V compared to the AIScN sensor, the lower quality factor and different stiffness tensors have the opposite effect. Simulations with the identical model geometry and quality factor show that AIScN as a piezoelectric material results in ≈ 7.5 times higher electrical sensitivity and voltage sensitivity compared to AlN.

SUMMARY AND CONCLUSION

In summary, we identified the influence of the piezoelectric material on the sensing characteristics of delta-E effect sensors. Experiments were performed on AIScN- and AlN-based cantilever sensors of identical design. The results were analyzed regarding sensitivity, noise, linearity, and limit of detection (LOD). The measurements are supported by an electromechanical finite element and a signal-and-noise model.

Within the simulated parameter range, both the electrical magnitude sensitivity $S_{el,am}$ and the voltage sensitivity S_V scale quadratically with the dominating components d_{ij} of the piezoelectric coefficient tensor \mathbf{d} . In the regime of intrinsic thermal–mechanical noise, the $\text{LOD} \propto 1/d_{ij}$ because the thermal–mechanical noise $\propto d_{ij}$. Consequently, our delta-E effect sensors could benefit from an increase in the piezoelectric coefficients much stronger than conventional magnetoelectric sensors, where the LOD is constant due to a merely linear increase in the output signal amplitude.³⁷

Considering not only d_{ij} but also the complete piezoelectric material properties, the model predicts a $7.5\times$ enhanced $S_{el,am}$ and S_V for the AIScN sensor. In the present case, the two analyzed sensors additionally differ in geometry and slightly in their quality factors. In total, this results in an $8\times$ improved voltage sensitivity and LOD measured with the AIScN sensor. This is well reproduced by

the model. The improvement in LOD is limited to small excitation amplitudes where thermal–electrical noise is dominant. With an increase in the excitation amplitude, the factor of 8 decreases and resonator nonlinearities of magnetic origin occur. They can be described and quantified with a nonlinear equivalent circuit model and are up to an order of magnitude larger in the AIScN sensor. Overall, the minimum LOD does not change due to an earlier onset of magnetic noise in the AIScN sensor. This result supports theoretical magnetic noise considerations in Ref. 31 experimentally. Using exchange bias multilayers as in Refs. 55 and 56, it might be possible to reduce the magnetic noise in the future and push its onset to higher excitation voltage amplitudes. The large improvement in the output signal amplitude makes AIScN a promising candidate for tapping into new kinds of resonance modes that are otherwise poorly excited.

SUPPLEMENTARY MATERIAL

See the [supplementary material](#) for the material parameters used, details on the models, the fitting parameters found, and additional measurements.

ACKNOWLEDGMENTS

We thank the German Research Foundation (DFG) for funding this work through the Collaborative Research Centre CRC 1261 “Magnetoelectric Sensors”: From Composite Materials to Biomagnetic Diagnostics. The authors thank Lars Thormählen for the deposition of the magnetic layers.

DATA AVAILABILITY

The data that support the findings of this study are available from the corresponding author upon reasonable request.

REFERENCES

- V. Sakkalis, *Comput. Biol. Med.* **41**, 1110 (2011).
- J. S. W. Kwong, B. Leithäuser, J.-W. Park, and C.-M. Yu, *Int. J. Cardiol.* **167**, 1835 (2013).
- L. Duez, S. Beniczky, H. Tankisi, P. O. Hansen, P. Sidenius, A. Sabers, and A. Fuglsang-Frederiksen, *Clin. Neurophysiol.* **127**, 3301 (2016).
- R. Jahns, R. Knochel, H. Greve, E. Woltermann, E. Lage, and E. Quandt, in *Proceedings of the 2011 IEEE International Symposium on Medical Measurement and Applications, MeMeA 2011* (IEEE, 2011).
- J. Reermann, P. Durdaut, S. Salzer, T. Demming, A. Piorra, E. Quandt, N. Frey, M. Höft, and G. Schmidt, *Meas. J. Int. Meas. Conf.* **116**, 230 (2018).
- R. M. Friedrich, S. Zabel, A. Galka, N. Lukat, J. M. Wagner, C. Kirchhof, E. Quandt, J. McCord, C. Selhuber-Unkel, M. Siniatchkin, and F. Faupel, *Sci. Rep.* **9**, 2086 (2019).
- S. Zuo, J. Schmalz, M.-O. Ozden, M. Gerken, J. Su, F. Niekil, F. Lofink, K. Nazarpour, and H. Heidari, *IEEE Trans. Biomed. Circuits Syst.* **14**, 971 (2020).
- C. Tu, Z.-Q. Chu, B. Spetzler, P. Hayes, C.-Z. Dong, X.-F. Liang, H.-H. Chen, Y.-F. He, Y.-Y. Wei, I. Lisenkov, H. Lin, Y.-H. Lin, J. McCord, F. Faupel, E. Quandt, and N. Sun, *Materials* **12**, 2259 (2019).
- C. W. Nan, M. I. Bichurin, S. Dong, D. Viehland, and G. Srinivasan, *J. Appl. Phys.* **103**, 031101 (2008).
- R. Kleiner, D. Koelle, F. Ludwig, and J. Clarke, *Proc. IEEE* **92**, 1534 (2004).
- C. N. Johnson, P. D. D. Schwindt, and M. Weisend, *Phys. Med. Biol.* **58**, 6065 (2013).

- ¹²W. C. Griffith, S. Knappe, and J. Kitching, *Opt. Express* **18**, 27167 (2010).
- ¹³E. Yarar, S. Salzer, V. Hrkac, A. Piorra, M. Höft, R. Knöchel, L. Kienle, and E. Quandt, *Appl. Phys. Lett.* **109**, 022901 (2016).
- ¹⁴J. Reermann, S. Zabel, C. Kirchhof, E. Quandt, F. Faupel, and G. Schmidt, *IEEE Sens. J.* **16**, 4891 (2016).
- ¹⁵R. Osiander, S. A. Ecelberger, R. B. Givens, D. K. Wickenden, J. C. Murphy, and T. J. Kistenmacher, *Appl. Phys. Lett.* **69**, 2930 (1996).
- ¹⁶N. Yoshizawa, I. Yamamoto, and Y. Shimada, *IEEE Trans. Magn.* **41**, 4359 (2005).
- ¹⁷M. Li, A. Matyushov, C. Dong, H. Chen, H. Lin, T. Nan, Z. Qian, M. Rinaldi, Y. Lin, and N. X. Sun, *Appl. Phys. Lett.* **110**, 143510 (2017).
- ¹⁸S. P. Bennett, J. W. Baldwin, M. Staruch, B. R. Matis, J. Lacombe, O. M. J. van 't Erve, K. Bussmann, M. Metzler, N. Gottron, W. Zappone, R. Lacombe, and P. Finkel, *Appl. Phys. Lett.* **111**, 252903 (2017).
- ¹⁹L. Bian, Y. Wen, Y. Wu, P. Li, Z. Wu, Y. Jia, and Z. Zhu, *IEEE Trans. Electron Devices* **65**, 2585 (2018).
- ²⁰B. Gojdka, R. Jahns, K. Meuris, H. Greve, R. Adelung, E. Quandt, R. Knöchel, and F. Faupel, *Appl. Phys. Lett.* **99**, 223502 (2011).
- ²¹T. Nan, Y. Hui, M. Rinaldi, and N. X. Sun, *Sci. Rep.* **3**, 1985 (2013).
- ²²J. Kiser, P. Finkel, J. Gao, C. Dolabdjian, J. Li, and D. Viehland, *Appl. Phys. Lett.* **102**, 042909 (2013).
- ²³R. Jahns, S. Zabel, S. Marauska, B. Gojdka, B. Wagner, R. Knöchel, R. Adelung, and F. Faupel, *Appl. Phys. Lett.* **105**, 2012 (2014).
- ²⁴S. Zabel, C. Kirchhof, E. Yarar, D. Meyners, E. Quandt, and F. Faupel, *Appl. Phys. Lett.* **107**, 152402 (2015).
- ²⁵Y. Hui, T. Nan, N. X. Sun, and M. Rinaldi, *J. Microelectromech. Syst.* **24**, 134 (2015).
- ²⁶S. Zabel, J. Reermann, S. Fichtner, C. Kirchhof, E. Quandt, B. Wagner, G. Schmidt, and F. Faupel, *Appl. Phys. Lett.* **108**, 222401 (2016).
- ²⁷M. Staruch, M.-T. Yang, J. F. Li, C. Dolabdjian, D. Viehland, and P. Finkel, *Appl. Phys. Lett.* **111**, 032905 (2017).
- ²⁸B. Spetzler, C. Kirchhof, E. Quandt, J. McCord, and F. Faupel, *Phys. Rev. Appl.* **12**, 064036 (2019).
- ²⁹B. Spetzler, E. V. Golubeva, C. Müller, J. McCord, and F. Faupel, *Sensors* **19**, 4769 (2019).
- ³⁰P. Durdaut, J. Reermann, S. Zabel, C. Kirchhof, E. Quandt, F. Faupel, G. Schmidt, R. Knöchel, and M. Höft, *IEEE Trans. Instrum. Meas.* **66**, 2771 (2017).
- ³¹P. Durdaut, E. Rubiola, J. Friedt, C. Müller, B. Spetzler, C. Kirchhof, D. Meyners, E. Quandt, F. Faupel, J. McCord, R. Knöchel, and M. Höft, *J. Microelectromech. Syst.* **29**, 1347 (2020).
- ³²B. Spetzler, C. Kirchhof, J. Reermann, P. Durdaut, M. Höft, G. Schmidt, E. Quandt, and F. Faupel, *Appl. Phys. Lett.* **114**, 183504 (2019).
- ³³N. Lukat, R. M. Friedrich, B. Spetzler, C. Kirchhof, C. Arndt, L. Thormählen, F. Faupel, and C. Selhuber-Unkel, *Sens. Actuators, A* **309**, 112023 (2020).
- ³⁴L. Bian, Y. Wen, P. Li, Y. Wu, X. Zhang, and M. Li, *Sens. Actuators, A* **247**, 453 (2016).
- ³⁵S. Fichtner, T. Reimer, S. Chemnitz, F. Lofink, and B. Wagner, *APL Mater.* **3**, 116102 (2015).
- ³⁶S. Fichtner, N. Wolff, G. Krishnamurthy, A. Petraru, S. Bohse, F. Lofink, S. Chemnitz, H. Kohlstedt, L. Kienle, and B. Wagner, *J. Appl. Phys.* **122**, 035301 (2017).
- ³⁷J. Su, F. Niekiel, S. Fichtner, L. Thormaehlen, C. Kirchhof, D. Meyners, E. Quandt, B. Wagner, and F. Lofink, *Appl. Phys. Lett.* **117**, 132903 (2020).
- ³⁸S. Marauska, M. Claus, T. Lisec, and B. Wagner, *Microsyst. Technol.* **19**, 1119 (2013).
- ³⁹J. Su, F. Niekiel, S. Fichtner, C. Kirchhof, D. Meyners, E. Quandt, B. Wagner, and F. Lofink, *J. Micromech. Microeng.* **30**, 075009 (2020).
- ⁴⁰J. D. Livingston, *Phys. Status Solidi A* **70**, 591 (1982).
- ⁴¹P. T. Squire, *J. Magn. Magn. Mater.* **140-144**, 1829 (1995).
- ⁴²P. Durdaut, V. Penner, C. Kirchhof, E. Quandt, R. Knöchel, and M. Höft, *IEEE Sens. J.* **17**, 7364 (2017).
- ⁴³S. Avdiaj, J. Setina, and N. Sylva, *Mater. Technol.* **43**, 283 (2009).
- ⁴⁴J. Yang, *An Introduction to the Theory of Piezoelectricity*, 2nd ed. (Springer International Publishing, Cham, 2018).
- ⁴⁵IEEE Standards Board, *IEEE Trans. Sonics Ultrason.* **20**, 67 (1973).
- ⁴⁶M. A. Caro, S. Zhang, T. Riekkinen, M. Ylilampi, M. A. Moram, O. Lopez-Acevedo, J. Molarius, and T. Laurila, *J. Phys.: Condens. Matter* **27**, 245901 (2015).
- ⁴⁷J. Segovia-Fernandez and G. Piazza, *J. Microelectromech. Syst.* **22**, 976 (2013).
- ⁴⁸M. Kersten, *Z. Phys.* **85**, 708 (1933).
- ⁴⁹E. W. Lee, *Rep. Prog. Phys.* **18**, 184 (1955).
- ⁵⁰S. Datta, J. Atulashimha, C. Mudivarthi, and A. B. Flatau, *J. Magn. Magn. Mater.* **322**, 2135 (2010).
- ⁵¹S. Atalay and P. T. Squire, *J. Appl. Phys.* **70**, 6516 (1991).
- ⁵²P. T. Squire, S. Atalay, and H. Chiriach, *IEEE Trans. Magn.* **36**, 3433 (2000).
- ⁵³N. O. Urs, E. Golubeva, V. Röbisch, S. Toxvaerd, S. Deldar, R. Knöchel, M. Höft, E. Quandt, D. Meyners, and J. McCord, *Phys. Rev. Appl.* **10**, 024018 (2020).
- ⁵⁴D. Castilla, R. Yanes, M. Sinusia, G. Fuentes, J. Grandal, M. Maicas, T. E. G. Álvarez-arenas, M. Muñoz, L. Torres, L. López, and J. L. Prieto, *Sci. Rep.* **10**, 9413 (2020).
- ⁵⁵V. Röbisch, E. Yarar, N. O. Urs, I. Teliban, R. Knöchel, J. McCord, E. Quandt, and D. Meyners, *J. Appl. Phys.* **117**, 17B513 (2015).
- ⁵⁶M. Jovičević Klug, L. Thormählen, V. Röbisch, S. D. Toxvaerd, M. Höft, R. Knöchel, E. Quandt, D. Meyners, and J. McCord, *Appl. Phys. Lett.* **114**, 192410 (2019).
- ⁵⁷P. Durdaut, S. Salzer, J. Reermann, V. Röbisch, P. Hayes, A. Piorra, D. Meyners, E. Quandt, G. Schmidt, R. Knöchel, and M. Höft, *IEEE Sens. J.* **17**, 2338 (2017).
- ⁵⁸P. Durdaut, *Ausleseverfahren Und Rauschmodellierung Für Magnetoelastische Und Magnetoelastische Sensorsysteme* (Kiel University, 2019).
- ⁵⁹A. Ludwig and E. Quandt, *IEEE Trans. Magn.* **38**, 2829 (2002).
- ⁶⁰W. N. Sharpe, K. T. Turner, and R. L. Edwards, *Exp. Mech.* **39**, 162 (1999).
- ⁶¹W. N. Sharpe, B. Yuan, R. Vaidyanathan, and R. L. Edwards, in *Proceedings of the IEEE Micro Electro Mechanical Systems* (IEEE, 1997), p. 424.
- ⁶²M. J. Madou, *Fundamentals of Microfabrication: The Science of Miniaturization*, 2nd ed. (CRC Press, Boca Raton, FL, 2002).
- ⁶³A. Khan, J. Philip, and P. Hess, *J. Appl. Phys.* **95**, 1667 (2004).
- ⁶⁴G. Krotz, W. Legner, C. Wagner, H. Moeller, H. Sonntag, and G. Mueller, in *Proceedings of the International Solid-State Sensors and Actuators Conference - TRANSDUCERS '95* (IEEE, 1995), Vol. 2, p. 186.
- ⁶⁵K. E. Petersen, *IEEE Trans. Electron Devices* **25**, 1241 (1978).
- ⁶⁶M. T. Kim, *Thin Solid Films* **283**, 12 (1996).
- ⁶⁷J. G. Noel, *IET Circuits, Devices Syst.* **10**, 156 (2016).
- ⁶⁸A. T. Collins, E. C. Lightowlers, and P. J. Dean, *Phys. Rev.* **158**, 833 (1967).
- ⁶⁹G. A. Slack, *J. Phys. Chem. Solids* **34**, 321 (1973).
- ⁷⁰R. Lifshitz and M. C. Cross, in *Reviews of Nonlinear Dynamics and Complexity*, edited by G. Radons, B. Rumpf, and H. G. Schuster (Wiley-VCH Verlag GmbH & Co. KGaA, Weinheim, 2010), p. 221.
- ⁷¹V. Kaajakari, T. Mattila, A. Oja, and H. Seppä, *J. Microelectromech. Syst.* **13**, 715 (2004).

SUPPLEMENTARY MATERIAL

Linear mBvD fit

In the linear mBvD model (Fig. S1), a series LCR circuit with inductance L , capacitance C , and resistance R is connected in parallel with a capacitance C_p and a resistance R_p , as shown in Fig. S1.

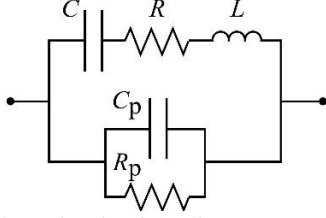


Fig. S1 Equivalent circuit of the linear mBvD model used to describe the sensor admittance at small excitation voltages \hat{u}_{ex} .

Table S1: mBVD parameters extracted from the two example measurements in Fig. 3a at $B_{AIN} = -1.7$ mT and $B_{AlScN} = -1.3$ mT.

	L [kH]	R [M Ω]	C [fF]	R _p [M Ω]	C _p [pF]	Q	f _r [kHz]
AIN	233. 7	23.34	1.3 2	10 ²⁰	24. 3	57 0	9045. 5
AlSc N	50.1	3.72	8.9 6	10 ²⁰	29. 4	63 5	7508. 2

Linear mBvD fits were performed for 20 admittance measurements at $B_{AIN} = -1.7$ mT and $B_{AlScN} = -1.3$ mT with a voltage amplitude of $\hat{u}_{ex} = 10$ mV. The fits were evaluated at the respective resonance frequency. Averaging results in mean values and standard deviations for the impedance magnitudes Y_0 , phase angles ϕ_0 and the electrical sensitivities $S_{el,am}$, and $S_{el,pm}$. The amplitude sensitivities S_{am} and phase sensitivities S_{pm} were calculated from the mean values using $S_{mag} = 40$ Hz/mT. All results are shown in Table S2.

Table S2: Mean values and standard deviations resulting from averaging over 20 measurements at an excitation voltage amplitude of $\hat{u}_{ex} = 10$ mV and $B_{AIN} = -1.7$ mT and $B_{AlScN} = -1.3$ mT. The amplitude and phase sensitivities S_{am} and S_{pm} are calculated with the mean values and $S_{mag} = 40$ Hz/mT.

	AIN	AlScN
$S_{el,am}$ [nS/Hz]	-4.6 \pm 0.6	-38.9 \pm 2.6
$S_{el,pm}$ [mrad/Hz]	-0.7 \pm 0.5	-5.5 \pm 1.9
Y_0 [μ S]	1.38 \pm 0.003	1.37 \pm 0.01
ϕ_0 [rad]	1.54.9 \pm 0.02	1.43 \pm 0.14
Q	496 \pm 249	624 \pm 8
S_{am} [mS/T]	-0.18	-1.60
S_{pm} [rad/T]	-28.3	-220.6

Finite element method model

The material parameters of the mechanically isotropic materials used in the finite element model are summarized in Table S3. With profilometer and microbalance measurements we experimentally determined the density of the sputter deposited FeCoSiB. The measurements were performed on a

6-inch wafer with a mean FeCoSiB layer thickness of approximately 1.5 μ m. A density of $\rho = (7870 \pm 1350)$ kg/m³ was obtained for the FeCoSiB. In the simulation, a density of $\rho = 7700$ kg/m³ is used.

Table S3: Young's modulus E , Poisson's ratio ν , and density ρ of the isotropic materials used in the finite element model. Their values are chosen in a range given by the respective reference. The density of FeCoSiB was estimated from measurements.

Material	E [GPa]	ν	ρ [kg/m ³]
FeCoSiB	150 ^{28,59}	0.30 ²⁸	7700
Poly-Si	160 ^{60,61}	0.22 ⁶¹	2330 ⁶²
Si ₃ N ₄	250 ⁶³	0.23 ⁶³	3100 ⁶⁴
SiO ₂	70 ^{65,66}	0.17 ⁶⁶	2200 ⁶⁵
Au	75 ⁶⁷	0.40 ⁶⁷	19300

The components C_{ij} of the hexagonal stiffness tensor of AlN and AlScN, the components $\epsilon_{r,ij}$ of the relative electric permittivity, and the density ρ are given in Table S4. The components of the piezoelectric coupling tensor are given in Table 1 of the main text.

Table S4: Components C_{ij} of the hexagonal stiffness tensor⁴⁶, components $\epsilon_{r,ij}$ ^{35,46,68} of the relative electrical permittivity tensor and density ρ ⁶⁹ used for AlN and AlScN in the finite element model.

Parameter	AIN	AlScN
C_{11} [GPa]	410.2	337.7
C_{12} [GPa]	142.2	145.2
C_{13} [GPa]	110.1	132.5
C_{33} [GPa]	385.0	254.6
C_{44} [GPa]	122.9	108.4
C_{66} [GPa]	134.0	96.25
$\epsilon_{r,11}$	9.208	9.208
$\epsilon_{r,22}$	9.208	9.208
$\epsilon_{r,33}$	9.800	16.90
ρ [kg/m ³]	3300	3300

In the finite element model, we consider all layers thicker than 0.15 μ m (Table S5). The model consists of an anchor region and a cantilever. Its long axis is oriented along the x_1 -axis and its short axis along the x_2 -axis. The cantilever's geometry is approximated by a structure of stratified blocks. The centroids of the piezoelectric layer (either AlN or AlScN) and the FeCoSiB layer are located at the centroid of the poly-Si layer. Hence, the AlN layer starts at 36 μ m from the clamping and the FeCoSiB layer at 46 μ m. This is alluded to in the sketch of Fig. 1a where the clamping is drawn significantly left of the AlN and the FeCoSiB film.

For Si₃N₄ the same dimensions are given as for the poly-Si layer in Table S5. Because it is deposited after the piezoelectric material, it covers not only the AlN/AlScN but also the free SiO₂ surface. This is considered in the model geometry with two overlapping Si₃N₄ domains, one on the free SiO₂ surface and one on the AlN/AlScN domain. They overlap by 4 μ m. Si₃N₄ coverage on the sides of the beam is neglected.

With a thickness of 4 μ m, the Au top contact line and the contact pads are not negligible and considered in the finite element model as well. The x_1x_2 -dimensions of the Au contact pad are 52 μ m \times 52 μ m and its centroid are located at 30 μ m from the centerline of the cantilever and 96 μ m from

the clamping. It extends through the Si_3N_4 layer, down to the piezoelectric layer. A straight, $32\ \mu\text{m}$ wide Au conduction line extends the Au contact on top of the Si_3N_4 to the clamping. Due to the high thickness of the Au, the FeCoSiB layer deposited on top is elevated relative to the rest of the magnetic film that is deposited on the Si_3N_4 . Both FeCoSiB domains are connected by an overlap of $4\ \mu\text{m}$ in the model.

Table S5: Layer dimension of all layers thicker than $0.15\ \mu\text{m}$ (schematic in Fig. 1a). The geometry of the Au contact line and pad is described in the text.

Material	Length L [μm]	Width W [μm]	Thickness T [μm]
FeCoSiB	908	158	2
Si_3N_4	1000	200	1
AlN/AlScN	928	178	1
SiO_2 (Top)	1000	200	0.65
Poly-Si	1000	200	5
SiO_2 (Bottom)	1000	200	0.99

The underetched region at the cantilever clamping is modeled with a three-layer rectangular plate (anchor plate) that continues the SiO_2 and poly-Si layers of the cantilever. Its width along the x_2 -dimension is set to $200\ \mu\text{m}$. A further increase in width does neither influence the resonance frequency nor the admittance characteristic, significantly. Its length along the x_1 -axis is given by d_{etch} , which represents the degree of underetching. Fixed displacement boundary conditions are applied to all x_1x_3 - and x_2x_3 -faces of the anchor plate, except for the one at which the cantilever is attached.

Nonlinearity in magnetic saturation

To gain insights into the origin of the resonator nonlinearity, we measured the admittance curve of the AlScN sensor at two different excitation voltage amplitude of $10\ \text{mV}$ and $150\ \text{mV}$ at a magnetic bias field of approximately $80\ \text{mT}$ provided by a permanent magnet. In Fig. S2 the results (Fig. S2a) are compared with measurements at the magnetic operation point (Fig. S2b). Whereas the delta-E effect and the resonator nonlinearities are visible in Fig. S2b, they do not occur at $B = 80\ \text{mT}$. Instead, the admittance is independent of the excitation voltage amplitude.

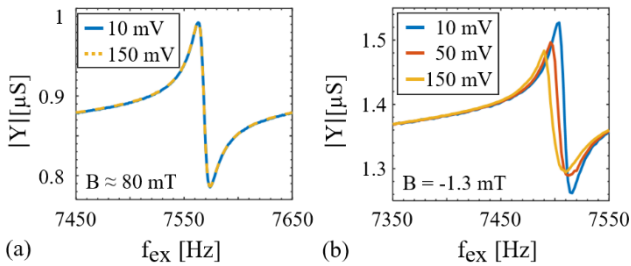


Fig. S2 a) Admittance measurements of the AlScN sensor at two different excitation voltage amplitudes and a magnetic bias field of approximately $80\ \text{mT}$. b) Corresponding measurements at the magnetic operation field of $B = -1.3\ \text{mT}$.

Nonlinear equivalent circuit model

For the nonlinear mBvD fit, the restoring force was assumed to be a function of the current I , which is represented as a variable capacitance C in the LCR circuit (Fig. S3).

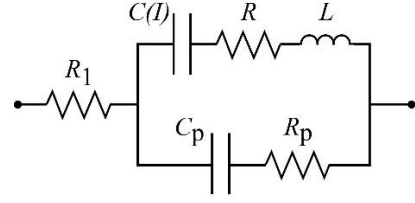


Fig. S3 Equivalent circuit of the nonlinear mBvD model used to describe the sensor admittance at large excitation voltages \hat{u}_{ex} .

As a result, the equation of motion of the current I through the LCR circuit can then be described as a Duffing oscillator:

$$L \frac{d^2 I}{dt^2} + R \frac{dI}{dt} + \frac{1}{C_r} I + \frac{1}{C_3} I^3 = i\omega \cdot u_{\text{ex}}(t) \quad (\text{S1})$$

$$\rightarrow \frac{d^2 I}{dt^2} + \frac{R}{L} \frac{dI}{dt} + \frac{1}{LC} I = \frac{i\omega}{L} \cdot u_{\text{ex}}(t).$$

In Eq. S1, the time is given by t , the angular frequency by ω and it is $i := \sqrt{-1}$. The resistance in the LCR circuit is R and the inductance L . A discussion on the mathematics of nonlinear resonators is given in Ref. ^{70,71}.

The capacity C depends quadratically on the current I , on the capacity C_r of the linear response and the capacity C_3 of the nonlinear term:

$$\frac{1}{C} = \frac{1}{C_r} + \frac{1}{C_3} I^2. \quad (\text{S2})$$

With Eq. S1, the admittance Y_{LCR} of the LCR series circuit in Fig. S3 can be expressed as

$$Y_{\text{LCR}} = \frac{I}{V} = \frac{i\omega/L}{\omega_0^2 \left(1 + \frac{C_r}{C_3} I^2\right) - \omega^2 + 2i\delta\omega}, \quad (\text{S3})$$

where $\omega_0 := 1/(LC_r)$ is the linear eigenfrequency and $\delta := R/(2L)$ the damping factor. It is used to calculate the admittance Y of the overall nonlinear mBvD equivalence circuit. The current I can be calculated numerically from solving a nonlinear system of equations that can be derived from Eq. S1, considering only the harmonic response term. For each admittance fit, a set of initial parameters was found by fitting a linear mBvD model to the electrical admittance magnitude. Next, the nonlinear capacitance C_3 was included and iterated until a good fit was achieved. Note, that the parallel resistance R_p in this equivalent circuit model is connected in series with C_p , in contrast to the linear model described earlier.

Electrical sensitivity as a function of u_{ex}

In the following, we show the measurements of the mean electrical magnitude sensitivity $S_{el,am}$ (Fig. S4a) and the mean electrical phase sensitivity $S_{el,pm}$ (Fig. S4b), as functions of the excitation voltage amplitude u_{ex} . The sensitivities were obtained at an excitation frequency $f_{ex} = f_r$. Compared to $S_{el,am}$, the contribution of the electrical phase sensitivity $S_{el,pm}$ to the output voltage amplitude is small and only shown for completeness.

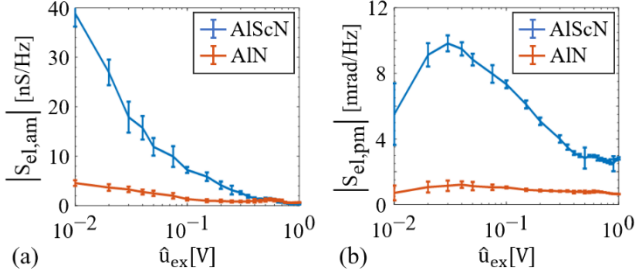


Fig. S4 Measured magnitude and standard deviation of the a) mean electrical magnitude sensitivity $S_{el,am}$ and b) electrical phase sensitivity $S_{el,pm}$, both as functions of the excitation voltage amplitude \hat{u}_{ex} , operating the sensor in mechanical resonance.

Electric amplitude sensitivity as a function of d_{ij}

In the following, we show the simulated electrical sensitivity of the non-zero components of the piezoelectric charge-stress coefficient tensor (Fig. S5) with components d_{ij} . The resulting $S_{el,am}$ curves are fitted with a function $f_{ij} = a_{ij} + b_{ij}x + c_{ij}x^2$. Significant quadratic contributions $c > 0$ are obtained for d_{31} and d_{33} . The coefficients are given in Table S6. For d_{15} and d_{24} , the electrical sensitivity $S_{el,am}$ is constant as a function of x and not plotted.

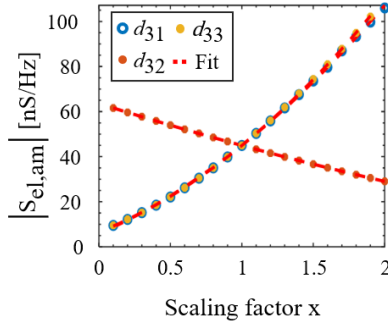


Fig. S5 Simulated electrical sensitivity as a function of the factor x that scales the piezoelectric charge-stress coefficient tensor $\mathbf{d} = x \cdot \mathbf{d}_{AlScN}$. Polynomial functions $f_{ij} = a_{ij} + b_{ij}x + c_{ij}x^2$ are fitted to the data.

Table S6: Coefficients found from the polynomial fits in Fig. S5.

ij	a_{ij} [nS/Hz]	b_{ij} [nS/Hz]	c_{ij} [nS/Hz]
31	5.83	27.80	11.42
32	63.59	-19.93	1.32
33	6.55	25.00	13.42

6.3 Influence of Magnetic Material

The last two sections demonstrated that large improvements in the output signal amplitude can be achieved by increasing Q or changing the piezoelectric material. Such improvements are also reflected in the significantly improved LOD if thermal-mechanical or thermal-electrical noise dominates the noise floor. Although this condition often holds at small amplitudes \hat{u}_{ex} of the excitation voltage, the sensor-intrinsic noise starts to dominate the noise floor at larger values of \hat{u}_{ex} . In both examples, a larger sensitivity is correlated with an earlier onset of noise, and this prevents an overall improvement in the LOD. Hence, an improvement in sensitivity could be accompanied by an increase in the noise level. At this point, it remains unclear whether this is a general phenomenon, i.e., if it is independent of how sensitivity improvement is achieved. The \hat{u}_{ex} dependent sensor-intrinsic noise correlates with the magnetic configuration such that it vanishes in the magnetic saturation. This is a strong indicator for the noise source being stress-induced and of a magnetic origin. The results lead to the following major questions that are addressed in this section: Is there a general connection between sensitivity and magnetic noise that can explain the observed behavior of the LOD? What parameters can potentially permit the improvement of the LOD?

In this section, the various noise contributions are reviewed and an attempt is made at explaining the LOD theoretically using a simplified magnetic noise model. This model connects the LOD with the complex effective magnetic susceptibility in a regime where magnetic noise dominates the noise floor.

Contribution

- Conceptualization (shared)
- Modeling (shared)

The following publication is reprinted, with permission, from Ref. [169], © 2020 IEEE.

Fundamental Noise Limits and Sensitivity of Piezoelectrically Driven Magnetoelastic Cantilevers

Phillip Durdaut¹, *Member, IEEE*, Enrico Rubiola², *Member, IEEE*, Jean-Michel Friedt, Cai Müller, Benjamin Spetzler, *Member, IEEE*, Christine Kirchhof³, Dirk Meyners, Eckhard Quandt, Franz Faupel, Jeffrey McCord, *Senior Member, IEEE*, Reinhard Knöchel, *Life Fellow, IEEE*, and Michael Höft⁴, *Senior Member, IEEE*

Abstract—Magnetoelastic sensors for the detection of low-frequency and low-amplitude magnetic fields are in the focus of research for more than 30 years. In order to minimize the limit of detection (LOD) of such sensor systems, it is of high importance to understand and to be able to quantify the relevant noise sources. In this contribution, cantilever-type electromechanical and magnetoelastic resonators, respectively, are comprehensively investigated and mathematically described not only with regard to their phase sensitivity but especially to the extent of the sensor-intrinsic phase noise. Both measurements and calculations reveal that the fundamental LOD is limited by additive phase noise due to thermal-mechanical noise of the resonator, i.e. by thermally induced random vibrations of the cantilever, and by thermal-electrical noise of the piezoelectric material. However, due to losses in the magnetic material parametric flicker phase noise arises, limiting the overall performance. In particular, it is shown that the LOD is virtually independent of the magnetic

sensitivity but is solely determined by the magnetic losses. Instead of the sensitivity, the magnetic losses, represented by the material's effective complex permeability, should be considered as the most important parameter for the further improvement of such sensors in the future. This implication is not only valid for magnetoelastic cantilevers but also applies to any type of magnetoelastic resonator. [2020-0219]

Index Terms—Cantilever, delta-E effect, flicker phase noise, limit of detection, magnetic field sensor, magnetic noise, magnetoelastic sensor, phase noise, phase sensitivity, resonator, thermal noise.

I. INTRODUCTION

IN 1989 Brendel *et al.* reported on a parasitic influence of magnetic fields on the oscillation frequency of quartz crystal oscillators which could be explained by magnetically induced deformations in the partly ferromagnetic springs used to hold the quartz plate [1], [2]. Since then, various micromechanical sensors based on the ΔE effect (Sec. II-A) have been presented, whose mechanical properties depend on an external magnetic field through interaction with a magnetostrictive layer. Although realizations in the form of highly sensitive magnetoelastic surface acoustic wave delay lines were also presented [3]–[9], magnetoelastic sensors are most commonly based on resonant structures [10]–[18], especially cantilevers [19]–[23], with resonance frequencies in the range between 550 Hz and 226 MHz.

Besides properties like e.g. dynamic range and frequency bandwidth, the limit of detection (LOD), frequently also referred to as detectivity or equivalent magnetic noise floor, is often considered as one of the most important figures of merit of a magnetic field sensor. Similar to a signal-to-noise ratio (SNR), the LOD is determined by both the sensor's signal, i.e. the sensitivity, as well as by the sensor's noise properties. In the existing articles reporting about magnetoelastic resonators, the focus has mostly been on modified sensor structures and their properties with an emphasis on enhancing the effect, i.e. the detuning of the sensing resonator. Although articles reported on measured values for the limit of detection in the microtesla [10], [12], [19], nanotesla [13], [16], [18], [20], [21], and even in the picotesla [11], [15], [22] range, the physical causes for noise in magnetoelastic magnetic field sensors based on the ΔE effect have not been investigated and described yet.

Manuscript received May 24, 2020; revised July 26, 2020; accepted July 27, 2020. Date of publication August 13, 2020; date of current version October 7, 2020. This work was supported in part by the German Research Foundation (Deutsche Forschungsgemeinschaft, DFG) through the Collaborative Research Centre CRC 1261 (Magnetolectric Sensors: From Composite Materials to Biomagnetic Diagnostics), in part by the ANR Programme d'Investissement d'Avenir (PIA) through the Oscillator IMP Project under Grant 11-EQPX-0033, in part by the FIRST-TF Network under Grant 10-LABX-0048, and in part by the Région Bourgogne Franche-Comté intended to support the PIA. Subject Editor R. N. Candler. (*Corresponding author: Phillip Durdaut.*)

Phillip Durdaut, Reinhard Knöchel, and Michael Höft are with the Chair of Microwave Engineering, Institute of Electrical Engineering and Information Technology, Kiel University, 24143 Kiel, Germany (e-mail: pd@tf.uni-kiel.de).

Enrico Rubiola is with the Department of Time and Frequency, FEMTO-ST Institute, Université Bourgogne Franche-Comté (UBFC), 25000 Besançon, France, also with CNRS, ENSMM, Université Bourgogne Franche-Comté (UBFC), 25000 Besançon, France, and also with the Physics Metrology Division, Istituto Nazionale di Ricerca Metrologica (INRiM), 10135 Turin, Italy.

Jean-Michel Friedt is with the Department of Time and Frequency, FEMTO-ST Institute, Université Bourgogne Franche-Comté (UBFC), 25000 Besançon, France, and also with CNRS, ENSMM, Université Bourgogne Franche-Comté (UBFC), 25000 Besançon, France.

Cai Müller and Jeffrey McCord are with the Chair of Nanoscale Magnetic Materials and Magnetic Domains, Institute for Materials Science, Kiel University, 24143 Kiel, Germany.

Benjamin Spetzler and Franz Faupel are with the Chair for Multicomponent Materials, Institute for Materials Science, Kiel University, 24143 Kiel, Germany.

Christine Kirchhof, Dirk Meyners, and Eckhard Quandt are with the Chair of Inorganic Functional Materials, Institute for Materials Science, Kiel University, 24143 Kiel, Germany.

Color versions of one or more of the figures in this article are available online at <http://ieeexplore.ieee.org>.

Digital Object Identifier 10.1109/JMEMS.2020.3014402

1057-7157 © 2020 IEEE. Personal use is permitted, but republication/redistribution requires IEEE permission. See <https://www.ieee.org/publications/rights/index.html> for more information.

In previous studies, we focused on thermal noise of magneto-electric cantilevers in passive mode [24], on the realization and analysis of low-noise preamplifiers for such sensors [25], on noise contributions of the readout electronics [26], [27] and the suppression of the local oscillator's phase noise in active mode magnetoelastic sensor systems [28]. Based on this, in this article the influence of the sensor's thermal noise on the phase noise is analyzed both metrologically and analytically. In addition, the impact of losses in the magnetic material on the phase noise characteristics, and thus on the overall sensor performance is shown.

This article is organized as follows: Sec. II introduces the sensor principle and the actual structure of the magnetoelastic cantilever under investigation. Based on the dynamics of resonant mechanical structures, expressions for the various sensitivities are derived, yielding the overall phase sensitivity. In addition, both an electrical equivalent circuit of the sensor covering for the various loss mechanisms as well a phase detecting readout system is presented. In comparison to previous studies the latter has been modified in order to allow for the neutralization of the sensor's parasitic static capacitance responsible for asymmetric transmission characteristics and a reduced sensitivity. Based on the sensor's loss mechanisms, expressions for thermally induced phase noise are derived and verified by measurements in Sec. III. Additional flicker phase noise clearly related to the losses in the magnetic material are traced back to fluctuations of the magnetization. Based on the fluctuation-dissipation theorem analytical expressions for the magnetically induced phase noise as well as for the resulting limit of detection are deduced. This article finishes with a summary of the findings in Sec. IV.

II. MAGNETOELASTIC SENSOR SYSTEM

A. ΔE Effect

The Young's modulus of any material is defined by the ratio between stress σ and elastic strain ε_{el} that is measured in the direction parallel to the applied stress [29]. However, for magnetic materials the relation $E_{sat} = \sigma/\varepsilon_{el}$ is only valid for magnetically saturated specimen [29]. In the general case, the problem has to be treated using tensors. As a consequence of the magnetostrictive effect, an additional magnetoelastic strain ε_{mel} occurs in magnetic materials [30, p. 270]. According to $\Delta\varepsilon_{mel} = d^m \Delta H$ (for positive magnetostriction) the magnetoelastic strain directly changes with the magnetic field H and proportionally to the piezomagnetic constant d^m [31] if ε_{mel} is linearized around a certain magnetic operating point H_{bias} . Considering both types of elastic strain, the resulting Young's modulus [30, p. 270]

$$E(H) = \frac{\sigma}{\varepsilon_{el} + \varepsilon_{mel}(H)} \leq E_{sat} \quad (1)$$

depends on the magnetic field H and is always lower than the Young's modulus of the same material in magnetic saturation. The magnetically induced change of the Young's modulus in the normalized form

$$\Delta E \text{ effect} \equiv \frac{\Delta E}{E} = \frac{E_{sat} - E}{E} = \frac{\varepsilon_{mel}(H)}{\varepsilon_{el}} \quad (2)$$

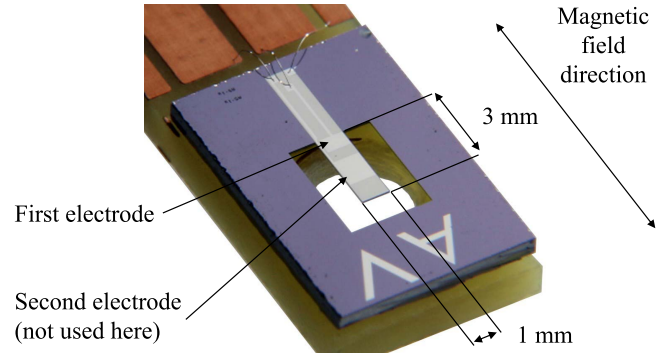


Fig. 1. Photograph of the utilized cantilever-type magnetoelastic sensor with a size of 3 mm x 1 mm mounted to a carrier PCB. The magnetic flux densities B_{bias} and B_x are applied along the long mechanical axis of the cantilever.

is known as the ΔE effect [31]. In the literature values for $\Delta E/E$ as high as approximately 700% for alloys of terbium-dysprosium (TbDy) [31] and approximately 30% for an alloy of iron-cobalt-silicon-boron ((Fe₉₀Co₁₀)₇₈Si₁₂B₁₀) [32] that is used in this work, respectively, are reported. It should be noted, however, that very large magnetic fields are required to change the Young's modulus in terbium-dysprosium by such a large value. With regard to the use of magnetostrictive materials for sensor applications, it is rather important how strong E is changed by a low amplitude magnetic measurement signal $B_x = \mu_0 H_x$ in a certain magnetic operating point $B_{bias} = \mu_0 H_{bias}$, thus requiring materials with large piezomagnetic constants d^m . An overview of piezomagnetic coefficients of various materials can be found in [33]. For (Fe₉₀Co₁₀)₇₈Si₁₂B₁₀ a value of 60 nm/A is reported that is only exceeded by (Fe₉₀Ga₁₉)₈₈B₁₂ with a value of 151 nm/A.

B. Magnetoelastic Sensor

The magnetoelastic sensor used for the investigations in this contribution as depicted in Fig. 1 is based on a poly-silicon cantilever of 3 mm length, 1 mm width and 50 μm thickness. The lower side is coated with 2 μm of soft magnetic amorphous metal ((Fe₉₀Co₁₀)₇₈Si₁₂B₁₀, magnetic easy axis perpendicular to the cantilever's long axis), and 2 μm of aluminum-nitride (AlN) piezoelectric material [34] are deposited on the cantilever's top. Details about the MEMS fabrication process can be found in [22]. In addition, the sensor offers two independent types of electrodes (see Fig. 1) that form plate capacitors with the piezoelectric AlN being the dielectric material. The investigations in this contribution focus on the first bending mode for which the first electrode performs best [35].

C. Resonance Detuning and Magnetic Sensitivity

The resonance frequency of a composite cantilever with N layers is given by [22]

$$f_{res} = \frac{1}{2\pi} \frac{\lambda^2}{l^2} \cdot \sqrt{\frac{\sum_{n=1}^N E_n J_n}{\sum_{n=1}^N m_n}} \quad (3)$$

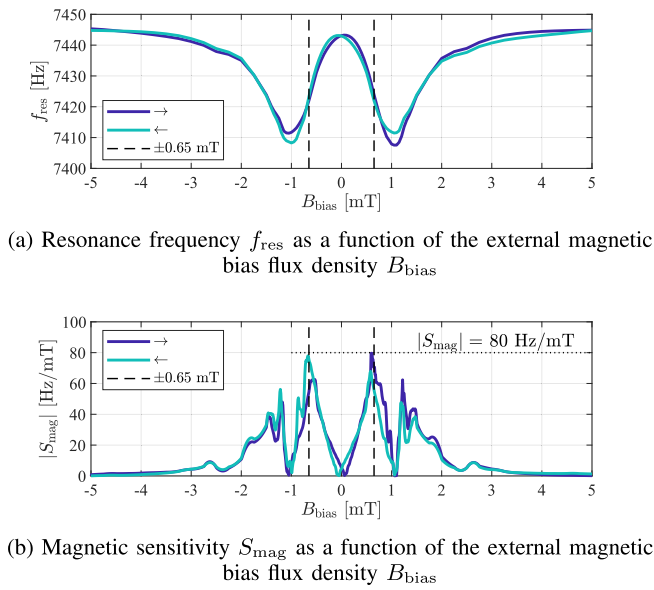


Fig. 2. Detuning of the magnetoelastic cantilever's resonance frequency with an external magnetic flux density (a). High magnetic sensitivities (b) are reached where the resonance frequency changes particularly strong with an external magnetic flux density, i.e. at $B_{\text{bias}} = \pm 0.65$ mT (vertical dashed lines).

where $\lambda = 1.875$ is the eigenvalue of the first characteristic bending mode, $l = 3$ mm is the free-standing length of the cantilever, and E_n is the Young's modulus, J_n is the second moment of area, and m_n is the mass per unit length of the n -th layer, respectively. Thus, the sensor's resonance frequency is proportional to the square root of the composite's effective Young's modulus E_{eff}

$$f_{\text{res}}(B_{\text{bias}}, B_x) \propto \sqrt{E_{\text{eff}}(B_{\text{bias}}, B_x)} \quad (4)$$

that depends on an external magnetic field, i.e. on the bias flux density B_{bias} and on the bias flux density of the measurement signal to be detected B_x (both applied along the long mechanical axis of the cantilever). As visible from a measurement in Fig. 2a, the cantilever's resonance frequency depends on the external magnetic field and changes particularly strong around $B_{\text{bias}} = \pm 0.65$ mT. The corresponding slope is known as the magnetic sensitivity towards low amplitude and low frequency magnetic measurement signals B_x

$$S_{\text{mag}}(B_{\text{bias}}) = \frac{\partial f_{\text{res}}}{\partial B_x} \quad (5)$$

for which a maximum value of $|S_{\text{mag}}| = 80$ Hz/mT is reached for the sensor under investigation (Fig. 2b). That value is often given normalized to f_{res} in saturation (here 7445 Hz), thus leading to a normalized magnetic sensitivity of $|S_{\text{mag}}| \approx 1.07 \% f_{\text{res}}/\text{mT}$ which is a typical value for thin-film magnetoelastic resonators [10], [11], [15], [21], [22].

In addition to the magnetic sensitivity determinable based on the magnetic field dependent resonance frequency, the measured characteristic in Fig. 2a reveals further insights into the sensor's magnetic behavior. The different results depending on the sweep direction of the applied magnetic bias flux

density are an indication of magnetic hysteresis. This reflects that the magnetic state of the piezomagnetic layer depends on the history of the applied magnetic bias flux density. During a sweep of the applied magnetic bias flux density the magnetic domain state changes, rearranging into different domain states at various points of the magnetization loop. These magnetic domain states and their dependence on the magnetic history of the applied magnetic bias flux density can be rather complex [36] and strongly influence the magnetic reversal process. Depending on the field amplitude and orientation magnetic domain behavior will change. It is often accompanied by nucleation, annihilation, and irreversible movement of magnetic domain walls. Similar magnetoelastic cantilever structures revealed magnetic Barkhausen noise contributions [37] due to magnetic domain reorganization processes during reversal. Especially, the variable domain structures also lead to variations in the effective sensitivity [37] and thus magnetic domain alterations relate to magnetic noise in such sensors [38]. Magnetic hysteresis losses are moreover linked to energy conversion into heat [39] and, thus, as discussed further below, correspond to additional noise contributions.

Contrary to all measurements for this investigation performed in an ultra-high magnetic field shielding mu-metal cylinder (Aaronia AG, ZG1), the magnetic operating point of the sensor can change due to ambient static fields outside magnetic shielding. For the sensor under investigation the impact of e.g. earth's magnetic field with magnetic flux densities between $25 \mu\text{T}$ and $60 \mu\text{T}$ [40, p. 43] is relatively low. To compensate for such external fields, self-regulating operating point stabilization approaches such as those already developed for giant magnetoimpedance (GMI) sensors [41] can be used. However, an operating point stabilization, i.e. providing a very stable and adjustable magnetic bias field, is not trivial because the required electronics also introduce additional noise [42]. Furthermore, the piezomagnetic layer of this sensor exhibits a uniaxial magnetic anisotropy. The orientation of the anisotropy favors the orientation of the magnetic field along the long axis of the cantilever. While additionally biasing the sensor in other directions proves useful in special cases [43], deviations of B_{bias} from the long axis in this case generally deteriorates the sensitivity due to the quadratic nature of the magnetoelastic effect. This affects the sensor's linearity, i.e. the dynamic range. As discussed above, a different alignment of the magnetic field will lead to a different magnetic domain structure and thus a different contribution to the magnetic noise, leading to a change in LOD. These effects are currently under investigation.

D. Mechanical Behavior and Electrical Sensitivity

Generally, the mechanical behavior of a resonant cantilever with the quality factor Q can be described by the unitless frequency response of a simple damped harmonic oscillator [44, pp. 427] [45]

$$G(f) = \frac{1}{1 - \left(\frac{f}{f_{\text{res}}}\right)^2 + j \frac{f}{f_{\text{res}} Q}} = |G(f)| \cdot \exp(j \gamma(f)) \quad (6)$$

with the magnitude frequency response

$$|G(f)| = \frac{1}{\sqrt{\left(1 - \left(\frac{f}{f_{\text{res}}}\right)^2\right)^2 + \left(\frac{f}{f_{\text{res}}Q}\right)^2}} \quad (7)$$

and the phase response

$$\gamma(f) = \arctan\left(\frac{-\frac{f}{f_{\text{res}}}}{Q\left(1 - \left(\frac{f}{f_{\text{res}}}\right)^2\right)}\right). \quad (8)$$

Eq. (8) describes the relation between phase and frequency where the slope of $\gamma(f)$ at f_{res} yields the well-known expression

$$S_{\text{elec}} = \left.\frac{d\gamma(f)}{df}\right|_{f=f_{\text{res}}} = -\frac{2Q}{f_{\text{res}}} \quad (9)$$

which, in the following, is referred to as the electrical sensitivity S_{elec} of a resonant sensor in units of rad/Hz [46].

E. Dynamic Frequency Response and Overall Phase Sensitivity

The higher the quality factor Q of a resonant sensor, the narrower the bandwidth of the characteristic band-pass behavior. Assuming a magnetic measurement signal $B_x(t) = \hat{B}_x \cos(2\pi f_x t)$, the sensor's response to such a signal with the frequency f_x can be determined by replacing f with $f_{\text{res}} \pm f_x$ [45] in Eq. (6)

$$G(f_{\text{res}} \pm f_x) = \frac{-jQ}{1 \pm \frac{f_x}{f_{\text{res}}} + j\frac{Qf_x^2}{f_{\text{res}}^2} \pm j\frac{2Qf_x}{f_{\text{res}}}} \quad (10)$$

$$\approx \frac{-jQ}{1 \pm j\frac{2Qf_x}{f_{\text{res}}}}. \quad (11)$$

Based on that result, an expression for the unitless dynamic sensitivity S_{dyn} can be deduced

$$S_{\text{dyn}}(f_x) = \frac{G(f_{\text{res}} \pm f_x)}{G(f_{\text{res}})} \quad (12)$$

$$\approx \frac{1}{\sqrt{1 + \left(\frac{f_x}{f_c}\right)^2}} \cdot \exp\left(j \arctan\left(-\frac{f_x}{f_c}\right)\right) \quad (13)$$

which exhibits the characteristic of a simple first-order low-pass filter with a cutoff frequency of $f_c = f_{\text{res}}/(2Q)$. This result agrees with theoretical expectations in [47] and with measurement results in [48]. Thus, the overall phase sensitivity of the resonant sensor in units of rad/T yields

$$S_{\text{PM}}(B_{\text{bias}}, f_x) = S_{\text{mag}}(B_{\text{bias}}) \cdot S_{\text{elec}} \cdot S_{\text{dyn}}(f_x). \quad (14)$$

F. Electrical Equivalent Circuit and Loss Mechanisms

According to the physical structure of the electromechanical resonator it can be described by an electrical equivalent circuit as depicted in the dashed box in Fig. 5 whose element's values can be determined utilizing a conventional impedance analyzer [22], [24], [26]. Based on electromechanical analogies [49] the

mechanical structure's resonant behavior is taken into account by an electrical series resonant circuit with the impedance $Z_r = R_r + R_{\text{mag}} + j\omega L_r + 1/(j\omega C_r)$ where $\omega = 2\pi f$ is the angular frequency. Due to the magnetically induced changes of the resonance frequency $f_{\text{res}} = 1/(2\pi\sqrt{L_r C_r})$, both the inductance L_r as well as the capacitance C_r change with the magnetic field. In parallel to the series resonant circuit the static capacitance due to the electrodes surrounding the piezoelectric material is considered by an additional capacitor with a capacitance of $C_{\text{ME}} = 44$ pF for the sensor under investigation.

A piezoelectric cantilever-type magnetoelastic sensor comprises several loss mechanisms that, according to the fluctuation-dissipation theorem, correspond with fluctuations, i.e. with noise. Generally, such losses can be taken into account in an electrical equivalent circuit in the form of dissipative elements, i.e. by resistors.

The predominant loss mechanism of micromechanical cantilevers under atmospheric pressure is air damping, commonly referred to as viscous damping. In addition, e.g. thermoelastic friction intrinsic to the solid structure, support losses, surface losses, and mounting losses (compare [50] for a more detailed analysis for a cantilever like the one investigated here or e.g. [51] for a general overview) may further attenuate the cantilever's deflection, also expressed by its quality factor Q . In the electrical equivalent circuit model (dashed box in Fig. 5) these losses are taken into account by the resistance R_r .

For the special case of a magnetoelastic cantilever, additional losses occur as a function of its magnetic state, i.e. as a function of the external magnetic bias flux density B_{bias} which are considered as an additional resistance R_{mag} . As measurement results in Fig. 3a reveal, these losses are particularly high for bias flux densities that also lead to high magnetic sensitivities S_{mag} (illustrated by the vertical dashed lines, compare also Fig. 2b). Conversely, this means that the overall quality factor

$$Q(B_{\text{bias}}) = \frac{1}{R_r + R_{\text{mag}}(B_{\text{bias}})} \sqrt{\frac{L_r(B_{\text{bias}})}{C_r(B_{\text{bias}})}} \quad (15)$$

is also a function of the bias flux density and that Q is lower in the vicinity of the sensor's operating point (here $B_{\text{bias}} = \pm 0.65$ mT) than in magnetic saturation (Fig. 3b). Results of a similar series of measurements in Fig. 4, but in dependence of the electrical excitation amplitude V_{ex} , clearly confirm the influence of the magnetic state on the losses and on the quality factor, respectively. In fact, the magnetic losses distinctly increase with higher excitation amplitudes in case the magnetic material is not in saturation.

As already hypothesized in [22], these additional losses can be explained by magnetic hysteresis losses that occur from the periodic bending of the cantilever which, in turn, lead to changes in the magnetization due to the inverse magnetostrictive effect, also referred to as Villari effect [52]. Dynamic magnetic hysteresis losses imply irreversible mechanisms due to domain activity that lead to energy dissipation in the form of heat during each cycle of periodic changes of the magnetization [53], [54]. Amongst other loss mechanisms related to the

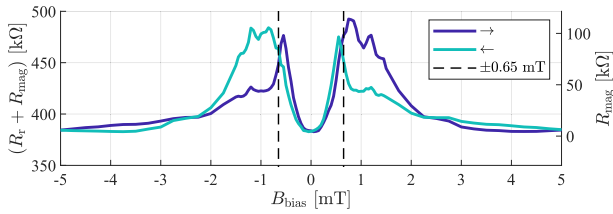
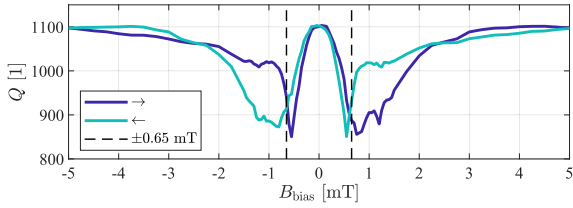
(a) Loss-representing values of the resistances R_r and R_{mag} as a function of the external magnetic bias flux density B_{bias} (b) Quality factor Q as a function of the external magnetic bias flux density B_{bias}

Fig. 3. Losses, represented by the resistances R_r and R_{mag} (a), and corresponding quality factor Q (b) as a function of the external magnetic bias flux density B_{bias} measured for an amplitude of the electrical excitation signal of $\hat{V}_{\text{ex}} = 100$ mV. The losses are particularly high for bias flux densities that also lead to high magnetic sensitivities Δ_{mag} (illustrated by the vertical dashed lines, compare also Fig. 2b) whereas highest values for Q are obtained in magnetic saturation.

magnetic material like e.g. eddy current losses, the hysteresis losses are considered by the imaginary part μ_r'' of the magnetic material's relative permeability $\mu_r = \mu_r' - j\mu_r''$ [54].

Further losses are affiliated to the sensor's plate capacitor, i.e. to the piezoelectric material. These dielectric losses are considered by the loss tangent $\tan \delta_{\text{ME}}$ with reported values for thin-film piezoelectric materials as low as e.g. $2.5 \cdot 10^{-4}$ (aluminium-nitride, AlN) [55], $1.3 \cdot 10^{-3}$ (aluminium-scandium-nitride, AlScN) [56], and $4 \cdot 10^{-3}$ (lead-zirconate-titanate, PZT) [57]. The sensor under investigation exhibits a value of $\tan \delta_{\text{ME}} = 5 \cdot 10^{-3}$, thus resulting in a resistance $R_{\text{ME}} = (\tan \delta_{\text{ME}} \omega C_{\text{ME}})^{-1}$ in parallel to the static capacitance C_{ME} and with a value in the vicinity of the resonance frequency of approximately 100 M Ω . With a corresponding conductance $1/R_{\text{ME}}$ in the nanosiemens range its influence is usually negligible. However, in Sec. III it will be shown that the noise associated with these losses might degrade the sensor's performance under certain circumstances.

G. Readout Structure

For sensor operation, i.e. for the reconstruction of a magnetic measurement signal $B_x(t)$ due to an induced detuning of the resonator an electrical readout system as depicted in Fig. 5 is utilized. The basic principle is based on a resonant excitation of the sensor with a voltage signal $v_{\text{ex}}(t) = \hat{V}_{\text{ex}} \cos(2\pi f_{\text{ex}} t)$ with $f_{\text{ex}} = f_{\text{res}}$ (first bending mode) leading to a magnetically modulated current through the sensor $i_{\text{sensor}}(t)$ that, in turn, is transformed into a proportional voltage signal $v_{\text{sensor}}(t)$ utilizing a transimpedance amplifier and subsequent phase demodulation. For all measurements a low-noise JFET charge

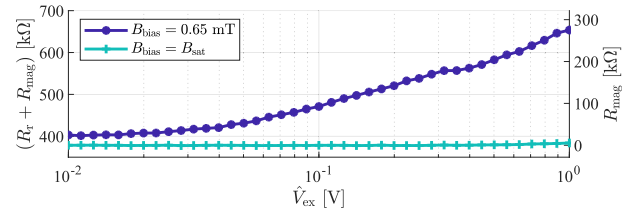
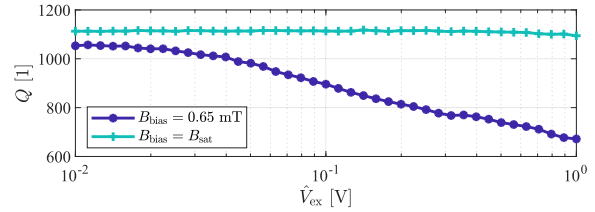
(a) Loss-representing values of the resistances R_r and R_{mag} as a function of the excitation amplitude \hat{V}_{ex} (b) Quality factor Q as a function of the excitation amplitude \hat{V}_{ex}

Fig. 4. Losses, represented by the resistances R_r and R_{mag} (a), and corresponding quality factor Q (b) as a function of the electrical excitation signal's amplitude \hat{V}_{ex} . If the sensor is not magnetically saturated the magnetic losses distinctly increase with the excitation amplitude due to dynamic magnetic hysteresis losses.

amplifier [25] with a feedback capacitance of $C_f = 30$ pF and a feedback resistance of $R_f = 5$ G Ω is utilized whose transimpedance in the vicinity of f_{res} , i.e. far above the amplifier's lower cutoff frequency $(2\pi R_f C_f)^{-1} \approx 1$ Hz, is given by

$$T(f) = \frac{V_{\text{sensor}}(f)}{I_{\text{sensor}}(f)} = -\frac{1}{j2\pi f C_f}. \quad (16)$$

However, as already mentioned above, this type of electro-mechanical sensor has an additional static capacitance C_{ME} due to its electrodes that, with regard to the electrical equivalent circuit, appears in parallel to the series resonant circuit with the impedance Z_r leading to an overall admittance of the electromechanical sensor of

$$Y_{\text{sensor}} = \frac{1}{Z_r} + \frac{1}{R_{\text{ME}}} + j\omega C_{\text{ME}}. \quad (17)$$

As a consequence of the additional static capacitance C_{ME} , a parallel resonance (also referred to as antiresonance) with a frequency $f_{\text{ares}} = f_{\text{res}} \sqrt{1 + C_r/C_{\text{ME}}}$ slightly above f_{res} [58, p. 204] appears which distorts the line shape of both the magnitude (Fig. 6a) and the phase (Fig. 6b) of Y_{sensor} compared to that of a bare resonator described by $G(f)$ (Eq. (6)). As a result, the electrical sensitivity resulting by differentiation of the admittance's phase is smaller than stated in Eq. (9) (Fig. 6d). The Nyquist plot in Fig. 6c illustrates that effect by means of the phasor of the excitation signal, i.e. the carrier signal (gray lines), and by the highlighted resonance frequencies (red crosses) of the slightly detuned resonator. Although the effect is not as pronounced for the sensor under investigation due to its comparatively low static capacitance of only $C_{\text{ME}} = 44$ pF, one can easily imagine that the larger the sensor's static capacitance (shift of the locus curve to the top), the lower the resulting phase modulation. This is

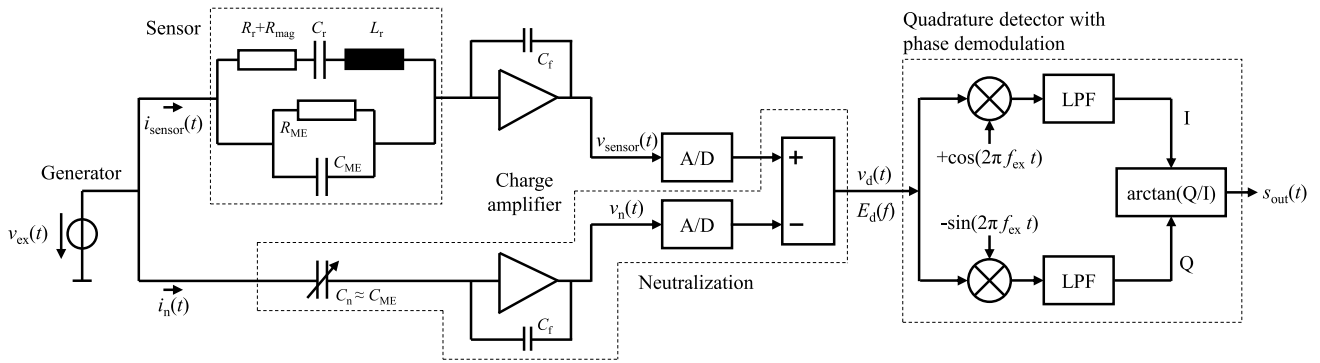
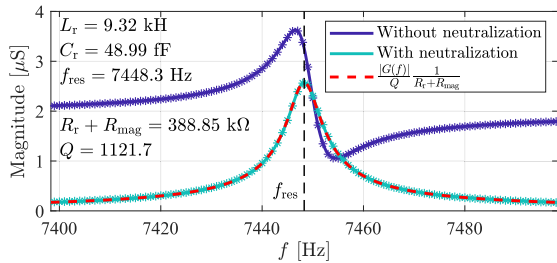
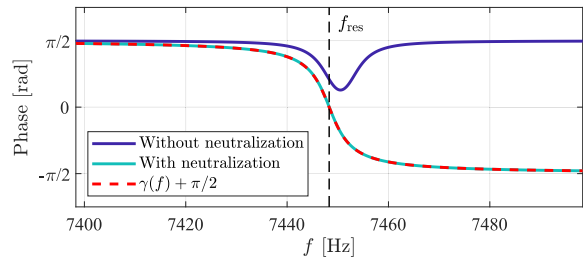


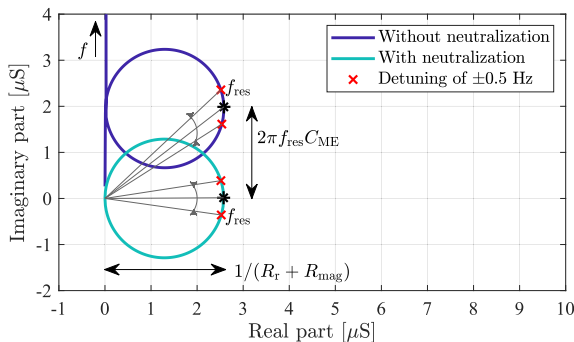
Fig. 5. Electrical readout system for the reconstruction of a magnetic measurement signal due to an induced detuning of the resonant sensor. The sensor (upper branch) is driven at its resonance frequency by an electrical excitation signal $v_{\text{ex}}(t)$, leading to a magnetically modulated voltage signal $v_{\text{sensor}}(t)$ at the output of the subsequent charge amplifier. An additional signal branch together with a subtractor is used to neutralize the parasitic effect of the sensor's static capacitance. The phase demodulation is performed in the digital domain by means of a conventional quadrature detector.



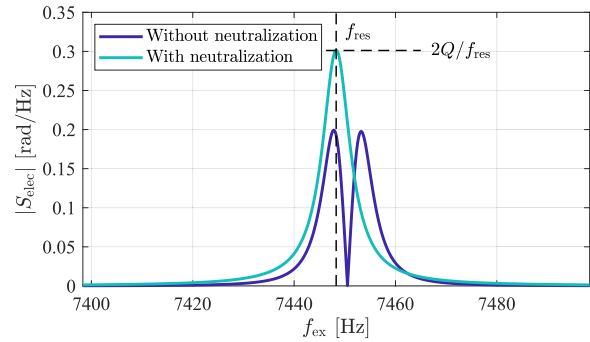
(a) Magnitude of the sensor's admittance



(b) Phase of the sensor's admittance



(c) Nyquist plot of the sensor's admittance



(d) Electrical sensitivity

Fig. 6. Measured (stars) and calculated (solid lines) trajectories of magnitude (a) and phase (b) of the sensor's admittance Y_{sensor} . Due to the parasitic influence of the sensor's static capacitance C_{ME} both line shapes are distorted, i.e. the locus curve (c) is shifted to higher imaginary parts. Neutralizing this effect not only leads to symmetric line shapes but also to an increase in the electrical sensitivity (d). The measurements have been conducted in magnetic saturation and for $V_{\text{ex}} = 1$ mV.

the reason why various methods for neutralizing the sensor's static capacitance have been reported [59]–[62], especially for large capacitance sensors. On the contrary, for this contribution, a neutralization is performed for symmetrizing the sensor's behavior. Thus, the admittance can be described by the frequency response of a simple harmonic oscillator $G(f)$ (compare Fig. 6a and Fig. 6b) which simplifies the noise considerations in the following section.

In the actual system as depicted in Fig. 5 the neutralization is perceived by a second branch that contains a trimming capacitor with a capacitance of $C_n \approx C_{\text{ME}}$ and an identical charge amplifier as in the sensor branch. When neglecting the

influence of the dielectric losses (R_{ME}) on the sensor signal $v_{\text{sensor}}(t)$ (see above) its amplitude spectrum yields

$$V_{\text{sensor}}(f) = T I_{\text{sensor}}(f) = T V_{\text{ex}} Y_{\text{sensor}}(f) \quad (18)$$

$$= T V_{\text{ex}} \left(\frac{1}{Z_r(f)} + j 2\pi f C_{\text{ME}} \right). \quad (19)$$

Similarly, the amplitude spectrum at the output of the second charge amplifier is given by

$$V_n(f) = T I_n(f) = T V_{\text{ex}} j 2\pi f C_{\text{ME}}, \quad (20)$$

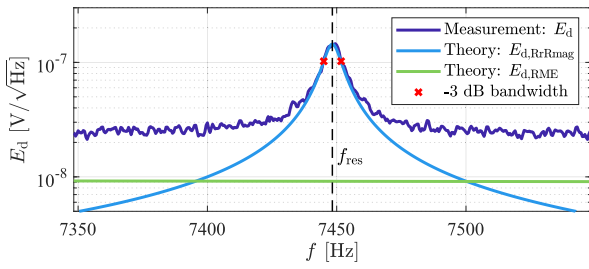


Fig. 7. Measured noise at the output of the subtractor in comparison to the theoretical expectations according to Eq. (27) and (29). In the vicinity of the resonance frequency the overall noise is dominated by the sensor-intrinsic thermal-mechanical noise $E_{d,RrRmag}$. Far beyond the sensor's -3 dB bandwidth the measured noise is approximately frequency independent but higher than predicted ($E_{d,RME}$) because of further contributions of the system electronics. The measurement has been conducted in magnetic saturation and for $\hat{V}_{ex} = 0$.

thus resulting in an amplitude spectrum of the differential signal $v_d(t)$

$$V_d(f) = V_{sensor}(f) - V_n(f) = \frac{TV_{ex}}{Z_r(f)} \quad (21)$$

in which the parasitic influence of the static capacitance C_{ME} is suppressed. For a resonant excitation $Z_r(f_{res})$ is purely ohmic. Consequently, the differential signal's amplitude can be written as (compare Fig. 6a)

$$\hat{V}_d = \sqrt{2} |V_d(f_{res})| = \frac{\hat{V}_{ex}|T(f_{res})||G(f_{res})|}{Q(R_r + R_{mag})} \quad (22)$$

$$= \frac{\hat{V}_{ex}|T(f_{res})|}{R_r + R_{mag}}. \quad (23)$$

When neglecting the amplitude modulation and the static phase delays due to the sensor and the amplifiers, the associated time domain signal can be written as

$$v_d(t) = \hat{V}_d \cos(2\pi f_{res}t + S_{PM}B_x(t) + \varphi(t)) \quad (24)$$

which contains the phase modulation with the phase sensitivity S_{PM} (Eq. (14)) and phase fluctuations $\varphi(t)$ due to the sensor and the electronics that are analyzed in more detail in the following section.

By means of a quadrature detector the phase demodulation is performed in the digital domain. For $f_{ex} = f_{res}$ the output signal is then equal to

$$s_{out}(t) = S_{PM}B_x(t) + \varphi(t). \quad (25)$$

For all measurements in this article, a high-resolution analog-to-digital (A/D) and digital-to-analog (D/A) converter, respectively, of type *Fireface UFX* from *RME* running at a sampling rate of 32 kHz has been used for digitizing $v_{sensor}(t)$ and $v_n(t)$ and for generating the excitation signal $v_{ex}(t)$. The digital low-pass filters (LPF) in the quadrature detector are third-order Butterworth filters with -3 dB cutoff frequencies of 3 kHz.

III. PHASE NOISE ANALYSIS

A. Thermal-Mechanical and Thermal-Electrical Noise

As discussed in Sec. II-F, an electromechanical cantilever exhibits several loss mechanisms that, in the electrical equivalent circuit, are covered by two resistors with the resistances

$R_r + R_{mag}$ and R_{ME} . In previous studies [24], [25] it has already been shown that both the related thermal-mechanical noise of the resonant structure $E_{d,RrRmag}$ as well as the thermal-electrical noise $E_{d,RME}$ of the dielectric material can accurately be predicted. Adjusting the previously published expressions to the readout structure as depicted in Fig. 5, the amount of the sensor's thermal voltage noise at the output of the subtractor can be calculated by

$$E_{d,RrRmag}(f) = \left| \frac{T(f)}{Z_r(f)} \right| \sqrt{4k_B T_0 (R_r + R_{mag})} \quad (26)$$

$$= \frac{|T(f)||G(f)|\sqrt{4k_B T_0}}{Q\sqrt{R_r + R_{mag}}} \quad (27)$$

and

$$E_{d,RME}(f) = \frac{|T(f)|}{R_{ME}(f)} \sqrt{4k_B T_0 R_{ME}(f)} \quad (28)$$

$$= \frac{|T(f)|\sqrt{4k_B T_0}}{\sqrt{R_{ME}(f)}} \quad (29)$$

where $k_B \approx 1.381 \cdot 10^{-23}$ J/K is the Boltzmann constant and $T_0 = 290$ K the room temperature. A noise measurement without any external excitation of the sensor ($\hat{V}_{ex} = 0$) and in comparison to the theoretical expectations is depicted in Fig. 7. Due to the sensor's resonant behavior the thermal-mechanical noise $E_{d,RrRmag}$ is weighted by $G(f)$ and perfectly agrees with the measurement in the vicinity of the resonance frequency. Far beyond the sensor's -3 dB bandwidth the measured noise is approximately frequency independent but higher than predicted ($E_{d,RME}$) because of further contributions due to the system electronics, i.e. that of the two charge amplifiers and the D/A and A/D converters, respectively.

B. Relation Between Voltage Noise Density and Phase Noise

Various and statistically independent voltage noise densities due to the sensor and the system electronics ($E_{d,system}$) add up at the output of the subtractor

$$E_d^2 = E_{d,RrRmag}^2 + E_{d,RME}^2 + E_{d,system}^2. \quad (30)$$

To determine their relation to the power spectral density $S_\varphi(f)$ of the random phase fluctuations $\varphi(t)$, Eq. (24) is written as

$$v_d(t) = \hat{V}_d \cos(2\pi f_{res}t + \hat{\varphi}(f_x) \cos(2\pi f_x t)) \quad (31)$$

in which one noise component with the modulation index $\hat{\varphi}$ at f_x represents other spectral components that can be taken into account by linear superposition. In addition, for this noise consideration the measurement signal $B_x(t)$ is assumed to be zero. Based on basic trigonometric identities Eq. (31) can be rearranged into

$$v_d(t) = \hat{V}_d \left[\cos(2\pi f_{res}t) - \frac{\hat{\varphi}(f_x)}{2} [\sin(2\pi(f_{res} - f_x)t) + \sin(2\pi(f_{res} + f_x)t)] \right] \quad (32)$$

revealing the typical structure of a narrow band small signal phase modulated signal with a carrier at f_{res} and two symmetrical sidebands at $f_{res} \pm f_x$. Following the concept of noise

sidebands [63, pp. 243] the carrier-to-noise sideband ratio

$$\frac{\hat{V}_d}{\hat{V}_d \frac{\hat{\phi}(f_x)}{2}} = \frac{2}{\hat{\phi}(f_x)} = \frac{\hat{V}_d}{E_d(f_{\text{res}} \pm f_x) \sqrt{2} \sqrt{\Delta f}} \quad (33)$$

is equal to the carrier-to-voltage noise ratio if a symmetrical noise distribution ($E_d(f_{\text{res}} - f_x) = E_d(f_{\text{res}} + f_x)$) around the resonance frequency is assumed. The additional term $\sqrt{\Delta f}$ transforms the voltage noise density into an effective voltage noise in the bandwidth Δf . From Eq. (33) the phase modulation index

$$\hat{\phi}(f_x) = \frac{2 E_d(f_{\text{res}} \pm f_x) \sqrt{2} \sqrt{\Delta f}}{\hat{V}_d} \quad (34)$$

can be deduced which directly yields the power spectral density

$$S_\phi(f_x) = \left(\frac{2 E_d(f_{\text{res}} \pm f_x)}{\hat{V}_d} \right)^2 \quad (35)$$

of the random phase fluctuations $\phi(t)$ in units of rad^2/Hz . For voltage noise distributed asymmetrically around the resonance frequency ($E_d(f_{\text{res}} - f_x) \neq E_d(f_{\text{res}} + f_x)$) the more generally valid power spectral density is given by

$$S_\phi(f_x) = \left(\frac{E_d(f_{\text{res}} - f_x) + E_d(f_{\text{res}} + f_x)}{\hat{V}_d} \right)^2. \quad (36)$$

However, for the frequency range in the vicinity of f_{res}

$$|T(f_{\text{res}})| \approx \frac{1}{2} (|T(f_{\text{res}} - f_x)| + |T(f_{\text{res}} + f_x)|) \quad (37)$$

and

$$R_{\text{ME}}(f_{\text{res}}) \approx \frac{1}{2} (R_{\text{ME}}(f_{\text{res}} - f_x) + R_{\text{ME}}(f_{\text{res}} + f_x)) \quad (38)$$

are generally good approximations. Because of the neutralization $E_{d,\text{RrRmag}}(f)$ is also symmetric around f_{res} , thus leading to expressions for the power spectral densities of random phase fluctuations due to thermal-mechanical noise

$$S_{\phi,\text{RrRmag}}(f_x) = \left(\frac{2 |T(f_{\text{res}})| S_{\text{dyn}}(f_x) |\sqrt{4k_B T_0}|}{\hat{V}_d \sqrt{R_r + R_{\text{mag}}}} \right)^2 \quad (39)$$

$$\stackrel{\text{Eq. (23)}}{=} \left(\frac{2 |S_{\text{dyn}}(f_x)| |\sqrt{4k_B T_0} (R_r + R_{\text{mag}})|}{\hat{V}_{\text{ex}}} \right)^2 \quad (40)$$

and due to thermal-electrical noise of the loss in the dielectric material

$$S_{\phi,\text{RME}} = \left(\frac{2 |T(f_{\text{res}})| |\sqrt{4k_B T_0}|}{\hat{V}_d \sqrt{R_{\text{ME}}(f_{\text{res}})}} \right)^2 \quad (41)$$

$$\stackrel{\text{Eq. (23)}}{=} \left(\frac{2 \sqrt{4k_B T_0} (R_r + R_{\text{mag}})}{\hat{V}_{\text{ex}} \sqrt{R_{\text{ME}}(f_{\text{res}})}} \right)^2. \quad (42)$$

Obviously, the thermal-electrical noise $E_{d,\text{RME}}$ leads to additive white phase noise that decreases with the excitation amplitude since $\hat{V}_d \propto \hat{V}_{\text{ex}}$. The phase noise, which is caused by the thermal-mechanical noise $E_{d,\text{RrRmag}}$, also decreases with \hat{V}_{ex} . However, due to the influence of the resonator this additive phase noise decreases with 20 dB/decade for frequencies f_x

above the cutoff frequency $f_c = f_{\text{res}}/(2Q)$. In contrast to this, thermal-mechanical noise also leads to white phase noise for frequencies well below the cutoff frequency ($f_x \ll f_c$).

C. Phase Noise Measurements

With the system described above (Fig. 5), several series of noise measurements were performed to analyze the sensor's phase noise behavior. Without any additional magnetic measurement signal ($B_x(t) = 0$), the system's output signal $s_{\text{out}}(t)$ is then equal to the random phase fluctuations $\phi(t)$ which were transformed to the frequency domain based on Welch's method [64], thus leading to the power spectral densities of random phase fluctuations S_ϕ . In the following, $S_\phi(f_x)$ is given as a function of the frequency f_x to clarify that this phase noise is effective in the same frequency range as the measurement signal. Formally it would be just as correct to use f here.

For all measurements the sensor was placed inside an ultra-high magnetic field shielding mu-metal cylinder (Aaronia AG ZG1) which, in turn, is placed inside a vibrationally decoupled box with lined absorbers against airborne sound. In addition, the whole box is coated with a copper fleece, which shields electrical fields. Furthermore, the sensor is surrounded by two solenoids inside the mu-metal that are used for generating both the magnetic bias flux density B_{bias} as well as the magnetic measurement signal $B_x(t)$. The latter is generated with a commercially available current source (Keithley 6221). However, no commercially available power source was suitable for generating comparatively large bias fields in the millitesla range while keeping the resulting low-frequency noise well below $100 \text{ pT}/\sqrt{\text{Hz}}$. Therefore, an in-house built setup based on several batteries (capacity > 100 Ah) and a stepper motor controlled potentiometer in series to the coil was used.

In a first series of noise measurements the sensor was magnetically saturated by means of a strong permanent magnet generating a magnetic bias flux density of $B_{\text{bias}} \approx 20 \text{ mT}$ which is distinctly higher than the sensor's saturation flux density < 5 mT (compare e.g. Fig. 2a). At the same time the amplitude \hat{V}_{ex} of the electrical excitation signal $V_{\text{ex}}(t)$ was increased incrementally. For several values of \hat{V}_{ex} , the measured phase noise is depicted in Fig. 8a together with the phase noise contributions due to thermal-mechanical noise $S_{\phi,\text{RrRmag}}$ (Eq. (40), dashed lines) and due to thermal-electrical noise of the dielectric material $S_{\phi,\text{RME}}$ (Eq. (42), dotted lines). As expected, the measured noise spectra decrease with increasing excitation amplitudes, thus confirming the additive character of both thermal noise contributions. In addition, values of measured phase noise and calculated phase noise $S_{\phi,\text{RrRmag}}$ (dashed lines) agree well for the low frequency range in the range of the sensor's passband, indicated by the respective cutoff frequency (black crosses). Due to the impact of the mechanical resonator, the phase noise decreases with higher frequencies proportional to f_x^{-2} until the white phase noise floor beyond the sensor's passband is reached. According to previous calculations, the crossover frequency between frequency-dependent and white phase noise due to thermal-electrical noise of the dielectric material

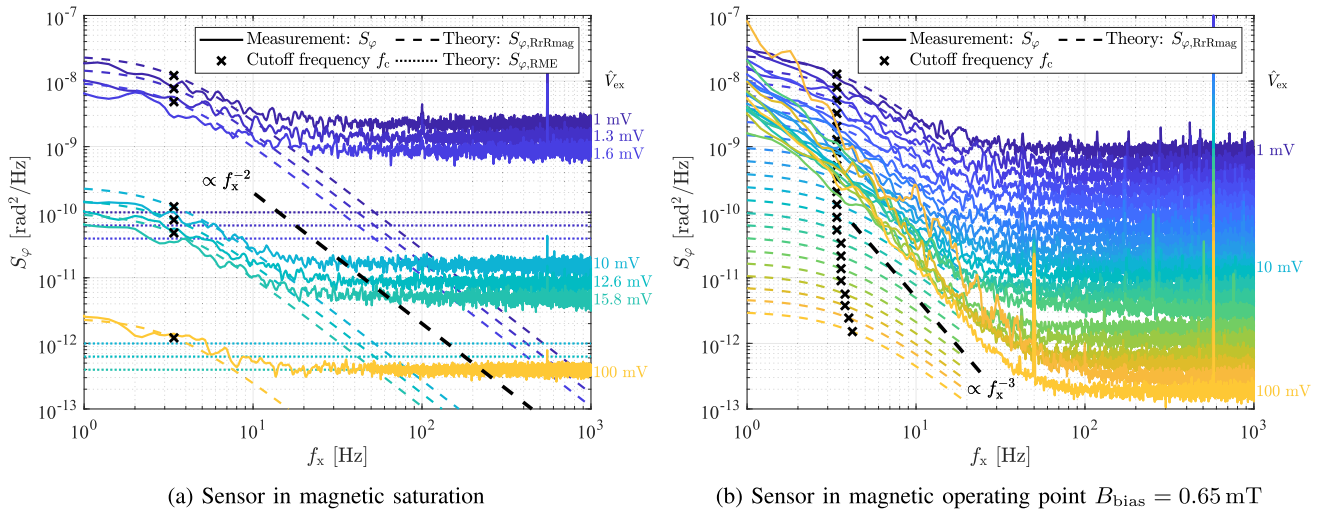


Fig. 8. Power spectral densities of the measured random phase fluctuations $\varphi(t)$ at the sensor system's output for the sensor in magnetic saturation (a) and for the sensor in its magnetic operating point (b) for various amplitudes of the excitation signal. For the magnetically saturated sensor, the additive phase noise due to thermal-mechanical (Eq. (40), dashed lines) and due to thermal-electrical noise (Eq. (42), dotted lines) decreases with the excitation amplitude \hat{V}_{ex} . For the sensor in its magnetic operating point low-frequency parametric phase noise occurs whose underlying physical noise process must exhibit a f_x^{-1} characteristic because an amount of f_x^{-2} is attributed to the influence of the resonator. The slightly different levels of white phase noise floors between the measurements in (a) and (b) are probably due to different states of charge of the battery supplying the amplifier, thus leading to different drain currents in the amplifier's discrete JFET front-end [25].

($S_{\varphi,RrRmag} = S_{\varphi,RME}$) is about 50 Hz. However, as already discussed in the context of Fig. 7, the overall noise floor outside the sensor's passband is dominated by noise contributions of the system electronics, thus leading to a crossover frequency at about 10 Hz for the system under investigation.

The same series of measurements was repeated for the sensor not being saturated anymore but brought into its magnetic operating point of $B_{bias} = 0.65$ mT after saturating the sensor in negative direction and stepwise incrementing B_{bias} . The measured phase noise acquired in this way is shown in Fig. 8b, again in comparison to the theoretical expectations (dashed lines) according to Eq. (40) (phase noise due to thermal-mechanical noise $S_{\varphi,RrRmag}$). The measured phase noise at low excitation amplitudes of about 1 mV still corresponds to the contribution of the thermal-mechanical noise. However, for increasing amplitudes \hat{V}_{ex} the measured phase noise in the sensor's passband no longer decreases significantly as for the magnetically saturated case (Fig. 8a). Thus, the noise contribution of the magnetic material leads to so-called parametric noise which is independent from the amplitude of the carrier signal [65, p. 36], at least if the noise process itself or material properties do not depend on the amplitude. Such a behavior is well-known from $1/f$ flicker phase noise, e.g. of amplifiers [66]. And indeed, considering the slope of f_x^{-3} with which the measured phase noise decreases, the underlying physical noise process must exhibit a f_x^{-1} characteristic because an amount of f_x^{-2} is attributed to the influence of the resonator.

To further verify the relationship between the sensor's magnetic state and the magnetically induced phase noise, measurements as a function of the magnetic bias flux density B_{bias} from negative to positive saturation were conducted (inverse measurement gives results mirrored on the axis of

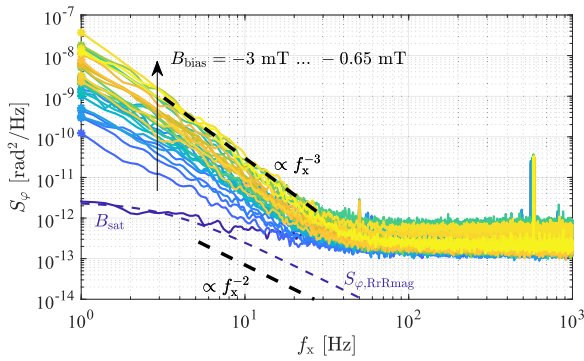
ordinates). As depicted by the corresponding power spectral densities of the random phase fluctuations in Fig. 9a, the f_x^{-1} flicker phase noise and the f_x^{-3} phase noise at the sensor system's output, respectively, clearly depend on the sensor's magnetic state. In fact, as shown by the measured phase noise at a frequency of 1 Hz in Fig. 9b, the induced phase noise is unambiguously related to the magnetic losses, represented by R_{mag} . For operating points with low losses, i.e. at which the magnetic sensitivity is low, e.g. near saturation and for $B_{bias} = 0$, also the phase noise adopts lower values. In contrast, the phase noise is particularly high when the losses or the magnetic sensitivity is high (dashed lines at $B_{bias} = \pm 0.65$ mT). In investigations on magnetoresistive sensors, an identical behavior could be observed in the past [67], [68]. These sensors also show largest noise for operating points of maximum sensitivity which was attributed to random fluctuations of the magnetization due to magnetic domain wall movements and rotations [68], [69].

D. Magnetically Induced Flicker Phase Noise

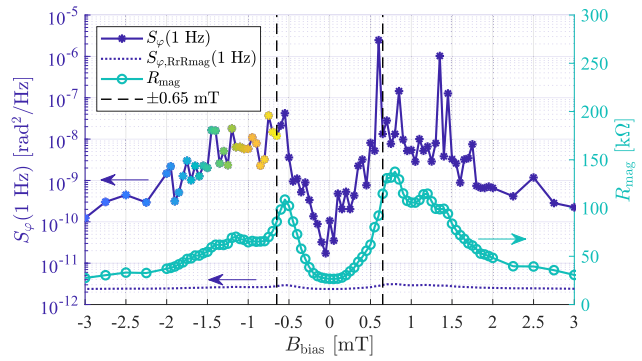
Due to the significant relation to the magnetic losses it is obvious to describe the magnetically induced phase noise using the fluctuation-dissipation theorem. Based on that theorem, the power spectral density of random fluctuations of the magnetization M

$$S_M(f_x) = \frac{4k_B T_0}{2\pi f_x} \frac{\mu_{r,eff}''}{V_{mag} \mu_0} \quad (43)$$

with the physical dimension (A/m)²/Hz can be derived [70], [71] which can be referred to as flicker magnetization noise since the power density decreases with $1/f_x$. This expression is typically given as a function of the imaginary part μ_r'' of



(a) Phase noise for various magnetic bias flux densities in the frequency domain



(b) Phase noise at a frequency of 1 Hz and magnetic losses as a function of the magnetic bias flux density

Fig. 9. Power spectral densities of the measured random phase fluctuations $\varphi(t)$ at the sensor system's output for a constant excitation amplitude of $\hat{V}_{ex} = 100$ mV as a function of the magnetic bias flux density B_{bias} measured increasingly from negative to positive magnetic saturation. The magnetically induced phase noise significantly changes with B_{bias} while the slope stays constant as far as the sensor is not in magnetic saturation (a). Obviously, the measured phase noise is directly linked to the magnetic losses, represented by R_{mag} , and for this excitation amplitude always higher than the phase noise due to the sensor's thermal-mechanical noise $S_{\varphi,RrRmag}$ (b).

the magnetic material's complex permeability $\mu_r = \mu'_r - j\mu''_r$. In general, however, μ''_r is also used to account for other losses, in particular eddy current losses, which in turn do not correspond with flicker noise but with frequency-independent white noise [72]. Therefore, in this article, an effective complex permeability $\mu_{r,eff} = \mu'_r - j\mu''_{r,eff}$ is used to cover only for magnetic hysteresis losses corresponding with $1/f$ flicker noise. Furthermore, $\mu_0 = 4\pi \cdot 10^{-7}$ Vs/(Am) and V_{mag} denote the vacuum permeability and the volume of the magnetic material, respectively. Thus, fluctuations of the magnetization can be decreased by larger magnetic volumes, at least if the magnetic losses $\mu''_{r,eff}$ do not rise proportionally with V_{mag} . However, literature shows that volume and losses are generally not independent of each other [73].

The expression for changes of the resonant sensor's phase response $\gamma(f)$ (Eq. 8) at the resonance frequency f_{res} due to changes of the magnetization M

$$\frac{\partial \gamma(f_{res})}{\partial M} = \frac{\partial \gamma(f)}{\partial f} \Big|_{f=f_{res}} \frac{\partial f_{res}}{\partial M} \quad (44)$$

can be factorized into two terms. The first term describes the changes of the sensor's phase response at f_{res} due to a detuning of the resonator. As discussed above, this term is equal to the electrical sensitivity S_{elec} (Eq. (9)). The second term covers the detuning of the resonator due to changes of the magnetization. With the magnetic susceptibility $\chi = \partial M / \partial H = \mu'_r - 1$, with $B = \mu_0 H$, and with $S_{mag} = \partial f_{res} / \partial B$ (Eq. (5)) the second term

$$\frac{\partial f_{res}}{\partial M} = \frac{\partial f_{res}}{\partial H} \frac{\partial H}{\partial M} = \frac{\partial f_{res}}{\partial H} \frac{1}{\chi} = \frac{\partial f_{res}}{\mu_0 \partial H} \frac{\mu_0}{\chi} \quad (45)$$

$$= S_{mag} \frac{\mu_0}{\chi} \approx S_{mag} \frac{\mu'_r}{\mu'_r} \quad (46)$$

can be expressed as a function of the magnetic sensitivity S_{mag} and the real part μ'_r of the effective permeability. The approximation is generally valid for commonly utilized magnetic materials with high permeabilities ($\mu'_r \gg 1$).

Using these relations, the power spectral density of random phase fluctuations due to random fluctuations of the

magnetization yields

$$S_{\varphi,M}(f_x) = S_M(f_x) \left| \frac{\partial \gamma(f_{res})}{\partial M} \right|^2 |S_{dyn}(f_x)|^2 \quad (47)$$

$$= S_M(f_x) |S_{elec}|^2 \left| S_{mag} \frac{\mu_0}{\mu'_r} \right|^2 |S_{dyn}(f_x)|^2 \quad (48)$$

in which the dynamic sensitivity S_{dyn} (Eq. (13)) accounts for the additional decrease in phase noise with increasing frequency due to the resonator. With Eq. (43) and the sensor's overall phase sensitivity S_{PM} (Eq. (14)) the expression further simplifies to

$$S_{\varphi,M}(f_x) = \frac{4k_B T_0}{2\pi f_x V_{mag}} |S_{PM}(f_x)|^2 \frac{\mu_0 \mu''_{r,eff}}{(\mu'_r)^2}, \quad (49)$$

clarifying that the magnetically induced phase noise is proportional to the sensor's sensitivity.

E. Limit of Detection

The limit of detection (LOD) of a magnetic field sensor system denotes the frequency-dependent noise floor, i.e. an amplitude spectral density, in units of T/ $\sqrt{\text{Hz}}$ [46]. Thus, the LOD is given by the ratio of the amplitude spectral density of random phase fluctuations and the phase sensitivity.

Considering only the phase noise $S_{\varphi,RrRmag}$ (Eq. (40)) due to the resonator's thermal-mechanical noise, the fundamental LOD is given by

$$\text{LOD}_{RrRmag}(f_x) = \frac{\sqrt{S_{\varphi,RrRmag}(f_x)}}{|S_{PM}(f_x)|} \quad (50)$$

$$= \frac{f_{res} \sqrt{4k_B T_0 (R_r + R_{mag})}}{\hat{V}_{ex} Q |S_{mag}|} \quad (51)$$

which is frequency-independent, deteriorates with the losses, and improves with the magnetic sensitivity. In particular, this fundamental LOD could be improved simply by increasing the excitation amplitude because the phase noise due to thermal-mechanical noise is additive (Fig. 8a). For the sensor under investigation, with typical values (compare Fig. 6a) of $f_{res} = 7450$ Hz, $R_r + R_{mag} = 388.85$ k Ω , $Q = 1121.7$, and

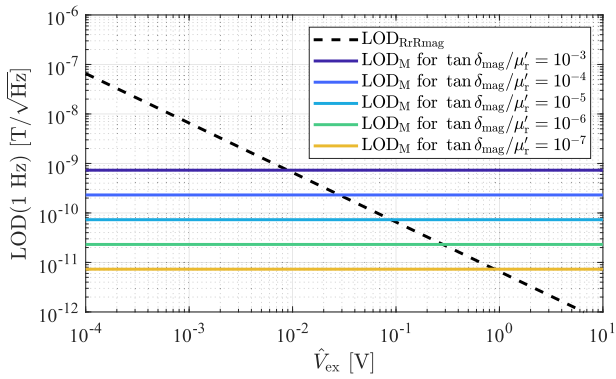


Fig. 10. Calculated limit of detection (LOD) at a frequency of 1 Hz and for typical sensor parameters ($f_{\text{res}} = 7450$ Hz, $R_r + R_{\text{mag}} = 388.85$ k Ω , $Q = 1121.7$, $S_{\text{mag}} = 80$ Hz/mT, $V_{\text{mag}} = 6 \cdot 10^{-12}$ m 3) at room temperature ($T_0 = 290$ K). The fundamental LOD is limited by additive thermal-mechanical noise, thus $\text{LOD}_{RrR\text{mag}}$ (Eq. (51)) improves with the excitation amplitude \hat{V}_{ex} . Parametric magnetically induced phase noise $S_{\phi,M}$ (Eq. (49)) limits the LOD of real sensors. However, LOD_M (Eq. (52) and (54)) can be improved by decreasing the relative magnetic loss factor $\tan \delta_{\text{mag}}/\mu'_r$.

$S_{\text{mag}} = 80$ Hz/mT the frequency-independent LOD would result, e.g. in a value as low as 6.5 pT/ $\sqrt{\text{Hz}}$ for an electrical driving amplitude of $\hat{V}_{\text{ex}} = 1$ V (dashed line in Fig. 10).

However, because the sensor system's overall noise floor is dominated by magnetically induced phase noise (as shown in Fig. 9b this noise is usually distinctly higher than phase noise due to the resonator's thermal-mechanical noise when the magnetic material is not saturated) it is more convenient to consider $S_{\phi,M}(f_x)$ (Eq. (49)) for the determination of the detectivity

$$\text{LOD}_M(f_x) = \frac{\sqrt{S_{\phi,M}(f_x)}}{S_{\text{PM}}(f_x)} = \sqrt{\frac{4k_B T_0}{2\pi f_x V_{\text{mag}}} \frac{\mu_0 \mu''_{r,\text{eff}}}{(\mu'_r)^2}} \quad (52)$$

which improves with $1/\sqrt{f_x}$. Remarkably, in that case, the limit of detection does not depend on the sensor's sensitivity at all but is solely determined by the volume and the magnetic properties μ'_r and $\mu''_{r,\text{eff}}$ of the magnetostrictive film which, in turn, depend on the sensor's operating point in terms of bias field, excitation frequency, and excitation power. A basically identical result was reported e.g. for giant magnetoimpedance sensors, for which the fundamental detectivity is also independent of the sensitivity [74]. A recently published article [38] about magnetic domain activities confirms the relation between magnetic losses and magnetic noise in periodically driven magnetoelectric cantilevers. The authors also come to the conclusion that controlling the magnetic domain behavior is the key to optimum sensor performance.

For the sensor under investigation magnetically coated with a volume of $V_{\text{mag}} = 3 \text{ mm} \cdot 1 \text{ mm} \cdot 2 \text{ } \mu\text{m} = 6 \cdot 10^{-12}$ m 3 , the expression for the LOD can be further simplified to

$$\text{LOD}_M(f_x) = \frac{23.1 \text{ nT} \sqrt{\mu''_{r,\text{eff}}}}{\sqrt{f_x} \mu'_r} \quad (53)$$

$$= \frac{23.1 \text{ nT}}{\sqrt{f_x}} \sqrt{\frac{\tan \delta_{\text{mag}}}{\mu'_r}}, \quad (54)$$

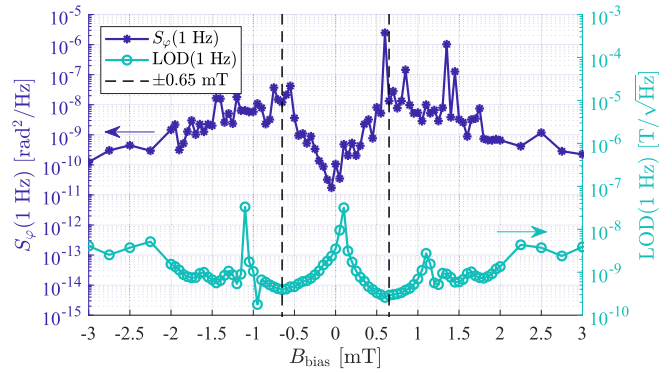


Fig. 11. Measured phase noise at a frequency of 1 Hz (same data as in Fig. 9b) and measured limit of detection (LOD), also at a frequency of 1 Hz for a constant excitation amplitude of $\hat{V}_{\text{ex}} = 100$ mV as a function of B_{bias} measured increasingly from negative to positive magnetic saturation. Best values as low as $\text{LOD}(1 \text{ Hz}) = 292$ pT/ $\sqrt{\text{Hz}}$ are obtained in the sensor's magnetic operating point at $B_{\text{bias}} = 0.65$ mT.

clarifying the exclusive dependence on the magnetostrictive film's magnetic properties. The best value for the detectivity of $\text{LOD}(1 \text{ Hz}) = 292$ pT/ $\sqrt{\text{Hz}}$ is measured around a bias flux density of $B_{\text{bias}} = +0.65$ mT (Fig. 11) despite the higher losses compared to the operating point around $B_{\text{bias}} = -0.65$ mT (Fig. 9b) for which a value of $\text{LOD}(1 \text{ Hz}) = 394$ pT/ $\sqrt{\text{Hz}}$ is achieved. The reason is the higher magnetic sensitivity in this measurement of $S_{\text{mag}} = 61.3$ Hz/mT at $B_{\text{bias}} = +0.65$ mT compared to a value of $S_{\text{mag}} = 42.5$ Hz/mT at $B_{\text{bias}} = -0.65$ mT. Thus, an optimum LOD is achieved at an operating point at which the sensitivity-to-loss ratio $S_{\text{mag}}/R_{\text{mag}}$ is maximized.

From a measured value $\text{LOD}(1 \text{ Hz}) = 292$ pT/ $\sqrt{\text{Hz}}$ at $B_{\text{bias}} = +0.65$ mT the relative magnetic loss factor can be determined to $\tan \delta_{\text{mag}}/\mu'_r = 1.6 \cdot 10^{-4}$ ($\tan \delta_{\text{mag}}/\mu'_r = 2.9 \cdot 10^{-4}$ at $B_{\text{bias}} = -0.65$ mT). Due to the dependence of the magnetic properties on e.g. the material composition, thickness, magnetic domain configuration, shape, etc. and also due to their interdependencies it is difficult to compare the determined value with other values from the literature. However, values reported in [70] are at least in the same order of magnitude even though the investigated samples were measured at cryogenic temperatures. For typical parameters of the sensor under investigation, Fig. 10 depicts resulting limits of detection at a frequency of 1 Hz for various relative magnetic loss factors. Because the LOD is proportional to the square root of this loss factor, $\tan \delta_{\text{mag}}/\mu'_r$ needs to be decreased by two orders of magnitude in order to improve the LOD by a factor of ten.

IV. CONCLUSION

In this article, a cantilever-type magnetoelastic resonant sensor, representative for other kinds of magnetoelastic resonators, has been investigated. Such sensors for the detection of low-frequency and low-amplitude magnetic fields utilize the ΔE effect which leads to a magnetically induced resonance detuning. For the detection of the resonator's detuning, the sensor is preferably driven by an electrical excitation signal

which, in turn, is then phase modulated by the magnetic measurement signal. Based on the dynamics of resonant mechanical structures an expression for the overall phase sensitivity has been derived. Such sensors exhibit several loss mechanisms that lead to random vibrations of the structure (thermal-mechanical noise) as well as to random agitation of the charge carriers flowing through the sensor (thermal-electrical noise). The phase noise resulting from these thermal noise sources can not only be predicted accurately but also decreased easily by increasing the excitation amplitude (additive noise). However, it has been shown that losses appearing in the sensor's magnetic material due to domain wall actions clearly generate additional flicker phase noise that can not be decreased by increasing the excitation amplitude (parametric noise). Based on the fluctuation-dissipation theorem indicating random fluctuations of the magnetization, an analytical expression for the magnetically induced phase noise could be derived. With this result, not only the fundamental LOD due to thermal vibrations of the mechanical structure but also the LOD for sensors impaired by magnetically induced phase noise could be described. In particular, in the latter case, the LOD does not depend on the sensitivity but is solely determined by the dynamic loss properties of the magnetic layer, at least if the magnetic sensitivity is high enough such that thermal noise sources are negligible. Hence, instead of the sensitivity, the magnetic losses, represented by the material's effective complex permeability, should be considered as the most important parameter for the further improvement of such sensors. This implication is not only valid for magnetoelastic cantilevers but also applies to any type of magnetoelastic resonator.

Please note that all statements made in this article refer to magnetic fields oriented along the long axis of the cantilever as depicted in Fig. 1. If the low-amplitude magnetic measurement signal $B_x(t)$ is applied at a different angle, only the sensitivity decreases cosinusoidally while all noise contributions remain unchanged. Thus, independently of the dominant noise source, the LOD worsens by the same factor the sensitivity is decreased. Contrary, if the ambient magnetic bias flux density B_{bias} is applied at a different angle, the sensor's magnetic state might be altered significantly. Due to the tight relation between the magnetic state and the magnetic losses, not only the magnetic sensitivity but also the noise contributions will change (with exception of the thermal-electrical noise caused by the dielectric losses of the piezoelectric material). As long as the overall noise floor is dominated by random fluctuations of the magnetization, the LOD is still exclusively determined by the relative magnetic loss factor (Eq. (54)).

REFERENCES

- [1] R. Brendel, C. El Hassani, M. Brunet, and E. Robert, "Influence of magnetic field on quartz crystal oscillators," in *Proc. 43rd Annu. Symp. Freq. Control*, Denver, CO, USA, May/June 1989, pp. 268–274.
- [2] R. Brendel, "Influence of a magnetic field on quartz crystal resonators," *IEEE Trans. Ultrason., Ferroelectr., Freq. Control*, vol. 43, no. 5, pp. 818–831, Sep. 1996.
- [3] S. M. Hanna, "Magnetic field sensors based on SAW propagation in magnetic films," *IEEE Trans. Ultrason., Ferroelectr., Freq. Control*, vol. UFFC-34, no. 2, pp. 191–194, Mar. 1987.
- [4] W. Li, P. Dhagat, and A. Jander, "Surface acoustic wave magnetic sensor using galferol thin film," *IEEE Trans. Magn.*, vol. 48, no. 11, pp. 4100–4102, Nov. 2012.
- [5] M. Elhosni *et al.*, "Experimental study of multilayer Piezo-magnetic SAW delay line for magnetic sensor," *Procedia Eng.*, vol. 120, pp. 870–873, Jan. 2015.
- [6] A. Kittmann *et al.*, "Wide band low noise love wave magnetic field sensor system," *Sci. Rep.*, vol. 8, no. 1, pp. 278–287, Jan. 2018.
- [7] A. Mazzamuro *et al.*, "Highly sensitive surface acoustic wave magnetic field sensor using multilayered TbCo₂/FeCo thin film," *Proceedings*, vol. 2, no. 13, p. 902, Nov. 2018.
- [8] W. Wang, Y. Jia, X. Xue, Y. Liang, and Z. Du, "Magnetostrictive effect in micro-dotted FeCo film coated surface acoustic wave devices," *Smart Mater. Struct.*, vol. 27, no. 10, Oct. 2018, Art. no. 105040.
- [9] V. Schell *et al.*, "Magnetic anisotropy controlled FeCoSiB thin films for surface acoustic wave magnetic field sensors," *Appl. Phys. Lett.*, vol. 116, no. 7, pp. 073503-1–073503-5, Feb. 2020.
- [10] N. Yoshizawa, I. Yamamoto, and Y. Shimada, "Magnetic field sensing by an electrostrictive/magnetostrictive composite resonator," *IEEE Trans. Magn.*, vol. 41, no. 11, pp. 4359–4361, Nov. 2005.
- [11] T. Nan, Y. Hui, M. Rinaldi, and N. X. Sun, "Self-biased 215 MHz magnetoelastic NEMS resonator for ultra-sensitive DC magnetic field detection," *Sci. Rep.*, vol. 3, no. 1, p. 1985, Dec. 2013.
- [12] J. Kiser, P. Finkel, J. Gao, C. Dolabdjian, J. Li, and D. Viehland, "Stress reconfigurable tunable magnetoelastic resonators as magnetic sensors," *Appl. Phys. Lett.*, vol. 102, no. 4, pp. 042909-1–042909-4, Jan. 2013.
- [13] Y. Hui, T. Nan, N. X. Sun, and M. Rinaldi, "High resolution magnetometer based on a high frequency magnetoelastic MEMS-CMOS oscillator," *J. Microelectromech. Syst.*, vol. 24, no. 1, pp. 134–143, Feb. 2015.
- [14] L. Bian, Y. Wen, P. Li, Y. Wu, X. Zhang, and M. Li, "Magnetostrictive stress induced frequency shift in resonator for magnetic field sensor," *Sens. Actuators A, Phys.*, vol. 247, pp. 453–458, Aug. 2016.
- [15] M. Li *et al.*, "Ultra-sensitive NEMS magnetoelastic sensor for picotesla DC magnetic field detection," *Appl. Phys. Lett.*, vol. 110, no. 14, pp. 143510-1–143510-4, Apr. 2017.
- [16] M. Staruch, M.-T. Yang, J. F. Li, C. Dolabdjian, D. Viehland, and P. Finkel, "Frequency reconfigurable phase modulated magnetoelastic sensors using ΔE effect," *Appl. Phys. Lett.*, vol. 111, no. 3, pp. 032905-1–032905-4, Jul. 2017.
- [17] S. P. Bennett *et al.*, "Magnetic field response of doubly clamped magnetoelastic microelectromechanical AlN-FeCo resonators," *Appl. Phys. Lett.*, vol. 111, no. 25, p. 252903 1–5, Dec. 2017.
- [18] L. Bian *et al.*, "A resonant magnetic field sensor with high quality factor based on quartz crystal resonator and magnetostrictive stress coupling," *IEEE Trans. Electron Devices*, vol. 65, no. 6, pp. 2585–2591, Jun. 2018.
- [19] R. Oslander, S. A. Ecelberger, R. B. Givens, D. K. Wickenden, J. C. Murphy, and T. J. Kistenmacher, "A microelectromechanical-based magnetostrictive magnetometer," *Appl. Phys. Lett.*, vol. 69, no. 19, pp. 2930–2931, Nov. 1996.
- [20] B. Gojdka *et al.*, "Fully integrable magnetic field sensor based on delta-E effect," *Appl. Phys. Lett.*, vol. 99, no. 22, pp. 223502-1–223502-3, Nov. 2011.
- [21] R. Jahns *et al.*, "Microelectromechanical magnetic field sensor based on ΔE effect," *Appl. Phys. Lett.*, vol. 105, no. 5, pp. 052414-1–052414-3, Aug. 2014.
- [22] S. Zabel, C. Kirchhof, E. Yarar, D. Meyners, E. Quandt, and F. Faupel, "Phase modulated magnetoelastic delta-E effect sensor for sub-nano tesla magnetic fields," *Appl. Phys. Lett.*, vol. 107, no. 15, pp. 152402-1–152402-4, Oct. 2015.
- [23] Y. Park, E. Lee, and T. Kouh, "Field-dependent resonant behavior of thin nickel film-coated microcantilever," *Micromachines*, vol. 8, no. 4, p. 109, Apr. 2017.
- [24] P. Durdaut *et al.*, "Thermal-mechanical noise in resonant thin-film magnetoelastic sensors," *IEEE Sensors J.*, vol. 17, no. 8, pp. 2338–2348, Apr. 2017.
- [25] P. Durdaut, V. Penner, C. Kirchhof, E. Quandt, R. Knöchel, and M. Hoft, "Noise of a JFET charge amplifier for piezoelectric sensors," *IEEE Sensors J.*, vol. 17, no. 22, pp. 7364–7371, Nov. 2017.
- [26] P. Durdaut *et al.*, "Modeling and analysis of noise sources for thin-film magnetoelastic sensors based on the ΔE effect," *IEEE Trans. Instrum. Meas.*, vol. 66, no. 10, pp. 2771–2779, Oct. 2017.
- [27] P. Durdaut *et al.*, "Noise analysis and comparison of phase- and frequency-detecting readout systems: Application to SAW delay line magnetic field sensor," *IEEE Sensors J.*, vol. 19, no. 18, pp. 8000–8008, Sep. 2019.

- [28] P. Durdaut, A. Kittmann, A. Bahr, E. Quandt, R. Knöchel, and M. Hoft, "Oscillator phase noise suppression in surface acoustic wave sensor systems," *IEEE Sensors J.*, vol. 18, no. 12, pp. 4975–4980, Jun. 2018.
- [29] L. Daniel and O. Hubert, "An analytical model for the ΔE effect in magnetic materials," *The Eur. Phys. J. Appl. Phys.*, vol. 45, no. 3, p. 31101, Mar. 2009.
- [30] B. D. Cullity, *Introduction to Magnetic Materials*. Hoboken, NJ, USA: IEEE Press, 2009.
- [31] A. E. Clark, J. B. Restorff, M. Wun-Fogle, and J. F. Lindberg, "Magnetoelastic coupling and ΔE effect in $Tb_x Dy_{1-x}$ single crystals," *J. Appl. Phys.*, vol. 73, no. 10, pp. 6150–6152, May 1993.
- [32] A. Ludwig and E. Quandt, "Optimization of the ΔE effect in thin films and multilayers by magnetic field annealing," *IEEE Trans. Magn.*, vol. 38, no. 5, pp. 2829–2831, Sep. 2002.
- [33] C. Dong *et al.*, "Characterization of magnetomechanical properties in FeGaB thin films," *Appl. Phys. Lett.*, vol. 113, no. 26, pp. 262401-1–262401-5, Dec. 2018.
- [34] E. Yarar, V. Hrkac, C. Zamponi, A. Piorra, L. Kienle, and E. Quandt, "Low temperature aluminum nitride thin films for sensory applications," *AIP Adv.*, vol. 6, no. 7, pp. 075115-1–075115-11, Jul. 2016.
- [35] S. Zabel *et al.*, "Multimode delta-E effect magnetic field sensors with adapted electrodes," *Appl. Phys. Lett.*, vol. 108, no. 22, pp. 222401-1–222401-4, May 2016.
- [36] A. Hubert and R. Schäfer, *Magnetic Domains: The Analysis of Magnetic Microstructures*. Berlin, Germany: Springer, 2009.
- [37] N. O. Urs, I. Teliban, A. Piorra, R. Knöchel, E. Quandt, and J. McCord, "Origin of hysteretic magnetoelastic behavior in magnetolectric 2-2 composites," *Appl. Phys. Lett.*, vol. 105, no. 20, pp. 202406-1–202406-5, Nov. 2014.
- [38] N. O. Urs *et al.*, "Direct link between specific magnetic domain activities and magnetic noise in modulated magnetolectric sensors," *Phys. Rev. A, Gen. Phys. Appl.*, vol. 13, no. 2, pp. 024018-1–024018-10, Feb. 2020.
- [39] F. Brailsford, "Domain-wall energy and hysteresis loss in ferromagnetic material," *Proc. Inst. Electr. Eng.*, vol. 117, no. 5, pp. 1052–1055, 1970.
- [40] W. Campbell, *Introduction to Geomagnetic Fields*. Cambridge, U.K.: Cambridge Univ. Press, 2003.
- [41] D. Zhang, Z. Pan, H. Zhou, and W. Zhang, "Magnetic sensor based on giant magneto-impedance effect using the self-regulating technology on the bias magnetic field," *Sens. Actuators A, Phys.*, vol. 249, pp. 225–230, Oct. 2016.
- [42] H. Zhou, Z. M. Pan, and D. S. Zhang, "Operating point self-regulator for giant magneto-impedance magnetic sensor," *Sensors*, vol. 17, no. 5, p. 1103, May 2017.
- [43] E. Lage *et al.*, "Magnetic domain control and voltage response of exchange biased magnetolectric composites," *Appl. Phys. Lett.*, vol. 104, no. 13, pp. 132405-1–132405-4, Mar. 2014.
- [44] C. V. Heer, *Statistical Mechanics, Kinetic Theory, and Stochastic Processes*. New York, NY, USA: Academic, 1972.
- [45] K. Kobayashi, H. Yamada, and K. Matsushige, "Frequency noise in frequency modulation atomic force microscopy," *Rev. Sci. Instrum.*, vol. 80, no. 4, pp. 043708-1–043708-8, Apr. 2009.
- [46] P. Durdaut, M. Höft, J.-M. Friedt, and E. Rubiola, "Equivalence of open-loop and closed-loop operation of SAW resonators and delay lines," *Sensors*, vol. 19, no. 1, p. 185, Jan. 2019.
- [47] J. Mertz, O. Marti, and J. Mlynek, "Regulation of a microcantilever response by force feedback," *Appl. Phys. Lett.*, vol. 62, no. 19, pp. 2344–2346, May 1993.
- [48] J. Reermann, S. Zabel, C. Kirchhof, E. Quandt, F. Faupel, and G. Schmidt, "Adaptive readout schemes for thin-film magnetolectric sensors based on the delta-E effect," *IEEE Sensors J.*, vol. 16, no. 12, pp. 4891–4900, Jun. 2016.
- [49] A. Bloch, "Electromechanical analogies and their use for the analysis of mechanical and electromechanical systems," *J. Inst. Electr. Eng. I, Gen.*, vol. 92, no. 52, pp. 157–169, Apr. 1945.
- [50] C. Kirchhof *et al.*, "Giant magnetolectric effect in vacuum," *Appl. Phys. Lett.*, vol. 102, no. 23, Jun. 2013, Art. no. 232905.
- [51] M. Weinberg, R. Candler, S. Chandorkar, J. Varsanik, T. Kenny, and A. Duwel, "Energy loss in MEMS resonators and the impact on inertial and RF devices," in *Proc. 15th Int. Conf. Solid-State Sensors, Actuat. Microsyst.*, vol. 1, Denver, CO, USA, Jun. 2009, pp. 688–695.
- [52] E. Villari, "Ueber die änderungen Des.magnetischen moments, welche der zug und das hindurchleiten eines galvanischen stroms in einem stabe von stahl oder eisen hervorbringen," *Annalen der Physik und Chem.*, vol. 202, no. 9, pp. 87–122, 1865.
- [53] G. Bertotti, "General properties of power losses in soft ferromagnetic materials," *IEEE Trans. Magn.*, vol. 24, no. 1, pp. 621–630, Jan. 1988.
- [54] J. B. Goodenough, "Summary of losses in magnetic materials," *IEEE Trans. Magn.*, vol. 38, no. 5, pp. 3398–3408, Sep. 2002.
- [55] E. Yarar, V. Hrkac, C. Zamponi, A. Piorra, L. Kienle, and E. Quandt, "Low temperature aluminum nitride thin films for sensory applications," *AIP Adv.*, vol. 6, no. 7, Jul. 2016, Art. no. 075115.
- [56] S. Fichtner *et al.*, "Identifying and overcoming the interface originating c-axis instability in highly Sc enhanced AlN for piezoelectric micro-electromechanical systems," *J. Appl. Phys.*, vol. 122, no. 3, pp. 035301-1–035301-7, Jul. 2017.
- [57] A. Piorra *et al.*, "Magnetolectric thin film composites with interdigital electrodes," *Appl. Phys. Lett.*, vol. 103, no. 3, pp. 032902-1–032902-5, Jul. 2013.
- [58] T. B. Jones and N. G. Nenadic, *Electromechanics MEMS*. Cambridge, U.K.: Cambridge Univ. Press, 2013.
- [59] R. D. Grober *et al.*, "Fundamental limits to force detection using quartz tuning forks," *Rev. Sci. Instrum.*, vol. 71, no. 7, pp. 2776–2780, Jul. 2000.
- [60] A. Arnau, J. V. García, Y. Jimenez, V. Ferrari, and M. Ferrari, "Improved electronic interfaces for AT-cut quartz crystal microbalance sensors under variable damping and parallel capacitance conditions," *Rev. Sci. Instrum.*, vol. 79, no. 7, pp. 075110-1–075110-12, Jul. 2008.
- [61] Z. Hu, J. Hedley, N. Keegan, J. Spoors, B. Gallacher, and C. McNeil, "One-port electronic detection strategies for improving sensitivity in piezoelectric resonant sensor measurements," *Sensors*, vol. 16, no. 11, p. 1781, Oct. 2016.
- [62] A. G. Fowler, M. B. Coskun, and S. O. R. Moheimani, "Q control of a microfabricated piezoelectric cantilever with on-chip feedthrough cancellation," in *Proc. IEEE Conf. Control Technol. Appl.*, Kohala Coast, HI, USA, Aug. 2017, pp. 123–128.
- [63] A. L. Lance, W. D. Seal, and F. Labaar, "Phase noise and AM noise measurements in the frequency domain," in *Infrared and Millimeter Waves*, vol. 11. Orlando, FL, USA: Academic, 1984.
- [64] P. Welch, "The use of fast Fourier transform for the estimation of power spectra: A method based on time averaging over short, modified periodograms," *IEEE Trans. Audio Electroacoust.*, vol. AU-15, no. 2, pp. 70–73, Jun. 1967.
- [65] E. Rubiola, *Phase Noise and Frequency Stability in Oscillators*. Cambridge, U.K.: Cambridge Univ. Press, 2009.
- [66] R. Boudot and E. Rubiola, "Phase noise in RF and microwave amplifiers," *IEEE Trans. Ultrason., Ferroelectr., Freq. Control*, vol. 59, no. 12, pp. 2613–2624, Dec. 2012.
- [67] H. T. Hardner, M. B. Weissman, M. B. Salamon, and S. S. P. Parkin, "Fluctuation-dissipation relation for giant magnetoresistive 1/f noise," *Phys. Rev. B, Condens. Matter*, vol. 48, no. 21, pp. 16156–16159, Dec. 1993.
- [68] R. J. M. van de Veerdonk *et al.*, "1/f noise in anisotropic and giant magnetoresistive elements," *J. Appl. Phys.*, vol. 82, no. 12, pp. 6152–6164, Dec. 1997.
- [69] S. Ingvarsson, G. Xiao, S. S. P. Parkin, W. J. Gallagher, G. Grinstein, and R. H. Koch, "Low-frequency magnetic noise in micron-scale magnetic tunnel junctions," *Phys. Rev. Lett.*, vol. 85, no. 15, pp. 3289–3292, Oct. 2000.
- [70] G. Durin, P. Falferi, M. Cerdonio, G. A. Prodi, and S. Vitale, "Low temperature properties of soft magnetic materials: Magnetic viscosity and 1/f thermal noise," *J. Appl. Phys.*, vol. 73, no. 10, pp. 5363–5365, 1993.
- [71] J. Briaire, "1/f noise in permalloy," Ph.D. dissertation, Eindhoven Univ. Technol. Eindhoven, Eindhoven, The Netherlands, 2000.
- [72] S.-K. Lee and M. V. Romalis, "Calculation of magnetic field noise from high-permeability magnetic shields and conducting objects with simple geometry," *J. Appl. Phys.*, vol. 103, no. 8, pp. 084904-1–084904-10, Apr. 2008.
- [73] W. P. Jayasekara, J. A. Bain, and M. H. Kryder, "High frequency initial permeability of NiFe and FeAlN," *IEEE Trans. Magn.*, vol. 34, no. 4, pp. 1438–1440, Jul. 1998.
- [74] L. G. C. Melo, D. Ménard, A. Yelon, L. Ding, S. Saez, and C. Dolabdjian, "Optimization of the magnetic noise and sensitivity of giant magnetoimpedance sensors," *J. Appl. Phys.*, vol. 103, no. 3, pp. 033903-1–033903-6, Feb. 2008. [Online]. Available: <http://aip.scitation.org/doi/10.1063/1.2837106>

Chapter 7

First Steps Towards Sensor Arrays

7.1 Exchange Biased ΔE -Effect Sensors for Localization

All ΔE -effect sensors presented previously were characterized and operated under the application of an external magnetic bias field. Magnetic bias fields are often created by external coils around the sensor, which makes the device occupy a large volume, and renders it unhandy for practical applications. Other potential solutions include the integration of permanent magnets into stationary measurement setups. Such a setup has been used to localization magnetically labeled cells, and it is presented in Appendix B. However, for nonstationary setups and for sensor arrays with many sensor elements, the additional electronics and potentially interfering stray fields of the coils or the permanent magnet may be highly disadvantageous.

This section presents a step towards the application by discussing the first ΔE -effect magnetometer, which is based on exchange-biased multilayers and does not require external coils for operating. A dual-mode operating scheme is demonstrated to localize the sensor and simultaneously measure a small-amplitude and low-frequency magnetic field.

Contribution

- Conceptualization (shared)
- Writing of original manuscript (shared)
- Modeling and simulations (shared)
- Measurements (shared)
- Data analysis and interpretation (shared)



OPEN

Exchange biased delta-E effect enables the detection of low frequency pT magnetic fields with simultaneous localization

B. Spetzler¹, C. Bald², P. Durdaut², J. Reermann², C. Kirchhof¹, A. Teplyuk², D. Meyners¹, E. Quandt¹, M. Höft², G. Schmidt² & F. Faupel¹✉

Delta-E effect sensors are based on magnetoelectric resonators that detune in a magnetic field due to the delta-E effect of the magnetostrictive material. In recent years, such sensors have shown the potential to detect small amplitude and low-frequency magnetic fields. Yet, they all require external magnetic bias fields for optimal operation, which is highly detrimental to their application. Here, we solve this problem by combining the delta-E effect with exchange biased multilayers and operate the resonator in a low-loss torsion mode. It is comprehensively analyzed experimentally and theoretically using various kinds of models. Due to the exchange bias, no external magnetic bias fields are required, but still low detection limits down to $350 \text{ pT} / \sqrt{\text{Hz}}$ at 25 Hz are achieved. The potential of this concept is demonstrated with a new operating scheme that permits simultaneous measurement and localization, which is especially desirable for typical biomedical inverse solution problems. The sensor is localized with a minimum spatial resolution of 1 cm while measuring a low-frequency magnetic test signal that can be well reconstructed. Overall, we demonstrate that this class of magnetic field sensors is a significant step towards first biomedical applications and compact large number sensor arrays.

The detection of low-frequency magnetic fields and the localization of its source is of interest for many biological and biomedical applications^{1–3}. Because these fields result in very small signal amplitudes in the pT regime and below, SQUID magnetometers⁴ are traditionally used. These sensors are extensive and expensive in operation, as they base on superconducting devices that must be cooled and magnetically well-shielded during the measurements. Significant progress has been made with optically pumped magnetometers^{5,6}. They sense magnetic fields by the change of transmission of a laser beam through a gas cell upon application of a magnetic field. With this concept detection limits in the order of a few $\text{fT} / \sqrt{\text{Hz}}$ were achieved in a frequency range from about 1–100 Hz⁷. Although their handling is improved compared to SQUID magnetometers, they still require a magnetically shielded environment and external temperature control. For both types of sensors, the limited integrability and the comparatively large size limit the number of sensors that can be used in typical biomedical array applications. Such applications are mainly inverse solution problems, such as MEG source localization⁸ or source imaging of the heart⁹. For a correct solution the precise knowledge of the sensor's position and orientation is essential¹⁰ as well as a large number of measurements.

In recent years, strain-mediated magnetoelectric composite magnetic field sensors have been investigated for similar purposes^{11–13}. They consist of mechanically coupled magnetostrictive and piezoelectric materials and can be processed on a large scale by MEMS technology with dimensions of a few millimeters¹⁴ down to a few micrometers^{15,16}. Such small devices are of special interest for array applications due to the potentially improved spatial resolution and reduced equipment costs.

Utilizing the magnetoelectric effect¹², limits of detection $< 1 \text{ pT} / \sqrt{\text{Hz}}$ can be reached¹⁷ with cm sized sensors, but only in mechanical resonance. Hence, the low detection limits are restricted to rather high-frequency magnetic fields within a narrow bandwidth around the device's resonance frequency. Such high frequencies and small bandwidths do not match the requirements of many biomedical applications.

¹Institute of Materials Science, Faculty of Engineering, Kiel University, Kaiserstraße 2, 24143 Kiel, Germany. ²Institute of Electrical Engineering and Information Technology, Faculty of Engineering, Kiel University, Kaiserstraße 2, 24143 Kiel, Germany. ✉email: ff@tf.uni-kiel.de

One way to overcome the limitations is the utilization of modulation techniques used e.g. in the delta-E effect read-out scheme. The delta-E effect of the magnetic material^{18–21}, is the change of the Young's modulus upon application of a magnetic field or a mechanical stress. Using the sensor concept with plate and cantilever magnetolectric resonators, detection limits in the sub-nT regime have been achieved in frequency bandwidths up to 100 Hz^{16,22–25}. Such low detection limits are achieved by applying a magnetic bias field with external coils to operate the sensor at its optimum signal-to-noise ratio, close to the maximum curvature of the magnetostriction curve. This comes at the expense of integrability and size of the sensor system with direct consequences for the application.

In general, coils require additional electronics and are difficult to integrate, which diminishes the advantage of using integrable technology for the magnetolectric resonators. In previously presented delta-E effect sensors^{16,22–25}, the coils increase the size of the system to several centimeters, even though the actual resonators have only dimensions in the hundreds of μm to mm range. As a result, the minimum distance of sensor and source increases, which can reduce the measured signal amplitude significantly. Moreover, the size and stray fields of the coils can be problematic for building dense, large number sensor arrays that are desirable for many biological and biomedical applications. Consequently, replacing the coils is an important step towards application.

A few devices avoid external magnetic bias fields using magnetic hysteresis^{16,22} at the expense of the detection limit. Magnetic hysteresis is connected with statistical magnetization or domain reorientation processes, which are intrinsically linked to magnetic noise²⁶. Consequently, this approach is potentially problematic for the reproducibility, stability, and the noise performance of magnetic field sensors.

A different way of achieving self-biased systems is the implementation of exchange biased multilayers^{27,28}. Such multilayers consist of a sequence of antiferromagnetic and ferromagnetic layers. The magnetization of these layers is coupled at their interface by a unidirectional exchange interaction that defines a preferable direction of the magnetization in the ferromagnetic layers²⁹. Overall, the effect on the ferromagnetic layers is similar to an external magnetic field.

Here we report on mm-sized delta-E effect sensors based on exchange biased multilayers and analyze their potential for the detection of small amplitude and low-frequency magnetic fields. A domain model³⁰ is extended to describe the magnetoelastic properties of the multilayer. Various other models are used to analyze measurements of the electromechanical and the sensing characteristics. Further, we demonstrate an operation technique that combines the advantages of direct magnetolectric and delta-E operation. It permits the detection of low-frequency magnetic fields using the delta-E effect in a higher resonance mode (RM), while simultaneously using the direct detection of the first mode to localize the sensor. The simultaneous measurement of location and signal is expected to be especially advantageous if the source can move, which is typically the case for source localization or imaging on patients. As a proof of concept, we use this technique to measure the magnetic field of a low frequency magnetic test signal with the delta-E effect, while localizing the sensor via the direct detection scheme.

Results

Exchange biased MEMS sensor. The magnetolectric composite sensors presented in this study are made by MEMS technology on a polysilicon cantilever surrounded by a silicon frame (Fig. 1a). The $W = 1$ mm wide, $L = 3$ mm long, and $50 \mu\text{m}$ thick cantilevers are covered by a magnetic multilayer and a piezoelectric AlN layer (Fig. 1c). The magnetic layer is made of a sequence of $20 \times (\text{Ta} / \text{Cu} / \text{Mn}_{70}\text{Ir}_{30} / \text{Fe}_{70.2}\text{Co}_{7.8}\text{Si}_{12}\text{B}_{10})$ with a total thickness of about $4 \mu\text{m}$. The multilayer is tempered under application of a strong magnetic field applied at an angle of 55° relative to the long cantilever axis. This process induces a magnetic easy axis and sets the exchange bias field. The $2 \mu\text{m}$ thick AlN layer³¹ on top of the magnetic film is used for excitation and read-out simultaneously. It is sandwiched by two Ta-Pt electrodes. An adapted electrode design²³ permits the efficient excitation of the 1st and 2nd bending mode. In this study both electrodes E_1 and E_2 (Fig. 1b) are used. Process details are described in the “Materials and methods” section. As shown in Fig. 1a, the MEMS chip with the magnetolectric cantilever is placed on a printed circuit board (PCB) and connected to a low noise JFET charge amplifier. Its equivalent circuit is given in Ref.³². The PCB is mounted on a 3D-printed holder and encapsulated in a brass cylinder (brass thickness: 2.1 mm) for electrical shielding and mechanical protection.

Magnetic properties. For the analysis of the magnetic properties, a magnetoelastic model is built. Simple single-domain models are accompanied by strong magnetic hysteresis for magnetic fields that are not applied along the magnetic hard axis³³. In soft-magnetic FeCoSiB thin-films, domain wall motion is expected to dominate the magnetization reversal process²⁶. This causes a significantly smaller coercive field than predicted by single-domain Stoner-Wohlfarth models, especially for magnetic fields applied close to the magnetic easy axis. Consequently, domain wall motion must be considered to describe the magnetization and the delta-E effect. The few numerical domain models that exist^{30,34} include neither exchange bias fields, nor arbitrary magnetic field directions and are therefore extended by the respective energy contributions (“Materials and methods” section).

In Fig. 2a measured and modeled magnetization curves are compared for a magnetic flux density \bar{B} applied along the long axis ($\varphi_H = 0^\circ$), the short axis ($\varphi_H = 90^\circ$), and for an example angle in between ($\varphi_H = 60^\circ$). The model matches the measurements well. Only small deviations occur around the transition from a dominant wall motion to a dominant moment rotation, which results in a larger curvature of the modeled magnetization curves. In a real multi-domain sample, the spatially distributed magnetic domains and effective anisotropies are expected to smooth out this transition. Overall, the model does reproduce the measured magnetization behavior correctly, even over the full range of φ_H (Fig. 2b). An effective easy axis orientation of $\theta = 1.5^\circ$ relative to the x-axis is found from the fit, with an effective uniaxial anisotropy energy density of $K_u = 1.8 \text{ kJ/m}^3$. The exchange bias field is found to be oriented $\varphi_{\text{ex}} = 46^\circ$ with a magnitude $B_{\text{ex}} \approx 0.8 \text{ mT}$. This is identical to the

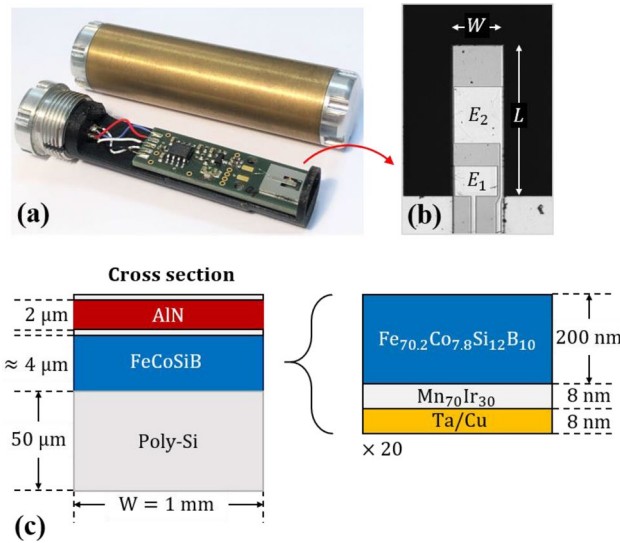


Figure 1. Exchange biased delta-E effect sensor. **(a)** Exchange biased magnetoelastic composite cantilever sensors presented in this study with (top) and without (bottom) encapsulation. The devices consist of a MEMS chip with a magnetoelastic resonator on a printed circuit board (PCB) with a JFET charge amplifier³². The PCB is mounted on a 3D-printed holder (black) with a ring at its end for mechanical protection of the cantilever. A brass encapsulation (brass thickness: 2.1 mm) is used for electrical shielding. **(b)** Microscopy image of a cantilever ($W = 1$ mm, $L = 3$ mm) with top electrodes E_1 and E_2 . **(c)** Schematic cross section of the cantilever with thicknesses of the functional layers and the structure of the exchange biased magnetic multilayer. Details are given in the “Materials and methods” section.

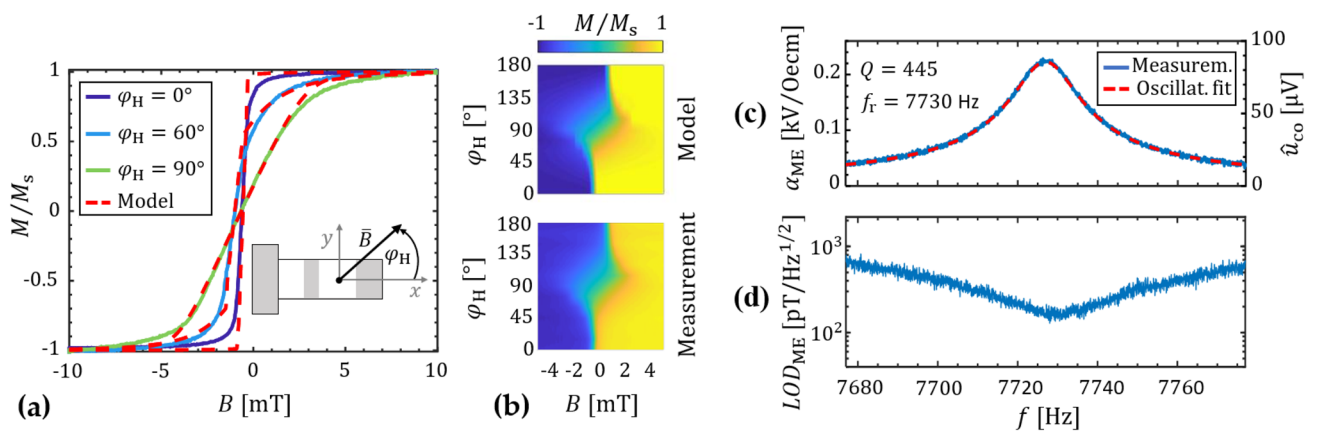


Figure 2. Magnetic and magnetoelastic properties. **(a)** Magnetization loops measured with a BH-loop tracer in three different directions are compared with the simulations: along the long axis ($\varphi_H = 0^\circ$), the short axis ($\varphi_H = 90^\circ$), and an example orientation in between ($\varphi_H = 60^\circ$). For the exchange bias field a magnitude $B_{ex} \approx 0.8$ mT and orientation of ($\varphi_{ex} = 46^\circ$) is obtained. **(b)** Comparison of measured and modeled magnetization curves in the range of $\varphi_H = 0^\circ - 180^\circ$. **(c)** Magnetoelastic coefficient α_{ME} of the first bending mode (RM1), calculated via Eq. (1) from the measurements. The ac magnetic flux density is applied along the x-axis (a) with an amplitude of $\hat{B}_{ac} = 100$ nT. From a harmonic oscillator fit a quality factor of $Q_1 \approx 445$ and a resonance frequency of about $f_{r,1} = 7728$ Hz are calculated. **(d)** Detection limit measured around the first bending mode. A minimum value of about $LOD_{ME} = 150$ pT/ $\sqrt{\text{Hz}}$ is obtained at $f_{r,1}$ with encapsulation, and an estimated value of approximately $LOD_{ME} = 30$ pT/Hz without.

orientation and magnitude found experimentally from the x-axis offset of the two measured hysteresis curves along $\varphi_H = 0^\circ$ and $\varphi_H = 90^\circ$.

Direct operation. For the sensor localization, the direct detection mode will be used. It utilizes the direct magnetoelastic effect in the first resonance mode (RM1), the first bending mode. The magnetoelastic effect is often characterized by the magnetoelastic coefficient

$$\alpha_{ME} = \frac{\hat{u}_p}{t_p \hat{B}_{ac}}, \text{ with } \hat{u}_p = \hat{u}_{co} \frac{C_f}{C_{ME}} \tag{1}$$

which can be calculated from the voltage amplitude \hat{u}_p across the piezoelectric layer, the thickness t_p of the piezoelectric layer and the ac amplitude \hat{B}_{ac} of the field to be measured, applied along the x-axis (Fig. 2). The voltage amplitude \hat{u}_p across the piezoelectric layer relates to the output voltage amplitude \hat{u}_{co} of the charge amplifier via the feedback capacitance $C_f = 33$ pF of the charge amplifier and the capacitance C_{ME} of the magnetoelectric sensor, which is determined in the following section as $C_{ME} = 63$ pF. All amplitudes in this paper are tagged with a hat in contrast to root mean square values.

For the characterization of the first bending mode (RM1) in the direct detection mode, a sinusoidal magnetic field was applied along the x-axis with an amplitude $\hat{B}_{ac} = 100$ nT and frequencies f_{ac} around the expected first bending resonance frequency. The magnetoelectric coefficient α_{ME} is calculated with Eq. (1) and a harmonic oscillator fit is used to characterize the resonance mode (“Materials and methods” section). The results are plotted in Fig. 2c. In resonance of the first bending mode we obtain $\alpha_{ME} = 0.22$ kV/(Oe · cm) = 220 MV/(T · m) and a voltage sensitivity at the output of the charge amplifier of $S_{ME} = 856$ V/T. A quality factor of $Q_1 \approx 445$ and a resonance frequency of $f_{r,1} = 7728$ Hz are obtained from the harmonic oscillator fit. This yields a -3 dB signal bandwidth of $bw_1 \approx 8.6$ Hz via $bw_1 = f_r/(2Q)^{35}$. With an additional noise measurement, we achieve a limit of detection of about $LOD_{ME} = 150$ pT/ $\sqrt{\text{Hz}}$ (Fig. 2d) for the direct detection in resonance. The voltage sensitivity and the limit of detection are in the same range but slightly improved compared to recent values of smaller, externally biased devices³⁶. It is worth noting that the ac magnetic field is damped due to the -3 dB cut-off frequency of the brass cylinder at 1.5 kHz. Without the cylinder, the ME voltage sensitivity around the resonance frequency increases by a factor of about 5, which improves the limit of detection to an estimated value of approximately $LOD_{ME} = 30$ pT/Hz. Here, a limit of detection in the lower pT-regime is not required, because the direct detection mode is only used for the sensor localization.

Delta-E operation. For the detection of low-frequency magnetic fields, the sensor is operated in delta-E mode. During the delta-E operation, a sinusoidal voltage is applied to the piezoelectric layer to drive the resonator close to its mechanical resonance frequency. A change in the magnetic field leads to a shift of the resonance frequency due to the delta-E effect. This frequency shift leads to a corresponding change of the sensor’s electrical admittance. Hence, an alternating magnetic field modulates the current through the sensor, which can be measured as a voltage u_{co} with a charge amplifier. In general, the modulation occurs in amplitude and in phase, depending on the excitation frequency f_{ex} . In our case, the operating point is chosen such that the phase modulation can be neglected in good approximation. For small signals, the output voltage at the charge amplifier is then approximately:

$$u_{co}(t) \approx |Z_f(f_{ex})| \cdot \hat{u}_{ex} \cdot [Y_0 + S_{dyn} S_{am} B_{ac}(t)] \cdot \cos(2\pi f_{ex} t). \tag{2}$$

Here \hat{u}_{ex} is the amplitude of the excitation voltage and $|Z_f(f_{ex})|$ the impedance magnitude of the charge amplifier’s feedback network. In the equation, $Y_0 := |Y(f_{ex}, B_0)|$ is the magnitude of the electrical admittance at f_{ex} and the magnetic dc bias flux density B_0 optionally applied in x-direction during operation or for characterization. The alternating magnetic flux density B_{ac} along the x-axis modulates the amplitude \hat{u}_{co} of u_{co} via the amplitude sensitivity S_{am} . The sensor’s bandpass characteristic is included in S_{dyn} and can be described by a first-order Bessel filter³⁷. We define the amplitude sensitivity in accordance with³⁸ as:

$$S_{am} = S_{mag} S_{el} := \left. \frac{df_r}{dB} \right|_{B=B_0} \left. \frac{d|Y|}{df} \right|_{f=f_{ex}, B=B_0} \tag{3}$$

with the electrical amplitude sensitivity S_{el} and the magnitude B of the dc flux density along the x-axis. The magnetic sensitivity S_{mag} can be obtained from the slope of the resonance frequency f_r as a function of the applied magnetic flux density B at B_0 . To compare the electric and magnetic sensitivities of different devices, relative sensitivities $S_{mag,r} := (df_r/dB)f_r^{-1}$ and $S_{el,r} := (d|Y|/df)f_r$ are defined. To reconstruct the magnetic measurement signal $B_{ac}(t)$, the charge amplifier’s output signal $u_{co}(t)$ is fed into a quadrature amplitude demodulator. Its output voltage is given by

$$u(t) = \frac{1}{2} |Z_f(f_{ex})| \cdot \hat{u}_{ex} \cdot [Y_0 + S_{dyn} S_{am} B_{ac}(t)], \tag{4}$$

yielding a voltage sensitivity of

$$S_V = \frac{1}{2} |Z_f(f_{ex})| \cdot \hat{u}_{ex} \cdot S_{am} S_{dyn} \tag{5}$$

The limit of detection (LOD), also referred to as equivalent magnetic noise floor or detectivity can be estimated by

$$LOD(f) = \frac{U(f)}{S_V(f)}, \tag{6}$$

	f_r [kHz]	Q	L [kH]	C [fF]	R [k Ω]	C_{ME} [pF]
RM2	47.961	1410	1.4114	7.8	301.68	63
RM3	48.082	1156	0.9937	11	259.62	

Table 1. Results of the mBVD fit. Equivalent circuit parameters, resonance frequencies f_r and quality factors Q of the two higher resonance modes RM2 and RM3 at zero bias field.

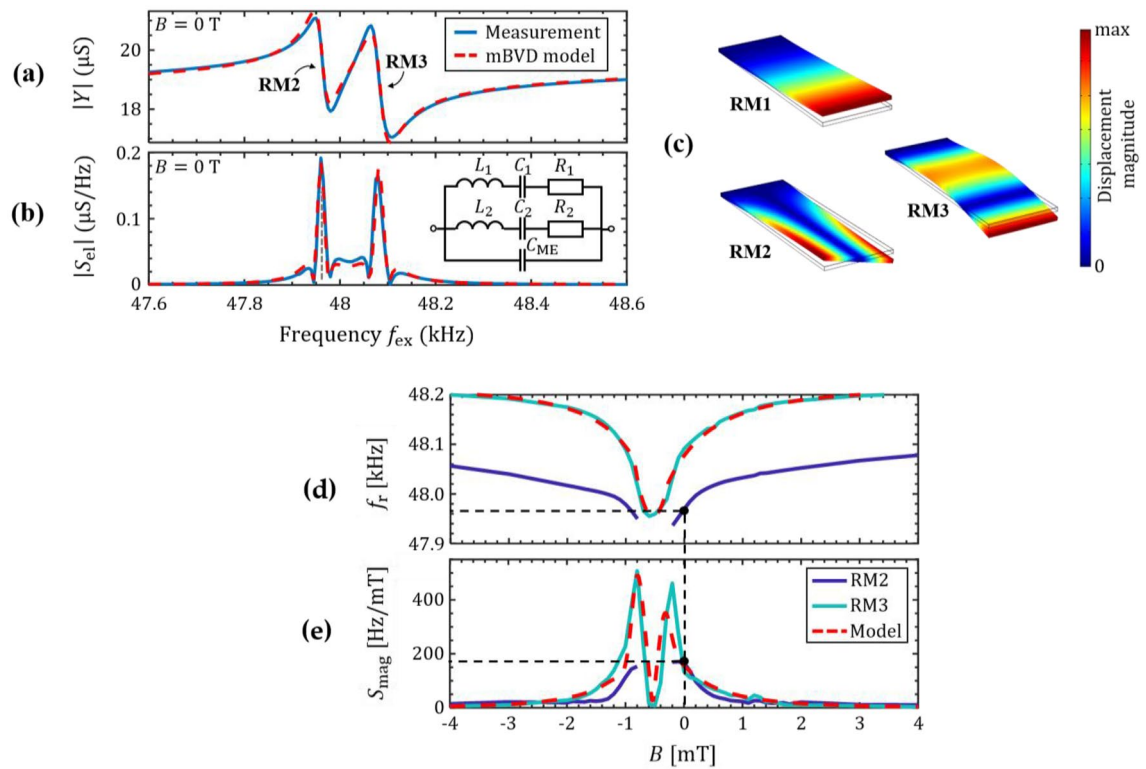


Figure 3. Sensitivity of delta-E operation. (a) Measured and modeled electrical admittance of the sensor at $B=0$ and (b) the absolute of its derivative. The modified BVD equivalence circuit used for the fit is shown as inset and the resulting values are given in Table 1. (c) Solutions of the finite element study for the first three resonance modes (RM1-RM3) with eigenfrequencies $f_{r,1} < f_{r,2} < f_{r,3}$, (d) Simulation and measurements of the resonance frequencies and (e) its first derivative the magnetic sensitivity S_{mag} , as a function of the magnetic bias field applied along the x-axis. The black, dashed lines mark the frequency of operation at zero bias and the corresponding magnetic sensitivity S_{mag} and resonance frequency. The measurement was started in the negative magnetic field regime along the cantilever's long axis.

With U being the voltage noise spectral density at the demodulator's output for $B_{ac} = 0$. For the delta-E operation we use a higher resonance mode (RM). Compared to the first bending mode (RM1) the higher resonance frequency yields a larger signal bandwidth and previous studies have shown a superior sensitivity and LOD ^{23,38}. To find the optimum operating point parameters for the delta-E operation, the admittance Y is measured as a function of the excitation frequency f_{ex} over a frequency range in which the second bending mode is expected.

The measurement is performed with an excitation amplitude of $\hat{u}_{ex} = 650$ mV and a magnetic bias field of $B = 0$ mT. As shown in Fig. 3a, the measurement reveals two resonance modes, we refer to as RM2 and RM3, approximately 100 Hz apart from each other. To analyze these modes a modified Butterworth van Dyke (mBVD) model³⁹ is fitted to the data. Within this model, each resonance mode is described by an LCR series circuit, both in parallel to each other and to the sensor capacitance C_{ME} . A sketch of the mBVD model is shown in Fig. 3b together with the magnitude $|S_{el}|$ of the electrical sensitivity derived from $|Y|$. The model fits the measurements well with the parameters given in Table 1. From these parameters, the resonance frequencies $f_r = (2\pi\sqrt{LC})^{-1}$ and the quality factors $Q = R^{-1}\sqrt{L/C}$ are calculated.

The resonance frequencies are found to be $f_{r,2} = 47.961$ kHz and $f_{r,3} = 48.082$ kHz. Both modes exhibit high quality factors of $Q_2 \approx 1400$ and $Q_3 \approx 1160$, respectively. Especially Q_2 is higher compared to typical values of $Q \approx 1000$ ^{22,23,25} for cantilever sensors of a comparable geometry in the first and second bending mode. Among other influence factors, the quality factor depends on the local magnetic properties^{22,40}, and significantly on the

air damping of the specific resonance mode⁴¹. Hence, the higher Q_2 of RM2 could indicate the excitation of a different kind of resonance mode.

With a finite element-based eigenfrequency study (“Materials and methods”) the eigenfrequencies of the first three resonance modes (RM1–RM3) of the beam are calculated. Consistent with the measurements, we find the first bending mode at about 7700 Hz and the second bending mode and the first torsional mode both at about 48 kHz. The resulting mode shapes are shown in Fig. 3c. Details on the model and the material parameters used are given in the “Materials and methods” section. As a consequence of the high Q -factors, the -3 dB bandwidths $bw = f_r/(2Q)$ ³⁵ with values of $bw_2 = 17$ Hz and $bw_3 = 21$ Hz are slightly smaller than typical bandwidths of the second bending mode. A maximum electrical sensitivity of $S_{el} \approx 0.2 \mu\text{S}/\text{Hz}$ ($S_{el,r} \approx 1$ S/%) is found at an excitation frequency of $f_{ex} = 47.96$ kHz $\approx f_{r,2}$. To analyze the magnetic sensitivities S_{mag} of the two resonance modes, the sensor’s admittance is measured for different magnetic bias flux densities B applied along the x -axis (Fig. 2), starting close to negative magnetic saturation at $B = -8$ mT. The resonance frequencies f_r are then extracted with the mBVD model and plotted in Fig. 3d.

With the Euler–Bernoulli eigenfrequency equation (“Materials and methods” section) of the second bending mode we calculate f_r using the Young’s modulus $E(B)$ predicted by the domain model [“Materials and methods”, Eq. (16)]. Using the same model parameters as in Fig. 2 leads to an excellent match between modeled and measured $f_r(B)$ curve of RM3 in Fig. 3d and e. The only parameter altered is the effective anisotropy energy density, which is reduced to $K = 1160$ J/m³. The smaller K_u could be caused by the simplified domain structure of the model, but it is also expected because the 2nd bending mode was found to weight the magnetic properties locally and thereby avoid regions of large effective anisotropy energy densities at the clamping of the cantilever³⁸.

Whereas for RM3, $f_r(B)$ data are given over the complete range of B , no data are shown for RM2 between -0.9 and -0.2 mT. In this flux density range, the resonance mode RM2 is no longer excited and hence, not present in the measured admittance characteristic. It is observed in all sensors investigated here and not a unique property of this sample. The magnetic sensitivity S_{mag} , as defined in Eq. (3) is calculated from the measured and modeled data in Fig. 5a and plotted in Fig. 3e. Whereas the maximum magnetic sensitivity of RM2 is located at zero bias field, for RM3 it is shifted to -0.8 mT. This is a direct consequence of the implemented exchange bias and well reflected by the domain model. At this bias field (-0.8 mT) the magnetic sensitivity of RM3 is $S_{mag} \approx 500$ Hz/mT ($S_{mag,r} \approx 1\%$ /mT). The magnetic sensitivity S_{mag} at $B=0$ is approximately the same for both resonance modes. Due to the exchange bias it is non-zero and with $S_{mag} \approx 175$ Hz/mT ($S_{mag,r} \approx 0.36\%$ /mT) only a factor of about three times smaller than the maximum value at -0.8 mT. Using Eq. (3) the amplitude sensitivities of RM2 and RM3 are $S_{am,2} \approx 35$ $\mu\text{S}/\text{mT}$ and $S_{am,3} \approx 31.5$ $\mu\text{S}/\text{mT}$ at $B=0$. These sensitivity values are within the typical range measured at the optimum bias field of non-exchange biased delta-E effect sensors^{22,23,25,42}. Consequently, the implemented exchange bias enables high sensitivity delta-E measurements without an externally applied magnetic bias field.

In the following, all measurements are performed at $B=0$. An important parameter for the maximum voltage sensitivity S_V and the optimum limit of detection LOD , is the excitation voltage amplitude \hat{u}_{ex} . To find the optimum \hat{u}_{ex} , the sensor is operated in RM2 at the determined operating point of $f_{ex} = 47.96$ kHz and $B=0$ for increasing \hat{u}_{ex} . A sinusoidal magnetic test signal $B_{ac}(t)$ with an amplitude of $\hat{B}_{ac} = 100$ nT and a frequency of $f_{ac} = 10$ Hz is applied. The sensor’s output signal is demodulated to obtain the voltage amplitude \hat{u} , required to calculate the voltage sensitivity S_V . Noise measurements are performed at each \hat{u}_{ex} to obtain the demodulated voltage noise density U , necessary to estimate the LOD with Eq. (6). The results are plotted in Fig. 4a for S_V and U , and in Fig. 4b the LOD as a function of \hat{u}_{ex} . It can be seen that, in accordance with Eq. (5), S_V increases linearly with \hat{u}_{ex} , consequently S_{am} is approximately constant with \hat{u}_{ex} . In contrast to the voltage sensitivity, the voltage noise density U increases more than linearly with \hat{u}_{ex} . We obtain a minimum LOD (at 10 Hz and $\hat{u}_{ex} = 650$ mV) of about $LOD = 450$ pT/ $\sqrt{\text{Hz}}$. This signal-and-noise behavior has been shown previously on similar sensors without exchange bias²⁵, where the minimum LOD was slightly worse, but at a similar excitation amplitude. It was argued that magnetic noise is induced by inverse magnetostriction during the cantilever oscillation and therefore increases with the excitation amplitude. The magnetic noise has been linked directly to magnetic domain activity in other magnetoelectric sensor devices, which might also apply here²⁶.

Delta-E signal-and-noise measurements are performed at the optimum operating conditions of $\hat{u}_{ex} = 650$ mV and $B=0$ with frequencies of the magnetic test signal between $f_{ac} = 1 - 300$ Hz and an amplitude of $\hat{B}_{ac} = 100$ nT. The measured output amplitude \hat{u} and the corresponding voltage sensitivity S_V [Eq. (5)] as functions of the signal frequency f_{ac} are shown in Fig. 4c. As observed in sensors without exchange bias²⁵ the output amplitude decreases with f_{ac} due to the low pass characteristic of the mechanical resonator. At about 100 Hz, an additional maximum is present in the data that correlates with the appearance of the third resonance mode RM3 seen in the admittance measurements. With the voltage sensitivity S_V , the detection limit (LOD) is calculated as a function of f_{ac} [Eq. (6)] and plotted in Fig. 4d. We obtain an $LOD_2 \leq 450$ pT/ $\sqrt{\text{Hz}}$ in the range of 10 – 50 Hz, with a minimum of about 350 pT/ $\sqrt{\text{Hz}}$ at 25 Hz. These detection limits are in the range of 100 – 500 pT/ $\sqrt{\text{Hz}}$ as reported for externally biased sensors of a comparable geometry^{22,23,25}.

Dual-mode operation. In this section, the sensor is operated with a scheme we refer to as dual-mode operation. In dual-mode operation, we localize the sensor using the direct detection scheme and simultaneously measure small amplitude and low-frequency magnetic fields via the delta-E effect. To distinguish the signals picked up by the respective operation scheme from each other, two different resonance modes are used. For the direct detection, the small bandwidth 1st bending mode (RM1) is excited. For the detection of the small-amplitude signal via the delta-E effect, a higher-order resonance mode is used to benefit from the larger bandwidth. In this example, we use the RM2 mode for the delta-E measurement, which was thoroughly analyzed in the previous section.

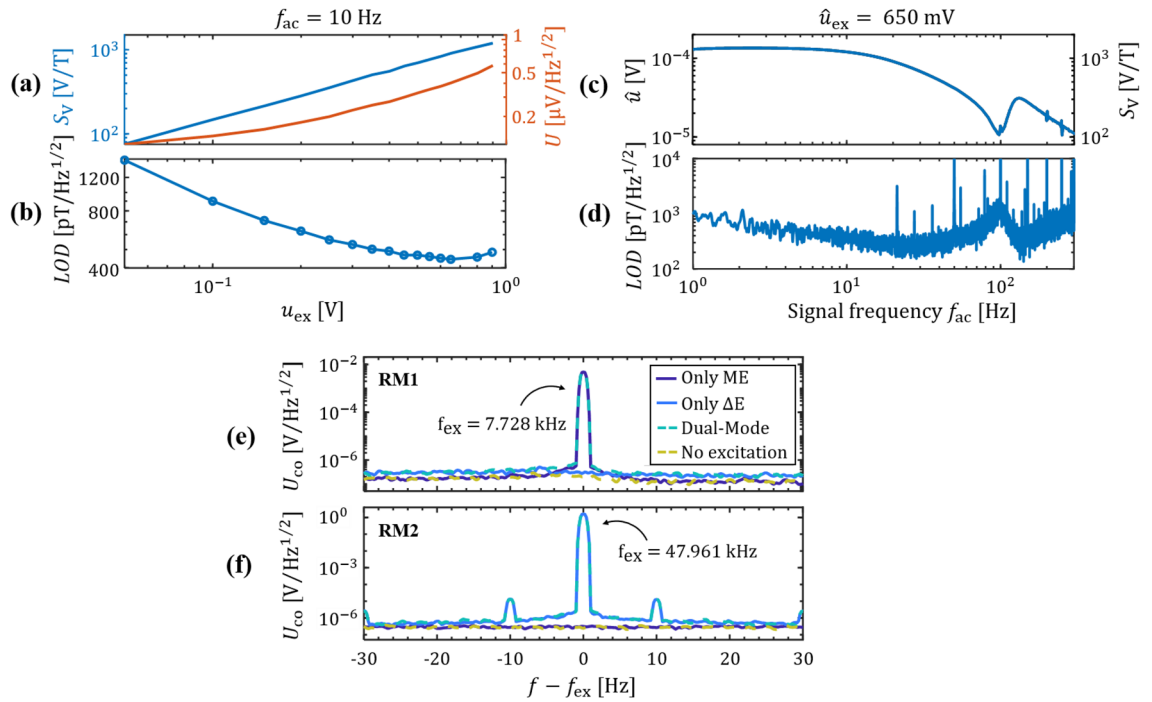


Figure 4. Signal, noise, and LOD. (a) Delta-E voltage sensitivity S_V and demodulated voltage noise density U at $f = 10$ Hz and $B = 0$ as functions of the excitation voltage amplitude \hat{u}_{ex} , and (b) the corresponding limit of detection with a minimum of about $450 \text{ pT}/\sqrt{\text{Hz}}$ found at an optimal excitation amplitude of $\hat{u}_{ex} = 650 \text{ mV}$. (c) Signal amplitude and (d) LOD, both at the optimal operation conditions of $\hat{u}_{ex} = 650 \text{ mV}$ as functions of the signal frequency, with a minimum of about $350 \text{ pT}/\sqrt{\text{Hz}}$ at 25 Hz . The disturbances visible for $f_{ac} > 200 \text{ Hz}$ are caused by insufficient electrical shielding. (e) and (f) Amplitude density spectra of the sensor for only direct detection (Only ME), only delta-E detection with a 10 Hz test signal (Only ΔE), parallel operation (Dual-Mode) and no excitation at all (No excitation). The x-axes are centered around the excitation frequency f_{ex} which equals the resonance frequency of the respective resonance mode. The results are shown for (e) the 1st bending mode (RM1) and (f) the first higher resonance mode (RM2).

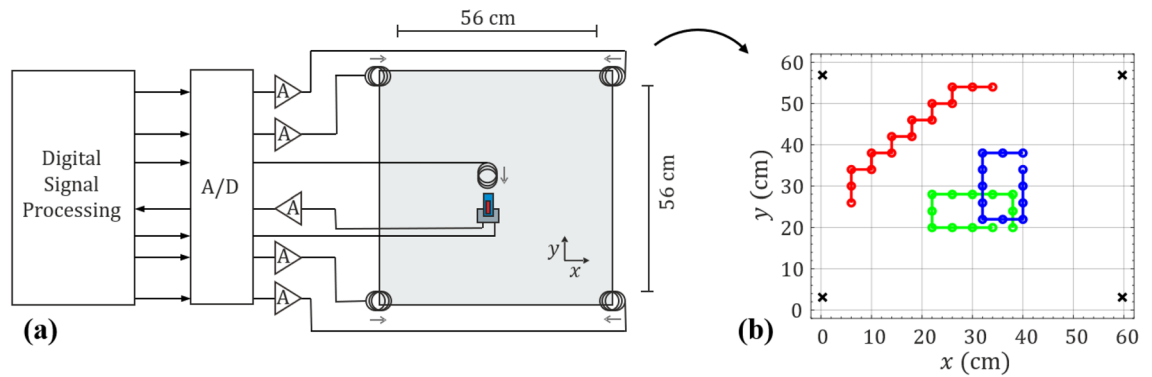


Figure 5. Dual-mode and localization test setup. (a) Measurement setup for the dual-mode operation of the exchange bias ME sensors. Four coils are positioned around the measurement area for the localization of the ME sensor and one additional coil is generating a magnetic test signal. The orientations of the coils are denoted by the grey arrows. The source coil is always oriented towards the sensor and shown here for the example of the sensor being oriented along the y -axis. (b) Sensor positions used for testing the localization of the ME sensor. Three different sets of positions (green, blue, and red circles) have been tested. The black crosses mark the positions of the transmitting coils. In total, 39 different positions were tested. With two different orientations each this results in a total of 78 different position-orientation pairs.

In the following, the influence of the parallel operation on the noise floor is analyzed. Measurements of the sensor are performed in four different ways as shown in Fig. 4e and f. First, it is operated in direct detection in the first bending mode (Only ME). Secondly, it is operated only in the delta-E read-out scheme in RM2 with a 10 Hz test signal (Only ΔE). Thirdly, both modes are operated simultaneously (Dual-Mode). For the delta-E excitation voltage, we use the optimum value of $\hat{u}_{ex} = 650 \text{ mV}$ and for the magnetic excitation of the first bending mode

a field amplitude of $\hat{B}_{ac} \approx 5 \mu\text{T}$. Additional to the three measurements the noise floor was quantified without any active excitation (No excitation). The measurements were operated outside of the magnetic shielding in a similar setup as used for the localization in the next section.

As expected, a carrier peak is visible at the excitation frequency of RM1 (Fig. 4e) for only ME and dual-mode operation. Correspondingly, a carrier peak is visible at RM2 (Fig. 4f) for only delta-E and dual-mode operation. In RM2 sidebands are visible at ± 10 Hz around the carrier. They result from the modulation of the sensor current by the 10 Hz magnetic test signal via the delta-E effect [Eq. (2)]. In RM1 the smaller bandwidth results in a larger attenuation of the low-frequency test signal compared to the higher frequency RM2 mode. Additionally, the carrier amplitude is more than two orders of magnitude smaller than in RM2 and hence also the sidebands. Consequently, no sidebands are visible in RM1, although the delta-E modulation does occur. The suppression of sidebands below the noise level is advantageous for simultaneous measurement and localization in dual-mode operation. It simplifies the signal processing by separating the source signal from the localization ME-signal in the frequency regime. The main requirement for the localization is a clear separation of the ME-signal from the noise floor. Hence, the ME-signal can be tuned within a large amplitude range to provide a measurable signal with still sufficient sideband suppression.

Dual-mode measurements with localization. The measurements were performed outside of the magnetically shielded setup using the sensor analyzed before and four coils transmitting orthogonal signals for the localization of the sensor. Two of the coils were oriented in the positive x-direction and the other two coils in the negative x-direction. All coils were calibrated, and the coil signals were amplified after D/A conversion. An additional coil generates a low-frequency magnetic test signal with frequency components similar to those of a human heart signal. It is to be measured in the delta-E operation mode in RM2. The coil is oriented towards the sensor with a fixed distance and an amplitude of the r-wave of approximately 250 nT at the sensor's position. A sketch of the measurement setup is shown in Fig. 5a. The position and orientation of the sensor is estimated by solving an inverse problem using a minimum least squares algorithm⁴³. A forward model was designed considering the positions and orientations of the coils as well as various position-orientation pairs the sensor could occupy. The coils were approximated by a magnetic point dipole model⁴⁴. Details on the localization algorithm and the calculation of the forward model can be found in the “Materials and methods” section.

In this study we use a $56 \times 56 \text{ cm}^2$ test area with a grid size of 1 cm used for the minimum least squares algorithm. The long axis of the sensor is always oriented along one of the unit vectors e_x and e_y of the Cartesian coordinate system. Three different sets of positions were tested (Fig. 5b), each set for both orientations. This results in a total of 78 different position-orientation pairs measured. These position-orientation-pairs were localized using different tilts γ of the sensor's sensitivity axis relative to the long axis of the sensor in the forward problem. The tilts were varied between -45° and 45° in 1° steps. The mean magnitude position estimation error μ_e as well as the median magnitude position estimation error m_e and the percentage of correct estimated sensor orientations d_e for all the tested position-orientation-pairs are shown in Fig. 6a,b.

A minimum of the localization error results for a tilt of $\gamma \approx 20^\circ \pm 10^\circ$ of the sensor's sensitivity axis. One reason for this broad minimum is the robustness of the localization algorithm against smaller orientation mismatches. The results show a minimum mean localization error of about $\mu_e = 4.82$ cm and a minimum median error of about $m_e = 2.532$ cm for the positions shown in Fig. 5b. The large difference between μ_e and m_e indicates outliers in the localization results. This error depends on the positions measured. Considering, for instance, only the blue set of sensor locations (Fig. 5b) with orientations in e_y led to better results as shown in Fig. 6c-d. The localization error is $\mu_e = 0.991$ cm and $m_e = 1$ cm. The results depicted in Fig. 6a-d are comparable with the results of other magnetic localization approaches, where no signal was measured simultaneously. For instance, in⁴⁵ an average error of 5.3 cm could be achieved by spanning a $3 \times 3 \text{ m}^2$ grid with three transmitter coils. In⁴⁶ a 1D coil and a 3D sensor were used for localization. The grid size was $8 \times 7 \text{ cm}^2$ for the 2D localization case and the average localization error was about 2 mm.

For the proof of concept, only simple models of the coils and the sensor were used here. With improved models, based on the Biot-Savart-Law for the coils and a more accurate model for the sensor that considers its geometry we anticipate a significant reduction of the localization error¹⁰. Further improvement could be achieved by e.g. increasing the number of transmitting coils to reduce ambiguities. The demodulated signal of RM2 for an example dual-mode measurement is depicted in Fig. 6e. Due to the higher bandwidth of RM2 the magnetic test signal can be almost entirely reconstructed. After demodulation, the signal is lowpass-filtered with a cut-off frequency of 30 Hz for the removal of noise and linearly detrended.

Summary and conclusion

We presented a fully integrable low-field delta-E effect sensor with MnIr-based exchange biased multilayer. It was thoroughly analyzed, and its potential was demonstrated with a dual-mode operation technique for simultaneous measurement and localization. A magnetic domain model was extended to analyze the magnetic properties of an example sensor. The model matches the magnetization curves well over the full angular range of the applied magnetic field. It confirms the implementation of an internal bias field at an angle $\varphi_{ex} = 46^\circ$ and a magnitude $B_{ex} \approx 0.8$ mT.

For the localization of the sensor, the first bending mode was analyzed in the direct detection mode. At zero bias field, a detection limit of $LOD_{ME} = 150 \text{ pT}/\sqrt{\text{Hz}}$ is found in mechanical resonance at $f_{r,1} = 7.728$ kHz with brass cylinder, and $LOD_{ME} = 30 \text{ pT}/\text{Hz}$ without. This is higher than measured with externally biased, cm-sized sensors^{17,47} optimized for the direct detection, but significantly improved compared to mm-sized sensors³⁶. A

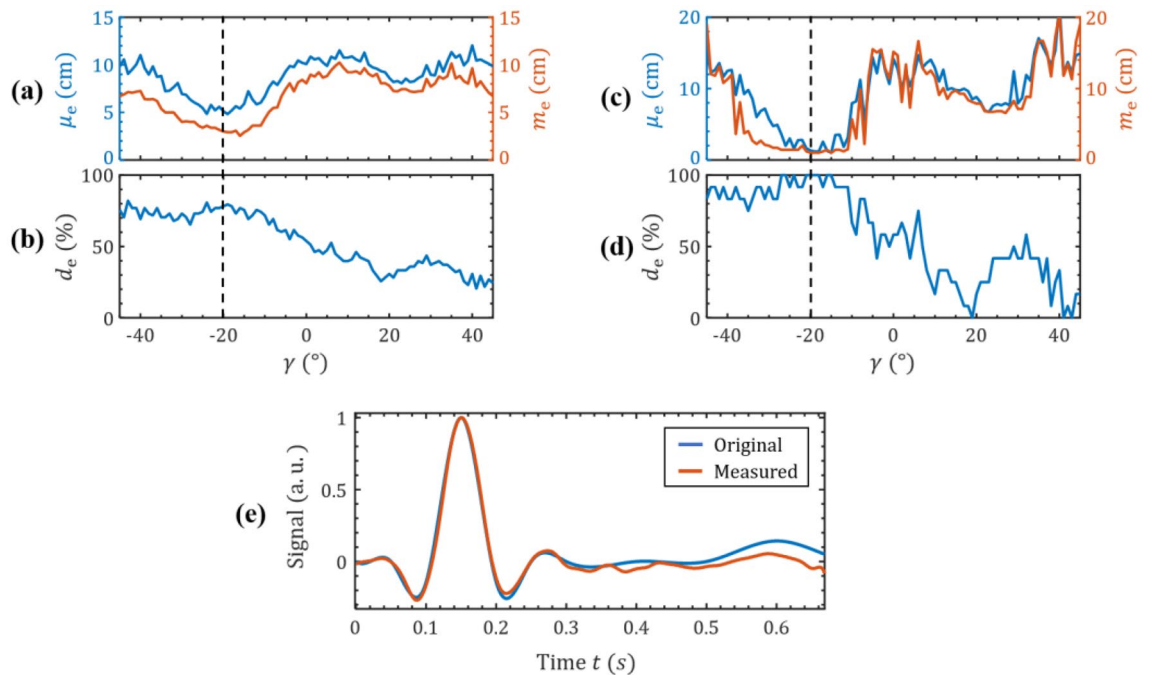


Figure 6. Localization and dual-mode measurement. Average localization error as a function of the tilt γ of the sensor's sensitivity axis for the localization for all of the tested position-orientation-pairs shown in Fig. 5b. In (a) the mean μ_e and median m_e Euclidean distance between real and estimated sensor positions and in (b) the percentage of correct estimated sensor orientations are shown. (c) Average localization error as a function of γ for the localization of the blue set of positions in Fig. 5b, (c) The mean μ_e and median m_e Euclidean distance between real and estimated sensor positions and in (d) the percentage of correct estimated sensor orientations is shown. (e) Demodulated, detrended, lowpass-filtered and normalized magnetic test signal measured by the ME sensor in the 2nd bending mode and original normalized transmitted signal. Due to the larger bandwidth of the sensor in resonance mode RM2 the signal can be reconstructed well.

detection limit in the low pT-regime is not required here, because the direct detection mode is only used for the sensor localization.

Two higher resonance modes (RM2 and RM3) are found around 48 kHz and analyzed for the delta-E operation. Compelling evidence from the models and measurements suggests that RM2 is the first torsional mode and RM3 the second bending mode. The measurements of RM2 match with the magnetic delta-E model. The quality factor at zero bias field of the RM3 mode $Q_3 = 1100$ is around typical values of $Q \approx 1000$ ^{22,23,25} for bending modes, whereas $Q_2 = 1400$ of RM2 is notably higher. At the optimum excitation voltage and $B = 0$, detection limits of $LOD_2 \leq 450 \text{ pT}/\sqrt{\text{Hz}}$ (RM2) are measured in the range between 10 and 50 Hz, with a minimum of about $350 \text{ pT}/\sqrt{\text{Hz}}$ at 25 Hz. Overall, we demonstrated that delta-E sensor characteristics in the same range of externally biased devices^{22,23,25} are possible with exchange biased multilayers on small sensors. Hence, problems detrimental to the application which arise from using coils are avoided.

Operating the sensor in dual-mode was shown to have no measurable impact on the detectivity of the signal detection in delta-E effect mode (RM2), for the excitation amplitudes used. Vice-versa, additional magnetic noise from the delta-E operation does slightly increase the noise floor in the lower frequency regime, which is used for the direct detection (RM1). Because the power of the localization signal can always be adjusted to provide a sufficient signal-to-noise ratio the additional noise is not detrimental for the localization. It was also shown that sidebands that would occur around RM1 from the delta-E modulation are naturally suppressed by the small bandwidth and the small carrier amplitude of the lower frequency RM1 mode. This is key for simultaneous measurement and localization in dual-mode operation. It significantly simplifies the signal processing by separating the source signal from the localization signal in the frequency domain. We demonstrated the feasibility of this concept and its application for the simultaneous sensor localization and measurement of a low-frequency magnetic signal. Mean localization errors between approximately 1–5 cm were obtained and mean median errors between 1 and 2.5 cm. These promising results were achieved despite the simple models used for the coils and the sensor in the forward problem. More accurate models are anticipated to reduce the localization error further¹⁰. The current results are comparable with those of other magnetic localization approaches, where no signal was measured simultaneously^{45,46}.

In conclusion, we presented and analyzed the first exchange biased delta-E effect sensor. With the internal bias, severe problems are avoided that accompany the usage of external coils. Dense, large number sensor arrays are now potentially feasible and a significant step towards real applications is made. Additionally, the concept of the dual-mode operation technique was demonstrated. The combination of both enables the detection of extremely small, low-frequency magnetic fields while localizing the sensor. The simultaneous localization might

	t [μm]	E [GPa]	ν	ρ [kg/m^3]
Substrate	52	160	0.22	2340
FeCoSiB	4	140	0.35	7900

Table 2. Model parameters. Layer thicknesses t , Young's modulus E , Poisson's ratio ν and density ρ used in the finite element simulation.

also bear the potential to reduce errors from source movements during the measurement and will be investigated with this regard in the future.

Materials and methods

Sensor fabrication. The sensor is fabricated starting from a 700 μm oxidized double side polished silicon wafer, covered by 50 μm polysilicon and another 650 nm oxide layer. All functional layers are deposited by magnetron sputtering from a von Ardenne CS730 S and structured by optical lithography and a combination of wet and dry etching techniques. The magnetic layer is deposited first and made of a sequence of $20 \times (\text{Ta} / \text{Cu} / \text{Mn}_{70}\text{Ir}_{30} / \text{Fe}_{70.2}\text{Co}_{7.8}\text{Si}_{12}\text{B}_{10})$ with individual layer thicknesses of Ta 5 nm, Cu 3 nm, MnIr 8 nm and FeCoSiB 200 nm. For a detailed structural characterization see⁴⁸. Ion beam etching is used to structure the magnetic layer. A bottom electrode of Ta 40 nm Pt 150 nm is deposited over the whole cantilever, also serving as seed layer for the following piezoelectric layer (AlN, 2 μm), which is deposited without additional heating by a pulsed DC generator as published in³¹. The AlN is structured by 80 °C H_3PO_4 (85%). After the lift off formation of the 150 nm thick Ta/Pt top electrodes (E1: 0.2 mm \times 1 mm, E2: 0.38 mm \times 0.2 mm), the silicon carrier wafer is etched with TMAH (25%) at 80 °C, leaving a silicon frame off 7.5 mm \times 11 mm for handling. The cantilever (width 1 mm, length 3 mm) is released by deep reactive ion etching using a modified Bosch-Process in a Sentech S1500 ICP-RIE. After separating the MEMS Chips by dicing saw, the sensors are annealed in an oil bath at 250 °C for 40 min with an applied field of 55° with respect to the length axis of the cantilever.

Magnetization measurements. To analyze the magnetic properties of the device, measurements were performed with a BH-loop tracer at 16 Hz and angles φ_{H} from 0° to 345° in steps of 15° relative to the sensor's long axis. The applied magnetic field was swept from -10 mT to 10 mT.

Signal and noise measurements. All electrical measurements are performed with a high-resolution A/D and D/A converter *Fireface UFX+* (*RME*, Germany) in a magnetically shielded setup⁴⁹ if not stated differently. The charge amplifier used has a feedback capacitance $C_f = 33$ pF and a feedback resistance $R_f = 5$ G Ω . The signal and noise measurements in Figs. 2 and 4 are performed six times for 4 min and then averaged in the frequency domain over segments of 5 s to obtain a smooth noise floor. The measurements in Fig. 4e and f and Fig. 6 are performed outside of the magnetically shielded setup. Each signal was measured over 1 min and averaged in the frequency domain using segments of 5 s to obtain a smooth noise floor and to better show the influence of the dual-mode operation scheme.

Numerical eigenfrequency study. For the calculation of the first three eigenfrequencies of the cantilever we use an eigenfrequency study in *COMSOL Multiphysics 5.4*. The simplified model geometry is a rectangular beam with in-plane dimensions of 3 mm \times 1 mm and fixed boundary conditions at the left end. The model cantilever consists of only two layers: one for the magnetic (FeCoSiB) layer and one substrate layer (Substrate) that includes all other layers via effective material properties. The material parameters used are given in the following table (Table 2). For the Young's modulus of the magnetic layer we consider the delta-E effect, using a value smaller than its saturation value of $E_m \approx 150$ GPa. The values used are consistent with material parameters used previously³⁸. Slight differences can occur from stress, curvature and process related deviations from the targeted geometry¹⁵.

Damped harmonic oscillator fit. The resonance amplitude $\hat{X} = |X(\omega)|$ of the oscillator model is fitted to the data and obtained from the frequency response

$$X(\omega) = \frac{A_m}{c_m i \omega + \omega_0^2 - \omega^2}, \quad (7)$$

with the angular frequency $\omega = 2\pi f$, the angular eigenfrequency ω_0 , and the complex number $i = \sqrt{-1}$. The oscillation amplitude $A = A_m m$ and the damping constant $c = c_m m$ are both normalized to the effective mass m . The parameters ω_0 , A_m and c_m are obtained from the fit. The effective mass m is calculated using ω_0 and the effective spring constant k

$$m = \frac{\omega_0^2}{k} \text{ with } k = \frac{3(EI)_{\text{eff}}}{L^3}. \quad (8)$$

The term $(EI)_{\text{eff}} := E_1 I_1 + E_2 I_2$ is the effective bending stiffness for the same simplified 2-layer cantilever geometry considered in the finite element model ("**Numerical eigenfrequency study**"). In $(EI)_{\text{eff}}$ the Young's moduli

of the substrate and of the FeCoSiB film are given by E_1, E_2 and the corresponding second moments of area by I_1 and I_2 . The quality factor $Q = 1/(2\xi)$ is then calculated from the damping ratio

$$\xi = \frac{c}{2\sqrt{mk}} = \frac{c}{2\sqrt{\omega_0^2}}. \tag{9}$$

Exchange bias magnetic domain model. In this section we extend a numerical domain model³⁰ by including an exchange bias and arbitrary external magnetic field direction. In the model a pair of simplified 180° domains is considered, consisting of two magnetic moments and a movable domain wall. It represents an average configuration of all domains in the sample. The original total enthalpy density u of the system is extended by an exchange anisotropy energy density u_{ex} and a more general Zeeman energy density term u_Z . The total enthalpy density u is

$$u = u_K + u_Z + u_{ex} + u_{me} + u_w. \tag{10}$$

The expressions used for the effective uniaxial anisotropy u_K , the magnetoelastic anisotropy energy density u_{me} and the phenomenological domain wall term u_w can be found in³⁰. For u_Z we use the magnetic vacuum permeability μ_0 , saturation magnetization M_s , magnitude H and angle φ_H of the external magnetic field vector \vec{H} . It is

$$u_Z = \mu_0 M_s H \cdot [v_2 \cos(\theta + \varphi_2 - \varphi_H) - v_1 \cos(\theta - \varphi_1 - \varphi_H)] \tag{11}$$

with the angles φ_1 and φ_2 of m_1 and m_2 relative to the easy axis with angle θ . All angles except of φ_1 and φ_2 are defined relative to the long axis of the cantilever (x-axis). The contribution of each domain is weighted by its respective volume fraction v_1 and v_2 . The exchange anisotropy energy density is defined via the magnitude H_{ex} and the angle φ_{ex} of the exchange bias field vector to the x-axis and results to

$$u_{ex} = \mu_0 M_s H_{ex} \cdot [v_2 \cos(\theta + \varphi_2 - \varphi_{ex}) - v_1 \cos(\theta - \varphi_1 - \varphi_{ex})]. \tag{12}$$

Following the method in³⁰ we obtain the normalized wall displacement equation

$$\frac{x_w}{d} = \frac{1}{2Ad^2w \sin^2 \theta} \cdot \left[\mu_0 M_s H_{ex} \cdot C + \mu_0 M_s H \cdot D - \frac{3}{2} \lambda_s \sigma \cdot E - K \cdot F \right], \tag{13}$$

with

$$\begin{aligned} C &:= \cos(\theta - \varphi_1 - \varphi_{ex}) + \cos(\theta + \varphi_2 - \varphi_{ex}), \\ D &:= \cos(\theta - \varphi_1 - \varphi_H) + \cos(\theta + \varphi_2 - \varphi_H), \\ E &:= \sin^2(\theta - \varphi_1) - \sin^2(\theta + \varphi_2), \\ F &:= \sin^2(\varphi_1) - \sin^2(\varphi_2). \end{aligned} \tag{14}$$

The initial domain width is denoted as d . Having the wall displacement Eqs. (13), (10) can be minimized numerically to obtain the residual unknowns φ_1 and φ_2 . The projection of the reduced magnetization m on the axis of the external magnetic field is then obtained from

$$m = v_1 \cos(\theta - \varphi_1 - \varphi_H) - v_2 \cos(\theta + \varphi_2 - \varphi_H). \tag{15}$$

With the Young's modulus E_m at fixed magnetization, the effective magnetization dependent Young's modulus can be described by²⁰

$$E = \left[\frac{\partial e}{\partial \sigma} + \frac{\partial \lambda}{\partial \sigma} \right]^{-1} := \left[\frac{1}{E_m} + \frac{1}{\Delta E} \right]^{-1}, \tag{16}$$

For the magnetostrictive part we obtain

$$\begin{aligned} \frac{1}{\Delta E} &= v_1 \frac{9\lambda_s^2 \sin^2(2[\theta - \varphi_1])}{4u_{\varphi\varphi_1}} \\ &- v_2 \frac{9\lambda_s^2 \sin^2(2[\theta + \varphi_2])}{4u_{\varphi\varphi_2}}, \end{aligned} \tag{17}$$

with the second order derivatives $u_{\varphi\varphi_{1,2}}$

$$\begin{aligned} u_{\varphi\varphi_1} &= v_1 [3\lambda_s \sigma \cos(2[\theta - \varphi_1]) + 2K \cos(2\varphi_1) \\ &+ \mu_0 M_s H_{ex} \cos(\theta - \varphi_1 - \varphi_{ex}) \\ &+ \mu_0 M_s H \cos(\theta - \varphi_1 - \varphi_H)], \end{aligned} \tag{18}$$

and

$$\begin{aligned}
 u_{\varphi\varphi_2} = & -v_2[3\lambda_s\sigma \cos(2[\theta + \varphi_2]) + 2K \cos(2\varphi_2) \\
 & + \mu_0 M_s H_{ex} \cos(\theta + \varphi_2 - \varphi_{ex}) \\
 & + \mu_0 M_s H \cos(\theta + \varphi_2 - \varphi_H)].
 \end{aligned}
 \tag{19}$$

For the simulations a saturation magnetostriction of $\lambda_s = 35$ ppm is used and a saturation flux density of $\mu_0 M_s = 1.5 \text{ T}^{50}$. A wall stiffness parameter of $w = 5 \cdot 10^8 \text{ J/m}^4$ is found from the fit and an initial domain wall width of $d = 50 \text{ }\mu\text{m}$ is used.

Analytical eigenfrequency calculation. The Eigenfrequency $f_{r,n}$ of the n^{th} bending mode of a Euler-Bernoulli beam is given by²²

$$f_{r,n} = \frac{\lambda_n^2}{2\pi L^2} \sqrt{\frac{\sum_k E_k I_k}{\sum_k \rho_k A_k}},
 \tag{20}$$

with the mode factor λ_i , the cantilever length L the mass density ρ_k , cross section area A_k the Young's modulus E_k and the second moment of area I_k all of the k^{th} layer. For the second bending mode it is $\lambda_2 = 4.694$. The material and geometry parameters are identical to those used in the eigenfrequency study in Table 2. The Young's modulus of the substrate was slightly adjusted to 162.7 GPa to match the measured resonance frequency of RM3. The Young's modulus of the magnetic layer as a function of the applied flux density is obtained from the domain model [Eqs. (16)–(19)] using a saturation Young's modulus of $E_m = 150 \text{ GPa}$.

Localization algorithm. For the localization of the sensor, coils positioned at the edge of the localization area transmit artificial signals. The coils used for localization consist of approximately 350 windings and have a radius of about 1.25 cm. The maximum rms value of the coil excitation current was about 164 mA. Position and orientation of the sensor can be inferred from the signals received at the sensor by solving an inverse problem. The magnetic flux density of the coil at the sensor's position is approximated by a magnetic dipole field⁴⁴

$$\bar{B}_i(t) = \frac{\mu_0}{4\pi} \cdot \frac{3[\bar{r}_s - \bar{r}_{c_i}] [\bar{m}_i(t) (\bar{r}_s - \bar{r}_{c_i})] - \bar{m}_i(t) \|\bar{r}_s - \bar{r}_{c_i}\|_2^2}{\|\bar{r}_s - \bar{r}_{c_i}\|_2^5}
 \tag{21}$$

with the permeability of vacuum μ_0 , the position \bar{r}_s of the sensor, the position \bar{r}_{c_i} of the coil i and the magnetic dipole moment $\bar{m}_i(t)$. The operator $\langle \bar{x} | \bar{y} \rangle$ denotes the scalar product of the vectors \bar{x} and \bar{y} . Equation (21) is a good approximation if the distance between the transmitting coil and the sensor is large enough⁴⁴. The sensitivity of the sensor is anisotropic and thus the measured signal

$$u(t) = h_s(t) * \left\langle \bar{d}_s \left| \sum_{i=1}^N \bar{B}_i(t) \right. \right\rangle
 \tag{22}$$

is the scalar product of the directivity \bar{d}_s of the sensor with the superposition of all N coil signals and a convolution with the impulse response $h_s(t)$ of the sensor system including the charge amplifier. This equation is valid at least for the considered frequency range around the first bending mode. To determine the signal components of each coil the transmitted signals must be orthogonal⁵¹. This is achieved here with a Time Division Multiple Access (TDMA) approach⁵². Moreover, the frequency of the signals should be as close as possible to the resonance frequency of the resonance mode used to benefit from the sensor's high sensitivity in resonance. Thus, the coil i transmits the sinusoidal signal

$$s_i(t) = \cos(2\pi f_{r,1}[t - \tau_i]) \cdot w[t - \tau_i] \text{ with } \tau_i = [i - 1] \cdot [T_{coil} + T_p]
 \tag{23}$$

with the resonance frequency $f_{r,1}$ of the sensor in the first bending mode, the transmitting time T_{coil} of the signal, and the pausing time T_p between two signals. The quantity $w(t)$ corresponds to a Hann window function of length T_{coil} . The localization area is divided into M different positions and orientations the sensor could occupy $\bar{P} = [\bar{p}^1, \dots, \bar{p}^j, \dots, \bar{p}^M]$ and a forward solution generating a lead field matrix \bar{A} for these possible states is calculated. The lead field matrix consists of the signal component that each coil would contribute if the sensor occupied the possible position and orientation. The inverse solution is determined by solving a minimum least squares problem

$$\min_j \sum_{i=1}^N \left(\frac{|\bar{A}(i,j)|}{|\bar{A}(i_{max},j)|} - \frac{|\tilde{s}(i)|}{|\tilde{s}(i_{max})|} \right)^2
 \tag{24}$$

comparable with the one presented in⁴³. The lead field matrix entries of each possible position-orientation-combination j are compared with the estimated signal components \tilde{s} of the coils measured by the sensor. Due to the sinusoidal excitation and the comparison of ratios the impulse response of the sensor denoted in Eq. (21) can be neglected. The signal components are extracted by applying a matched filter⁵³. The lead field matrix entries as well as the extracted signal components are normalized by the entry i_{max} . The entry i_{max} corresponds to the

maximal absolute signal component. The position and orientation leading to the best fitting entry j_{\max} are most likely the position and orientation of the sensor $\hat{p}_s = \hat{p}^{j_{\max}}$.

Received: 4 August 2020; Accepted: 8 January 2021

Published online: 05 March 2021

References

1. Duez, L. *et al.* Added diagnostic value of magnetoencephalography (MEG) in patients suspected for epilepsy, where previous, extensive EEG workup was unrevealing. *Clin. Neurophysiol.* **127**, 3301–3305 (2016).
2. Kwong, J. S. W., Leithäuser, B., Park, J. W. & Yu, C. M. Diagnostic value of magnetocardiography in coronary artery disease and cardiac arrhythmias: A review of clinical data. *Int. J. Cardiol.* **167**, 1835–1842 (2013).
3. Sakkalis, V. Review of advanced techniques for the estimation of brain connectivity measured with EEG/MEG. *Comput. Biol. Med.* **41**, 1110–1117 (2011).
4. Kleiner, R., Koelle, D., Ludwig, F. & Clarke, J. Superconducting quantum interference devices: State of the art and applications. *Proc. IEEE* **92**, 1534–1548 (2004).
5. Johnson, C. N., Schwindt, P. D. D. & Weisend, M. Multi-sensor magnetoencephalography with atomic magnetometers. *Phys. Med. Biol.* **58**, 6065–6077 (2013).
6. Griffith, W. C., Knappe, S. & Kitching, J. Femtotesla atomic magnetometry in a microfabricated vapor cell. *Opt. Express* **18**, 27167 (2010).
7. Osborne, J., Orton, J., Alem, O. & Shah, V. Fully integrated, standalone zero field optically pumped magnetometer for biomagnetism. *Proc. SPIE* **10548**, 51 (2018).
8. Baillet, S., Mosher, J. C. & Leahy, R. M. Electromagnetic brain mapping. *IEEE Signal Process. Mag.* **18**, 14–30 (2001).
9. Habboush, N., Hamid, L., Siniatchkin, M., Stephani, U. & Galka, A. Pipeline for Forward Modeling and Source Imaging of Magnetocardiographic Recordings via Spatiotemporal Kalman Filtering, in *40th Annual International Conference of the IEEE Engineering in Medicine and Biology Society (EMBC)* 199–202 (IEEE, 2018). <https://doi.org/10.1109/EMBC.2018.8512188>.
10. Dong, J., Zhang, G., Geng, Y. & Wang, J. Influence of magnetic measurement modeling on the solution of magnetostatic inverse problems applied to current distribution reconstruction in switching air arcs. *IEEE Trans. Magn.* **54**, 3–6 (2018).
11. Tu, C. *et al.* Mechanical-resonance-enhanced thin-film magnetolectric heterostructures for magnetometers, mechanical antennas, tunable RF inductors, and filters. *Materials* **2**, 2259 (2019).
12. Nan, C. W., Bichurin, M. I., Dong, S., Viehland, D. & Srinivasan, G. Multiferroic magnetolectric composites: Historical perspective, status, and future directions. *J. Appl. Phys.* **103**, 12 (2008).
13. Reermann, J. *et al.* Evaluation of magnetolectric sensor systems for cardiological applications. *Meas. J. Int. Meas. Conf.* **116**, 230–238 (2018).
14. Röbisch, V. *et al.* Exchange biased magnetolectric composites for magnetic field sensor application by frequency conversion. *J. Appl. Phys.* **117**, 1–5 (2015).
15. Töpfer, H. Automated parameter extraction of ScAlN MEMS devices using an extended Euler – Bernoulli beam theory. *Sensors* **20**, 1001 (2020).
16. Nan, T., Hui, Y., Rinaldi, M. & Sun, N. X. Self-biased 215 MHz magnetolectric NEMS resonator for ultra-sensitive DC magnetic field detection. *Sci. Rep.* **3**, 1985 (2013).
17. Yarar, E. *et al.* Inverse bilayer magnetolectric thin film sensor. *Appl. Phys. Lett.* **109**, 022901 (2016).
18. Honda, K. & Terada, T. II. On the change of elastic constants of ferromagnetic substances by magnetization. *Philos. Mag. Ser. 6*, 13 (1907).
19. Lee, E. W. Magnetostriction and magnetomechanical effects. *Rep. Prog. Phys.* **18**, 184–229 (1955).
20. Livingston, J. D. Magnetomechanical properties of amorphous metals. *Phys. Status Solidi A* **70**, 591–596 (1982).
21. Spetzler, B., Golubeva, E. V., Müller, C., McCord, J. & Faupel, F. Frequency dependency of the delta-e effect and the sensitivity of delta-e effect magnetic field sensors. *Sensors* **19**, 1–14 (2019).
22. Zabel, S. *et al.* Phase modulated magnetolectric delta-E effect sensor for sub-nano tesla magnetic fields. *Appl. Phys. Lett.* **107**, 152402 (2015).
23. Zabel, S. *et al.* Multimode delta-E effect magnetic field sensors with adapted electrodes. *Appl. Phys. Lett.* **108**, 222401 (2016).
24. Li, M. *et al.* Ultra-sensitive NEMS magnetolectric sensor for picotesla DC magnetic field detection. *Appl. Phys. Lett.* **110**, 143510 (2017).
25. Durdaut, P. *et al.* Modeling and analysis of noise sources for thin-film magnetolectric sensors based on the delta-E effect. *IEEE Trans. Instrum. Meas.* **66**, 2771–2779 (2017).
26. Urs, N. O. *et al.* Direct link between specific magnetic domain activities and magnetic noise in modulated magnetolectric sensors. *Phys. Rev. Appl.* **10**, 1 (2020).
27. Lage, E. *et al.* Exchange biasing of magnetolectric composites. *Nat. Mater.* **11**, 523–529 (2012).
28. Lage, E., Woltering, F., Quandt, E. & Meyners, D. Exchange biased magnetolectric composites for vector field magnetometers. *J. Appl. Phys.* **113**, 88–91 (2013).
29. Nogués, J. & Schuller, I. K. Exchange bias. *J. Magn. Magn. Mater.* **192**, 203–232 (1999).
30. Squire, P. T. Phenomenological model for magnetization, magnetostriction and ΔE effect in field-annealed amorphous ribbons. *J. Magn. Magn. Mater.* **87**, 299–310 (1990).
31. Yarar, E. *et al.* Low temperature aluminum nitride thin films for sensory applications. *AIP Adv.* **6**, 075115 (2016).
32. Durdaut, P. *et al.* Noise of a JFET charge amplifier for piezoelectric sensors. *IEEE Sens. J.* **17**, 7364–7371 (2017).
33. Stoner, E. C. & Wohlfarth, E. P. A mechanism of magnetic hysteresis in heterogeneous alloys. *Philos. Trans. R. Soc. Lond. A* **240**, 599–642 (1948).
34. Squire, P. T. Domain model for magnetoelastic behaviour of uniaxial ferromagnets. *J. Magn. Magn. Mater.* **140–144**, 1829–1830 (1995).
35. Mertz, J., Marti, O. & Mlynek, J. Regulation of a microcantilever response by force feedback. *Appl. Phys. Lett.* **62**, 2344–2346 (1993).
36. Zuo, S. *et al.* Ultrasensitive magnetolectric sensing system for pico-tesla magnetomyography. *IEEE Trans. Biomed. Circuits Syst.* **1**, 1–1. <https://doi.org/10.1109/tbcas.2020.2998290> (2020).
37. Reermann, J. *et al.* Adaptive readout schemes for thin-film magnetolectric sensors based on the delta-E effect. *IEEE Sens. J.* **16**, 4891–4900 (2016).
38. Spetzler, B., Kirchoff, C., Quandt, E., McCord, J. & Faupel, F. Magnetic sensitivity of bending-mode delta-E-effect sensors. *Phys. Rev. Appl.* **12**, 1 (2019).
39. Varadan, V. K., Vinoy, K. J. & Gopalakrishnan, S. Smart material systems and MEMS: Design and development methodologies. *Des. Dev. Methodol.* <https://doi.org/10.1002/0470093633> (2007).
40. Herzer, G. Magnetomechanical damping in amorphous ribbons with uniaxial anisotropy. *Mater. Sci. Eng. A* **226–228**, 631–635 (1997).

41. Spetzler, B. *et al.* Influence of the quality factor on the signal to noise ratio of magnetoelectric sensors based on the delta-E effect. *Appl. Phys. Lett.* **114**, 183504 (2019).
42. Durdaut, P. *Ausleseverfahren und Rauschmodellierung für Magnetoelektrische und Magnetoelastische Sensorsysteme.* (Kiel University, 2019). <https://doi.org/10.13140/RG.2.2.17043.84009>
43. Wang, J. Z., Williamson, S. J. & Kaufman, L. Magnetic source images determined by a lead-field analysis: The unique minimum-norm least-squares estimation. *IEEE Trans. Biomed. Eng.* **39**, 665–675 (1992).
44. Bao, J., Hu, C., Lin, W. & Wang, W. On the magnetic field of a current coil and its localization. *IEEE Int. Conf. Autom. Logist.* **1**, 573–577. <https://doi.org/10.1109/ICAL.2012.6308143> (2012).
45. De Angelis, G. *et al.* An indoor AC magnetic positioning system. *IEEE Trans. Instrum. Meas.* **64**, 1275–1283 (2015).
46. Dai, H. *et al.* 6-D electromagnetic tracking approach using uniaxial transmitting coil and tri-axial magneto-resistive sensor. *IEEE Sens. J.* **18**, 1178–1186 (2018).
47. Salzer, S. *et al.* Tuning fork for noise suppression in magnetoelectric sensors. *Sens. Actuators A Phys.* **237**, 91–95 (2016).
48. Hrkac, V. *et al.* Amorphous FeCoSiB for exchange bias coupled and decoupled magnetoelectric multilayer systems: Real-structure and magnetic properties. *J. Appl. Phys.* **116**, 134302 (2014).
49. Jahns, R. *et al.* Magnetolectric sensors for biomagnetic measurements. in *MeMeA 2011 - 2011 IEEE International Symposium on Medical Measurements and Applications, Proceedings* (2011). <https://doi.org/10.1109/MeMeA.2011.5966676>
50. Ludwig, A. & Quandt, E. Optimization of the delta E effect in thin films and multilayers by magnetic field annealing. *IEEE Trans. Magn.* **38**, 2829–2831 (2002).
51. Psiuk, R. *et al.* Simultaneous 2D localization of multiple coils in an LF magnetic field using orthogonal codes. *Proc. IEEE Sens.* **2017**, 1–3 (2017).
52. Lcev, S. D. Time Division Multiple Access (TDMA) applicable for mobile satellite communications. in *2011 21st International Crimean Conference "Microwave & Telecommunication Technology* 365–367 (IEEE, 2011).
53. Turin, G. L. An introduction to matched filters. *IRE Trans. Inf. Theory* **6**, 311–329 (1960).

Author contributions

B.S. and C.B. performed and designed the experiments. B.S. performed the magnetic and mechanical simulations. C.B. set up the sensor localization and the inverse solution problem. P.D. and J.R. built the sensor electronics. C.K. produced the thin film samples. B.S., C.B. and P.D. analyzed the results and wrote the manuscript with contribution from all authors. All authors reviewed the manuscript.

Funding

Open Access funding enabled and organized by Projekt DEAL. The research is funded by the German Research Foundations (DFG) via the collaborative research center CRC 1261.

Competing interests

The authors declare no competing interests.

Additional information

Correspondence and requests for materials should be addressed to F.F.

Reprints and permissions information is available at www.nature.com/reprints.

Publisher's note Springer Nature remains neutral with regard to jurisdictional claims in published maps and institutional affiliations.



Open Access This article is licensed under a Creative Commons Attribution 4.0 International License, which permits use, sharing, adaptation, distribution and reproduction in any medium or format, as long as you give appropriate credit to the original author(s) and the source, provide a link to the Creative Commons licence, and indicate if changes were made. The images or other third party material in this article are included in the article's Creative Commons licence, unless indicated otherwise in a credit line to the material. If material is not included in the article's Creative Commons licence and your intended use is not permitted by statutory regulation or exceeds the permitted use, you will need to obtain permission directly from the copyright holder. To view a copy of this licence, visit <http://creativecommons.org/licenses/by/4.0/>.

© The Author(s) 2021

7.2 Parallel Operation of Sensor Elements

A major benefit of the exchange-biased ΔE -effect sensors is the possibility of operating them without an external magnetic bias field. This permits keeping the measurement setup compact and handy for applications where several sensors are required or beneficial, such as spatial magnetic field mapping of the heart and source localization.

Instead of using sensor arrays to measure the magnetic field simultaneously at various locations, spatial resolution can be traded off by averaging the outputs of the sensors to improve the LOD. An improvement in the $\text{LOD} \propto \sqrt{N}$ (N : Number of sensor) can be expected under two main conditions [154]: (1) All sensors have an identical LOD and (2) each sensor element is operated with its own operating and read-out electronics. The first condition is limited by the manufacturing process, and if it is not fulfilled, we expect an LOD improvement $< \sqrt{N}$ or no improvement at all [154]. The second condition limits the number of sensors owing to the large number of hardware channels required when a large improvement in the LOD is pursued. As a possible solution to this problem, sensor elements could be connected in parallel using the same electronics to reduce the number of operating and read-out channels required. This approach permits the use of many sensor elements; however, it accompanies other challenges and constraints analyzed and discussed further in this section.

In the following, the previously presented noise model is modified and extended to permit the description of the signal, noise, and LOD of a sensor system with N parallel sensor elements. The model is validated with measurements and then used to discuss and analyze challenges, limits, and requirements for LOD improvement.

Contribution

- Conceptualization
- Writing of original manuscript
- Modeling and simulations (shared)
- Measurements (shared)
- Data analysis and interpretation (shared)

Article

Modeling and Parallel Operation of Exchange-Biased Delta-E Effect Magnetometers for Sensor Arrays

Benjamin Spetzler ^{*}, Patrick Wiegand, Phillip Durdaut , Michael Höft , Andreas Bahr , Robert Rieger 
and Franz Faupel 

Institute of Materials Science, Faculty of Engineering, Kiel University, 24143 Kiel, Germany; pw@tf.uni-kiel.de (P.W.); pd@tf.uni-kiel.de (P.D.); michael.hoeft@tf.uni-kiel.de (M.H.); andreas.bahr@tf.uni-kiel.de (A.B.); rri@tf.uni-kiel.de (R.R.); ff@tf.uni-kiel.de (F.F.)

* Correspondence: benjamin.spetzler@tu-ilmenau.de

Abstract: Recently, Delta-E effect magnetic field sensors based on exchange-biased magnetic multilayers have shown the potential of detecting low-frequency and small-amplitude magnetic fields. Their design is compatible with microelectromechanical system technology, potentially small, and therefore, suitable for arrays with a large number N of sensor elements. In this study, we explore the prospects and limitations for improving the detection limit by averaging the output of N sensor elements operated in parallel with a single oscillator and a single amplifier to avoid additional electronics and keep the setup compact. Measurements are performed on a two-element array of exchange-biased sensor elements to validate a signal and noise model. With the model, we estimate requirements and tolerances for sensor elements using larger N . It is found that the intrinsic noise of the sensor elements can be considered uncorrelated, and the signal amplitude is improved if the resonance frequencies differ by less than approximately half the bandwidth of the resonators. Under these conditions, the averaging results in a maximum improvement in the detection limit by a factor of \sqrt{N} . A maximum $N \approx 200$ exists, which depends on the read-out electronics and the sensor intrinsic noise. Overall, the results indicate that significant improvement in the limit of detection is possible, and a model is presented for optimizing the design of delta-E effect sensor arrays in the future.

Keywords: magnetometer; delta-E effect; sensor array; magnetoelectric; cantilever; exchange bias



Citation: Spetzler, B.; Wiegand, P.; Durdaut, P.; Höft, M.; Bahr, A.; Rieger, R.; Faupel, F. Modeling and Parallel Operation of Exchange-Biased Delta-E Effect Magnetometers for Sensor Arrays. *Sensors* **2021**, *21*, 7594. <https://doi.org/10.3390/s21227594>

Academic Editor: Iren E. Kuznetsova

Received: 9 October 2021

Accepted: 14 November 2021

Published: 16 November 2021

Publisher's Note: MDPI stays neutral with regard to jurisdictional claims in published maps and institutional affiliations.



Copyright: © 2021 by the authors. Licensee MDPI, Basel, Switzerland. This article is an open access article distributed under the terms and conditions of the Creative Commons Attribution (CC BY) license (<https://creativecommons.org/licenses/by/4.0/>).

1. Introduction

The detection of small amplitude magnetic fields is of interest for various fields of application, e.g., in magnetic recording, geomagnetism, and aerospace engineering [1]. Specific engineering and development challenges arise for biomedical applications, such as cell and particle mapping [2,3], magnetomyography [4,5], or magnetocardiography [6–9]. Such applications are often connected to inverse solution problems that benefit from large arrays with many sensor elements and the possibility of quick spatial field mapping [10,11]. Magnetic flux densities in this field of application are of the order of tens of picotesla and less [12] with frequency components often well below 1 kHz [5,13]. Therefore, research on sensor systems for biomedical applications is devoted to improving the minimum detectable field at low frequencies while minimizing critical parameters such as size, power consumption, and cost [13].

The gold standard for detecting such small magnetic fields is superconducting quantum interference device (SQUID) magnetometry [14,15]. These sensors must be cooled and magnetically well-shielded during operation, which makes them expensive and extensive to operate. Such setups are limited in the number of sensor elements and their minimum distance to the magnetic source. Atomic magnetometers [16–18] have been investigated as an affordable alternative to SQUIDS and have achieved limits of detection (LOD) in the fT/\sqrt{Hz} regime at low signal frequencies between 1–200 Hz [16]. Despite this progress,

atomic magnetometers often require magnetic shielding, and their limited CMOS integrability and downsizing reduce the number and density of sensor elements that can be used in array applications. Miniaturization and MEMS fabrication of atomic magnetometers is currently an active field of research [19,20]. Many magnetometers are being investigated to overcome such limitations [4,15], and an overview and comparison of magnetic field sensors for biomedical applications can be found [13].

In this work, we study magnetic field sensors based on magnetoelectric composite resonators. Previously, sensor systems utilizing the direct magnetoelectric effect were discussed for magnetocardiography [21] and magnetomyography [5], and limits of detection in the low and sub-pT/ $\sqrt{\text{Hz}}$ regime have been reached with a linear response over several orders of magnitude [22]. Magnetoelectric sensors can be produced on a large scale with standard micro-electro-mechanical system (MEMS) technology and dimensions down to the micrometer range [23]. They are potentially cost-efficient, feature low power consumption, and are integrable with CMOS electronics. These aspects make magnetoelectric sensors promising candidates for sensor arrays. On the other hand, detecting small magnetic flux densities is limited to a narrow bandwidth of a few hertz around the resonance frequency, which is usually in the kilohertz regime for millimeter-sized resonators or the megahertz regime for micrometer-sized devices. Such high and narrow frequency regimes are not suitable for many applications [21]. Shifting them down increases the contributions of $1/f$ noise and requires large resonators with low resonance frequencies, which are susceptible to mechanical vibrations and reduce the spatial resolution.

Delta-E effect magnetometers extend the measurement range of magnetoelectric sensors and shift it to low frequencies while avoiding $1/f$ noise and keeping the advantages of magnetoelectric composites and the MEMS fabrication technology. In contrast to sensors based on the direct magnetoelectric effect, delta-E effect sensors benefit from high resonance frequencies because they operate on a modulation scheme. The higher resonance frequencies permit miniaturization and render the devices robust against mechanical disturbances. The modulation occurs via the magnetoelastic delta-E effect [24–26], i.e., the magnetization induced change of the stiffness of the material, which leads to a detuning of the resonance frequency upon the application of a magnetic field. This detuning can be measured as a change of the electrical admittance of the sensor and causes a modulation of the current through the sensor [27]. Although precursor steps towards the delta-E effect sensor concept were already made in the 1990s [28], it took another two decades until fully integrable delta-E effect sensors [29] were developed based on microelectromechanical magnetoelectric composite cantilevers [26,30–34], plate resonators [35,36], or other designs [37], including macroscopic laminate structures [38,39]. MEMS cantilever sensors achieved LODs $< 100 \text{ pT}/\sqrt{\text{Hz}}$ in the frequency range from approximately 10–100 Hz [32]. This is currently of a similar order of magnitude as the LODs of some magnetoresistive sensors [40,41]. As an application example of delta-E effect sensors, magnetic particle mapping was recently demonstrated for cell localization [42]. In this setup, the sensor was operated under a magnetic bias field provided by a permanent magnet. Most studies rely on an external magnetic bias field to operate the sensor at an optimum signal-to-noise ratio. Instead of a permanent magnet, the magnetic bias field is often created with external coils. For delta-E effect sensor arrays with many sensor elements, coils and permanent magnets can be inconvenient because their stray fields shift the operation points of adjacent sensor elements, and the additional electrical components increase the volume of the sensor system.

Recently, we demonstrated a first delta-E effect magnetometer based on exchange biased magnetic multilayers that circumvents such complications and still achieves a minimum detection limit of $350 \text{ pT}/\sqrt{\text{Hz}}$ at 25 Hz [34]. The exchange bias provides an internal bias field and thereby paves the way to flexible and compact delta-E effect sensor arrays with many sensor elements. Only recently were sensor arrays based on magnetoelectric sensor elements reported [43–47], and were limited to direct magnetoelectric detection and were mostly based on macroscopic resonators. A CMOS integrated array of magnetoelastic

sensor elements was presented for vector magnetometry [48], but the sensor elements were only characterized individually and without a signal and noise analysis. No attempts of parallel operating delta-E effect sensor elements in array configurations or thorough signal and noise analyses of such have yet been presented.

In this study, we explore the operation of delta-E effect sensor elements in arrays to improve the signal, noise, and limit of detection. Instead of measuring the magnetic field at different locations, spatial resolution can be sacrificed by averaging the outputs of several sensors operating simultaneously. However, the large number of hardware channels required to achieve the desired improvement in the LOD increases the size of the setup and limits the number and density of sensors. As a solution, sensor elements are connected in parallel and operated and read out simultaneously with one set of electronics. This method of parallel operation is accompanied by other complications, and they are analyzed here to identify the potential of such a setup. After presenting the sensor system, which is based on exchange-biased delta-E effect sensors, a signal-and-noise model is developed and validated with measurements. The model is used to analyze the sensor characteristics as functions of the number of sensor elements and variations in the resonance frequency that can occur during fabrication. Implications for the design of delta-E effect sensor arrays are derived and requirements on the reproducibility are identified and discussed.

2. Sensor System

In this study, two MEMS fabricated sensor elements are used, based on 50 μm thick poly-Si cantilevers with a length of 3 mm and a width of 1 mm. They are covered with a 4 μm thick exchange-biased magnetic multilayer [49] and a 2 μm thick piezoelectric AlN layer [50] on the top. The AlN layer is contacted via two Ta-Pt electrodes on its top and rear-side for excitation and read-out. The magnetic multilayer is based on alternating anti-ferromagnetic $\text{Mn}_{70}\text{Ir}_{30}$ (8 nm) and soft ferromagnetic $\text{Fe}_{70.2}\text{Co}_{7.8}\text{Si}_{12}\text{B}_{10}$ (200 nm) layers. In this configuration, the antiferromagnetic layer provides an exchange bias that serves as an internal bias field for the ferromagnetic layer to ensure a nonzero sensitivity without an externally applied magnetic field. Hence, all measurements shown in this study are performed without a magnetic bias field. Details about the layer structure and fabrication process and a comprehensive analysis of sensors with a similar geometry can be found elsewhere [34]. Two sensor elements are mounted on a printed circuit board, respectively, as shown in Figure 1. They are connected in parallel to each other and connected to the input of a low-noise JFET-based charge amplifier [51]. A high-resolution A/D and D/A converter (*Fireface UFX+*, RME, Chemnitz, Germany) is used for excitation and read-out (24 bit, 32 kHz). For the measurements, the sensors are placed in a magnetically and electrically shielded setup [52], based on a mu-metal shielding cylinder (ZG1, Aaronia AG, Strickscheid, Germany), and are located in a copper fleece coated box that is mechanically decoupled to reduce the impact of mechanical vibrations. All magnetic flux densities are applied along the long axis of the cantilever.

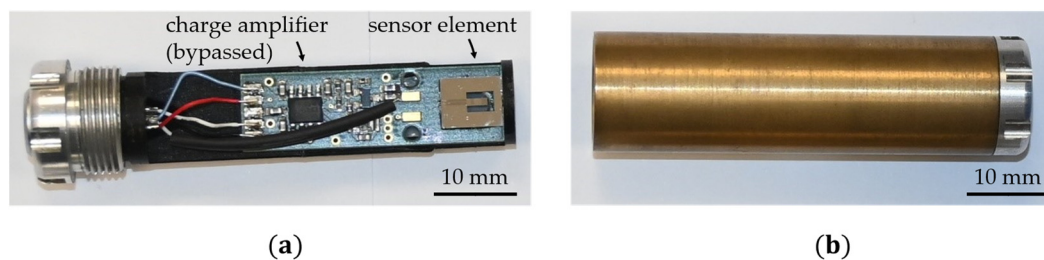


Figure 1. (a) Example sensor (without encapsulation) used in this study; it comprises a MEMS-fabricated cantilever resonator as a sensing element mounted on a printed circuit board (PCB). The JFET charge amplifier on the PCB was used in a previous study and is bypassed here and replaced by an external one. (b) Brass encapsulation for mechanical protection and electrical shielding during the measurements. Further details are reported in Ref. [34].

3. Array Modeling

In an alternating magnetic field, the delta-E effect causes an oscillation of the mechanical stiffness of the cantilever. The response of the cantilever to this stiffness change is damped with increasing magnetic field frequencies because of its mass inertia. Previously, this behavior was modeled with a first-order Bessel filter [27,53], applied to the demodulated simulated output signal of the charge amplifier. Later, a dynamic sensitivity was introduced [54] to consider the low-pass filter characteristics of the sensor as a function of the magnetic field frequency. The dynamic sensitivity was derived from the frequency response of a simple damped harmonic oscillator; however, it is only fully valid if the sensor is excited at its mechanical resonance frequency. For many previously analyzed sensors [33,53,55], this approximation was well justified, as their resonance frequency was close to their optimum excitation frequency, i.e., the excitation frequency with the largest signal-to-noise ratio. This is not a general property of such sensors but depends on their geometry, material, and electrical capacitance. Significant quantitative and qualitative deviations between measurements and simulations can occur if the excitation is not in mechanical resonance [56] (p. 139). In an array, not all sensor elements can be excited in mechanical resonance because of variations in their resonance frequencies that occur during fabrication. In this section, a signal and noise model is developed based on an altered approach, and it permits describing the output signal of an array of N sensor elements excited at an arbitrary excitation frequency.

3.1. Signal Model

During operation of the sensor array, a sinusoidal voltage $u_{\text{ex}}(t)$ with amplitude \hat{u}_{ex} and frequency f_{ex} is applied. It excites the magnetoelectric resonators of each sensor element at, or close to, its respective resonance frequency $f_{r,n}$. In linear approximation, the voltage at the charge amplifier's output can be described by:

$$u_{\text{co}}(t) \approx -Z_f(f_{\text{ex}}) \cdot i_s(t). \quad (1)$$

In this equation, the time is denoted by t and the feedback impedance of the charge amplifier by Z_f . The current i_s through the array of parallel-connected sensor elements can be expressed as the sum of all individual currents $i_{s,n}$ that flow through the respective sensor element n . To describe $i_{s,n}$, we use a modified Butterworth-van Dyke (mBvD) equivalent circuit representation, illustrated in detail in Appendix A. It consists of a series resonant circuit with a resistance $R_{r,n}$, inductance $L_{r,n}$, and capacitance $C_{r,n}$ that consider the resonant behavior of the cantilever. The electrodes of each sensor element form a capacitor with the piezoelectric layer. It is described by a capacitance $C_{p,n}$ and resistance $R_{p,n}$, both in parallel to the series LCR-circuit. Further, the current $i_{s,n}$ can be separated into a current $i_{r,n}$, which passes through the resonant LCR circuit, and a current $i_{p,n}$, which passes through the parallel pathway. A sketch of the circuit model is provided in Figure A1 (Appendix A). For N parallel-connected sensor elements, i_s can be described by:

$$i_s(t) = \sum_{n=1}^N i_{s,n} = \sum_{n=1}^N (i_{p,n} + i_{r,n}). \quad (2)$$

The current $i_{p,n}$ is described as a function of the magnitude $|Y_{p,n}|$ and the phase angle $\phi_{p,n}$ of the electrical admittance $Y_{p,n}$ of the parallel pathway, and results in:

$$i_{p,n} = \hat{u}_{\text{ex}} \cdot |Y_{p,n}(f_{\text{ex}})| \cdot \cos(2\pi f_{\text{ex}} t + \phi_{p,n}(f_{\text{ex}})). \quad (3)$$

This current is independent of the magnetic field, and the corresponding electrical admittance $Y_{p,n}(f) = R_{p,n}^{-1} + 2\pi f C_{p,n}$ as a function of frequency f is entirely determined by the capacitance $C_{p,n}$ of the respective piezoelectric layer-electrode configuration and its resistance $R_{p,n}$. Similarly, the current $i_{r,n}$ can be described as a function of the magnitude $|Y_{r,n}|$ and the phase angle $\phi_{r,n}$ of the magnetic-field and frequency-dependent

admittance $Y_{r,n}$ of the resonant circuit of a sensor element n . The current $i_{r,n}$ is filtered in the time domain to consider the frequency response of the resonator. We use a second-order digital peaking (resonator) filter with a rational transfer function \mathcal{H}_r that is determined by the resonance frequency f_r and the quality factor Q (Appendix B). It is given by:

$$i_{r,n} = \mathcal{H}_r\{\hat{u}_{ex} \cdot |Y_{r,n}(f_{ex}, B, t)| \cdot \cos(2\pi f_{ex}t + \phi_{r,n}(f_{ex}, B, t))\}. \quad (4)$$

In contrast to $i_{p,n}$, the resonant current $i_{r,n}$ depends on the magnetic flux density $B = B_0 + B_{ac}(t)$, which can be expressed as a static magnetic flux density B_0 , superposed by a small, time t dependent contribution $B_{ac}(t)$. For small amplitudes \hat{B}_{ac} of $B_{ac}(t)$, the admittance $Y_{r,n}(f, B)$ around B_0 and at $f = f_{ex}$ can be approximated by a first-order Taylor series:

$$|Y_{r,n}(f_{ex}, B, t)| \approx |Y_{r,n}(f_r, B_0)| + \left. \frac{d|Y_{r,n}(f, B_0)|}{df} \right|_{f=f_{ex}} \left. \frac{df_{r,n}(B)}{dB} \right|_{B=B_0} \cdot B_{ac}(t), \quad (5)$$

and

$$\phi_{r,n}(f_{ex}, B, t) \approx \phi_{r,n}(f_r, B_0) + \left. \frac{d\phi_{r,n}(f, B_0)}{df} \right|_{f=f_{ex}} \left. \frac{df_{r,n}}{dB} \right|_{B=B_0} \cdot B_{ac}(t). \quad (6)$$

Because the damping of the carrier relative to its maximum value at $f_{ex} = f_r$ is already considered by \mathcal{H}_r , the zero-order element in the series expansion is taken at $f = f_r$ instead of $f = f_{ex}$. If not stated differently, we always use $B_0 = 0$ because the exchange bias sensors used here do not require an externally applied magnetic bias field.

3.2. Definition of Sensitivities

The derivatives in the previous two equations describe the influence of the magnetic field on the electrical admittance and can be referred to as sensitivities. A magnetic sensitivity can be defined as:

$$S_{mag,n} = \left. \frac{df_{r,n}}{dB} \right|_{B=B_0}, \quad (7)$$

and two electrical sensitivities $S_{el,am,n}$ and $S_{el,pm,n}$ as:

$$S_{el,am,n} = \left. \frac{d|Y_{r,n}(f, B_0)|}{df} \right|_{f=f_{ex}}, S_{el,pm,n} = \left. \frac{d\phi_{r,n}(f, B_0)}{df} \right|_{f=f_{ex}}. \quad (8)$$

These definitions of electrical sensitivities differ from previous work [26,53,57], which is further discussed at the end of this section. A normalization, as in Refs. [26,57], is still required to compare the electric and magnetic sensitivity of sensors with different resonance frequencies. After amplification by the charge amplifier, the output signal $u_{co}(t)$ is fed into a quadrature amplitude demodulator to obtain the demodulated signal $u(t)$. The amplitude spectrum $\hat{U}(f)$ of $u(t)$ can then be used to define the voltage sensitivity $S_V(f)$ as a normalized measure for the sensor's signal response:

$$S_V(f_{ac}) = \frac{\hat{U}(f_{ac})}{\hat{B}_{ac}} \text{ with } [S_V] = \frac{V}{T}. \quad (9)$$

The voltage sensitivity $S_V(f_{ac})$ can be estimated by applying a sinusoidal magnetic test signal $B_{ac} = \hat{B}_{ac} \sin(2\pi f_{ac}t)$, with well-defined amplitude \hat{B}_{ac} and frequency f_{ac} , to obtain $U(f_{ac})$ from the measurement. With $S_V(f_{ac})$, a measure for the smallest detectable magnetic field can be defined. This measure is frequently referred to as limit of detection (LOD) [22,27], equivalent magnetic noise [58,59], or detectivity [40]:

$$\text{LOD}(f_{ac}) = \frac{E(f_{ac})}{S_V(f_{ac})} \text{ with } [\text{LOD}] = \frac{T}{\sqrt{\text{Hz}}}, \quad (10)$$

where $E(f_{ac})$ is the voltage noise density of $u(t)$ at f_{ac} , after demodulation and measured without any magnetic field applied. The response of Delta-E effect magnetometers to magnetic fields depends on the mutual orientation of the magnetic field and sensor element. Consequently, the sensitivities and LOD (Equations (7)–(10)) are generally functions of the orientation of the magnetic field. Details about the signal-and-noise characterization of ΔE -effect magnetometers can be found elsewhere [27,53,54].

The definitions of the electrical sensitivities (Equation (8)) differ from previous formulations [26,53,57] limited to the special case of one sensor element excited in resonance ($f_{ex} = f_r$). The electrical sensitivities defined within those models use the total sensor admittance $Y_s Y_r + Y_p$ instead of Y_r to form the derivatives with respect to the frequency. Here, the parallel admittance Y_p is considered in the total sensor current i_s . This definition arises naturally from separating the sensor current into the resonator current and the current through the capacitor, and it is used to consider the response of the resonator to the alternating magnetic field.

3.3. Noise Model

In the following, we modify and extend the model presented in Ref. [54] to analyze the noise of the array sensor system and how it is influenced by adding parallel sensor elements. Additional sensor elements are considered and minor noise sources, e.g., of the cables, are omitted. The equivalent circuit noise model is shown in Figure 2 and a summary of the parameters is given in Table A1 in Appendix C. The noise of the excitation source is described by a thermal-electrical noise source E_{ex} of the D/A converter's output resistance R_{ex} and the D/A converter's quantization noise E_{Vex} . Similarly, E_{AD} describes the noise that occurs during the analog-digital conversion. The noise source of the JFET charge amplifier is calculated from the model in [51] and is summarized in E_{JCA} . Each sensor element of the array is described by the mBvD equivalent circuit (Figure 2b). For the sensor intrinsic noise of the n th sensor element, we consider the thermal-electrical noise source $E_{p,n}$ of the piezoelectric layer and the thermal-mechanical noise source $E_{r,n}$ of the resonator. The value of the thermal-electrical noise sources can be calculated from:

$$E_x = \sqrt{4k_B T R_x} \text{ with } x \in \{ex, p, r\}, \quad (11)$$

with Boltzmann's constant $k_B = 1.38 \times 10^{-23} \text{ J/K}$ and the temperature $T = 290 \text{ K}$. The noise source E_{Vex} and E_{AD} were obtained from measurements. Here, we consider small excitation amplitudes $\hat{u}_{ex} < 100 \text{ mV}$ only and obtain $E_{Vex} = 26.8 \text{ nV}/\sqrt{\text{Hz}}$ and $E_{AD} = 6.9 \text{ nV}/\sqrt{\text{Hz}}$ in this case. Each noise source is transformed to the output of the charge amplifier to analyze its contribution to the total noise density at the charge amplifier's output. To simplify the final expressions, the following impedances are defined. The impedance $Z_{s,n}$ of the n th sensor is obtained from:

$$Z_{s,n} = Z_{r,n} \parallel Z_{p,n}, \quad (12)$$

$$Z_{r,n} = R_{r,n} + j\omega L_{r,n} + \frac{1}{j\omega C_{r,n}}, \quad (13)$$

$$Z_{p,n} = \frac{1}{j\omega C_{p,n}} \parallel R_{p,n}, \quad (14)$$

where \parallel denotes the parallel operator ($a \parallel b = (a^{-1} + b^{-1})^{-1}$).

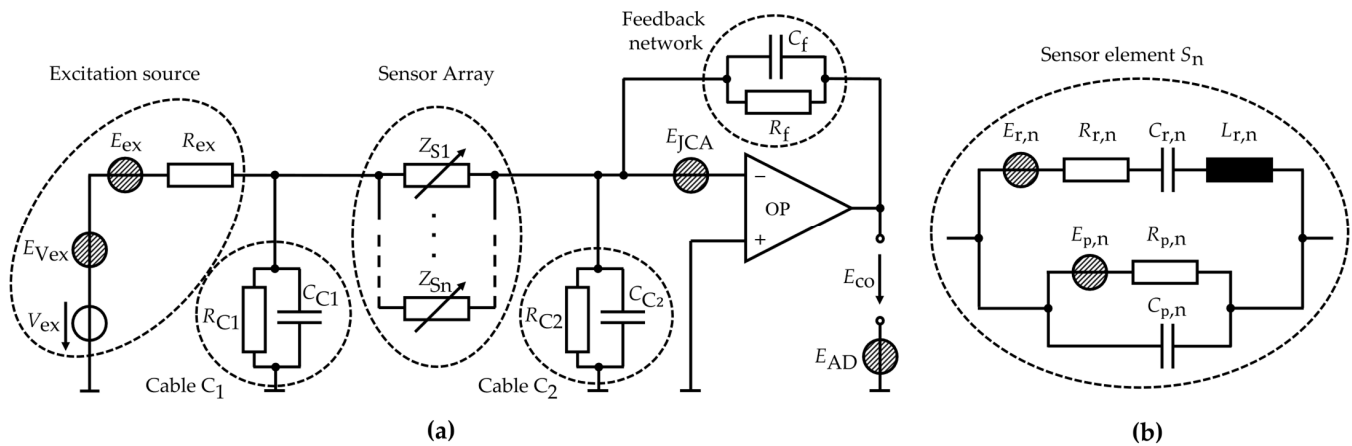


Figure 2. (a) Noise model of the sensor system comprising an excitation source, charge amplifier, and N sensor elements S_n with impedances Z_{S_n} , connected in parallel. (b) Equivalent circuit noise model of each sensor element S_n , with resonator intrinsic noise source $E_{r,n}$ and piezoelectric noise source $E_{p,n}$.

The total impedance of all N sensor elements connected in parallel is:

$$Z_s = \left[\sum_{n=1}^N Z_{s,n}^{-1} \right]^{-1}. \quad (15)$$

The impedance Z_{C_2} of the cable with capacitance C_{C_2} and resistance R_{C_2} between the sensor elements and the charge amplifier is given by:

$$Z_{C_2} = \frac{1}{j\omega C_{C_2}} \parallel R_{C_2}, \quad (16)$$

and the feedback impedance of the charge amplifier by:

$$Z_f = \frac{1}{j\omega C_f} \parallel R_f, \quad (17)$$

with the capacitance C_f and the resistance R_f . The total voltage noise density at the output of the charge amplifier is obtained from the superposition of the individual output referred noise sources,

$$E_{co}^2 = E_{co,JCA}^2 + E_{co,Vex}^2 + E_{co,AD}^2 + E_{co,s}^2, \quad (18)$$

$E_{co,JCA}$ of the charge amplifier, $E_{co,Vex}$ of the D/A converter, $E_{co,AD}$ of the A/D converter, and the contribution $E_{co,s}$ of the parallel sensor elements. These noise contributions are given by:

$$E_{co,JCA}^2 = E_{JCA}^2 \left| 1 + \frac{Z_f}{Z_s + Z_{C_2}} \right|^2, \quad (19)$$

$$E_{co,Vex}^2 = E_{Vex}^2 \left| \frac{Z_f}{Z_s} \right|^2, \quad (20)$$

$$E_{co,AD}^2 = E_{AD}^2, \quad (21)$$

$$E_{co,s}^2 = \sum_{n=1}^N \left(E_{r,n}^2 \left| \frac{Z_f}{Z_{r,n}} \right| + E_{p,n}^2 \left| \frac{Z_f}{R_{p,n}} \right| \right) E_{co,r}^2 + E_{co,p}^2. \quad (22)$$

4. Characterization and Validation of the Signal-and-Noise Model

In this section, the sensor elements and the array are characterized regarding their impedance, signal, and noise as well as their frequency response. The measurements

are compared with simulations to demonstrate the validity of the model. Details on the implementation of the model are given in Appendix D.

4.1. Electrical Sensitivity and Admittance Characterization

To eventually compare simulations with measurements, the admittance of the sensor elements is characterized. Measurements of the admittance magnitude $|Y_s|$ as functions of frequency f are shown in Figure 3a (top) for the two sensor elements S_1 , S_2 , and both connected in parallel ($S_1 || S_2$). All measurements were made at $B_0 = 0$ and an excitation voltage amplitude of $\hat{u}_{ex} = 10$ mV. An mBvD equivalent circuit as described earlier and illustrated in Appendix A is fitted to the magnitude data. The parameters obtained from the fit are given in Table A1 in Appendix C. From the mBvD parameters, we obtain resonance frequencies of $f_{r,1} = 7674.9$ Hz and $f_{r,2} = 7676.5$ Hz and quality factors of $Q_1 = 642$ and $Q_2 = 558$ (equations in Appendix A). This results in resonator bandwidths $f_{BW,n} \approx f_{r,n}/Q_n$ of $f_{BW,1} \approx 12$ Hz and $f_{BW,2} \approx 14$ Hz. Hence, the difference in resonance frequencies $\Delta f_r = |f_{r,2} - f_{r,1}| = 1.6$ Hz is significantly smaller than the bandwidth of the sensor elements.

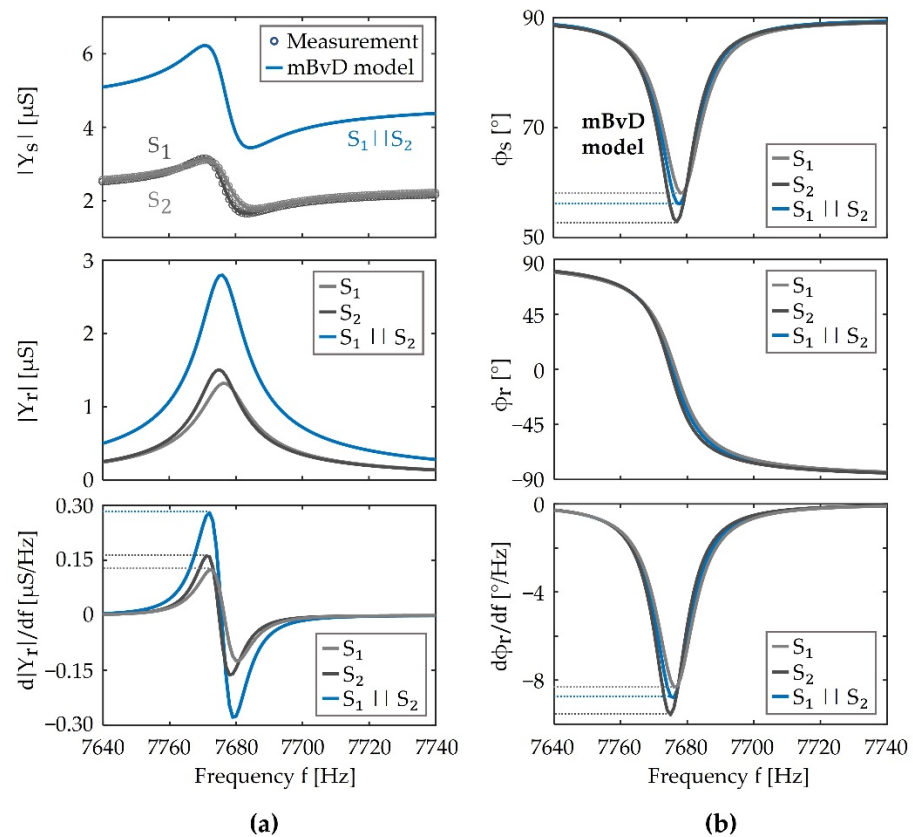


Figure 3. (a) Top: magnitudes $|Y_s|$ of the admittance of the sensor elements S_1 , S_2 and both connected in parallel ($S_1 || S_2$) measured at an applied magnetic flux density of $B = 0$ and an excitation voltage amplitude of $\hat{u}_{ex} = 10$ mV, compared with a modified Butterworth-van Dyke (mBvD) equivalent circuit fit; middle: magnitude $|Y_r|$ of the electrical admittance of the LCR series circuit of the mBvD model; bottom: derivative of $|Y_r|$ with respect to the frequency f , which we refer to as electrical amplitude sensitivity. (b) Top: corresponding phase angles ϕ_s of the sensor elements obtained from the mBvD model; middle: phase angles ϕ_r of the admittance of the LCR series circuits; bottom: their derivatives, which we refer to as electrical phase sensitivities.

With the mBvD parameters, the phase angle $\phi_{s,n}$ is calculated and plotted in Figure 3b (top). It shows the typical minimum of an electromechanical resonator that is caused by the superposition of the current through the resonator and the current through the parallel capacitance $C_{p,n}$ and resistance $R_{p,n}$. The values of $Y_{s,n}$ and $\phi_{s,n}$ are similar

to other electromechanical resonators that have been operated as delta-E effect sensors (e.g., [32,34,54]). Hence, the chosen sensor elements are representative examples. The admittance magnitude $|Y_{r,n}|$ and phase angle $\phi_{r,n}$ of the series resonance circuit are obtained from the mBvD model by omitting the parallel current $i_{p,n}$ and are plotted in Figure 3a,b (middle). They exhibit the behavior expected from a linear resonator and the main difference between the two sensor elements is the small difference in their resonance frequencies. The electrical sensitivities $S_{el,am,n}$ and $S_{el,pm,n}$ are calculated following the definitions in Equation (8) from the derivatives of $|Y_{r,n}|$ and $\phi_{r,n}$ with respect to the frequency. They are plotted in Figure 3a,b (bottom). Both sensor elements have similar electrical sensitivities with extrema of $S_{el,am,1}^{\max} \approx S_{el,am,2}^{\max} \approx \pm 0.15 \mu\text{S}/\text{Hz}$ and $S_{el,pm,1}^{\max} \approx S_{el,pm,2}^{\max} \approx -8.5/\text{Hz}$. Note that $S_{el,am,n} = 0$ at $f_{ex} = f_{r,n}$, but $S_{el,pm,n} = S_{el,pm,n}^{\max}$. Because the two sensor elements have very similar resonance frequencies, their total electrical admittance $Y_s = Y_{s,1} + Y_{s,2}$ in parallel connection ($S_1 || S_2$) shows qualitatively the same behavior but with a much increased admittance magnitude and electrical amplitude sensitivity by approximately a factor of two compared to the single sensor elements. The corresponding plots are shown in Figure 3. Comparing the magnitude and phase of $Y_s(S_1 || S_2)$ emphasizes that an improvement in the sensitivity is only expected for the electrical amplitude sensitivity $S_{el,am}$, because the magnitudes $|Y_{r,n}|$ add up. In contrast, the electrical phase sensitivity $S_{el,pm}$ does not improve, as it results from averaging $S_{el,pm,1}$ and $S_{el,pm,2}$. For a more comprehensive and general discussion, signal and noise must be considered and, in particular, their dependencies on the magnetic field frequency and the differences in resonance frequency. For that, the signal model is validated in the following section.

4.2. Frequency Response of the Sensor

The electrical sensitivities and sensor parameters found in the previous section are used here in the signal model and the simulations are compared with measurements. In Figure 4a, the spectrum \hat{U}_{co} of the modulated signal is shown from a measurement of the sensor element S_1 (top) and $S_1 || S_2$ (bottom) using an excitation signal with a voltage amplitude of $\hat{u}_{ex} = 25$ mV, a frequency $f_{ex} = 7680$ Hz and a sinusoidal magnetic test signal with an arbitrarily chosen frequency of $f_{ac} = 5.8$ Hz, and an amplitude of $\hat{B}_{ac} = 1 \mu\text{T}$. Besides the carrier peak at f_{ex} , both spectra show one pair of peaks at $f_{ex} \pm f_{ac}$, which corresponds to the modulating signal caused by the magnetic field. Following the magnitude-frequency response of the transfer function of the resonator, the side peak closest to the resonance frequency at $f_{r,1} = 7674.9$ Hz (S_1) is the largest. The signal model fits the measurements very well for magnetic sensitivities of $S_{mag,1} \approx S_{mag,2} = 24$ Hz/mT. Considering the normalization required for a comparison [26,57], $S_{mag,n}/f_{r,n}$ is in the typical range expected from similar sensor elements [34,57].

Several $f_{ex} \neq f_r$ are chosen to analyze the sensor's magnitude-frequency response for operating out of resonance. They are indicated in Figure 4b for S_1 (top) and $S_1 || S_2$ (bottom) as the difference $\Delta f_{ex,1} = f_{ex} - f_{r,1}$ of f_{ex} to the resonance frequency $f_{r,1}$ of S_1 , and the difference $\Delta f_{ex,2} = f_{ex} - f_{r,2}$ of f_{ex} to $f_{r,2}$, respectively. For each excitation frequency, the voltage sensitivity S_V as a function of the magnetic field frequency f_{ac} was measured four times, averaged, and plotted in Figure 4c. As expected, the measurements of both configurations (S_1 and $S_1 || S_2$) show qualitatively the same behavior. For excitation frequencies close to f_r , the sensor's voltage sensitivity S_V exhibits a low-pass behavior with a maximum voltage sensitivity at the lowest magnetic field frequency f_{ac} .

With an increasing deviation of f_{ex} from f_r , the maximum shifts to larger values of f_{ac} and further reduces its value. The reduction of the voltage sensitivity is caused by a change of the electrical sensitivities as well as the transfer function of the resonator. The model matches the measurements well with deviations mostly smaller than a factor of two and well within the estimated errors of the measurements. In line with the estimation based on the electrical sensitivity in the previous section, the simulations, and measurements of $S_1 || S_2$, show an overall improved voltage sensitivity compared to S_1 . A more detailed

analysis of this is given in Section 5, where the model is used to estimate the influence of a resonance mismatch for otherwise identical sensor elements.

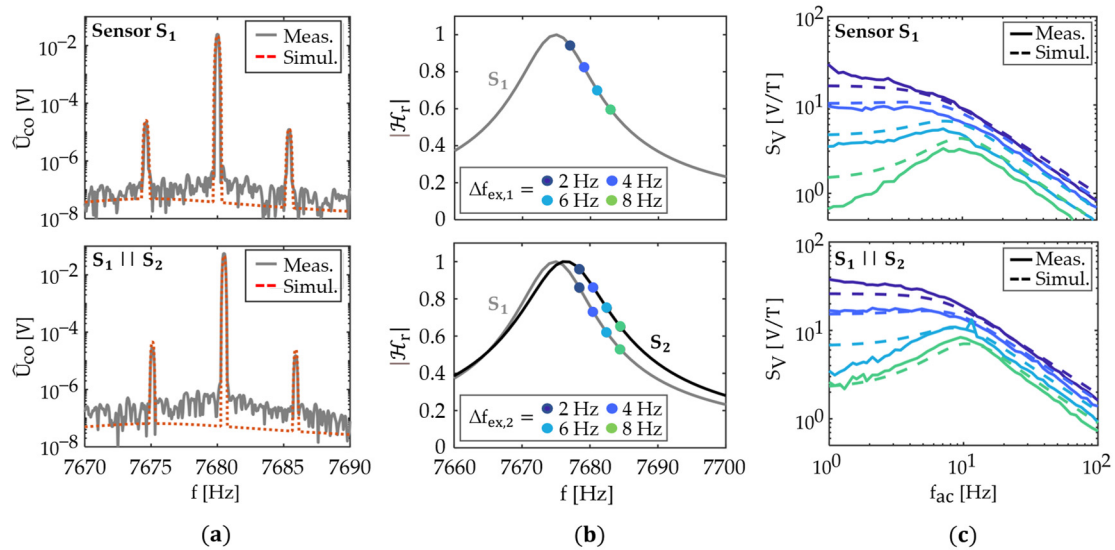


Figure 4. Comparison of simulations with measurements. (a) Example amplitude spectrum of the measured and simulated output signal using only the sensor element S_1 (top) and both sensor elements in parallel $S_1 || S_2$ (bottom) ($\hat{u}_{ex} = 25$ mV). (b) Magnitude $|H_r|$ of the transfer function H_r of the resonator used to indicate several excitation frequencies f_{ex} by $\Delta f_{ex,1} f_{ex} - f_{r,1}$, relative to the resonance frequency $f_{r,1} = 7674.9$ Hz of the sensor element S_1 (top), and $\Delta f_{ex,2} f_{ex} - f_{r,2}$, relative to the resonance frequency $f_{r,2} = 7676.5$ Hz of the sensor element S_2 (bottom). (c) Measured and simulated voltage sensitivity S_V (Equation (9)) as a function of the magnetic field frequency f_{ac} for the excitation frequencies indicated in (b) for the sensor element S_1 (top) and both sensor elements in parallel $S_1 || S_2$ (bottom) ($\hat{u}_{ex} = 10$ mV).

4.3. Validation of the Noise Model

We omit the effect of \hat{u}_{ex} on the quality factor and noise floor for the small \hat{u}_{ex} used in this work, in line with previous investigations [53,54]. Noise measurements are performed for $\hat{u}_{ex} = 0$, i.e., the sensor's input is shortened to ground potential, and data are recorded for 5 min with a sample rate of 32 kHz. The measured noise density spectra are compared with the simulations in Figure 5. The contributions of the sensor intrinsic thermal-mechanical noise $E_{co,r}$, and piezoelectric thermal-electric noise $E_{co,p}$, as well as the operational amplifier's noise $E_{co,JCA}$, are shown. The measurements and simulations match well and show what is expected for no excitation, or small excitation amplitudes. Thermal-mechanical noise dominates the noise floor around the resonance frequency and, further away, thermal-electrical noise of the piezoelectric resistance. The maximum noise density peak in Figure 5 is increased by a factor of approximately 1.3 compared to the single sensor elements. This is slightly less than the maximum increase by a factor of $\sqrt{2}$ expected from Equation (22), and it is likely caused by the resonance mismatch.

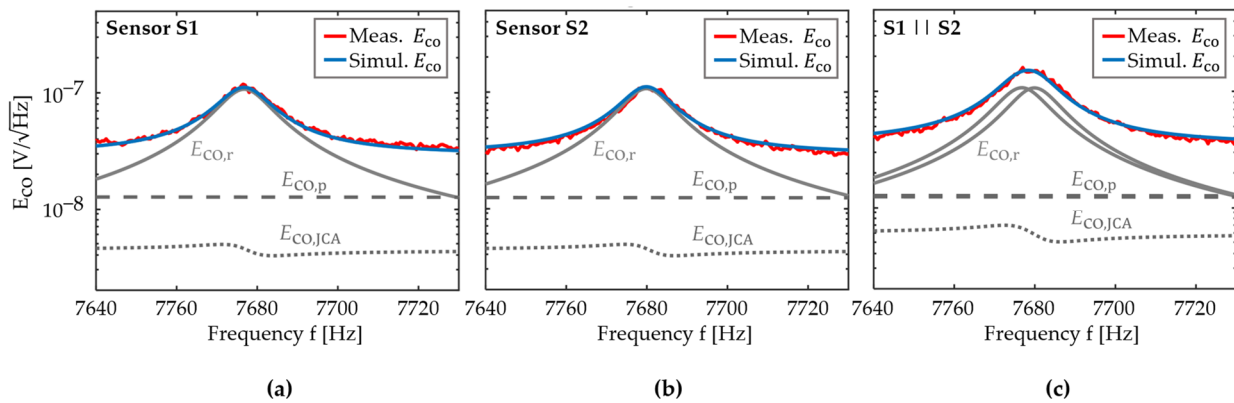


Figure 5. Comparison of the simulated and measured total voltage noise density E_{co} (Equation (18)) around the sensor's resonance frequency. The simulated contributions of the thermal-mechanical noise density $E_{co,r}$, the thermal-electrical noise density $E_{co,p}$ of the piezoelectric layer, and the operational amplifier's noise density $E_{co,JCA}$ are shown as well. Measurements and simulations are compared for a sensor system with (a) a single sensor element S_1 , (b) a single sensor element S_2 , and (c) two sensor elements connected in parallel ($S_1 || S_2$).

5. Implications for Sensor Arrays

5.1. Influence of the Number of Sensor Elements

The noise model is used to estimate the influence of the number N of sensor elements on the minimum detectable magnetic flux density. First, we consider the ideal case of identical sensor elements described with the mBvD parameters of the sensor S_1 . In this case, the signal magnitude increases linearly with N . The change of the total voltage noise density is less trivial because the various noise contributions depend differently on N . A simulation of the voltage noise density at the resonance frequency is shown in Figure 6 as a function of N . While the sensor intrinsic thermal-mechanical noise and thermal-electrical noise increase $\propto \sqrt{N}$, the noise of the JFET charge amplifier is $\propto N$. This linear relationship can be explained with the expression for the noise gain $|1 + Z_f / (Z_s + Z_{C2})|$ of the amplifier in Equation (19). According to this expression, the noise gain is in good approximation ($Z_s \gg Z_{C2}, 1$) inversely proportional to the impedance Z_s of the array. Each additional sensor element increases the capacitance and reduces Z_s (Equation (15)), and therefore, the noise gain increases linearly with N if all sensor elements are identical. The thermal-mechanical noise and the thermal-electrical noise of the amplifier dominate the noise floor at different N owing to their different dependencies on N . At small N , the thermal-mechanical noise dominates the noise floor and the LOD $\propto 1/\sqrt{N}$ can be improved by adding sensor elements. At large N , the noise contribution of the amplifier dominates and no improvement in the LOD can be achieved because signal and noise are both $\propto N$. A transition region exists at intermediate values of N where the improvement in LOD decreases continuously with N . This transition region is approximately around $N = 200N_{max}$ for the set of sensor parameters considered.

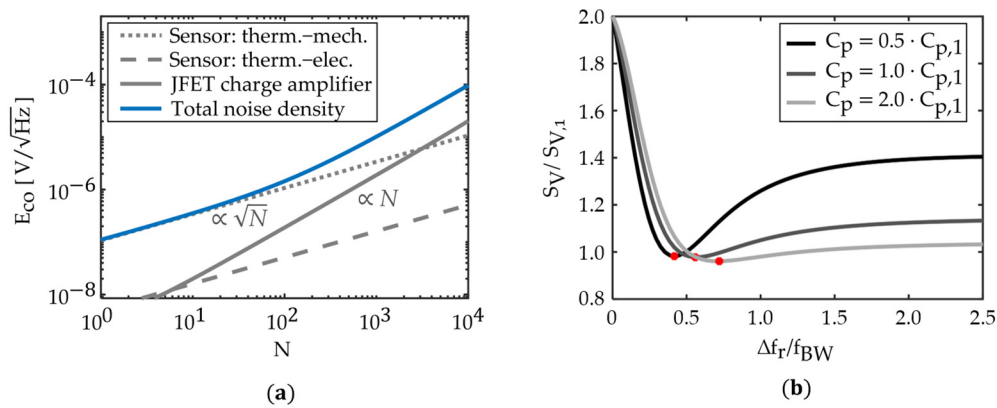


Figure 6. (a) Simulation of the voltage noise density at the resonance frequency as a function of the number N of the parallel connected sensor elements. Below approximately $N = 200$, the noise level is dominated by the sensor intrinsic thermal-mechanical noise and increases $\propto \sqrt{N}$. At approximately $N > N_{max} \approx 200$, the noise of the charge amplifier dominates the noise floor and is $\propto N$. No significant improvement in the signal-to-noise ratio is expected for $N > N_{max} \approx 200$ because the signal amplitude increases $\propto N$ as well. (b) Simulated gain $S_V/S_{V,1}$ in the voltage sensitivity S_V of a system with two parallel connected sensor elements relative to the voltage sensitivity $S_{V,1}$ of a single sensor element as a function of the difference Δf_r in their resonance frequencies, normalized to the bandwidth $f_{BW}f_r/Q$ of the resonator. Examples are shown for three different parallel capacities, expressed as multiples of the parallel capacitance $C_{p,1}$ of the sensor element S_1 . The minima are indicated with red dots.

5.2. Influence of Resonance Frequency Mismatch

The reproducibility of sensor elements can be considerably impaired by the relaxation of small stress during fabrication [60] and by small variations in the resonator geometry. The condition $f_{ex} = f_r$ cannot be fulfilled simultaneously for all N sensor elements because both mechanisms cause a distribution in resonance frequency f_r . At this point, it remains unclear to what extent such a distribution impairs signal, noise, and LOD. However, knowing the tolerable variation in resonance frequency is important for the design of sensor arrays because it imposes limitations on the resonator geometry and on the tolerances of the fabrication process.

First, the voltage sensitivity S_V is calculated as a function of the resonance frequency mismatch because it must be known to estimate the LOD (Equation (10)). The model sensor system considered comprises two sensor elements connected in parallel. Both sensor elements have identical resonance frequencies and sensitivities, and they are described by the same set of mBvD equivalent circuit parameters of the sensor element S_1 . The resonance frequency $f_r \propto 1/\sqrt{L_r C_r}$ of one sensor element is altered by increasing the mBvD parameters L_r and C_r in equal ratios. This keeps the quality factor $Q \propto L_r/C_r$ constant (Appendix A), and it causes only a negligible change in the bandwidth for the range of resonance frequencies tested. For each difference Δf_r in the two resonance frequencies, we simulate the output signal using a magnetic test signal with a frequency of $f_{ac} = 1$ Hz, and calculate the voltage sensitivity S_V (Equation (9)). This procedure is repeated for three different example capacities C_p with values that are multiples of the parallel capacitance $C_{p,1}$ of the sensor element S_1 . We define the sensitivity gain $S_V/S_{V,1}$ by the voltage sensitivity S_V of the two parallel sensor elements, normalized to the voltage sensitivity $S_{V,1}$ of the single sensor element. The results are plotted in Figure 6b as functions of Δf_r normalized to the bandwidth $f_{BW} = f_r/Q$ of S_1 .

For all three values of C_p , the sensitivity gain reaches a maximum value of $S_V/S_{V,1} = 2$, when the resonance frequencies are identical $\Delta f_r/f_{BW} = 0$. It decreases to a minimum of around $S_V/S_{V,1} = 1$ at roughly $\Delta f_r/f_{BW} = 0.5$, indicated in Figure 6b with red dots. For larger $\Delta f_r/f_{BW}$, $S_V/S_{V,1}$ increases slightly but it does not reach its maximum value again. The influence of the parallel capacitance C_p on $S_V/S_{V,1}$ is distinct but it does not change the curves qualitatively in the considered range. A larger C_p reduces $S_V/S_{V,1}$ at high $\Delta f_r/f_{BW}$ and shifts the location of the minimum to a larger $\Delta f_r/f_{BW}$; hence, it slightly broadens

the peak around the maximum of $S_V/S_{V,1}$. Consequently, the condition of approximately $\Delta f_r/f_{BW} < 0.5$ (depending on C_p) should be fulfilled to increase the signal magnitude in an array with two sensor elements. This condition can be expressed as:

$$\Delta f_{r,BW} \frac{\Delta f_r}{f_{BW}} \approx \frac{\Delta f_r}{f_r} \cdot Q < 0.5. \quad (23)$$

The simulations in Figure 6b demonstrate that Equation (23) is not a strict criterium because the locations of the minima on the $\Delta f_{r,BW}$ -axis vary by up to 50% for different tested values of C_p (e.g., for $C_p = 2C_{p,1}$ the minimum is at $\Delta f_{r,BW} \approx 0.75$). The exact location of the minimum depends on the contribution of the current through the LCR pathway to the total sensor current, relative to the capacitive contribution of C_p . For all practical purposes, these two contributions can hardly be varied independently because changing the parallel capacitance is accompanied by a change of the excitation efficiency, e.g., by altering the electrode geometry [32] or the piezoelectric material [33].

Not only for the voltage sensitivity, but also the sensor intrinsic thermal-mechanical noise referred to as the output follows the transfer function of the resonator; this is demonstrated with the measurements and simulations in Figure 5. Therefore, the LOD is constant if the sensor intrinsic thermal-mechanical noise dominates the noise floor, which is typically fulfilled for excitation frequencies f_{ex} within the bandwidth of the resonator and sufficiently small magnetic field frequencies f_{ac} . This conclusion is in line with other experimental results [55] (Figure 6) and does still hold for two parallel operating sensor elements with different resonance frequencies. Consequently, it is also $LOD(\Delta f_{r,BW}) = const.$ if the thermal-mechanical noise dominates the voltage noise density at $f_{ex} + f_{ac}$. The frequency band around the resonance frequency where the LOD is constant depends on the difference between the thermal-electric noise level and the resonance-amplified thermal-mechanical noise level and changes with N . For the sensors analyzed, this range is approximately $< f_{BW}$ around f_r , as shown in Figure 5.

6. Discussion and Conclusions

The signal-and-noise model developed matches well with measurements on exchange-biased sensor elements operated separately and in parallel in a setup with a single oscillator and amplifier. The model does still hold for excitation frequencies out of resonance and more than one sensor element. Hence, two major limitations of previous models have been solved and a tool is presented that can further support the design of delta-E effect sensors and sensor arrays. From the good match of the model and consistency with noise measurements, we find that the sensor intrinsic noise in our setup can be considered as uncorrelated, despite the parallel connection of sensor elements and their operation and read-out by a single oscillator and single amplifier. This is an essential precondition for improving the sensor performance by operating in parallel while using fewer electronic elements to keep the setup compact. Additional requirements were identified, which must be fulfilled to improve the signal and the limit of detection by operating many sensor elements in parallel. For the given sensor system, no significant improvement in the limit of detection can be achieved if a maximum number $N_{max} \approx 200$ of sensor elements is exceeded. Above this number, the noise contribution of the amplifier dominates the noise floor and increases, like the signal amplitude $\propto N$. Below, the sensor intrinsic noise dominates around the resonance and increases merely $\propto \sqrt{N}$, which results in $LOD \propto 1/\sqrt{N}$. With the given N_{max} , this would correspond to an LOD improvement by a factor of approximately 14. The value of N_{max} depends on the contribution of the thermal-mechanical noise relative to the thermal-electric noise. Therefore, N_{max} can potentially be improved by reducing the noise contribution of the charge amplifier. The proportionalities found do only hold strictly if all sensor elements are identical. Simulations of the voltage sensitivity confirmed that the improvement in signal amplitude depends significantly on the difference in the resonance frequencies of the sensor elements. It vanishes at a bandwidth normalized resonance frequency difference of approximately $\Delta f_{r,BW} \approx 0.5$, depending on the value of

the parallel capacitance of the sensor element. Consequently, a large signal improvement by parallel operation requires tight tolerances on the resonance frequency and, therefore, on the reproducibility provided by the fabrication process. Because the sensor intrinsic noise follows the same resonator transfer function as the signal, we expect the LOD to be constant with $\Delta f_{r,BW}$ for sufficiently small $\Delta f_{r,BW}$, and here at approximately $\Delta f_{r,BW} < 2$. This value depends on the level of the thermal-mechanical noise, relative to the thermal-electrical noise of the piezoelectric layer and the noise contribution of the amplifier.

In conclusion, a model was presented that overcomes previous limitations and can be used to explore the signal and noise characteristics of delta-E effect sensor arrays. The results from measurements and simulations indicate that large arrays of parallel operating sensor elements can be an option to improve the signal and limit of detection in the future.

Author Contributions: Conceptualization, B.S.; methodology, B.S. and P.D.; formal analysis, B.S. and P.W.; investigation, B.S., P.W. and P.D.; data curation, B.S. and P.W.; writing—original draft preparation, B.S.; writing—review and editing, B.S., P.W., P.D., M.H., A.B., R.R. and F.F.; visualization, B.S.; project administration, M.H., A.B., R.R. and F.F.; funding acquisition, M.H., A.B., R.R. and F.F. All authors have read and agreed to the published version of the manuscript.

Funding: This research was funded by the German Research Foundation (DFG) via the collaborative research center CRC 1261.

Institutional Review Board Statement: Not applicable.

Informed Consent Statement: Not applicable.

Data Availability Statement: The data presented in this study are available on reasonable request from the corresponding author.

Acknowledgments: The authors gratefully thank Christine Kirchhof for the fabrication of the sensor elements.

Conflicts of Interest: The authors declare no conflict of interest.

Appendix A. Equivalent Circuit Model

The equivalent circuit model used to describe the electrical admittance of each sensor element is illustrated in Figure A1a and the structure of the modeled sensor array in Figure A1b.

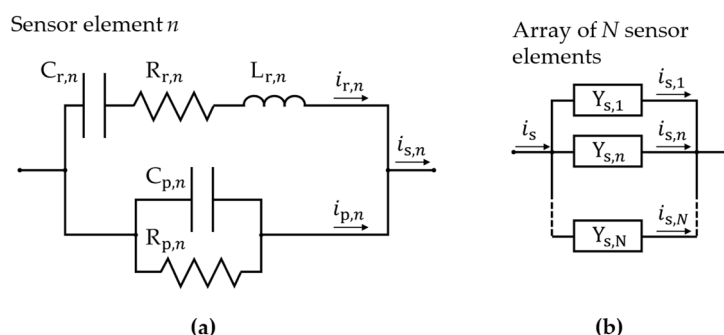


Figure A1. Illustration of (a) the modified Butterworth-van Dyke equivalent-circuit model used to describe the sensor elements, with the current $i_{r,n}$ through the resonator LCR-circuit and $i_{p,n}$ as the parallel capacitive pathway, and (b) all N parallel-connected sensor elements of the array, with the current $i_{s,n}$ through the n th sensor element and the total current i_s through the array.

The following equations are used to estimate the resonance frequency $f_{r,n}$ and the quality factor Q_n of the n th sensor element:

$$Q_n = \frac{1}{R_{r,n}} \sqrt{\frac{L_{r,n}}{C_{r,n}}}, \quad (\text{A1})$$

and

$$f_{r,n} = \frac{1}{2\pi\sqrt{L_{r,n}C_{r,n}}} . \quad (\text{A2})$$

Appendix B. Transfer Function of the Resonator

The frequency response of the resonator is modeled as second-order infinite impulse response (IIR) peaking filter with the transfer function $\mathcal{H}_r(z)$ [61]:

$$\mathcal{H}_r(z) = \frac{n_1 + n_2z^{-1} + n_3z^{-2}}{d_1 + d_2z^{-1} + d_3z^{-2}} , \quad (\text{A3})$$

and the components n_i of the numerator coefficients as well as d_i of the denominator coefficients, which are functions of the quality factor Q and the resonance frequency f_r [62]:

$$n = \begin{pmatrix} 1 - g \\ 0 \\ g - 1 \end{pmatrix} , \quad d = \begin{pmatrix} 1 - g \\ -2g \cdot \cos(\pi f_r) \\ 2g - 1 \end{pmatrix} . \quad (\text{A4})$$

To ensure a gain of -3 dB at the bandwidth, the factor g is set to:

$$g = \left[1 + \sqrt{2} \cdot \tan\left(\frac{\pi}{2} \frac{f_r}{Q}\right) \right]^{-1} . \quad (\text{A5})$$

Appendix C. System Parameters

In the following Table A1, the model parameters of the sensor system and the equivalent circuit parameters of the two sensor elements S_1 and S_2 are summarized.

Table A1. Parameters of the equivalent circuit noise model and the modified Butterworth-van Dyke (mBvD) model.

Component	Parameter	Value	Parameter	Value
Excitation	R_{ex}	75 Ω		
Cable C_1	R_{C1}	147 M Ω	C_{C1}	208 pF
Cable C_2	R_{C2}	184 M Ω	C_{C2}	36 pF
Sensor element S_1	$R_{p,1}$	295 M Ω	$C_{ME,1}$	47.157 pF
	$R_{r,1}$	663.47 k Ω	$C_{r,1}$	48.725 fF
	$L_{r,1}$	8.826 kH	$f_{r,1}$	7674.9 Hz
Sensor element S_2	$R_{p,2}$	310 M Ω	$C_{ME,2}$	48.568 pF
	$R_{r,2}$	755.96 k Ω	$C_{r,2}$	49.112 fF
	$L_{r,2}$	8.753 kH	$f_{r,2}$	7676.4 Hz
Amplifier	R_f	5 G Ω	C_f	30 pF

Appendix D. Implementation of the Model

The equations, which describe the signal-and-noise model (Equations (1)–(22)), are implemented in MATLAB (The MathWorks, Inc., Natick, MA, USA). The voltage at the charge amplifier's output $u_{co}(t)$ is calculated in the time domain using Equations (1)–(6), and the electric sensitivities (Equations (7) and (8)) obtained from the impedance measurements in Section 4.1. Estimated magnetic sensitivities of $S_{mag,1} \approx S_{mag,2} = 24$ Hz/mT are used, which is in the typical range expected from similar sensor elements [34,57]. The simulated time domain signal is demodulated with a quadrature amplitude demodulator and subsequently converted to the frequency domain using Welch's method [63]. From the power spectral density estimate, we calculate the amplitude spectrum $\hat{U}(f)$ of the demodulated signal $u(t)$ and the voltage sensitivity following the definition provided by

Equation (9). For the noise simulations, Equations (11)–(22) are implemented to obtain the voltage noise density at the output of the charge amplifier in the frequency domain.

References

1. Lenz, J.; Edelstein, S. Magnetic Sensors and Their Applications. *IEEE Sens. J.* **2006**, *6*, 631–649. [[CrossRef](#)]
2. Gleich, B.; Weizenecker, J. Tomographic Imaging Using the Nonlinear Response of Magnetic Particles. *Nature* **2005**, *435*, 1214–1217. [[CrossRef](#)]
3. Friedrich, R.-M.; Zabel, S.; Galka, A.; Lukat, N.; Wagner, J.-M.; Kirchof, C.; Quandt, E.; McCord, J.; Selhuber-Unkel, C.; Siniatchkin, M.; et al. Magnetic Particle Mapping Using Magnetolectric Sensors as an Imaging Modality. *Sci. Rep.* **2019**, *9*, 2086. [[CrossRef](#)]
4. Cohen, D.; Givler, E. Magnetomyography: Magnetic Fields around the Human Body Produced by Skeletal Muscles. *Appl. Phys. Lett.* **1972**, *21*, 114–116. [[CrossRef](#)]
5. Zuo, S.; Schmalz, J.; Özden, M.-Ö.; Gerken, M.; Su, J.; Niekief, F.; Lofink, F.; Nazarpour, K.; Heidari, H. Ultrasensitive Magneto-electric Sensing System for Pico-Tesla MagnetoMyoGraphy. *IEEE Trans. Biomed. Circuits Syst.* **2020**, *14*, 971–984. [[CrossRef](#)]
6. Koch, H. Recent Advances in Magnetocardiography. *J. Electrocardiol.* **2004**, *37*, 117–122. [[CrossRef](#)]
7. Fenici, R.; Brisinda, D.; Meloni, A.M. Clinical Application of Magnetocardiography. *Expert Rev. Mol. Diagn.* **2005**, *5*, 291–313. [[CrossRef](#)]
8. Kwong, J.S.W.; Leithäuser, B.; Park, J.-W.; Yu, C.-M. Diagnostic Value of Magnetocardiography in Coronary Artery Disease and Cardiac Arrhythmias: A Review of Clinical Data. *Int. J. Cardiol.* **2013**, *167*, 1835–1842. [[CrossRef](#)] [[PubMed](#)]
9. Duez, L.; Beniczky, S.; Tankisi, H.; Hansen, P.O.; Sidenius, P.; Sabers, A.; Fuglsang-Frederiksen, A. Added Diagnostic Value of Magnetoencephalography (MEG) in Patients Suspected for Epilepsy, Where Previous, Extensive EEG Workup Was Unrevealing. *Clin. Neurophysiol.* **2016**, *127*, 3301–3305. [[CrossRef](#)] [[PubMed](#)]
10. Fenici, R.; Brisinda, D.; Nenonen, J.; Fenici, P. Phantom Validation of Multichannel Magnetocardiography Source Localization. *Pacing and Clin. Electrophysiol.* **2003**, *26*, 426–430. [[CrossRef](#)] [[PubMed](#)]
11. Bertero, M.; Piana, M. Inverse problems in biomedical imaging: Modeling and methods of solution. In *Complex Systems in Biomedicine*; Quarteroni, A., Formaggia, L., Veneziani, A., Eds.; Springer: Milano, Italy, 2006; pp. 1–33. ISBN 978-88-470-0396-5.
12. Yang, J.; Poh, N. *Recent Application in Biometrics*; IntechOpen: London, UK, 2011; ISBN 978-953-307-488-7.
13. Murzin, D.; Mapps, D.J.; Levada, K.; Belyaev, V.; Omelyanchik, A.; Panina, L.; Rodionova, V. Ultrasensitive Magnetic Field Sensors for Biomedical Applications. *Sensors* **2020**, *20*, 1569. [[CrossRef](#)] [[PubMed](#)]
14. Kleiner, R.; Koelle, D.; Ludwig, F.; Clarke, J. Superconducting Quantum Interference Devices: State of the Art and Applications. *Proc. IEEE* **2004**, *92*, 1534–1548. [[CrossRef](#)]
15. Robbes, D. Highly Sensitive Magnetometers—A Review. *Sens. Actuators A Phys.* **2006**, *129*, 86–93. [[CrossRef](#)]
16. Griffith, W.C.; Knappe, S.; Kitching, J. FemtoTesla Atomic Magnetometry in a Microfabricated Vapor Cell. *Opt. Express* **2010**, *18*, 27167–27172. [[CrossRef](#)] [[PubMed](#)]
17. Johnson, C.N.; Schwindt, P.D.D.; Weisend, M. Multi-Sensor Magnetoencephalography with Atomic Magnetometers. *Phys. Med. Biol.* **2013**, *58*, 6065–6077. [[CrossRef](#)]
18. Osborne, J.; Orton, J.; Alem, O.; Shah, V. Fully Integrated Standalone Zero Field Optically Pumped Magnetometer for Biomagnetism. In Proceedings of the Steep Dispersion Engineering and Opto-Atomic Precision Metrology XI, San Francisco, CA, USA, 29 January–1 February 2018; Volume 10548, pp. 89–95.
19. Mhaskar, R.R.; Knappe, S.; Kitching, J. Low-Frequency Characterization of MEMS-Based Portable Atomic Magnetometer. In Proceedings of the 2010 IEEE International Frequency Control Symposium, Newport Beach, CA, USA, 1–4 June 2010; pp. 376–379.
20. Oelsner, G.; IJsselsteijn, R.; Scholtes, T.; Krüger, A.; Schultze, V.; Seyffert, G.; Werner, G.; Jäger, M.; Chwala, A.; Stolz, R. Integrated Optically Pumped Magnetometer for Measurements within Earth’s Magnetic Field. *arXiv* **2021**, arXiv:2008.01570.
21. Reermann, J.; Durdaut, P.; Salzer, S.; Demming, T.; Piorra, A.; Quandt, E.; Frey, N.; Höft, M.; Schmidt, G. Evaluation of Magnetolectric Sensor Systems for Cardiological Applications. *Measurement* **2018**, *116*, 230–238. [[CrossRef](#)]
22. Yasar, E.; Salzer, S.; Hrkac, V.; Piorra, A.; Höft, M.; Knöchel, R.; Kienle, L.; Quandt, E. Inverse Bilayer Magnetolectric Thin Film Sensor. *Appl. Phys. Lett.* **2016**, *109*, 022901. [[CrossRef](#)]
23. Tu, C.; Chu, Z.-Q.; Spetzler, B.; Hayes, P.; Dong, C.-Z.; Liang, X.-F.; Chen, H.-H.; He, Y.-F.; Wei, Y.-Y.; Lisenkov, I.; et al. Mechanical-Resonance-Enhanced Thin-Film Magnetolectric Heterostructures for Magnetometers, Mechanical Antennas, Tunable RF Inductors, and Filters. *Materials* **2019**, *12*, 2259. [[CrossRef](#)]
24. Lee, E.W. Magnetostriction and Magnetomechanical Effects. *Rep. Prog. Phys.* **1955**, *18*, 184–229. [[CrossRef](#)]
25. Spetzler, B.; Golubeva, E.V.; Müller, C.; McCord, J.; Faupel, F. Frequency Dependency of the Delta-E Effect and the Sensitivity of Delta-E Effect Magnetic Field Sensors. *Sensors* **2019**, *19*, 4769. [[CrossRef](#)] [[PubMed](#)]
26. Spetzler, B.; Golubeva, E.V.; Friedrich, R.-M.; Zabel, S.; Kirchof, C.; Meyners, D.; McCord, J.; Faupel, F. Magnetoelastic Coupling and Delta-E Effect in Magnetolectric Torsion Mode Resonators. *Sensors* **2021**, *21*, 2022. [[CrossRef](#)] [[PubMed](#)]
27. Reermann, J.; Zabel, S.; Kirchof, C.; Quandt, E.; Faupel, F.; Schmidt, G. Adaptive Readout Schemes for Thin-Film Magnetolectric Sensors Based on the Delta-E Effect. *IEEE Sens. J.* **2016**, *16*, 4891–4900. [[CrossRef](#)]
28. Osiander, R.; Ecelberger, S.A.; Givens, R.B.; Wickenden, D.K.; Murphy, J.C.; Kistenmacher, T.J. A Microelectromechanical-based Magnetostrictive Magnetometer. *Appl. Phys. Lett.* **1996**, *69*, 2930–2931. [[CrossRef](#)]

29. Gojdka, B.; Jahns, R.; Meurisch, K.; Greve, H.; Adelung, R.; Quandt, E.; Knöchel, R.; Faupel, F. Fully Integrable Magnetic Field Sensor Based on Delta-E Effect. *Appl. Phys. Lett.* **2011**, *99*, 223502. [[CrossRef](#)]
30. Jahns, R.; Zabel, S.; Marauska, S.; Gojdka, B.; Wagner, B.; Knöchel, R.; Adelung, R.; Faupel, F. Microelectromechanical Magnetic Field Sensor Based on ΔE Effect. *Appl. Phys. Lett.* **2014**, *105*, 052414. [[CrossRef](#)]
31. Zabel, S.; Kirchhof, C.; Yarar, E.; Meyners, D.; Quandt, E.; Faupel, F. Phase Modulated Magnetoelectric Delta-E Effect Sensor for Sub-Nano Tesla Magnetic Fields. *Appl. Phys. Lett.* **2015**, *107*, 152402. [[CrossRef](#)]
32. Zabel, S.; Reermann, J.; Fichtner, S.; Kirchhof, C.; Quandt, E.; Wagner, B.; Schmidt, G.; Faupel, F. Multimode Delta-E Effect Magnetic Field Sensors with Adapted Electrodes. *Appl. Phys. Lett.* **2016**, *108*, 222401. [[CrossRef](#)]
33. Spetzler, B.; Su, J.; Friedrich, R.-M.; Niekkel, F.; Fichtner, S.; Lofink, F.; Faupel, F. Influence of the Piezoelectric Material on the Signal and Noise of Magnetoelectric Magnetic Field Sensors Based on the Delta-E Effect. *APL Mater.* **2021**, *9*, 031108. [[CrossRef](#)]
34. Spetzler, B.; Bald, C.; Durdaud, P.; Reermann, J.; Kirchhof, C.; Teplyuk, A.; Meyners, D.; Quandt, E.; Höft, M.; Schmidt, G.; et al. Exchange Biased Delta-E Effect Enables the Detection of Low Frequency PT Magnetic Fields with Simultaneous Localization. *Sci. Rep.* **2021**, *11*, 5269. [[CrossRef](#)]
35. Nan, T.; Hui, Y.; Rinaldi, M.; Sun, N.X. Self-Biased 215 MHz Magnetoelectric NEMS Resonator for Ultra-Sensitive DC Magnetic Field Detection. *Sci. Rep.* **2013**, *3*, 1985. [[CrossRef](#)]
36. Li, M.; Matyushov, A.; Dong, C.; Chen, H.; Lin, H.; Nan, T.; Qian, Z.; Rinaldi, M.; Lin, Y.; Sun, N.X. Ultra-Sensitive NEMS Magnetoelectric Sensor for Picotesla DC Magnetic Field Detection. *Appl. Phys. Lett.* **2017**, *110*, 143510. [[CrossRef](#)]
37. Staruch, M.; Matis, B.R.; Baldwin, J.W.; Bennett, S.P.; van't Erve, O.; Lofland, S.; Bussmann, K.; Finkel, P. Large Non-Saturating Shift of the Torsional Resonance in a Doubly Clamped Magnetoelastic Resonator. *Appl. Phys. Lett.* **2020**, *116*, 232407. [[CrossRef](#)]
38. Zhuang, X.; Sing, M.L.C.; Dolabdjian, C.; Wang, Y.; Finkel, P.; Li, J.; Viehland, D. Sensitivity and Noise Evaluation of a Bonded Magneto(Elasto) Electric Laminated Sensor Based on In-Plane Magnetocapacitance Effect for Quasi-Static Magnetic Field Sensing. *IEEE Trans. Magn.* **2015**, *51*, 1–4. [[CrossRef](#)]
39. Staruch, M.; Yang, M.-T.; Li, J.F.; Dolabdjian, C.; Viehland, D.; Finkel, P. Frequency Reconfigurable Phase Modulated Magnetoelectric Sensors Using ΔE Effect. *Appl. Phys. Lett.* **2017**, *111*, 032905. [[CrossRef](#)]
40. Stutzke, N.A.; Russek, S.E.; Pappas, D.P.; Tondra, M. Low-Frequency Noise Measurements on Commercial Magnetoresistive Magnetic Field Sensors. *J. Appl. Phys.* **2005**, *97*, 10Q107. [[CrossRef](#)]
41. Deak, J.G.; Zhou, Z.; Shen, W. Tunneling Magnetoresistance Sensor with PT Level 1/f Magnetic Noise. *AIP Adv.* **2017**, *7*, 056676. [[CrossRef](#)]
42. Lukat, N.; Friedrich, R.-M.; Spetzler, B.; Kirchhof, C.; Arndt, C.; Thormählen, L.; Faupel, F.; Selhuber-Unkel, C. Mapping of Magnetic Nanoparticles and Cells Using Thin Film Magnetoelectric Sensors Based on the Delta-E Effect. *Sens. Actuators A Phys.* **2020**, *309*, 112023. [[CrossRef](#)]
43. Chu, Z.; Shi, W.; Shi, H.; Chen, Q.; Wang, L.; PourhosseiniAsl, M.J.; Xiao, C.; Xie, T.; Dong, S. A 1D Magnetoelectric Sensor Array for Magnetic Sketching. *Adv. Mater. Technol.* **2019**, *4*, 1800484. [[CrossRef](#)]
44. Cuong, T.D.; Viet Hung, N.; Le Ha, V.; Tuan, P.A.; Duong, D.D.; Tam, H.A.; Duc, N.H.; Giang, D.T.H. Giant Magnetoelectric Effects in Serial-Parallel Connected Metglas/PZT Arrays with Magnetostrictively Homogeneous Laminates. *J. Sci. Adv. Mater. Devices* **2020**, *5*, 354–360. [[CrossRef](#)]
45. Xi, H.; Lu, M.-C.; Yang, Q.X.; Zhang, Q.M. Room Temperature Magnetoelectric Sensor Arrays For Application of Detecting Iron Profiles in Organs. *Sens. Actuators A Phys.* **2020**, *311*, 112064. [[CrossRef](#)] [[PubMed](#)]
46. Lu, Y.; Cheng, Z.; Chen, J.; Li, W.; Zhang, S. High Sensitivity Face Shear Magneto-Electric Composite Array for Weak Magnetic Field Sensing. *J. Appl. Phys.* **2020**, *128*, 064102. [[CrossRef](#)]
47. Li, H.; Zou, Z.; Yang, Y.; Shi, P.; Wu, X.; Ou-Yang, J.; Yang, X.; Zhang, Y.; Zhu, B.; Chen, S. Microbridge-Structured Magnetoelectric Sensor Array Based on PZT/FeCoSiB Thin Films. *IEEE Trans. Magn.* **2020**, *56*, 1–4. [[CrossRef](#)]
48. Kim, H.J.; Wang, S.; Xu, C.; Laughlin, D.; Zhu, J.; Piazza, G. Piezoelectric/Magnetostrictive MEMS Resonant Sensor Array for in-Plane Multi-Axis Magnetic Field Detection. In Proceedings of the 2017 IEEE 30th International Conference on Micro Electro Mechanical Systems (MEMS), Las Vegas, NV, USA, 22–26 January 2017; pp. 109–112.
49. Lage, E.; Kirchhof, C.; Hrkac, V.; Kienle, L.; Jahns, R.; Knöchel, R.; Quandt, E.; Meyners, D. Exchange Biasing of Magnetoelectric Composites. *Nat. Mater.* **2012**, *11*, 523–529. [[CrossRef](#)]
50. Yarar, E.; Hrkac, V.; Zamponi, C.; Piorra, A.; Kienle, L.; Quandt, E. Low Temperature Aluminum Nitride Thin Films for Sensory Applications. *AIP Adv.* **2016**, *6*, 075115. [[CrossRef](#)]
51. Durdaud, P.; Penner, V.; Kirchhof, C.; Quandt, E.; Knöchel, R.; Höft, M. Noise of a JFET Charge Amplifier for Piezoelectric Sensors. *IEEE Sens. J.* **2017**, *17*, 7364–7371. [[CrossRef](#)]
52. Jahns, R.; Knöchel, R.; Greve, H.; Woltermann, E.; Lage, E.; Quandt, E. Magnetoelectric Sensors for Biomagnetic Measurements. In Proceedings of the 2011 IEEE International Symposium on Medical Measurements and Applications, Bari, Italy, 30–31 May 2011; pp. 107–110.
53. Durdaud, P.; Reermann, J.; Zabel, S.; Kirchhof, C.; Quandt, E.; Faupel, F.; Schmidt, G.; Knöchel, R.; Höft, M. Modeling and Analysis of Noise Sources for Thin-Film Magnetoelectric Sensors Based on the Delta-E Effect. *IEEE Trans. Instrum. Meas.* **2017**, *66*, 2771–2779. [[CrossRef](#)]

54. Durdaut, P.; Rubiola, E.; Friedt, J.-M.; Müller, C.; Spetzler, B.; Kirchhof, C.; Meyners, D.; Quandt, E.; Faupel, F.; McCord, J.; et al. Fundamental Noise Limits and Sensitivity of Piezoelectrically Driven Magnetoelastic Cantilevers. *J. Microelectromech. Syst.* **2020**, *29*, 1347–1361. [[CrossRef](#)]
55. Spetzler, B.; Kirchhof, C.; Reermann, J.; Durdaut, P.; Höft, M.; Schmidt, G.; Quandt, E.; Faupel, F. Influence of the Quality Factor on the Signal to Noise Ratio of Magnetolectric Sensors Based on the Delta-E Effect. *Appl. Phys. Lett.* **2019**, *114*, 183504. [[CrossRef](#)]
56. Durdaut, P. Ausleseverfahren Und Rauschmodellierung Für Magnetoelektrische Und Magnetoelastische Sensorsysteme. Ph.D. Thesis, Kiel University, Kiel, Germany, 2019.
57. Spetzler, B.; Kirchhof, C.; Quandt, E.; McCord, J.; Faupel, F. Magnetic Sensitivity of Bending-Mode Delta-E-Effect Sensors. *Phys. Rev. Appl.* **2019**, *12*, 064036. [[CrossRef](#)]
58. Wang, Y.J.; Gao, J.Q.; Li, M.H.; Shen, Y.; Hasanyan, D.; Li, J.F.; Viehland, D. A Review on Equivalent Magnetic Noise of Magnetolectric Laminate Sensors. *Philos. Trans. R. Soc. A Math. Phys. Eng. Sci.* **2014**, *372*, 20120455. [[CrossRef](#)] [[PubMed](#)]
59. Ding, L.; Saez, S.; Dolabdjian, C.; Melo, L.G.C.; Yelon, A.; Menard, D. Equivalent Magnetic Noise Limit of Low-Cost GMI Magnetometer. *IEEE Sens. J.* **2009**, *9*, 159–168. [[CrossRef](#)]
60. Matyushov, A.D.; Spetzler, B.; Zaeimbashi, M.; Zhou, J.; Qian, Z.; Golubeva, E.V.; Tu, C.; Guo, Y.; Chen, B.F.; Wang, D.; et al. Curvature and Stress Effects on the Performance of Contour-Mode Resonant ΔE Effect Magnetometers. *Adv. Mater. Technol.* **2021**, *6*, 2100294. [[CrossRef](#)]
61. Oppenheim, A.V.; Schafer, R.W.; Buck, J.R. *Discrete-Time Signal Processing*, 2nd ed.; Prentice Hall: Upper Saddle River, NJ, USA, 1998.
62. Orfanidis, S.J. *Introduction to Signal Processing*; Prentice Hall: Hoboken, NJ, USA, 1996; ISBN 978-0-13-240334-4.
63. Welch, P.D. The Use of Fast Fourier Transform for the Estimation of Power Spectra: A Method Based on Time Averaging Over a Short, Modified Periodograms. *IEEE Trans. Audio Electroacoust.* **1967**, *15*, 70–73. [[CrossRef](#)]

Part III
Outlook

Chapter 8

Compact Sensor Arrays

We took the first steps toward the development of arrays based on ΔE -effect sensors in the previous chapters. Sensors based on exchange-biased multilayers were presented, which do not require external magnetic fields during operation. Cantilever-based sensor elements were mounted with a low-noise charge amplifier on a dedicated, printed circuit board. Such compact sensors potentially enable measurement arrangements with several sensors, e.g., for spatial field mapping or source localization. In Section 7.2, we indicated that a large number of sensor elements could be beneficial for the LOD, presuming a sufficient reproducibility of the resonator structure. The comparatively large size of the previously used sensor elements prevents using a large number of sensor elements and high densities. In such cases, where many sensors or high spatial resolution are required, the size of the sensor element can become an important parameter. In addition, the increased resonance frequency connected with the reduced size can significantly increase the bandwidth of the sensor if the quality factor is kept the same.

We present the first concept for compact ΔE -effect sensor arrays that comprise a large number of miniaturized sensor elements, that are suitable for integration with CMOS operating and read-out electronics¹. This concept attempts to address other major challenges identified in the previous chapters. The examples include reproducibility, as pointed out in Section 7.2, and the control of anisotropic stress. With the micro-contour-mode resonators in Section 4.3, reproducibility was significantly impaired by anisotropic stress that enters the magnetic layer upon the release of the resonator. Here, we present a method to reduce the effects of stress by depositing a magnetic layer on the released resonator structure. In Section 4.1, we showed that bending modes suffer from the properties of the magnetic layer close to its edge. Here, a new resonator design is suggested to reduce such problems.

After briefly introducing the technology platform used for sensor processing, the first experimental and theoretical results are evaluated. Finally, potential advantages and drawbacks of the suggested concept are discussed.

8.1 PiezoMUMPs Technology Platform

The approach selected in this chapter is based on microresonators fabricated by standard microelectromechanical system (MEMS) technology provided by the PiezoMUMPs design and technology package of the company MEMSCAP Inc. This platform permits the design of piezoelectric microstructures with a given sequence of layers of a fixed thickness. The limited design freedom affords the great advantage of short tape-out times of approximately 3 months and well-defined tolerances. The layer sequence is shown in Fig. 8.1 for the example of a cantilever structure. The layers comprise a silicon-on-insulator (SOI) starting substrate with a poly-silicon

¹Part of this project is conducted in collaboration with Patrick Wiegand, Chair of Networked Electronic Systems, Kiel University.

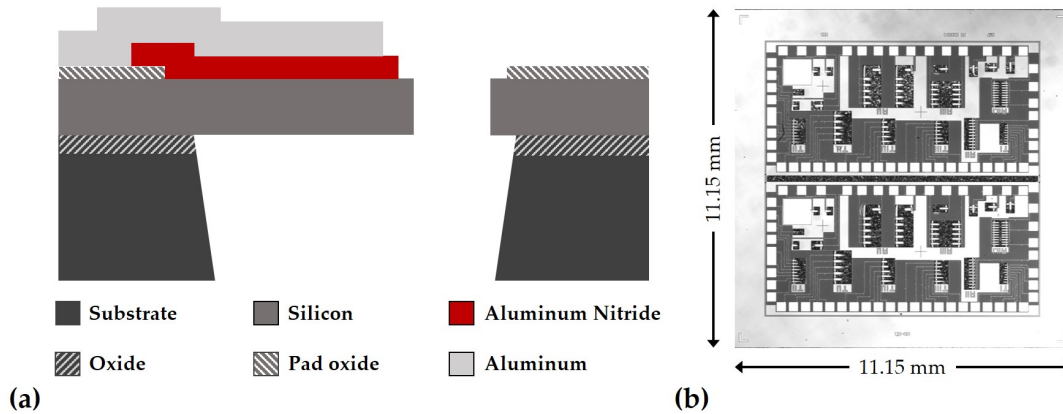


Figure 8.1: (a) Cross-sectional illustration of a cantilever structure produced with MEMSCAP Inc.'s PiezoMUMPS design platform (not to scale). The sketch is adapted from Ref. [404]. (b) Top-view of a chip with test structures to analyze the feasibility of the proposed concept. It comprises two identical half-chips that can be separated at a predetermined breaking line in the middle.

thickness of $10\ \mu\text{m}$. The poly-silicon is doped and can serve as a rear-side electrode. After doping, it is patterned and etched to the oxide layer to obtain a free-standing resonator structure. Where necessary, an $0.2\text{-}\mu\text{m}$ -thin thermal oxide layer is added on the top of the doped silicon layer to insulate it electrically from the subsequent layers. On top of the silicon or the thermal oxide, a $0.5\text{-}\mu\text{m}$ -thick piezoelectric layer is deposited, and a $1\text{-}\mu\text{m}$ -thick patterned aluminum layer can be used as top electrode. Details on the fabrication process and tolerances can be found in the *PiezoMUMPs Design Handbook* [403].

8.2 First Array Design

The first test structure was designed to assess the reproducibility of the resonators and the possibility of depositing a magnetic layer on the released structure. The chip has in-plane dimensions of $11.15\ \text{mm} \times 11.15\ \text{mm}$ with an area of $8.5\ \text{mm} \times 8.5\ \text{mm}$, which can be used for placing the resonators. For the first design, 186 cantilever resonators are placed on the chip with lengths from $130\text{-}500\ \mu\text{m}$ and widths from $40\text{-}100\ \mu\text{m}$. Besides single cantilevers that can be operated with their own pair of electrodes, arrays of parallel-connected cantilevers are placed on the chip. Example images are shown below in Figs. 8.2 and 8.4. An important parameter that limits the resonator dimensions is the resonance frequency. It was designed to stay below $1\ \text{MHz}$ in the first bending mode to reduce the requirements on the read-out electronics.

8.2.1 Electromechanical Properties

A representative example for an array structure is shown in Fig 8.2a; it comprises ten cantilevers of identical design, with nine of them connected in parallel. A curvature is visible at the edge of the cavity, and this results in an approximately symmetric distribution of the length of the cantilever in Fig. 8.2a. Accordingly, the measured magnitude of the admittance shows a distribution of the resonance frequencies. In Fig. 8.2b, five electromechanical resonance peaks (A-E) are visible. They are analyzed with an mBvD model used in Section 7.1 but with nine parallel LCR circuits instead of two. The fit reveals that A-D are the superposition of two resonance modes with very similar resonance frequency. All resonance frequencies and quality factors are extracted from the mBvD fit. The mean quality factor of this set of data is slightly

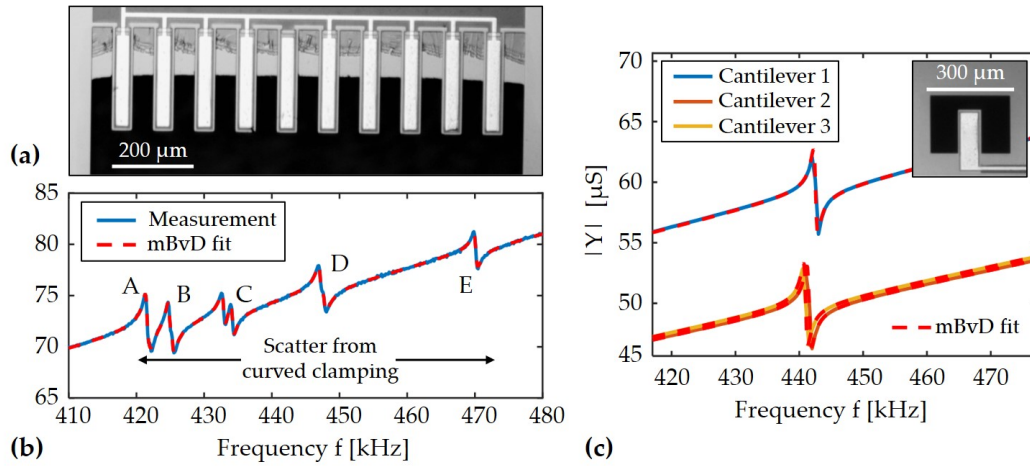


Figure 8.2: (a) Optical microscopy image (top-view) of an example of an array of parallel sensor elements and (b) the corresponding measured magnitude of the admittance with a scatter of the resonance frequencies caused by the curved clamping region. An mBvD model is fitted to the measurements to characterize the resonance modes. (c) Representative example of the measured and fitted admittance magnitudes of three cantilevers where the silicon layer is extended to the edge of the cavity. A straight clamping region is visible in the example top-view photograph in the inset.

smaller compared to that for the macroscopic cantilevers presented in the previous chapters, with $Q \approx 750$ and a standard deviation of $\Delta Q \approx 20\%$. A mean resonance frequency of $f_r \approx 436$ kHz is obtained with a standard deviation of $\Delta f_r \approx 3.7\%$; therefore, the mean bandwidth of the resonators is $BW \approx 0.6$ kHz (Section 2, Equation 2.6), which corresponds to a bandwidth-normalized resonance frequency deviation of $\Delta f_{r,BW} \approx 28$ (Section 7.2, Equation 22). This is far away from the condition $\Delta f_{r,BW} < 0.5$ that must be approximately fulfilled to improve the LOD by averaging.

Standard deviations can be improved significantly by matching the edge of the trench with the edge of the hole in the poly-silicon layer. Three cantilevers on the chip were designed in this manner. Their measured admittance magnitude curves are shown in Fig. 8.2c together with the top-view photograph provided in the inset. A clean and straight edge is visible at the clamping of the cantilever, and correspondingly, a considerably improved standard deviation $\Delta f_r \approx 0.18\%$ of the resonance frequency. This results in $\Delta f_{r,BW} \approx 1.1$ and including the data of six other chips $\Delta f_{r,BW} \approx 0.9$, which is in the range of the reproducibility requirement. Compared to the other two cantilevers, cantilever 1 has a significantly higher admittance magnitude, which can be attributed to the larger parasitic capacitance caused by a longer conducting line on the chip. The relative electrical magnitude sensitivity (Section 4.4, Equation 1) of the three cantilevers in Fig. 8.2c is estimated to be $|S_{Y,r}| \approx (8.5 \pm 0.3)$ mS on average and a mean quality factor of $Q \approx 630 \pm 20$. Here, $S_{Y,r}$ is similar to the values of the previous analyzed millimeter sized cantilevers ($|S_{Y,r}| \approx 9.6$ mS, Section 7.1), and Q is a bit lower than the typical values around $Q = 1000$. In general, the differences are expected because of the different geometry.

The results demonstrate the feasibility of miniaturization from an electromechanical point of view and show that no significant compromises are made in terms of the electrical sensitivity. Although the small value of $\Delta f_{r,BW}$ seems to be promising, more data are required to determine a reliable value for the means and standard deviations.

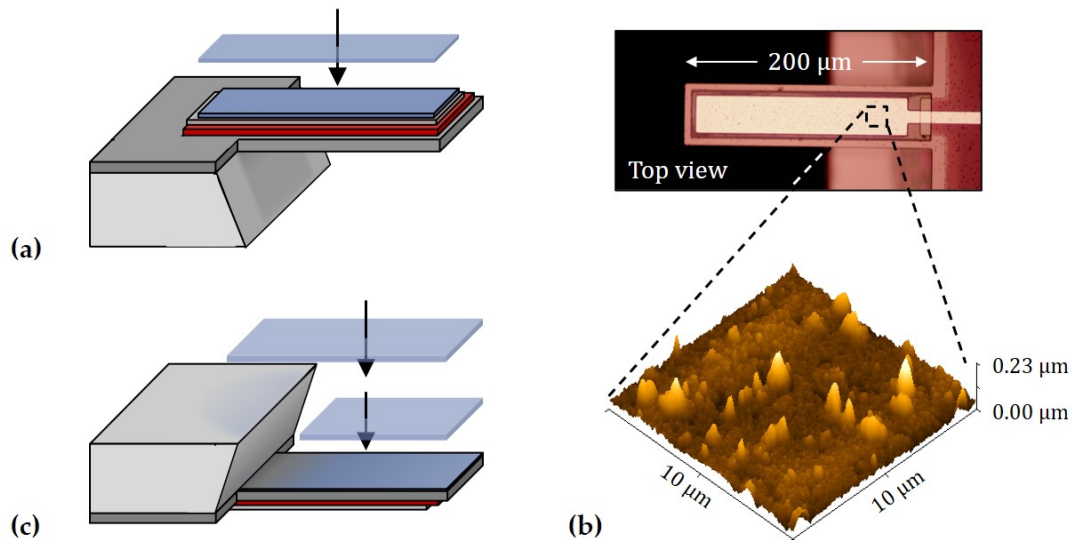


Figure 8.3: (a) Illustration of a deposition of the magnetic layer (blue) on top of the free-standing cantilever with a shadow mask. To avoid short circuits, high tolerances are required. (b) Light-microscopy image of the top of a typical cantilever of the sensor array. Atomic force microscopy (AFM) measurement of the oxidized Al top electrode, showing a high roughness. (c) Illustration of an alternative deposition from the rear side that avoids the rough top oxide and reduces the required tolerances of the shadow mask at the expense of potentially depositing magnetic material in unwanted regions around the clamping area of the cantilever.

8.2.2 Magnetic Layer Deposition

Magnetic layer is to be deposited on the free-standing resonator. Consequently, the stress in the magnetic layer can occur only from the deposition of the magnetic layer itself. However, there is a trade off with structuring as the deposition has to be performed with a shadow mask. The two options are illustrated in Fig. 8.3. Depositing the magnetic layer from the top may be desirable for two reasons. First, it permits extending the magnetic layer over the clamping region as indicated in Fig. 8.3a to avoid the sample edges to be present directly at the clamping. This can be advantageous for the magnetoelastic properties as shown in Section 4.1. Second, the shadow mask can be brought into direct contact with the cantilever, and this can enable us to precisely structure the deposited layer. Such a method requires high precision to avoid short circuiting the electrodes when depositing the magnetic layer from the top. Consequently, this approach comes with tight tolerances for the shadow mask itself and its positioning, which places high demands on the experimental procedure and the technical equipment. Another condition is the surface smoothness of the top electrode. Atomic force microscopy measurements of a typical top electrode (Fig. 8.3b) show a roughness of the order of the envisioned magnetic layer thickness of 100-200 nm. An alternative is to deposit the magnetic layer from the rear-side of the resonator. As illustrated in Fig. 8.3c, the shadow mask cannot be placed in direct contact with the resonator because of the approximately 400- μm -thick substrate and oxide in between. The comparatively large distance might lead to non-ideal magnetic layer properties at the clamping or the edges of the cantilever but the tolerances on the mask alignment and the risk of short circuits are significantly reduced for sufficiently thin magnetic layers. To test the feasibility of this approach, a $(\text{Fe}_{90}\text{Co}_{10})_{78}\text{Si}_{12}\text{B}_{10}$ layer with a target thickness of 200 nm is deposited². For a first demonstration, the chip is flipped over to use the etched trenches as a shadow mask. Neither

²Magnetic layer deposition by Anne Kittmann, Inorganic Functional Materials, Kiel University.

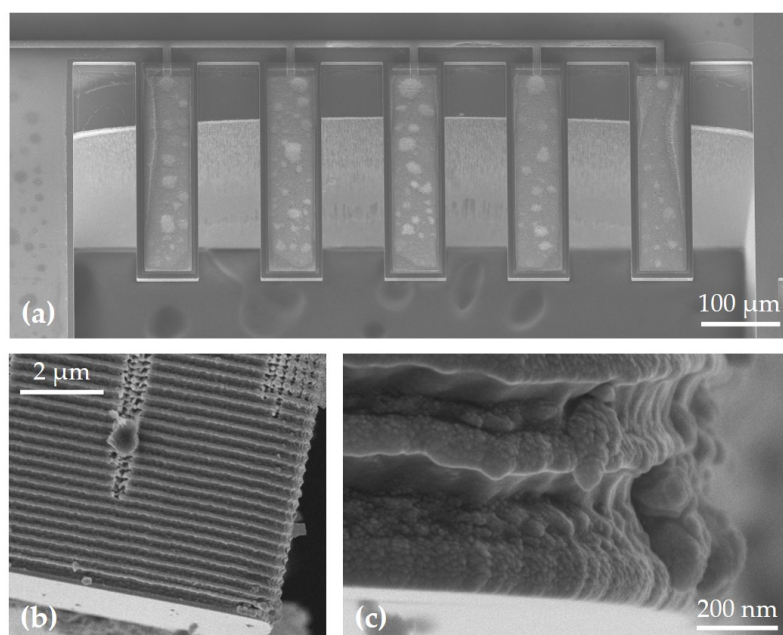


Figure 8.4: (a) Scanning electron microscopy (SEM) image of the top of an example cantilever array on the chip processed with the PiezoMUMPS technology platform. (b) SEM image shows a close-up and (c) an overview of a rear-side corner of a cantilever with an approximately 200-nm-thick magnetic layer deposited on top.

a magnetic field was applied during the deposition, nor were the samples annealed afterwards.

8.2.3 Scanning Electron Microscopy Measurements

Scanning electron microscopy (SEM) images were obtained to analyze the cantilever arrays, and in particular, the edges of the magnetic layer deposited on the rear-side. A detailed top-view³ of a representative electromechanical cantilever array is shown in Fig. 8.4a. A clear curvature is visible in the etched trench and the inclined profile of the trench wall under the cantilevers. The oxidized surface of the aluminum electrodes is clearly visible on the silicon cantilevers because of its high roughness. Additional SEM images were taken⁴ to evaluate the structure at the edges of the deposited magnetic layer. An example image shows an overview (Fig. 8.4b) of a rear-side corner of a cantilever with an approximately 200-nm-thick magnetic layer on top. The periodic ripple structure is characteristic for the Bosch process used to structure the cantilever. The edge of the magnetic layer and its surface is mostly smooth, and the large impurities in the background on the layer could be caused by dust particles or residuals from the etching process that were still present during sputter deposition. At the side of the cantilever in Fig. 8.4b, columnar structures are visible that seem to extend from the top-side of the cantilever to the rear-side where the magnetic layer is deposited. They are more dominant closer to the top-side from where the etching process was started, and it can be caused by insufficient passivation. A close-up (Fig. 8.4c) of the edge reveals a granular nanostructure at the side of the magnetic layer that is expected from the stochastic layer growth and local shadowing. Such a granular structure is also present on the Bosch-ripples protruding from the cantilever side. Reference measurements (not shown) of cantilevers without a magnetic layer confirm that the magnetic material has grown there as well. A magnetic characterization is required to understand if this

³SEM imaging performed by Lars Thormählen, Inorganic Functional Materials, Kiel University

⁴SEM imaging performed by Jonas Drewes, Multicomponent Materials, Kiel University

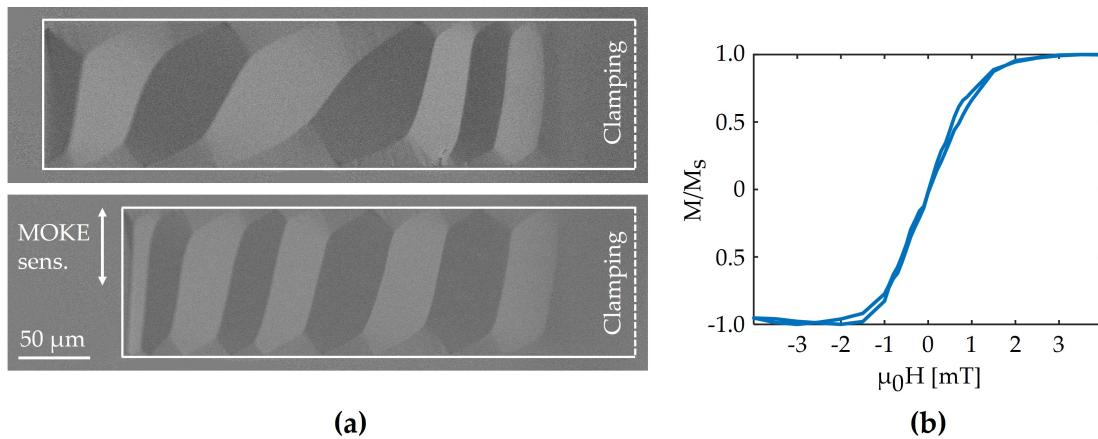


Figure 8.5: (a) Magneto-optical Kerr effect (MOKE) microscopy images of two example cantilevers captured without an applied magnetic field. The MOKE sensitivity axis was set along the short axis of the cantilevers. The background image was captured in magnetic saturation with the magnetic field applied along the long axis of the cantilevers. Clamping of the cantilevers is indicated by the dashed lines. Close to the clamping, the cantilever is obscured by the inclined side of the etched trench. (b) Reduced magnetization curve M/M_s , as a function of the magnetic flux density $\mu_0 H$ applied along the long axis of the shorter cantilever.

is problematic for achieving the desired magnetic properties.

Magneto-Optical Imaging

Magneto-optical Kerr effect (MOKE) microscopy [405] was used⁵ to assess the magnetic properties of the deposited layer. The MOKE images of two example cantilevers are shown in Fig. 8.5a. They were recorded at zero applied magnetic field after saturating the samples along the long axis of the cantilever. The MOKE sensitivity axis is set along the short axis. Both samples show Landau-like magnetic domain patterns [406] that indicate a small effective anisotropy with a mean magnetic easy axis oriented approximately 15° relative to the short axis of the cantilever. Such an anisotropy can be caused by the deposition process itself or by small anisotropic residual stress in the magnetic layer. An example hysteresis curve plotted in Fig. 8.5b is extracted from the MOKE measurements of the shorter cantilever, with the magnetic flux density applied along its long axis. The magnetization curve demonstrates the soft-magnetic properties of the magnetic layer that is similar to that achieved with larger structures [115, 395]. The right ends of the cantilevers close to the clamping are obscured by the angled side of the etched trench. A comprehensive analysis of the entire magnetic layer requires altering the resonator design.

8.3 Revised Resonator Design

The magnetic properties close to the clamping are important for bending modes. This can be problematic for several reasons. First, initial isotropic stress at the clamping relaxes differently compared to the rest of the cantilever because of the different geometric situation. This can lead to altered magnetoelastic anisotropy around the clamping and to inhomogeneous magnetic properties. Second, if the magnetic layer is deposited on the rear-side of the cantilever, it cannot be extended beyond the clamping region and the edge properties of the magnetic layer contribute significantly. For the process used here, the shadowing of the clamping region prevents the

⁵MOKE microscopy measurements by Elizaveta V. Golubeva, Nanoscale Magnetic Materials, Kiel University.

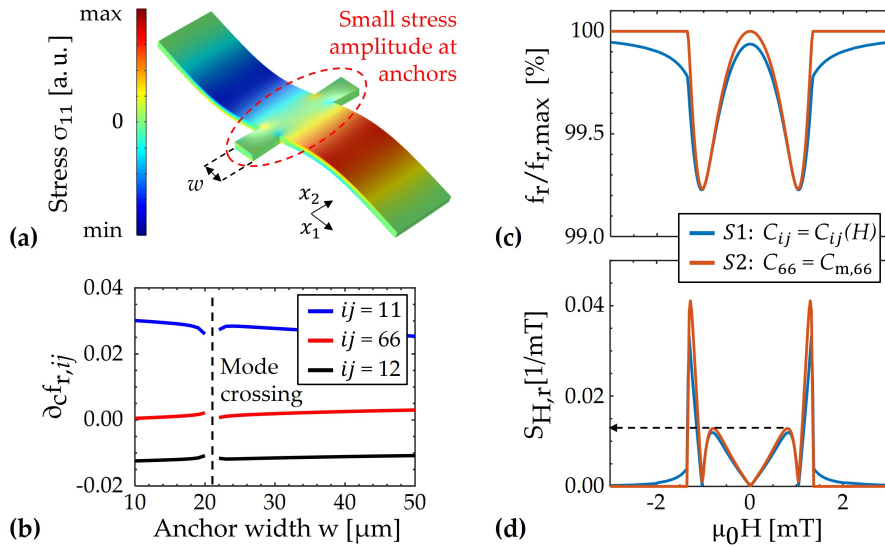


Figure 8.6: Simulation and analysis of antisymmetric second-order bending mode of a free-free beam, following the method and model established in Section 4.4. The beam is $400\ \mu\text{m}$ long and $80\ \mu\text{m}$ wide, with an anchor length of $50\ \mu\text{m}$ and an anchor width $w = 30\ \mu\text{m}$ (except in (b)). (a) Rear-side view of mode shape and σ_{11} component of the stress tensor. (b) Simulated normalized frequency factors $\partial_c f_{r,ij}$ as a function of the anchor width w , to estimate the contribution of the stiffness tensor components C_{ij} to the resonance frequency f_r . (c) Simulation (S1) of the normalized resonance frequency $f_r/f_{r,\max}$ as a function of the applied magnetic flux density $\mu_0 H$, with the magnetic field H and vacuum permeability μ_0 . A second simulation (S2) was performed where C_{66} was set constant to $C_{66} = C_{m,66}$ ($C_{m,66}$: value at fixed magnetization). (d) Relative magnetic sensitivity $S_{H,r}$ calculated from the data in (c) via Equation 1 (Section 4.4).

analysis of the magnetic properties, and it is expected to influence the magnetic layer formation, which can cause an inhomogeneous magnetic layer thickness.

Most issues may be resolvable by revising the current resonator design. Instead of a cantilever clamped at one end, a free-free beam can be used that is anchored symmetrically in the middle of its two long sides as illustrated in Fig. 8.6a. Based on the length of the anchors, they are mostly shadowed by the etched trench, whereas the complete beam stays visible. It is not expected that the deposition of magnetic material on the anchors can be completely avoided, but it is possible to reduce its contribution to the resonance frequency by selecting a suitable resonance mode. The resonance mode should oscillate with a small amplitude of anisotropic stress at its anchor, and the resonance frequency should be in the desired frequency range and well excitable electrically. A resonance mode that fulfills these conditions is the antisymmetric second-order bending mode.

A simulation of this mode is illustrated in Fig. 8.6 for a $400\ \mu\text{m}$ long and $80\ \mu\text{m}$ wide beam with two $50\ \mu\text{m}$ long and $w = 30\ \mu\text{m}$ wide anchors fixed at their respective free end. A 200-nm-thick magnetic layer covers the complete rear-side of the beam, including the anchor structures. The model and analysis are based on the finite element and magnetoelastic model described in Section 4.4. For the simulation, the layer sequence prescribed by the technology platform is used, with the material parameters provided by the company [403]. The mode shape and σ_{11} component of the stress tensor (in arbitrary units) are plotted in Fig. 8.6 for fixed magnetization. Due to the antisymmetric displacement profile, σ_{11} has a zero transition at the anchor line along

x_2 . The extrema of σ_{11} are in the middle of each wing where consequently, the magnetic properties are most weighted. During the oscillation, the anchors are twisted around the x_2 -axis. The torsion in this case is mechanically mediated by the C_{66} component, and therefore, it is expected to contribute to the resonance frequency f_r . With increasing anchor width w , the shear stress increases and changes the contribution to f_r . The normalized frequency factors $\partial_c f_{r,ij}$ (Equation 3, Section 4.4) were simulated as a function of the anchor width w to estimate this contribution of the stiffness tensor components C_{11} , C_{12} and C_{66} to f_r . The results are plotted in Fig. 8.6b. In line with the expectations, $\partial_c f_{r,11}$ and $|\partial_c f_{r,12}|$ decrease with w , whereas $\partial_c f_{r,66}$ slightly increases. Yet, over the range of w , $\partial_c f_{r,66}$ is more than one order of magnitude smaller than $\partial_c f_{r,11}$. A gap is visible in the data at around $w = 21 \mu\text{m}$. At this width, it intersects a different resonance mode that has a dominant displacement in the anchors. This gap could be at different anchor widths for other beam geometries and should be avoided during the design. In the previously analyzed bending modes in cantilevers (c.f. Section 4.4), $|\partial_c f_{r,12}|$ was more than an order of magnitude smaller than $\partial_c f_{r,11}$. Here, $|\partial_c f_{r,12}| \approx \partial_c f_{r,11}$, which corresponds to a considerably larger contribution of C_{12} to f_r compared to the cantilever design. This may be caused by the symmetric anchoring that partially constrains a lateral strain along the x_2 -axis. Because both components C_{12} and C_{11} cause resonance detuning in the same direction, it is not expected to be problematic for the magnetic sensitivity (c.f. Section 4.4).

In the following we illustrate the effect of different $\partial_c f_{r,ij}$ on the resonance frequency and magnetic sensitivity. Magnetoelastic simulations were performed with the model from Section 4.4, considering a magnetic field along x_1 and a effective magnetic anisotropy energy density of $K_{\text{eff}} = 800 \text{ J/m}^3$ with an easy axis along the x_2 -axis. For the first simulation (S1), the magnetic field dependency of all stiffness tensor components C_{ij} is considered. For the second simulation (S2), $C_{66} = C_{m,66}$ is kept constant with its value $C_{m,66}$ at fixed magnetization. The resonance frequency curves $f_r(H)$ of both simulations are normalized to their maximum $f_{r,\text{max}}$ and plotted in Fig. 8.6c. The influence of $C_{66}(H)$ in S1 is clearly visible as the difference between the two $f_r(H)$ curves. While $f_r(H)$ of S2 with $C_{66} = C_{m,66}$ follows the shape of the $C_{11}(H)$ component (c.f. Section 4.4, Fig. 3a), substantial deviations occur in S2, but only at magnetic field values around $H = 0$ and close to saturation. The corresponding relative magnetic sensitivities $S_{H,r}$ (Equation 1, Section 4.4) of the two resonance frequency curves are shown in Fig. 8.6d. They deviate only slightly and are approximately the same around the two local maxima at $\approx \pm 0.8 \text{ mT}$ indicated in the plot. These maxima are with $S_{H,r} \approx 1.3 \text{ mT}^{-1}$ approximately the same as the corresponding peaks in the magnetic sensitivity measured with second-order bending modes (c.f. Section 4.1, Fig. 7b). Owing to the macrospin approximation, discontinuities occur in $f_r(H)$, which cause infinite peaks in $S_{H,r}$ at $\approx \pm 1.3 \text{ mT}$. Here, the peaks are finite because of the limited resolution of the numerical differentiation, and their values have no physical relevance for the sensitivity estimation in this case.

In conclusion, the small contribution of C_{66} to the resonance mode does not seem to deteriorate the magnetic sensitivity significantly. With a magnetic layer thickness of $\approx 200 \text{ nm}$, a similar magnetic sensitivity is estimated as measured previously with second-order bending modes.

8.4 Summary and Conclusion

The preliminary results demonstrated that the required reproducibility of the electromechanical MEMS structure can be met with the selected fabrication process. Yet, the magnetic layer deposition eventually has to follow these requirements. The roughness analysis showed that the magnetic layer must be deposited on the rear-side of the cantilever. A first trial proved that a single magnetic layer can be deposited on the free-standing resonator with a very small anisotropic stress and effective magnetic anisotropy, which is promising for sensor application. Further, the simplicity of the deposition approach because of the loose tolerances required for

the shadow mask were demonstrated. Cantilevers were shown to be unsuitable as a sensing element because of the shadowing of the clamping region. Based on numerical estimations, a new resonator design was suggested that seems to be suitable for avoiding the conceptual problems of the previous design. Overall, the suggested procedure and improved resonator design are a promising starting point for the development and investigation of integrated sensor arrays based on the ΔE effect. Further investigations will be required to quantify potential sensor cross-talk, the possibility of depositing magnetic multilayers, and the optimum sensor geometry for a given electrical read-out and operating system.

Conclusion

This work focused on the investigation of magnetoelectric ΔE -effect magnetometers for the detection of small-amplitude and low-frequency magnetic fields. In this study, essential parameters of ΔE -effect magnetometers such as the geometry, material, and operating parameters were connected with the sensing characteristics to identify current limitations and possible methods of sensor improvement. The conclusions drawn provide promising prospects for the further development of ΔE -effect sensors in the future.

Initial studies were focused on the ΔE effect and magnetic sensitivity. Both were analyzed as functions of fundamental sensor design parameters such as the resonator geometry, and the magnetic and mechanical material parameters. Analytical and numerical models were used and developed to describe the ΔE effect and the magnetic sensitivity. Among other aspects, the importance of homogeneous magnetic material properties and the magnetization for a large ΔE effect and magnetic sensitivity was emphasized and quantified for the bending mode and contour mode resonators. While material parameters such as a high saturation magnetostriction and low induced magnetic anisotropy may seem desirable according to previous analyses and simple models, they were not identified as the limiting factors when more realistic scenarios were considered. Maximizing these parameters affects the sensitivity of the magnetization to small magnitudes of stress, and this makes achieving a good uniformity of magnetization challenging. For large magnetic volume fractions, which is desirable from an entirely mechanical point of view, the relaxation of homogeneous residual stress can cause the stress neutral axis to be within the magnetic layer. This can significantly pronounce the inhomogeneity of the effective anisotropy and rotate the magnetization over the layer thickness. In the experimental demonstration with contour mode resonators, this phenomenon reduced the magnetic sensitivity and ΔE effect by orders of magnitude. Hence, a major source for spatial magnetic inhomogeneity is revealed. The results improved the qualitative understanding of the current limitations in the magnetic sensitivity and the device reproducibility and helped provide guidance for resonator designs that could reduce such effects in the future.

The ΔE effect and magnetic sensitivity depend significantly on the mode number, which was demonstrated with experiments on cantilever resonators in the bending and torsion modes, where a relative magnetic sensitivity difference of more than a factor of four between the 1st and 3rd order modes was measured. The dependence of the sensitivity on the mode number showed an opposite behavior in bending modes compared to torsion modes. To this end, two different mechanisms were identified and described with theoretical models. The mechanisms are closely connected to the spatial inhomogeneity of the effective magnetic anisotropy, and the tensor character of the ΔE effect. Although these mechanisms were mostly ignored before, both turned out to be relevant factors that should be considered for sensor development. With the models and methodology the impact of such effects can be estimated and they can support sensor design. Operating the ΔE -effect sensors at high-frequency resonance modes improved the measurement bandwidth but introduced the question of the frequency dependency of the ΔE effect. It was estimated that operating the sensor at resonance frequencies in the high megahertz regime could change the sign of the ΔE effect and reduce the magnetic sensitivity caused by the

magneto-dynamic effects around the ferromagnetic resonance frequency. Hence, the simplified dynamic model demonstrates a physical limitation of the operating frequency and consequently of the bandwidth. These limitations are intrinsic to the ΔE effect and can be important for high-frequency devices and extremely soft-magnetic materials.

Studies on resonance modes confirmed that the magnetic sensitivity of torsion modes can be considerably larger compared to that of the bending modes. Yet, improving the magnetic sensitivity of torsion modes in cantilever resonators is connected with a smaller electrical sensitivity, which is intrinsic to the resonance mode and the electrical excitation method. Hence, torsion modes did not improve overall sensitivity compared to bending modes, although the ΔE effect in the shear modulus seems promising. A different method to utilize the shear modulus was analyzed with a first sensor system based on the ΔE effect in the Love-wave surface acoustic wave devices that operate at ≈ 150 MHz. The study on these sensors showed the LOD of the order of $100 \text{ pT}/\sqrt{\text{Hz}}$ with a considerably improved bandwidth in the kilohertz regime compared to previous cantilever sensors; however, there is a trade-off with integrability and size. These results represent the first proof of the large potential of SAW devices for the detection of low-frequency and small-amplitude magnetic fields.

Voltage sensitivity and signal amplitude can be improved significantly by increasing the quality factor Q and tuning the piezoelectric material parameters. The experimental results confirmed the theoretic dependencies and demonstrated improvements by more than a factor of ten by operating in vacuum and eight with AlScN as the piezoelectric material. At large amplitudes of the excitation voltage, the sensitivity was limited by magnetoelastic nonlinearities. The increase in sensitivity translates into a greater linear improvement of the LOD with Q and a similarly large improvement with the piezoelectric coefficients as long as either thermal-mechanical or thermal-electrical noise is dominant. Improving the LOD is eventually limited by the loss in the magnetic material that dominates the noise floor at large amplitudes of the excitation voltage. Following a first magnetic noise model, the LOD could be improved by reducing the imaginary part of the effective magnetic susceptibility that corresponds to magnetic loss while increasing its real part, which contributes to sensitivity. Other parts of the sensitivity do not contribute to the LOD in this regime. Yet, it should be emphasized that this holds only as long as the signal amplitude is sufficiently large to overcome the thermal-electrical and thermal-mechanical noise floor. Consequently, a sufficiently large sensitivity in conjunction with reduced magnetic loss is key for improving the LOD further in the future. Further investigations on this matter should be focused on gaining a detailed understanding of the specific micromagnetic origin of the magnetic noise and loss to support the design of low-noise magnetoelastic films and multilayers.

In addition to the theoretical aspects, a first step towards application was made with a new operating scheme that permits measuring small amplitude and low-frequency signals, while simultaneously localizing the sensor. The operating scheme uses a first ΔE -effect sensor based on magnetic exchange-bias multilayers. This sensor does not require an external magnetic bias field during operating and thus ensures a compact measurement setup that is interesting for scenarios where many sensor elements are necessary or beneficial. Consequently, such sensors open up new perspectives for applying the ΔE -effect magnetic field sensors and create an opportunity to develop new applications in the future. Instead of operating all sensor elements of the array individually, they can also be operated in parallel using the same local oscillator and read-out electronics. A more detailed analysis points out the tolerances on the reproducibility that must be met to improve the signal, noise, and LOD with this approach. The simulation results indicated that the LOD could be improved until the maximum number of sensor elements was reached. This number depends on the sensor intrinsic noise level and the thermal-electrical

noise of the amplifier. Sensor elements could be grouped into individually operating sub-arrays to benefit from a larger number of sensor elements. Hence, the first guidelines for the design of sensor arrays and grouping strategies are provided to achieve an improved LOD with a minimum number of separated read-out channels. Such an approach could be another alternative to improve the LOD in the future.

In the outlook, a first experimental realization of compact sensor arrays was demonstrated with a new resonator concept intended to circumvent some of the previous limitations. The analysis indicates a promising reproducibility that seems suitable for further studies on the parallel operation of sensor arrays with a large number of elements. It provides a starting point for studies on the origin of magnetic loss and noise, and for application specific aspects of the sensor designs, e.g., for vector magnetometry or high spatial resolution mapping of magnetic fields.

Bibliography

- [1] D. Robbes, “Highly sensitive magnetometers - a review,” *Sensors and Actuators, A: Physical*, vol. 129, no. 1–2, pp. 86–93, 2006, doi: [10.1016/j.sna.2005.11.023](https://doi.org/10.1016/j.sna.2005.11.023).
- [2] H. Koch, “Recent advances in magnetocardiography,” *Journal of Electrocardiology*, vol. 37, pp. 117–122, 2004, doi: [10.1016/j.jelectrocard.2004.08.035](https://doi.org/10.1016/j.jelectrocard.2004.08.035).
- [3] J. R. Claycomb, “Impedance magnetocardiography: experiments and modeling,” *Journal of Applied Physics*, vol. 96, no. 12, pp. 7650–7654, 2004, doi: [10.1063/1.1818716](https://doi.org/10.1063/1.1818716).
- [4] R. Fenici, D. Brisinda, and A. M. Meloni, “Clinical application of magnetocardiography,” *Expert Review of Molecular Diagnostics*, vol. 5, no. 3, pp. 291–313, 2005, doi: [10.1586/14737159.5.3.291](https://doi.org/10.1586/14737159.5.3.291).
- [5] J. S. W. Kwong, B. Leithäuser, J.-W. Park, and C.-M. Yu, “Diagnostic value of magnetocardiography in coronary artery disease and cardiac arrhythmias: A review of clinical data,” *International Journal of Cardiology*, vol. 167, no. 5, pp. 1835–1842, 2013, doi: [10.1016/j.ijcard.2012.12.056](https://doi.org/10.1016/j.ijcard.2012.12.056).
- [6] L. Duez, S. Beniczky, H. Tankisi, P. O. Hansen, P. Sidenius, A. Sabers, and A. Fuglsang-Frederiksen, “Added diagnostic value of magnetoencephalography (MEG) in patients suspected for epilepsy, where previous, extensive EEG workup was unrevealing,” *Clinical Neurophysiology*, vol. 127, no. 10, pp. 3301–3305, 2016, doi: [10.1016/j.clinph.2016.08.006](https://doi.org/10.1016/j.clinph.2016.08.006).
- [7] R. Salmelin and S. Baillet, “Electromagnetic brain imaging,” *Human Brain Mapping*, vol. 30, no. 6, pp. 1753–1757, 2009, doi: [10.1002/hbm.20795](https://doi.org/10.1002/hbm.20795).
- [8] V. Sakkalis, “Review of advanced techniques for the estimation of brain connectivity measured with EEG/MEG,” *Computers in Biology and Medicine*, vol. 41, no. 12, pp. 1110–1117, 2011, doi: [10.1016/j.compbiomed.2011.06.020](https://doi.org/10.1016/j.compbiomed.2011.06.020).
- [9] B. Gleich and J. Weizenecker, “Tomographic imaging using the nonlinear response of magnetic particles,” *Nature*, vol. 435, no. 7046, pp. 1214–1217, 2005, doi: [10.1038/nature03808](https://doi.org/10.1038/nature03808).
- [10] R. M. Friedrich, S. Zabel, A. Galka, N. Lukat, J. M. Wagner, C. Kirchhof, E. Quandt, J. McCord, C. Selhuber-Unkel, M. Siniatchkin, and F. Faupel, “Magnetic particle mapping using magnetoelectric sensors as an imaging modality,” *Scientific Reports*, vol. 9, 2019, doi: [10.1038/s41598-018-38451-0](https://doi.org/10.1038/s41598-018-38451-0).
- [11] D. Cohen and E. Givler, “Magnetomyography: magnetic fields around the human body produced by skeletal muscles,” *Applied Physics Letters*, vol. 21, no. 3, pp. 114–116, 1972, doi: [10.1063/1.1654294](https://doi.org/10.1063/1.1654294).
- [12] S. Zuo, J. Schmalz, M.-O. Ozden, M. Gerken, J. Su, F. Niekiel, F. Lofink, K. Nazarpour, and H. Heidari, “Ultrasensitive magnetoelectric sensing system for pico-tesla magnetomyography,” *IEEE Transactions on Biomedical Circuits and Systems*, vol. 14, no. 5, pp. 971–984, 2020, doi: [10.1109/tbcas.2020.2998290](https://doi.org/10.1109/tbcas.2020.2998290).

- [13] O. Dössel, “Inverse problem of electro- and magnetocardiography: review and recent progress,” *International Journal of Bioelectromagnetism*, vol. 2, no. 2, pp. 1–43, 2000, doi: [available online](#).
- [14] R. R. Fenici, D. Brisinda, J. Nenonen, and P. Fenici, “Phantom validation of multichannel magnetocardiography source localization,” *Pacing and Clinical Electrophysiology*, vol. 26, no. 1p2, pp. 426–430, 2003, doi: [10.1046/j.1460-9592.2003.00063.x](#).
- [15] M. Bertero and M. Piana, “Inverse problems in biomedical imaging: modeling and methods of solution,” in *Complex Systems in Biomedicine*, A. Quarteroni, L. Formaggia, and A. Veneziani, Eds. Milano: Springer, 2006, doi: [10.1007/88-470-0396-2_1](#).
- [16] F. N. Hooge, “1/f noise,” *Physica B+C*, vol. 83, no. 1, pp. 14–23, 1976, doi: [10.1016/0378-4363\(76\)90089-9](#).
- [17] M. S. Keshner, “1/f noise,” *Proceedings of the IEEE*, vol. 70, no. 3, pp. 212–218, 1982, doi: [10.1109/PROC.1982.12282](#).
- [18] R. Kleiner, D. Koelle, F. Ludwig, and J. Clarke, “Superconducting quantum interference devices: state of the art and applications,” *Proceedings of the IEEE*, vol. 92, no. 10, pp. 1534–1548, 2004, doi: [10.1109/JPROC.2004.833655](#).
- [19] D. Murzin, D. J. Mapps, K. Levada, V. Belyaev, A. Omelyanchik, L. Panina, and V. Rodionova, “Ultrasensitive magnetic field sensors for biomedical applications,” *Sensors*, vol. 20, no. 6, 2020, doi: [10.3390/s20061569](#).
- [20] C. N. Johnson, P. D. D. Schwindt, and M. Weisend, “Multi-sensor magnetoencephalography with atomic magnetometers,” *Physics in Medicine and Biology*, vol. 58, no. 17, pp. 6065–6077, 2013, doi: [10.1088/0031-9155/58/17/6065](#).
- [21] J. Osborne, J. Orton, O. Alem, and V. Shah, “Fully integrated, standalone zero field optically pumped magnetometer for biomagnetism,” in *Proc. SPIE 10548, Steep Dispersion Engineering and Opto-Atomic Precision Metrology XI*, vol. 105481G, San Francisco, USA, 2018, pp. 51–58, doi: [10.1117/12.2299197](#).
- [22] J. Reermann, P. Durdaut, S. Salzer, T. Demming, A. Piorra, E. Quandt, N. Frey, M. Höft, and G. Schmidt, “Evaluation of magnetoelectric sensor systems for cardiological applications,” *Measurement*, vol. 116, pp. 230–238, 2018, doi: [10.1016/j.measurement.2017.09.047](#).
- [23] J. Reermann, E. Elzenheimer, and G. Schmidt, “Real-time biomagnetic signal processing for uncooled magnetometers in cardiology,” *IEEE Sensors Journal*, vol. 19, no. 11, pp. 4237–4249, 2019, doi: [10.1109/JSEN.2019.2893236](#).
- [24] S. Zuo, H. Heidari, D. Farina, and K. Nazarpour, “Miniaturized magnetic sensors for implantable magnetomyography,” *Advanced Materials Technologies*, vol. 5, no. 6, 2020, doi: [10.1002/admt.202000185](#).
- [25] H. Xi, M. C. Lu, Q. X. Yang, and Q. M. Zhang, “Room temperature magnetoelectric sensor arrays for application of detecting iron profiles in organs,” *Sensors and Actuators A: Physical*, vol. 311, 2020, doi: [10.1016/j.sna.2020.112064](#).
- [26] W. Eerenstein, N. D. Mathur, and J. F. Scott, “Multiferroic and magnetoelectric materials,” *Nature*, vol. 442, pp. 759–765, 2006, doi: [10.1038/nature05023](#).
- [27] D. K. Pradhan, S. Kumari, and P. D. Rack, “Magnetoelectric composites: applications, coupling mechanisms, and future directions,” *Nanomaterials*, vol. 10, no. 10, 2020, doi: [10.3390/nano10102072](#).

- [28] H. Greve, E. Woltermann, H.-J. Quenzer, B. Wagner, and E. Quandt, “Giant magnetoelectric coefficients in $(\text{Fe}_{90}\text{Co}_{10})_{78}\text{Si}_{12}\text{B}_{10}$ -AlN thin film composites,” *Applied Physics Letters*, vol. 96, no. 18, 2010, doi: [10.1063/1.3377908](https://doi.org/10.1063/1.3377908).
- [29] V. Röbisch, E. Yarar, N. O. Urs, I. Teliban, R. Knöchel, J. McCord, E. Quandt, and D. Meyners, “Exchange biased magnetoelectric composites for magnetic field sensor application by frequency conversion,” *Journal of Applied Physics*, vol. 117, no. 17, 2015, doi: [10.1063/1.4913814](https://doi.org/10.1063/1.4913814).
- [30] S. Marauska, R. Jahns, H. Greve, E. Quandt, R. Knöchel, and B. Wagner, “MEMS magnetic field sensor based on magnetoelectric composites,” *Journal of Micromechanics and Microengineering*, vol. 22, no. 6, 2012, doi: [10.1088/0960-1317/22/6/065024](https://doi.org/10.1088/0960-1317/22/6/065024).
- [31] R. Jahns, S. Zabel, S. Marauska, B. Gojdka, B. Wagner, R. Knöchel, R. Adelung, and F. Faupel, “Microelectromechanical magnetic field sensor based on the delta-E effect,” *Applied Physics Letters*, vol. 105, no. 5, pp. 2012–2015, 2014, doi: [10.1063/1.4891540](https://doi.org/10.1063/1.4891540).
- [32] J. Su, F. Niekil, S. Fichtner, C. Kirchhof, D. Meyners, E. Quandt, B. Wagner, and F. Lofink, “Frequency tunable resonant magnetoelectric sensors for the detection of weak magnetic field,” *Journal of Micromechanics and Microengineering*, vol. 30, no. 7, 2020, doi: [10.1088/1361-6439/ab8dd0](https://doi.org/10.1088/1361-6439/ab8dd0).
- [33] T. Nan, Y. Hui, M. Rinaldi, and N. X. Sun, “Self-biased 215 MHz magnetoelectric NEMS resonator for ultra-sensitive DC magnetic field detection,” *Scientific Reports*, vol. 3, 2013, doi: [10.1038/srep01985](https://doi.org/10.1038/srep01985).
- [34] C. Tu, Z.-Q. Chu, B. Spetzler, P. Hayes, C.-Z. Dong, X.-F. Liang, H.-H. Chen, Y.-F. He, Y.-Y. Wei, I. Lisenkov, H. Lin, Y.-H. Lin, J. McCord, F. Faupel, E. Quandt, and N.-X. Sun, “Mechanical-resonance-enhanced thin-film magnetoelectric heterostructures for magnetometers, mechanical antennas, tunable RF inductors, and filters,” *Materials*, vol. 12, no. 14, 2019, doi: [10.3390/ma12142259](https://doi.org/10.3390/ma12142259).
- [35] V. Röbisch, S. Salzer, N. O. Urs, J. Reermann, E. Yarar, A. Piorra, C. Kirchhof, E. Lage, M. Höft, G. U. Schmidt, R. Knöchel, J. McCord, E. Quandt, and D. Meyners, “Pushing the detection limit of thin film magnetoelectric heterostructures,” *Journal of Materials Research*, vol. 32, pp. 1009–1019, 2017, doi: [10.1557/jmr.2017.58](https://doi.org/10.1557/jmr.2017.58).
- [36] Y. Wang, J. Li, and D. Viehland, “Magnetoelectrics for magnetic sensor applications: status, challenges and perspectives,” *Materials Today*, vol. 17, no. 6, pp. 269–275, 2014, doi: [10.1016/j.mattod.2014.05.004](https://doi.org/10.1016/j.mattod.2014.05.004).
- [37] J. Zhai, Z. Xing, S. Dong, J. Li, and D. Viehland, “Detection of pico-tesla magnetic fields using magneto-electric sensors at room temperature,” *Applied Physics Letters*, vol. 88, no. 6, pp. 5–8, 2006, doi: [10.1063/1.2172706](https://doi.org/10.1063/1.2172706).
- [38] K. Honda and T. Terada, “II. On the change of elastic constants of ferromagnetic substances by magnetization,” *Philosophical Magazine Series 6*, vol. 13, no. 73, pp. 36–83, 1907, doi: [10.1080/14786440709463584](https://doi.org/10.1080/14786440709463584).
- [39] E. W. Lee, “Magnetostriction and magnetomechanical effects,” *Reports on progress in physics*, vol. 18, no. 1, pp. 184–229, 1955, doi: [10.1088/0034-4885/18/1/305](https://doi.org/10.1088/0034-4885/18/1/305).
- [40] J. D. Livingston, “Magnetomechanical properties of amorphous metals,” *Physica Status Solidi (a)*, vol. 70, no. 2, pp. 591–596, 1982, doi: [10.1002/pssa.2210700228](https://doi.org/10.1002/pssa.2210700228).

- [41] S. M. Hanna, "Magnetic field sensors based on SAW propagation in magnetic films," *IEEE Transactions on Ultrasonics, Ferroelectrics, and Frequency Control*, vol. 34, no. 2, pp. 191–194, 1987, doi: [10.1109/T-UFFC.1987.26931](https://doi.org/10.1109/T-UFFC.1987.26931).
- [42] C. Barus, "The effect of magnetization on the viscosity and rigidity of iron and of steel," *American Journal of Science*, vol. s3-34, no. 201, pp. 175–186, 1887, doi: [10.2475/ajs.s3-34.201.175](https://doi.org/10.2475/ajs.s3-34.201.175).
- [43] K. Honda, S. Shimizu, and S. Kusakabe, "LX. Change of modulus of rigidity of ferromagnetic substances by magnetization," *The London, Edinburgh, and Dublin Philosophical Magazine and Journal of Science*, vol. 4, no. 23, pp. 537–546, 1902, doi: [10.1080/14786440209462877](https://doi.org/10.1080/14786440209462877).
- [44] D. V. Malyugin, "On the theory of Wiedemann effects," *Journal of Magnetism and Magnetic Materials*, vol. 97, no. 1-3, pp. 193–197, 1991, doi: [10.1016/0304-8853\(91\)90180-I](https://doi.org/10.1016/0304-8853(91)90180-I).
- [45] H. Rensing, "Über magneto-elastische Wechselbeziehungen in paramagnetischen Substanzen," *Annalen der Physik*, vol. 319, no. 7, pp. 363–377, 1904, doi: [10.1002/andp.19043190708](https://doi.org/10.1002/andp.19043190708).
- [46] N. Akulov and E. Kondorsky, "Über einen magnetomechanischen Effekt," *Zeitschrift für Physik*, vol. 78, no. 11-12, pp. 801–807, 1932, doi: [10.1007/BF01342040](https://doi.org/10.1007/BF01342040).
- [47] A. Heydweiller, "Zur Theorie der magneto-elastischen Wechselbeziehungen," *Annalen der Physik*, vol. 317, no. 11, pp. 602–607, 1903, doi: [10.1002/andp.19033171108](https://doi.org/10.1002/andp.19033171108).
- [48] W. Heisenberg, "Zur Theorie des Ferromagnetismus," *Zeitschrift für Physik*, vol. 49, no. 9-10, pp. 619–636, 1928, doi: [10.1007/BF01328601](https://doi.org/10.1007/BF01328601).
- [49] K. Honda, S. Kaya, and Y. Masuyama, "On the magnetic properties of single crystals of iron," *Nature*, vol. 117, no. 2952, pp. 753–754, 1926, doi: [10.1038/117753a0](https://doi.org/10.1038/117753a0).
- [50] N. Akulov, "Über die Magnetostriktion der Eiseneinkristalle," *Zeitschrift für Physik*, vol. 52, no. 5-6, pp. 389–405, 1929, doi: [10.1007/BF01339430](https://doi.org/10.1007/BF01339430).
- [51] M. Kersten, "Über die Abhängigkeit der mechanischen Eigenschaften des Nickels von den elastischen Spannungen," *Zeitschrift für Physik*, vol. 71, pp. 553–592, 1931, doi: [10.1007/BF01339568](https://doi.org/10.1007/BF01339568).
- [52] W. Heisenberg, "Zur Theorie der Magnetostriktion und der Magnetisierungskurve," *Zeitschrift für Physik*, vol. 69, no. 5-6, pp. 287–297, 1931, doi: [10.1007/BF01391350](https://doi.org/10.1007/BF01391350).
- [53] N. Akulov and E. Kondorsky, "Über Mechanostriktion und δE -Effekt," *Zeitschrift für Physik*, vol. 85, no. 9-10, pp. 661–671, 1933, doi: [10.1007/BF01331006](https://doi.org/10.1007/BF01331006).
- [54] K. Nakamura, "Untersuchung der Variationen des Elastizitätskoeffizienten der Metallegierung Ni-Fe durch Magnetisierung," *Zeitschrift für Physik*, vol. 94, no. 11-12, pp. 707–716, 1935, doi: [10.1007/BF01330079](https://doi.org/10.1007/BF01330079).
- [55] M. Kersten, "Über den Temperaturkoeffizienten des Elastizitätsmoduls ferromagnetischer Stoffe," *Zeitschrift für Physik*, vol. 85, no. 11-12, pp. 708–716, 1933, doi: [10.1007/BF01330318](https://doi.org/10.1007/BF01330318).
- [56] R. Becker and M. Kornetzki, "Einige magneto-elastische Torsionsversuche," *Zeitschrift für Physik*, vol. 88, no. 9-10, pp. 634–646, 1934, doi: [10.1007/BF01333112](https://doi.org/10.1007/BF01333112).

- [57] W. F. Brown, "The variation of the internal friction and elastic constants with magnetization in iron. Part II," *Physical Review*, vol. 50, no. 12, pp. 1165–1172, 1936, doi: [10.1103/PhysRev.50.1165](https://doi.org/10.1103/PhysRev.50.1165).
- [58] W. T. Cooke, "The variation of the internal friction and elastic constants with magnetization in iron. Part I," *Physical Review*, vol. 50, no. 12, pp. 1158–1164, 1936, doi: [10.1103/PhysRev.50.1158](https://doi.org/10.1103/PhysRev.50.1158).
- [59] O. Engler, "Der Elastizitätsmodul ferromagnetischer Stoffe in Abhängigkeit von der Temperatur und vom Magnetfeld," *Annalen der Physik*, vol. 423, no. 2, pp. 145–163, 1938, doi: [10.1002/andp.19384230205](https://doi.org/10.1002/andp.19384230205).
- [60] R. Becker and W. Döring, *Ferromagnetismus*, 1st ed. Berlin, Heidelberg: Julius Springer, 1939, p. 353, doi: [10.1007/978-3-642-47366-1](https://doi.org/10.1007/978-3-642-47366-1).
- [61] R. Kimura, "On the elastic moduli of ferromagnetic materials. part II. The change in Young's modulus, due to magnetisation and temperature," *Proceedings of the Physico-Mathematical Society of Japan. 3rd Series*, vol. 21, no. 12, pp. 786–799, 1939, doi: [10.11429/ppmsj1919.21.12_786](https://doi.org/10.11429/ppmsj1919.21.12_786).
- [62] W. P. Mason, "Domain wall relaxation in nickel," *Physical Review*, vol. 83, no. 3, pp. 683–684, 1951, doi: [10.1103/PhysRev.83.683.2](https://doi.org/10.1103/PhysRev.83.683.2).
- [63] S. J. Johnson and T. F. Rogers, "Magnetically induced ultrasonic velocity changes in polycrystalline nickel," *Journal of Applied Physics*, vol. 23, no. 5, pp. 574–577, 1952, doi: [10.1063/1.1702253](https://doi.org/10.1063/1.1702253).
- [64] W. P. Mason, "Rotational relaxation in nickel at high frequencies," *Reviews of Modern Physics*, vol. 25, no. 1, pp. 136–139, 1953, doi: [10.1103/RevModPhys.25.136](https://doi.org/10.1103/RevModPhys.25.136).
- [65] C. Kittel, "Physical theory of ferromagnetic domains," *Reviews of Modern Physics*, vol. 21, no. 4, pp. 541–583, 1949, doi: [10.1103/RevModPhys.21.541](https://doi.org/10.1103/RevModPhys.21.541).
- [66] E. C. Stoner and E. P. Wohlfarth, "A mechanism of magnetic hysteresis in heterogeneous alloys," *Philosophical Transactions of the Royal Society of London. Series A, Mathematical and Physical Sciences*, vol. 240, no. 826, pp. 599–642, 1948, doi: [10.1098/rsta.1948.0007](https://doi.org/10.1098/rsta.1948.0007).
- [67] E. R. Callen and H. B. Callen, "Static magnetoelastic coupling in cubic crystals," *Physical Review*, vol. 129, no. 2, pp. 578–593, 1963, doi: [10.1103/PhysRev.129.578](https://doi.org/10.1103/PhysRev.129.578).
- [68] E. Callen and H. B. Callen, "Magnetostriction, forced magnetostriction, and anomalous thermal expansion in ferromagnets," *Physical Review*, vol. 139, no. 2A, pp. 455–471, 1965, doi: [10.1103/PhysRev.139.A455](https://doi.org/10.1103/PhysRev.139.A455).
- [69] C. Kittel, "Interaction of spin waves and ultrasonic waves in ferromagnetic crystals," *Physical Review*, vol. 110, no. 4, pp. 836–841, 1958, doi: [10.1103/PhysRev.110.836](https://doi.org/10.1103/PhysRev.110.836).
- [70] E. Schlömann, "Generation of phonons in high-power ferromagnetic resonance experiments," *Journal of Applied Physics*, vol. 31, no. 9, pp. 1647–1656, 1960, doi: [10.1063/1.1735909](https://doi.org/10.1063/1.1735909).
- [71] W. P. Robbins and A. Young, "SAW phase modulator using magnetostrictive thin films," *IEEE Transactions on Sonics and Ultrasonics*, vol. 32, no. 3, pp. 423–427, 1985, doi: [10.1109/T-SU.1985.31611](https://doi.org/10.1109/T-SU.1985.31611).
- [72] A. K. Ganguly, K. L. Davis, D. C. Webb, and C. Vittoria, "Magnetoelastic surface waves in a magnetic film-piezoelectric substrate configuration," *Journal of Applied Physics*, vol. 47, no. 6, pp. 2696–2704, 1976, doi: [10.1063/1.322991](https://doi.org/10.1063/1.322991).

- [73] W. Strauss, "Elastic and magnetoelastic waves in yttrium iron garnet," *Proceedings of the IEEE*, vol. 53, no. 10, pp. 1485–1495, 1965, doi: [10.1109/PROC.1965.4261](https://doi.org/10.1109/PROC.1965.4261).
- [74] H. Van De Vaart, "Magnetoelastic love-wave propagation in metal-coated layered substrates," *Journal of Applied Physics*, vol. 42, no. 13, pp. 5305–5312, 1971, doi: [10.1063/1.1659940](https://doi.org/10.1063/1.1659940).
- [75] H. Matthews and H. van de Vaart, "Magnetoelastic love waves," *Applied Physics Letters*, vol. 15, no. 11, pp. 373–375, 1969, doi: [10.1063/1.1652865](https://doi.org/10.1063/1.1652865).
- [76] J. P. Parekh and H. L. Bertoni, "Magnetoelastic Rayleigh waves on a YIG substrate magnetized normal to its surface," *Journal of Applied Physics*, vol. 45, no. 4, pp. 1860–1868, 1974, doi: [10.1063/1.1663504](https://doi.org/10.1063/1.1663504).
- [77] A. K. Ganguly, K. L. Davis, D. C. Webb, C. Vittoria, and D. W. Forester, "Magnetically tuned surface-acoustic-wave phase shifter," *Electronic Letters*, vol. 11, no. 25/26, pp. 610–611, 1975, doi: [10.1049/el:19750465](https://doi.org/10.1049/el:19750465).
- [78] W. P. Robbins and E. M. Simpson, "Tunable surface acoustic wave oscillators using magnetostrictive thin films," *Proceedings of the IEEE*, vol. 67, no. 11, pp. 1572–1573, 1979, doi: [10.1109/PROC.1979.11525](https://doi.org/10.1109/PROC.1979.11525).
- [79] M. Yamaguchi, K. Y. Hashimoto, H. Kogo, and M. Naoe, "Variable SAW delay line using amorphous TbFe₂ film," *IEEE Transactions on Magnetics on magnetism*, vol. Mag-16, no. 5, pp. 916–918, 1980, doi: [10.1109/TMAG.1980.1060738](https://doi.org/10.1109/TMAG.1980.1060738).
- [80] M. Inoue, Y. Tsuboi, N. Yokokawa, and T. Fujii, "Love-type magento-surface-acoustic-wave in multilayer highly magnetostrictive films separated by insulating layers," *IEEE Transactions on Magnetics*, vol. 26, no. 5, pp. 1465–1467, 1990, doi: [10.1109/20.104413](https://doi.org/10.1109/20.104413).
- [81] D. W. Forester, C. Vittoria, D. C. Webb, and K. L. Davis, "Variable delay lines using magnetostrictive metallic-glass film overlays," *Journal of Applied Physics*, vol. 49, no. 3, pp. 1794–1796, 1978, doi: [10.1063/1.324869](https://doi.org/10.1063/1.324869).
- [82] A. E. Clark, H. S. Belson, and R. E. Strakna, "Elastic properties of rare-earth-iron compounds," *Journal of Applied Physics*, vol. 44, no. 6, pp. 2913–2914, 1973, doi: [10.1063/1.1662676](https://doi.org/10.1063/1.1662676).
- [83] A. E. Clark and H. T. Savage, "Giant magnetically induced changes in the elastic moduli in Tb₃DY₇Fe₂," *IEEE Transactions on Sonics and Ultrasonics*, vol. 22, no. 1, pp. 50–51, 1975, doi: [10.1109/T-SU.1975.30775](https://doi.org/10.1109/T-SU.1975.30775).
- [84] K. I. Arai and N. Tsuya, "Magnetomechanical coupling and variable delay characteristics by means of a giant delta-E effect in iron-rich amorphous ribbon," *Journal of Applied Physics*, vol. 49, no. 3, pp. 1718–1720, 1978, doi: [10.1063/1.324845](https://doi.org/10.1063/1.324845).
- [85] M. Brouha and J. van der Borst, "The effect of annealing conditions on the magneto-mechanical properties of Fe-B-Si amorphous ribbons," *Journal of Applied Physics*, vol. 50, no. 11, pp. 7594–7596, 1979, doi: [10.1063/1.326769](https://doi.org/10.1063/1.326769).
- [86] T. H. O'Dell, "Measurement of magnetomechanical coupling factor in amorphous ribbons," *Physica Status Solidi (a)*, vol. 74, no. 2, pp. 565–572, 1982, doi: [10.1002/pssa.2210740223](https://doi.org/10.1002/pssa.2210740223).
- [87] L. Lanotte, C. Luponio, and F. Porreca, "Magnetoelastic coupling coefficient and anisotropy induced by magnetic annealing in strips of noncrystalline material," *Il Nuovo Cimento D*, vol. 9, no. 6, pp. 633–645, 1987, doi: [10.1007/BF02457025](https://doi.org/10.1007/BF02457025).

- [88] N. P. Kobelev, Y. M. Soifer, V. G. Shteinberg, and Y. B. Levin, "Giant" ΔE -effect and magnetomechanical damping in amorphous ferromagnetic ribbons," *Physica Status Solidi (a)*, vol. 102, no. 2, pp. 773–780, 1987, doi: [10.1002/pssa.2211020240](https://doi.org/10.1002/pssa.2211020240).
- [89] P. T. Squire, "Magnetomechanical measurements of magnetically soft amorphous materials," *Measurement Science and Technology*, vol. 5, no. 2, pp. 67–81, 1994, doi: [10.1088/0957-0233/5/2/001](https://doi.org/10.1088/0957-0233/5/2/001).
- [90] L. M. Małkiński, "The role of residual stresses in magnetostrictive metallic glasses," *Journal of Magnetism and Magnetic Materials*, vol. 140-144, no. Part 1, pp. 267–268, 1995, doi: [10.1016/0304-8853\(94\)01341-1](https://doi.org/10.1016/0304-8853(94)01341-1).
- [91] J. Gutiérrez, A. García-Arribas, J. S. Garitaonandia, J. M. Barandiarán, and P. T. Squire, " ΔE effect and anisotropy distribution in metallic glasses with oblique easy axis induced by field annealing," *Journal of Magnetism and Magnetic Materials*, vol. 157-158, pp. 543–544, 1996, doi: [10.1016/0304-8853\(95\)01119-6](https://doi.org/10.1016/0304-8853(95)01119-6).
- [92] G. Herzer, "Magnetomechanical damping in amorphous ribbons with uniaxial anisotropy," *Materials Science and Engineering: A*, vol. 226-228, pp. 631–635, 1997, doi: [10.1016/S0921-5093\(96\)10697-3](https://doi.org/10.1016/S0921-5093(96)10697-3).
- [93] D. Y. Kim, C. G. Kim, H. C. Kim, and U. H. Sung, "Stress dependence of ΔE in amorphous ribbon," *Journal of Applied Physics*, vol. 81, no. 8, pp. 5811–5813, 1997, doi: [10.1063/1.364676](https://doi.org/10.1063/1.364676).
- [94] P. Squire, "Magnetostrictive materials for sensors and actuators," *Ferroelectrics*, vol. 228, no. 1, pp. 305–319, 1999, doi: [10.1080/00150199908226144](https://doi.org/10.1080/00150199908226144).
- [95] J. Gutiérrez, V. Muto, and P. T. Squire, "Induced anisotropy and magnetoelastic properties in Fe-rich metallic glasses," *Journal of Non-Crystalline Solids*, vol. 287, no. 1–3, pp. 417–420, 2001, doi: [10.1016/S0022-3093\(01\)00599-3](https://doi.org/10.1016/S0022-3093(01)00599-3).
- [96] G. Herzer, "Effect of domain size on the magneto-elastic damping in amorphous ferromagnetic metals," *Zeitschrift für Metallkunde*, vol. 93, no. 10, pp. 978–982, 2002, doi: [10.3139/146.020978](https://doi.org/10.3139/146.020978).
- [97] J. M. Barandiarán, J. Gutiérrez, Z. Kaczkowski, and D. de Cos, "Influence of annealing temperature on the magnetic and magnetoelastic properties in Fe-Co-B metallic glasses," *Journal of Non-Crystalline Solids*, vol. 329, no. 1-3, pp. 43–47, 2003, doi: [10.1016/j.jnoncrysol.2003.08.010](https://doi.org/10.1016/j.jnoncrysol.2003.08.010).
- [98] S. Atalay and P. T. Squire, "Magnetomechanical damping in FeSiB amorphous wires," *Journal of Applied Physics*, vol. 73, no. 2, pp. 871–875, 1993, doi: [10.1063/1.353299](https://doi.org/10.1063/1.353299).
- [99] D. Atkinson, P. T. Squire, M. R. J. Gibbs, S. Atalay, and D. G. Lord, "The effect of annealing and crystallization on the magnetoelastic properties of Fe-Si-B amorphous wire," *Journal of Applied Physics*, vol. 73, no. 7, pp. 3411–3417, 1993, doi: [10.1063/1.352942](https://doi.org/10.1063/1.352942).
- [100] P. T. Squire, S. Atalay, and H. Chiriac, " ΔE effect in amorphous glass covered wires," *IEEE Transactions on Magnetics*, vol. 36, no. 5, pp. 3433–3435, 2000, doi: [10.1109/20.908850](https://doi.org/10.1109/20.908850).
- [101] P. T. Squire and M. R. J. Gibbs, "Shear-wave magnetometry using metallic glass ribbon," *Electronic Letters*, vol. 23, no. 4, pp. 147–148, 1987, doi: [10.1049/el:19870103](https://doi.org/10.1049/el:19870103).
- [102] F. K. Charles, "Development of the shear wave magnetometer," Ph.D. dissertation, University of Bath, 1992, [available online](#).

- [103] S. Atalay and P. T. Squire, “Comparative measurements of the field dependence of Young’s modulus and shear modulus in Fe-based amorphous wire,” *Journal of Applied Physics*, vol. 70, no. 10, pp. 6516–6518, 1991, doi: [10.1063/1.349892](https://doi.org/10.1063/1.349892).
- [104] G. Herzer, “Magnetic materials for electronic article surveillance,” *Journal of Magnetism and Magnetic Materials*, vol. 254–255, pp. 598–602, 2003, doi: [10.1016/S0304-8853\(02\)00930-7](https://doi.org/10.1016/S0304-8853(02)00930-7).
- [105] Q. Su, J. Morillo, Y. Wen, and M. Wuttig, “Young’s modulus of amorphous Terfenol-D thin films,” *Journal of Applied Physics*, vol. 80, no. 6, pp. 3604–3606, 1996, doi: [10.1063/1.363269](https://doi.org/10.1063/1.363269).
- [106] M. R. J. Gibbs, “Applications of magmems,” *Journal of Magnetism and Magnetic Materials*, vol. 290–291, pp. 1298–1303, 2005, doi: [10.1016/j.jmmm.2004.11.572](https://doi.org/10.1016/j.jmmm.2004.11.572).
- [107] M. R. J. Gibbs, C. Shearwood, J. L. Dancaster, P. E. M. Frere, and A. J. Jacobs-Cook, “Piezomagnetic tuning of a micromachined resonator,” *IEEE Transactions on Magnetics*, vol. 32, no. 5, pp. 4950–4952, 1996, doi: [10.1109/20.539298](https://doi.org/10.1109/20.539298).
- [108] M. R. J. Gibbs, R. Watts, W. Karl, A. I. Powell, and R. B. Yates, “Microstructures containing piezomagnetic elements,” *Sensors and Actuators A: Physical*, vol. 59, no. 1–3, pp. 229–235, 1997, doi: [10.1016/S0924-4247\(97\)80180-X](https://doi.org/10.1016/S0924-4247(97)80180-X).
- [109] P. T. Squire, “Phenomenological model for magnetization, magnetostriction and ΔE effect in field-annealed amorphous ribbons,” *Journal of Magnetism and Magnetic Materials*, vol. 87, no. 3, pp. 299–310, 1990, doi: [10.1016/0304-8853\(90\)90764-H](https://doi.org/10.1016/0304-8853(90)90764-H).
- [110] Z. Sárközi, K. Mackay, and J. C. Peuzin, “Elastic properties of magnetostrictive thin films using bending and torsion resonances of a bimorph,” *Journal of Applied Physics*, vol. 88, no. 10, pp. 5827–5832, 2000, doi: [10.1063/1.1318388](https://doi.org/10.1063/1.1318388).
- [111] T. Bourouina, A. Garnier, and H. Fujita, “Effect of direct current bias field and alternating current excitation field on vibration amplitudes and resonance frequencies of a magnetostrictively actuated bimorph microresonator,” *Journal of Applied Physics*, vol. 91, no. 1, pp. 112–120, 2002, doi: [10.1063/1.1417998](https://doi.org/10.1063/1.1417998).
- [112] G. Petculescu, K. B. Hathaway, T. A. Lograsso, M. Wun-Fogle, and A. E. Clark, “Magnetic field dependence of galfenol elastic properties,” *Journal of Applied Physics*, vol. 97, no. 10, pp. 2003–2006, 2005, doi: [10.1063/1.1855711](https://doi.org/10.1063/1.1855711).
- [113] R. Kellogg and A. Flatau, “Experimental investigation of terfenol-D’s elastic modulus,” *Journal of Intelligent Material Systems and Structures*, vol. 19, no. 5, pp. 583–595, 2008, doi: [10.1177/1045389X07077854](https://doi.org/10.1177/1045389X07077854).
- [114] S. Datta, J. Atulasimha, C. Mudivarthi, and A. B. Flatau, “Stress and magnetic field-dependent young’s modulus in single crystal iron-gallium alloys,” *Journal of Magnetism and Magnetic Materials*, vol. 322, no. 15, pp. 2135–2144, 2010, doi: [10.1016/j.jmmm.2010.01.046](https://doi.org/10.1016/j.jmmm.2010.01.046).
- [115] A. Ludwig and E. Quandt, “Optimization of the delta-E effect in thin films and multilayers by magnetic field annealing,” *IEEE Transactions on Magnetics*, vol. 38, no. 5, pp. 2829–2831, 2002, doi: [10.1109/TMAG.2002.802467](https://doi.org/10.1109/TMAG.2002.802467).
- [116] A. Ludwig, M. Tewes, S. Glasmachers, M. Löhndorf, and E. Quandt, “High-frequency magnetoelastic materials for remote-interrogated stress sensors,” *Journal of Magnetism and Magnetic Materials*, vol. 242–245, no. Part 2, pp. 1126–1131, 2002, doi: [10.1016/S0304-8853\(01\)00979-9](https://doi.org/10.1016/S0304-8853(01)00979-9).

- [117] C. Dong, M. Li, X. Liang, H. Chen, H. Zhou, X. Wang, Y. Gao, M. E. McConney, J. G. Jones, G. J. Brown, B. M. Howe, and N. X. Sun, "Characterization of magnetomechanical properties in FeGaB thin films," *Applied Physics Letters*, vol. 113, no. 26, 2018, doi: [10.1063/1.5065486](https://doi.org/10.1063/1.5065486).
- [118] R. Osiander, S. A. Ecelberger, R. B. Givens, D. K. Wickenden, J. C. Murphy, and T. J. Kistenmacher, "A microelectromechanical-based magnetostrictive magnetometer," *Applied Physics Letters*, vol. 69, no. 19, pp. 2930–2931, 1996, doi: [10.1063/1.117327](https://doi.org/10.1063/1.117327).
- [119] N. Yoshizawa, I. Yamamoto, and Y. Shimada, "Magnetic field sensing by an electrostrictive/magnetostrictive composite resonator," *IEEE Transactions on Magnetics*, vol. 41, no. 11, pp. 4359–4361, 2005, doi: [10.1109/TMAG.2005.855168](https://doi.org/10.1109/TMAG.2005.855168).
- [120] H. Zhou, A. Talbi, N. Tiercelin, and O. B. Matar, "Theoretical and experimental study of multilayer piezo-magnetic structure based surface acoustic wave devices for high sensitivity magnetic sensor," in *2013 IEEE International Ultrasonics Symposium (IUS)*. IEEE, 2013, pp. 212–215, doi: [10.1109/ULTSYM.2013.0055](https://doi.org/10.1109/ULTSYM.2013.0055).
- [121] V. Polewczyk, K. Dumesnil, D. Lacour, M. Moutaouekkil, H. Mjahed, N. Tiercelin, S. Petit Watelot, H. Mishra, Y. Dusch, S. Hage-Ali, O. Elmazria, F. Montaigne, A. Talbi, O. Bou Matar, and M. Hehn, "Unipolar and bipolar high-magnetic-field sensors based on surface acoustic wave resonators," *Physical Review Applied*, vol. 8, no. 2, 2017, doi: [10.1103/PhysRevApplied.8.024001](https://doi.org/10.1103/PhysRevApplied.8.024001).
- [122] J. Tong, Y. Jia, W. Wang, Y. Wang, S. Wang, X. Liu, and Y. Lei, "Development of a magnetostrictive FeNi coated surface acoustic wave current sensor," *Applied Sciences*, vol. 7, no. 8, 2017, doi: [10.3390/app7080755](https://doi.org/10.3390/app7080755).
- [123] W. Wang, J. Yana, X. Liu, Y. Liang, X. Xue, and Z. Du, "Enhanced sensitivity of temperature-compensated SAW-based current sensor using the magnetostrictive effect," *Smart Materials and Structures*, vol. 26, no. 2, 2017, doi: [10.1088/1361-665X/aa5137](https://doi.org/10.1088/1361-665X/aa5137).
- [124] W. Wang, Y. Jia, X. Xue, Y. Liang, and Z. Du, "Grating-patterned FeCo coated surface acoustic wave device for sensing magnetic field," *AIP Advances*, vol. 8, no. 1, 2018, doi: [10.1063/1.5012579](https://doi.org/10.1063/1.5012579).
- [125] X. Liu, B. Tong, J. Ou-Yang, X. Yang, S. Chen, Y. Zhang, and B. Zhu, "Self-biased vector magnetic sensor based on a Love-type surface acoustic wave resonator," *Applied Physics Letters*, vol. 113, no. 8, 2018, doi: [10.1063/1.5044478](https://doi.org/10.1063/1.5044478).
- [126] T. Jagielinski, K. I. Arai, N. Tsuya, S. Ohnuma, and T. Masumoto, "Saturation magnetostriction and volume magnetostriction of Fe-Ni-Co amorphous ribbons," *IEEE Transaction on Magnetics*, vol. 13, no. 5, pp. 1553–1555, 1977, doi: [10.1109/TMAG.1977.1059635](https://doi.org/10.1109/TMAG.1977.1059635).
- [127] P. T. Squire, M. R. J. Gibbs, and A. P. Thomas, "Magnetostriction of obliquely annealed metallic glass," *Journal of Magnetism and Magnetic Materials*, vol. 83, no. 1-3, pp. 179–180, 1990, doi: [10.1016/0304-8853\(90\)90477-8](https://doi.org/10.1016/0304-8853(90)90477-8).
- [128] X. Liang, C. Dong, H. Chen, J. Wang, Y. Wei, M. Zaeimbashi, Y. He, A. Matyushov, C. Sun, and N. X. Sun, "A review of thin-film magnetoelastic materials for magnetoelectric applications," *Sensors*, vol. 20, no. 5, 2020, doi: [10.3390/s20051532](https://doi.org/10.3390/s20051532).
- [129] J. R. Cullen, S. Rinaldi, and G. V. Blessing, "Elastic versus magnetoelastic anisotropy in rare earth-iron alloys," *Journal of Applied Physics*, vol. 49, no. 3, pp. 1960–1965, 1978, doi: [10.1063/1.324764](https://doi.org/10.1063/1.324764).

- [130] R. C. O’Handley, *Modern magnetic materials - principles and applications*, 1st ed. New York: Wiley-Interscience, 2000, pp. 224–229.
- [131] B. Spetzler, E. V. Golubeva, C. Müller, and F. Faupel, “Frequency dependency of the delta-E effect and the sensitivity of delta-E effect magnetic field sensors,” *Sensors*, vol. 19, no. 21, 2019, doi: [10.3390/s19214769](https://doi.org/10.3390/s19214769).
- [132] B. Spetzler, E. V. Golubeva, R. M. Friedrich, S. Zabel, C. Kirchhof, D. Meyners, J. McCord, and F. Faupel, “Magnetoelastic coupling and delta-E effect in magnetoelectric torsion mode resonators,” *Sensors*, vol. 21, no. 6, 2021, doi: [10.3390/s21062022](https://doi.org/10.3390/s21062022).
- [133] R. C. O’Handley, *Modern magnetic materials - principles and applications*, 1st ed. New York: Wiley-Interscience, 2000, pp. 229–235.
- [134] Z. Chu, C. Dong, C. Tu, Y. He, X. Liang, J. Wang, Y. Wei, H. Chen, X. Gao, C. Lu, Z. Zhu, Y. Lin, S. Dong, J. McCord, and N. X. Sun, “Voltage-driven nonlinearity in magnetoelectric heterostructures,” *Physical Review Applied*, vol. 12, no. 4, 2019, doi: [10.1103/PhysRevApplied.12.044001](https://doi.org/10.1103/PhysRevApplied.12.044001).
- [135] IEEE, “319-1990 - IEEE standard on magnetostrictive materials: piezomagnetic nomenclature.” IEEE, 1991, doi: [10.1109/IEEESTD.1991.101048](https://doi.org/10.1109/IEEESTD.1991.101048).
- [136] B. Spetzler, C. Kirchhof, E. Quandt, J. McCord, and F. Faupel, “Magnetic sensitivity of bending-mode delta-E-effect sensors,” *Physical Review Applied*, vol. 12, no. 6, 2019, doi: [10.1103/PhysRevApplied.12.064036](https://doi.org/10.1103/PhysRevApplied.12.064036).
- [137] W. C. Young and R. G. Budynas, *Roark’s formula for stress and strain*, p. 765, table 16.1, 7th ed. New York: McGraw-Hill, 2002.
- [138] M. Kupnik, I. O. Wygant, and T. B. Khuri-Yakub, “Finite element analysis of stress stiffening effects in CMUTs,” in *2008 IEEE Ultrasonic Symposium*. Beijing, China: IEEE, 2008, pp. 487–490, doi: [10.1109/ULTSYM.2008.0119](https://doi.org/10.1109/ULTSYM.2008.0119).
- [139] J. Zhang, X. Rui, B. Li, and G. Chen, “Study on the stress-stiffening effect and modal synthesis methods for the dynamics of a spatial curved beam,” *Journal of Applied Mechanics, Transactions ASME*, vol. 83, no. 8, pp. 1–8, 2016, doi: [10.1115/1.4033515](https://doi.org/10.1115/1.4033515).
- [140] S. Wang, C. Bi, B. Zi, and C. Zheng, “Vibration characteristics of rotating mistuned bladed disks considering the coriolis force, spin softening, and stress stiffening effects,” *Shock and Vibration*, vol. 8, 2019.
- [141] M. X. Shi, B. Liu, Z. Q. Zhang, Y. W. Zhang, and H. J. Gao, “Direct influence of residual stress on the bending stiffness of cantilever beams,” *Proceedings of the Royal Society A*, vol. 468, no. 2145, pp. 2595–2613, 2012, doi: [10.1098/rspa.2011.0662](https://doi.org/10.1098/rspa.2011.0662).
- [142] V. Pini, J. J. Ruz, P. M. Kosaka, O. Malvar, M. Calleja, and J. Tamayo, “How two-dimensional bending can extraordinarily stiffen thin sheets,” *Scientific Reports*, vol. 8, 2016, doi: [10.1038/srep29627](https://doi.org/10.1038/srep29627).
- [143] V. H. Guerrero and R. C. Wetherhold, “Magnetostrictive bending of cantilever beams and plates,” *Journal of Applied Physics*, vol. 94, no. 10, pp. 6659–6666, 2003, doi: [10.1063/1.1621710](https://doi.org/10.1063/1.1621710).
- [144] B. C. Stipe, H. J. Mamin, T. D. Stowe, T. W. Kenny, and D. Rugar, “Magnetic dissipation and fluctuations in individual nanomagnets measured by ultrasensitive cantilever magnetometry,” *Physical Review Letters*, vol. 86, no. 13, pp. 2874–2877, 2001, doi: [10.1103/PhysRevLett.86.2874](https://doi.org/10.1103/PhysRevLett.86.2874).

- [145] J. W. van Honschoten, W. W. Koelmans, S. M. Konings, L. Abelmann, and M. Elwenspoek, "Nanotesla torque magnetometry using a microcantilever," in *Euroensors XXII*. Dresden: Euroensors Committee, 2008, pp. 597–600, [available online](#).
- [146] S. Zabel, C. Kirchhof, E. Yarar, D. Meyners, E. Quandt, and F. Faupel, "Phase modulated magnetoelectric delta-E effect sensor for sub-nano tesla magnetic fields," *Applied Physics Letters*, vol. 107, no. 15, 2015, doi: [10.1063/1.4932575](#).
- [147] S. Zabel, J. Reermann, S. Fichtner, C. Kirchhof, E. Quandt, B. Wagner, G. Schmidt, and F. Faupel, "Multimode delta-E effect magnetic field sensors with adapted electrodes," *Applied Physics Letters*, vol. 108, no. 22, 2016, doi: [10.1063/1.4952735](#).
- [148] A. Kittmann, P. Durdaut, S. Zabel, J. Reermann, J. Schmalz, B. Spetzler, D. Meyners, N. X. Sun, J. McCord, M. Gerken, G. Schmidt, M. Höft, R. Knöchel, F. Faupel, and E. Quandt, "Wide Band Low Noise Love Wave Magnetic Field Sensor System," *Scientific Reports*, vol. 8, no. 1, pp. 1–10, 2018, doi: [10.1038/s41598-017-18441-4](#).
- [149] A. D. Matyushov, B. Spetzler, M. Zaeimbashi, J. Zhou, Z. Qian, E. V. Golubeva, C. Tu, Y. Guo, B. F. Chen, D. Wang, A. Will-Cole, H. Chen, M. Rinaldi, J. McCord, F. Faupel, and N. X. Sun, "Curvature and stress effects on the performance of contour-mode resonant ΔE effect magnetometers," *Advanced Materials Technologies*, 2021, doi: [10.1002/admt.202100294](#).
- [150] B. Gojdka, R. Jahns, K. Meurisch, H. Greve, R. Adelung, E. Quandt, R. Knöchel, and F. Faupel, "Fully integrable magnetic field sensor based on delta-E effect," *Applied Physics Letters*, vol. 99, no. 22, 2011, doi: [10.1063/1.3664135](#).
- [151] Y. Hui, T. Nan, N. X. Sun, and M. Rinaldi, "High resolution magnetometer based on a high frequency magnetoelectric MEMS-CMOS oscillator," *Journal of Microelectromechanical Systems*, vol. 24, no. 1, pp. 134–143, 2014, doi: [10.1109/JMEMS.2014.2322012](#).
- [152] M. Li, A. Matyushov, C. Dong, H. Chen, H. Lin, T. Nan, Z. Qian, M. Rinaldi, Y. Lin, and N. X. Sun, "Ultra-sensitive NEMS magnetoelectric sensor for picotesla DC magnetic field detection," *Applied Physics Letters*, vol. 110, no. 14, 2017, doi: [10.1063/1.4979694](#).
- [153] H. J. Kim, S. Wang, C. Xu, D. Laughlin, J. Zhu, and G. Piazza, "Piezoelectric / magnetostrictive MEMS resonant sensor array for in-plane multi-axis magnetic field detection," in *IEEE MEMS*, Las Vegas, NV, USA, 2017, pp. 109–112, doi: [10.1109/MEMSYS.2017.7863352](#).
- [154] J. Reermann, S. Zabel, C. Kirchhof, E. Quandt, F. Faupel, and G. Schmidt, "Adaptive readout schemes for thin-film magnetoelectric sensors based on the delta-E effect," *IEEE Sensors Journal*, vol. 16, no. 12, pp. 4891–4900, 2016, doi: [10.1109/JSEN.2016.2553962](#).
- [155] P. Durdaut, J. Reermann, S. Zabel, C. Kirchhof, E. Quandt, F. Faupel, G. Schmidt, R. Knöchel, and M. Höft, "Modeling and analysis of noise sources for thin-film magnetoelectric sensors based on the delta-E effect," *IEEE Transactions on Instrumentation and Measurement*, vol. 66, no. 10, pp. 2771–2779, 2017, doi: [10.1109/TIM.2017.2709478](#).
- [156] X. Zhuang, A. M. C. Sing, C. Dolabdjian, Y. Wang, P. Finkel, J. Li, and D. Viehland, "Sensitivity and noise evaluation of a bonded magneto(elasto) electric laminated sensor based on in-plane magnetocapacitance effect for quasi-static magnetic field sensing," *IEEE Transactions on Magnetics*, vol. 51, no. 1, 2015, doi: [10.1109/TMAG.2014.2356852](#).
- [157] M. Staruch, M.-T. Yang, J. Li, C. Dolabdjian, D. Viehland, and P. Finkel, "Frequency reconfigurable phase modulated magnetoelectric sensors using ΔE effect," *Applied Physics Letters*, vol. 111, no. 3, 2017, doi: [10.1063/1.4994663](#).

- [158] M. Staruch, B. R. Matis, J. W. Baldwin, S. P. Bennett, O. van 't Erve, S. Lofland, K. Bussmann, and P. Finkel, "Large non-saturating shift of the torsional resonance in a doubly clamped magnetoelastic resonator," *Applied Physics Letters*, vol. 116, no. 23, 2020, doi: [10.1063/5.0010975](https://doi.org/10.1063/5.0010975).
- [159] P. T. Squire and M. R. J. Gibbs, "Shear-wave magnetometry," *IEEE Transactions on Magnetics*, vol. 24, no. 2, pp. 1755–1757, 1988, doi: [10.1109/20.11592](https://doi.org/10.1109/20.11592).
- [160] P. F. Blomley and J. N. Gooding, "A S.A.W. frequency discriminator," in *Ultrasonics Symposium*. Monterey, CA, USA: IEEE, 1973, pp. 468–471, doi: [10.1109/ULTSYM.1973.196243](https://doi.org/10.1109/ULTSYM.1973.196243).
- [161] M. F. Lewis, "Surface acoustic wave devices and applications: 6. oscillators - the next successful surface acoustic wave device?" *Ultrasonics*, vol. 12, no. 3, pp. 115–123, 1974, doi: [10.1016/0041-624X\(74\)90068-7](https://doi.org/10.1016/0041-624X(74)90068-7).
- [162] T. E. Parker, "Precision surface acoustic wave (SAW) oscillators," in *Ultrasonics Symposium*. San Diego, CA, USA: IEEE, 1982, pp. 268–274, doi: [10.1109/ULTSYM.1982.197827](https://doi.org/10.1109/ULTSYM.1982.197827).
- [163] T. E. Parker and G. K. Montress, "Precision surface-acoustic-wave (SAW) oscillators," *IEEE Transactions on Ultrasonics, Ferroelectrics, and Frequency Control*, vol. 35, no. 3, pp. 342–364, 1988, doi: [10.1109/58.20455](https://doi.org/10.1109/58.20455).
- [164] P. Durdaut, M. Höft, J.-M. Friedt, and E. Rubiola, "Equivalence of open-loop and closed-loop operation of SAW resonators and delay lines," *Sensors*, vol. 19, no. 1, 2019, doi: [10.3390/s19010185](https://doi.org/10.3390/s19010185).
- [165] H. Barkhausen, *Lehrbuch der Elektronen-Röhren und Ihrer Technischen Anwendungen*. Leipzig, Germany: S. Hirzel Verlag, 1935.
- [166] G.-C. Hsieh and J. C. Hung, "Phase-locked loop techniques - a survey," *IEEE Transactions on Industrial Electronics*, vol. 43, no. 6, pp. 609–615, 1996, doi: [10.1109/41.544547](https://doi.org/10.1109/41.544547).
- [167] D. Rabus, J.-M. Friedt, S. Ballandras, G. Martin, É. Carry, and V. Blondeau-Patissier, "High-sensitivity open-loop electronics for gravimetric acoustic-wave-based sensors," *IEEE Transactions on Ultrasonics, Ferroelectrics, and Frequency Control*, vol. 60, no. 6, pp. 1219–1226, 2013, doi: [10.1109/TUFFFC.2013.2685](https://doi.org/10.1109/TUFFFC.2013.2685).
- [168] H. Liu, C. Zhang, Z. Weng, Y. Guo, and Z. Wang, "Resonance frequency readout circuit for a 900 MHz SAW device," *Sensors*, vol. 17, no. 9, 2017, doi: [10.3390/s17092131](https://doi.org/10.3390/s17092131).
- [169] P. Durdaut, E. Rubiola, J.-M. Friedt, C. Müller, B. Spetzler, C. Kirchhof, D. Meyners, E. Quandt, F. Faupel, J. McCord, R. Knöchel, and M. Höft, "Fundamental noise limits and sensitivity of piezoelectrically driven magnetoelastic cantilevers," *Journal of Microelectromechanical Systems*, vol. 29, no. 5, 2020, doi: [10.1109/JMEMS.2020.3014402](https://doi.org/10.1109/JMEMS.2020.3014402).
- [170] J. Mertz, O. Marti, and J. Mlynek, "Regulation of a microcantilever response by force feedback," *Applied Physics Letters*, vol. 62, no. 19, pp. 2344–2346, 1993, doi: [10.1063/1.109413](https://doi.org/10.1063/1.109413).
- [171] K. S. van Dyke, "The piezo-electric resonator and its equivalent network," *Proceedings of the Institute of Radio Engineers*, vol. 16, no. 6, pp. 742–764, 1928, doi: [10.1109/JRPROC.1928.221466](https://doi.org/10.1109/JRPROC.1928.221466).
- [172] E. Hafner, "The piezoelectric crystal unit-definitions and methods of measurement," *Proceedings of the IEEE*, vol. 57, no. 2, pp. 179–201, 1969, doi: [10.1109/PROC.1969.6912](https://doi.org/10.1109/PROC.1969.6912).

- [173] IEEE, “An american national standard: IEEE standard on piezoelectricity,” in *IEEE Standard 176-1987*. IEEE, 1988, doi: [10.1109/IEEESTD.1988.79638](https://doi.org/10.1109/IEEESTD.1988.79638).
- [174] C. Enz and A. Kaiser, *MEMS-based circuits and systems for wireless communication*, C. Enz and A. Kaiser, Eds. New York: Springer, 2013, doi: [10.1007/978-1-4419-8798-3](https://doi.org/10.1007/978-1-4419-8798-3).
- [175] A. Vorobiev, S. Gevorgian, M. Löffler, and E. Olsson, “Correlations between microstructure and Q-factor of tunable thin film bulk acoustic wave resonators,” *Journal of Applied Physics*, vol. 110, no. 5, 2011, doi: [10.1063/1.3626939](https://doi.org/10.1063/1.3626939).
- [176] S. Lee, V. Lee, S. A. Sis, and A. Mortazawi, “A simple nonlinear mBVD model parameter extraction method for intrinsically switchable ferroelectric FBARs,” in *2013 European Microwave Conference*. Nuremberg, Germany: IEEE, 2013, pp. 1355–1358, doi: [10.23919/EuMC.2013.6686917](https://doi.org/10.23919/EuMC.2013.6686917).
- [177] J. Segovia-Fernandez and G. Piazza, “Thermal nonlinearities in contour mode AlN resonators,” *Journal of Microelectromechanical Systems*, vol. 22, no. 4, pp. 976–985, 2013, doi: [10.1109/JMEMS.2013.2252422](https://doi.org/10.1109/JMEMS.2013.2252422).
- [178] D. A. Feld, R. Parker, R. Ruby, P. Bradley, and S. Dong, “After 60 Years: a new formula for computing quality factor is warranted,” in *IEEE Ultrasonic Symposium Proceedings*, no. 6, 2008, pp. 431–436, doi: [10.1109/ULTSYM.2008.0105](https://doi.org/10.1109/ULTSYM.2008.0105).
- [179] T. B. Jones and N. G. Nenadic, *Electromechanics and MEMS*. Cambridge: Cambridge University Press Textbooks, 2013.
- [180] P. Durdaut, “Ausleseverfahren und Rauschmodellierung für magnetoelastische und magnetoelastische Sensorsysteme,” Ph.D. dissertation, Kiel University, 2019.
- [181] L. G. C. Melo, D. Mnard, A. Yelon, L. Ding, S. Saez, and C. Dolabdjian, “Optimization of the magnetic noise and sensitivity of giant magnetoimpedance sensors,” *Journal of Applied Physics*, vol. 103, no. 3, 2008, doi: [10.1063/1.2837106](https://doi.org/10.1063/1.2837106).
- [182] E. Portalier, B. Dufay, S. Saez, and C. Dolabdjian, “Noise behavior of high sensitive GMI-based magnetometer relative to conditioning parameters,” *IEEE Transactions on Magnetics*, vol. 51, no. 1, pp. 6–9, 2015, doi: [10.1109/TMAG.2014.2355414](https://doi.org/10.1109/TMAG.2014.2355414).
- [183] Y. J. Wang, J. Q. Gao, M. H. Li, Y. Shen, D. Hasanyan, J. F. Li, and D. Viehland, “A review on equivalent magnetic noise of magnetoelectric laminate sensors,” *Philosophical Transactions of the Royal Society A*, vol. 372, no. 2009, 2014, doi: [10.1098/rsta.2012.0455](https://doi.org/10.1098/rsta.2012.0455).
- [184] C. Reig and M.-D. Cubells-Belrán, “Giant magnetoresistance (GMR) magnetometers,” in *High sensitivity magnetometers. smart sensors, seasurement and instrumentation, vol. 19*, 1st ed., A. Grosz, M. J. Haji-Sheikh, and S. C. Mukhopadhyay, Eds. Cham: Springer, 2016, ch. 4, pp. 225–252, doi: [10.1007/978-3-319-34070-8_8](https://doi.org/10.1007/978-3-319-34070-8_8).
- [185] L. Ding, S. Saez, C. Dolabdjian, L. G. C. Melo, A. Yelon, and D. Ménard, “Equivalent magnetic noise limit of low-cost GMI magnetometer,” *IEEE Sensors Journal*, vol. 9, no. 2, pp. 159–168, 2009, doi: [10.1109/JSEN.2008.2011067](https://doi.org/10.1109/JSEN.2008.2011067).
- [186] N. A. Stutzke, S. E. Russek, D. P. Pappas, and M. Tondra, “Low-frequency noise measurements on commercial magnetoresistive magnetic field sensors,” *Journal of Applied Physics*, vol. 97, no. 10, pp. 9–11, 2005, doi: [10.1063/1.1861375](https://doi.org/10.1063/1.1861375).
- [187] E. Yarar, S. Salzer, V. Hrkac, A. Piorra, M. Höft, R. Knöchel, L. Kienle, and E. Quandt, “Inverse bilayer magnetoelectric thin film sensor,” *Applied Physics Letters*, vol. 109, no. 2, 2016, doi: [10.1063/1.4958728](https://doi.org/10.1063/1.4958728).

- [188] J. W. S. Rayleigh, “Notes on electricity and magnetism.—III. On the behaviour of iron and steel under the operation of feeble magnetic forces,” *The London, Edinburgh, and Dublin Philosophical Magazine and Journal of Science*, vol. 23, no. 142, pp. 225–245, 1887, doi: [10.1080/14786448708628000](https://doi.org/10.1080/14786448708628000).
- [189] J. D. Lavers, “An efficient method of calculating parameters for induction and resistance heating installations with Magnetic Loads,” *IEEE Transactions on Industry Applications*, vol. IA-14, no. 5, pp. 427–432, 1978, doi: [10.1109/TIA.1978.4503564](https://doi.org/10.1109/TIA.1978.4503564).
- [190] N. A. Demerdash and T. W. Nehl, “Use of numerical analysis of nonlinear eddy current problems by finite elements in the determination of parameters of electrical machines with solid iron rotors,” *IEEE Transactions on Magnetics*, vol. 15, no. 6, pp. 1482–1484, 1979, doi: [10.1109/TMAG.1979.1060386](https://doi.org/10.1109/TMAG.1979.1060386).
- [191] J. D. Lavers, “Finite element solution of nonlinear two dimensional TE-mode eddy current problems,” *IEEE Transactions on Magnetics*, vol. 19, no. 5, pp. 2201–2203, 1983, doi: [10.1109/TMAG.1983.1062731](https://doi.org/10.1109/TMAG.1983.1062731).
- [192] S. N. M. Willcock and B. K. Tanner, “Harmonic analysis of B-H loops,” *IEEE Transaction on Magnetics*, vol. 19, no. 5, pp. 2265 – 2270, 1983, doi: [10.1109/TMAG.1983.1062588](https://doi.org/10.1109/TMAG.1983.1062588).
- [193] R. Rabinovici, “Nonlinear eddy current effects in ferromagnetic materials in the presence of DC magnetic fields,” *IEEE Transactions on Magnetics*, vol. 27, no. 4, pp. 3704–3709, 1991, doi: [10.1109/20.102941](https://doi.org/10.1109/20.102941).
- [194] J. C. Li and Y. P. Wu, “FFT algorithms for the harmonic analysis of three-phase transformer banks with magnetic saturation,” *IEEE Transactions on Power Delivery*, vol. 6, no. 1, pp. 158–165, 1991, doi: [10.1109/61.103735](https://doi.org/10.1109/61.103735).
- [195] C. E. Lin, C. L. Cheng, and C. L. Huang, “Hysteresis characteristic analysis of transformer under different excitations using real time measurement,” *IEEE Transactions on Power Delivery*, vol. 6, no. 2, pp. 873–879, 1991, doi: [10.1109/61.131147](https://doi.org/10.1109/61.131147).
- [196] A. Savini, “Modelling hysteresis loops for finite element magnetic field calculations,” *IEEE Transaction on Magnetics*, vol. 18, no. 2, pp. 552–557, 1982, doi: [10.1109/TMAG.1982.1061908](https://doi.org/10.1109/TMAG.1982.1061908).
- [197] R. M. Del Vecchio, “The calculation of eddy current losses associated with rotating magnetic fields in thin laminations,” *IEEE Transaction on Magnetics*, vol. 18, no. 6, pp. 1707–1709, 1982, doi: [10.1109/TMAG.1982.1062076](https://doi.org/10.1109/TMAG.1982.1062076).
- [198] F. C. Trutt, E. A. Erdelyi, and R. E. Hopkins, “Representation of the magnetization characteristic of DC machines for computer use,” *IEEE Transactions on Power Apparatus and Systems*, vol. PAS-87, no. 3, pp. 665–669, 1968, doi: [10.1109/TPAS.1968.292178](https://doi.org/10.1109/TPAS.1968.292178).
- [199] J. Rivas, C. Pereira, and E. Martín, “Simple approximation for magnetization curves and hysteresis loops,” *IEEE Transactions on Magnetics*, vol. 17, no. 4, pp. 1498–1502, 1981, doi: [10.1109/TMAG.1981.1061241](https://doi.org/10.1109/TMAG.1981.1061241).
- [200] I. D. Mayergoyz, F. M. Abdel-Kader, and F. P. Emad, “On penetration of electromagnetic fields into nonlinear conducting ferromagnetic media,” *Journal of Applied Physics*, vol. 55, no. 3, pp. 618–629, 1984, doi: [10.1063/1.333114](https://doi.org/10.1063/1.333114).
- [201] S. A. Nasar, G. Y. Xiong, and Z. X. Fu, “Eddy-current losses in a tubular linear induction motor,” *IEEE Transactions on Magnetics*, vol. 30, no. 4, pp. 1437–1445, 1994, doi: [10.1109/20.305544](https://doi.org/10.1109/20.305544).

- [202] G. F. Dionne, “Determination of magnetic anisotropy and porosity from the approach to saturation of polycrystalline ferrites,” *Journal of Applied Physics*, vol. 40, no. 4, pp. 1839–1848, 1969, doi: [10.1063/1.1657855](https://doi.org/10.1063/1.1657855).
- [203] G. F. Dionne, J. A. Weiss, and G. A. Allen, “Anisotropy and microstructure analysis by magnetic measurement,” *IEEE Transactions on Magnetics*, vol. 22, no. 5, pp. 656–658, 1986, doi: [10.1109/TMAG.1986.1064413](https://doi.org/10.1109/TMAG.1986.1064413).
- [204] G. F. Dionne, J. A. Weiss, and G. A. Allen, “Hysteresis loops modeled from coercivity, anisotropy, and microstructure parameters,” *Journal of Applied Physics*, vol. 61, no. 8, pp. 3862–3864, 1987, doi: [10.1063/1.338621](https://doi.org/10.1063/1.338621).
- [205] M. K. El-Sherbiny, “Representation of the magnetization characteristic by a sum of exponentials,” *IEEE Transactions on Magnetics*, vol. 9, no. 1, pp. 60–61, 1973, doi: [10.1109/TMAG.1973.1067562](https://doi.org/10.1109/TMAG.1973.1067562).
- [206] K. W. Macfadyen, R. R. S. Simpson, R. D. Slater, and W. S. Wood, “Representation of magnetisation curves by exponential series,” in *Proceedings of the Institution of Electrical Engineers*, vol. 120, no. 8, 1973, pp. 902–904, doi: [10.1049/piee.1973.0198](https://doi.org/10.1049/piee.1973.0198).
- [207] G. F. T. Widger, “Representation of magnetisation curves over extensive range by rational-fraction approximations,” *Proceedings of the Institution of Electrical Engineers*, vol. 116, no. 1, pp. 156–160, 1969, doi: [10.1049/piee.1969.0032](https://doi.org/10.1049/piee.1969.0032).
- [208] M. Akbaba, “A modified Froelich’s type equation for accurate modeling of magnetising characteristic of magnetic cores,” *Electric Machines and Power Systems*, vol. 19, no. 3, pp. 303–311, 1991, doi: [10.1080/07313569108909525](https://doi.org/10.1080/07313569108909525).
- [209] R. M. Josephs, D. S. Crompton, and C. S. Krafft, “Characterization of magnetic oxide recording media using fourier analysis of static hysteresis loops,” *IEEE Transaction on Magnetics*, vol. 22, no. 5, pp. 653–655, 1986, doi: [10.1109/TMAG.1986.1064501](https://doi.org/10.1109/TMAG.1986.1064501).
- [210] F. Preisach, “Über die magnetische Nachwirkung,” *Zeitschrift für Physik*, vol. 94, pp. 277–302, 1935, doi: [10.1007/BF01349418](https://doi.org/10.1007/BF01349418).
- [211] I. D. Mayergoyz, *Mathematical models of hysteresis and their applications*, 2nd ed. Elsevier Inc., 2003, doi: [10.1016/B978-0-12-480873-7.X5000-2](https://doi.org/10.1016/B978-0-12-480873-7.X5000-2).
- [212] R. Skomski, *Simple Models of Magnetism*. New York: Oxford University Press, 2008.
- [213] A. Iványi, *Hysteresis models in electromagnetic computations*, O. Benda and G. Fodor, Eds. Hungary: Iványi, A., 1997.
- [214] I. D. Mayergoyz, “Dynamic Preisach models of hysteresis,” *IEEE Transactions on Magnetics*, vol. 24, no. 6, pp. 2925–2927, 1988, doi: [10.1109/20.92290](https://doi.org/10.1109/20.92290).
- [215] G. Bertotti, “Generalized Preisach model for the description of hysteresis and eddy current effects in metallic ferromagnetic materials,” *Journal of Applied Physics*, vol. 69, no. 8, pp. 4608–4610, 1991, doi: [10.1063/1.348325](https://doi.org/10.1063/1.348325).
- [216] A. Bergqvist and G. Engdahl, “A stress-dependent magnetic Preisach hysteresis model,” *IEEE Transactions on Magnetics*, vol. 27, no. 6, pp. 4796–4798, 1991, doi: [10.1109/20.278950](https://doi.org/10.1109/20.278950).
- [217] T. Suzuki and E. Matsumoto, “Magnetoelastic behavior of ferromagnetic materials using stress dependent Preisach model based on continuum theory,” *International Journal of Applied Electromagnetics and Mechanics*, vol. 19, no. 1–4, pp. 485–489, 2004, doi: [10.3233/jae-2004-613](https://doi.org/10.3233/jae-2004-613).

- [218] I. D. Mayergoyz and G. Friedman, “Isotropic vector Preisach model of hysteresis,” *Journal of Applied Physics*, vol. 61, no. 8, pp. 4022–4024, 1987, doi: [10.1063/1.338565](https://doi.org/10.1063/1.338565).
- [219] I. D. Mayergoyz, “Vector Preisach hysteresis models (invited),” *Journal of Applied Physics*, vol. 63, no. 8, pp. 2995–3000, 1988, doi: [10.1063/1.340926](https://doi.org/10.1063/1.340926).
- [220] L. Chua and K. Stromsmoe, “Lumped-circuit models for nonlinear inductors exhibiting hysteresis loops,” *IEEE Transactions on Circuit Theory*, vol. 17, no. 4, pp. 564–574, 1970, doi: [10.1109/TCT.1970.1083192](https://doi.org/10.1109/TCT.1970.1083192).
- [221] L. Chua and S. Bass, “A generalized hysteresis model,” *IEEE Transactions on Circuit Theory*, vol. 19, no. 1, pp. 36–48, 1972, doi: [10.1109/TCT.1972.1083416](https://doi.org/10.1109/TCT.1972.1083416).
- [222] Y. Saito, “Three-dimensional analysis of magnetodynamic fields in electromagnetic devices taken into account the dynamic hysteresis loop,” *IEEE Transactions on Magnetics*, vol. 18, no. 2, pp. 546–551, 1982, doi: [10.1109/TMAG.1982.1061853](https://doi.org/10.1109/TMAG.1982.1061853).
- [223] Y. Saito, H. Saotome, S. Hayano, and T. Yamamura, “Modelling of nonlinear inductor exhibiting hysteresis loops and its application to the single phase parallel inverters,” *IEEE Transaction on Magnetics*, vol. 19, no. 5, pp. 2189–2191, 1983, doi: [10.1109/TMAG.1983.1062734](https://doi.org/10.1109/TMAG.1983.1062734).
- [224] M. Song, H. Yoon, H. Yang, and C. S. Koh, “A generalized Chua-type vector hysteresis model for both the non-oriented and grain-oriented electrical steel sheets,” *IEEE Transactions on Magnetics*, vol. 47, no. 5, pp. 1146–1149, 2011, doi: [10.1109/TMAG.2010.2073686](https://doi.org/10.1109/TMAG.2010.2073686).
- [225] Y. Saito, S. Hayano, T. Yamamura, and N. Tsuya, “A representation of magnetic hysteresis,” *IEEE Transaction on Magnetics*, vol. 20, no. 5, pp. 1434–1436, 1984, doi: [10.1109/TMAG.1984.1063217](https://doi.org/10.1109/TMAG.1984.1063217).
- [226] Y. Saito, S. Hayano, Y. Kishino, K. Fukushima, H. Nakamura, and N. Tsuya, “A representation of magnetic aftereffect,” *IEEE Transaction on Magnetics*, vol. 22, no. 5, pp. 647–649, 1986, doi: [10.1109/TMAG.1986.1064567](https://doi.org/10.1109/TMAG.1986.1064567).
- [227] Y. Sato, K. Kawano, D. Hou, J. Morroni, and H. Igarashi, “Cauer-equivalent circuit for inductors considering hysteresis magnetic properties for SPICE simulation,” *IEEE Transactions on Power Electronics*, vol. 35, no. 9, pp. 9661–9668, 2020, doi: [10.1109/TPEL.2020.2968749](https://doi.org/10.1109/TPEL.2020.2968749).
- [228] P. J. Leonard, D. Rodger, T. Karaguler, and P. C. Coles, “Finite element modelling of magnetic hysteresis,” *IEEE Transaction on Magnetics*, vol. 31, no. 3, pp. 1801–1804, 1995, doi: [10.1109/20.376386](https://doi.org/10.1109/20.376386).
- [229] A. Benabou, S. Clénet, and F. Piriou, “Comparison of Preisach and Jiles – Atherton models to take into account hysteresis phenomenon for finite element analysis,” *Journal of Magnetism and Magnetic Materials*, vol. 261, no. 1–2, pp. 139–160, 2003, doi: [10.1016/S0304-8853\(02\)01463-4](https://doi.org/10.1016/S0304-8853(02)01463-4).
- [230] A. Bermúdez, L. Dupré, D. Gómez, and P. Venegas, “Electromagnetic computations with Preisach hysteresis model,” *Finite Elements in Analysis and Design*, vol. 126, pp. 65–74, 2017, doi: [10.1016/j.finel.2016.11.005](https://doi.org/10.1016/j.finel.2016.11.005).
- [231] W. Nolting and A. Ramakanth, *Quantum theory of magnetism*. Berlin Heidelberg: Springer-Verlag, 2009, chapter 2, p. 28, doi: [10.1007/978-3-540-85416-6](https://doi.org/10.1007/978-3-540-85416-6).
- [232] W. Nolting and A. Ramakanth, *Quantum theory of magnetism*. Berlin Heidelberg: Springer-Verlag, 2009, chapter 8.2, p. 388, doi: [10.1007/978-3-540-85416-6](https://doi.org/10.1007/978-3-540-85416-6).

- [233] G. Bihlmayer, “Density-functional theory of magnetism,” in *Handbook of magnetism and advanced magnetic materials. Volume 1: fundamentals and theory*, H. Kronmüller, Ed. John Wiley & Sons, Ltd, 2007, doi: [10.1002/9780470022184.hmm101](https://doi.org/10.1002/9780470022184.hmm101).
- [234] R. F. L. Evans, “Atomistic Spin Dynamics,” in *Handbook of materials modeling: applications: current and emerging materials*, S. Sanvito, Ed. Cham: Springer, 2020, p. 438, doi: [10.1007/978-3-319-50257-1_147](https://doi.org/10.1007/978-3-319-50257-1_147).
- [235] R. F. L. Evans, W. J. Fan, P. Chureemart, T. A. Ostler, M. O. A. Ellis, and R. W. Chantrell, “Atomistic spin model simulations of magnetic nanomaterials,” *Journal of Physics: Condensed Matter*, vol. 26, no. 10, 2014, doi: [10.1088/0953-8984/26/10/103202](https://doi.org/10.1088/0953-8984/26/10/103202).
- [236] D. Perera, M. Eisenbach, D. M. Nicholson, G. M. Stocks, and D. P. Landau, “Reinventing atomistic magnetic simulations with spin-orbit coupling,” *Physical Review B*, vol. 93, no. 6, 2016, doi: [10.1103/PhysRevB.93.060402](https://doi.org/10.1103/PhysRevB.93.060402).
- [237] M. O. A. Ellis, R. F. L. Evans, and T. A. Ostler, “The Landau-Lifshitz equation in atomistic models,” *Low Temperature Physics*, vol. 41, no. 9, pp. 705–712, 2015, doi: [10.1063/1.4930971](https://doi.org/10.1063/1.4930971).
- [238] K. Schwarz, P. Mohn, P. Blaha, and J. Kübler, “Electronic and magnetic structure of BCC Fe-Co alloys from band theory,” *Journal of Physics F: Metal Physics*, vol. 14, no. 11, pp. 2659–2671, 1984, doi: [10.1088/0305-4608/14/11/021](https://doi.org/10.1088/0305-4608/14/11/021).
- [239] R. F. L. Evans, “Atomistic spin models,” in *Handbook of materials modeling: applications: current and emerging materials*, S. Sanvito, Ed. Cham: Springer, 2020, p. 429, doi: [10.1007/978-3-319-50257-1_147](https://doi.org/10.1007/978-3-319-50257-1_147).
- [240] O. Eriksson, A. Bergman, L. Bergqvist, and J. Hellsvik, *Atomistic spin-dynamics: foundations and applications*. New York: Oxford University Press, 2017, doi: [10.1093/oso/9780198788669.001.0001](https://doi.org/10.1093/oso/9780198788669.001.0001).
- [241] R. F. L. Evans, “Atomistic spin dynamics: advanced models of magnetic materials,” in *Handbook of materials modeling: applications: current and emerging materials*, S. Sanvito, Ed. Cham: Springer, 2020, pp. 433–437, doi: [10.1007/978-3-319-50257-1_147](https://doi.org/10.1007/978-3-319-50257-1_147).
- [242] Z. Nedelkoski, D. Kepaptsoglou, L. Lari, T. Wen, R. A. Booth, S. D. Oberdick, P. L. Galindo, Q. M. Ramasse, R. F. L. Evans, S. Majetich, and V. K. Lazarov, “Origin of reduced magnetization and domain formation in small magnetite nanoparticles,” *Scientific Reports*, vol. 7, 2017, doi: [10.1038/srep45997](https://doi.org/10.1038/srep45997).
- [243] L. Szunyogh, B. Lazarovits, L. Udvardi, J. Jackson, and U. Nowak, “Giant magnetic anisotropy of the bulk antiferromagnets IrMn and IrMn₃ from first principles,” *Physical Review B*, vol. 79, no. 2, 2009, doi: [10.1103/PhysRevB.79.020403](https://doi.org/10.1103/PhysRevB.79.020403).
- [244] R. Yanes, J. Jackson, L. Udvardi, L. Szunyogh, and U. Nowak, “Exchange bias driven by Dzyaloshinskii-Moriya interactions,” *Physical Review Letters*, vol. 111, no. 21, 2013, doi: [10.1103/PhysRevLett.111.217202](https://doi.org/10.1103/PhysRevLett.111.217202).
- [245] J. Barker and G. E. W. Bauer, “Thermal spin dynamics of yttrium iron garnet,” *Physical Review Letters*, vol. 117, no. 21, 2016, doi: [10.1103/PhysRevLett.117.217201](https://doi.org/10.1103/PhysRevLett.117.217201).
- [246] J. Barker and R. W. Chantrell, “Higher-order exchange interactions leading to metamagnetism in FeRh,” *Physical Review B*, vol. 92, no. 9, pp. 1–5, 2015, doi: [10.1103/PhysRevB.92.094402](https://doi.org/10.1103/PhysRevB.92.094402).

- [247] Y. Toga, M. Matsumoto, S. Miyashita, H. Akai, S. Doi, T. Miyake, and A. Sakuma, “Monte Carlo analysis for finite-temperature magnetism of $\text{Nd}_2\text{Fe}_{14}\text{B}$ permanent magnet,” *Physical Review B*, vol. 94, no. 17, 2016, doi: [10.1103/PhysRevB.94.174433](https://doi.org/10.1103/PhysRevB.94.174433).
- [248] O. N. Mryasov, U. Nowak, K. Y. Guslienko, and R. W. Chantrell, “Temperature-dependent magnetic properties of FePt: effective spin hamiltonian model,” *Europhysics Letters*, vol. 69, no. 5, pp. 805–811, 2005, doi: [10.1209/epl/i2004-10404-2](https://doi.org/10.1209/epl/i2004-10404-2).
- [249] T. A. Ostler, R. F. L. Evans, R. W. Chantrell, U. Atxitia, O. Chubykalo-Fesenko, I. Radu, R. Abrudan, F. Radu, A. Tsukamoto, A. Itoh, A. Kirilyuk, T. Rasing, and A. Kimel, “Crystallographically amorphous ferrimagnetic alloys: comparing a localized atomistic spin model with experiments,” *Physical Review B*, vol. 84, no. 2, 2011, doi: [10.1103/PhysRevB.84.024407](https://doi.org/10.1103/PhysRevB.84.024407).
- [250] R. F. L. Evans, “Vampire 5,” [available online](#).
- [251] A. Bergman, L. Bergqvist, and L. Nordström, “Uppsala atomistic spin dynamics (Up-ASD),” Uppsala University 2017, [available online](#).
- [252] O. Muthsam, C. Vogler, and D. Suess, “Curie temperature modulated structure to improve the performance in heat-assisted magnetic recording,” *Journal of Magnetism and Magnetic Materials*, vol. 474, pp. 442–447, 2019, doi: [10.1016/j.jmmm.2018.11.035](https://doi.org/10.1016/j.jmmm.2018.11.035).
- [253] M. Strungaru, S. Ruta, R. F. L. Evans, and R. W. Chantrell, “Model of magnetic damping and anisotropy at elevated temperatures: application to granular FePt films,” *Physical Review Applied*, vol. 14, no. 1, 2020, doi: [10.1103/PhysRevApplied.14.014077](https://doi.org/10.1103/PhysRevApplied.14.014077).
- [254] P. Asselin, R. F. L. Evans, J. Barker, R. W. Chantrell, R. Yanes, O. Chubykalo-Fesenko, D. Hinzke, and U. Nowak, “Constrained Monte Carlo method and calculation of the temperature dependence of magnetic anisotropy,” *Physical Review B*, vol. 82, no. 5, 2010, doi: [10.1103/PhysRevB.82.054415](https://doi.org/10.1103/PhysRevB.82.054415).
- [255] P.-W. Ma and C. H. Woo, “Large-scale simulation of the spin-lattice dynamics in ferromagnetic iron,” *Physical Review B*, vol. 78, no. 2, pp. 1–12, 2008, doi: [10.1103/PhysRevB.78.024434](https://doi.org/10.1103/PhysRevB.78.024434).
- [256] D. Perera, D. M. Nicholson, M. Eisenbach, G. M. Stocks, and D. P. Landau, “Collective dynamics in atomistic models with coupled translational and spin degrees of freedom,” *Physical Review B*, vol. 95, no. 1, 2017, doi: [10.1103/PhysRevB.95.014431](https://doi.org/10.1103/PhysRevB.95.014431).
- [257] R. F. L. Evans, “Atomistic spin dynamics,” in *Handbook of materials modeling: applications: current and emerging materials*, S. Sanvito, Ed. Cham: Springer, 2020, doi: [10.1007/978-3-319-50257-1_147](https://doi.org/10.1007/978-3-319-50257-1_147).
- [258] L. D. Landau and E. M. Lifshitz, “On the Theory of the Dispersion of Magnetic Permeability in Ferromagnetic Bodies,” *Physikalische Zeitschrift der Sowjetunion*, vol. 8, pp. 153–164, 1935, doi: [10.1016/B978-0-08-036364-6.50008-9](https://doi.org/10.1016/B978-0-08-036364-6.50008-9).
- [259] W. F. Brown, “Theory of the approach to magnetic saturation,” *Physical Review*, vol. 58, no. 8, 1940, pp. 736–743, doi: [10.1103/PhysRev.58.736](https://doi.org/10.1103/PhysRev.58.736).
- [260] Gilbert, T. L., “A Lagrangian formulation of the gyromagnetic equation of the magnetization field,” *Physical Review*, vol. 100, p. 1243, 1955.
- [261] W. F. Brown, *Micromagnetics*, R. E. Marshak, Ed. New York, London: John Wiley & Sons, Inc., 1963, ISBN: 9780470110379.

- [262] Y. Nakatani, Y. Uesaka, and N. Hayashi, “Direct solution of the Landau-Lifshitz-Gilbert equation for micromagnetics,” *Japanese Journal of Applied Physics*, vol. 28, no. 12 R, pp. 2485–2507, 1989, doi: [10.1143/JJAP.28.2485](https://doi.org/10.1143/JJAP.28.2485).
- [263] T. Schrefl, D. Suess, W. Scholz, H. Forster, V. Tsiantos, and J. Fidler, “Finite element micromagnetics,” in *Computational electromagnetics. Lecture notes in computational science and engineering, vol. 28*, P. Monk, C. Carstensen, S. Funken, W. Hackbusch, and R. H. W. Hoppe, Eds. Berlin, Heidelberg: Springer, 2003, pp. 165–181, doi: [10.1007/978-3-642-55745-3_11](https://doi.org/10.1007/978-3-642-55745-3_11).
- [264] T. Schrefl, G. Hrkac, S. Bance, D. Suess, O. Ertl, and J. Fidler, “Numerical methods in micromagnetics (finite element method),” in *Handbook of magnetism and advanced magnetic materials*, H. Kronmüller, S. Parkin, J. E. Miltat, and M. R. Scheinfein, Eds. John Wiley & Sons, Ltd., 2007, doi: [10.1002/9780470022184.hmm203](https://doi.org/10.1002/9780470022184.hmm203).
- [265] J. Fidler and T. Schrefl, “Micromagnetic modelling - the current state of the art,” *Journal of Physics D: Applied Physics*, vol. 33, no. 15, pp. R135–R156, 2000, doi: [10.1088/0022-3727/33/15/201](https://doi.org/10.1088/0022-3727/33/15/201).
- [266] M. E. Schabes and H. N. Bertram, “Magnetization processes in ferromagnetic cubes,” *Journal of Applied Physics*, vol. 64, no. 3, pp. 1347–1357, 1988, doi: [10.1063/1.341858](https://doi.org/10.1063/1.341858).
- [267] Y. Nakatani, Y. Uesaka, N. Hayashi, and H. Fukushima, “Computer simulation of thermal fluctuation of fine particle magnetization based on Langevin equation,” *Journal of Magnetism and Magnetic Materials*, vol. 168, no. 3, pp. 347–351, 1997, doi: [10.1016/S0304-8853\(96\)00725-1](https://doi.org/10.1016/S0304-8853(96)00725-1).
- [268] J. G. Zhu, “Modeling of multilayer thin film recording media,” *IEEE Transactions on Magnetics*, vol. 28, no. 5, pp. 3267–3269, 1992, doi: [10.1109/20.179779](https://doi.org/10.1109/20.179779).
- [269] M. J. Vos, R. L. Brott, J. G. Zhu, and L. W. Carlson, “Computed hysteresis behavior and interaction effects in spheroidal particle assemblies,” *IEEE Transactions on Magnetics*, vol. 29, no. 6, pp. 3652–3657, 1993, doi: [10.1109/20.281259](https://doi.org/10.1109/20.281259).
- [270] R. Ramesh and K. Srikrishna, “Magnetization reversal in nucleation controlled magnets. I. Theory,” *Journal of Applied Physics*, vol. 64, no. 11, pp. 6406–6415, 1988, doi: [10.1063/1.342054](https://doi.org/10.1063/1.342054).
- [271] T. Schrefl, “Finite elements in numerical micromagnetics. Part I: granular hard magnets,” *Journal of Magnetism and Magnetic Materials*, vol. 207, no. 1-3, pp. 45–65, 1999, doi: [10.1016/S0304-8853\(99\)00532-6](https://doi.org/10.1016/S0304-8853(99)00532-6).
- [272] A. Hubert and R. Schäfer, *Magnetic domains - the analysis of magnetic microstructures*, 3rd ed. Berlin Heidelberg: Springer Verlag, 2017, doi: [10.1007/978-3-319-59409-5_2](https://doi.org/10.1007/978-3-319-59409-5_2).
- [273] L. Torres, E. Martínez, L. Lopez-Díaz, and O. Alejos, “About the inclusion of eddy currents in micromagnetic computations,” *Physica B: Condensed Matter*, vol. 343, no. 1–4, pp. 257–261, 2004, doi: [10.1016/j.physb.2003.08.104](https://doi.org/10.1016/j.physb.2003.08.104).
- [274] S. Zhang and Z. Li, “Roles of nonequilibrium conduction electrons on the magnetization dynamics of ferromagnets,” *Physical Review Letters*, vol. 93, no. 12, 2004, doi: [10.1103/PhysRevLett.93.127204](https://doi.org/10.1103/PhysRevLett.93.127204).
- [275] C. Abert, “Micromagnetics and spintronics: models and numerical methods,” *The European Physical Journal B*, vol. 92, 2019, doi: [10.1140/epjb/e2019-90599-6](https://doi.org/10.1140/epjb/e2019-90599-6).

- [276] U. Atxitia, D. Hinzke, and U. Nowak, “Fundamentals and applications of the Landau-Lifshitz-Bloch equation,” *Journal of Physics D*, vol. 50, no. 3, 2017, doi: [10.1088/1361-6463/50/3/033003](https://doi.org/10.1088/1361-6463/50/3/033003).
- [277] D. V. Berkov, “Magnetization dynamics including thermal fluctuations: Basic phenomenology, fast remagnetization processes and transitions over high-energy barriers,” in *Handbook of magnetism and advanced magnetic materials. Volume 2: micromagnetism*, H. Kronmüller, Ed. John Wiley & Sons, Ltd, 2007, doi: [10.1002/9780470022184.hmm204](https://doi.org/10.1002/9780470022184.hmm204).
- [278] M. B. Hahn, “Temperature in micromagnetism: cell size and scaling effects of the stochastic Landau–Lifshitz equation,” *Journal of Physics Communications*, vol. 3, no. 7, 2019, doi: [10.1088/2399-6528/ab31e6](https://doi.org/10.1088/2399-6528/ab31e6).
- [279] M. J. Donahue and D. G. Porter, “OOMMF user’s guide, version 1.0, - 6376,” *National Institute of Standards and Technology, Gaithersburg*, no. 6376, 1999, doi: [10.6028/NIST.IR.6376](https://doi.org/10.6028/NIST.IR.6376).
- [280] C. Abert, L. Exl, F. Bruckner, A. Drews, and D. Suess, “Magnum.fe: a micromagnetic finite-element simulation code based on FEniCS,” *Journal of Magnetism and Magnetic Materials*, vol. 345, pp. 29–35, 2013, doi: [10.1016/j.jmmm.2013.05.051](https://doi.org/10.1016/j.jmmm.2013.05.051).
- [281] A. Vansteenkiste, J. Leliaert, M. Dvornik, M. Helsen, F. Garcia-Sanchez, and B. Van Waeyenberge, “The design and verification of MuMax3,” *AIP Advances*, vol. 4, no. 10, 2014, doi: [10.1063/1.4899186](https://doi.org/10.1063/1.4899186).
- [282] J. Leliaert and J. Mulkers, “Tomorrow’s micromagnetic simulations,” *Journal of Applied Physics*, vol. 125, no. 18, 2019, doi: [10.1063/1.5093730](https://doi.org/10.1063/1.5093730).
- [283] J. Leliaert, M. Dvornik, J. Mulkers, J. de Clercq, M. V. Milošević, and B. van Waeyenberge, “Fast micromagnetic simulations on GPU - recent advances made with mumax3,” *Journal of Physics D*, vol. 51, no. 12, 2018, doi: [10.1088/1361-6463/aaab1c](https://doi.org/10.1088/1361-6463/aaab1c).
- [284] C. L. Jermain, G. E. Rowlands, R. A. Buhrman, and D. C. Ralph, “GPU-accelerated micromagnetic simulations using cloud computing,” *Journal of Magnetism and Magnetic Materials*, vol. 401, no. 1, pp. 320–322, 2016, doi: [10.1016/j.jmmm.2015.10.054](https://doi.org/10.1016/j.jmmm.2015.10.054).
- [285] R. Streubel, P. Fischer, F. Kronast, V. P. Kravchuk, D. D. Sheka, Y. Gaididei, O. G. Schmidt, and D. Makarov, “Magnetism in curved geometries,” *Journal of Physics D*, vol. 49, no. 36, 2016, doi: [10.1088/0022-3727/49/36/363001](https://doi.org/10.1088/0022-3727/49/36/363001).
- [286] D. D. Sheka, O. V. Pylypovskyi, P. Landeros, Y. Gaididei, A. Kákay, and D. Makarov, “Nonlocal chiral symmetry breaking in curvilinear magnetic shells,” *Communications Physics*, vol. 3, 2020, doi: [10.1038/s42005-020-0387-2](https://doi.org/10.1038/s42005-020-0387-2).
- [287] J. X. Zhang and L. Q. Chen, “Phase-field microelasticity theory and micromagnetic simulations of domain structures in giant magnetostrictive materials,” *Acta Materialia*, vol. 53, no. 9, pp. 2845–2855, 2005, doi: [10.1016/j.actamat.2005.03.002](https://doi.org/10.1016/j.actamat.2005.03.002).
- [288] T. Koyama, “Phase-field modeling of microstructure evolutions in magnetic materials,” *Science and Technology of Advanced Materials*, vol. 9, no. 1, 2008, doi: [10.1088/1468-6996/9/1/013006](https://doi.org/10.1088/1468-6996/9/1/013006).
- [289] J. Wang and J. Zhang, “A real-space phase field model for the domain evolution of ferromagnetic materials,” *International Journal of Solids and Structures*, vol. 50, no. 22–23, pp. 3597–3609, 2013, doi: [10.1016/j.ijsolstr.2013.07.001](https://doi.org/10.1016/j.ijsolstr.2013.07.001).

- [290] S. Cui, J. Wan, N. Chen, and Y. Rong, “Phase-field simulation of magnetic field induced microstructure evolution in γ Mn-based alloys,” *Journal of Applied Physics*, vol. 127, no. 9, 2020, doi: [10.1063/1.5141110](https://doi.org/10.1063/1.5141110).
- [291] C. Adelman, F. Vanderveken, J. Mulkers, J. Leliaert, B. Van Waeyenberge, B. Sorée, O. Zografos, and F. Ciubotaru, “Finite difference magnetoelastic simulator,” *Open Research Europe*, vol. 1, no. 35, 2021, doi: [10.12688/openreseurope.13302.1](https://doi.org/10.12688/openreseurope.13302.1).
- [292] R. Hertel, “Applications of multi-scale modeling to spin dynamics in spintronics devices,” in *Handbook of materials modeling: applications: current and emerging materials*, W. Andreoni and S. Yip, Eds. Cham: Springer, 2020, pp. 401–426, doi: [10.1007/978-3-319-44680-6_104](https://doi.org/10.1007/978-3-319-44680-6_104).
- [293] R. E. Miller and E. B. Tadmor, “A unified framework and performance benchmark of fourteen multiscale atomistic/continuum coupling methods,” *Modelling and simulation in materials science and engineering*, vol. 17, no. 5, 2009, doi: [10.1088/0965-0393/17/5/053001](https://doi.org/10.1088/0965-0393/17/5/053001).
- [294] F. Garcia-Sanchez, O. Chubykalo-Fesenko, O. Mryasov, R. W. Chantrell, and K. Y. Guslienko, “Exchange spring structures and coercivity reduction in FePtFeRh bilayers: a comparison of multiscale and micromagnetic calculations,” *Applied Physics Letters*, vol. 87, no. 12, 2005, doi: [10.1063/1.2051789](https://doi.org/10.1063/1.2051789).
- [295] T. Jourdan, A. Marty, and F. Lançon, “Multiscale method for heisenberg spin simulations,” *Physical Review B*, vol. 77, no. 22, 2008, doi: [10.1103/physrevb.77.224428](https://doi.org/10.1103/physrevb.77.224428).
- [296] C. Andreas, A. Kákay, and R. Hertel, “Multiscale and multimodel simulation of Bloch-point dynamics,” *Physical Review B*, vol. 89, no. 13, 2014, doi: [10.1103/PhysRevB.89.134403](https://doi.org/10.1103/PhysRevB.89.134403).
- [297] B. Schweflinghaus, B. Zimmermann, M. Heide, G. Bihlmayer, and S. Blügel, “Role of Dzyaloshinskii-Moriya interaction for magnetism in transition-metal chains at Pt step edges,” *Physical Review B*, vol. 94, no. 2, 2016, doi: [10.1103/PhysRevB.94.024403](https://doi.org/10.1103/PhysRevB.94.024403).
- [298] N. Kazantseva, U. Nowak, R. W. Chantrell, J. Hohlfeld, and A. Rebei, “Slow recovery of the magnetisation after a sub-picosecond heat pulse,” *EPL (Europhysics Letters)*, vol. 81, no. 2, 2007, doi: [10.1209/0295-5075/81/27004](https://doi.org/10.1209/0295-5075/81/27004).
- [299] G. Hrkac, T. G. Woodcock, C. Freeman, A. Goncharov, J. Dean, T. Schrefl, and O. Gutfleisch, “The role of local anisotropy profiles at grain boundaries on the coercivity of Nd₂Fe₁₄B magnets,” *Applied Physics Letters*, vol. 97, no. 23, pp. 2010–2013, 2010, doi: [10.1063/1.3519906](https://doi.org/10.1063/1.3519906).
- [300] O. Ertl, G. Hrkac, D. Suess, M. Kirschner, F. Dorfbauer, J. Fidler, and T. Schrefl, “Multi-scale micromagnetic simulation of giant magnetoresistance read heads,” *Journal of Applied Physics*, vol. 99, no. 8, 2006, doi: [10.1063/1.2162812](https://doi.org/10.1063/1.2162812).
- [301] F. Bruckner, D. Suess, M. Feischl, T. Führer, P. Goldenits, M. Page, D. Praetorius, and M. Ruggieri, “Multiscale modeling in micromagnetics: existence of solutions and numerical integration,” *Mathematical Models and Methods in Applied Sciences*, vol. 24, no. 13, pp. 2627–2662, 2014, doi: [10.1142/S0218202514500328](https://doi.org/10.1142/S0218202514500328).
- [302] Z. Szabó and A. Iványi, “Computer-aided simulation of stoner-wohlfarth model,” *Journal of Magnetism and Magnetic Materials*, vol. 215–216, pp. 33–36, 2000, doi: [10.1016/S0304-8853\(00\)00059-7](https://doi.org/10.1016/S0304-8853(00)00059-7).

- [303] M. A. Chuev and J. Hesse, “Nanomagnetism: extension of the Stoner-Wohlfarth model within Néel’s ideas and useful plots,” *Journal of Physics Condensed Matter*, vol. 19, no. 50, 2007, doi: [10.1088/0953-8984/19/50/506201](https://doi.org/10.1088/0953-8984/19/50/506201).
- [304] E. Myrovali, N. Maniotis, A. Makridis, A. Terzopoulou, V. Ntomprougkidis, K. Simeonidis, D. Sakellari, O. Kalogirou, T. Samaras, R. Salikhov, M. Spasova, M. Farle, U. Wiedwald, and M. Angelakeris, “Arrangement at the nanoscale: effect on magnetic particle hyperthermia,” *Scientific Reports*, vol. 6, 2016, doi: [10.1038/srep37934](https://doi.org/10.1038/srep37934).
- [305] S. A. Mathews, A. C. Ehrlich, and N. A. Charipar, “Hysteresis branch crossing and the Stoner–Wohlfarth model,” *Scientific Reports*, vol. 10, 2020, doi: [10.1038/s41598-020-72233-x](https://doi.org/10.1038/s41598-020-72233-x).
- [306] P. Mohn, “Weiss molecular field model,” in *Magnetism in the Solid State*. Berlin, Heidelberg: Springer, 2003, ch. 6, pp. 53–61, doi: [10.1007/3-540-30981-0](https://doi.org/10.1007/3-540-30981-0).
- [307] D. C. Jiles and D. L. Atherton, “Theory of ferromagnetic hysteresis (invited),” *Journal of Applied Physics*, vol. 55, no. 6, pp. 2115–2120, 1984, doi: [10.1063/1.333582](https://doi.org/10.1063/1.333582).
- [308] A. Ramesh, D. C. Jiles, and J. M. Roderick, “A model of anisotropic anhysteretic magnetization,” *IEEE Transactions on Magnetics*, vol. 32, no. 5, pp. 4234–4236, 1996, doi: [10.1109/20.539344](https://doi.org/10.1109/20.539344).
- [309] R. Szewczyk, “Validation of the anhysteretic magnetization model for soft magnetic materials with perpendicular anisotropy,” *Materials*, vol. 7, no. 7, pp. 5109–5116, 2014, doi: [10.3390/ma7075109](https://doi.org/10.3390/ma7075109).
- [310] G. Szymański and M. Waszak, “Vectorized Jiles-Atherton hysteresis model,” *Physica B: Condensed Matter*, vol. 343, no. 1–4, pp. 26–29, 2004, doi: [10.1016/j.physb.2003.08.048](https://doi.org/10.1016/j.physb.2003.08.048).
- [311] F. T. Calkins, R. C. Smith, and A. B. Flatau, “Energy-based hysteresis model for magnetostrictive transducers,” *IEEE Transactions on Magnetics*, vol. 36, no. 2, pp. 429–439, 2000, doi: [10.1109/20.825804](https://doi.org/10.1109/20.825804).
- [312] M. J. Dapino, R. C. Smith, and A. B. Flatau, “Model for the delta-E effect in magnetostrictive transducers,” *Proceedings SPIE 3985, Smart Structures and Materials 2000: Smart Structures and Integrated Systems*, vol. 2, pp. 174–185, 2000, doi: [10.1117/12.388821](https://doi.org/10.1117/12.388821).
- [313] J. Zheng, S. Cao, and H. Wang, “Modeling of magnetomechanical effect behaviors in a giant magnetostrictive device under compressive stress,” *Sensors and Actuators A: Physical*, vol. 143, no. 2, pp. 204–214, 2008, doi: [10.1016/j.sna.2007.10.063](https://doi.org/10.1016/j.sna.2007.10.063).
- [314] B. O. Moldovanu, C. Moldovanu, and A. Moldovanu, “Computer simulation of the transient behaviour of a fluxgate magnetometric circuit,” *Journal of Magnetism and Magnetic Materials*, vol. 157–158, pp. 565–566, 1996, doi: [10.1016/0304-8853\(95\)01101-3](https://doi.org/10.1016/0304-8853(95)01101-3).
- [315] W. D. Armstrong, “Magnetization and magnetostriction processes in Tb(0.27-0.30)Dy(0.73-0.70)Fe(1.9-2.0),” *Journal of Applied Physics*, vol. 81, no. 5, pp. 2321–2326, 1997.
- [316] W. D. Armstrong, “A directional magnetization potential based model of magnetoelastic hysteresis,” *Journal of Applied Physics*, vol. 91, no. 4, pp. 2202–2210, 2002, doi: [10.1063/1.1431433](https://doi.org/10.1063/1.1431433).
- [317] J. Atulasimha, A. B. Flatau, and E. Summers, “Characterization and energy-based model of the magnetomechanical behavior of polycrystalline iron-gallium alloys,” *Smart Materials and Structures*, vol. 16, no. 4, pp. 1265–1276, 2007, doi: [10.1088/0964-1726/16/4/039](https://doi.org/10.1088/0964-1726/16/4/039).

- [318] J. Atulasima, A. B. Flatau, and J. R. Cullen, “Energy-based quasi-static modeling of the actuation and sensing behavior of single-crystal iron-gallium alloys,” *Journal of Applied Physics*, vol. 103, no. 1, 2008, doi: [10.1063/1.2826946](https://doi.org/10.1063/1.2826946).
- [319] J. Atulasimha and A. B. Flatau, “A review of magnetostrictive iron-gallium alloys,” *Smart Materials and Structures*, vol. 20, no. 4, 2011, doi: [10.1088/0964-1726/20/4/043001](https://doi.org/10.1088/0964-1726/20/4/043001).
- [320] D. L. Atherton and J. R. Beattie, “A mean field Stoner-Wohlfarth hysteresis model,” *IEEE Transactions on Magnetics*, vol. 26, no. 6, pp. 3059–3063, 1990, doi: [10.1109/20.102891](https://doi.org/10.1109/20.102891).
- [321] L. Lanci and D. V. Kent, “Introduction of thermal activation in forward modeling of hysteresis loops for single-domain magnetic particles and implications for the interpretation of the Day diagram,” *Journal of Geophysical Research: Solid Earth*, vol. 108, no. B3, pp. 1–9, 2003, doi: [10.1029/2001jb000944](https://doi.org/10.1029/2001jb000944).
- [322] P. T. Squire, “Domain model for magnetoelastic behaviour of uniaxial ferromagnets,” *Journal of Magnetism and Magnetic Materials*, vol. 140-144, no. Part 3, pp. 1829–1830, 1995, doi: [10.1016/0304-8853\(94\)00918-X](https://doi.org/10.1016/0304-8853(94)00918-X).
- [323] V. H. Guerrero and R. C. Wetherhold, “Strain and stress calculation in bulk magnetostrictive materials and thin films,” *Journal of Magnetism and Magnetic Materials*, vol. 271, no. 2-3, pp. 190–206, 2004, doi: [10.1016/j.jmmm.2003.09.028](https://doi.org/10.1016/j.jmmm.2003.09.028).
- [324] O. Hubert, “Multiscale magneto-elastic modeling of magnetic materials including isotropic second order stress effect,” *Journal of Magnetism and Magnetic Materials*, vol. 491, 2019, doi: [10.1016/j.jmmm.2019.165564](https://doi.org/10.1016/j.jmmm.2019.165564).
- [325] P. Bruno and J. P. Renard, “Magnetic surface anisotropy of transition metal ultrathin films,” *Applied Physics A Solids and Surfaces*, vol. 49, no. 5, pp. 499–506, 1989, doi: [10.1007/BF00617016](https://doi.org/10.1007/BF00617016).
- [326] R. C. O’Handley, *Modern magnetic materials - principles and applications*, 1st ed. New York: Wiley-Interscience, 2000, p. 16.
- [327] R. B. Goldfarb, “Electromagnetic units, the Giorgi system, and the revised international system of units,” *IEEE Magnetics Letters*, vol. 9, 2017, doi: [10.1109/LMAG.2018.2868654](https://doi.org/10.1109/LMAG.2018.2868654).
- [328] A. Hubert and R. Schäfer, *Magnetic domains - the analysis of magnetic microstructures*, 3rd ed. Berlin Heidelberg: Springer Verlag, 2017, pp. 101–104, doi: [10.1007/978-3-319-59409-5_2](https://doi.org/10.1007/978-3-319-59409-5_2).
- [329] A. S. Arrott, B. Heinrich, and D. S. Bloomberg, “Micromagnetics of magnetization processes in toroidal geometries,” *IEEE Transaction on Magnetics*, vol. 10, no. 3, pp. 950–953, 1974, doi: [10.1109/TMAG.1974.1058423](https://doi.org/10.1109/TMAG.1974.1058423).
- [330] R. C. O’Handley, *Modern magnetic materials - principles and applications*, 1st ed. New York: Wiley-Interscience, 2000, p. 122.
- [331] H. Kronmüller, *General micromagnetic theory and applications*. American Cancer Society, 2019, doi: [10.1002/9783527603978.mst0460](https://doi.org/10.1002/9783527603978.mst0460).
- [332] R. C. O’Handley, *Modern magnetic materials - principles and applications*, 1st ed. New York: Wiley-Interscience, 2000, pp. 183–188.
- [333] A. Hubert and R. Schäfer, *Magnetic domains - the analysis of magnetic microstructures*, 3rd ed. Berlin Heidelberg: Springer Verlag, 2017, pp. 104–105, doi: [10.1007/978-3-319-59409-5_2](https://doi.org/10.1007/978-3-319-59409-5_2).

- [334] W. H. Meiklejohn, “Exchange anisotropy - a review,” *Journal of Applied Physics*, vol. 33, no. 3, pp. 1328–1335, 1962, doi: [10.1063/1.1728716](https://doi.org/10.1063/1.1728716).
- [335] A. P. Malozemoff, “Mechanisms of exchange anisotropy (invited),” *Journal of Applied Physics*, vol. 63, no. 8, pp. 3874–3879, 1988, doi: [10.1063/1.340591](https://doi.org/10.1063/1.340591).
- [336] F. Radu and H. Zabel, “Exchange bias effect of ferro-/antiferromagnetic heterostructures,” in *Magnetic heterostructures*, F. Radu and H. Zabel, Eds. Berlin, Heidelberg: Springer, 2007, vol. 227, ch. 3, pp. 97–184, doi: [10.1007/978-3-540-73462-8_3](https://doi.org/10.1007/978-3-540-73462-8_3).
- [337] M. F. Hansen and G. Rizzi, “Exchange-biased AMR bridges for magnetic field sensing and biosensing,” *IEEE Transactions on Magnetics*, vol. 53, no. 4, 2017, doi: [10.1109/TMAG.2016.2614012](https://doi.org/10.1109/TMAG.2016.2614012).
- [338] Y. Guo, Y. Ouyang, N. Sato, C. C. Ooi, and S. X. Wang, “Exchange-biased anisotropic magnetoresistive field sensor,” *IEEE Sensors Journal*, vol. 17, no. 11, pp. 3309–3315, 2017, doi: [10.1109/JSEN.2017.2695238](https://doi.org/10.1109/JSEN.2017.2695238).
- [339] V. S. Luong, A. T. Nguyen, Q. K. Hoang, T. N. Nguyen, A. T. Nguyen, T. A. Nguyen, and V. C. Giap, “Magnetoresistive performances in exchange-biased spin valves and their roles in low-field magnetic sensing applications,” *Journal of Science: Advanced Materials and Devices*, vol. 3, no. 4, pp. 399–405, 2018, doi: [10.1016/j.jsamd.2018.09.004](https://doi.org/10.1016/j.jsamd.2018.09.004).
- [340] A. E. Berkowitz and K. Takano, “Exchange anisotropy - a review,” *Journal of Magnetism and Magnetic Materials*, vol. 200, no. 1–3, pp. 552–570, 1999, doi: [10.1016/S0304-8853\(99\)00453-9](https://doi.org/10.1016/S0304-8853(99)00453-9).
- [341] R. C. O’Handley, *Modern magnetic materials - principles and applications*, 1st ed. New York: Wiley-Interscience, 2000, pp. 437–449.
- [342] E. Lage, C. Kirchhof, V. Hrkac, L. Kienle, R. Jahns, R. Knöchel, E. Quandt, and D. Meyners, “Exchange biasing of magnetoelectric composites,” *Nature Materials*, vol. 11, no. 6, pp. 523–529, 2012, doi: [10.1038/nmat3306](https://doi.org/10.1038/nmat3306).
- [343] V. Hrkac, E. Lage, G. Köppel, J. Strobel, J. McCord, E. Quandt, D. Meyners, and L. Kienle, “Amorphous FeCoSiB for exchange bias coupled and decoupled magnetoelectric multilayer systems: real-structure and magnetic properties,” *Journal of Applied Physics*, vol. 116, no. 13, 2014, doi: [10.1063/1.4896662](https://doi.org/10.1063/1.4896662).
- [344] E. Lage, N. O. Urs, V. Röbisch, I. Teliban, R. Knöchel, D. Meyners, J. McCord, and E. Quandt, “Magnetic domain control and voltage response of exchange biased magnetoelectric composites,” *Applied Physics Letters*, vol. 104, no. 13, 2014, doi: [10.1063/1.4870511](https://doi.org/10.1063/1.4870511).
- [345] A. Aharoni, “Magnetostatic energy calculations,” *IEEE Transactions on Magnetics*, vol. 27, no. 4, pp. 3539–3547, 1991, doi: [10.1109/20.102925](https://doi.org/10.1109/20.102925).
- [346] E. P. Furlani, “Chapter 2 - review of maxwell’s equations,” in *Permanent magnet and electromechanical devices*, ser. Electromagnetism, E. P. Furlani, Ed. San Diego: Academic Press, 2001, pp. 73–95, doi: [10.1016/B978-012269951-1/50003-6](https://doi.org/10.1016/B978-012269951-1/50003-6).
- [347] L. Exl, N. J. Mauser, T. Schrefl, and D. Suess, “The extrapolated explicit midpoint scheme for variable order and step size controlled integration of the Landau–Lifschitz–Gilbert equation,” *Journal of Computational Physics*, vol. 346, pp. 14–24, 2017, doi: [10.1016/j.jcp.2017.06.005](https://doi.org/10.1016/j.jcp.2017.06.005).

- [348] A. Hubert and R. Schäfer, *Magnetic domains - the analysis of magnetic microstructures*, 3rd ed. Berlin Heidelberg: Springer Verlag, 2017, pp. 112–113, doi: [10.1007/978-3-319-59409-5_2](https://doi.org/10.1007/978-3-319-59409-5_2).
- [349] A. Aharoni, “Demagnetizing factors for rectangular ferromagnetic prisms,” *Journal of Applied Physics*, vol. 83, no. 6, pp. 3432–3434, 1998, doi: [10.1063/1.367113](https://doi.org/10.1063/1.367113).
- [350] A. Aharoni, “Local demagnetization in a rectangular ferromagnetic prism,” *Physica Status Solidi (B) Basic Research*, vol. 229, no. 3, pp. 1413–1416, 2002, doi: [10.1002/1521-3951\(200202\)229:3<1413::AID-PSSB1413>3.0.CO;2-Q](https://doi.org/10.1002/1521-3951(200202)229:3<1413::AID-PSSB1413>3.0.CO;2-Q).
- [351] A. Aharoni, L. Pust, and M. Kief, “Comparing theoretical demagnetizing factors with the observed saturation process in rectangular shields,” *Journal of Applied Physics*, vol. 87, no. 9, pp. 6564–6566, 2000, doi: [10.1063/1.372771](https://doi.org/10.1063/1.372771).
- [352] E. du Trémolet de Lacheisserie, *Magnetostriction: theory and applications of magnetoelasticity*. Boca Raton, Florida: CRC Press Inc, 1993.
- [353] C. Mudivarthi, S. Datta, J. Atulasimha, P. G. Evans, M. J. Dapino, and A. B. Flatau, “Anisotropy of constrained magnetostrictive materials,” *Journal of Magnetism and Magnetic Materials*, vol. 322, no. 20, pp. 3028–3034, 2010, doi: [10.1016/j.jmmm.2010.05.024](https://doi.org/10.1016/j.jmmm.2010.05.024).
- [354] J. P. Joule, “On the effects of magnetism upon the dimensions of iron and steel bars,” *The London, Edinburgh, and Dublin Philosophical Magazine and Journal of Science*, vol. 30, no. Third Series, pp. 76–87, 1847, doi: [10.1080/14786444708645656](https://doi.org/10.1080/14786444708645656).
- [355] R. Becker and W. Döring, *Ferromagnetismus*, 1st ed. Berlin, Heidelberg: Julius Springer, 1939, p. 291, doi: [10.1007/978-3-642-47366-1](https://doi.org/10.1007/978-3-642-47366-1).
- [356] A. Reid, X. Shen, P. Maldonado, T. Chase, P. Granitzka, K. Carva, R. Li, J. Li, L. Wu, T. Vecchione, T. Liu, Z. Chen, D. J. Higley, N. Hartmann, R. Coffee, J. Wu, G. L. Dakovski, W. F. Schlotter, H. Ohldag, Y. K. Takahashi, V. Mehta, O. Hellwig, A. Fry, Y. Zhu, J. Cao, E. E. Fullerton, J. Stöhr, P. M. Oppeneer, E. Jal, X. J. Wang, and H. A. Dürr, “Beyond a phenomenological description of magnetostriction,” *Nature Communications*, vol. 9, 2018, doi: [10.1038/s41467-017-02730-7](https://doi.org/10.1038/s41467-017-02730-7).
- [357] A. E. Green and R. S. Rivlin, “On Cauchy’s equations of motion,” in *Collected Papers of R. S. Rivlin*, G. I. Barenblatt and D. D. Joseph, Eds. New York: Springer, 1997, pp. 1359–1361, doi: [10.1007/978-1-4612-2416-7_83](https://doi.org/10.1007/978-1-4612-2416-7_83).
- [358] D. Royer and E. Dieulesaint, *Elastic waves in solids 1 - free and guided propagation*. Berlin Heidelberg: Springer-Verlag, 2000.
- [359] W. V. Chaves, “The Fundamental Equations of Continuum Mechanics,” in *Notes on Continuum Mechanics*, 1st ed. Springer, 2013, ch. 5, pp. 297–301, doi: [10.1007/978-94-007-5986-2](https://doi.org/10.1007/978-94-007-5986-2).
- [360] F. R. Blom, “Dependence of the quality factor of micromachined silicon beam resonators on pressure and geometry,” *Journal of Vacuum Science & Technology B: Microelectronics and Nanometer Structures*, vol. 10, no. 1, pp. 19–26, 1992, doi: [10.1116/1.586300](https://doi.org/10.1116/1.586300).
- [361] J. E. Sader, “Frequency response of cantilever beams immersed in viscous fluids with applications to the atomic force microscope,” *Journal of Applied Physics*, vol. 84, no. 1, pp. 64–76, 1998, doi: [10.1063/1.368002](https://doi.org/10.1063/1.368002).

- [362] C. P. Green and J. E. Sader, “Torsional frequency response of cantilever beams immersed in viscous fluids with applications to the atomic force microscope,” *Journal of Applied Physics*, vol. 92, no. 10, pp. 6262–6274, 2002, doi: [10.1063/1.1512318](https://doi.org/10.1063/1.1512318).
- [363] J. F. Vignola, J. A. Judge, J. Jarzynski, M. Zalalutdinov, B. H. Houston, and J. W. Baldwin, “Effect of viscous loss on mechanical resonators designed for mass detection,” *Applied Physics Letters*, vol. 88, no. 4, 2006, doi: [10.1063/1.2165186](https://doi.org/10.1063/1.2165186).
- [364] S. Gorelick, J. R. Dekker, M. Leivo, and U. Kantojärvi, “Air damping of oscillating MEMS structures: modeling and comparison with experiment,” in *Proceeding of the 2013 COM-SOL Conference in Rotterdam*, Rotterdam, 2013, pp. 1–6.
- [365] A. T. Liem, C. Ti, V. Kara, A. B. Ari, J. G. McDaniel, and K. L. Ekinici, “Acoustic radiation of MEMS and NEMS resonators in fluids,” *Journal of Applied Physics*, vol. 129, no. 6, 2021, doi: [10.1063/5.0037959](https://doi.org/10.1063/5.0037959).
- [366] R. Lifshitz and M. L. Roukes, “Thermoelastic damping in micro- and nanomechanical systems,” *Physical Review B*, vol. 61, no. 8, pp. 5600–5609, 2000, doi: [10.1103/PhysRevB.61.5600](https://doi.org/10.1103/PhysRevB.61.5600).
- [367] Y. B. Yi, “Geometric effects on thermoelastic damping in MEMS resonators,” *Journal of Sound and Vibration*, vol. 309, no. 3–5, pp. 588–599, 2008, doi: [10.1016/j.jsv.2007.07.055](https://doi.org/10.1016/j.jsv.2007.07.055).
- [368] X. Guo, Y. B. Yi, and S. Pourkamali, “A finite element analysis of thermoelastic damping in vented MEMS beam resonators,” *International Journal of Mechanical Sciences*, vol. 74, pp. 73–82, 2013, doi: [10.1016/j.ijmecsci.2013.04.013](https://doi.org/10.1016/j.ijmecsci.2013.04.013).
- [369] J. A. Judge, D. M. Photiadis, J. F. Vignola, B. H. Houston, and J. Jarzynski, “Attachment loss of micromechanical and nanomechanical resonators in the limits of thick and thin support structures,” *Journal of Applied Physics*, vol. 101, no. 1, 2007, doi: [10.1063/1.2401271](https://doi.org/10.1063/1.2401271).
- [370] B. Chouvion, S. McWilliam, A. A. Popov, and C. Fox, “Review and comparison of different support loss models for micro-electro-mechanical systems resonators undergoing in-plane vibration,” *Journal of Mechanical Engineering Science*, vol. 226, pp. 283–295, 2011, doi: [10.1063/1.2401271](https://doi.org/10.1063/1.2401271).
- [371] M. Pandey, R. B. Reichenbach, A. T. Zehnder, A. Lal, and H. G. Craighead, “Reducing anchor loss in MEMS resonators using mesa isolation,” *Journal of Microelectromechanical Systems*, vol. 18, no. 4, pp. 836–844, 2009, doi: [10.1109/JMEMS.2009.2016271](https://doi.org/10.1109/JMEMS.2009.2016271).
- [372] W. K. Blake, “The radiation from free-free beams in air and in water,” *Journal of Sound and Vibration*, vol. 33, no. 4, pp. 427–450, 1974, doi: [10.1016/S0022-460X\(74\)80227-0](https://doi.org/10.1016/S0022-460X(74)80227-0).
- [373] E. G. Williams, “A series expansion of the acoustic power radiated from a planar source,” *The Journal of the Acoustical Society of America*, vol. 73, no. 5, pp. 1520–1524, 1983, doi: [10.1121/1.389412](https://doi.org/10.1121/1.389412).
- [374] J. Yang, T. Ono, and M. Esashi, “Energy dissipation in submicrometer thick single-crystal silicon cantilevers,” *Journal of Microelectromechanical Systems*, vol. 11, no. 6, pp. 775–783, 2002, doi: [10.1109/JMEMS.2002.805208](https://doi.org/10.1109/JMEMS.2002.805208).
- [375] J. Yang, “Surface dissipations in NEMS/MEMS,” in *Encyclopedia of Nanotechnology*, B. Bhushan, Ed. Dordrecht: Springer Science and Business Media, 2016, doi: [10.1007/978-94-007-6178-0_101000-1](https://doi.org/10.1007/978-94-007-6178-0_101000-1).
- [376] F. Lochon, I. Dufour, and D. Rebière, “Influence of losses on microcantilever-based chemical sensor design,” in *Euroensors XIX*, Barcelone, Spain, 2005, doi: [available online](https://doi.org/10.1007/978-3-540-28111-1_10).

- [377] M. Weinberg, R. Candler, S. Chandorkar, J. Varsanik, T. Kenny, and A. Duwel, "Energy loss in MEMS resonators and the impact on inertial and RF devices," in *Transducers 2009 - 2009 International Solid-State Sensors, Actuators and Microsystems Conference*. Denver, CO, USA: IEEE, 2009, pp. 688–695, doi: [10.1109/SENSOR.2009.5285418](https://doi.org/10.1109/SENSOR.2009.5285418).
- [378] R. Abdolvand, B. Bahreyni, J. E. Y. Lee, and F. Nabki, "Micromachined resonators: a review," *Micromachines*, vol. 7, no. 9, 2016, doi: [10.3390/mi7090160](https://doi.org/10.3390/mi7090160).
- [379] N. Nakamura, "Extended rayleigh damping model," *Frontiers in Built Environment*, vol. 2, 2016, doi: [10.3389/fbuil.2016.00014](https://doi.org/10.3389/fbuil.2016.00014).
- [380] S. Onitsuka, Y. Ushio, N. Ojima, and T. Iijima, "Modeling method of element Rayleigh damping for the seismic analysis of a 3D FEM model with multiple damping properties," *Journal of Vibration and Control*, vol. 24, no. 17, 2018, doi: [10.1177/1077546317718969](https://doi.org/10.1177/1077546317718969).
- [381] G. A. Lesieutre, "Damping in fe models," in *Encyclopedia of Vibration*, S. Braun, Ed. Oxford: Elsevier, 2001, pp. 321–327, doi: [10.1006/rwvb.2001.0021](https://doi.org/10.1006/rwvb.2001.0021).
- [382] A. M. R. Ribeiro and J. M. M. Silva, "Free and forced vibration with viscous and hysteretic damping: a different perspective," in *5th international conference on mechanics and materials in design*, Porto, Portugal, 2006, doi: [10.13140/2.1.3019.5207](https://doi.org/10.13140/2.1.3019.5207).
- [383] D. J. Inman and C. H. Park, "Damping: an introduction to viscoelastic models," in *Modal Analysis and Testing*, J. M. M. Silva and N. M. M. Maia, Eds. Springer, Dordrecht, 1999, pp. 395–408, doi: [10.1007/978-94-011-4503-9_19](https://doi.org/10.1007/978-94-011-4503-9_19).
- [384] G. Genta and N. Amati, "Hysteretic damping in rotordynamics : An equivalent formulation," *Journal of Sound and Vibration*, vol. 329, no. 22, pp. 4772–4784, 2010, doi: [10.1016/j.jsv.2010.04.036](https://doi.org/10.1016/j.jsv.2010.04.036).
- [385] T. Liu, T. Zordan, Q. Zhang, and B. Briseghella, "Equivalent viscous damping of bi-linear hysteretic oscillators," *Journal of Structural Engineering*, vol. 141, no. 11, 2015, doi: [10.1061/\(ASCE\)ST.1943-541X.0001262](https://doi.org/10.1061/(ASCE)ST.1943-541X.0001262).
- [386] T. L. Gilbert, "A phenomenological theory of damping in ferromagnetic materials," *IEEE Transactions on Magnetism*, vol. 40, no. 6, pp. 3443–3449, 2004, doi: [10.1109/TMAG.2004.836740](https://doi.org/10.1109/TMAG.2004.836740).
- [387] M. Lakshmanan, "The fascinating world of the Landau-Lifshitz-Gilbert equation: an overview," *Philosophical Transactions of the Royal Society A: Mathematical, Physical and Engineering Sciences*, vol. 369, no. 1939, pp. 1280–1300, 2011, doi: [10.1098/rsta.2010.0319](https://doi.org/10.1098/rsta.2010.0319).
- [388] R. Kikuchi, "On the minimum of magnetization reversal time," *Journal of Applied Physics*, vol. 27, no. 11, pp. 1352–1357, 1956, doi: [10.1063/1.1722262](https://doi.org/10.1063/1.1722262).
- [389] Z. Diao, Z. Li, S. Wang, Y. Ding, A. Panchula, E. Chen, L. C. Wang, and Y. Huai, "Spin-transfer torque switching in magnetic tunnel junctions and spin-transfer torque random access memory," *Journal of Physics: Condensed Matter*, vol. 19, no. 16, 2007, doi: [10.1088/0953-8984/19/16/165209](https://doi.org/10.1088/0953-8984/19/16/165209).
- [390] M. Iwayama, T. Kai, M. Nakayama, H. Aikawa, Y. Asao, T. Kajiyama, S. Ikegawa, H. Yoda, and A. Nitayama, "Reduction of switching current distribution in spin transfer magnetic random access memories," *Journal of Applied Physics*, vol. 103, no. 7, 2008, doi: [10.1063/1.2838140](https://doi.org/10.1063/1.2838140).

- [391] R. F. L. Evans, D. Hinzke, U. Atxitia, U. Nowak, R. W. Chantrell, and O. Chubykalo-Fesenko, “Stochastic form of the Landau-Lifshitz-Bloch equation,” *Physical Review B*, vol. 85, no. 1, 2012, doi: [10.1103/PhysRevB.85.014433](https://doi.org/10.1103/PhysRevB.85.014433).
- [392] J. M. Barandiarán, A. García-Arribas, and J. Gutiérrez, “Magnetic anisotropy distribution in transverse and obliquely field annealed amorphous ribbons,” *Journal of Magnetism and Magnetic Materials*, vol. 133, no. 1-3, pp. 46–48, 1994, doi: [10.1016/0304-8853\(94\)90485-5](https://doi.org/10.1016/0304-8853(94)90485-5).
- [393] A. García-Arribas, E. Fernández, I. Orue, and J. M. Barandiaran, “Determination of the distribution of transverse magnetic anisotropy in thin films from the second harmonic of Kerr signal,” *Applied Physics Letters*, vol. 103, no. 14, 2013, doi: [10.1063/1.4824647](https://doi.org/10.1063/1.4824647).
- [394] T. M. L. Alves, C. G. Bezerra, A. D. C. Viegas, S. Nicolodi, M. A. Corrêa, and F. Bohn, “Quantifying magnetic anisotropy dispersion: theoretical and experimental study of the magnetic properties of anisotropic FeCuNbSiB ferromagnetic films,” *Journal of Applied Physics*, vol. 117, no. 8, 2015, doi: [10.1063/1.4913249](https://doi.org/10.1063/1.4913249).
- [395] B. Spetzler, C. Kirchhof, J. Reermann, P. Durdaut, M. Höft, G. Schmidt, E. Quandt, and F. Faupel, “Influence of the quality factor on the signal to noise ratio of magnetoelectric sensors based on the delta-E effect,” *Applied Physics Letters*, vol. 114, no. 18, 2019, doi: [10.1063/1.5096001](https://doi.org/10.1063/1.5096001).
- [396] G. Piazza, V. Felmetzger, P. Mural, R. H. O. Iii, and R. Ruby, “Piezoelectric aluminum nitride thin films for microelectromechanical systems,” *MRS Bulletin*, vol. 37, no. 11, pp. 1051–1061, 2012, doi: [10.1557/mrs.2012.268](https://doi.org/10.1557/mrs.2012.268).
- [397] M. Akiyama, T. Kamohara, K. Kano, A. Teshigahara, Y. Takeuchi, and N. Kawahara, “Enhancement of piezoelectric response in scandium aluminum nitride alloy thin films prepared by dual reactive cosputtering,” *Advanced Materials*, vol. 21, no. 5, pp. 593–596, 2009, doi: [10.1002/adma.200802611](https://doi.org/10.1002/adma.200802611).
- [398] M. Akiyama, K. Umeda, A. Honda, and T. Nagase, “Influence of scandium concentration on power generation figure of merit of scandium aluminum nitride thin films,” *Applied Physics Letters*, vol. 102, no. 2, 2013, doi: [10.1063/1.4788728](https://doi.org/10.1063/1.4788728).
- [399] S. Fichtner, T. Reimer, S. Chemnitz, F. Lofink, and B. Wagner, “Stress controlled pulsed direct current co-sputtered $\text{Al}_{1-x}\text{Sc}_x\text{N}$ as piezoelectric phase for micromechanical sensor applications,” *APL Materials*, vol. 3, no. 11, 2015, doi: [10.1063/1.4934756](https://doi.org/10.1063/1.4934756).
- [400] M. A. Caro, S. Zhang, T. Riekkinen, M. Ylilammi, M. A. Moram, O. Lopez-Acevedo, J. Molarius, and T. Laurila, “Piezoelectric coefficients and spontaneous polarization of ScAlN ,” *Journal of Physics: Condensed Matter*, vol. 27, no. 24, p. 245901, 2015, doi: [10.1088/0953-8984/27/24/245901](https://doi.org/10.1088/0953-8984/27/24/245901).
- [401] P. M. Mayrhofer, H. Euchner, A. Bittner, and U. Schmid, “Circular test structure for the determination of piezoelectric constants of $\text{Sc}_x\text{Al}_{1-x}\text{N}$ thin films applying laser doppler vibrometry and FEM simulations,” *Sensors and Actuators, A: Physical*, vol. 222, pp. 301–308, 2015, doi: [10.1016/j.sna.2014.10.024](https://doi.org/10.1016/j.sna.2014.10.024).
- [402] S. Fichtner, “Development of high performance piezoelectric $\text{Al}_{1-x}\text{Sc}_x\text{N}$ for microelectromechanical systems: towards a ferroelectric wurzite structure,” Ph.D. dissertation, Kiel University, 2019.
- [403] A. Cowe, G. Hames, K. Glukh, and B. Hardy, *PiezoMUMPs^(TM) Design Handbook*, 1st ed. MEMSCAP Inc., 2014, [available online](#).

-
- [404] G. Pillai, A. A. Zope, and S. S. Li, “Piezoelectric-based support transducer design to enable high-performance bulk mode resonators,” *Journal of Microelectromechanical Systems*, vol. 28, no. 1, pp. 4–13, 2019, doi: [10.1109/JMEMS.2018.2877784](https://doi.org/10.1109/JMEMS.2018.2877784).
- [405] J. McCord, “Progress in magnetic domain observation by advanced magneto-optical microscopy,” *Journal of Physics D: Applied Physics*, vol. 48, no. 33, 2015, doi: [10.1088/0022-3727/48/33/333001](https://doi.org/10.1088/0022-3727/48/33/333001).
- [406] A. Hubert and R. Schäfer, *Magnetic domains - the analysis of magnetic microstructures*, 3rd ed. Berlin Heidelberg: Springer Verlag, 2017, chapter 3.7.4, pp. 296–311, doi: [10.1007/978-3-319-59409-5_2](https://doi.org/10.1007/978-3-319-59409-5_2).
- [407] J. Tamayo, J. J. Ruz, V. Pini, P. Kosaka, and M. Calleja, “Quantification of the surface stress in microcantilever biosensors: revisiting Stoney’s equation,” *Nanotechnology*, vol. 23, no. 47, 2012, doi: [10.1088/0957-4484/23/47/475702](https://doi.org/10.1088/0957-4484/23/47/475702).

Acknowledgments

Finally, I would like to express my gratitude to everyone who directly or indirectly contributed to this work. I cordially thank Prof. Franz Faupel for the opportunity to work on such an interesting project and in particular his trust and support, which has permitted me to follow my own ideas and endeavors. I sincerely enjoyed working in his group "Chair for Multicomponent Materials", and thank all members, especially Ron-Marco Friedrich and Stefan Rehders for the stimulating discussions and the realization of experimental setups. At the beginning of the project, Sebastian Zabel provided me an excellent introduction to the sensor concept. Thank you a lot, Sebastian. Your critical thoughts leveraged the project, and I very much enjoyed our work together. It is a great pleasure to see the project now being continued by Fatih Ilgaz, and I feel that it is in best hands.

I would like to extend my gratitude to all members of the collaborative research center CRC 1261. The activities in this highly interdisciplinary research project have benefited considerably from the active thought exchange and collaborations with many colleagues from other groups and various disciplines. For always being on hand with words and deeds I thank Prof. Jeffrey McCord, Phillip Durdaut, Elizaveta Golubeva, Cai Müller, Christin Bald, Patrick Wiegand, Julius Schmalz, Lars Thormählen, Patrick Hayes and Dirk Meyners. Further, I would like to recognize the invaluable work of Christine Kirchhof, Anne Kittmann and Lars Thormählen from the group of Prof. Eckhard Quandt, who spent lots of hours in the clean room, as well as our colleagues from the ISIT, Jingxiang Su, Florian Niekiel, Simon Fichtner and Fabian Lofink. I would also like to thank Prof. Nian X. Sun and his group for always being welcome there. Especially, I must thank Alexei D. Matyushov for our fruitful discussions and collaboration on ΔE -effect sensors.

After all, this project would have turned out differently without the everlasting support and patience of Liza. Beyond her many direct contributions, I am deeply grateful for all our passionate discussions on the magic of magnetism and for her sharing life with me.



List of Figures

1.1	<p>(a) Simulated reduced magnetization $m := M/M_s$, defined by the magnetization M and saturation magnetization M_s, and plotted as a function of the applied magnetic flux density $\mu_0 H$. (b) Simulated reduced magnetization m as a function of uniaxial stress σ, which starts at the magnetization states marked in (a). (c) Corresponding magnetostriction λ calculated from the data in (b) via a quadratic approximation and normalized to the saturation magnetostriction λ_s. (d) Stress σ as a function of the total strain ε^0 calculated from λ in (c) and the mechanical strain e with Equation 1.1.</p>	8
1.2	<p>(a) Effective Young's modulus E, as a function of stress σ for various magnetic flux densities $\mu_0 H$, with the magnetic field H and vacuum permeability μ_0. The E-curves are obtained from the derivatives of the stress-strain curves in Fig. 1.1d, and they are normalized to the Young's modulus E_m at fixed magnetization. (b) Young's modulus $E(\mu_0 H)$ for two different stress values, σ_0 and σ_1. The red, bold lines in both plots indicate the minimum of E.</p>	9
2.1	<p>(a) Photograph (left) and illustration (right) of a surface acoustic wave (SAW) sensor element based on a quartz-crystal structure with a soft-magnetic FeCoSiB thin-film deposited on the delay line in between a pair of interdigital transducers. Image adapted from Ref. [148]. (b) Schematic structure (left) and top view (right) of a typical sensor element comprising a MEMS-fabricated, free-standing magnetoelectric composite cantilever. The piezoelectric layer is sandwiched by a rear-side electrode and two top electrodes that are as visible as white squares in the photograph. Image adapted from Ref. [132]; copyright 2019 by the American Physical Society. (c) Example of a free-standing magnetoelectric plate-resonator that is fabricated with standard MEMS technology. Interdigital electrodes shown in the schematic (top) are used to excite a higher-order bulk mode (bottom). Image adapted from Ref. [149].</p>	14
2.2	<p>(a) Schematic setup of an open-loop and a (b) closed-loop operation and read-out system. The sketch is adapted from [164].</p>	16
2.3	<p>(a) Simplified equivalent-circuit representation of an open-loop operation and read-out system adapted from [155]. It comprises an excitation source with output resistance R_{ex}, a sensor element with an impedance $Z_s = 1/Y_s$ that depends on the applied magnetic flux density $\vec{B}(t) = \mu_0 \vec{H}(t)$ (t: time, μ_0: magnetic vacuum permeability, \vec{H}: magnetic field), and a charge amplifier with an operational amplifier (OP) and a feedback impedance Z_f. The impedance of the two cables is denoted with Z_{C1} and Z_{C2}, respectively. (b) The example of a typical modified Butterworth-Van Dyke (mBvD) equivalent circuit as used in [146] to describe the electrical behavior of the sensor element.</p>	17

- 2.4 Example of measured sensor admittance Y_s as a function of excitation frequency f_{ex} compared with a Butterworth-van Dyke equivalent circuit fit. The mechanical eigenfrequency f_r obtained from the model is indicated. **(a)** Magnitude $|Y_s|$ of the electrical sensor admittance Y_s and magnitude $|\partial|Y_s|/\partial f_{\text{ex}}|$ of the derivative with respect to the excitation frequency f_{ex} . **(b)** Phase angle $\arg\{Y_s\}$ of Y_s and magnitude $|\partial\arg\{Y_s\}/\partial f_{\text{ex}}|$ of the derivative of the phase angle. 19
- 2.5 **(a)** Mechanical resonance frequency f_r as a function of the magnetic flux density B obtained from a series of admittance measurements and BvD fits as shown in Fig. 2.4. The measurement was started close to magnetic saturation at -5 mT . **(b)** The magnitude $|\partial f_r/\partial B|$ of the derivative of f_r with respect to the magnetic flux density B ; We refer to this derivative as the magnetic sensitivity S_m 21
- 2.6 Example spectra from measurements with a typical cantilever-based ΔE -effect magnetic field sensor around the resonance frequency $f_r = 9070\text{ Hz}$. **(a)** Voltage spectrum $\hat{U}_{\text{co}}(f)$ (f:frequency) of the output signal $u_{\text{co}}(t)$ of the charge amplifier with the applied magnetic test signal with a frequency of $f_{\text{ac}} = 10\text{ Hz}$, and voltage noise density spectrum $U_{\text{co}}(f)$ without the applied test signal; **(b)** amplitude spectrum $\hat{A}(f)$ of the amplitude demodulated signal $u_A(t)$ with the applied magnetic test signal and amplitude noise density spectrum $A(f)$ without the applied test signal. **(c)** Illustration of the voltage sensitivity S_V and the amplitude noise density A as a function of f_{ac} of an example sensor operated in the first and second bending mode (BM 1 and BM 2), where the sensor-intrinsic noise sources dominate the noise floor around f_r . The data in (c) are obtained from [146]. 23
- 8.1 **(a)** Cross-sectional illustration of a cantilever structure produced with MEMSCAP Inc.'s PiezoMUMPS design platform (not to scale). The sketch is adapted from Ref. [404]. **(b)** Top-view of a chip with test structures to analyze the feasibility of the proposed concept. It comprises two identical half-chips that can be separated at a predetermined breaking line in the middle. 202
- 8.2 **(a)** Optical microscopy image (top-view) of an example of an array of parallel sensor elements and **(b)** the corresponding measured magnitude of the admittance with a scatter of the resonance frequencies caused by the curved clamping region. An mBvD model is fitted to the measurements to characterize the resonance modes. **(c)** Representative example of the measured and fitted admittance magnitudes of three cantilevers where the silicon layer is extended to the edge of the cavity. A straight clamping region is visible in the example top-view photograph in the inset. 203
- 8.3 **(a)** Illustration of a deposition of the magnetic layer (blue) on top of the free-standing cantilever with a shadow mask. To avoid short circuits, high tolerances are required. **(b)** Light-microscopy image of the top of a typical cantilever of the sensor array. Atomic force microscopy (AFM) measurement of the oxidized Al top electrode, showing a high roughness. **(c)** Illustration of an alternative deposition from the rear side that avoids the rough top oxide and reduces the required tolerances of the shadow mask at the expense of potentially depositing magnetic material in unwanted regions around the clamping area of the cantilever. 204
- 8.4 **(a)** Scanning electron microscopy (SEM) image of the top of an example cantilever array on the chip processed with the PiezoMUMPS technology platform. **(b)** SEM image shows a close-up and **(c)** an overview of a rear-side corner of a cantilever with an approximately 200-nm-thick magnetic layer deposited on top. 205

- 8.5 **(a)** Magneto-optical Kerr effect (MOKE) microscopy images of two example cantilevers captured without an applied magnetic field. The MOKE sensitivity axis was set along the short axis of the cantilevers. The background image was captured in magnetic saturation with the magnetic field applied along the long axis of the cantilevers. Clamping of the cantilevers is indicated by the dashed lines. Close to the clamping, the cantilever is obscured by the inclined side of the etched trench. **(b)** Reduced magnetization curve M/M_s , as a function of the magnetic flux density $\mu_0 H$ applied along the long axis of the shorter cantilever. 206
- 8.6 Simulation and analysis of antisymmetric second-order bending mode of a free-free beam, following the method and model established in Section 4.4. The beam is $400\ \mu\text{m}$ long and $80\ \mu\text{m}$ wide, with an anchor length of $50\ \mu\text{m}$ and an anchor width $w = 30\ \mu\text{m}$ (except in (b)). **(a)** Rear-side view of mode shape and σ_{11} component of the stress tensor. **(b)** Simulated normalized frequency factors $\partial_c f_{r,ij}$ as a function of the anchor width w , to estimate the contribution of the stiffness tensor components C_{ij} to the resonance frequency f_r . **(c)** Simulation (*S1*) of the normalized resonance frequency $f_r/f_{r,\text{max}}$ as a function of the applied magnetic flux density $\mu_0 H$, with the magnetic field H and vacuum permeability μ_0 . A second simulation (*S2*) was performed where C_{66} was set constant to $C_{66} = C_{m,66}$ ($C_{m,66}$: value at fixed magnetization). **(d)** Relative magnetic sensitivity $S_{H,r}$ calculated from the data in (c) via Equation 1 (Section 4.4). 207

Appendices

Appendix A

Additional Calculations

A.1 Simplified Mean-Field Model

Energy Density Equation

One of the first models that described ferromagnetic hysteresis is the Stoner-Wohlfarth model [66]. Here, this model is extended by a simplified magnetoelastic energy density term that considers uniaxial stress σ . The extended total energy density is

$$u = u_K + u_Z + u_{me} = K_u \sin^2(\theta_H - \theta_K) - \mu_0 M_s H \cos(\theta_H) - \frac{3}{2} \lambda_s \sigma \cos^2(\theta_H - \theta_{me}). \quad (\text{A.1})$$

The uniaxial anisotropy energy density u_K with the first-order anisotropy energy density constant K_u defines a magnetic easy axis ($K_u > 0$). The Zeeman energy density u_Z describes the effect of a magnetic field with magnitude H and u_{me} represents the magnetoelastic energy density term that captures the effect of uniaxial stress with magnitude σ on the macrospin for a material with saturation magnetotrixtion λ_s . All angles θ_H , θ_K , and θ_{me} are defined in relation to the orientation of the applied magnetic field vector \vec{H} with magnitude H . Angle θ_H describes the orientation of the macrospin vector with magnitude M_s ; θ_K , the orientation of the magnetic easy axis; and θ_{me} , the orientation of the uniaxial stress. Hence, $(\theta_H - \theta_K)$ represents the orientation of the macrospin to the magnetic easy axis and $(\theta_H - \theta_{me})$, the orientation to the uniaxial stress. The quasi-static equilibrium orientation is found by numerically minimizing the energy density of the magnetization vector. A detailed and more general description of the energy density contributions is presented in Chapter 3.

Simulation Parameters

For the calculations in Section 1.2, we minimize Equation A.1 numerically to obtain θ_H at various values of applied H and σ . The examples are calculated using typical values for soft-magnetic amorphous FeCoSiB [115] $\mu_0 M_s = 1.5$ T, $\lambda_s = 35$ ppm. The magnetization was averaged over 500 uncoupled simulations with different values of K_u . The values are distributed following a normal distribution with a mean value of $K_u = 850$ J/m³ and a standard deviation of $\Delta K_u = 100$ J/m³. The easy axis is oriented at $\theta_K = 88^\circ$ to the applied magnetic field direction.

A.2 Resonance Detuning Effects

Different effects can potentially contribute to detuning a resonant ferromagnetic structure. Here, we consider the pole effect, change of cantilever length and curvature, and the effect of induced equilibrium stress. Simple estimations presented in this chapter confirm that the dominant contribution can be addressed to the ΔE effect arising from stress-induced Joule magnetostriction, which is discussed in detail in Chapter 3.

A.2.1 Magnetostrictive Elongation

The first bending resonance frequency of a cantilever, as obtained from the Euler-Bernoulli beam theory is a function of the cantilever's length L (Equation A.2). Consequently, a pure magnetostrictive elongation of the beam results in detuning of its natural frequency. For the estimation of the maximum-effect, the cantilever is assumed to be of a homogeneous ferromagnetic material with a constant Young's modulus E , cross section area A , density ρ and bending stiffness κ . The i^{th} eigenfrequency with the mode factor λ_i ($\lambda_1 \approx 1.875$) is then given by [137]

$$f_i = \frac{\lambda_i^2}{2\pi L^2} \sqrt{\frac{\kappa}{\rho A}} = \frac{\text{const.}}{L^2}. \quad (\text{A.2})$$

Here, an increase ΔL in length from L_0 to L_1 reduces the resonance frequency. If the strain originates from magnetostriction, it is given as

$$\lambda = \frac{\Delta L}{L_0} = \frac{L_1 - L_0}{L_0} \Rightarrow L_1 = L_0 + L_0 \lambda \quad (\text{A.3})$$

Using Equations A.2 and A.3, the relative change in the resonance frequency can be described by the magnetostrictive strain only as

$$\frac{\Delta f}{f_r} = -\frac{3\lambda}{1 + 3\lambda} \approx -3\lambda \quad (\text{A.4})$$

The maximum magnetostrictive strain of a ferromagnetic material is its saturation magnetostriction λ_s . Depending on the material, λ_s is in the range between 10^{-6} and 10^{-3} [128], and therefore, $\lambda_s \ll 1$. This justifies the approximation in Equation A.4. For FeCoSiB with $\lambda_s = 35 \cdot 10^{-6}$ [115] this results in a relative change of about $\frac{\Delta f}{f_r} \approx 10^{-4}$, which is less than one Hertz for a resonance at about 7000 Hz in the first bending mode. This estimation is only fully valid for a free ferromagnetic film. However, the sensor device is a composite structure, where the magnetostrictive strain rather bends the device and induces stress than elongates the cantilever homogeneously. Consequently, the frequency shift from the elongation is expected to be strongly overestimated.

A.2.2 Stress Stiffening and Geometric Nonlinearity

Detuning by Induced Stress

Magnetoelastic stress is induced on the magnetization of the ferromagnetic thin film. This magnetization-dependent stress can, in principle, influence the bending stiffness and thereby the natural frequency. The linear elasticity theory is not capable of this effect because it originates from geometric nonlinearity. The resulting bending stiffness as a function of equilibrium stress σ_{s0} along the long axis of the cantilever can be approximated for a mechanically isotropic material as [141]

$$\kappa(\sigma_{s0}) = \frac{Eh^3}{12(1-v^2)} - \frac{vhh_s(h-h_s)}{6(1-v)}\sigma_{s0} - \frac{(1-v-2v^2)h_s^2(4h+5h_s)}{30E(1-v)(h-h_s)}\sigma_{s0}^2, \quad (\text{A.5})$$

where h denotes the total beam thickness and h_s represents the thickness of the substrate. In the absence of mechanical residual stress, and considering isotropic magnetostriction, the stress along the long axis is induced by a magnetization component along this axis. The maximum field-induced stress occurs if the material is saturated magnetically. In this case, the film stress is provided by the magnetoelastic stress component b_{11} . The specific value depends on the initial zero-stress configuration with respect to its magnetization configuration; however, it does not change over orders of magnitude. Using literature values, the film stress along the long axis is $\sigma_{s0} = -b_{11} \approx -6$ Mpa [115]. The eigenfrequency equation (Equation A.2) is used to estimate the shift of natural frequency. Instead of the multilayer composite cantilever, a homogeneous beam is considered with a constant Young's modulus $E_m = 150$ GPa and Poisson's ratio $\nu = 0.3$. This results in a relative frequency shift of

$$\frac{\Delta f}{f_r} = \frac{\sqrt{\kappa(\sigma_{s0})} - \sqrt{\kappa_0}}{\sqrt{\kappa_0}} \approx 10^{-6}. \quad (\text{A.6})$$

The estimation holds only if the film is completely constraint by the substrate and therefore no curvature occurs.

Effect of Curvature

Transverse curvature increases the bending stiffness of thin plates in contrasts to longitudinal curvature, substantially [142]. The magnetic easy axis of the ΔE -effect sensors is often aligned along the short cantilever axis (y-axis). Considering a strongly simplified picture, the magnetization at the zero magnetic field ($H = 0$) is oriented along that axis and induces a magnetostrictive strain resulting in a curvature along the y-axis of the beam. Applying a magnetic field in the longitudinal direction results in the reduction of magnetization and magnetostriction in the transverse direction (x-axis). The curvature decreases with decreasing magnetostriction along the y-direction, and it is accompanied by the softening of the effective bending stiffness. Whether the resonance frequency increases or decreases depends on the initial magnetostrictive state of the sample, and this is not known a priori. Here, only the described process is assumed, which does not influence the order of magnitude of this effect. In this case, the initial film strain equals the saturation magnetostriction λ_s . The relative stiffness change can be obtained from the relative change in the effective spring constant k of the beam [142]

$$\frac{\Delta k}{k} = \frac{L^2 \beta^4}{60 \eta^2} e^{-c\beta} (\kappa_y - \nu \kappa_x)^2, \quad (\text{A.7})$$

with height-to-length ratio $\eta = h/L$ and width-to-length ratio $\beta = b/L$. This equation is valid only for a homogeneous beam with Poisson's ratio ν . For the estimation, it is assumed to be $\nu \approx 0.3$, which does not change the order of magnitude of the effect. The numerically determined constant c depends on the vibrational mode and considers a reduced curvature at the clamping. For the first (fundamental) bending mode, it is $c \approx 3.095$. The maximum curvature in the x- and y- direction is represented by κ_x and κ_y , respectively [407]. A completely unstrained initial state and a final magnetized state with magnetostrictive strains $\lambda_y = \lambda_s$ and $\lambda_x = -\frac{1}{2}\lambda_s$ is considered for the estimation. The maximum curvature results for a free plate and it is calculated using [143]:

$$\kappa_{x,y} t_s = \frac{6 \lambda_{x,y} (1 + \zeta)}{(\chi \zeta)^{-1} + 4(1 + \zeta^2) + \chi \zeta^3 + 6\zeta}, \quad (\text{A.8})$$

$$\chi = \frac{E_f (1 - \nu_s^2)}{E_s (1 - \nu_f^2)}. \quad (\text{A.9})$$

In (A.8), $\zeta = t_f/t_s$ represents the ratio of the film-to-substrate thickness and E_f and E_s represent the corresponding Young's moduli with Poisson's ratios ν_f and ν_s , respectively. This results in

curvatures of $\kappa_x \approx 0.17 \text{ m}^{-1}$ and $\kappa_y \approx -0.08 \text{ m}^{-1}$. With these curvatures and Equation A.7, a relative stiffness change of $\Delta k/k \approx 5 \cdot 10^{-8}$ can be estimated, which corresponds to a relative change in the resonance frequency of $\Delta f/f_r \approx 5 \cdot 10^{-6} \%$.

A.2.3 Pole Effect

The pole effect describes how a resonator with a magnetic component effectively stiffens in an applied magnetic field. We consider a cantilever covered by a magnetic thin film with magnetization along its longitudinal axis. The energy per unit length can be expressed using the area of cross section A_f of the film [145]

$$U(x) = K_s A \sin^2 \phi(x) - \mu_0 H M_s A_f \cos(\theta(x) - \phi(x)), \quad (\text{A.10})$$

where the first term represents the shape anisotropy, which is approximated using the shape anisotropy coefficient $K_s = \frac{1}{2} \mu_0 M_s^2$. Thus, the equation is valid for the approximation of an infinitely thin film compared to that of other dimensions. Further, ϕ represents the angle at which the magnetic moment cants out of plane. The second term is the Zeeman energy with θ representing the cantilever angle to the field vector; this angle depends on position x along the cantilever and varies among different mode shapes. Consequently, U is a function of position. No intrinsic anisotropy is considered here, and this is a suitable approximation for the ΔE -effect sensors because the out-of-plane shape anisotropy coefficient is considerably larger than the induced anisotropy. The equilibrium angular orientation is obtained from the force equilibrium condition $\partial U / \partial \phi = 0$ as a function of the cantilever orientation θ . An analytical expression can be found using a small angle approximation, and it is justified because of the large shape anisotropy coefficient. Similarly, the local torque $\tau(x)$ can be obtained as a function of ϕ by minimizing U with respect to θ . Merging both equations $\tau(x)$ can be expressed as a function of the local cantilever orientation θ , which is known for a given mode shape from the Euler-Bernoulli beam theory. The total torque T on the cantilever is obtained by integration of $\tau(x)$ over the beam length, which results for the first bending mode in [145]

$$T = 0.785 \mu_0 M_s^2 V \frac{H}{M_s + H} \left(\frac{d}{L} \right). \quad (\text{A.11})$$

Consequently, the torque increases linearly with the tip deflection d and the volume of magnetic material V . The constant arises directly from the integration over the x -dimension. Using T , the stiffening of the cantilever can be described by the change Δk of the effective spring constant k_0 with

$$\Delta k = \frac{1}{L_{\text{eff}}} \left(\frac{\partial T}{\partial d} \right). \quad (\text{A.12})$$

In this equation, L_{eff} represents the effective beam length, which is characteristic for a specific bending mode. For the first mode, it is $L_{\text{eff}} = 0.725L$. Combining Equation A.11 and Equation A.12, the relative change of frequency can be expressed as [145]

$$\frac{\Delta f}{f_r} = \frac{1}{2} \frac{\Delta k}{k_0} = \frac{1.085 A_f \mu_0 M_s^2}{L k_0} \left(\frac{H}{H + M_s} \right) \quad (\text{A.13})$$

This result is only valid for $\Delta k/k_0 \ll 1$ because of the linearization used in Equation A.13. Further, the relative change in the natural frequency is independent of the tip deflection, which is a direct consequence of the linear dependency of T on d in Equation A.11. The result is only valid for small beam deflections. Nevertheless, the relative resonance shift is nonlinear with H , and it arises from the parenthetical term in Equation A.13. This nonlinearity originates from the out-of-plane canting of the magnetization vector, which essentially reduces the relative frequency

shift at large fields where the shape anisotropy is successively overcome. Consequently, an upper limit exists at which the magnetization is always oriented along H . Thus, Equation A.13 becomes

$$\lim_{H \rightarrow \infty} \frac{\Delta f(H)}{f_r} = 1.084 A_f \frac{\mu_0 M_s^2}{L k_0}. \quad (\text{A.14})$$

The effective spring constant $k_0 = 3\kappa_{\text{eff}}/L^3$ of the beam, defined by the ratio of force applied on the tip and the corresponding tip displacement, is used for the calculation. The effective flexural rigidity of the multilayer cantilever is obtained from a sum over all layers with the Young's modulus E_i and second moment of area I_i of the i^{th} layer. If the substrate is significantly thicker than the magnetic thin film, it dominates the mechanical behavior. Then, the flexural rigidity can be further simplified to

$$\kappa_{\text{eff}} := \sum E_i I_i \approx E_s \frac{bh}{12}, \quad (\text{A.15})$$

with the Young's modulus E_s of the substrate, width b , and total thickness h of the cantilever. Using k_0 and Equation A.15, Equation A.16 can be expressed as

$$\lim_{H \rightarrow \infty} \frac{\Delta f(H)}{f_r} \approx \frac{4\mu_0 M_s^2 L^2 t_f}{E_s t_s} \text{ for } (t_f \ll t_s), \quad (\text{A.16})$$

with the magnetic layer thickness t_f and substrate thickness t_s . For a realistic estimation, we consider a cantilever with length $L = 3 \text{ mm}$, $\mu_0 M_s = 1.5 \text{ T}$, $t_f = 2 \mu\text{m}$, $t_s = 50 \mu\text{m}$, and $E_s = 150 \text{ GPa}$, and $\lambda_s = 35 \text{ ppm}$. This results in the maximum relative frequency shift of about $\Delta f/f_r \approx 6 \cdot 10^{-3}$. However, this requires flux densities in the tesla range. For small fields on the order of a few millitesla, shifts occur in the range of $\Delta f/f_r \approx 10^{-6}$.

A.3 Note on Cauchy's Equation of Motion

A simple explanation of Cauchy's equation of motion is provided to illustrate its connection with Newton's second law. Newton's second law for a system with a mass m that is constant in time is

$$\bar{F} = m\bar{a}, \quad (\text{A.17})$$

with the force vector \bar{F} , and the acceleration $\bar{a} := d^2\bar{u}/dt^2$, which is defined as the second derivative of the displacement vector with respect to time t . The right-hand side of Equation A.17 can be formulated as

$$m\bar{a} = \frac{d^2\bar{u}}{dt^2} \int \rho \cdot dV \quad (\text{A.18})$$

by expressing the acceleration using the displacement vector \bar{u} and the mass in terms of the volume integral over the mass density ρ . The force

$$\bar{F} = \int \bar{\nabla}\sigma dV + f_V, \quad (\text{A.19})$$

on the left-hand side of Equation A.17 is described by the gradient $\bar{\nabla}\sigma$ of the stress tensor σ integrated over the volume (surface forces), superposed by all forces f_V that are constant throughout the volume (body forces). A typical example for the latter includes the gravitational force, which can often be ignored for small structures. Inserting Equations A.18 and A.19 into Equation A.17 yields

$$\int \bar{\nabla}\sigma dV + f_V = \frac{d^2\bar{u}}{dt^2} \int \rho \cdot dV. \quad (\text{A.20})$$

Approximating $f_V \approx 0$ and integrating the equation to cancel out the volume, we arrive at a simple form of Cauchy's equation of motion (or Cauchy's momentum equation):

$$\rho \frac{d^2\bar{u}}{dt^2} = \bar{\nabla}\sigma. \quad (\text{A.21})$$

In contrast to the original form of Newton's second law, Equation A.21 can be easily expressed as a function of only the displacement field \bar{u} , which makes it convenient for computational purposes. This becomes evident when considering the example of a linear elastic material with the constitutive relation

$$\sigma_{ij} = C_{ijkl}\varepsilon_{kl} \quad \text{with} \quad \varepsilon_{kl} = \frac{1}{2} \left(\frac{\partial u_k}{\partial x_l} + \frac{\partial u_l}{\partial x_k} \right), \quad (\text{A.22})$$

with the components C_{ijkl} of the stiffness tensor, ε_{kl} of the linear strain tensor, u_i of the displacement vector, and the spatial coordinates x_i .

Appendix B

Additional Publications

B.1 Love-Wave Magnetic-Field Sensor Modeling

Contribution

- Modeling (shared)

Love Wave Magnetic Field Sensor Modeling – from 1D to 3D Model

Julius Schmalz*, Benjamin Spetzler†, Franz Faupel† and Martina Gerken*

*Institute of Electrical Engineering and Information Technology

Kiel University, Kaiserstraße 2, 24143 Kiel, Germany

Email: {jusc, mge}@tf.uni-kiel.de

†Institute for Materials Science

Kiel University, Kaiserstraße 2, 24143 Kiel, Germany

Email: {besp, ff}@tf.uni-kiel.de

Abstract—Three different finite element method (FEM) models of a surface acoustic wave (SAW) based magnetic field sensor with increasing complexity from one dimensional to three dimensional model are presented and compared. These sensors are designed to measure weak biomagnetic fields in an unshielded environment at room temperature, using a magnetostrictive layer at the surface to convert a magnetic signal to a change in SAW velocity.

Index Terms—SAW, Love wave, magnetic field sensor, FEM

I. INTRODUCTION

Wearable sensors for contact-free measurement of brain or cardiac magnetic signals require a linear response over many orders of magnitude for unshielded measurements, as well as room-temperature operation, low power consumption and system miniaturization. One approach of a suitable sensor is a surface acoustic wave (SAW) based magnetic field sensor [1]. Section II introduces the SAW sensor principle [1]–[4]. The change of elastic constants with magnetization is known as the delta-E effect [5], [6]. Here, Love waves are utilized because the shear modulus of the magnetostrictive layer shows a large change upon application of an external magnetic field [8]. The sensitivity of the SAW sensors are calculated using different models, as presented in section III. Section IV discusses the results and compares the models.

II. SENSOR PRINCIPLE

The sensor consists of a piezoelectric quartz substrate with two interdigital transducers (IDT), a guiding layer consisting of fused silica (SiO_2), and a FeCoBSi magnetostrictive layer [7] in the region between the IDTs as shown in Fig. 1. In this delay-line configuration an electric signal at the IDT causes a deformation of the piezoelectric quartz substrate and excites a Love wave, i.e., a shear surface wave. To excite only Love waves an st-cut quartz is used. The wavelength and wave velocity in the propagation region with the magnetostrictive layer depend on the applied magnetic field. The transmitted wave is detected at the second IDT and the phase change due to a magnetic field is evaluated.

As depicted in Fig. 2, a bias field is applied to tune the sensor to its operating point. An applied magnetic field causes a phase delay due to a different wave velocity. This is caused by a reduced shear modulus μ of the magnetostrictive layer

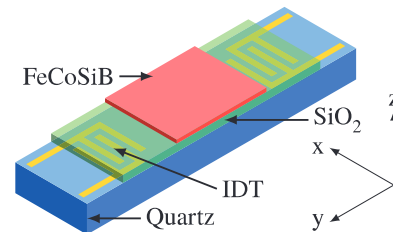


Fig. 1. The surface acoustic wave (SAW) sensor structure with substrate, interdigital transducers, guiding layer, and magnetostrictive layer is shown. The sensor dimensions are $14 \times 2.2 \text{ mm}^2$ with a delay line length of 3.8 mm. The IDT finger pitch is $28 \mu\text{m}$ and the finger width is $7 \mu\text{m}$.

due to the delta-E effect [1] and correspondingly a changed wave velocity of shear waves, which is given by $v_s = \sqrt{\mu/\rho}$ with the density ρ .

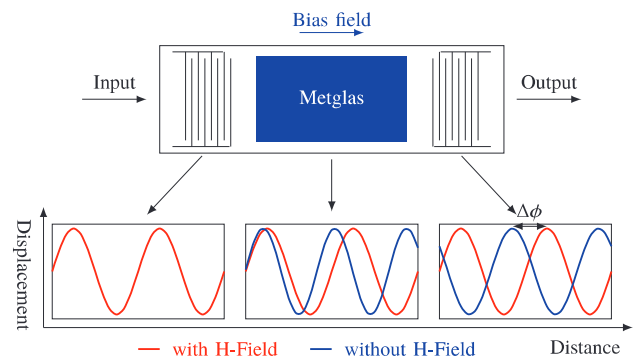


Fig. 2. Sensor principle using a delay line configuration. Due to the applied magnetic field a phase delay $\Delta\phi$ is caused being the indicator.

III. MODELS

Accurate simulations of the sensor are necessary for sensor design and optimization. They require a multiphysics approach and the finite element method (FEM, Comsol Multiphysics®) is used to solve the coupled electric-magnetic-mechanic problem employing different levels of simplification in the model.

There are other approaches for solving SAW devices, such as the use of an Legendre and Laguerre polynomials [9] or

solving the eigenvalue problem using the Inner-Node-Matrix and the Schur-Complement method [2]. However, these methods are less flexible to changes in the layer stack or geometry changes.

Here, the different modeling approaches with their equations and boundary conditions are presented. Common to all models, the small signal behavior is modeled using linear material equations. The effect of the magnetostrictive layer is simplified to a change in the elasticity tensor. Hence, the simulation does not contain equations for magnetic field and their coupling to the solid mechanics. For the three- and two-and-a-half-dimensional approaches there are unit cell models as well as delay line models, where the delay line of the SAW sensor is considered. The different use cases are examined in section IV.

A. One-dimensional (1D) model

The one-dimensional model only considers the thicknesses of the different layers and only uses isotropic material parameters. The mechanical system is described by Newton's law (1), the linear constitutive material equation (2) and the elastic relation (3).

$$\nabla \cdot \mathbf{T} = -\rho\omega^2 \vec{u} \quad (1)$$

$$\mathbf{T} = \mathbf{c}\mathbf{S} \quad (2)$$

$$\mathbf{S} = \frac{1}{2} \left[(\nabla \vec{u})^\top + \nabla \vec{u} \right] \quad (3)$$

Here, \vec{u} is the displacement in x , y and z direction, \mathbf{T} is the stress tensor, \mathbf{S} the strain tensor, \mathbf{c} the elasticity tensor, ω is the angular frequency and ρ the mass density.

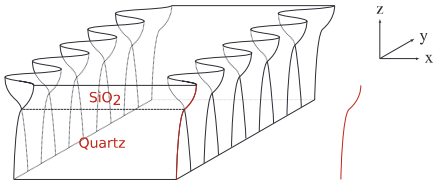


Fig. 3. Simplified view of the sensor with indicated Love wave displacement. The red line represents the one-dimensional approximation of the sensor which is considered for the calculation.

For an approximate calculation, the anisotropic parameters of the st-cut quartz substrate and the magnetostrictive layer are reduced to the isotropic values (Appendix A). In this isotropic approximation, the material parameters are only z dependent and the displacement is described by

$$u_2(k, z, \omega) = U(k, z, \omega)e^{i(kx - \omega t)} \quad (4)$$

with the wave vector k . After transformations and substitutions, we get the differential equation for Love waves [10]:

$$\frac{d}{dz} \left[c_{66}(z) \frac{dU}{dz} \right] = [k^2 c_{66}(z) - \omega^2 \rho(z)] U(k, z, \omega) \quad (5)$$

The boundary conditions are given as follows: The displacement must vanish for $z \rightarrow \infty$ and the mechanical stress T_{12} should be zero at the surface.

$$T_{12} = 2c_{66}S_{12} = c_{66} \frac{\partial u_1}{\partial u_2} \quad (6)$$

At the interface, continuity of displacement and continuity of stress are required. The c_{66} component is the corresponding shear modulus μ of this Love wave.

B. Three-dimensional (3D)

The three-dimensional model uses the full set of partial differential equations. Hence, anisotropic material parameters are incorporated. To reduce the computational complexity, only a thin slice of the geometry is modeled in a 3D model with only one mesh element in the third direction.

The 3D simulation of the ME-Sensor is performed using COMSOL Multiphysics® by implementing the following linear equations in the “general form partial differential equation” interface as a small-signal approximation.

Newton's law and Maxwell's equations are given by:

$$\nabla \cdot \mathbf{T} = -\rho\omega^2 \vec{u} \quad (7)$$

$$\nabla \cdot \vec{D} = 0 \quad (8)$$

$$\nabla \cdot \vec{B} = 0, \quad (9)$$

where \mathbf{T} is the stress tensor, ρ the mass density, ω the angular frequency, \vec{u} the displacement vector and \vec{D} , \vec{B} are the electric and magnetic flux density.

The linear constitutive material equations are:

$$\mathbf{T} = \mathbf{c}^{EH}\mathbf{S} - \mathbf{e}\vec{E} - \mathbf{e}_m^\top \vec{H} \quad (10)$$

$$\vec{D} = \mathbf{e}\mathbf{S} + \boldsymbol{\epsilon}\vec{E} + \boldsymbol{\alpha}\vec{H} \quad (11)$$

$$\vec{B} = \mathbf{e}_m\mathbf{S} + \boldsymbol{\alpha}\vec{E} + \boldsymbol{\mu}^S\vec{H}, \quad (12)$$

where \mathbf{S} is the strain tensor, \mathbf{c}^{EH} the stiffness tensor, \mathbf{e} , \mathbf{e}_m the strain to field coupling constants, \vec{E} , \vec{H} the electric and magnetic field, $\boldsymbol{\epsilon}$, $\boldsymbol{\mu}$ the permittivity and permeability, V the electric potential and V_m the magnetic potential.

The elasticity relations and scalar potentials are:

$$\mathbf{S} = 1/2 \left[(\nabla \vec{u})^\top + \nabla \vec{u} \right] \quad (13)$$

$$\vec{E} = -\nabla V \quad (14)$$

$$\vec{H} = -\nabla V_m. \quad (15)$$

With these equations, the resonance frequency, the stress distribution and the electrical voltage of the piezoelectric layer due to a magnetic excitation are calculated.

C. Two-and-a-half-dimensional (2.5D)

Compared to the interdigital electrode size, the width of the sensor is assumed as infinitely long. Hence, a plane strain approximation, assuming the out-of-plane strain to be zero, is an appropriate assumption. In contrast to a pure 2D model, a displacement in out-of-plane direction is allowed for the 2.5D model, which is the main component of the Love wave. This two-and-a-half-dimensional model reduces the amount of mesh knots and therefore the computational time significantly.

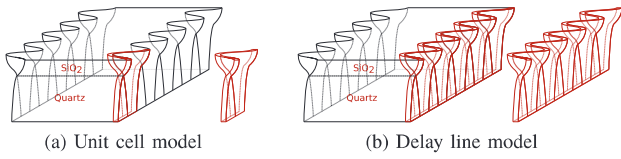


Fig. 4. Simplified view of the sensor with indicated Love wave displacement. The red line represents the three-dimensional approximation of the sensor which is considered for the calculation.

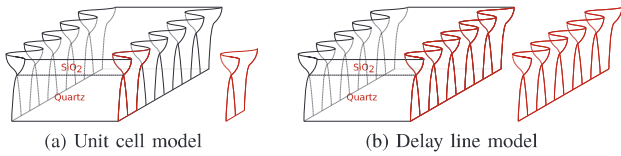


Fig. 5. Simplified view of the sensor with indicated Love wave displacement. The red line represents the two-and-a-half-dimensional approximation of the sensor which is considered for the calculation.

IV. RESULTS AND COMPARISON

For the comparison of the different models, a constant mesh size of $1\ \mu\text{m}$ is used for the FEM models. Nevertheless, the amount of elements increases with increased dimensionality. All simulations are performed on a server equipped with an Intel® Xeon® E5-2697A v4 processor running at 2.60 GHz and with 512 GB RAM. Table I shows an overview of the different models and Fig. 6 shows an overview of typical simulation results.

The main benefit of the one-dimensional model is its very fast computational time of 200 ms. This is achieved by the reduced complexity of the differential equations as shown in III-A. The drawback is the reduced accuracy due to the approximation of the material parameters to isotropic values. Fig. 6a shows the wave velocity for a given frequency range.

The elasticity tensor of the quartz substrate and the magnetostrictive layer are both anisotropic. Hence, it is necessary to use either an enhanced two-dimensional model or a three-dimensional model to consider this. Both, unit cell and delay line configuration of a three-dimensional model have relatively long simulation times compared to the one-dimensional model. A unit cell model takes 1000 ms and a delay line model with a length of 3.8 mm takes 100 min and needs 250 GB of memory. This large amount of memory and time consumption is caused by the high number of degrees of freedom. Another aspect of the delay line model is the post-processing to extract the wave velocity. A sine equation has to be fitted to the displacement to get the wavelength to calculate the phase velocity. In a three dimensional unit cell model on the other hand, the frequency has to be swept to get the resonant frequency for the given width of the cell.

A three-dimensional model simulating the full delay line length takes up to several hours using hundreds of GB of RAM due to a drastic increase of the complexity. However, the full three-dimensional model provides a very detailed view of the wave propagation including reflections at position of

layer changes, interference effects and more. This gives such a detailed simulation that the benefit of getting a deeper understanding of secondary wave propagation effects outweighs the costs of higher simulation times.

A two-and-a-half-dimensional model is a compromise between a three-dimensional and a one-dimensional model considering anisotropic material parameters. A unit cell model takes only 200 ms compared to 1000 ms for the three-dimensional case. This reduction in time is achieved by the reduction of mesh elements due to the reduced dimensionality, but with the ability to obtain a displacement field in the out of plane direction.

A delay line model takes 3200 ms to calculate and its specialty to show wave propagation effects along the delay line. In Fig. 6c a whole sensor of input interdigital transducer, delay line with magnetostrictive layer on top and output interdigital transducer is shown. The reflections and interferences are seen at each boundary change.

The use of fully anisotropic material parameters allows the investigation of the influence of the changed tensor elements of the magnetostrictive layer due to a magnetic field. Fig. 6b shows that for zero magnetic field the wave is a pure shear wave but for 1.36 mT there is a significant e_{yz} -component as shown in Fig. 6b. This influences the performance of the sensor and is only considered using a three- or two-and-a-half-dimensional model.

V. CONCLUSIONS

We presented different modeling approaches to calculate a surface acoustic wave sensor with a magnetostrictive layer on top of the delay line. Starting with a simple one-dimensional model with fast computation time but less accuracy to an optimized two-and-a-half-dimensional model with anisotropic material parameters. Whether a unit cell model or a delay line model should be used depends on the use case of the simulation. To investigate interference patterns at boundary discontinuities along the delay line or the inter digital transducers, a delay line model needs to be used. To calculate the sensitivity of the sensor, a unit cell model is sufficient.

APPENDIX A

MATERIAL PARAMETERS

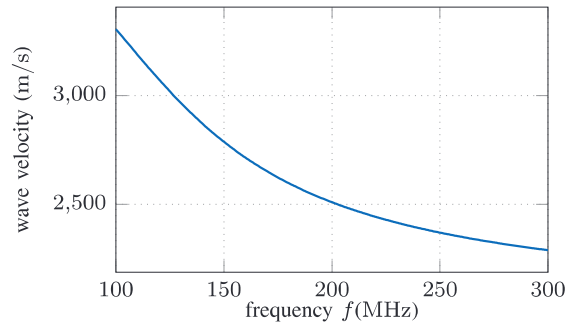
For one-dimensional model

$$\begin{aligned} \mu_{\text{Quartz}} &= 41.75\ \text{GPa}, \rho_{\text{Quartz}} = 2200\ \text{kg/m}^3, \\ \mu_{\text{SiO}_2} &= 33.35\ \text{GPa}, \rho_{\text{SiO}_2} = 2200\ \text{kg/m}^3, \\ \mu_{\text{MS}} &= 52.50\ \text{GPa}, \text{ and } \rho_{\text{MS}} = 7250\ \text{kg/m}^3. \end{aligned}$$

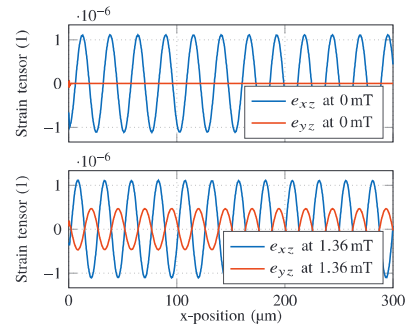
For 2.5D and 3D

St-cut quartz (SiO_2) rotated from [11]:

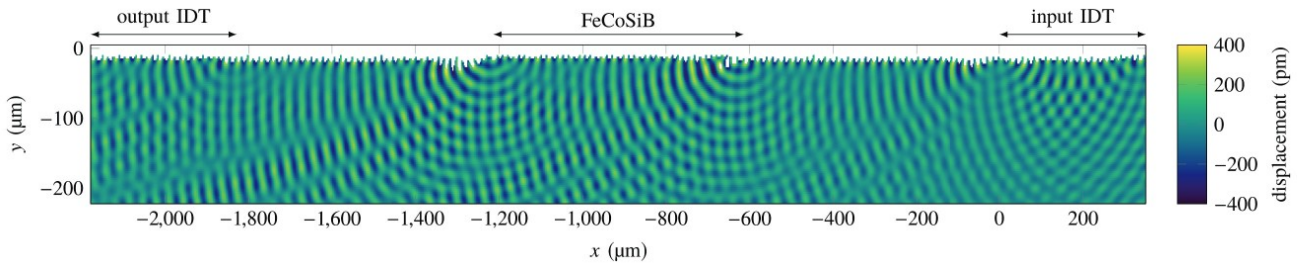
$$\begin{aligned} \mathbf{c}_{\text{Quartz}}^{EH} &= \begin{pmatrix} 86.74 & 27.49 & -8.60 & 1.05 & 0.00 & 0.00 \\ 27.49 & 96.64 & -4.81 & 13.44 & 0.00 & 0.00 \\ -8.60 & -4.81 & 130.74 & -1.84 & 0.00 & 0.00 \\ 1.05 & 13.44 & -1.84 & 41.22 & 0.00 & 0.00 \\ 0.00 & 0.00 & 0.00 & 0.00 & 30.35 & 7.58 \\ 0.00 & 0.00 & 0.00 & 0.00 & 7.58 & 67.50 \end{pmatrix} \text{GPa}, \\ \mathbf{e}_{\text{Quartz}} &= \begin{pmatrix} 0.17 & -0.04 & -0.13 & 0.08 & 0.00 & 0.00 \\ 0.00 & 0.00 & 0.00 & 0.00 & 0.07 & -0.10 \\ 0.00 & 0.00 & 0.00 & 0.00 & -0.07 & 0.11 \end{pmatrix} \text{N/Vm}, \end{aligned}$$



(a) 1D result showing the wave velocity v over a frequency range of 100–300 MHz.



(b) The e_{xz} - and e_{yz} -component of the strain tensor of a 3D SAW sensor with the material parameters of the magnetostrictive layer for 0 mT and for 1.36 mT.



(c) 2.5D result of a whole sensor with input IDT, delay line, magnetostrictive layer and output IDT. Reflections and interference patterns are visible at each boundary discontinuity. (Displacement field is clipped to 400 pm for better visibility.)

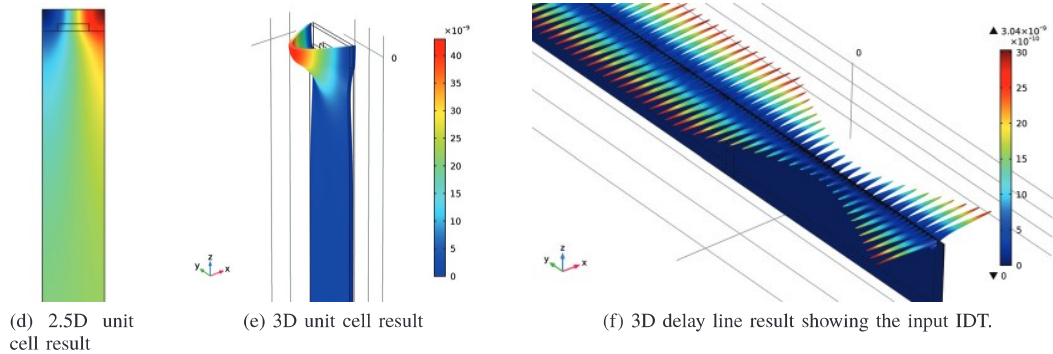


Fig. 6. Overview of typical results of the described models.

TABLE I
COMPARISON OF SIMULATION METHODS FOR LOVE WAVE BASED MAGNETIC FIELD SENSORS.

Method	Mat. Prop.	Comp.time	Memory usage	Pros	Cons
Love wave Eq.	1D isotropic	200 ms	1.5 GB	no post processing necessary	no delay line or other geometries
Unit cell FEM	2.5D anisotropic	200 ms	2.8 GB	fastest anisotropic model	freq sweep necessary to get f_{res}
	3D anisotropic	1000 ms	5.5 GB	-	freq sweep necessary to get f_{res}
Delay Line FEM	2.5D anisotropic	3200 ms	140 GB	wave propagation effects can be observed	sine fit of displacement necessary to get wave velocity
	3D anisotropic	100 min	220 GB	wave propagation effects can be observed	sine fit of displacement necessary to get wave velocity

$$\epsilon_{r, \text{Quartz}} = \begin{pmatrix} 4.43 & 0.00 & 0.00 \\ 0.00 & 4.54 & 0.10 \\ 0.00 & 0.10 & 4.52 \end{pmatrix},$$

$$\rho_{\text{Quartz}} = 2651 \text{ kg/m}^3.$$

Silica glass (SiO₂) [12]:

$$c_{\text{SiO}_2}^{EH} = \begin{pmatrix} 77.46 & 15.6 & 15.6 & 0 & 0 & 0 \\ 15.6 & 77.46 & 15.6 & 0 & 0 & 0 \\ 15.6 & 15.6 & 77.46 & 0 & 0 & 0 \\ 0 & 0 & 0 & 30.91 & 0 & 0 \\ 0 & 0 & 0 & 0 & 30.91 & 0 \\ 0 & 0 & 0 & 0 & 0 & 30.91 \end{pmatrix} \text{ GPa},$$

$$e_{\text{SiO}_2} = \begin{pmatrix} 0 & 0 & 0 & 0 & 0 & 0 \\ 0 & 0 & 0 & 0 & 0 & 0 \\ 0 & 0 & 0 & 0 & 0 & 0 \end{pmatrix} \text{ N/Vm},$$

$$\epsilon_{r, \text{SiO}_2} = \begin{pmatrix} 2.2 & 0.0 & 0.0 \\ 0.0 & 2.2 & 0.0 \\ 0.0 & 0.0 & 2.2 \end{pmatrix},$$

$$\rho_{\text{SiO}_2} = 2200 \text{ kg/m}^3.$$

Metglas (MG) [7]:

$$c_{\text{MG}}^{EH} = \begin{pmatrix} 202 & 86.5 & 86.5 & 0 & 0 & 0 \\ 86.5 & 202 & 86.5 & 0 & 0 & 0 \\ 86.5 & 86.5 & 202 & 0 & 0 & 0 \\ 0 & 0 & 0 & 57.7 & 0 & 0 \\ 0 & 0 & 0 & 0 & 57.7 & 0 \\ 0 & 0 & 0 & 0 & 0 & 57.7 \end{pmatrix} \text{ GPa},$$

$$e_{\text{MG}} = \begin{pmatrix} 0 & 0 & 0 & 0 & 0 & 0 \\ 0 & 0 & 0 & 0 & 0 & 0 \\ 0 & 0 & 0 & 0 & 0 & 0 \end{pmatrix} \text{ N/Vm},$$

$$\epsilon_{r, \text{MG}} = \begin{pmatrix} 1 & 0 & 0 \\ 0 & 1 & 0 \\ 0 & 0 & 1 \end{pmatrix},$$

$$\rho_{\text{MG}} = 7250 \text{ kg/m}^3.$$

ACKNOWLEDGMENT

This work was supported by the German Research Foundation (Deutsche Forschungsgemeinschaft, DFG) through the Collaborative Research Centre CRC 1261 *Magnetolectric Sensors: From Composite Materials to Biomagnetic Diagnostics*.

REFERENCES

- [1] A. Kittmann, P. Durdaut, S. Zabel, J. Reermann, J. Schmalz, B. Spetzler, D. Meyners, N. X. Sun, J. McCord, M. Gerken, G. Schmidt, M. Höft, R. Knöchel, F. Faupel, and E. Quandt, "Wide Band Low Noise Love Wave Magnetic Field Sensor System," *Scientific Reports*, vol. 8, no. 1, p. 278, dec 2018.
- [2] S. Zaglmayr, J. Schöberl, and U. Langer, "Eigenvalue Problems in Surface Acoustic Wave," *Progress in Industrial Mathematics at ECMI 2004*, pp. 74–98, 2006.
- [3] J. Schmalz, S. Zabel, E. Yarar, A. Kittmann, F. Faupel, E. Quandt, and M. Gerken, "Influence of a magnetostrictive layer on the mode shape and wave velocity of a Love-wave based SAW-device," in *3rd Euro Intelligent Materials*, 2017.
- [4] M. Inoue, S. Yamamoto, N. Fujita, and T. Fujii, "Local detection of magneto-surface-acoustic-wave in highly magnetostrictive amorphous film by light probing technique," *IEEE Transactions on Magnetics*, vol. 23, no. 5, pp. 3334–3336, 1987.
- [5] J. D. Livingston, "Magnetomechanical properties of amorphous metals," *physica status solidi (a)*, vol. 70, no. 2, pp. 591–596, apr 1982. [Online]. Available: <http://doi.wiley.com/10.1002/pssa.2210700228>
- [6] E. W. Lee, "Magnetostriction and Magnetomechanical Effects," *Reports on Progress in Physics*, vol. 18, no. 1, p. 305, jan 1955. [Online]. Available: <http://stacks.iop.org/0034-4885/18/i=1/a=305?key=crossref.a61b9abd3c8c20db2592051c27f0944e>
- [7] A. Ludwig and E. Quandt, "Optimization of the ΔE-effect in thin films and multilayers by magnetic field annealing," in *IEEE International Digest of Technical Papers on Magnetics Conference*. IEEE, 2002, p. AE2. [Online]. Available: <http://ieeexplore.ieee.org/document/1000626/>
- [8] Z. Sárközi, K. Mackay, and J. C. Peuzin, "Elastic properties of magnetostrictive thin films using bending and torsion resonances of a bimorph," *Journal of Applied Physics*, vol. 88, no. 10, pp. 5827–5832, nov 2000. [Online]. Available: <http://aip.scitation.org/doi/10.1063/1.1318388>
- [9] O. Bou Matar, N. Gasmí, H. Zhou, M. Goueygou, and A. Talbi, "Legendre and Laguerre polynomial approach for modeling of wave propagation in layered magneto-electro-elastic media," *The Journal of the Acoustical Society of America*, vol. 133, no. 3, pp. 1415–24, 2013.
- [10] L. D. Landau and E. M. Lifshitz, *Theory of Elasticity*, 2nd ed., ser. Course of theoretical physics. Oxford: Pergamon, 1970.
- [11] R. Bechmann, "Elastic and Piezoelectric Constants of Alpha-Quartz," *Physical Review*, vol. 110, no. 5, pp. 1060–1061, jun 1958. [Online]. Available: <https://link.aps.org/doi/10.1103/PhysRev.110.1060>
- [12] W. Pabst and E. Gregorová, "Elastic properties of silica polymorphs - A review," *Ceramics-Silikáty*, vol. 57, no. 3, pp. 167–184, 2013. [Online]. Available: http://www.ceramics-silikaty.cz/2013/2013_03_167.htm
- [13] J. L. Gugat, M. C. Krantz, and M. Gerken, "Two-Dimensional Versus Three-Dimensional Finite-Element Method Simulations of Cantilever Magnetolectric Sensors," *IEEE Transactions on Magnetics*, vol. 49, no. 10, pp. 5287–5293, 2013. [Online]. Available: <http://dx.doi.org/10.1109/TMAG.2013.2260346>

B.2 Multimode Love-Wave SAW Magnetic-Field Sensors

Contribution

- Modeling (shared)

Letter

Multi-Mode Love-Wave SAW Magnetic-Field Sensors

Julius Schmalz ^{1,*} , Anne Kittmann ² , Phillip Durdaut ³ , Benjamin Spetzler ⁴ ,
Franz Faupel ⁴ , Michael Höft ³ , Eckhard Quandt ² and Martina Gerken ¹ 

¹ Integrated Systems and Photonics, Institute of Electrical Engineering and Information Technology, Kiel University, Kaiserstraße 2, 24143 Kiel, Germany; mge@tf.uni-kiel.de

² Inorganic Functional Materials, Institute for Materials Science, Kiel University, Kaiserstraße 2, 24143 Kiel, Germany; anki@tf.uni-kiel.de (A.K.); eq@tf.uni-kiel.de (E.Q.)

³ Chair of Microwave Engineering, Institute of Electrical Engineering and Information Technology, Kiel University, Kaiserstraße 2, 24143 Kiel, Germany; pd@tf.uni-kiel.de (P.D.); mh@tf.uni-kiel.de (M.H.)

⁴ Multicomponent Materials, Institute for Materials Science, Kiel University, Kaiserstraße 2, 24143 Kiel, Germany; bsep@tf.uni-kiel.de (B.S.); ff@tf.uni-kiel.de (F.F.)

* Correspondence: jusc@tf.uni-kiel.de; Tel.: +49-431-880-6262

Received: 19 May 2020; Accepted: 14 June 2020; Published: 17 June 2020



Abstract: A surface-acoustic-wave (SAW) magnetic-field sensor utilizing fundamental, first- and second-order Love-wave modes is investigated. A 4.5 μm SiO_2 guiding layer on an ST-cut quartz substrate is coated with a 200 nm $(\text{Fe}_{90}\text{Co}_{10})_{78}\text{Si}_{12}\text{B}_{10}$ magnetostrictive layer in a delay-line configuration. Love-waves are excited and detected by two interdigital transducers (IDT). The delta-E effect in the magnetostrictive layer causes a phase change with applied magnetic field. A sensitivity of $1250^\circ/\text{mT}$ is measured for the fundamental Love mode at 263 MHz. For the first-order Love mode a value of $45^\circ/\text{mT}$ is obtained at 352 MHz. This result is compared to finite-element-method (FEM) simulations using one-dimensional (1D) and two-and-a-half-dimensional (2.5 D) models. The FEM simulations confirm the large drop in sensitivity as the first-order mode is close to cut-off. For multi-mode operation, we identify as a suitable geometry a guiding layer to wavelength ratio of $h_{\text{GL}}/\lambda \approx 1.5$ for an IDT pitch of $p = 12 \mu\text{m}$. For this layer configuration, the first three modes are sufficiently far away from cut-off and show good sensitivity.

Keywords: SAW; FEM; Love-wave; higher modes; multi-mode; magnetic-field sensing; delta-E effect

1. Introduction

Within the last 30 years, Love-wave-based SAW sensors have been proposed for (bio)chemical measurements [1–3]. These sensors use shear-wave surface modes (Love-waves) supported by a guiding layer. Recently, Love-wave SAW sensors have been developed for highly sensitive magnetic-field sensing [4–6] using either resonant [7,8] or delay-line structures [5,9–11]. In Love-wave magnetic-field sensors, the delay line of the SAW device is coated with a magnetostrictive (MS) layer as shown in Figure 1. The propagation delay line is between two interdigital electrodes (IDT), a transmitter and a receiver electrode. The wavelength of the wave generated at the transmitter IDT is given by the IDT finger pitch p , while the wave velocity depends on the layer thicknesses and material parameters. Due to the different layer stack of the delay-line region with the MS layer, the wave velocity and the wavelength decrease, before returning to its original velocity and wavelength at the receiver IDT. Applying a magnetic field changes the effective mechanical stiffness of the MS material via the delta-E effect [12–15]. This results in a change of the wave velocity and thereby in a magnetic field dependent phase change $\Delta\varphi$ as illustrated in Figure 1. From the phase change $\Delta\varphi$ the magnetic-field strength can be calculated. Besides other SAW sensors [5–7,16–18], the delta-E effect is used for magnetic-field sensing with piezoelectric composite resonators operating in bending or

bulk modes [19–22]. In contrast to such sensors, the sensitivity of Love-wave magnetic-field sensors is expected to benefit from shear-resonance, as the elastic modulus change of the magnetostrictive material was reported to be largest for shear stress [14]. A focus of current research is to maximize the sensitivity, which is essential to overcome thermal phase noise, thus allowing measurements of small amplitude magnetic fields. An increase in sensitivity can be achieved, e.g., with smaller wavelengths by adjusting the sensor geometry. With decreased wavelength and thus increased frequency, the wave energy concentrates further at the surface. By this, higher energies within the MS layer result in increased sensitivity, as the influence on the wave velocity of a magnetically induced elastic modulus change is increased. Because changing the sensor geometry implies production of new sensor types, modifications of existing sensors in terms of excitation is beneficial to increase the sensitivity. Higher harmonics can be used to excite waves with smaller wavelengths resulting in an increase in velocity variation [23]. As the sensitivity rises with decreased wavelength and increased frequency, an alternative approach is to investigate higher order Love-modes, optionally combined with multi-mode operation, to maximize the sensor sensitivity. In the present study, we analyze whether the use of higher order Love-modes increases the sensitivity and if multi-mode operation is possible with this approach. Here, we experimentally demonstrate magnetic-field sensor operation in the fundamental (0th order) mode and in the 1st order mode of a single sensor device and investigate the respective sensitivities. Furthermore, we compare the experimental results to finite-element-method (FEM) simulations of the 0th, 1st, and 2nd order mode. The results are of high importance for the development of SAW sensors for multi-mode operation.

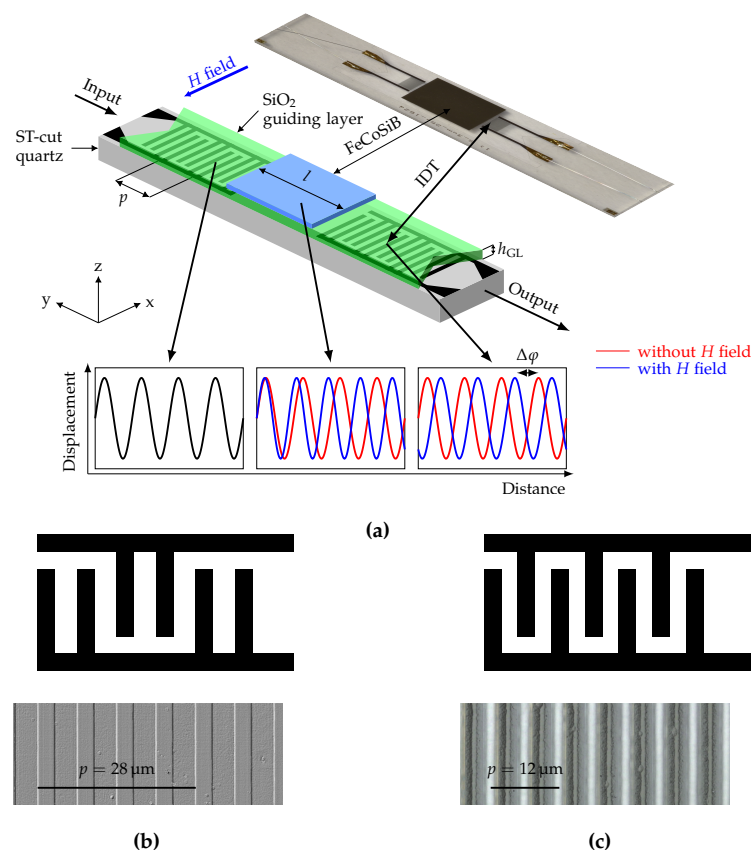


Figure 1. (a) Sensor schematic of a SAW-based magnetic-field delay-line sensor and photograph of fabricated sensor including the materials of the different layers and important design parameters. Microscope image and schematic overview of the interdigital transducer (IDT) structure (b) for a 28 μm pitch with double-finger electrodes and (c) for a 12 μm pitch with single-finger electrodes. The experimental data in this study is based on the 12 μm IDT pitch design. The 28 μm design is included for comparison and described in more detail in [5].

2. Experimental Data

For sensor fabrication, first interdigital transducer (IDT) electrodes are structured by ion-beam etching on a 500 μm ST-cut quartz substrate. The electrodes consist of 300 nm Au with 12 nm Cr adhesion layer to the substrate and to the guiding layer on top and are deposited via magnetron sputtering onto the quartz substrate. The sputter deposition rate is determined for all layers prior final sensor fabrication by profilometry. The IDT electrodes have 25 pairs in a single-finger structure with a periodicity of 12 μm and a finger width of 3 μm . For comparison, IDTs with 25 pairs of double-finger electrodes with a periodicity of 28 μm are used. Apart from the IDT structure, the fabrication process of the sensors is identical. The propagation direction is aligned orthogonal to the x -axis of the ST-cut quartz wafer for shear-wave excitation. A 4.5 μm thick SiO_2 guiding layer is deposited with a PECVD process covering the IDT electrodes. Finally, a 200 nm $(\text{Fe}_{90}\text{Co}_{10})_{78}\text{Si}_{12}\text{B}_{10}$ (FeCoSiB) magnetostrictive layer is deposited by magnetron sputtering from a single target with composition of $(\text{Fe}_{90}\text{Co}_{10})_{78}\text{Si}_{12}\text{B}_{10}$ and structured using a lift-off process [24] to yield the geometry shown in Figure 1. To promote adhesion and prevent oxidation, 10 nm Ta layers on both sides of the FeCoSiB layer were deposited. During deposition, a magnetic field is applied along the y -axis to saturate the film and introduce an easy axis of magnetization [11]. The total stack thicknesses for IDTs and MS layer (Cr/Au/Cr and Ta/FeCoSiB/Ta) are controlled by profilometer after structuring. The IDT pitch is chosen supporting the fundamental Love-wave mode and the 1st order mode in the guiding layer with 4.5 μm thickness. This permits excitation of both modes in the same device, while keeping all other material and geometry parameters the same. To achieve this, the IDT pitch and thus the wavelength need to be chosen sufficiently small to enable the wave guide to support higher order Love-wave modes. Hence, the smallest IDT pitch according to the manufacturing limits $p = 4 \mu\text{m}$ was chosen and the presence of the 1st mode for this was verified using the 2.5D FEM model described in Section 3.

For the determination of the magnetically induced phase shift, the sensor is placed in a homogeneous magnetic field of a solenoid, which in turn is placed in a magnetic-field shielding mu-metal cylinder ZG1 (Aaronia AG) to avoid significant offsets due to the earth's magnetic field. The calibrated solenoid is driven by a programmable current source (KEPCO BOP20-10ML) to successively generate magnetic flux densities B_{bias} between negative and positive saturation. Due to the expected hysteresis of the magnetic material, the measurement is performed for increasing ambient fields from -5 mT to 5 mT and vice versa. The static phase response of the sensor is determined with a lock-in amplifier UHFLI (Zurich Instruments) at a sensor input power of 0 dBm. The resulting phase responses are shown in Figure 2, in which blue lines correspond to a change of the magnetic flux density from negative to positive values and red lines from positive to negative values. Due to the significant group delay of the sensor $> 1 \mu\text{s}$, a single-frequency measurement of the phase leads to an ambiguity of $n \cdot 2\pi$. Therefore, the depicted phase responses (Figure 2) are each normalized to the value in magnetic saturation. The measured phase shift results from the delta-E effect, dominated here by the change of the shear modulus. The bias field dependent sensitivity S is given by the derivative of the measured phase change (Figure 2). The fundamental mode is at 263 MHz, exhibiting a maximum sensitivity of $1250^\circ/\text{mT}$ at a bias field of 0.6 mT. The 1st order mode is at 352 MHz and has a much lower maximum sensitivity of only $45^\circ/\text{mT}$ at a bias field of 0.7 mT. To explain this strong reduction in sensitivity, finite-element-method (FEM) simulations were carried out.

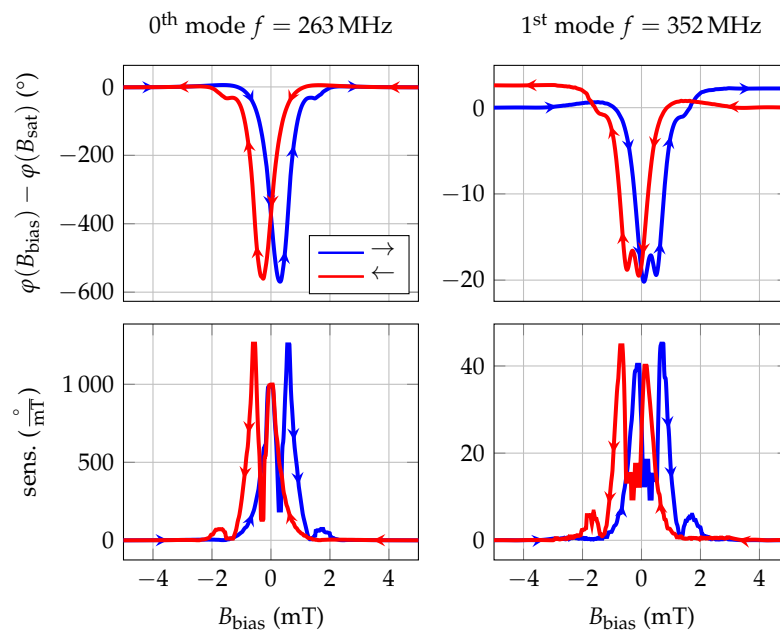


Figure 2. Experimental phase change and sensitivity derived from phase change for 0th and 1st order mode of a delay-line SAW sensor with IDT pitch $p = 12 \mu\text{m}$, guiding layer thickness $h_{\text{GL}} = 4.5 \mu\text{m}$ and magnetostrictive layer thickness $h_{\text{MS}} = 200 \text{nm}$. The arrow marks represent the direction of the magnetization process starting from a magnetically saturated state. The phase of the sensor in the magnetically saturated state is chosen as phase reference for the measurement.

The sensitivity of the fundamental mode measured here is only outperformed by the sensors described by Schell et al. [11] with $2000^\circ/\text{mT}$ using a magnetic anisotropy controlled magnetostrictive layer or sensors with higher MS layer thicknesses [24]. Potentially, using these more enhanced layers, the overall sensitivity of the sensor geometry in this study could even surpass the one described there due to its enhanced magnetic sensitivity. In the literature, various sensor types with lower performance have been described. Ganguly et al. [25] and Robbins and Simpson [26] started the development of SAW-based magnetically tunable phase shifters and did not provide a sensitivity value. To be able to classify their devices anyway, the sensitivities of up to $5^\circ/\text{mT}$ were extracted from the phase responses. Forester et al. [9] reported an enhanced SAW device with $240^\circ/\text{mT}$ (value extracted from phase response), while Li et al. [27] describe the performance by giving the maximum phase change of 0.64% and Yokokawa et al. [4] mention a phase shift normalized to the delay-line length of $1500^\circ/\text{cm}$. With $6944^\circ/\text{cm}$, the sensitivity of the sensors described here is significantly higher using a delay-line length of 1.8mm . Hanna [16] and Wang et al. [28] describe the limit of detection (LOD) of their sensors to be $1 \mu\text{T}$ and 140nT , respectively. As only the sensor dimension and the frequency is changed and the same layer thicknesses and material deposition processes were used, the sensor investigated here with $p = 12 \mu\text{m}$ can be expected to have a similar LOD than the sensor described in a previous study with $250 \text{pT}/\sqrt{\text{Hz}}$ at 10Hz [5]. Nevertheless, the main problem remains that the comparison of these sensors using different surface waves, materials, geometries and ambiguous specifications of the sensor performance is difficult. However, within this study, the sensitivity measured in $^\circ/\text{mT}$ is used for comparison, as this value can be specified for the measurement, as well as for our FEM simulations.

For completeness, the limit of detection results from this sensor are shown in Figure A2 in the Appendix C, as the focus of this study is based on sensitivities. The fundamental mode reaches an LOD of $700 \text{pT}/\sqrt{\text{Hz}}$ and the first mode $3 \text{nT}/\sqrt{\text{Hz}}$ both at 10Hz .

As the noise increases with the sensitivity due to the magnetic layer properties (see Appendix C), an LOD-improvement of the sensors described here was not observed. However, the improvement of the sensor sensitivity will be beneficial for the development of future sensors with more sophisticated magnetic layers.

3. FEM Modelling

For FEM simulations, 1D and 2.5D unit cell models were implemented as described in [29] and solved using Comsol Multiphysics[®]. For the 1D model, the geometry of the device is reduced to a stack of layers with different thicknesses assuming isotropic material parameters. By this, the displacement u_1 in x -direction is only z -dependent and is described by

$$u_1(k, z, \omega) = U(k, z, \omega)e^{i(ky - \omega t)} \quad (1)$$

with the wave vector k , the time t and the angular frequency ω . After transformations and substitutions, the differential equation for Love-waves [30] is obtained:

$$\frac{d}{dz} \left[G(z) \frac{dU}{dz} \right] = \left[k^2 G(z) - \omega^2 \rho(z) \right] U(k, z, \omega). \quad (2)$$

with the shear modulus G and the density ρ . This equation is solved using a partial differential equation interface in Comsol Multiphysics[®] with the following boundary conditions: The bottom interface is clamped (displacement $u_1 = 0$) and the top interface is a free surface (stress $T_{13} = 0$). At the layer interfaces, continuity of displacement and stress is required. The stress component T_{13} must be continuous at the interfaces of the different layers, which is executed automatically by the program.

The 2.5D simulation solves the 3-dimensional problem assuming that the stress and strain distributions do not depend on the x -coordinate and no stress in x -direction, using a so-called plain-strain conditions. As the width of our device is large compared to the wavelength, these conditions can be assumed. In y -direction periodic boundary conditions are used. The 2.5D model reduces the amount of mesh knots and therefore the computational time significantly in contrast to a full 3D model. The used material parameters for both models are described in Appendix A and the delta-E effect is represented by a linear approximation at the sensor operating point. A linear approximation of the delta-E effect was considered, because the targeted magnetic fields are significantly low and thus, a small signal approximation is suitable. While the 1D model only considers different layer thickness using isotropic material parameters, the 2.5D model additionally includes the IDT structure as shown in Figure 3d and uses anisotropic material parameters to obtain more realistic results.

The simulation setup consists of an ST-cut quartz substrate with a thickness of $h_{\text{sub}} = 200 \mu\text{m}$, a guiding layer of varying thickness h_{GL} and a magnetostrictive layer with a thickness of $h_{\text{MS}} = 200 \text{ nm}$. The electrode thickness h_{el} is 300 nm. The wave is excited using single-finger IDTs at the top of the substrate by applying an electric potential.

3.1. Mode Profile

The mode profiles showing the amplitude of the displacement for all positions z in the layer are evaluated for IDT pitches of $12 \mu\text{m}$ and $28 \mu\text{m}$. The IDT pitch corresponds to the mode wavelength. Figure 3a,b show the displacement profiles in the x -direction for 0th and 1st order Love-wave modes propagating along the y -direction for a pitch of $12 \mu\text{m}$ obtained with the 2.5D model. From the graphs, the displacement profiles shown in Figure 3c are extracted. For comparison, the fundamental mode for a pitch of $28 \mu\text{m}$ is additionally shown. Only the top 200 nm region consists of magnetostrictive material, while the guiding layer has a thickness of $18 \mu\text{m}$ in Figure 3. This guiding layer thickness was chosen for better visibility of the wave concentration effect.

Of the three modes, the 0th mode at $p = 12 \mu\text{m}$ has the highest concentration at the surface, because the largest fraction of the area between the displacement graph and the zero line is localized in the MS layer. For the 1st order mode at 332 MHz, a large part of the displacement is in the guiding layer and not only at the surface. Thus, a significantly reduced sensitivity is expected already from this qualitative analysis.

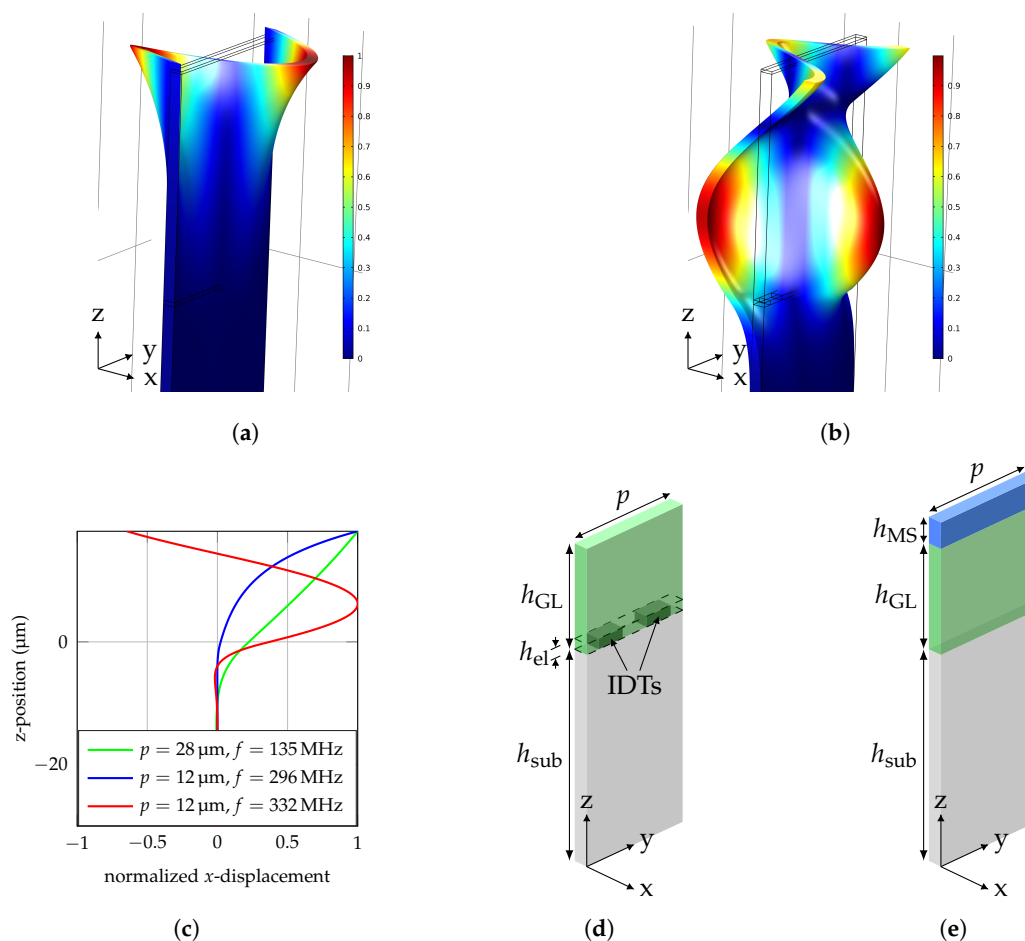


Figure 3. Normalized displacement of a delay-line SAW device with $\lambda = 12 \mu\text{m}$ and $h_{\text{GL}} = 4.5 \mu\text{m}$ for the (a) 0th mode and (b) 1st mode calculated using a frequency domain study. (c) Mode profile of Love-waves at different wavelengths with a $500 \mu\text{m}$ thick quartz substrate for $z < 0$ and a $18 \mu\text{m}$ thick guiding layer above $z = 0$. Schematic simulation setup of the unit cell for the excitation region (d) and the delay-line region (e). With a width of p , substrate thickness h_{sub} , guiding layer thickness h_{GL} , electrode thickness h_{el} , magnetostrictive layer thickness h_{MS} and the interdigital transducers (IDTs).

3.2. Two-Part Simulation

Since the Love-wave is generated at the IDT without a magnetostrictive layer on top before propagating through the delay line, the simulation must take into account the altered layer structure with the magnetostrictive layer. This is done by dividing the simulation into two parts: the wave excitation and propagation. Neglecting the changed layer structure by using the same wavelength for both simulation parts, with and without an MS layer, respectively, would lead to a drastic frequency shift and thus, distort sensitivity results. The frequency of a sensor with $h_{\text{GL}} = 4.5 \mu\text{m}$ is, e.g., reduced from 329 MHz without an MS layer to 300 MHz with an MS layer of 200 nm thickness. To avoid the influence of this effect on the sensitivity, we implemented the two-part study.

In the excitation region (Figure 3d), the wavelength is given by the IDT pitch, as the waves are constructively interfering with a periodicity of p . The resonance frequency is given by the different layer thicknesses and their properties. Hence, the first part calculates the mode frequency for the given guiding layer thickness without an MS layer, but with IDTs to address the wave's excitation at the IDT structure. This is achieved by a frequency sweep using a frequency domain study and the 2.5D model. The resonance frequency is identified, where the displacement of the Love-wave is maximized.

After the excitation, the wave is propagating through the delay line with an MS layer on top and without IDTs (Figure 3e). This change in the layer stack leads to an altered wavelength of the Love-wave. Since the frequency of the wave cannot change after excitation, it is set to the resonance

frequency of the first part. Hence, the second part uses the excitation frequency from the first part to calculate the influence of the changed layer stack. Using unit cell models, this is only possible using a sweep, until the unit cell width fits to the mode's wavelength at that given frequency. In particular, a frequency domain study is carried out for unit cell widths near the expected wavelength and the resonance wavelength is identified at the point of maximum displacement.

3.3. 1D vs. 2.5D

For model verification, we compared the 1D and 2.5D results. The 1D model uses isotropic material parameters. Therefore, we used an isotropic material tensor for the 2.5D simulation. This enables a comparison of the models using the same material parameters. For comparison, the resonance frequency from the 1D model is used in the 2.5D model. Comparing the 1D model with the 2.5D model with isotropic material parameters, reveals a deviation between the two models of $< 0.2\%$ for our parameter sets (results exemplary shown for $p = 12 \mu\text{m}$ and $h_{\text{GL}} = 18 \mu\text{m}$ for the 0th and 1st order mode, Table 1). Comparing the 2.5D model with isotropic material parameters with the same model with anisotropic material parameters, there is a deviation $< 2\%$. The wavelength as well as the wave velocity are clearly reduced, as the wave is not at the IDT resonance wavelength. At the resonance frequency of 295 MHz, the wavelength reaches approximately $12 \mu\text{m}$, again. The anisotropic material parameters used in the 2.5D model cause a frequency shift in the resonance frequency and there are other strain components than the targeted shear component ϵ_{yx} caused by the anisotropy of the material parameters (Figure 4).

Table 1. Comparison of results from 1D and 2.5D model with isotropic parameters, 2.5D model with anisotropic parameters for $p = 12 \mu\text{m}$ and $h_{\text{GL}} = 18 \mu\text{m}$ for the 0th and 1st order mode.

	0th			1st		
	$p/\mu\text{m}$	f/MHz	$v/\text{m/s}$	$p/\mu\text{m}$	f/MHz	$v/\text{m/s}$
1D isotropic	12.000	304.1	3648.0	12.000	336.7	4040.0
2.5D isotropic	12.012	304.1	3652.8	12.019	336.7	4046.8
2.5D anisotropic	11.682	304.1	3552.5	11.826	336.7	3981.8
2.5D anisotropic resonant	12.022	295.0	3546.5	11.995	332.0	3982.3

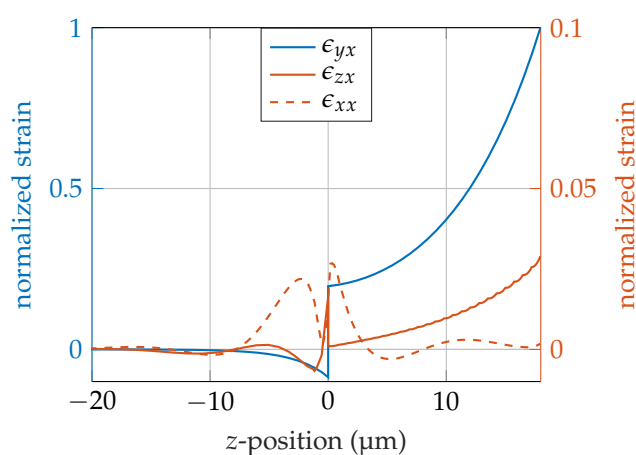


Figure 4. Comparison of strain tensor components of a SAW sensor at the first mode with $18 \mu\text{m}$ guiding layer thickness and substrate for $z < 0$. The components are normalized to the maximum of the main shear component ϵ_{yx} . The magnitude of the components ϵ_{zx} and ϵ_{xx} are shown on the right axis.

4. Sensitivity Calculation

With the use of the FEM models, the influence of the concentration of the energy at the surface on the sensitivity is investigated. In a previous study, we showed that the sensitivity S of the present SAW sensors can be separated into three parts: the magnetic sensitivity S_{mag} , the structural sensitivity S_{str} and the geometrical sensitivity S_{geo} [5]. The sensitivity S is calculated using Equation (3) with the shear modulus G and the magnetic field H .

$$S = \frac{\partial \varphi}{\partial H} = \frac{\partial G}{\partial H} \cdot \frac{\partial v}{\partial G} \cdot \frac{\partial \varphi}{\partial v} = S_{\text{mag}} \cdot S_{\text{str}} \cdot S_{\text{geo}} \quad (3)$$

The magnetic sensitivity S_{mag} describes the shear modulus change for a given magnetic-field change and depends on the magnetic properties of the material. It is also highly dependent on the bias magnetic-field B_{bias} , which is chosen to get maximal shear modulus change. The structural sensitivity S_{str} describes the amount of wave velocity change per shear modulus change and depends on the amount of wave energy propagating through the MS layer and is mainly determined by the layer structure of the sensor. The geometric sensitivity S_{geo} describes phase change per velocity change and depends on the excitation frequency and length l of the delay line. The magnetic sensitivity S_{mag} is approximated by Equation (4) at the operating point of 0.6 mT. For this operating point, the bias field B_{bias} was used, where the sensitivity reaches its maximum. The magnetic material properties were obtained by an iterative fit, until the phase change derived from the measurement and the FEM simulation using the assumed magnetic properties calculated by a micro-magnetic model [22] matched. As this process requires several iterations and the determination of the magnetic parameters is not trivial, this fit was carried out using the 1D and not the 2.5D model because of the faster computation time. The magnetic sensitivity at the operating point with the two shear moduli G_{MS}^+ and G_{MS}^- for a magnetic flux density change of $\Delta B = 0.1$ mT is given by:

$$S_{\text{mag}} = \frac{G_{\text{MS}}^+ - G_{\text{MS}}^-}{\Delta B} = \frac{29.8605 \text{ GPa} - 26.3380 \text{ GPa}}{0.1 \text{ mT}} = 35.225 \frac{\text{GPa}}{\text{mT}}. \quad (4)$$

The differential quotient of the structural sensitivity S_{str} is approximated by a difference quotient:

$$S_{\text{str}} = \frac{\partial v}{\partial G} = \frac{f \Delta \lambda}{\Delta G}. \quad (5)$$

For this, two simulations around the operating point $G = 28.1$ GPa are carried out. These two values of the elasticity tensor $c_{\text{MG}}^{\text{EH}}$ of the magnetostrictive layer (surrounding the operating point) are $c_{\text{MG}}^{\text{EH}+}$ and $c_{\text{MG}}^{\text{EH}-}$ being 0.1 mT apart from each other.

For this simulation, the frequency from the first part of the simulation was used to calculate the wave propagation constants. The eigen-wavelength of the mode is calculated for a respective geometry with the material parameters $c_{\text{MG}}^{\text{EH}+}$ and $c_{\text{MG}}^{\text{EH}-}$ at a given frequency.

The results of this two-stage approach are values for the wavelength and the frequency for the two different points near the operating point. With these, the structural sensitivity is calculated using (5), with the wave velocity $v = \lambda f$ with constant f and $\Delta G = 29.8605 \text{ GPa} - 26.3380 \text{ GPa}$. The wave propagates through the delay line with the length $l = 150p$ and according to its wave constant k , the phase shift accumulates to $\varphi = kl$. With this, the geometric sensitivity is given by Equation (6).

$$S_{\text{geo}} = \frac{\partial \varphi}{\partial v} = \frac{\partial kl}{\partial v} = \frac{\partial}{\partial v} \frac{2\pi fl}{v} = -\frac{2\pi fl}{v^2} \quad (6)$$

Using these equations, the overall sensitivity is calculated for different guiding layer thicknesses and IDT pitches for the fundamental, 1st, and 2nd mode. The 2.5D simulation results are added for several points in Figure 5, showing the sensitivity for different h_{GL}/λ -ratios. For comparison, results from a 1D setup with same layer thicknesses but isotropic material parameters are additionally shown. Similar to

the 2.5D simulation described above, the 1D simulation is split into two parts as well including the first part to determine the resonance frequency. In the second part, two simulations near the operating point are carried out using the values G_{MS}^+ and G_{MS}^- as the shear modulus of the magnetostrictive layer. In contrast to the 2.5D simulation, there are no parameter sweeps necessary to find the resonances, as the differential equation [29] can be solved directly. The 1D results are shown as continuous lines, since the computation time is a fraction of the 2.5D simulation.

5. Results and Discussion

The sensitivity curve for the Love-wave magnetic-field sensors at different h_{GL}/λ -ratios is shown in Figure 5 for $p = 12 \mu\text{m}$ and $p = 28 \mu\text{m}$. The sensitivity curve starts with an axial intercept for the 0th mode, because even with no guiding layer ($h_{GL} = 0 \mu\text{m}$), there is still a layer of 200 nm thick MS material. Due to the material properties this layer acts as a guiding layer itself and by this supports Love-waves. With increasing guiding layer thickness, the sensitivity reaches a maximum. Here, the highest part of the wave energy is at the surface. Thus, an additional guiding layer improves the performance. With even higher guiding layer thicknesses, the wave starts to concentrate within the guiding layer and less at the surface and the sensitivity decreases.

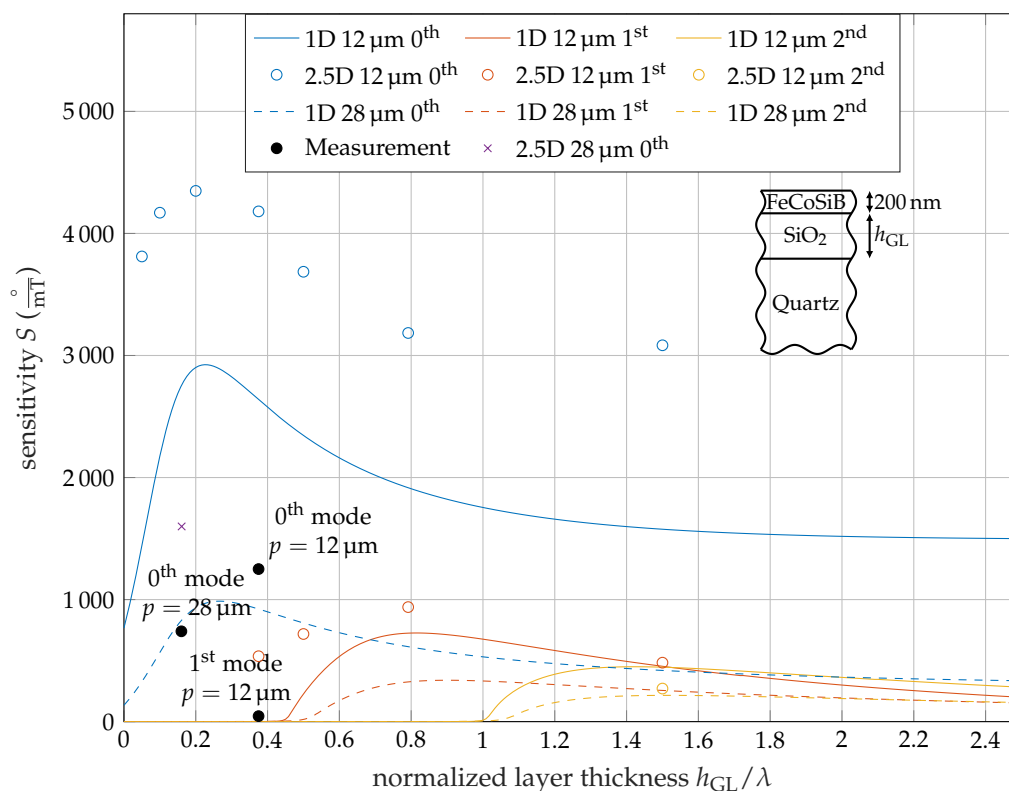


Figure 5. Comparison of sensitivity results for isotropic (1D) and anisotropic (2.5D) calculation for $p = 12 \mu\text{m}$ and $p = 28 \mu\text{m}$ for the fundamental, first- and second-order modes. Due to the fixed MS layer thickness, the normalized data are not entirely wavelength independent. For comparison, the measurement results are included.

Above a cut of ratio of $h_{GL}/\lambda \approx 0.5$ and $h_{GL}/\lambda \approx 1$ the 1st and 2nd order modes are supported and with further increasing guiding layer thickness, the sensitivity increases to a maximum similar to the fundamental mode (Figure 5).

The overall behavior of less sensitive higher modes is similar to the one published by Kovacs et al [31], where a Love-wave sensor with a silicon substrate and a SiO_2 guiding layer was examined. The authors described a sensor using the frequency shift due to mass absorption as detection mechanism, which is contrary to the sensor analyzed here using an MS layer causing a phase shift.

For the calculation, only isotropic material parameters are used and the higher 2.5D results were not predicted.

5.1. Qualitative Results

The 0th order modes sensitivity is significantly larger than the 1st and 2nd order modes sensitivity, as the wave is more concentrated at the surface. Figure 3 confirms this, as the displacement of the 1st order mode at the surface is lower than the maximal displacement resulting in an reduced influence of the MS layer to the wave propagation. Hence, the sensitivity is reduced.

The curve shapes of the 1D and 2.5D simulation results are similar, but with an offset. The overall shape of both the 1D and 2.5D simulations indicates a maximum near $h_{GL}/\lambda = 0.3$, $h_{GL}/\lambda = 0.7$ and $h_{GL}/\lambda = 1.5$ for the fundamental, 1st and 2nd mode. Regarding the isotropic material parameters for the 1D and 2.5D simulation, the results are in good agreement in terms of the propagation constants. The sensitivities match with an error below 3% according to Table 2. Consequently, the only difference between the models is the anisotropy of the quartz substrate. The 2.5D simulation takes more details of the materials into account and the results have a significant offset in the sensitivity. The frequency of the 2.5D simulation with anisotropic material parameters is lower than the isotropic results. This emphasizes the importance of using 2.5D models to get higher accuracy of SAW magnetic-field sensors.

According to Figure 5, multi-mode operation of the fundamental, 1st, and 2nd modes is possible and a ratio of $h_{GL}/\lambda = 1.5$ for $p = 12 \mu\text{m}$ is preferred, because all three modes have a reasonable high sensitivity level. Regarding overall sensitivity, the choice of the operating point is not optimal, since the fundamental mode's sensitivity is not at its maximum. Nevertheless, it still surpasses the maximal sensitivity of a sensor with $p = 28 \mu\text{m}$ and by this facilitates multi-mode operation.

5.2. Quantitative Results

Because the 1D and the 2.5D simulation uses the same values for the magnetic sensitivity according to Equation (4), which was fit to the 1D model, the 1D simulation results correspond better to the experimental data than the 2.5D simulation, especially the fundamental mode.

A surprisingly strong reduction of the 1st order modes sensitivity in the measurement was observed. The FEM simulation confirmed an overall lower performance of the higher modes, although the experimental values were even lower. This data point for the 1st order mode is extremely close to the cut-off ratio. Due to the steep curve near the cut-off ratio, small deviations between measurement and simulation can cause a significant influence on the sensitivity. One effect not considered in the simulation is the frequency dependency of the delta-E effect that might result in a slightly reduced magnetic sensitivity in higher frequency modes according to theoretical considerations [22].

Additionally, a lower S_{mag} due to fabrication variations, internal stress and material inhomogeneities probably causes the lower performance of the measurement in general, as even the fundamental modes sensitivity is lower than in the simulation. Because S_{mag} of the sensor with $p = 28 \mu\text{m}$ was used in the simulation a difference between simulation and measurement is expected for $p = 12 \mu\text{m}$. The magnetization curves (Figure A1) of the sensor with $p = 12 \mu\text{m}$ show a significant tilt of the mean easy axis (Figure A1a) compared to the sensor with $p = 28 \mu\text{m}$ (Figure A1c) [5]. It also exhibits a higher coercivity along the hard axis that might result from inhomogeneous magnetic anisotropies or shape effects. Both the easy axis tilt and the inhomogeneity are expected to reduce the delta-E effect and thereby S_{mag} [32–34].

Table 2. Comparison of the measured and simulated sensitivities for different wavelengths λ and guiding layer thicknesses h_{GL} .

$\lambda/\mu\text{m}$	$h_{GL}/\mu\text{m}$		0th		1st	
			f/MHz	$S/^\circ/\text{mT}$	f/MHz	$S/^\circ/\text{mT}$
28	4.5	measurement	148	740	–	–
		1D isotropic	162	750	–	–
		2.5D anisotropic	150	1600	–	–
12	4.5	measurement	263	1250	352	45
		1D isotropic	320	2640	420	0.6
		2.5D anisotropic	304	4180	368	530
	9.5	1D isotropic	306	1916	382	725
		2.5D anisotropic	297	3184	368	938
	18	1D isotropic	304	1574	336	453
		2.5D isotropic	304	1534	336	449
		2.5D anisotropic	295	3084	332	483

6. Conclusions

We investigated a Love-wave-based magnetic-field sensor operated in different modes in experiment and simulation. Our fabricated sensor with $p = 12 \mu\text{m}$ show a 250 % higher sensitivity compared to $p = 28 \mu\text{m}$ for the fundamental mode, corresponding to the prediction from [5]. The significant reduction of the first mode sensitivity is explained with the generally reduced sensitivity of the higher modes according to Figure 5 caused by the easy axis tilt and increased mean anisotropy (Figure A1) and in particular with this mode being close to cut-off. We also showed the necessity to use more detailed FEM models, as the one-dimensional model does not satisfy the anisotropy of the used materials and excitation effects due to the electrodes. This results in significant deviations, hence this model can only be used as an approximation.

We proposed a sensor with $h_{GL}/\lambda = 1.5$ for multi-mode operation possessing fundamental, 1st, and 2nd order Love-wave modes with sufficient sensitivity. Although the higher-mode sensitivity is generally reduced compared to the fundamental mode, the choice of this operating point enables the reduction of noise and distortions using signal processing approaches with mode- instead of time-domain averaging of the signal. Assuming an equal sensitivity of each mode, the sensitivity increases linearly with the number of averaged modes [35]. For non-identical values, the overall sensitivity is given by the sum of the individual sensitivities. Thus, for the proposed multi-mode operating point, the combined sensitivity is not increasing linearly with the number of modes, but is a result of the addition of the individual sensitivities. Since almost the entire wave energy is trapped in the guiding layer for higher h_{GL} , the material choice of the guiding layer is important in terms of loss minimization.

Author Contributions: Conceptualization, J.S., M.G., A.K. and E.Q.; validation, J.S. and B.S.; investigation, J.S., A.K. and P.D.; methodology, J.S., M.G., A.K. and E.Q.; writing—original draft preparation, J.S.; writing—review and editing, J.S., A.K., P.D., B.S., F.F., M.H., E.Q. and M.G.; visualization, J.S.; supervision, M.G., E.Q., F.F. and M.H.; funding acquisition, M.G., E.Q., F.F. and M.H. All authors have read and agreed to the published version of the manuscript.

Funding: This research was funded by the German Research Foundation (DFG) via the collaborative research center CRC 1261.

Acknowledgments: The authors would like to thank the group of Nanoscale Magnetic Materials-Magnetic Domains from Kiel University, especially C.M. (Cai Müller), for helping us out with the characterization of the FeCoSiB layer in their laboratory. We acknowledge financial support by DFG within the funding programme Open Access Publizieren.

Conflicts of Interest: The authors declare no conflict of interest. The funders had no role in the design of the study; in the collection, analyses, or interpretation of data; in the writing of the manuscript, and in the decision to publish the results.

Appendix A. Material Parameters

Appendix A.1. For One-Dimensional Model

$$G_{\text{Quartz}} = 67.50 \text{ GPa}, \rho_{\text{Quartz}} = 2200 \text{ kg/m}^3,$$

$$G_{\text{SiO}_2} = 33.35 \text{ GPa}, \rho_{\text{SiO}_2} = 2200 \text{ kg/m}^3,$$

$$G_{\text{MS}}^+ = 29.8605 \text{ GPa}, G_{\text{MS}}^- = 26.3380 \text{ GPa}, \text{ and } \rho_{\text{MS}} = 7250 \text{ kg/m}^3.$$

Appendix A.2. For 2.5D and 3D

ST-cut quartz (SiO_2) rotated from [36]:

$$c_{\text{Quartz}}^{EH} = \begin{pmatrix} 86.74 & 27.49 & -8.60 & 1.05 & 0.00 & 0.00 \\ 27.49 & 96.64 & -4.81 & 13.44 & 0.00 & 0.00 \\ -8.60 & -4.81 & 130.74 & -1.84 & 0.00 & 0.00 \\ 1.05 & 13.44 & -1.84 & 41.22 & 0.00 & 0.00 \\ 0.00 & 0.00 & 0.00 & 0.00 & 30.35 & 7.58 \\ 0.00 & 0.00 & 0.00 & 0.00 & 7.58 & 67.50 \end{pmatrix} \text{ GPa},$$

$$e_{\text{Quartz}} = \begin{pmatrix} 0.17 & -0.04 & -0.13 & 0.08 & 0.00 & 0.00 \\ 0.00 & 0.00 & 0.00 & 0.00 & 0.07 & -0.10 \\ 0.00 & 0.00 & 0.00 & 0.00 & -0.07 & 0.11 \end{pmatrix} \text{ N/Vm},$$

$$\varepsilon_{r,\text{Quartz}} = \begin{pmatrix} 4.43 & 0.00 & 0.00 \\ 0.00 & 4.54 & 0.10 \\ 0.00 & 0.10 & 4.52 \end{pmatrix},$$

$$\rho_{\text{Quartz}} = 2651 \text{ kg/m}^3.$$

Silica glass (SiO_2) [37]:

$$c_{\text{SiO}_2}^{EH} = \begin{pmatrix} 77.46 & 15.6 & 15.6 & 0 & 0 & 0 \\ 15.6 & 77.46 & 15.6 & 0 & 0 & 0 \\ 15.6 & 15.6 & 77.46 & 0 & 0 & 0 \\ 0 & 0 & 0 & 30.91 & 0 & 0 \\ 0 & 0 & 0 & 0 & 30.91 & 0 \\ 0 & 0 & 0 & 0 & 0 & 30.91 \end{pmatrix} \text{ GPa},$$

$$e_{\text{SiO}_2} = \begin{pmatrix} 0 & 0 & 0 & 0 & 0 & 0 \\ 0 & 0 & 0 & 0 & 0 & 0 \\ 0 & 0 & 0 & 0 & 0 & 0 \end{pmatrix} \text{ N/Vm},$$

$$\varepsilon_{r,\text{SiO}_2} = \begin{pmatrix} 2.2 & 0.0 & 0.0 \\ 0.0 & 2.2 & 0.0 \\ 0.0 & 0.0 & 2.2 \end{pmatrix},$$

$$\rho_{\text{SiO}_2} = 2200 \text{ kg/m}^3.$$

FeCoSiB [38]:

$$c_{\text{MG}}^{EH+} = \begin{pmatrix} 104.512 & 44.7907 & 44.7907 & 0 & 0 & 0 \\ 44.7907 & 104.512 & 44.7907 & 0 & 0 & 0 \\ 44.7907 & 44.7907 & 104.512 & 0 & 0 & 0 \\ 0 & 0 & 0 & 29.8605 & 0 & 0 \\ 0 & 0 & 0 & 0 & 29.8605 & 0 \\ 0 & 0 & 0 & 0 & 0 & 29.8605 \end{pmatrix} \text{ GPa},$$

$$c_{MG}^{EH-} = \begin{pmatrix} 92.1830 & 39.5070 & 39.5070 & 0 & 0 & 0 \\ 39.5070 & 92.1830 & 39.5070 & 0 & 0 & 0 \\ 39.5070 & 39.5070 & 92.1830 & 0 & 0 & 0 \\ 0 & 0 & 0 & 26.3380 & 0 & 0 \\ 0 & 0 & 0 & 0 & 26.3380 & 0 \\ 0 & 0 & 0 & 0 & 0 & 26.3380 \end{pmatrix} \text{ GPa,}$$

$$e_{MG} = \begin{pmatrix} 0 & 0 & 0 & 0 & 0 & 0 \\ 0 & 0 & 0 & 0 & 0 & 0 \\ 0 & 0 & 0 & 0 & 0 & 0 \end{pmatrix} \text{ N/Vm,}$$

$$\varepsilon_{r,MG} = \begin{pmatrix} 1 & 0 & 0 \\ 0 & 1 & 0 \\ 0 & 0 & 1 \end{pmatrix},$$

$$\rho_{MG} = 7250 \text{ kg/m}^3.$$

Appendix B. B-H Loops

The magnetization curve of the SAW device with $p = 12 \mu\text{m}$ are measured by a hysteresis loop tracer model 108 (Shb Instruments). The anisotropy is tilted by approximately 10° with respect to the propagation direction. The normalized magnetization parallel to the delay line is shown in Figure A1a and the normalized magnetization of the hard axis is depicted in Figure A1b. Figure A1c shows the magnetization curve of a SAW device with $p = 28 \mu\text{m}$ [5]. A small opening of the hysteresis curve can be seen, which is also visible in the phase change and sensitivity curves plotted in Figure 2.

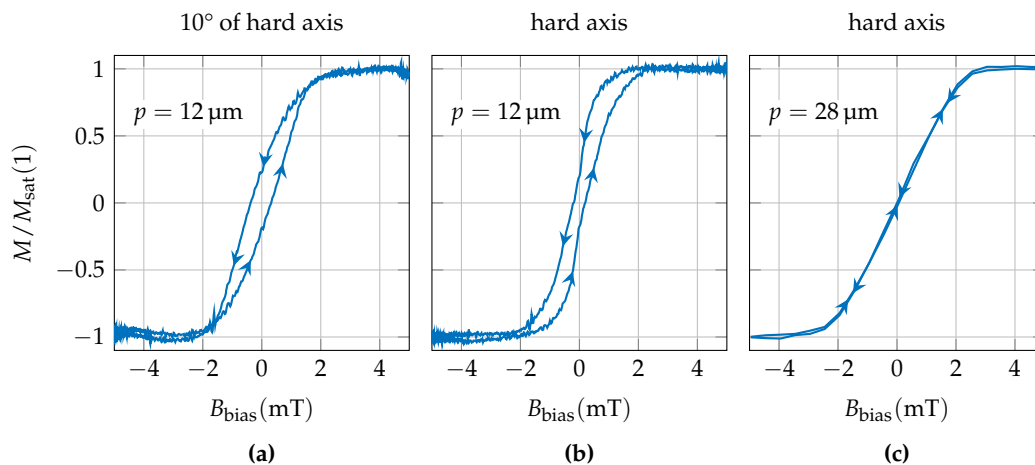


Figure A1. Magnetization curve of the SAW device with $p = 12 \mu\text{m}$ measured by a hysteresis loop tracer model 108 (Shb Instruments). The normalized magnetization parallel to the delay line (a) and to the hard axis (b) are shown. (c) Shows the Magnetization curve of a SAW device with $p = 28 \mu\text{m}$ [5]. The arrow marks represent the direction of the magnetization process starting from a magnetically saturated state.

Appendix C. Limit of Detection and Phase Noise Measurements

The frequency dependent noise floor of the SAW magnetic-field sensor in units of $\text{T}/\sqrt{\text{Hz}}$, often referred to as equivalent magnetic noise floor, detectivity, or limit of detection (LOD) is given by the ratio of the square root of the power spectral density of the sensor's random phase fluctuations in units of rad^2/Hz and the (phase) sensitivity in units of rad/T [39]. For the first two discussed modes of the sensor under investigation the power spectral densities of the sensor's random phase fluctuations were measured using a phase noise analyzer FSWP (Rohde & Schwarz) at an input power of 10 dBm. During these measurements, the sensor was placed inside an electrically, magnetically (ZG1 from Aaronia AG), and acoustically shielded measurement chamber. For each mode, the noise measurements were

performed twice: one measurement in the sensor's magnetic operating point and one measurement in magnetic saturation using a strong permanent magnet. The magnetic operating point was chosen at $B_{\text{bias}} = 0$. Compared to maximum possible sensitivities (Figure 2), this operating point is associated with only slightly reduced values for the sensitivities but offers the great advantage that during noise measurements, no additional, and with regard to its additional noise extremely critical, current source is required to generate the magnetic bias flux density. To ensure a largely comparable magnetic operating point for both modes, the sensor was magnetically initialized before each measurement. Using a coil surrounding the sensor and a current source (B2962A from Keysight), the magnetic bias flux density was gradually increased from -10 mT to 0 mT over a period of about 15 s. Subsequently, the current source was switched off before the actual noise measurement was performed. Due to high mismatch losses and corresponding high insertion losses of about 55 dB to 65 dB, two amplifiers (ZFL-1000LN+ from Mini-Circuits) with a total gain of 50 dB were additionally connected between the sensor and the input of the phase noise analyzer. Contrary to the determined sensitivities based on numerically differentiating the static phase responses (Figure 2), values for the sensitivities necessary for calculating the LOD were re-determined in the chosen magnetic operating point of $B_{\text{bias}} = 0$ by means of a dynamic sensitivity measurement as described in [24]. Values of $26.2 \text{ rad/mT} = 1504^\circ/\text{mT}$ (0th mode) and $0.67 \text{ rad/mT} = 38.2^\circ/\text{mT}$ (1st mode) were achieved. The results of the phase noise measurements are shown in Figure A2a. As already observed in a previous study [39], at low frequencies at which the thermal noise, i.e., the white phase noise, is negligible the power spectral density not only progresses proportional to $1/f$ but is also higher than for the magnetically saturated device indicating a magnetic origin for the increased noise. Recently, it was found [24] that the $1/f$ flicker phase noise in the sensor's magnetic operating point is associated with hysteresis losses in the magnetic layer which increase with the sensitivity. In fact, it could be shown that the magnetically induced flicker phase noise is directly proportional to the sensitivity, leading to a LOD theoretically being independent of the sensitivity. The determined limits of detection for both modes are depicted in Figure A2b yielding values of $700 \text{ pT}/\sqrt{\text{Hz}}$ (0th mode) and $3 \text{ nT}/\sqrt{\text{Hz}}$, each at an exemplary frequency of 10 Hz . Although the sensitivities of both modes differ by a factor of about 39, the difference in LOD in the flicker noise regime is only a factor of about 4.3. Even if, from a theoretical point of view, an identical LOD could have been expected in principle, the discrepancy can be easily explained. The hysteresis losses, represented by the imaginary part of the magnetic material's complex permeability, generally increase with higher excitation frequencies approaching ferromagnetic resonance [40–42], thus leading to a worse flicker phase noise-to-sensitivity ratio in the higher frequency 1st mode.

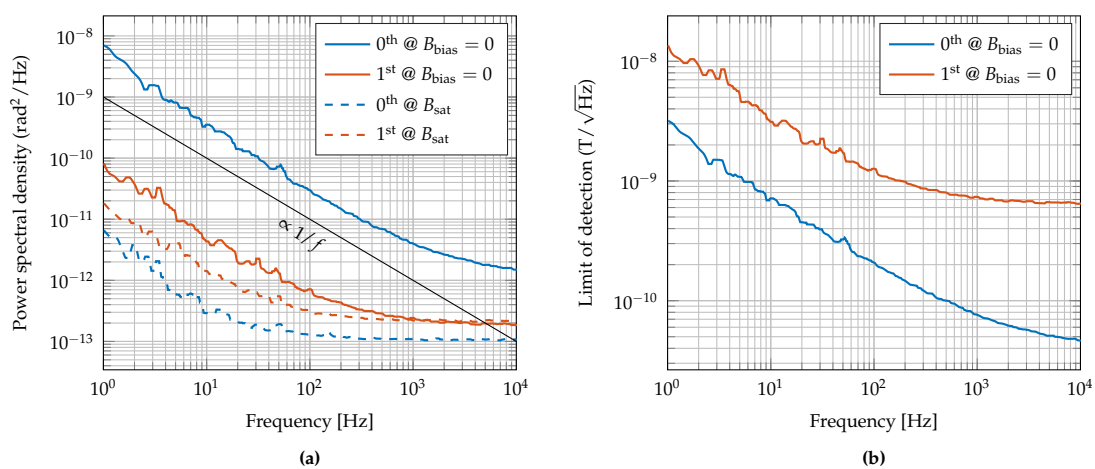


Figure A2. (a) Measured power spectral densities of random phase fluctuations in the magnetic operating point (continuous lines) and in magnetic saturation (dashed line) of the sensor with $p = 12 \mu\text{m}$ for fundamental and first-order mode. (b) Calculated limit of detection for both modes.

References

1. Gizeli, E.; Stevenson, A.; Goddard, N.; Lowe, C. A novel Love-plate acoustic sensor utilizing polymer overlayers. *IEEE Trans. Ultrason. Ferroelectr. Freq. Control* **1992**, *39*, 657–659. [[CrossRef](#)] [[PubMed](#)]
2. Kovacs, G.; Lubking, G.; Vellekoop, M.; Venema, A. Love waves for (bio)-chemical sensing in liquids. In Proceedings of the IEEE 1992 Ultrasonics Symposium Proceedings, Tucson, AZ, USA, 20–23 October 1992; pp. 281–285. [[CrossRef](#)]
3. Schlenso, M.D.; Gronewold, T.M.; Tewes, M.; Famulok, M.; Quandt, E. A Love-wave biosensor using nucleic acids as ligands. *Sens. Actuators B Chem.* **2004**, *101*, 308–315. [[CrossRef](#)]
4. Yokokawa, N.; Tanaka, S.; Fujii, T.; Inoue, M. Love-type surface-acoustic waves propagating in amorphous iron-boron films with multilayer structure. *J. Appl. Phys.* **1992**, *72*, 360–366. [[CrossRef](#)]
5. Kittmann, A.; Durdaut, P.; Zabel, S.; Reermann, J.; Schmalz, J.; Spetzler, B.; Meyners, D.; Sun, N.X.; McCord, J.; Gerken, M.; et al. Wide Band Low Noise Love Wave Magnetic Field Sensor System. *Sci. Rep.* **2018**, *8*, 278. [[CrossRef](#)]
6. Mazzamurro, A.; Dusch, Y.; Pernod, P.; Bou Matar, O.; Addad, A.; Talbi, A.; Tiercelin, N. Giant Magnetoelastic Coupling in a Love Acoustic Waveguide Based on TbCo₂/FeCo Nanostructured Film on ST-Cut Quartz. *Phys. Rev. Appl.* **2020**, *13*, 044001. [[CrossRef](#)]
7. Liu, X.; Tong, B.; Ou-Yang, J.; Yang, X.; Chen, S.; Zhang, Y.; Zhu, B. Self-biased vector magnetic sensor based on a Love-type surface acoustic wave resonator. *Appl. Phys. Lett.* **2018**, *113*, 082402. [[CrossRef](#)]
8. Mishra, H.; Streque, J.; Hehn, M.; Mengue, P.; M'Jahed, H.; Lacour, D.; Dumesnil, K.; Petit-Watelot, S.; Zhgoon, S.; Polewczyk, V.; et al. Temperature compensated magnetic field sensor based on love waves. *Smart Mater. Struct.* **2020**, *29*, 045036. [[CrossRef](#)]
9. Forester, D.W.; Vittoria, C.; Webb, D.C.; Davis, K.L. Variable delay lines using magnetostrictive metallic-glass film overlays. *J. Appl. Phys.* **1978**, *49*, 1794–1796. [[CrossRef](#)]
10. Yamaguchi, M.; Naoe, M.; Kogo, H. Variable saw delay line using amorphous TbFe₂ film. *IEEE Trans. Magn.* **1980**, *16*, 916–918. [[CrossRef](#)]
11. Schell, V.; Müller, C.; Durdaut, P.; Kittmann, A.; Thormählen, L.; Lofink, F.; Meyners, D.; Höft, M.; McCord, J.; Quandt, E. Magnetic anisotropy controlled FeCoSiB thin films for surface acoustic wave magnetic field sensors. *Appl. Phys. Lett.* **2020**, *116*. [[CrossRef](#)]
12. Livingston, J.D. Magnetomechanical properties of amorphous metals. *Phys. Status Solidi* **1982**, *70*, 591–596. [[CrossRef](#)]
13. Lee, E.W. Magnetostriction and Magnetomechanical Effects. *Rep. Prog. Phys.* **1955**, *18*, 229. [[CrossRef](#)]
14. Sárközi, Z.; Mackay, K.; Peuzin, J.C. Elastic properties of magnetostrictive thin films using bending and torsion resonances of a bimorph. *J. Appl. Phys.* **2000**, *88*, 5827–5832. [[CrossRef](#)]
15. Bou Matar, O.; Robillard, J.F.; Vasseur, J.O.; Hladky-Hennion, A.C.; Deymier, P.A.; Pernod, P.; Preobrazhensky, V. Band gap tunability of magneto-elastic phononic crystal. *J. Appl. Phys.* **2012**, *111*, 054901. [[CrossRef](#)]
16. Hanna, S.M. Magnetic Field Sensors Based on SAW Propagation in Magnetic Films. *IEEE Trans. Ultrason. Ferroelectr. Freq. Control* **1987**, *34*, 191–194. [[CrossRef](#)]
17. Wang, W.; Jia, Y.; Liu, X.; Liang, Y.; Xue, X.; Du, Z.; Wang, W.; Jia, Y.; Liu, X.; Liang, Y.; et al. Enhanced sensitivity of temperature-compensated SAW-based current sensor using the magnetostrictive effect. *SMA* **2017**, *26*, 025008. [[CrossRef](#)]
18. Polewczyk, V.; Dumesnil, K.; Lacour, D.; Moutaouekkil, M.; M'jahed, H.; Tiercelin, N.; Petit-Watelot, S.; Mishra, H.; Dusch, Y.; Hage-Ali, S.; et al. Unipolar and bipolar high-magnetic-field sensors based on surface acoustic wave resonators. *Phys. Rev. Appl.* **2017**, *8*, 024001. [[CrossRef](#)]
19. Nan, T.; Hui, Y.; Rinaldi, M.; Sun, N.X. Self-biased 215 MHz magnetoelectric NEMS resonator for ultra-sensitive DC magnetic field detection. *Sci. Rep.* **2013**, *3*, 1985. [[CrossRef](#)]
20. Zabel, S.; Reermann, J.; Fichtner, S.; Kirchhof, C.; Quandt, E.; Wagner, B.; Schmidt, G.; Faupel, F. Multimode delta-E effect magnetic field sensors with adapted electrodes. *Appl. Phys. Lett.* **2016**, *108*, 222401. [[CrossRef](#)]
21. Li, M.; Matyushov, A.; Dong, C.; Chen, H.; Lin, H.; Nan, T.; Qian, Z.; Rinaldi, M.; Lin, Y.; Sun, N.X. Ultra-sensitive NEMS magnetoelectric sensor for picotesla DC magnetic field detection. *Appl. Phys. Lett.* **2017**, *110*, 143510. [[CrossRef](#)]

22. Spetzler, B.; Golubeva, E.V.; Müller, C.; McCord, J.; Faupel, F. Frequency Dependency of the Delta-E Effect and the Sensitivity of Delta-E Effect Magnetic Field Sensors. *Sensors* **2019**, *19*, 4769. [[CrossRef](#)] [[PubMed](#)]
23. Zhou, H.; Talbi, A.; Tiercelin, N.; Bou Matar, O. Multilayer magnetostrictive structure based surface acoustic wave devices. *Appl. Phys. Lett.* **2014**, *104*. [[CrossRef](#)]
24. Kittmann, A.; Müller, C.; Durdaut, P.; Thormählen, L.; Schell, V.; Niekkel, F.; Lofink, F.; Meyners, D.; Knöchel, R.; Höft, M.; et al. Sensitivity and Noise Analysis of SAW Magnetic Field Sensors with varied Magnetostrictive Layer Thicknesses. *Sens. Actuators A Phys.* **2020**, *311*, 111998. [[CrossRef](#)]
25. Ganguly, A.K.; Davis, K.L.; Webb, D.C.; Vittoria, C.; Forester, D.W. Magnetically tuned surface-acoustic-wave phase shifter. *Electr. Lett.* **1975**, *11*, 610–611. [[CrossRef](#)]
26. Robbins, W.; Simpson, E. Surface Acoustic Wave Properties of RF Sputtered Nickel Films on Lithium Niobate. In Proceedings of the 1978 Ultrasonics Symposium, Cherry Hill, NJ, USA, 25–27 September 1978; pp. 658–661. [[CrossRef](#)]
27. Li, W.; Dhagat, P.; Jander, A. Surface acoustic wave magnetic sensor using galfenol thin film. *IEEE Trans. Magnet.* **2012**, *48*, 4100–4102. [[CrossRef](#)]
28. Wang, W.; Jia, Y.; Xue, X.; Liang, Y.; Du, Z. Grating-patterned FeCo coated surface acoustic wave device for sensing magnetic field. *AIP Adv.* **2018**, *8*, 015134. [[CrossRef](#)]
29. Schmalz, J.; Spetzler, B.; Faupel, F.; Gerken, M. Love Wave Magnetic Field Sensor Modeling—From 1D to 3D Model. In Proceedings of the 2019 International Conference on Electromagnetics in Advanced Applications (ICEAA), Granada, Spain, 9–13 September 2019; pp. 765–769. [[CrossRef](#)]
30. Landau, L.D.; Lifshitz, E.M. *Theory of Elasticity*, 2nd ed.; Course of Theoretical Physics: Oxford, UK, 1970; p. 101.
31. Kovacs, G.; Venema, A. Theoretical comparison of sensitivities of acoustic shear wave modes for (bio)chemical sensing in liquids. *Appl. Phys. Lett.* **1992**, *61*, 639–641. [[CrossRef](#)]
32. Atkinson, D.; Squire, P.T.; Gibbs, M.R.; Atalay, S.; Lord, D.G. The effect of annealing and crystallization on the magnetoelastic properties of Fe-Si-B amorphous wire. *J. Appl. Phys.* **1993**, *73*, 3411–3417. [[CrossRef](#)]
33. Gutiérrez, J.; Muto, V.; Squire, P.T. Induced anisotropy and magnetoelastic properties in Fe-rich metallic glasses. *J. Non-Cryst. Solids* **2001**, *287*, 417–420. [[CrossRef](#)]
34. Spetzler, B.; Kirchhof, C.; Quandt, E.; McCord, J.; Faupel, F. Magnetic Sensitivity of Bending-Mode Delta-E-Effect Sensors. *Phys. Rev. Appl.* **2019**, *12*, 064036. [[CrossRef](#)]
35. Reermann, J.; Zabel, S.; Kirchhof, C.; Quandt, E.; Faupel, F.; Schmidt, G. Adaptive Readout Schemes for Thin-Film Magnetoelectric Sensors Based on the delta-E Effect. *IEEE Sens. J.* **2016**, *16*, 4891–4900. [[CrossRef](#)]
36. Bechmann, R. Elastic and Piezoelectric Constants of Alpha-Quartz. *Phys. Rev.* **1958**, *110*, 1060–1061. [[CrossRef](#)]
37. Pabst, W.; Gregorová, E. Elastic properties of silica polymorphs—A review. *Ceramics-Silikáty* **2013**, *57*, 167–184.
38. Ludwig, A.; Quandt, E. Optimization of the ΔE -effect in thin films and multilayers by magnetic field annealing. In Proceedings of the IEEE International Digest of Technical Papers on Magnetics Conference, Amsterdam, The Netherlands, 28 April–2 May 2002; p. AE2. [[CrossRef](#)]
39. Durdaut, P.; Kittmann, A.; Rubiola, E.; Friedt, J.M.; Quandt, E.; Knöchel, R.; Höft, M. Noise Analysis and Comparison of Phase- and Frequency-Detecting Readout Systems: Application to SAW Delay Line Magnetic Field Sensor. *IEEE Sens. J.* **2019**, *19*, 8000–8008. [[CrossRef](#)]
40. Chen, L.H.; Klemmer, T.J.; Ellis, K.A.; Van Dover, R.B.; Jin, S. Soft-magnetic properties of Fe-Co-B thin films for ultra-high-frequency applications. *J. Appl. Phys. Am. Inst. Phys.* **2000**, *87*, 5858–5860. [[CrossRef](#)]
41. Frommberger, M.; McCord, J.; Quandt, E. High-frequency properties of FeCoSiB thin films with crossed anisotropy. *IEEE Trans. Magnet.* **2004**, *40*, 2703–2705. [[CrossRef](#)]
42. Glasmachers, S.; Frommberger, M.; McCord, J.; Quandt, E. Influence of strain on the high-frequency magnetic properties of FeCoSi thin films. *Phys. Status Solidi* **2004**, *201*, 3319–3324. [[CrossRef](#)]



B.3 Mapping of Magnetic Particles with ΔE -Effect Sensors

Contribution

- Methodology
- Resources
- Investigation



Mapping of magnetic nanoparticles and cells using thin film magnetoelectric sensors based on the delta-E effect



Nils Lukat^a, Ron-Marco Friedrich^b, Benjamin Spetzler^b, Christine Kirchhof^c,
Christine Arndt^a, Lars Thormählen^c, Franz Faupel^b, Christine Selhuber-Unkel^{a,*}

^a University of Kiel, Institute for Materials Science, Biocompatible Nanomaterials, Kaiserstr. 2, 24143 Kiel, Germany

^b University of Kiel, Institute for Materials Science, Chair for Multicomponent Materials, Kaiserstr. 2, 24143 Kiel, Germany

^c University of Kiel, Institute for Materials Science, Inorganic Functional Materials, Kaiserstr. 2, 24143 Kiel, Germany

ARTICLE INFO

Article history:

Received 11 February 2020

Received in revised form 7 April 2020

Accepted 22 April 2020

Available online 28 April 2020

Keywords:

Iron oxide nanoparticles

Magnetic imaging

Cell detection

Magnetoelectric sensor

Delta-E effect

Motion modulation

ABSTRACT

Superparamagnetic iron oxide nanoparticles (SPIONs) are an important tool for labeling cells and tissues in many therapeutic and diagnostic applications, such as magnetic resonance imaging (MRI) and magnetic particle imaging (MPI). However, these methods require large and expensive instrumentation. Here we show that our magnetic susceptibility particle mapping (MSPM) system can achieve the detection of magnetic nanoparticles in an inexpensive and small device. The system is based on magnetoelectric (ME) sensors utilizing the ΔE effect in combination with a permanent magnet that is generating a bias field for the sensor and at the same time is magnetizing the SPIONs in the sample. The permanent magnet is placed above the sensor, and the sample is rotated through the gap in between. The magnetized SPIONs in the sample generate an additional magnetic field that can be detected by the ME sensor. The clear novelty of our approach is the use of a rotating sample, generating a periodic signal, which enables an easy separation of the desired signal from the background signal and the possibility to compensate drift, which is commonly observed in ME sensor measurements. With this improvement and the use of a ME sensor that is sensitive for low frequencies the setup is able to measure significantly smaller amounts of magnetic nanoparticles than previous approaches described in the literature and we are even able to reconstruct 2D nanoparticle distributions. The noise floor, also referred to as limit of detection (LOD), of this measurement system is around $500 \text{ pT}/(\text{Hz})^{1/2}$. The detection threshold of our MSPM system is $20 \mu\text{g}$ SPIONs in a volume of 200 mm^3 and the spatial resolution is in the range of a few mm. The spatial resolution is determined by reconstructing the particle distribution in the sample layer by solving the inverse problem. To demonstrate the feasibility of the method for detecting living cells, we measured the field distribution originating from SPION-labeled fibroblast cells in an alginate-gelatin matrix, thus demonstrating the potential of our method for biomaterial applications.

© 2020 Elsevier B.V. All rights reserved.

1. Introduction

Superparamagnetic iron oxide nanoparticles (SPIONs) are highly relevant for many biological and medical applications. They are used for magnetic tumor targeting [1], for fighting cancer by hyperthermia [2], and for the intraoperative detection of sentinel

lymph nodes [3,4]. In magnetic resonance tomography (MRT) they serve as contrast agent [5] and their distribution can be directly imaged in 3D by magnetic particle imaging (MPI) [6]. SPIONs are ideally suited for imaging applications because of their high susceptibility at small magnetic fields and nonlinear magnetization in combination with the absence of a remanence field resulting in low particle-particle interactions. Therefore, the particles react directly and independently on the external magnetic field generating a magnetic signal. These properties and the facts that the magnetic signal generated by the human body does not show harmonic components and is very small compared to the signal generated by the SPIONs, make SPIONs ideally suited as contrast agents in magnetic imaging techniques [7].

Abbreviations: ME sensor, magnetoelectric sensor; SPION, superparamagnetic iron oxide nanoparticle; MRI, magnetic resonance imaging; MRT, magnetic resonance tomography; MPI, magnetic particle imaging; MPM, magnetical particle mapping; LOD, limit of detection; DC, direct current; AC, alternating current; S, sensitivity; ASD, amplitude spectral density; VSM, vibrating sample magnetometer.

* Corresponding author.

E-mail address: cse@tf.uni-kiel.de (C. Selhuber-Unkel).

<https://doi.org/10.1016/j.sna.2020.112023>

0924-4247/© 2020 Elsevier B.V. All rights reserved.

Here we present a novel method to map superparamagnetic nanoparticles that is based on the alignment of magnetic moments by moving the sample through the field of a permanent magnet. This results in a motion-modulated field at the sensor position showing spectral components at multiples of the rotation frequency. In contrast to a previous study on the direct measurement of DC magnetic fields with ME sensors [8], we employ a ME sensor and utilize the ΔE effect for sensing the motion modulated field, which in turn leads to a tremendous improvement of the LOD. Other magnetic particle imaging methods, such as MPI [6,9] and magnetic particle mapping (MPM) [10], require technically demanding single frequency AC fields to excite signals at higher harmonics for deriving information on the magnetic properties of the sample. A drawback of these methods is that a strong signal is generated by the sample at the excitation frequency. Due to the superposition of the sample and excitation signal, deciphering the information received at this frequency is not straightforward and the signal component sampled at the excitation frequency is therefore normally suppressed by filtering.

We therefore introduce Magnetic Susceptibility Particle Mapping (MSPM), which employs a permanent magnet that provides the bias field for a ΔE -effect sensor (Fig. 1a) [11,12] and a rotating sample that is magnetized by this magnet, resulting in a motion-modulated magnetic field at the sensor position. The magnetic field at the sample position magnetizes the sample by aligning the magnetic moment of the particles dependent on the magnetic field strength. This magnetic moment m is linked to the magnetization M by $M = m/V$, where V is the Volume. Accordingly, the alignment of magnetic moments can also be described as a change in the magnetization due to the field-dependent susceptibility of the SPIONs. The resulting additional field generated by the SPIONs in the sample is recorded with a ΔE -effect sensor. Besides a characterization of the sensitivity and resolution of MSPM, we also demonstrate that our method is able to detect magnetically labeled cells embedded in an alginate-gelatin hydrogel.

The strength of the sample-generated signal depends on the field-dependent susceptibility of the particles and on the position of the sample in the gap between the permanent magnet and the sensor. Two counteracting processes govern the sample position dependent signal: On the one hand, the absolute strength of the magnetic field and consequently the magnetic moment of the SPIONs (Fig. 1b, orange curve) decreases with decreasing distance of sample and sensor as the sample to magnet distance increases. On the other hand, the sample is at the same time closer to the sensor, which in turn results in an increase of the signal generated by the magnetic moments of the sample (Fig. 1b, blue curve). From this blue curve it is clearly visible that the signal is increasing when the distance between sample and sensor is decreased. Therefore, it would be ideal to place the sample as close to the sensor as possible. Mainly due to the wiring of the sensor and the thickness of the sample holder the smallest distance that can be chosen is 8 mm. We therefore use this distance for all measurements shown in this work.

For detecting the magnetic field generated by the SPIONs we use a thin-film magnetoelectric (ME) sensor as depicted in Fig. 2a. The working principle of ME sensors in general is based on the coupling of a magnetostrictive and a piezoelectric layer on a cantilever. The cantilever (length: 3 mm, width: 1 mm, thickness: 0.05 mm) is made of 50 μm poly-silicon, where the bottom side is coated with a 2 μm thick soft-magnetic magnetostrictive layer (FeCoSiB, easy axis perpendicular to the long axis of the cantilever) and the upper side is coated with a 2 μm thick AlN layer as piezoelectric material [13].

In this work, the ME sensor is operated as ΔE -effect sensor. The LOD of this ΔE -effect sensor in a magnetically shielded chamber is about 500 pT/(Hz)^{1/2} at 10 Hz and the noise sources for these

ME sensors are well-understood [14,15]. The ΔE effect describes the change of the effective elastic modulus that occurs upon magnetization of a magnetostrictive material [16]. It results from an additional, stress-induced magnetostrictive strain that adds up to the mechanical strain. The ME sensor is operated as ΔE -effect sensor by applying an AC voltage A_{ex} near the mechanical resonance frequency f_{res} to the piezoelectric layer. Depending on the electrode design and its excitation frequency, the sensor can be operated in different resonance modes. Here we excite the second bending mode with an adapted electrode design [12]. Due to the anisotropy of the sensitivity, only the projected field parallel to the long axis of the cantilever changes the resonance frequency.

The resonance frequency of the sensor as a function of an external magnetic bias field is shown in Fig. 2b. Magnetic field induced changes in the resonance frequency alter the admittance Y_s of the sensor and can be determined by measuring the current through the electro-mechanical sensor. From the dashed line in Fig. 2b it is obvious that the gradient df_{res}/dB at $B=0$ is small. This gradient is called magnetic sensitivity and determines the sensitivity of the sensor together with the electrical sensitivity ($d|Y|/df_{res}$). Therefore, it is important to use a bias field for shifting the operating point of the sensor to a region of maximum magnetic sensitivity. This is one of the tasks of the permanent magnet in our setup, where the optimum bias field is reached by adjusting the distance between the permanent magnet and the sensor (Fig. 2b). In our setup, the distance was adjusted such that a region of the highest sensitivity is around zero field originating from the sample position.

Determining the ideal operating frequency and amplitude of the detection system is achieved by measuring the output voltage of the sensor at different excitation amplitudes and frequencies in a known magnetic field. The calibrated sinusoidal field has an amplitude of 1.4 μT at a frequency of 2.5 Hz. Sensitivity values and the amplitude spectral density (ASD) of the noise floor at 2.5 Hz measured in an unshielded environment are shown in Fig. 2c. The best sensitivity (S) for this sensor is reached at an excitation amplitude of $A_{ex} = 1.4 \text{ V}$ and at an excitation frequency of $f_{ex} = 45.895 \text{ kHz}$. The sensitivity at these excitation parameters is $S = 12.3 \text{ mV}/\mu\text{T}$ and the ASD of the noise floor is $ASD = 5.5 \mu\text{V}/(\text{Hz})^{1/2}$. The resulting limit of detection (LOD = ASD/S) is 448 pT/(Hz)^{1/2} at 2.5 Hz.

The MSPM setup is shown in Fig. 2d. When rotating a SPION-containing tube through the 21 mm wide gap between the permanent magnet and the electrically shielded sensor at a rotation frequency of 2.5 Hz, the field generated by the magnetized sample is acquired (Fig. 2e). The rotation speed of 2.5 Hz is used for all measurements in this work. A slow rotation speed is advantageous as centrifugal forces on the sample are reduced and a signal with low frequency components at multiples of the rotation frequency is generated. This is favorable due to the sensor's limited bandwidth of approximately 40 Hz. As the acquired signal is periodic with one rotation the signals from different rotations can be averaged to reduce the drift in the signal that is commonly observed in measurements with ME sensors.

For the envisaged reconstruction of SPION distributions from the measured field profile, it is important to acquire the field distribution in a 2D plane parallel to the sample. The distance between the bottom of the sample and the sensor is about 8 mm for all measurements in this paper. 2D measurements of the field distribution are accomplished by radially moving the sensor. Depending on the radial extension of the sample and the acquisition time needed for one measurement at a single radius, the full sample area is scanned within several minutes. Due to the lack of 3D information in the system matrix of the current setup (see section "modelling and reconstruction") it is not possible to gain a 3D distribution of the particles in the sample. Due to the lack of 3D information the reconstruction is currently limited to 2D where we get the projection of the 3D particle distribution onto the layer of the sample holder.

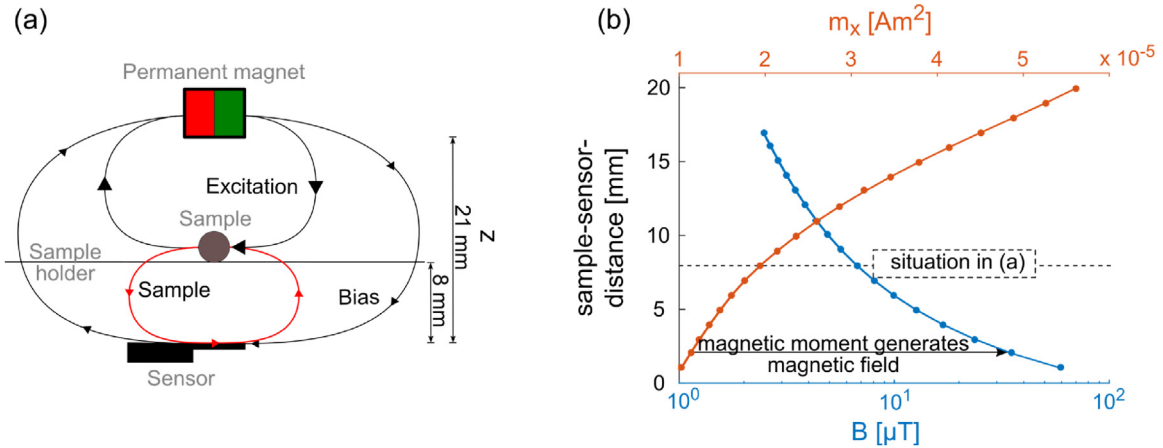


Fig. 1. (a) Working principle of Magnetic Susceptibility Particle Mapping (MSPM). The sample is moved through the gap in between the permanent magnet and the sensor. Magnetic moments are aligned in the field of a permanent magnet and generate an additional magnetic field at the sensor position (red field line). In this work the sample is positioned 8 mm above the sensor. At the sample position the magnetic field has a strength of approximately 6 mT and 1.6 mT at the sensor position. (b) Magnetic moment of a sample in the field of the permanent magnet at different distances to the sensor derived from a VSM curve (see supplementary information). The magnetic moment generates a magnetic field at the sensor position. This field is increasing with decreasing the distance between sample and sensor. (For interpretation of the references to colour in the text and figure legend, the reader is referred to the web version of this article.)

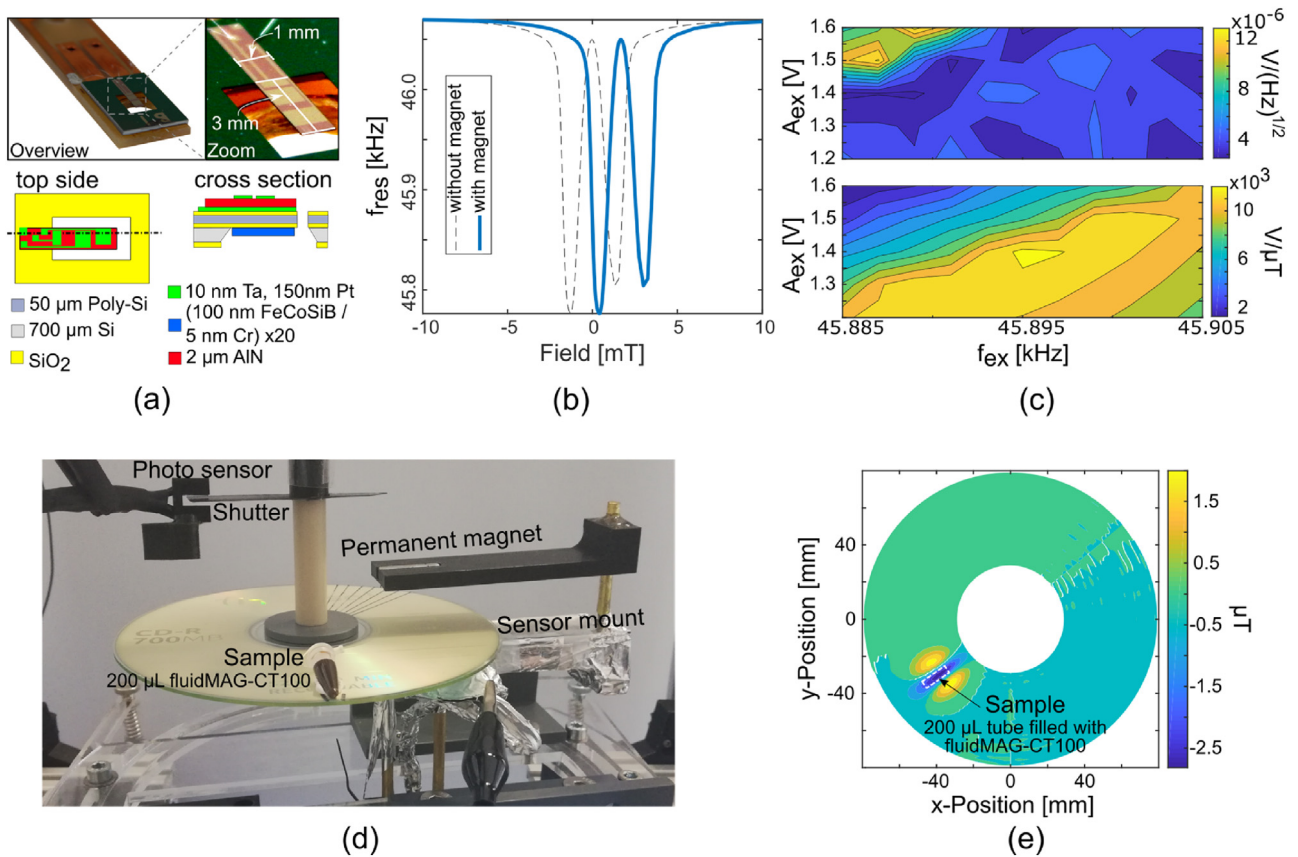


Fig. 2. (a) Image of ΔE-effect sensor (top) and a sketch of the layer stack (bottom). (b) Magnetic field dependent change in the resonance frequency. The curve is shifted by placing a permanent magnet at a distance of 21 mm from the sensor, thus providing a bias field of 1.6 mT to operate the sensor at maximum magnetic sensitivity (highest slope). (c) Excitation parameter dependent noise floor (top) and overall sensitivity (bottom). (d) Setup for measuring distributions of SPIONs in the field of a permanent magnet with a ΔE-effect sensor. By rotating the sample (tube filled with SPIONs) between the permanent magnet and the sensor and by varying the radial position of the sensor, the field distribution (e) generated by the magnetized sample shown in (d) can be measured.

2. Experimental

2.1. Detection limit

The sensor's output signal and thus the acquired signal is modulated by the moving magnetic sample in both amplitude and phase.

Reconstruction of the sample signal is achieved with a quadrature detector in the digital domain where we here only use the amplitude information (see Materials and Methods in the supplementary). Fig. 2e shows the measured 2D field distribution of samples containing SPIONs (fluidMAG-CT, Ø 100 nm, Chemicell, Berlin). This particle type is used for all measurements in this work.

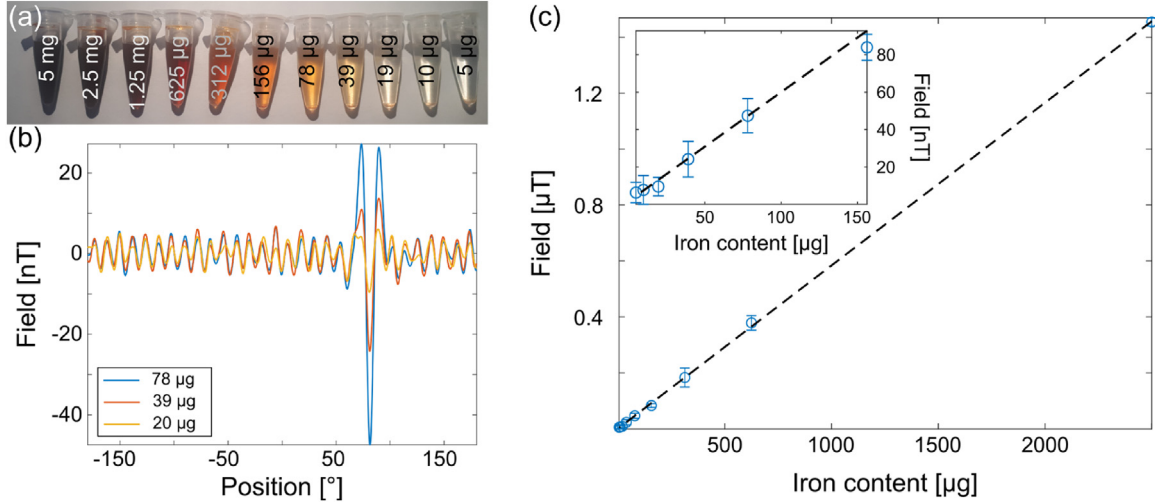


Fig. 3. (a) Tubes containing different amounts of SPIONs diluted in 200 µL water. (b) Angular position dependent signal at the radius where the center of the sample is located. The sample signal measured at a rotation speed of 2.5 Hz is overlaid by a position dependent oscillating background signal. (c) Maximum field amplitude measured for different iron contents. The signal is linearly increasing with increasing SPION mass. The inset shows a magnification for small SPION mass in the range between 5 and 150 µg.

The performance of the sensor setup is determined by measuring the magnetic signal originating from different concentrations of SPIONs (Fig. 3a). The lowest detectable iron content is at 20 µg (Fig. 3b). Due to the correlation in the background signal of single measurements, which are clearly depending on rotation angle, we expect the motor to be the origin of this signal. The amplitude of this background signal, which is limiting the performance in the current setup, is about 5 nT. Fig. 3c shows the maximum field measured by the sensor as a function of iron content in the sample. As expected, there is a linear relationship between the iron content and the measured signal.

2.2. Modelling and reconstruction

In general, the field distribution measured by the sensor can be explained via the superposition of magnetic fields originating from the magnetic dipoles that are aligned in the field of the permanent magnet. The degree of alignment, i.e. the magnetization is dependent on the magnetic field at the position of the sample and can be measured by VSM, resulting in a relation between the applied field and the magnetic moment as shown in the supplementary. A dipole at the origin generates a magnetic field $\mathbf{B}_D(\mathbf{r})$ at the position \mathbf{r} . The size of the magnetic field can be calculated by

$$\mathbf{B}_D(\mathbf{r}) = \frac{\mu_0}{4\pi} \left(\frac{3\hat{\mathbf{r}}(\mathbf{m} \cdot \hat{\mathbf{r}}) - \mathbf{m}}{r^3} \right) \quad (1)$$

here, μ_0 is the vacuum permeability, $\hat{\mathbf{r}}$ is the unit vector in the direction of \mathbf{r} and \mathbf{m} is the magnetic moment.

With this in mind, we also calculated the expected field distribution of a typical sample by solving the forward problem. In a first step, the source geometry is defined by approximating the flask as a cylinder with a height of 15 mm, a diameter of 4 mm and a mass of 5 mg SPIONs homogeneously distributed inside this cylinder. This volume is discretized into voxels of 1 mm³ size (Fig. 4a). For one radial position of the sensor and one angular position of the sample, the contribution from all voxels to the field at the sensor position is summed up. The contribution of a single voxel is determined by calculating the field from the permanent magnet at the voxel position causing a magnetic moment inside this voxel. According to Eq. 1, this magnetic moment generates a magnetic field at the sensor

position. Subsequently this calculation is performed for all angular positions between 0° and 360° of the sample.

Due to the filter characteristics of the sensor, the field calculated for a sample in the above described manner is not equal to the measured signal for this sample. The filter characteristics of the sensor can be described approximately with a first order Bessel filter [17]. By applying a Bessel filter to the calculated symmetric field shown in Fig. 4b we get the red curve shown in Fig. 4c.

To validate this simulation the symmetric field from Fig. 4b is generated in a Helmholtz coil setup. The coils create a temporally varying magnetic signal at the sensor position. The sensor recognizes this field as shown in Fig. 4c, blue curve. The measured signal is very similar but not equal to the simulated one, showing that the Bessel filter is just an approximation here. The asymmetric shape of the curves in Fig. 4c is the result of the filter characteristics of the sensor. Therefore, the temporal signal measured by the sensor is independent of the direction of rotation. But when the temporal signal is transferred to the angular position the signal is mirrored resulting in a higher peak at the higher angular position.

The filter characteristics of the sensor is needed to account for the transient motion influence on the measured data. To get an accurate representation of the corresponding magnetic field of the SPIONs distribution, an inverse filter needs to be applied to the measured signal. After this, we can compute the system matrix (spatial transfer function) by describing the individual matrix coefficients A_{ij} . They relate the magnetic field gained from the source voxel j to the measurement position i . The coefficients in A can be thought of as a spatial sensitivity with the dimensions magnetic field per mass of SPIONs [T/g_{SPIONs}] contributing to the measurement signal via the particle mass x_j stored in the magnetic source vector \mathbf{x} . The measured magnetic field b_i at position i can thus be described as the superposition of all magnetic fields from all voxels j , i.e. the system is described by a system of linear equations:

$$\mathbf{Ax} = \mathbf{b} \quad (2)$$

The matrix \mathbf{A} describes a convolution via a spatial transfer function given by the field distribution of the permanent magnet, which determines the orientation and the strength of the magnetic moment for all voxels. The matrix \mathbf{A} is thus a discretized integral operator and therefore performs a smoothing operation on the spatial particle distribution \mathbf{x} to the magnetic field \mathbf{b} . Therefore, high spatial frequencies in \mathbf{x} are attenuated in \mathbf{b} , i.e. it acts as a low pass

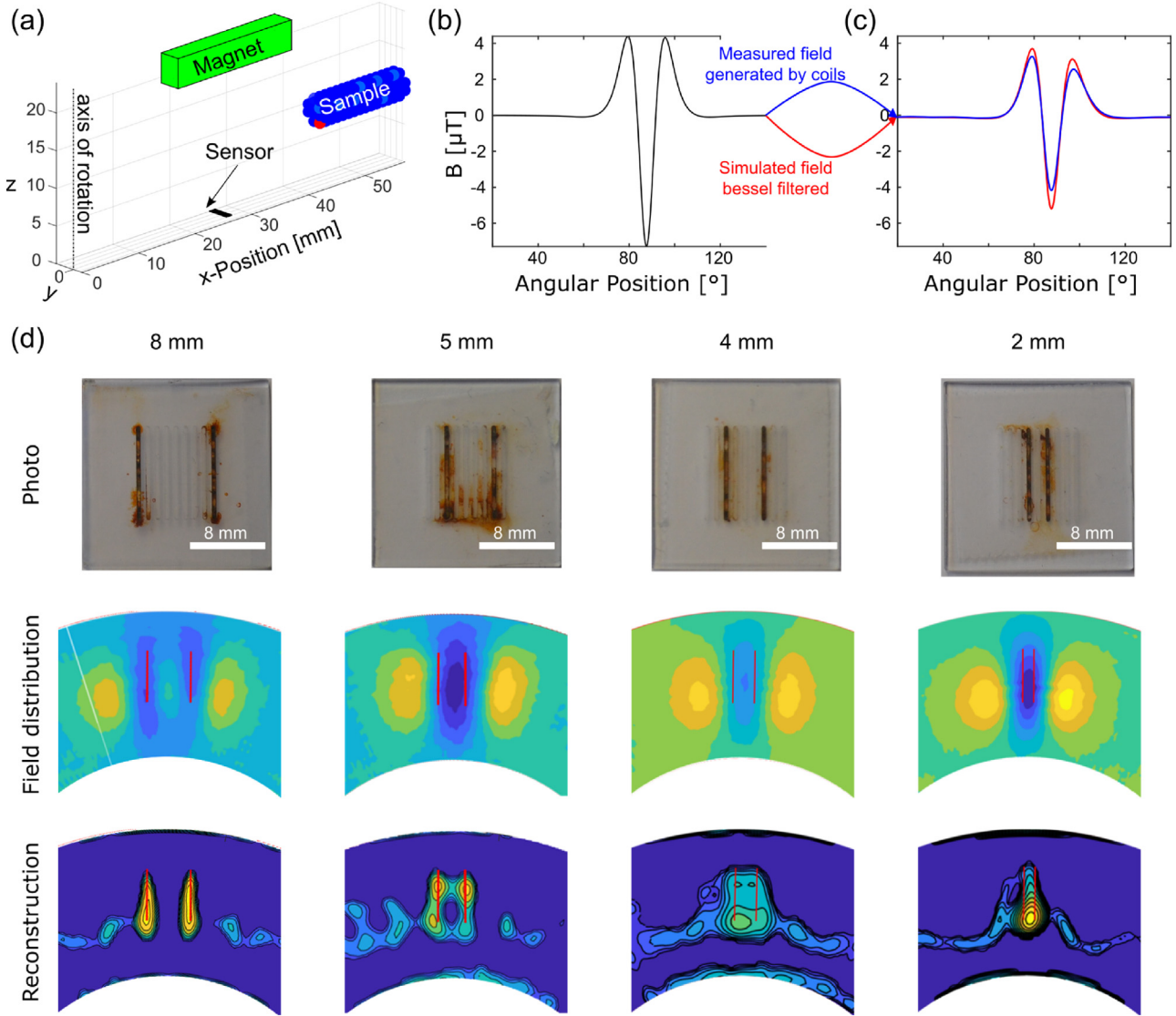


Fig. 4. (a) Sample geometry and setup design for the calculation of the forward problem. Permanent magnet (green), sensor (black), sample (blue) and an exemplary voxel (red) at one radial position of the sensor and one angular position of the sample are shown. (b) Calculated field distribution for the situation in (a) without taking the filter characteristics of the sensor into account. Due to the low pass filter characteristic of the sensor the shape of this calculated field is not equal to the measured field at a rotation frequency of 2.5 Hz. (c) Comparison of the waveforms, when the calculated field is filtered with a Bessel filter (red line) and when it is generated by a coil setup and measured with the sensor (blue line). The calculated and measured curves are in good agreement. (d) SPIONs dried in grooves with different spacing (top) and the measured field distributions for these arrangements (middle). Each groove contains 750 μg of SPIONs, corresponding to a magnetic moment of $10.8 \mu\text{A m}^2$ in a field of 6 mT. The red lines in the field distribution visualize the position of the grooves. From these measurements the particle distribution is reconstructed (bottom). (For interpretation of the references to colour in the text and figure legend, the reader is referred to the web version of this article.)

filter. In the inverse problem, we then have to increase the high spatial frequencies, but these may be distorted by noise, which would lead to unphysical reconstructions of the particle distribution. This effect would express itself by a large solution vector norm. A common approach to solve for an appropriate particle distribution is then to include a penalty term to the cost function for fitting, which involves the solution norm. Here, we choose to use the Iterative Regularization Toolbox IR Tools [18] implementation of the FISTA [19] algorithm, which minimizes the problem

$$\min_{\mathbf{x}} \|\mathbf{A}\mathbf{x} - \mathbf{b}\|_2^2 \text{ s.t. } \mathbf{x} \in C + \text{semiconvergence} \quad (3)$$

The set C describes a box constraint used here to enforce a nonnegative particle distribution. The semiconvergence of the algorithm gives us an appropriate solution, before converging to the unregularized solution, which is distorted by noise. Here, we use

visual inspection of the magnetic source vector \mathbf{x} to determinate the iterated solution.

2.3. Spatial resolution

An important specification of each imaging system is its spatial resolution. We here define the 2D spatial resolution of the setup as the distance at which two identical spatially separated specimens can be recognized as discrete objects in the reconstructed image (Fig. 4d). The sample for the determination of the spatial resolution consists of PMMA slices (width: 20 mm, length: 20 mm, height: 1 mm) containing grooves (width: 0.5 mm, length: 10 mm height: 0.5 mm) at a center to center distance of 1 mm. The grooves were repeatedly filled with 2 μL of fluidMAG-CT until each groove contained approximately 750 μg of SPIONs. This corresponds to a magnetic moment of $10.8 \mu\text{A m}^2$ at the sample position. Measure-

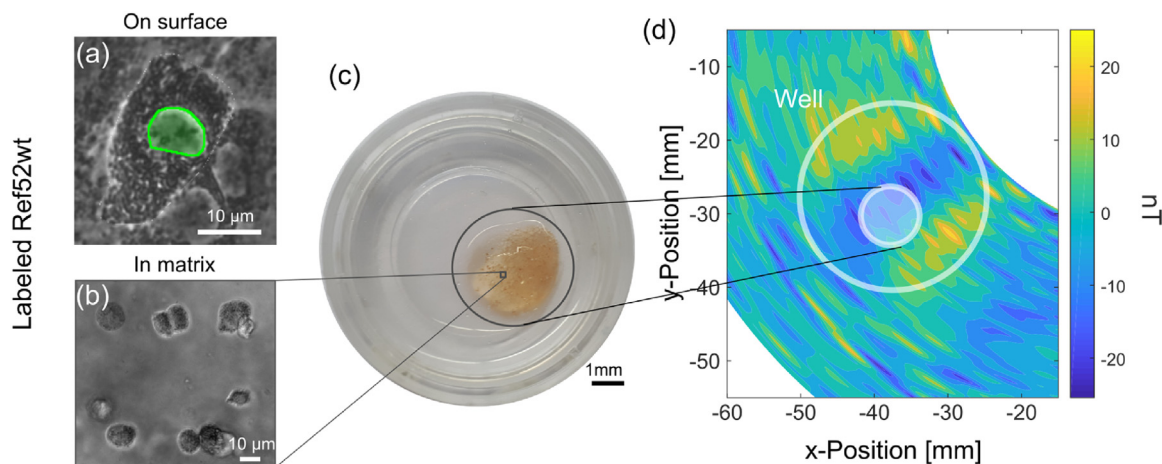


Fig. 5. (a) Ref52-wt cell labeled with SPIONs on a flat surface. The SPIONs surrounding the nucleus, which is highlighted in green, are clearly visible. (b) Magnetically labeled Ref52-wt cells inside an alginate-gelatin matrix and (c) magnetically labeled cells (approx. 1.4×10^6 cells) inside a hydrogel matrix. (d) Field distribution generated by the sample shown in c. Although the signal is much smaller than the strong signal from 5 mg SPIONs shown in Fig. 1, the field distribution looks similar as two regions with positive field (yellowish) surround a region with negative field (blueish). (For interpretation of the references to colour in the figure legend, the reader is referred to the web version of this article.)

ments were taken for samples with groove spacing between 1 mm and 8 mm.

Solving the inverse problem leads to the spatial distribution of SPIONs and indicates a high content of particles at the position of the grooves. Although the reconstruction proves the high content of SPIONs at the sample position, an artificial accumulation of the signal next to the samples appears. These spots are artifacts from the reconstruction and probably result from the discretized integral operator, which is amplifying high frequencies or approximations in the utilized model [20].

Whereas grooves at distances of 8 and 5 mm can be clearly separated in the reconstructed images, this is not possible for smaller distances. Therefore, the current spatial resolution of our setup is limited to 5 mm.

2.4. Cell measurements

An interesting application of MSPM is the determination of the distribution of magnetically labeled cells in biomaterial scaffolds. Essential for this application is a successful labeling of cells with magnetic particles that is crucial for every application that aims at the detection of magnetically labeled cells. The internalization capacity depends strongly on particle coating and shape [21]. Therefore we here use fluidMAG-CT SPIONs with a hydrodynamic diameter of 100 nm, as they are known to be well-internalized by cells due to their coating with citric acid [22]. To show the feasibility of MSPM to detect labeled cells inside a biomaterial scaffold, an alginate-gelatin sample was prepared. This material combination is very common in 3D bio printing [23]. Applying our setup to this sample reveals that the magnetic content of the sample is clearly visible in the magnetic field distribution (Fig. 5).

Hence, MSPM can indeed be used to detect magnetically labeled cells in biomaterial scaffolds. This is a particularly interesting application in the context of tissue engineering, where it is important to non-invasively monitor 3D cell growth *in vitro* [24,25]. Especially for non-transparent biomaterial scaffolds it is currently a time-consuming and destructive task to investigate cell distributions. For example, the sample must be cut into slices before optical investigation [26], or it is critically point dried and imaged in electron microscopy [27]. Hence, our strategy can lead to a strong improvement of *in situ* cell monitoring in scaffolds.

2.5. Perspectives

The concept of aligning magnetic moments inside a magnetic field has also clinical applications. Examples include the determination of the iron content in the liver by Xi et al. who used a thick ME sensor gradiometer [28], or the detection of SPIONs in sentinel lymph nodes with a Hall sensor, as reported by Sekino et al. [4]. Both methods have clear disadvantages for the detection of SPIONs compared to MSPM: The magnetic field in the work of Xi et al. is in the range of 100 mT, which is high enough to align magnetic moments in water and thus the contrast between water and magnetic particles decreases. Due to this alignment, the water present in the sample has a magnetic moment that is in the same range as the magnetic moment of the magnetic nanoparticles. Since water is diamagnetic the field generated by water is pointing in the opposite direction as the field from the nanoparticles and therefore screens the desired signal. For a detailed analysis of this context see the supplementary material. In contrast to the field used by Xi et al., our method uses much smaller external fields to reduce the screening effect of water. The Hall probe reported by Sekino et al. for sentinel lymph node detection uses instead an external field of 0 T. Zero field at the sensor position is often required to not saturate the sensor. The detriment here is that the distance between sample and sensor must be larger or more complicated arrangements of permanent magnets are required to create a field-free point. In our MSPM setup, the ideal field at the sensor position is about 1.6 mT and the field at the sample position is about 6 mT, thus resulting in a small distance between sample and sensor and a good contrast between water and SPIONs. Additionally, we use a scanning approach with a low limit of detection (LOD) of $500 \text{ pT}/(\text{Hz})^{1/2}$ in contrast to the LODs reported by Xi et al. ($0.99 \text{ nT}/(\text{Hz})^{1/2}$) and Sekino et al. ($1 \mu\text{T}$).

A further interesting approach to detect magnetically labeled SPIONs with ME sensors and magnetic modulation has been described by Huong Giang et al. [29]. This setup has a similar detectable minimum iron content as MSPM, but due to our motion-modulated approach the scanning speed in MSPM is about 4500 larger and we are in addition able to provide a 2D reconstruction of nanoparticle distributions.

3. Conclusion

In summary, we have developed a novel and versatile method for detecting SPIONs by a motion-modulated susceptibility mea-

surement that is based on a ΔE -effect sensor and solving of the inverse problem. We demonstrated that the system detects SPIONs effectively down to iron contents of 20 μg in a volume of 200 mm^3 , and with a spatial resolution in the range of a few mm. With further improvements in ME sensors, it will certainly be possible to improve the LOD of the setup and the detectable amount of SPIONs. An improvement of the spatial resolution in 2D is mandatory to map accurately the presence of SPIONs in biological samples. This improvement can be achieved by placing the sample closer to the sensor.

Furthermore, we have shown that it is possible to measure the magnetic signal originating from magnetically labeled cells in bio-material scaffolds. Therefore, we believe that our MSPM method has great potential as a detection method of magnetic nanoparticles, ranging from the detection of cells in 3D printed scaffolds to clinical applications, such as tumor detection.

Declaration of competing interests

The authors declare that they have no known competing financial interests or personal relationships that could have appeared to influence the work reported in this paper.

Funding sources

German Research Foundation (CRC 1261, project B7).
Volkswagen Foundation.

CRediT authorship contribution statement

Nils Lukat: Conceptualization, Methodology, Software, Formal analysis, Investigation, Writing - original draft, Visualization. **Ron-Marco Friedrich:** Writing - original draft, Software, Formal analysis. **Benjamin Spetzler:** Methodology, Resources, Investigation. **Christine Kirchhof:** Methodology, Resources. **Christine Arndt:** Investigation, Resources. **Lars Thormählen:** Investigation. **Franz Faupel:** Supervision, Funding acquisition. **Christine Selhuber-Unkel:** Writing - original draft, Project administration, Supervision, Funding acquisition.

Acknowledgments

We acknowledge the German Research Foundation (Deutsche Forschungsgemeinschaft, DFG) for funding through the collaborative Research Centre CRC 1261 "Magnetolectric Sensors: From Composite Materials to Biomagnetic Diagnostics", project B7. C.S. and C.A. thank the Volkswagen Foundation for funding the project "Molecularly controlled, stimuli-sensitive hydrogels for dynamically adjustable biohybrid actuators". Furthermore, we thank Michael Ortner for the furnishing of magpylib, an easy to use python package for calculating magnetic fields of magnets, currents and moments and Phillip Durdaut for stimulating discussions, the construction and preparation of the amplifier and advice in signal processing issues.

Appendix A. Supplementary data

Supplementary material related to this article can be found, in the online version, at doi:<https://doi.org/10.1016/j.sna.2020.112023>.

References

- [1] M. Mahmoudi, S. Sant, B. Wang, S. Laurent, T. Sen, Superparamagnetic iron oxide nanoparticles (SPIONs): development, surface modification and

- applications in chemotherapy, *Adv. Drug Deliv. Rev.* 63 (2011) 24–46, <http://dx.doi.org/10.1016/j.addr.2010.05.006>.
- [2] Z.W. Tay, P. Chandrasekharan, A. Chiu-Lam, D.W. Hensley, R. Dhavalikar, X.Y. Zhou, et al., magnetic particle imaging-guided heating in vivo using gradient fields for arbitrary localization of magnetic hyperthermia therapy, *ACS Nano* 12 (2018) 3699–3713, <http://dx.doi.org/10.1021/acsnano.8b00893>.
- [3] R. Madru, P. Kjellman, F. Olsson, K. Wingårdh, C. Ingvar, F. Ståhlberg, et al., 99mTc-labeled superparamagnetic iron oxide nanoparticles for multimodality SPECT/MRI of sentinel lymph nodes, *J. Nucl. Med.* 53 (2012) 459–463, <http://dx.doi.org/10.2967/jnumed.111.092437>.
- [4] M. Sekino, A. Kuwahata, T. Ookubo, M. Shiozawa, K. Ohashi, M. Kaneko, et al., Handheld magnetic probe with permanent magnet and Hall sensor for identifying sentinel lymph nodes in breast cancer patients, *Sci. Rep.* 8 (2018) 1195, <http://dx.doi.org/10.1038/s41598-018-19480-1>.
- [5] Y. Bao, J.A. Sherwood, Z. Sun, Magnetic iron oxide nanoparticles as T1 contrast agents for magnetic resonance imaging, *J. Mater. Chem. C* 6 (2018) 1280–1290, <http://dx.doi.org/10.1039/C7TC05854C>.
- [6] B. Gleich, J. Weizenecker, Tomographic imaging using the nonlinear response of magnetic particles, *Nature* 435 (2005) 1214–1217, <http://dx.doi.org/10.1038/nature03808>.
- [7] E.Y. Yu, M. Bishop, B. Zheng, R.M. Ferguson, A.P. Khandhar, S.J. Kemp, et al., Magnetic particle imaging: a novel in vivo imaging platform for cancer detection, *Nano Lett.* 17 (2017) 1648–1654, <http://dx.doi.org/10.1021/acs.nanolett.6b04865>.
- [8] Y. Ren, J. Ouyang, W. Wang, X. Wu, X. Yang, Y. Zhang, et al., Rotating magnetolectric sensor for DC magnetic field measurement, *IEEE Trans. Magn.* 54 (2018) 1–3, <http://dx.doi.org/10.1109/TMAG.2018.2840823>.
- [9] C. Bakenecker Anna, M. Ahlborg, C. Debbeler, C. Kaethner, M. Buzug Thorsten, K. Lüdtke-Buzug, Magnetic particle imaging in vascular medicine, *Innov. Surg. Sci.* (2018) 179, <http://dx.doi.org/10.1515/iss-2018-2026>.
- [10] R.-M. Friedrich, S. Zabel, A. Galka, N. Lukat, J.-M. Wagner, C. Kirchhof, et al., Magnetic particle mapping using magnetolectric sensors as an imaging modality, *Sci. Rep.* 9 (2019) 2086, <http://dx.doi.org/10.1038/s41598-018-38451-0>.
- [11] B. Gajdka, R. Jahns, K. Meurisch, H. Greve, R. Adelung, E. Quandt, et al., Fully integrable magnetic field sensor based on delta-E effect, *Appl. Phys. Lett.* 99 (2011), 223502, <http://dx.doi.org/10.1063/1.3664135>.
- [12] S. Zabel, J. Reermann, S. Fichtner, C. Kirchhof, E. Quandt, B. Wagner, et al., Multimode delta-E effect magnetic field sensors with adapted electrodes, *Appl. Phys. Lett.* 108 (2016), 222401, <http://dx.doi.org/10.1063/1.4952735>.
- [13] S. Zabel, C. Kirchhof, E. Yarar, D. Meyners, E. Quandt, F. Faupel, Phase modulated magnetolectric delta-E effect sensor for sub-nano tesla magnetic fields, *Appl. Phys. Lett.* 107 (2015), 152402, <http://dx.doi.org/10.1063/1.4932575>.
- [14] B. Spetzler, C. Kirchhof, J. Reermann, P. Durdaut, M. Höft, G. Schmidt, et al., Influence of the quality factor on the signal to noise ratio of magnetolectric sensors based on the delta-E effect, *Appl. Phys. Lett.* 114 (2019), 183504, <http://dx.doi.org/10.1063/1.5096001>.
- [15] P. Durdaut, J. Reermann, S. Zabel, C. Kirchhof, E. Quandt, F. Faupel, et al., Modeling and analysis of noise sources for thin-film magnetolectric sensors based on the delta-E effect, *IEEE Trans. Instrum. Meas.* 66 (2017) 2771–2779, <http://dx.doi.org/10.1109/TIM.2017.2709478>.
- [16] E.W. Lee, Magnetostriction and magnetomechanical effects, *Rep. Prog. Phys.* 18 (1955) 184–229, <http://dx.doi.org/10.1088/0034-4885/18/1/305>.
- [17] J. Reermann, S. Zabel, C. Kirchhof, E. Quandt, F. Faupel, G. Schmidt, Adaptive readout schemes for thin-film magnetolectric sensors based on the delta-E effect, *IEEE Sens. J.* 16 (2016) 4891–4900, <http://dx.doi.org/10.1109/JSEN.2016.2553962>.
- [18] S. Gazzola, P.C. Hansen, J.G. Nagy, IR tools: a MATLAB package of iterative regularization methods and large-scale test problems, *Numer. Algorithms* 81 (2019) 773–811, <http://dx.doi.org/10.1007/s11075-018-0570-7>.
- [19] A. Beck, M. Teboulle, A fast iterative shrinkage-thresholding algorithm for linear inverse problems, *SIAM J. Imag. Sci.* 2 (2009) 183–202, <http://dx.doi.org/10.1137/080716542>.
- [20] P.C. Hansen, 1. Introduction and motivation, in: *Discrete Inverse Problems, Society for Industrial and Applied Mathematics*, 2010, pp. 1–4.
- [21] J.A. Champion, S. Mitragotri, Role of target geometry in phagocytosis, *PNAS* 103 (2006) 4930–4934, <http://dx.doi.org/10.1073/pnas.0600997103>.
- [22] A. Plan Sangnier, A.B. Van de Walle, A. Curcio, R. Le Borgne, L. Motte, Y. Lalatonne, et al., Impact of magnetic nanoparticle surface coating on their long-term intracellular biodegradation in stem cells, *Nanoscale* 11 (2019) 16488–16498, <http://dx.doi.org/10.1039/C9NR05624F>.
- [23] Y. He, F. Yang, H. Zhao, Q. Gao, B. Xia, J. Fu, Research on the printability of hydrogels in 3D bioprinting, *Sci. Rep.* 6 (2016) 29977, <http://dx.doi.org/10.1038/srep29977>.
- [24] T.L. Jenkins, D. Little, Synthetic scaffolds for musculoskeletal tissue engineering: cellular responses to fiber parameters, *npj Regen. Med.* 4 (2019) 15, <http://dx.doi.org/10.1038/s41536-019-0076-5>.
- [25] E.S. Place, N.D. Evans, M.M. Stevens, Complexity in biomaterials for tissue engineering, *Nat. Mater.* 8 (2009) 457–470, <http://dx.doi.org/10.1038/nmat2441>.
- [26] C. Lamprecht, M. Taale, I. Paulowicz, H. Westerhaus, C. Grabosch, A. Schuchardt, et al., A tunable scaffold of microtubular graphite for 3D cell growth, *ACS Appl. Mater. Interfaces* 8 (2016) 14980–14985, <http://dx.doi.org/10.1021/acsami.6b00778>.

- [27] M. Taale, F. Schütt, K. Zheng, Y.K. Mishra, A.R. Boccaccini, R. Adelung, et al., Bioactive carbon-based hybrid 3D scaffolds for osteoblast growth, *ACS Appl. Mater. Interfaces* 10 (2018) 43874–43886, <http://dx.doi.org/10.1021/acsami.8b13631>.
- [28] H. Xi, X. Qian, M.-C. Lu, L. Mei, S. Rupprecht, Q.X. Yang, et al., A room temperature ultrasensitive magnetoelectric susceptometer for quantitative tissue iron detection, *Sci. Rep.* 6 (2016) 29740, <http://dx.doi.org/10.1038/srep29740>.
- [29] D.T.H. Giang, D.X. Dang, N.X. Toan, N.V. Tuan, A.T. Phung, N.H. Duc, Distance magnetic nanoparticle detection using a magnetoelectric sensor for clinical interventions, *Rev. Sci. Instrum.* 88 (2017), 015004, <http://dx.doi.org/10.1063/1.4973729>.

Biographies

Nils Lukat studied physics at the Christian-Albrecht University (CAU) in Kiel. He received his M.Sc. in 2016. Since 2016 he has been a Ph.D. candidate in the Collaborative Research Center (CRC) 1261 – Magnetoelectric Sensors: From Composite Materials to Biomagnetic Diagnostics under the supervision of Prof. Dr. Christine Selhuber-Unkel. In his research he is interested in the detection of magnetically labeled cells, strategies for labeling cells with magnetic nanoparticles and the dynamic of cells.

Ron-Marco Friedrich received his Master's degree in materials science and engineering from the Christian-Albrecht University (CAU) in Kiel, Germany, in the Chair for Multicomponent Materials. He is currently a Ph.D. candidate in the Collaborative Research Center (CRC) 1261 for Biomagnetic Sensing at the CAU under the supervision of Prof. Franz Faupel. His current research interest is focused on the imaging of magnetic nanoparticles using magnetoelectric sensors and the mathematical description and limitations of such systems.

Benjamin Spetzler received the M.Sc. degree in materials science and engineering from Kiel University, Germany, in 2017, where he is currently pursuing the Ph.D. degree in Collaborative Research Center (CRC) 1261. His main research interests are magnetic sensor systems utilizing the delta-E effect.

Christine Kirchhof received the Ph.D. degree in materials science and engineering from Kiel University, Kiel, Germany, in 2017 for her work on resonant magnetoelectric sensors for the detection of low frequency magnetic fields. Her current research interests include the magnetostrictive and MEMS-design aspects of magnetoelectric sensors. She works as research fellow in the CRC 1261 "Magnetoelectric Sensors: From Composite Materials to Biomagnetic Diagnostics" at the Kiel University.

Christine Arndt received her bachelor's (2015) and master's degrees (2017) in materials science and engineering from Kiel University, Germany. She is currently a Ph.D. candidate in the Biocompatible Nanomaterials group at Kiel University. Her work focuses on the development of dynamically adjustable hydrogel scaffolds for biohybrid soft robotics.

Lars Thormählen received a master's degree in materials science and engineering from Kiel University in 2017 and afterwards began his doctoral research in thin-film processes and the development of magnetic thin films. The research focus is on the development and improvement of magnetic thin films using PVD processes for magnetoelectric composite sensors in the project CRC 1261 "Magnetoelectric sensors: From composite materials to biomagnetic diagnostics".

Franz Faupel received his Ph.D. in physics from the University of Göttingen in 1985. From 1987 to 1988, he was postdoctoral fellow at the IBM Th. J. Watson Research Center in Yorktown Heights, and got his habilitation from the University of Göttingen in 1992. Since 1994, he holds the Chair for Multicomponent Materials within the Faculty of Engineering at Kiel University. Faupel published more than 300 peer reviewed papers and is listed in the Web of Science with an h-index of 48. His research interests include functional nanocomposites, magnetoelectric sensors, and plasma deposition.

Christine Selhuber-Unkel studied physics at the University of Heidelberg (Germany) and Uppsala University (Sweden). She received her Ph.D. in physics at the University of Heidelberg in 2006. From 2007 to 2009 she worked as a postdoctoral fellow at the Niels Bohr Institute at the University of Copenhagen. Since 2010 she has been a professor for Biocompatible Nanomaterials at Kiel University. In her research she is interested in cell-material interactions, with a particular focus on mechanotransduction and soft materials.





B.4 Mechanical-Resonance-Enhanced Thin-Film Magnetoelectric Heterostructures

Contribution

- Writing original manuscript (shared)

Review

Mechanical-Resonance-Enhanced Thin-Film Magnetolectric Heterostructures for Magnetometers, Mechanical Antennas, Tunable RF Inductors, and Filters

Cheng Tu ^{1,*} , Zhao-Qiang Chu ^{1,2}, Benjamin Spetzler ³, Patrick Hayes ³, Cun-Zheng Dong ¹ , Xian-Feng Liang ¹ , Huai-Hao Chen ¹, Yi-Fan He ¹, Yu-Yi Wei ¹, Ivan Lisenkov ⁴, Hwaider Lin ⁴, Yuan-Hua Lin ⁵, Jeffrey McCord ³, Franz Faupel ³ , Eckhard Quandt ³ and Nian-Xiang Sun ^{1,*}

¹ Department of Electrical and Computer Engineering, Northeastern University, Boston, MA 02115, USA

² College of Engineering, Peking University, Beijing 100871, China

³ Institute for Materials Science, Kiel University, Kaiserstraße 2, 24143 Kiel, Germany

⁴ Winchester Technologies LLC, Burlington, MA 01803, USA

⁵ Materials Science and Engineering, Tsinghua University, Beijing 100084, China

* Correspondence: c.tu@northeastern.edu (C.T.); n.sun@northeastern.edu (N.-X.S.);

Tel.: +1-217-607-3786 (C.T.); +1-617-373-3351 (N.-X.S.)

Received: 16 June 2019; Accepted: 11 July 2019; Published: 13 July 2019



Abstract: The strong strain-mediated magnetolectric (ME) coupling found in thin-film ME heterostructures has attracted an ever-increasing interest and enables realization of a great number of integrated multiferroic devices, such as magnetometers, mechanical antennas, RF tunable inductors and filters. This paper first reviews the thin-film characterization techniques for both piezoelectric and magnetostrictive thin films, which are crucial in determining the strength of the ME coupling. After that, the most recent progress on various integrated multiferroic devices based on thin-film ME heterostructures are presented. In particular, rapid development of thin-film ME magnetometers has been seen over the past few years. These ultra-sensitive magnetometers exhibit extremely low limit of detection (sub-pT/Hz^{1/2}) for low-frequency AC magnetic fields, making them potential candidates for applications of medical diagnostics. Other devices reviewed in this paper include acoustically actuated nanomechanical ME antennas with miniaturized size by 1–2 orders compared to the conventional antenna; integrated RF tunable inductors with a wide operation frequency range; integrated RF tunable bandpass filter with dual H- and E-field tunability. All these integrated multiferroic devices are compact, lightweight, power-efficient, and potentially integrable with current complementary metal oxide semiconductor (CMOS) technology, showing great promise for applications in future biomedical, wireless communication, and reconfigurable electronic systems.

Keywords: thin film; magnetolectric (ME) heterostructures; multiferroic devices; magnetometers; mechanical antennas; tunable RF devices

1. Introduction

Multiferroic materials, by definition, possess at least two of the ferroic properties (ferroelectricity, ferromagnetism, or ferroelasticity). In such materials, the interactions between the different order parameters can lead to new effects, such as magnetolectric (ME) effects [1–4]. According to the physical control mechanism, ME effects are classified as two types: direct ME coupling and converse ME coupling. By definition, direct ME coupling refers to magnetic field control of electric polarization. In contrast, converse ME effect refers to electric field manipulation of magnetization. From the view of material

constituents, the multiferroic ME materials can be categorized into two groups, namely single-phase and composite materials. The single-phase multiferroic materials are natural compounds, whereas the composites typically incorporate ferromagnetic and ferroelectric phases. The magnetoelectric responses of single-phase multiferroic materials, such as BiFeO_3 , are either weak or occur at temperatures too low for practical applications [5,6]. In contrast, multiferroic composites typically exhibit very large ME coupling (several orders of magnitude higher than that of single-phase multiferroics) above room temperature [7]. It should be noted that neither the ferromagnetic nor ferroelectric phase has a ME effect, but the cross elastic interaction between the phases yields a remarkable ME effect. The strong ME coupling found in multiferroic composites proves that efficient energy conversion occurs between the electric and magnetic fields via elastic interaction, making multiferroic ME composites promising candidate to realize a wide variety of devices such as magnetometers [8,9], tunable radio frequency (RF) devices [10–12], transformers [13–15], gyrators [16–19], energy harvesters [20,21], spintronics [22,23], and random access memory [23–25]. In addition to strain-mediated ME coupling, other ME coupling mechanisms such as charge-mediated ME effect [26,27] and exchange bias-mediated ME effect [28,29] have also received a lot of attention. However, these ME coupling mechanisms are still in the early research stages and not discussed in this paper. Some comprehensive review papers for various ME coupling mechanisms are available [5,6,30].

Generally, there are two types of ME composites, namely bulk ME composites and thin-film ME heterostructures. During the last two decades, much effort has been focused on the theoretical and experimental investigations of bulk ME composites. Excellent reviews on the bulk ME composites can be found elsewhere [3,5,7]. The investigation of thin-film ME heterostructures has recently accelerated due to the advances in thin-film growth techniques [31]. Compared to the bulk composites, thin-film ME heterostructures benefit from small form factor, lightweight, low cost due to batch fabrication, as well as the potential capability to integrate with CMOS circuit [32]. In addition, thanks to the advancement of thin-film deposition techniques, excellent elastic interactions can be readily achieved between the piezoelectric and magnetostrictive films. The ME coupling between the two types of films via elastic interaction becomes maximum at the mechanical resonant frequency of the heterostructures, which can be essentially considered as mechanical resonators. Such resonance-enhanced ME coupling inherent to the thin-film ME heterostructures, together with the excellent elastic interactions between the constituent phases, greatly benefit the performance of the integrated devices based on thin-film ME heterostructures. These unique characteristics make thin-film ME heterostructure more advantageous compared to its bulk counterpart in certain applications where miniaturization of the device is crucial. One good example is the magnetometer array which usually requires high spatial resolution and, thus, small size for each constituent magnetometer.

In this article, we present the most recent progress on several types of integrated multiferroic devices based on thin-film ME heterostructures, such as magnetometers, mechanical antennas, tunable RF inductors, and filters. Table 1 provides the summary of the physical mechanisms for different types of integrated devices. Among these devices, the working principles of magnetometers and mechanical antennas in receiving mode are both based on direct ME coupling, which refers to the occurrence of electrical polarization when the devices are subjected to a magnetic field (or waves). In contrast, the working principles of RF tunable devices and mechanical antennas in transmitting mode are both based on converse ME coupling, which refers to the change of magnetic properties due to the application of an electric field. Interestingly, both direct and converse ME coupling are employed in the mechanical antennas, which enables the function of receiving and transmitting using the same thin-film ME heterostructure.

Table 1. Summary of the physical mechanisms for various of integrated multiferroic devices.

Device	Type of ME Coupling	Physical Mechanism
Magnetometer	Direct ME coupling	H-field control of electric polarization
Mechanical antenna in transmitting mode	Converse ME coupling	E-field control of magnetization switching
Mechanical antenna in receiving mode	Direct ME coupling	H-field control of electric polarization
Tunable RF inductor	Converse ME coupling	E-field control of permeability
Tunable RF filter	Converse ME coupling	E-field control of magnetostatics surface waves

2. Thin-Film Characterization Techniques

The strength of ME coupling in the thin-film heterostructures is determined by many factors, such as the properties of the two constituent phases, the elastic interaction between them, the vibration mode of heterostructure, and the orientation of the magnetic and electric fields. Among these factors, the film properties of the two constituent phases are the most fundamental ones in determining the strength of ME coupling. For example, large ME coupling requires large a piezoelectric coefficient in the piezoelectric phase and a large piezomagnetic coefficient in the magnetostrictive phase due to the fact that ME coupling is a product tensor property which is a result of the product of the piezoelectric effect and magnetostrictive effect. In addition, film properties such as coupling coefficient, permittivity and dielectric loss of piezoelectric phase, magnetostriction, saturation field, anisotropic energy, coupling coefficient, permeability and loss tangents associated with the magnetostrictive phase also play significant roles in determining the performance of the thin-film ME heterostructures. Given that these film properties are varied a lot depending on the adopted fabrication processes and conditions, it is crucial to evaluate these properties using thin-film characterization techniques for the purpose of design, simulation, and performance optimization of the integrated multiferroic devices. Comprehensive summary of the film properties can be found for both piezoelectric [33,34] and magnetostrictive thin films [35,36].

2.1. Characterization of Piezoelectric Thin Films

Among all the piezoelectric thin films, lead zirconate titanate (PZT) and aluminium nitride (AlN) are considered as representative materials. PZT is a polycrystalline ceramic and belongs to ferroelectric materials. The advantage of PZT films is the high electromechanical coupling coefficient and piezoelectric coefficient. These superior properties are normally obtained at morphotropic phase boundary (MPB) composition, which corresponds to Zr/Ti ratios close to 58/42 [37]. The main drawback of PZT films is the presence of lead in this material, which causes higher probability of contamination during its processing and not suitable for biological applications. It is also reported that PZT films exhibit high acoustic loss at high frequency range [38]. In contrast to that, sputter-deposited AlN film, being textured polycrystalline non-ferroelectric material, is a better choice for high-frequency applications due to its low dissipation factor and moderate piezoelectric coefficient [39]. More importantly, AlN films are biocompatible and also compatible with the standard CMOS technology [40,41].

Extensive works have been carried out to develop the characterization techniques for PZT and AlN thin films [42–46]. For example, the crystallization quality in AlN film can be evaluated by the X-ray diffraction (XRD) technique. The scanning electron microscopy (SEM) and atomic force microscopy (AFM) techniques were commonly used to examine the topography and surface roughness of the films. The permittivity and dielectric loss of the films can be obtained by measurement using impedance analyzer. To measure the piezoelectric coefficient of the films, a direct measurement approach based on double-beam interferometer was often used, the main characteristic of which is to discriminate the true film expansion from the bimorph-like binding of the sample [42,47]. In addition, many indirect measurement techniques based on cantilever structures [37], surface-acoustic-wave (SAW) resonators [48], and bulk-acoustic-wave (BAW) resonators [38] were also demonstrated to be effective to extract the piezoelectric coefficients.

2.2. Characterization of Magnetostrictive Thin Films

The most commonly used magnetostrictive materials are magnetic alloys such as Terfenol-D, Galfenol, FeGaB, and FeCoSiB. Terfenol-D ($Tb_{0.3}Dy_{0.7}Fe_{1.92}$), with a saturation magnetostriction constant up to 1600 ppm, is well-known as a giant magnetostrictive material [49]. Although having large saturation magnetostriction, Terfenol-D also exhibits a saturation field as large as several kOe, which makes its piezomagnetic coefficient small [50]. On the other hand, Galfenol (binary FeGa alloy) shows a large saturation magnetostriction constant of near 300 ppm with low saturation field in the order of 100 Oe, but the problem of Galfenol is its large loss tangents at RF/microwave frequency range, which was manifested as large ferromagnetic resonance (FMR) linewidth of 450–600 Oe at X band [51]. It has also been demonstrated that incorporation of metalloid element (i.e., boron) into magnetic binary alloys help refine the grain size and reduce magnetic anisotropy, resulting in excellent soft magnetic properties such as low saturation field, large saturation magnetostriction as well as low loss tangents [52]. Among the thin films based on soft magnetic alloys, FeCoSiB and FeGaB thin films are most representative and have been successfully demonstrated to build ME heterostructures with giant ME voltage coefficients and low loss tangents at microwave frequencies [53,54].

Many characterization techniques were developed to evaluate these metallic soft magnetic films. Compositions and crystal structures of the films can be examined by X-ray photoelectron spectroscopy (XPS) and XRD, respectively. Magnetic properties, such as coercive field, saturation field, and saturation magnetization, can be measured using magnetometry techniques based on vibrating sample magnetometers (VSM), superconducting quantum interference devices (SQUID), or BH-loopers. The permeability, loss tangents and FMR linewidth can be extracted from the measured S parameters of a thin-film loaded waveguide which is immersed in a fixed magnetic field [55]. As for measurement of magnetostriction, several techniques have been proposed, which can be broadly classified as either direct or indirect methods [56]. Direct methods enable the magnetostriction to be measured directly as a function of the applied magnetic field. The most commonly used direct methods include the capacitance method based on cantilever structures [57], the optical method utilizing rotating magnetic fields [58], and the nano-indentation method [59]. In the capacitance method, the cantilever with the thin film on top forms one plate of a capacitor, which serves as a tuning capacitance in an oscillator. The magnetostriction can be derived by measuring the shift in resonant frequency of the oscillator, which is caused by the capacitance change due to deflection of the cantilever. The drawback of the capacitance method is that its accuracy is easily impacted by the environment, such as ambient temperature. The optical method utilizing rotating magnetic fields permits measurement with high accuracy and does not need any contact between the probe and sample. However, the method requires a large space and a sophisticated optical system. The nano-indentation method enables measurement of both elastic properties and magnetostrictions in thin films, but it requires a minimum penetration depth into the film (60 nm) and causes unrecoverable damage to the film. In addition to magnetostriction, the change in elastic modulus as a function of applied magnetic field (delta-E effect) is also an important magnetomechanical property of thin films, given that increased interest has recently been spurred in employing the delta-E effect to build sensitive magnetometer [32,60,61]. Unfortunately, few works have been reported to quantitatively characterize the delta-E effect [62].

Recently, Dong et al. [63] developed a simple, compact, and sensitive system to measure magnetostriction, the piezomagnetic coefficient, and the delta-E effect by using a non-contact optical technique. The system includes a magnetostriction tester and a delta-E tester, both of which were based on a similar structure and can be assembled with very few parts. Figure 1a shows the schematic of the proposed magnetostriction tester in three-view. An adjustable AC driving magnetic field ranging from 0 to 300 Oe is provided by two pairs of mutually perpendicular set Helmholtz coils. Equivalent amplitude and 90° phase shift current in the two pairs of Helmholtz coils can be configured to generate a rotating magnetic field. The sample under test is prepared by depositing the magnetostrictive thin film on a cantilever. An MTI-2000 fiber-optic sensor is utilized to detect the deflection of the cantilever tip due to strain changes in the magnetostrictive thin film. The displacement between the cantilever

tip and the optical probe can be detected and converted to an AC voltage signal, which is recorded using a SR-830 lock-in amplifier. As a result, the magnetostriction and piezomagnetic coefficient of the magnetostrictive thin-film can be deduced. It should be noted that the AC driving frequency should be set to off resonance to avoid mechanical amplification. The schematic of the proposed delta-E tester is shown in Figure 1b, where it can be seen that the measurement setup is very similar to that of magnetostriction tester. A 0.1 Oe AC driving field with the frequency swept around 1555 Hz (second resonant frequency of the cantilever) is provided by a solenoid, which will excite the cantilever to vibrate at its second resonant mode. The reason to choose the second resonant mode is that the frequency of the fundamental vibration mode is too low (280 Hz), and the resultant miniscule frequency shift is very difficult to distinguish. For the higher-order resonant modes, the signal strength becomes too weak to detect. Outside the solenoid, one pair of Helmholtz coils is set to provide the DC bias field, which will induce change in the magnetostrictive strain and, thus, leads to the change in Young's modulus. By measuring the shift in resonant frequency, the change of Young's modulus can be derived according to the modified Euler-Bernoulli beam theorem. To obtain the maximum magnetostrictive strain change and strongest vibration signal, the directions of the generated magnetic fields from the solenoid and Helmholtz coil should be set perpendicular to the easy axis of the thin films.

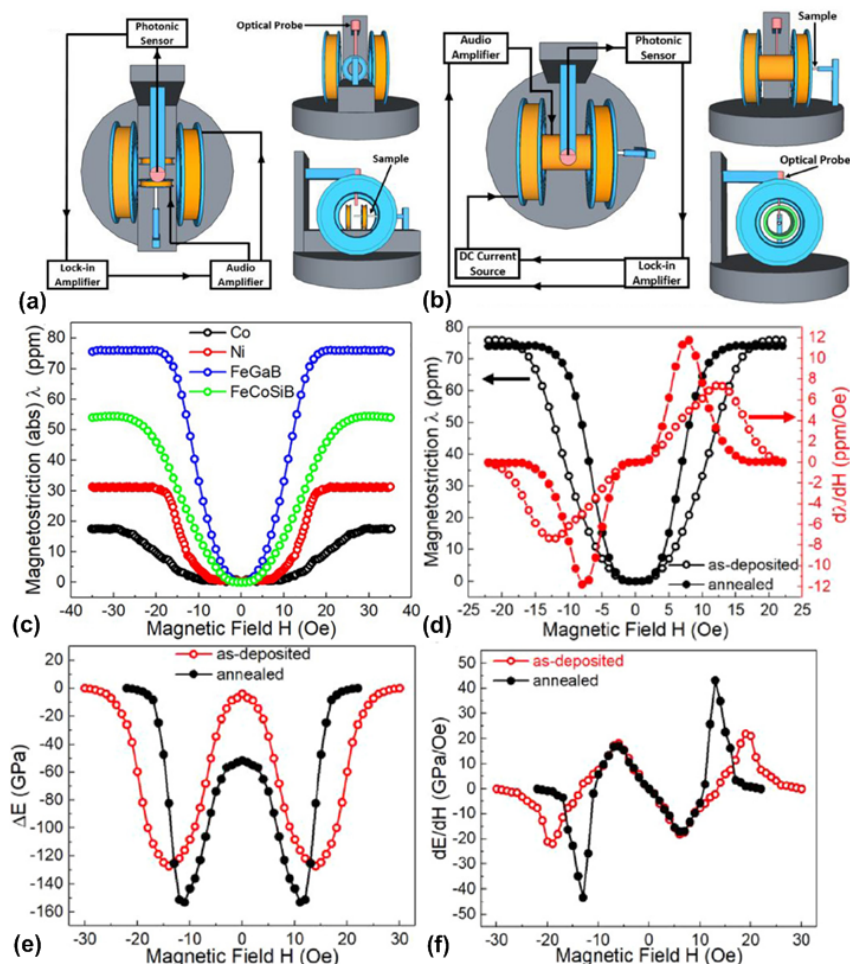


Figure 1. (a) Schematic of the proposed magnetostriction tester in three-view; (b) schematic of the proposed delta-E tester in three-view; (c) measured magnetostriction with respect to magnetic field for different magnetic thin films; (d) measured magnetostriction and piezomagnetic coefficient for as-deposited and annealed FeGaB thin films; (e) measured delta-E effect for as-deposited and annealed FeGaB thin films; and (f) measured dE/dH for as-deposited and annealed FeGaB thin films. This figure is reproduced with permission from American Institute of Physics (AIP) Publishing, [63].

To calibrate the system, some typical magnetostrictive thin films (e.g., Ni, Co, FeGa, and Permalloy) with reported magnetostriction should be used. Figure 1c shows the measured magnetostriction of some magnetostrictive thin films after system calibration. To confirm the accuracy of the system, magnetostriction characterizations were carried out for as-deposited and annealed FeGaB thin films, respectively. Figure 1d shows the measured magnetostriction and piezomagnetic coefficient for as-deposited and annealed FeGaB thin films. It can be seen that the saturation magnetostriction field (15 Oe) is smaller for annealed FeGaB film compared to that of as-deposited one (20 Oe). At the same time, magnetic annealing also enhances the piezomagnetic coefficient from 7.5 ppm/Oe to 12 ppm/Oe. These improvements show that the total anisotropy energy was reduced by magnetic annealing, which essentially released the residual stress in the films. By using a delta-E tester, one can measure the change in Young's modulus, as shown in Figure 1e. It can be seen that a larger reduction in Young's modulus (153 GPa) occurs for annealed FeGaB thin films compared to that of the as-deposited one (125 GPa). Figure 1f shows the derivative of Young's modulus in regard to the magnetic field (dE/dH), where it can be seen that the annealed FeGaB film exhibits a larger peak value of dE/dH (43 GPa/Oe). These measured results agree with the theoretical predictions, which suggests accurate measurement of the magnetostriction, piezomagnetic coefficient, and delta-E effect can be achieved by using the proposed system.

2.3. Magnetic Domain Characterization of Magnetostrictive Thin Films

Magnetic domain activity plays an important role for the noise characteristic in ME-based devices. Moreover, due to stress-strain effects [64,65] in the ME structures, the actual magnetic material properties, especially the effective magnetic anisotropy, may become local in nature. Only a few methods allow for a spatially resolved characterization of the magnetization response down to the device level. Magnetic domain observations techniques applied for the characterization of the piezomagnetic phase in ME heterostructures include magnetic force microscopy (MFM) [66], scanning electron microscopy with polarization analysis (SEMPA) [67], and soft X-ray magnetic circular dichroism–photoemission electron microscopy (XMCD-PEEM) [68]. In particular, magnetic domain imaging by magneto-optical Kerr effect (MOKE) microscopy [69,70] offers direct access to the local magnetization behavior on the ME device level [66,71–76]. MOKE microscopy allows in situ and time-resolved characterization of the magnetic phase of ME heterostructures. As shown in Figure 2a, characterization from a local level up to the extended ME structures is achievable. This includes obtaining quantitative information on the magnetic domain distribution. Figure 2b shows a quantitative domain image from the edge of a ME structure [65]. The characteristic domain pattern is because of stress relaxation at the device edges. The visible partial folding of magnetization is due to minimization of the magnetostrictive self-energy. Magnetoelastic interactions lead to an effective inversion of the magnetic anisotropy axis with effects on magnetization reversal and magnetic noise behavior in ME structures. Analyzing the spatial magnetic response also permits directly correlating the magnetic domain characteristics and ME response [65,70]. It was shown that the ME amplitude and working point, beyond material properties, are strongly dependent on the exhibited domain configuration.

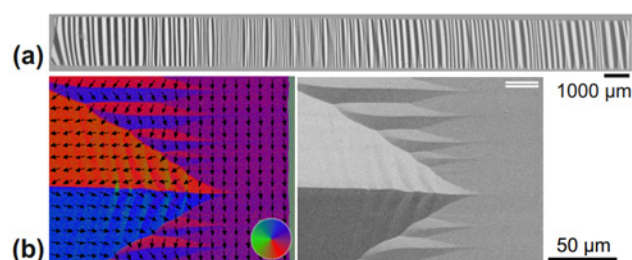


Figure 2. (a) Full magnetic domain distribution [70]; and (b) the quantitative magnetic domain evaluation and MOKE micrograph of edge closure domains states in a cantilever ME magnetometer based on FeCoSiB [67]. This figure is reproduced with permission from AIP Publishing, [70] and [67].

MOKE microscopy was also employed for process control for advanced ME schemes. In situ MOKE imaging during magnetic field annealing was utilized for magnetic domain engineering to improve ME device performance in terms of reducing the magnetic noise level [76].

3. Magnetometers

Until now, the gold standard for weak magnetic field measurement has been to use SQUIDs with a limit of detection (LOD) of a few $\text{fT}/\text{Hz}^{1/2}$ at 1 Hz [77]. However, SQUIDs are bulky and expensive because their optimal performance is usually achieved with the help of liquid helium cooling for near absolute-zero temperature. Thus, it is highly desirable to find alternative magnetometer techniques that work at room temperature while also having a low LOD value. Recently, much effort has been focused on building ultra-sensitive magnetometers using ME heterostructures, which have been demonstrated to exhibit LOD at a few $\text{pT}/\text{Hz}^{1/2}$ at 1 Hz without the need for cooling [78]. Such ME magnetometers are usually categorized into two groups, namely, bulk laminates or thin-film composites. The most important merit shared by bulk and thin-film ME magnetometers is their enhanced ME voltage coefficients and sensitivity (about 1 ~ 2 orders enhancement in magnitude) when driven at their mechanical resonant frequencies. This enhancement is due to the fact that much less energy loss, and thus much higher energy transduction efficiency, occurs at mechanical resonant frequencies compared to out-of-resonance frequency range. Different from the bulk ones, the thin-film ME magnetometers have much smaller size, which is essential for achieving high spatial resolution by forming magnetometer arrays [79]. Furthermore, thin-film ME laminates benefit from perfect elastic coupling between the magnetostrictive and piezoelectric phases. Another advantage of thin-film ME magnetometer is its capability to attain magnetic field sensitivity in only one direction, which is enabled by the in-plane anisotropy of the magnetostrictive layer. This feature makes it possible to realize magnetometer capable of three-dimensional vector field measurement. Currently, there are mainly three types of thin-film ME magnetometers based on direct or indirect detection schemes, which are respectively described in following three subsections.

3.1. Magnetometers Using Direct Detection

Magnetometers using direct detection are usually used for detecting AC magnetic fields. Their working principle is based on electrical polarization upon an applied magnetic field (direct ME effect). The applied AC magnetic field induces alternative magnetostriction in the magnetostrictive phase, which translates to stress variation in the piezoelectric phase and, thus, results in a change in the electrical polarization for output readout. A commonly used figure-of-merit to describe how sensitive the output electrical polarization responds to the applied magnetic field is the ME voltage coefficient. In 2009, Zhao et al. [80] demonstrated a thin-film ME magnetometer consisting of sol-gel-derived PZT and magnetron-sputtered FeGa layers on a micromachined silicon cantilever. The reported thin-film ME magnetometer shows ME voltage coefficient of $1.81 \text{ V}/\text{cm}\cdot\text{Oe}$ at a mechanical resonant frequency of 333 Hz under a DC bias magnetic field of 90 Oe. The purpose of the DC bias field was to shift the operating point of the magnetostrictive layer to the inflection point, where the derivative of the magnetostriction with respect to the magnetic field and, thus, the ME voltage coefficient reaches its maximum. With the help of magnetic field annealing, Greve et al. [53] demonstrated an extremely high ME voltage coefficient of $737 \text{ V}/\text{cm}\cdot\text{Oe}$ at a mechanical resonant frequency of 753 Hz under a DC bias magnetic field of 6 Oe in a ME magnetometer consisting of FeCoSiB/AlN thin-film ME heterostructures. The reported high ME voltage coefficient ($737 \text{ V}/\text{cm}\cdot\text{Oe}$) was two orders of magnitude higher than that at out-of-resonance frequency range ($3 \text{ V}/\text{cm}\cdot\text{Oe}$). The observed enhancement in ME voltage coefficient agrees with the measured quality factor (Q) of 140 at the resonant frequency. The demonstrated thin-film ME magnetometer exhibit pronounced magnetic field sensitivity only in the long axis of the cantilever, which was perpendicular to the magnetic field applied during the annealing process. This unique characteristic serves the possibility to realize a vector field magnetometer. To further enhance the ME voltage coefficient, Kirchhof et al. [81] operated

the thin-film ME magnetometer in vacuum (under pressure below 10^{-5} mbar), demonstrating a giant ME voltage coefficient of 20 kV/cm·Oe at resonant frequency of 152 Hz, which represents a five-fold increase compared to that at atmospheric pressure. It is also shown that operating the magnetometer in vacuum improves the LOD by 10-fold (from 3 nT/Hz^{1/2} to 300 pT/Hz^{1/2}). These improvements in ME voltage coefficient and LOD were attributed to much lower air damping in vacuum, which is manifested as a remarkable increase in Q from 1400 in air to 5800 in vacuum.

Most of the thin-film ME magnetometers mentioned above have similar laminate structures, which is FeCoSiB layer on top of AlN layer. The reason why AlN layer has to be deposited prior to deposition of FeCoSiB layer is due to that the conventional reactive magnetron sputter deposition of a high-quality AlN layer requires a substrate heating temperature as high as 400 °C [82], which negatively impacts the amorphous nature of FeCoSiB. However, it is also reported in [83] that this deposition sequence does not yield the best soft magnetic properties for FeCoSiB layer because of the higher roughness of AlN layer compared to that of silicon substrate. In 2016, Yarar et al. [84] developed an inversed deposition sequence, which allows depositing amorphous FeCoSiB on the smooth silicon substrate using magnetron sputter deposition, followed by sputter deposition of a high-quality AlN layer without intentional substrate heating [85]. The schematic illustration of the investigated magnetometer is shown in Figure 3a. The measured ME voltage coefficient as a function of the applied AC magnetic field was shown in Figure 3b, where it can be seen that a sharp peak (giant ME voltage coefficient as high as 5 kV/cm·Oe) occurs at the mechanical resonant frequency of 867 Hz. This suggests the resonance behavior of the ME heterostructure greatly enhances the ME voltage coefficient compared to that at out-of-resonance frequency range. Figure 3c depicts the measured ME voltage noise density as the magnitude of the applied 867 Hz magnetic field decreases. It can be seen that the measured data start to scatter as the magnetic field becomes smaller. This is due to the fact that the output electric signal from the magnetometer becomes indistinguishable from the noise when the signal-to-noise ratio (SNR) drops to 1. Thus, the value of LOD can be deduced from the readings marked by the red arrow, which is determined to be 400 fT/Hz^{1/2}. Figure 3d shows the measured LOD at different frequencies. At low frequency range from 1 to 100 Hz where noise with 1/f characteristic dominates, measured values of LOD are in the nT/Hz^{1/2} range. A remarkable improvement in LOD (below 1 pT/Hz^{1/2}) can be seen around the mechanical resonance. As the frequency is further increased, the noise restricts the LOD within a few pT/Hz^{1/2} range.

There is one potential problem for the cantilever-type ME magnetometer, which is that such a magnetometer is vulnerable to extrinsic acoustic and vibrational noise since these noises are usually in the same frequency range as the resonant frequencies of the bending modes. To reduce the noise contribution, Salzer et al. [86] proposed a noise cancellation scheme by placing two cantilever-type magnetometers in an inverse orientation (tuning fork). Such an orientation setup allows two cantilevers bending in opposite directions producing a differential-mode signal when a magnetic field is applied, but bending in the same direction resulting in a common-mode signal upon vibrational excitation. Thus, acoustic and vibrational noise can be highly suppressed when simply taking the difference of the signal components utilizing an instrumental amplifier. Using such a noise cancellation method, LOD of approximately 500 fT/Hz^{1/2} has been achieved at a resonant frequency of 958 Hz.

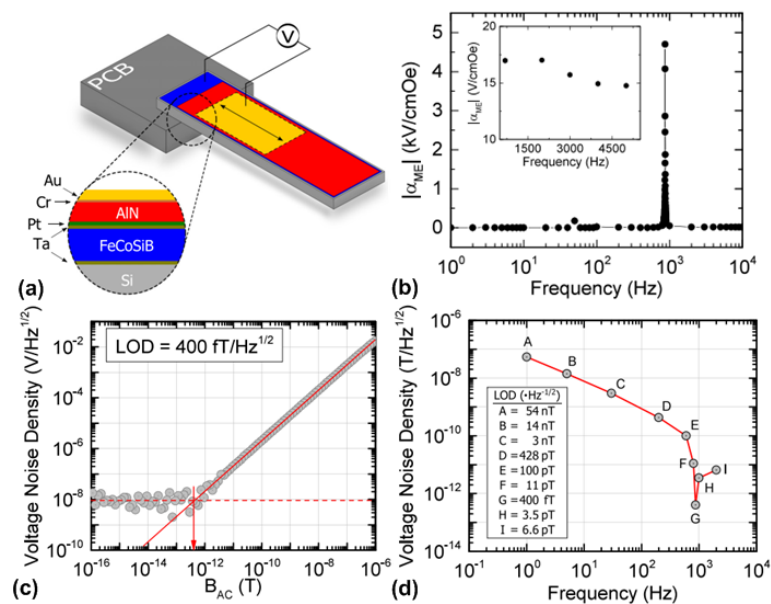


Figure 3. (a) Schematic of the cantilever-type magnetometer using inverted deposition sequence; (b) measured ME voltage coefficient as a function of the frequency of the applied AC magnetic field. The sharp peak marks the mechanical resonant frequency of 867 Hz. The inset shows the ME voltage coefficient above the resonance; (c) measured voltage noise density with respect to the magnitude of applied AC magnetic field with constant frequency of 867 Hz; and (d) measured voltage noise density with respect to the frequency of applied AC magnetic field with constant magnitude of 1×10^{-3} Oe. This figure is reproduced with permission from AIP Publishing, [84].

3.2. Magnetometers Based on Frequency Conversion

One problem for magnetometers using direct detection is narrow bandwidth. This problem occurs because the optimal ME voltage coefficient and LOD can only be obtained when the frequency of the magnetic signal to be detected matches the resonant frequency of the ME composite. For bio-magnetic applications such as measurement of heart signals, the frequency range of the magnetic signal to be detected is from 0.1 Hz to approximately 100 Hz. Mechanical resonators with such low resonant frequencies would have excessively large size, which makes it impractical to realize using thin-film ME heterostructure. Thus, most of the cantilever-type thin-film ME magnetometers have resonant frequencies from several hundred Hz to a few kHz. This means that the ME voltage coefficient will be much lower at the frequency range of interest below 100 Hz due to the missing resonance enhancement. Furthermore, LOD decreases due to dominating $1/f$ noise contribution towards the low frequency range. Recently, two indirect detection schemes have emerged showing promises to solve this problem: magnetometers using frequency conversion and magnetometers based on delta-E effect. The frequency conversion techniques allow transferring the desired low-frequency magnetic signal to the higher resonant frequency of the magnetometer structure. Currently, there are two available approaches to realize frequency conversion which are using magnetic frequency conversion or electric frequency conversion.

The frequency-conversion-approach for thin-film ME magnetometer was first demonstrated by Jahns et al. [87], which used a time-varying bias magnetic field (modulation signal) instead of a DC bias field commonly adopted in direct detection method. Due to the non-linear characteristics of the magnetostriction curve, the frequency of desired magnetic signal will be upconverted to the mechanical resonant frequency of the ME magnetometer under the premise that the amplitude of the desired signal is much smaller than that of the modulation signal. This technique offers the possibility to achieve resonance enhanced ME voltage coefficient and improved LOD at virtually arbitrary frequencies far below mechanical resonant frequency, which allows wideband measurement. It was shown in [87] that this frequency conversion technique using magnetic modulation improved LOD by three orders of magnitude

(from $1 \mu\text{T}/\text{Hz}^{1/2}$ to $1 \text{nT}/\text{Hz}^{1/2}$) upon desired magnetic signal at 1 Hz. However, this value of LOD is still much larger than that using direct detection method ($7.1 \text{pT}/\text{Hz}^{1/2}$ [87]). The reason for this is that the undesired occurrence of additional noise under modulation, which was systematically studied in [88].

To reduce the noise caused during magnetic frequency modulation, Röbisch et al. [75] reported an effective method, which utilize exchanged biased (EB) multilayers as a magnetostrictive phase. The introduction of the exchange bias coupling in magnetostrictive multilayers, magnetic domain configurations can be systematically altered, highly reducing the noise caused by magnetic frequency modulation. As a result, a LOD of $180 \text{pT}/\text{Hz}^{1/2}$ upon a desired magnetic signal at 10 Hz has been demonstrated, which represents an enhancement in the LOD by a factor of about five compared to the magnetometer without exchange bias layer. A further step in improving the noise characteristics of ME magnetometers has been taken by an almost complete elimination of magnetic domain activity using an antiparallel exchange bias scheme [76]. By this, the shape and demagnetization effects are overcome and stable single-domain configurations in the magnetic sensing layers of the employed magnetic multilayers are formed. As a result, magnetic noise contributions are eliminated and LODs down to $60 \text{pT}/\text{Hz}^{1/2}$ at a magnetic signal of 10 Hz are obtained [89]. The antiparallel bias arrangement can also be applied to other ME heterostructures. It offers the possibility of further improvement in LOD, envisioning LODs below $10 \text{pT}/\text{Hz}^{1/2}$. Another advantage of using exchange bias coupling refers to elimination of an external DC magnetic bias field, which favors reducing the complexity of the measurement setup.

One drawback for the magnetic modulation is the large power consumption for generating AC magnetic fields, thus prohibiting the construction of sensor arrays. To overcome this issue, Hayes et al. [90] reported a cantilever-type magnetometer using electric frequency conversion technique, which consumes much less power by employing electrical field to actively drive the ME heterostructure. Figure 4a shows the schematic of this device, where it can be seen that the ME heterostructure mainly consists of two electrically independent piezoelectric phases (AlN layer and PZT layer) and one magnetostrictive phase (EB-FeCoSiB layer). The electric modulation signal is applied across the unpoled PZT layer to excite the ME heterostructure to vibrate. This excitation method enables frequency conversion since PZT shows a nonlinear piezoelectric coefficient. The AlN layer is used for the detection of the output voltage. This readout scheme is considered to be more compact compared to the one using a pickup coil wound around the magnetometer [91]. Figure 4b shows the measured output spectrum taken from the AlN layer when a low frequency 2 Hz sinusoidal magnetic field with an amplitude of $1 \mu\text{T}$ is present. No DC magnetic bias field is required since the exchange biased magnetostrictive multilayer (EB-FeCoSiB layer) shows its maximum magnetoelectric response in zero field. It can be seen that the output signal reaches its maximum at 689 Hz, which agrees with the resonant frequency of the ME heterostructure. Two equally large side-band signals are formed at $f_{\text{mod}} \pm 2 \text{ Hz}$ due to the frequency modulation. A limit of detection of approximately $5 \text{nT}/\text{Hz}^{1/2}$ can be derived upon the fact that a $1 \mu\text{T}$ signal is about 45 dB above the noise floor. Figure 4c shows the case when a 20 Hz sinusoidal magnetic field with an amplitude of $1 \mu\text{T}$ is applied. The frequency of the modulation signal applied to the PZT layer is set to be 669 Hz. Thus, the sum of the modulation frequency (669 Hz) and the desired magnetic signal (20 Hz) matches the resonant frequency of the ME composite (689 Hz). It can be seen that the up sideband signal at 689 Hz is much stronger than the low sideband signal due to the enhancement of the Q at the resonant frequency. Figure 4d shows the linearity measurement performed at magnetic field of 10 Hz, where it can be seen that SNR drops to 1 at $10 \text{nT}/\text{Hz}^{1/2}$. This translates to a LOD value of $10 \text{nT}/\text{Hz}^{1/2}$.

In order to retain power consumption at a minimum and avoid external magnetic bias or driving fields, replacing one piezoelectric layer with a mechanically decoupled passive pickup coil is an option. The coil surrounds a similar thin film composite with which the converse magnetoelectric effect is exploited [91]. The setup is shown in Figure 5a. Exciting of a high frequency resonance mode at about 500 kHz, causes magnetoelastic interactions with the magnetostrictive phase, leading to periodic magnetic flux change within the coil. The coil voltage amplitude at this frequency shows a strong dependence towards external magnetic fields exceeding 2.2 kV/T, shown in Figure 5b. A linear

resolution of 1.2 nT at quasi-DC of 200 mHz is achieved in this way, indicated by 15 dBV of noise margin in Figure 5c,d. Utilizing such high resonant frequency modes provides inherently superior acoustic noise rejection.

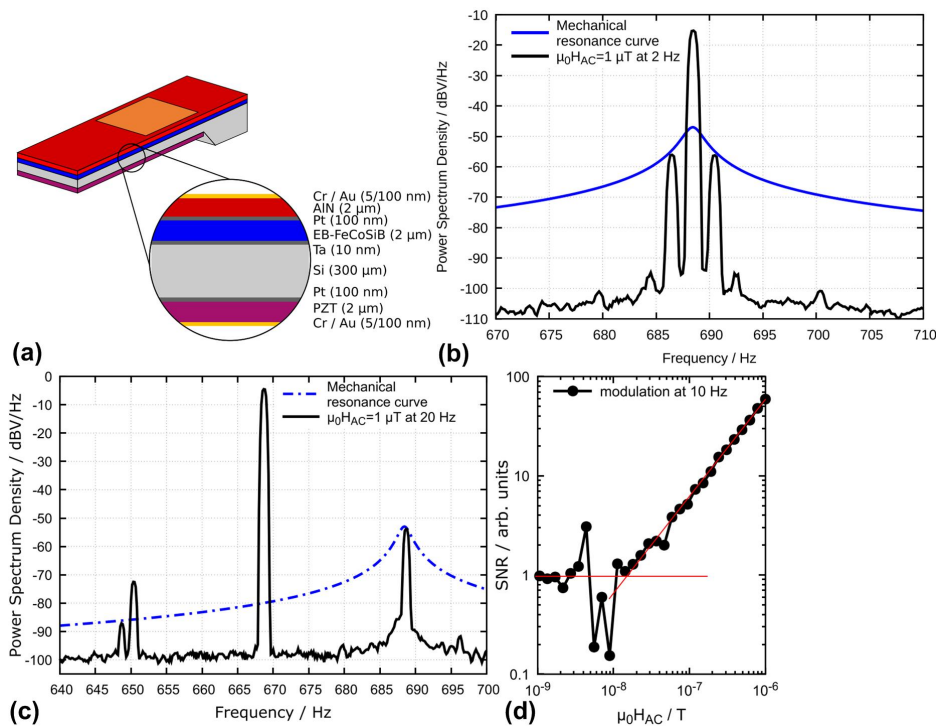


Figure 4. (a) Schematic of the cantilever-type magnetometer using electric frequency conversion; (b) measured output spectrum taken from the AlN layer when a low frequency 2 Hz sinusoidal magnetic field is present. The sensor’s PZT layer is excited in mechanical resonance at 689 Hz, and the blue line indicates the resonance behavior of the resonator; (c) the measured output spectrum taken from the AlN layer when a low frequency 20 Hz sinusoidal magnetic field is present. The sensor’s PZT layer is excited at 669 Hz, and the blue line indicates the resonance behavior of the resonator; and (d) the linearity measurement performed at a magnetic field of 10 Hz, where the noise floor is reached at about 10 nT/Hz^{1/2}. This figure is reproduced with permission from AIP Publishing, [90].

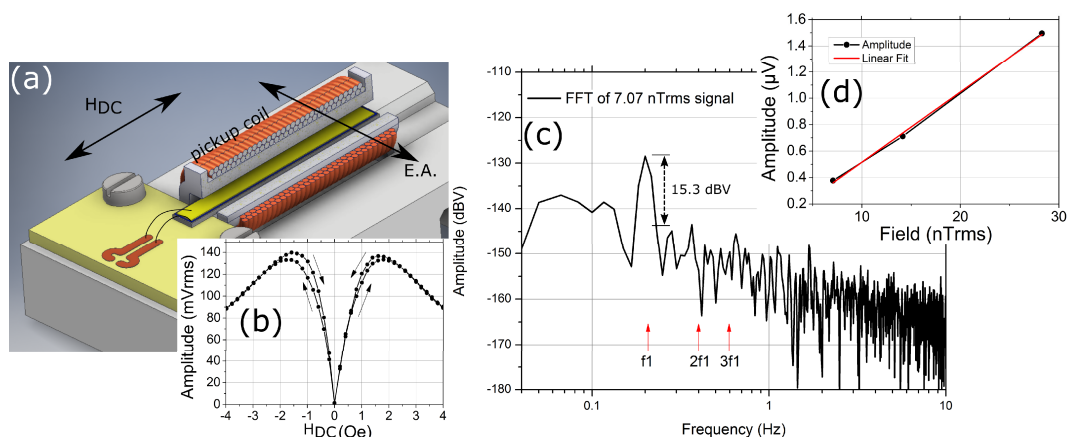


Figure 5. (a) Setup showing cantilevered ME composite surrounded by pickup coil (1200 windings). Magnetic easy axis (E.A.) transverse to external field axis (H_{DC}); (b) coil voltage at mechanical resonance frequency with respect to external magnetic field; (c) coil voltage spectrum showing magnetic field of 200 mHz and its margin of about 15 dBV towards noise floor. Absent harmonics at $2f_1$ and $3f_1$; and (d) linearity with respect to magnetic signal amplitude. This figure is reproduced with permission from IOP Publishing, [91].

3.3. Magnetometers Based on Delta-E Effect

An alternative method for magnetic field sensing utilizes the change of the elastic constants of magnetostrictive materials with magnetization. It arises from an additional magnetostrictive strain that adds up to the Hookean strain upon application of a stress. This effect is commonly referred to as the delta-E effect and has been extensively studied experimentally and theoretically in the beginning of the last century [92–97]. Later studies were focused on the Young's modulus and the shear modulus of soft magnetic amorphous ribbons and wires for magnetic field sensing [98–102], due to their soft magnetic properties and easy processing. Although, shear wave magnetometers demonstrated the detection of low frequency magnetic fields in the 100 pT regime [103], the usage of macroscopic amorphous ribbons limits the device integration. First integrable delta-E effect sensors [104] were improved using magnetolectric composites [60,61] with soft-magnetic amorphous thin films [63,102]. Via the piezoelectric layer the resonator is excited to oscillate at its resonant frequency and read-out simultaneously. Upon application of a magnetic AC field, the resonant frequency changes, which modulates the read-out current in amplitude and in phase [105] and mixes the signal up to higher frequencies. This permits delta-E effect magnetometers to detect DC or low-frequency magnetic signals in a comparatively large bandwidth, avoiding low frequency $1/f$ noise (f : frequency) and acoustic disturbances. Different resonator designs have been demonstrated. With cantilever resonators, equivalent magnetic noise levels of about $100 \text{ pT/Hz}^{1/2}$ between 10 and 100 Hz were reached [106] using the second transversal bending mode. Such devices benefit from magnetically well-oriented FeCoSiB-Cr multilayers and an electrode design adapted to the resonant mode of the cantilever, as shown in Figure 6a. To obtain the largest piezoelectric transduction for the second transversal bending mode as shown in Figure 6b, the location of the two electrodes (i.e., E_1 and E_2) was designed to match with the positions where maximum stress occurs along the cantilever.

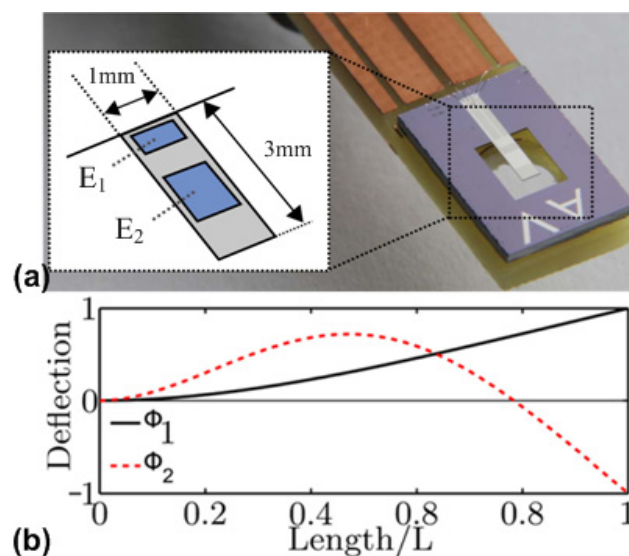


Figure 6. (a) Cantilever delta-E effect magnetometer with adapted electrode design, optimized for the second bending mode [107] (© 2016 IEEE); and (b) cantilever deflection in the 1st and 2nd transversal bending modes as calculated from Euler-Bernoulli beam theory [106]. This figure is reproduced with permission from AIP Publishing, [106].

Simultaneous excitation of different resonant modes was investigated for noise cancelling and detection limit improvement [107] under ambient conditions. Experimental and theoretical studies focused on the origin of signal and noise levels, whereas, at small carrier amplitudes and small signal frequencies, the thermal-mechanical noise [108] dominates the noise floor, the overall detection limit is currently restricted by the onset of magnetic noise at large excitation amplitudes [109,110]. In contrast

to the direct ME operation, the quality factor of the resonator has a more significant influence on the detection limit, which is found to be proportional to $Q^{-1.5}$ [110].

For array applications and a high local magnetic field resolution, smaller sensors are more advantageous. Nan et al. [61] demonstrated a thin-film ME magnetometers using a nano-plate structure with a resonant frequency of 215 MHz. This high resonant frequency is achieved using interdigital electrodes to launch Lamb waves in the nano-plate. The working principle of Lamb wave resonators can be found in [111,112]. As shown in Figure 7a, the nano-plate structure consists of a $(\text{FeGaB}/\text{Al}_2\text{O}_3) \times 10$ multilayer with total thickness of 250 nm, serving as magnetostrictive phase as well as a floating top electrode, and a 250 nm-thick AlN layer serving as piezoelectric phase. Patterned Pt layers are used as interdigital electrodes at the bottom of the AlN layer. The reason to choose an FeGaB/Al₂O₃ multilayer as magnetostrictive phase is because it exhibits a high piezomagnetic coefficient and low eddy current loss at radio frequencies [52,113]. When a magnetic field is applied, the Young's modulus of the FeGaB layer changes due to delta-E effect, thus resulting in a change in the resonant frequency of the nano-plate. An SEM image of the fabricated nano-plate magnetometer is shown in Figure 7b. Figure 7c shows the measured magnitude of the admittance for the magnetometer under different DC magnetic bias fields applied along the length direction of the device. The dependency of the resonant frequency and peak admittance on the DC bias magnetic field is plotted in in Figure 7d. It can be seen that both resonant frequency and peak admittance decrease with DC bias magnetic field at low bias level, reaching minimum values at 15 Oe bias field, and then increase until the magnetostrictive phase (FeGaB/Al₂O₃) is saturated at about 50 Oe. The observed enhancement of Q at large magnetic fields is due to the elimination of magnetic domain walls and reduction of magnetic losses. As shown in Figure 7e, the magnitude of the peak admittance was recorded as the magnetic field decreases from 200 nT to 0.1 nT in a magnetically unshielded environment. The magnitude of admittance starts to scatter at 300 pT, indicating that the signal to be detected cannot be distinguished from noise below 300 pT. This translates to minimum detectable DC magnetic fields of 300 pT. Moreover, a minimum detectable DC magnetic field of 600 pT is achieved under self-bias condition, which is shown in Figure 7f.

A completely different approach of using the delta-E effect for magnetic field sensing employs surface acoustic waves (SAW) devices [114]. In order to enhance the effect, Love wave SAW devices are used. Here, shear horizontal acoustic surface waves are concentrated at the surface of the device by an amorphous SiO₂ guiding layer which is coated with a thin amorphous magnetostrictive FeCoSiB film exhibiting the pronounced delta-E effect [115]. By this concentration of the acoustic waves at the surface, the influence of the delta-E effect on the wave propagation is maximized. This SAW magnetic field sensor can be operated in a delay line configuration and translates the magnetic field-induced changes of the shear modulus via the corresponding velocity changes of the Love waves to a time delay and a related phase shift. Another alternative is to measure the related frequency changes in a resonant configuration [116]. Figure 8a shows the sensor design of the Love wave surface acoustic wave sensor based on ST-cut quartz substrate and a 4.5 μm SiO₂ guiding layer. The 200 nm magnetostrictive FeCoSiB thin film is deposited on the delay line between the interdigital transducers, which have a periodicity of 28 μm. Important characteristics include a low noise level of 250 pT/Hz^{1/2} at 10 Hz as shown in Figure 8b, a dynamic range covering six orders of magnitude and a possible bandwidth exceeding 1 MHz.

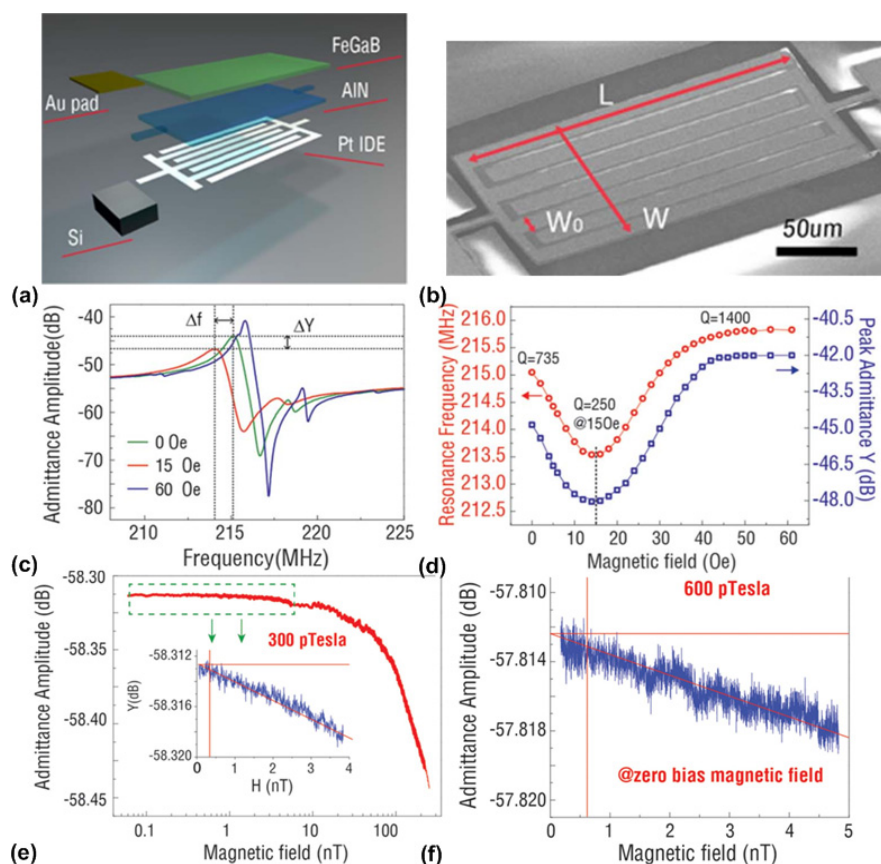


Figure 7. (a) Schematic of the layered structure for the nanoplate magnetometer; (b) SEM of the fabricated magnetometer; (c) measured admittance frequency spectrum of the magnetometer; (d) Measured resonant frequency and admittance of the magnetometer; (e) measured admittance showing the sensitivity and linearity of magnetometer under DC bias magnetic field of 5 Oe; and (f) measured admittance showing the sensitivity and linearity of magnetometer under zero bias magnetic field. This figure is reproduced from [61].

3.4. Practical Applications of Thin-Film ME Magnetometers

The thin-film ME magnetometers have shown LOD of $1 \text{ pT/Hz}^{1/2}$ or even below in mechanical resonant frequencies [75,86]. Given the reported low values of LOD, a hypothesis that thin-film magnetometer could be used for biomagnetic measurements was often mentioned but never proven. The first proof of this hypothesis was recently reported by Reermann et al. [117], where the first system using thin-film ME magnetometer for cardiological application was presented. Cantilever-type thin-film magnetometer was adopted with magnetic frequency modulation technique. In the reported system, sophisticated averaging techniques were applied to improve SNR and thus closed the gap between the measured LOD of the magnetometer and the magnetic signal from human heart. Moreover, to deal with various types of noise, different weighted averaging algorithms have been demonstrated to ensure convergence even in highly distorted environments.

Another practical application of thin-film ME magnetometers refers to magnetic particle mapping, which has been recently demonstrated by Friedrich et al. [118]. Imaging magnetic nanoparticles (MNPs) has gained widespread interest due to its great value in medical life science and diagnostic applications. The work presented in [118] shows that thin-film ME magnetometers can be used to localize MNPs, which is proven as a more cost-effective and efficient way compared to other available technologies. In the reported work, the nonlinear nature of the MNPs was utilized. When MNPs were exposed to a AC magnetic field that had $1/3$ of the resonant frequency of the magnetometer, the third harmonic excitation due to the nonlinear behavior of the MNPs was measured by magnetometer

with resonance enhanced performance, thus decoupling the desired and excitation magnetic fields. Furthermore, the reported work measured the magnetic response from 2D MNP distributions and reconstructed the distribution by solving the inverse problem. The measurement results suggests that the thin-film magnetometers hold great potential for mapping MNPs.

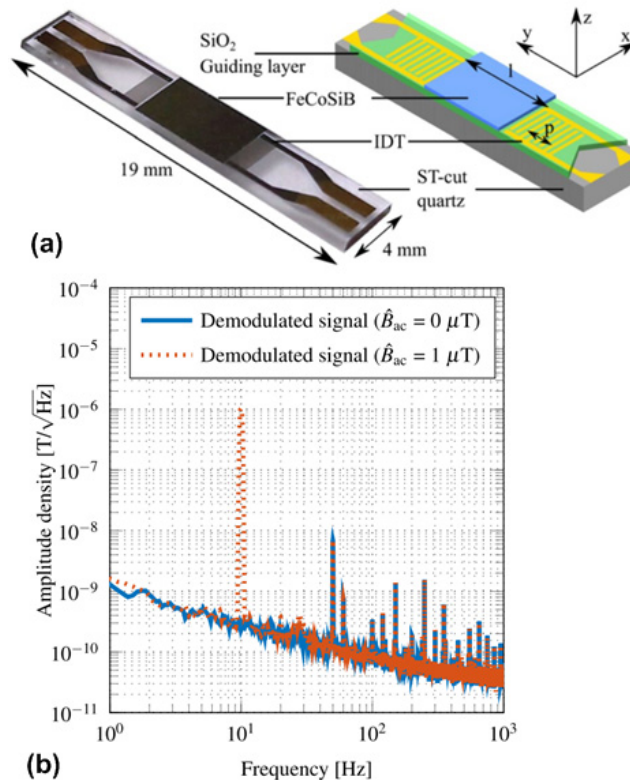


Figure 8. (a) A sensor design of the Love wave surface acoustic wave sensor based on ST-cut quartz substrate and a $4.5 \mu\text{m}$ SiO_2 guiding layer; and (b) equivalent magnetic noise floor of the output signal shows the frequency dependent LOD. An equivalent magnetic noise of $250 \text{ pT}/\text{Hz}^{1/2}$ at 10 Hz is achieved. This figure is reproduced from [115].

4. Mechanical Antenna

Conventional antennas using electric currents for electromagnetic wave radiation are ubiquitous in our daily life, which enables wireless communications in portable electronic devices such as smart phones, tablets, and radio frequency identification systems. A key challenge of conventional antennas is the size miniaturization since the size of the antenna should be designed to be comparable to the electromagnetic (EM) wavelength for optimal radiation efficiency. This miniaturization limitation causes difficulty in achieving compact antennas and antenna arrays at the very-high-frequency band (VHF, 30–300 MHz) and ultra-high frequency band (UHF, 0.3–3 GHz). Thus, new antenna concepts and radiation mechanisms for miniaturization of antennas are highly desired. To meet this demand, a novel antenna concept based on mechanically vibrating ME heterostructures were theoretically proposed recently in [119,120]. In 2017, Nan et al. [121] demonstrated the ultra-compact mechanical antennas based on suspended nano-mechanical ME resonators, which exhibit 1 ~ 2 orders of magnitude miniaturization over state-of-the-art compact antennas without performance degradation. The remarkable reduction in size benefits from the fact that the operation of mechanical antenna hinges on utilization of acoustic wave of the wavelength of which is about five orders of magnitude smaller than that of the electromagnetic wave at the same frequency. In [121], two types of structures for mechanical antennas based on laterally-vibrating or vertically-vibrating nano-mechanical resonators were proposed, which are described in the following subsections.

4.1. Mechanical Antenna Based on a Laterally-Vibrating Nano-Plate Resonator

Figure 9a shows the SEM image of the laterally-vibrating nano-plate resonator (NPR) with a length of 200 μm and a width of 50 μm . The rectangular resonator body consists of a 50-nm-thick bottom Pt electrode and a thin-film ME heterostructure ((45 nm FeGaB/ 5 nm Al_2O_3) \times 10/500 nm AlN) on top of the Pt layer. Another 100-nm-thick Au layer was patterned to form the ground-signal-ground (GSG) pads and top ground for electrical characterization. The multilayer nano-plate structure is fully released from the silicon substrate to minimize the substrate clamping effect, but mechanically supported by the anchors at two sides. The resonant frequency of the in-plane mechanical vibration mode of NPR is determined by the width of the structure, which offers designers great flexibility to choose the desired operation frequency. The working principle of such type of laterally-vibrating mechanical resonators is detailed in [122]. Figure 9b shows the measurement setup schematic with the structure of NPR. It can be seen that an RF coil, which was placed 14 mm away from the device under test, was used to generate an AC magnetic field at the frequency range around the mechanical resonant frequency of the NPR. Due to the direct ME effect, the AC magnetic field will induce strain variation in the magnetostrictive layer (FeGaB layer) which, in turn, transfers to the piezoelectric layer (AlN layer) and results in voltage output. The induced voltage output from the parallel-plate structure (FeGaB and Pt) can be detected by the lock-in amplifier. Figure 9c shows the measured amplitude of admittance of the NPR characterized by a network analyzer. The measured admittance spectrum was fitted into the Modified Butterworth-van Dyke model [123], from which the mechanical resonant frequency of 60.7 MHz, electromechanical coupling coefficient of 1.35% and quality factor of 930 were extracted. To confirm that the induced voltage output is due to the strain-mediated ME coupling, a nonmagnetic NPR using Cu as the top electrode instead of FeGaB was also measured using the same measurement setup. The measured result is shown in Figure 9d, where it can be seen that the nonmagnetic NPR exhibits a similar admittance spectrum compared to that of the NPR with magnetic film. Using the measurement setup illustrated in Figure 4b, the induced voltage output from the NPR under the RF coil excitation of 60 nT at 60.7 MHz was measured using a UHF lock-in amplifier. The measured result was shown in Figure 9e, where it can be seen that a peak voltage value of 180 μV occurs at the excitation frequency. This peak output voltage translates to ME voltage coefficient of 6 kV/cm·Oe, which suggests a strong ME coupling in the thin-film heterostructure. Figure 9f shows the measured output voltage from the Cu/AlN NPR under the same AC magnetic field excitation. It can be observed that the induced output voltage is about two orders of magnitude smaller than that in NPR with magnetic film. It is believed that this weak resonant signal is due to the inductive coupling between the RF coil and the device ground loop.

4.2. Mechanical Antenna Based on a Vertically-Vibrating Thin-Film Bulk Acoustic Wave Resonator

Acoustically-actuated antennas can also be designed to operate at the GHz range utilizing the thickness vibration mode of the ME heterostructure, which can be essentially seen as a thin-film bulk acoustic wave resonator (FBAR). The working principle of FBAR can be found in [124]. The same as other FBAR devices, the resonant frequency of the FBAR-type mechanical antenna is also set by the thickness of the ME heterostructure. Figure 10a shows the SEM of the vertically-vibrating FABR-type mechanical antenna, which has identical vertical laminate structure as NPR described in the previous section. The fully-released FBAR-type mechanical antenna has a lateral shape of a circular disk with a diameter of 200 μm . Figure 10b shows the schematic of the gain measurement setup for FABR-type mechanical antenna. It can be seen that this setup includes a calibrated linear polarization standard horn antenna and an FABR-type mechanical antenna under test. A network analyzer was used to electrically characterize the antenna by measuring its two-port S parameters. It is noted that this antennas measurement was performed in an anechoic chamber under a far-field configuration. In the receiving process, the magnetostrictive layer of the mechanical antenna detects the RF magnetic field component of electromagnetic waves, which induces oscillating strains in magnetostrictive layer. The strains are transferred to piezoelectric layer, and lead to AC voltage output, the magnitude of

which reaches its maximum at mechanical resonant frequency. Conversely, during the transmitting process, the oscillating strains occur in the piezoelectric layer of mechanical antenna under input AC voltage. The strains are transferred to magnetostrictive layer, and excite magnetization oscillation (or magnetic current), which results in radiation. The measured magnitude of reflection coefficient (S_{22}) of the FABR-type mechanical antenna is shown in Figure 10c, where the mechanical resonant frequency (2.53 GHz) can be found from the peak return loss of 10.3 dB. The inset of Figure 10c shows a simulated displacement profile of the device, which indicates a thickness vibration mode at 2.53 GHz. For comparison, a nonmagnetic control device using Al as the top electrode instead of FeGaB was also measured using the same measurement setup. The measured result was shown in Figure 10d, where a mechanical resonance frequency at 2.5 GHz can be found. Figure 10e shows a measured magnitude of transmission coefficients S_{21} and S_{12} , which represent the transmitting and receiving behaviors of the mechanical antenna, respectively. The antenna gain is measured to be -18 dBi at resonant frequency through gain comparison method. In contrast, as shown in Figure 10f, only a very weak peak at 2.5 GHz can be observed for the control device which is about 20 dB lower than the performance of FABR-type mechanical antenna. This suggests that the ME coupling effect dominates the performance of the antenna transmission.

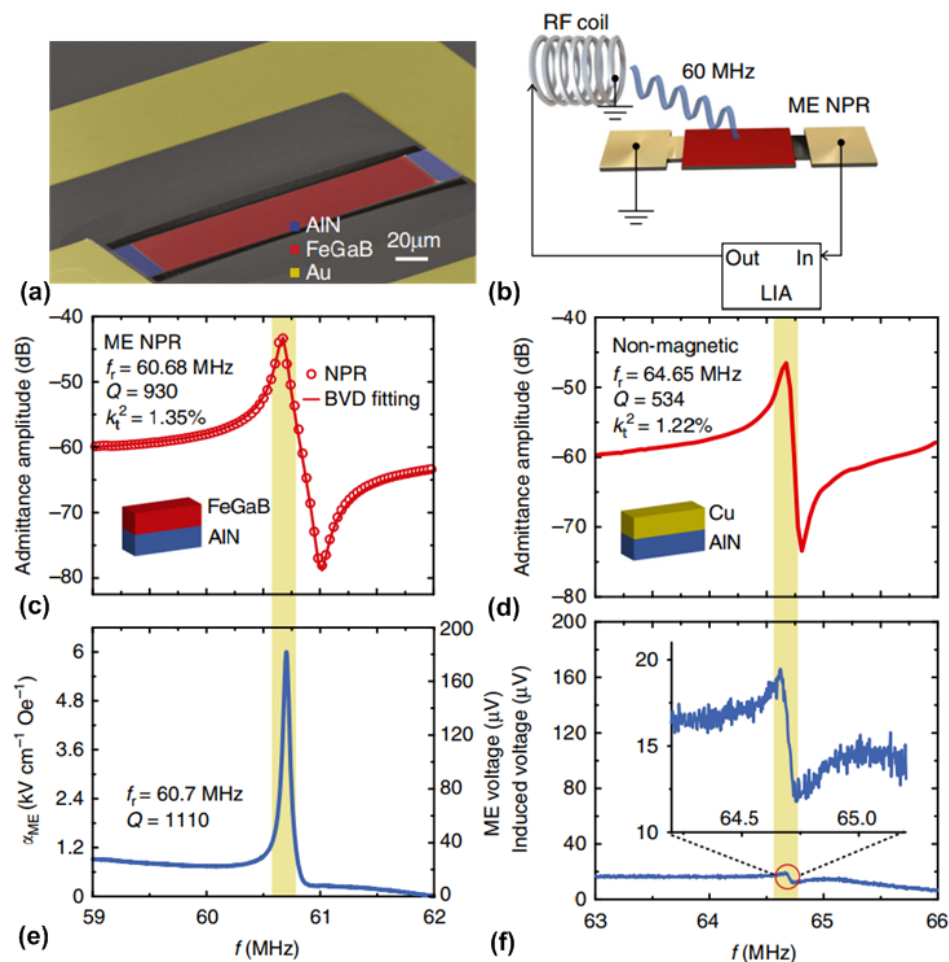


Figure 9. (a) SEM of the NPR-type mechanical antenna; (b) schematic of the measurement setup using RF coil and high-frequency lock-in amplifier; (c) measured admittance frequency spectrum of the NPR-type mechanical antenna; (d) measured admittance frequency spectrum of the nonmagnetic Cu/AlN control device; (e) ME coupling coefficient (left axis) and the induced ME voltage (right axis) versus the excitation frequency of RF-coil for NPR-type mechanical antenna; and (f) measured induced voltage versus the excitation frequency of RF-coil for Cu/AlN control device. The inset illustrates the zoomed-in view of the resonance peak area (red circle). This figure is reproduced from [121].

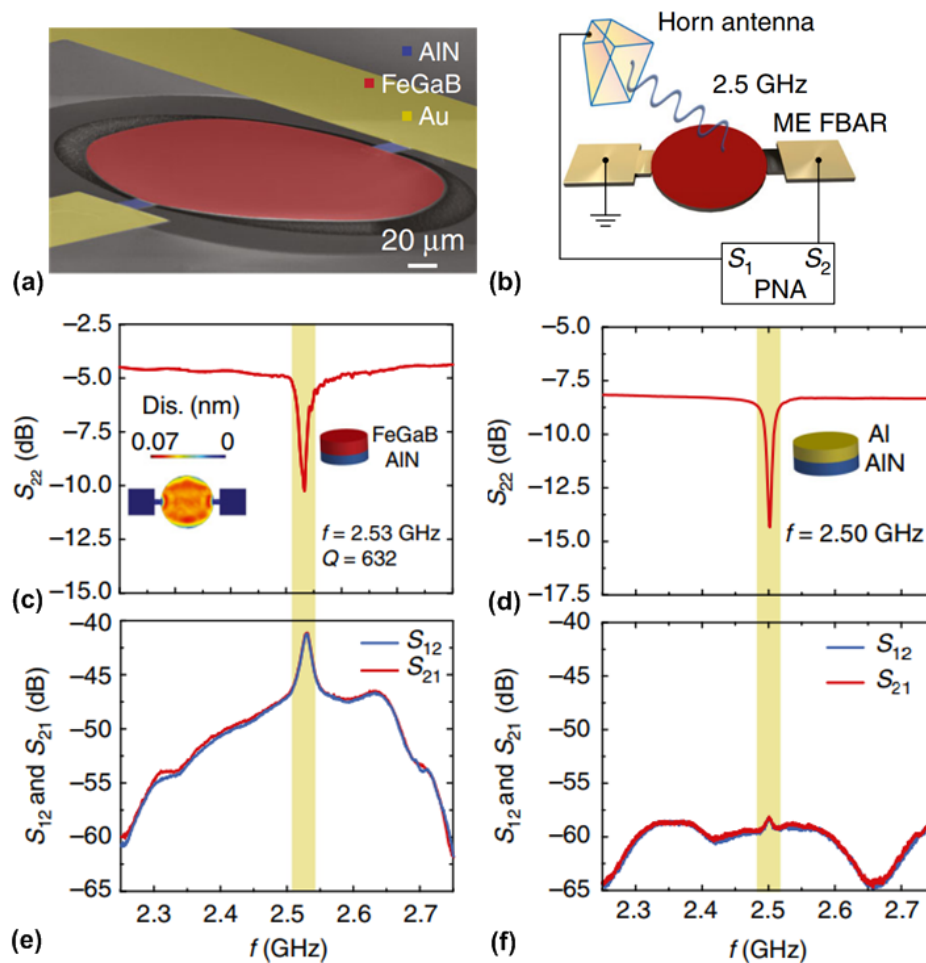


Figure 10. (a) SEM of the FABR-type mechanical antenna; (b) schematic of the gain measurement setup using Horn antenna and network analyzer; (c) measured reflection coefficient (S_{22}) of the FABR-type mechanical antenna. The inset shows the out-of-plane displacement of the circular disk at resonant frequency; (d) measured reflection coefficient (S_{22}) of the nonmagnetic Al/AlN control device; (e) Measured transmission coefficients (S_{21} and S_{12}) of the FABR-type mechanical antenna; and (f) measured transmission coefficients (S_{21} and S_{12}) of the nonmagnetic Al/AlN control device. This figure is reproduced from [121].

In summary, the ultra-compact mechanical antennas based on NPR or FBAR structures have antenna sizes one to two orders of magnitude smaller than the state-of-the-art compact antennas, thus providing great opportunities in realizing miniaturized antennas in future wireless communication systems such as Internet of Things, wearable monitoring systems, bio-implantable communication systems. Moreover, the mechanical antennas based on NPR or FBAR structures share the same five-mask microfabrication process on the same chip, which can be readily connected to CMOS oscillator circuits realizing reconfigurable mechanical antenna array with an operation frequency range from tens of MHz to tens of GHz.

5. Tunable RF/Microwave Devices

One important application of multiferroic heterostructure is to build electrostatically tunable RF/microwave devices, such as tunable inductors and filters. The function of tunability can be realized either by applying a magnetic field [125–127] or electrical field [128–130]. Compared to the conventional magnetically tunable devices, the electrostatically tunable multiferroic devices are more compact, lightweight, and power efficient. The working principle of electrostatically tunable multiferroic devices relies on the converse ME effect, which relates to E-field control of the magnetic permeability. Thus, it is

of paramount importance to realize strong ME coupling in multiferroic heterostructure, which enables large tunability. However, it has been an open challenge to obtain large ME coupling at RF/microwave frequencies due to large loss tangents of magnetic phase. Moreover, the ideal magnetic phase should have large piezomagnetic coefficient, which translates to large saturation magnetostriction (λ_s) and low saturation magnetic field (H_s). Much effort has been focused on developing such high-quality magnetic thin films and building multiferroic heterostructures with large ME coupling at RF/microwave frequencies. Lou et al. [52] reported a class of metallic magnetic FeGaB films that has a high λ_s of 70 ppm, a low H_s of 20 Oe, and a narrow ferromagnetic resonance linewidth of 16 Oe at 9.6 GHz. The maximum piezomagnetic coefficient is about 7 ppm/Oe, which is much larger than that of other well-known magnetostrictive materials, such as Terfenol-D (Tb-Dy-Fe) [131], Galfenol (Fe-Ga) [132], and Metglas (FeBSiC) [133]. By depositing FeGaB film onto lead zinc niobate-lead titanate (PZN-PT) single-crystal slabs using magnetron sputter deposition, Lou et al. [54] demonstrated a novel FeGaB/PZN-PT heterostructure that exhibit high electrostatically tunable FMR frequency range of 5.82 GHz and a giant electrostatically induced magnetic anisotropy field of 750 Oe at both DC and microwave frequencies. Xing et al. [113] studied the structure of FeCoB/Al₂O₃ multilayer and found significant reduced eddy current loss as well as lower coercivity.

5.1. Tunable RF/Microwave Inductors

As a fundamental type of electronic component, inductors have been used ubiquitously in all kinds of electronic circuits. Compared to voltage tunable capacitors, which have been widely applied in a variety of electronic circuits, voltage tunable inductors are not readily available due to low inductance areal density and low quality factor especially at RF/microwave frequencies. Many integrated tunable inductors using MEMS technology were reported, which typically exhibit high quality factors [134–136]. However, the problem for these inductors is their low inductance areal densities due to lack of magnetic material. Salvia et al. [137] demonstrated an on-chip tunable inductor using patterned permalloy film. Measured results show a 40% increase in inductance by introducing the permalloy film, a 15% tuning range, and a Q between 5 and 11 up to 5 GHz. The drawback of this tunable inductor is its large power consumption which stems from the large DC current required for generating the magnetic bias field. A more power efficient voltage-tunable inductor using multiferroic heterostructure was proposed by Lou et al. [130]. The reported device was based on a solenoid inductor with multiferroic core which exhibits a large inductance tuning range of 450% with negligible power consumption.

Gao et al. [138,139] demonstrated a voltage-tunable RF integrated inductor based on solenoid structures using FeGaB/Al₂O₃ multilayer films. Compared with a single FeGaB layer, FeGaB/Al₂O₃ multilayer film with the same total thickness provides less eddy current loss, lower out of plane anisotropy, and higher permeability. Thus, the reported tunable inductor exhibits significantly enhanced inductance (>100%) and higher quality factor at GHz frequencies over their air core counterparts. The optical image of the tunable inductor is shown in Figure 11a, where a solenoid structure can be seen. The tunable inductor was fabricated using micro-fabrication techniques [138] followed by bonding to lead magnesium niobate-lead titanate (PMN-PT) piezoelectric slab. As shown in the Figure 11b, the magnetic phase (FeGaB/Al₂O₃ multilayer films) and piezoelectric phase (PMN-PT slab) form the multiferroic heterostructure. The function of voltage tuning in inductance is due to the strain-mediated ME coupling within the multiferroic heterostructure, which enables E-field-induced changes of the permeability of the FeGaB/Al₂O₃ multilayer film. Using a vector network analyzer together with a RF probing system, the inductance and quality factor of the tunable inductor can be measured. Figure 11c shows the measured inductances of the inductor with magnetic multilayer films as the inductor core and the one with air core. It can be seen that introducing the magnetic multilayer as the core doubles the inductance at frequency below 2 GHz. Figure 11d shows the measured inductance under different E-field applied across the thickness of the PMN-PT slab. The applied voltage ranges from 0 to 400 V which corresponds to an E-field from 0 to 8 kV/cm. It can be seen from Figure 11d that a high tunable inductance of more than 100% is achieved over a large frequency range from 2 GHz to 4 GHz. It was

also reported that the measured Q of the inductor enhances by at least 50% over the frequency range from 0.5 GHz to 1 GHz.

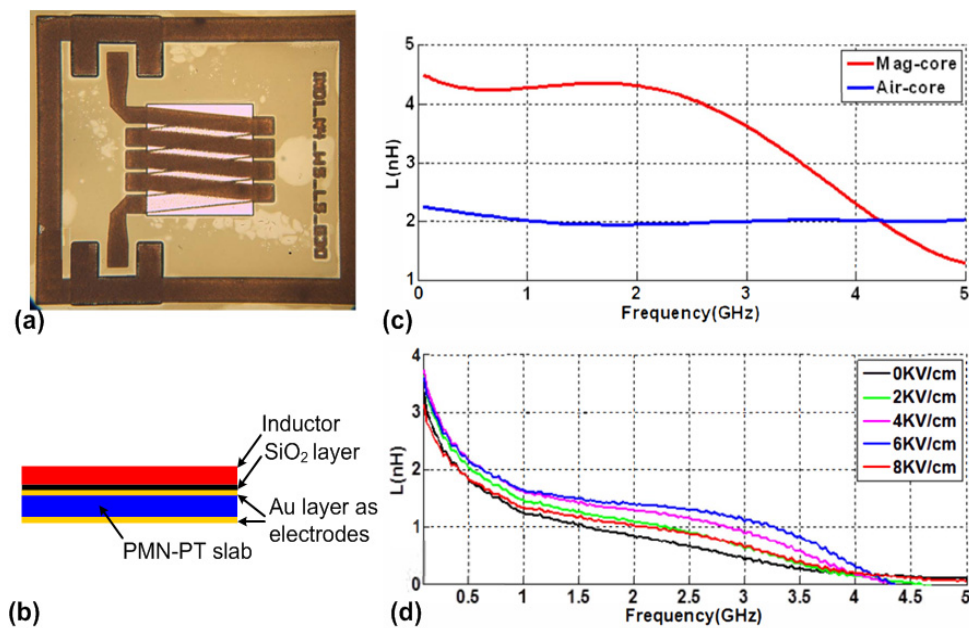


Figure 11. (a) Optical image of the tunable inductor; (b) schematic of the layered structure of the tunable inductor; (c) measured inductances of the inductor with magnetic multilayer films as the inductor core and the one with air core; and (d) measured inductance under different E-field applied across the thickness of the PMN-PT slab. This figure is reproduced from [138] and [139] (© 2014 IEEE).

5.2. Tunable RF/Microwave Filters

Filters are essential components in modern electronic systems since they provide the function of frequency selection. Wideband and low-loss tunable filters are highly desirable since they can greatly reduce the complexity in a wide variety of electronic systems such as reconfigurable electronic systems, multiband communication systems and wideband tracking receivers. One of the most practical implementation for RF/microwave tunable filters is based on yttrium-iron-garnet (YIG) resonators, which offers multi-octave bandwidths and high quality factor [140–143]. However, tunable filters based on YIG resonators are bulky and cannot be easily miniaturized for portable electronic systems. Moreover, the operation of YIG filters consumes considerable amount of DC power for generation of magnetic bias field [144]. Solid-state varactors have also been used to build tunable filters with wide tuning range, but they exhibit high loss and low linearity at RF/microwave frequencies [145–147]. In addition, it has been demonstrated that tunable filters based on MEMS switches and varactors provide low loss, low DC power consumption, and good linearity [148–150]. Another competitive alternative to realize a RF/microwave tunable filter is to utilize multiferroic heterostructures, which have been demonstrated to be compact, low-cost, and power-efficient. In particular, such a type of tunable filter provides the function of dual H- and E-field tunability, which offers more design flexibility.

Lin et al. [151] reported the first integrated dual H- and E-field tunable bandpass filters with nonreciprocal transmission characteristics. Figure 12a shows the schematic of the device, which mainly consists of an inverted-L-shape microstrip structure loaded with NiZn ferrite film, and a PMN-PT piezoelectric slab. The NiZn ferrite film is deposited using a spin spraying process, which is a low-temperature, low cost, and fast deposition method. The silicon substrate at the back side of the microstrip structure is removed using the deep reactive ion etching (DRIE) technique. A multiferroic heterostructure is formed by bonding the microstrip structure to the PMN-PT piezoelectric slab. By applying a magnetic bias field, the magnetostatic surface wave will be excited in the NiZn film [152]. The NiZn ferrite film is rotated by a certain angle and the reflection will propagate parallel to the

bias field, which is operating in the stopband of magnetostatic back volume wave to diminish the splitting modes and the standing-wave resonances. The nonreciprocity characteristic is achieved from the limited surface wave on the bottom surface due to the non-reflection edges. Figure 12b,c show the measured S_{11} parameters of the tunable bandpass filter under DC magnetic field and DC electric field, respectively. It can be seen from Figure 12b that a tunable frequency range from 3.78 GHz to 5.27 GHz is achieved by increasing the DC magnetic field from 100 Oe to 400 Oe, which translates to an H-field frequency tunability of about 5 MHz/Oe. As shown in Figure 12c, the center frequency changes from 2.075 GHz to 2.295 GHz when the applied electric field across the thickness of PMN-PT increases from 0 kV/cm to 4 kV/cm. This represents a E-field frequency tunability of 55 MHz/(kV/cm). Figure 12d shows the measured S_{21} and S_{12} for the device under DC magnetic bias field of 400 Oe. It can be seen that an isolation of 15.8 dB is obtained between S_{21} and S_{12} showing nonreciprocal transmission characteristics.

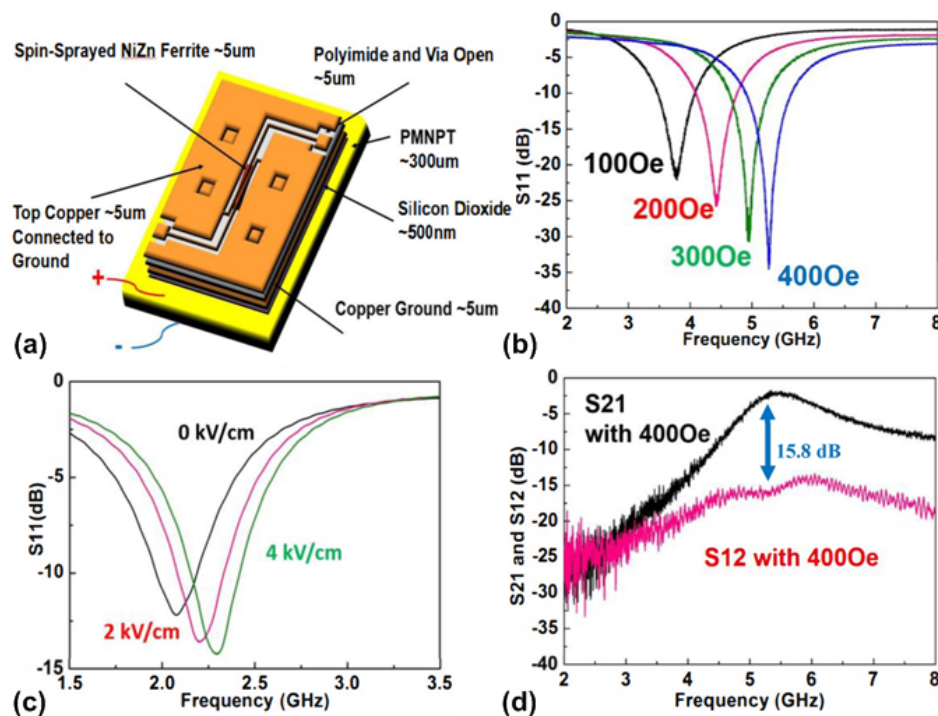


Figure 12. (a) Schematic of the tunable filter; (b) measured S_{11} of the tunable filter as a function of the DC magnetic field; (c) measured S_{11} of the tunable filter as a function of DC electric field across the thickness of the PMN-PT slab; and (d) measured S_{21} and S_{12} of the tunable filter at a magnetic bias field of 400 Oe. This figure is reproduced from [151] (© 2015 IEEE).

More recently, an integrated RF tunable bandpass filter based on two coupled elliptic-shape nano-mechanical resonators was reported with dual E- and H-field tunability [153]. Figure 13a shows the schematic of the device, where it can be seen that each elliptic-shape resonator consists of a multiferroic heterostructure of magnetostrictive multilayer films ($\text{FeGaB}/\text{Al}_2\text{O}_3$) and piezoelectric film (AlN), together with a Pt layer as the bottom electrode. Two resonators are placed in close proximity with 2 μm air gap. Both resonators are excited in in-plane contour mode, the resonant frequency of which is determined by the lateral dimension of the resonator. Due to the strong ME effect between the $\text{FeGaB}/\text{Al}_2\text{O}_3$ multilayer and AlN film, the acoustic wave within each resonator can be strongly coupled via the electromagnetic waves. Figure 13b shows the measured S parameters for the filter under zero-bias field, where it can be seen that return loss of 11.2 dB and insertion loss of 3.4 dB are achieved at center frequency of 93.165 MHz with an extracted quality factor of 252. When a magnetic field is applied, the center frequency will change due to the magnetic field-induced Young's modulus change in FeGaB film (ΔE effect). Figure 13c shows the measured resonant frequency as a function

of applied DC magnetic field, where the H-field frequency tunability of 5 kHz/Oe can be extracted. The measured E-field frequency tunability is 2.3 kHz/V as shown in Figure 13d. It can be observed that the change in resonant frequency due to ME coupling is much smaller compared to that caused by the delta-E effect. This is due to the remarkable change in the Young's modulus (up to 70%) due to the delta-E effect found in FeGaB film [63].

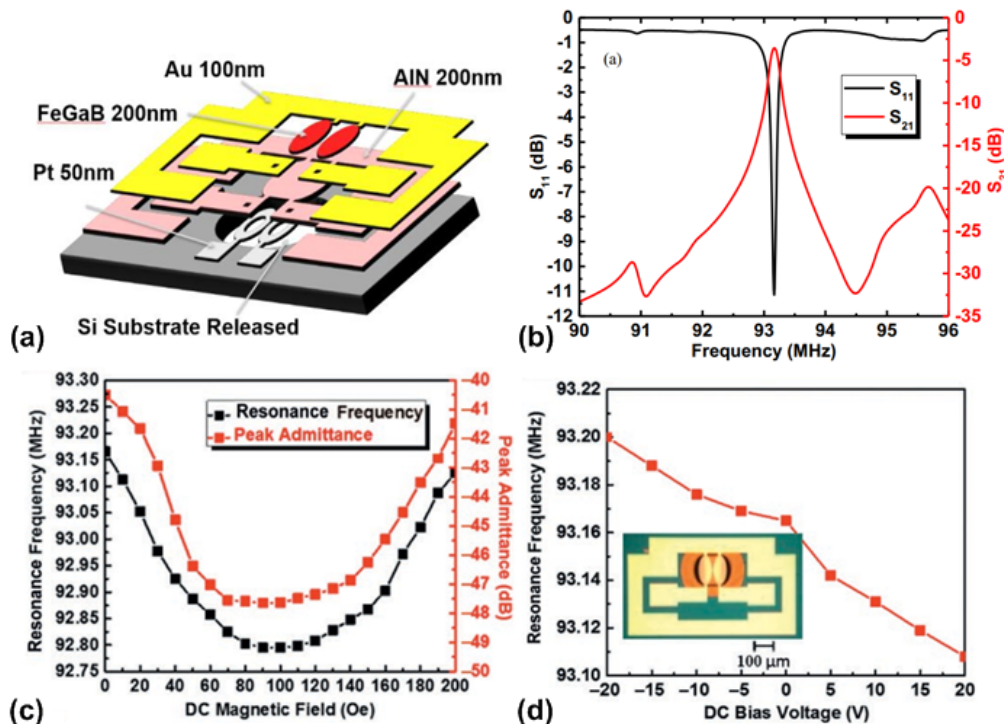


Figure 13. (a) Schematic of the tunable filter; (b) measured S_{11} and S_{21} of the tunable filter at zero bias field; (c) Measured resonant frequency as a function of DC magnetic field; (d) measured resonant frequency as a function of DC voltage across the thickness of the AlN film. This figure is reproduced from [153] (© 2016 IEEE).

6. Conclusions

During the last decade, considerable progress has been made for different types of integrated multiferroic devices that are based on thin-film ME heterostructures. The performance of these integrated devices greatly benefit from the strong strain-mediated ME coupling occurred at the mechanical resonance of the magnetic/piezoelectric heterostructure. Despite the advantages of small form factor, low power consumption, and the feasibility of batch fabrication, excellent elastic coupling between the magnetic and ferroelectric phases can be attained thanks to the advancement of thin-film deposition techniques. It can be foreseen that further improvement on the magnetic and piezoelectric properties of thin-film materials will greatly benefit the performance of the integrated multiferroic devices. On the other hand, the accurate determination of these film properties also relies on the development of the thin-film characterization techniques.

A summary of characteristics for some of the reviewed integrated multiferroic devices is provided in Table 2. Among the presented devices, thin-film ME magnetometers have seen fast development in recent years. The achievable LOD of the magnetometer has been significantly improved by many novel techniques, such as magnetic/electric frequency conversion, utilization of delta-E effect in the magnetic phase, noise suppression method of exploiting tuning-fork structure and introduction of exchange biased magnetostrictive multilayers. For both DC and AC magnetic field detection, the best reported values of LOD achieved have been lowered into the range of $\text{pT}/\text{Hz}^{1/2}$, making thin-film ME magnetometer a promising candidate for future biomedical and biomagnetic applications. In particular,

some practical applications of using thin-film ME magnetometer for cardiological application and magnetic nanoparticles mapping were recently reported.

Table 2. Summary of characteristics for some of the reviewed integrated multiferroic devices.

Device	Type	Characteristics	Performance	Ref
Magnetometer	Direct detection	(1) Lowest LOD at resonance (2) Narrow bandwidth	LOD = 400 fT/Hz ^{1/2} @ 867 Hz	[84]
	Magnetic frequency conversion	(1) Transfer desired low frequency magnetic signal to high frequency via magnetic modulation (2) Wide bandwidth (3) Large power consumption	LOD = 60 pT/Hz ^{1/2} @ 10 Hz	[76, 89]
	Electric frequency conversion	(1) Transfer desired low frequency magnetic signal to high frequency via electric modulation (2) Wide bandwidth (3) Low power consumption	LOD = 10 nT/Hz ^{1/2} @ 10 Hz	[90]
	Delta-E effect	(1) Change of elastic constants upon applied magnetic field (2) Large bandwidth (3) Low power consumption	LOD = 250 pT/Hz ^{1/2} @ 10 Hz	[115]
Mechanical antenna	NPR-type	(1) vibrate in lateral direction (2) work at several tens of MHz	α_V ¹ = 6 kV/cm-Oe @ 60.7 MHz	[121]
	FBAR-type	(1) vibrate in thickness direction (2) work at several GHz	G ² = -18 dBi @ 2.5 GHz	[121]
Tunable RF/Microwave devices	Tunable inductor	(1) E-field controlled (2) High Q at GHz	TIR ³ = 100% @ 2 ~ 4 GHz	[138]
	Tunable filter	(1) H- or E-field controlled (2) Nonreciprocity	TFR ⁴ = 39% @ 4 ~ 5 GHz	[151]

¹ α_V denotes the ME voltage coefficient; ² G denotes the measured antenna gain; ³ TIR denotes the tunable inductance range; ⁴ TFR denotes the tunable frequency range.

A novel antenna miniaturization approach has been recently demonstrated in the mechanical antennas which are based on thin-film ME heterostructures. In this new antenna concept, transmitting and receiving behavior are realized by converse and direct ME coupling effects, respectively. The operation frequency of such mechanical antenna ranges from several MHz to tens of GHz, which can be well-controlled by the physical geometries of the thin-film ME heterostructures with in-plane or thickness vibration modes. Although still in its early stage, the mechanical antennas based on thin-film ME heterostructures have already exhibited one to two orders of reduced size compared to conventional antenna and ground plane immunity from metallic surfaces. One problem of such mechanical antennas is that the antenna gain is still not ideal, which could be solved by further optimization of the ME heterostructures or implementation of mechanical antenna arrays. With the advantages of high magnetic field sensitivity in near field, the reported mechanical antennas hold great potential in the future systems of biomedical communication, wearable electronics, and the Internet-of-Things.

Based on the converse ME coupling effects, novel integrated tunable RF inductors and nonreciprocal RF bandpass filters have been demonstrated. These integrated RF devices are compact, lightweight, power efficient, and have the potential to integrate with CMOS technology, providing great opportunities for future reconfigurable electronic systems.

Funding: The financial supports from the NSF TANMS ERC Award 1160504, W.M. Keck Foundation. The views, opinions, and/or findings expressed are those of the author and should not be interpreted as representing the official views or policies of the Department of Defense or the U.S. Government. Patrick Hayes, Benjamin Spetzler, Jeffrey McCord, Franz Faupel, and Eckhard Quandt was funded by the Deutsche Forschungsgemeinschaft (DFG, German Research Foundation) through the Collaborative Research Center SFB 1261. Y.-H.L. was funded by NSFC 51729201.

Conflicts of Interest: The authors declare no conflict of interest.

References

1. Fiebig, M. Revival of the magnetoelectric effect. *J. Phys. D: Appl. Phys.* **2005**, *38*, R123–R152. [[CrossRef](#)]
2. Eerenstein, W.; Mathur, N.D.; Scott, J.F. Multiferroic and magnetoelectric materials. *Nature* **2006**, *442*, 759–765. [[CrossRef](#)] [[PubMed](#)]
3. Srinivasan, G. Magnetoelectric composites. *Annu. Rev. Mater. Res.* **2010**, *40*, 153–178. [[CrossRef](#)]
4. Wang, Y.; Hu, J.; Lin, Y.; Nan, C.-W. Multiferroic magnetoelectric composite nanostructures. *NPG Asia Mater.* **2010**, *2*, 61–68. [[CrossRef](#)]
5. Nan, C.-W.; Bichurin, M.I.; Dong, S.; Viehland, D.; Srinivasan, G. Multiferroic magnetoelectric composites: Historical perspective, status, and future directions. *J. Appl. Phys.* **2008**, *103*, 031101. [[CrossRef](#)]
6. Ma, J.; Hu, J.; Li, Z.; Nan, C.W. Recent progress in multiferroic magnetoelectric composites: From bulk to thin films. *Adv. Mater.* **2011**, *23*, 1062–1087. [[CrossRef](#)] [[PubMed](#)]
7. Zhai, J.; Xing, Z.; Dong, S.; Li, J.; Viehland, D. Magnetoelectric laminate composites: An overview. *J. Am. Ceram. Soc.* **2008**, *91*, 351–358. [[CrossRef](#)]
8. Zhai, J.; Xing, Z.; Dong, S.; Li, J.; Viehland, D. Detection of pico-tesla magnetic fields using magneto-electric sensors at room temperature. *Appl. Phys. Lett.* **2006**, *88*, 062510. [[CrossRef](#)]
9. Sreenivasulu, G.; Laletin, U.; Petrov, V.M.; Petrov, V.V.; Srinivasan, G. A permendur-piezoelectric multiferroic composite for low-noise ultrasensitive magnetic field sensors. *Appl. Phys. Lett.* **2012**, *100*, 173506. [[CrossRef](#)]
10. Tatarenko, A.S.; Srinivasan, G.; Bichurin, M.I. Magnetoelectric microwave phase shifter. *Appl. Phys. Lett.* **2006**, *88*, 183507. [[CrossRef](#)]
11. Yang, G.-M.; Sun, N.X. Tunable ultrawideband phase shifters with magnetodielectric disturber controlled by a piezoelectric transducer. *IEEE Trans. Magn.* **2014**, *50*, 1–4. [[CrossRef](#)]
12. Liu, G.; Cui, X.; Dong, S. A tunable ring-type magnetoelectric inductor. *J. Appl. Phys.* **2010**, *108*, 094106. [[CrossRef](#)]
13. Dong, S.; Li, J.F.; Viehland, D. Voltage gain effect in a ring-type magnetoelectric laminate. *Appl. Phys. Lett.* **2004**, *84*, 4188–4190. [[CrossRef](#)]
14. Dong, S.; Li, J.F.; Viehland, D.; Cheng, J.; Cross, L.E. A strong magnetoelectric voltage gain effect in magnetostrictive-piezoelectric composite. *Appl. Phys. Lett.* **2004**, *85*, 3534–3536. [[CrossRef](#)]
15. Gao, Y.; Zare, S.; Yang, X.; Nan, T.X.; Zhou, Z.Y.; Onabajo, M.; O'Brien, K.P.; Jalan, U.; Ei-tatani, M.; Fisher, P.; et al. High quality factor integrated gigahertz magnetic transformers with FeGaB/Al₂O₃ multilayer films for radio frequency integrated circuits applications. *J. Appl. Phys.* **2014**, *115*, 17E714. [[CrossRef](#)]
16. Jia, Y.; Or, S.W.; Chan, H.L.W.; Jiao, J.; Luo, H.; van der Zwaag, S. Bidirectional current-voltage converters based on magnetostrictive/piezoelectric composites. *Appl. Phys. Lett.* **2009**, *94*, 263504. [[CrossRef](#)]
17. Zhai, J.; Gao, J.; De Vreugd, C.; Li, J.; Viehland, D.; Filippov, A.V.; Bichurin, M.I.; Drozdov, D.V.; Semenov, G.A.; Dong, S.X. Magnetoelectric gyrator. *Eur. Phys. J. B* **2009**, *71*, 383–385. [[CrossRef](#)]
18. Leung, C.M.; Zhuang, X.; Gao, M.; Tang, X.; Xu, J.; Li, J.; Zhang, J.; Srinivasan, G.; Viehland, D. Enhanced stability of magnetoelectric gyrators under high power conditions. *Appl. Phys. Lett.* **2017**, *111*, 182901. [[CrossRef](#)]
19. Zhuang, X.; Leung, C.M.; Sreenivasulu, G.; Gao, M.; Zhang, J.; Srinivasan, G.; Li, J.; Viehland, D. Upper limit for power conversion in magnetoelectric gyrators. *Appl. Phys. Lett.* **2017**, *111*, 163902. [[CrossRef](#)]
20. Dong, S.; Zhai, J.; Li, J.F.; Viehland, D.; Priya, S. Multimodal system for harvesting magnetic and mechanical energy. *Appl. Phys. Lett.* **2008**, *93*, 103511. [[CrossRef](#)]
21. Onuta, T.-D.; Wang, Y.; Long, C.J.; Takeuchi, I. Energy harvesting properties of all-thin-film multiferroic cantilevers. *Appl. Phys. Lett.* **2011**, *99*, 203506. [[CrossRef](#)]
22. Chu, Y.H.; Martin, L.W.; Holcomb, M.B.; Gajek, M.; Han, S.J.; He, Q.; Balke, N.; Yang, C.H.; Lee, D.; Hu, W.; et al. Electric-field control of local ferromagnetism using a magnetoelectric multiferroic. *Nat. Mater.* **2008**, *7*, 478–482. [[CrossRef](#)] [[PubMed](#)]
23. Liu, M.; Li, S.; Obi, O.; Lou, J.; Rand, S.; Sun, N.X. Electric field modulation of magnetoresistance in multiferroic heterostructures for ultralow power electronics. *Appl. Phys. Lett.* **2011**, *98*, 222509. [[CrossRef](#)]
24. Hu, J.M.; Li, Z.; Chen, L.Q.; Nan, C.W. High-density magnetoresistive random access memory operating at ultralow voltage at room temperature. *Nat. Commun.* **2011**, *2*, 553. [[CrossRef](#)] [[PubMed](#)]
25. Nan, T.X.; Zhou, Z.Y.; Lou, J.; Liu, M.; Yang, X.; Gao, Y.; Rand, S.; Sun, N.X. Voltage impulse induced bistable magnetization switching in multiferroic heterostructures. *Appl. Phys. Lett.* **2012**, *100*, 132409. [[CrossRef](#)]

26. Rondinelli, J.M.; Stengel, M.; Spaldin, N.A. Carrier-mediated magnetoelectricity in complex oxide heterostructures. *Nat. Nanotechnol.* **2007**, *3*, 46. [[CrossRef](#)]
27. Duan, C.G.; Velev, J.P.; Sabirianov, R.F.; Zhu, Z.; Chu, J.; Jaswal, S.S.; Tsymbal, E.Y. Surface magnetoelectric effect in ferromagnetic metal films. *Phys. Rev. Lett.* **2008**, *101*, 137201. [[CrossRef](#)]
28. Catalan, G.; Scott, J.F. Physics and applications of bismuth ferrite. *Adv. Mater.* **2009**, *21*, 2463–2485. [[CrossRef](#)]
29. Lage, E.; Kirchof, C.; Hrkac, V.; Kienle, L.; Jahns, R.; Knochel, R.; Quandt, E.; Meyners, D. Exchange biasing of magnetoelectric composites. *Nat. Mater.* **2012**, *11*, 523–529. [[CrossRef](#)]
30. Hu, J.-M.; Duan, C.-G.; Nan, C.-W.; Chen, L.-Q. Understanding and designing magnetoelectric heterostructures guided by computation: progresses, remaining questions, and perspectives. *NPJ Comput. Mater.* **2017**, *3*. [[CrossRef](#)]
31. Martin, L.W.; Chu, Y.H.; Ramesh, R. Advances in the growth and characterization of magnetic, ferroelectric, and multiferroic oxide thin films. *Mat. Sci. Eng. R* **2010**, *68*, 89–133. [[CrossRef](#)]
32. Hui, Y.; Nan, T.; Sun, N.X.; Rinaldi, M. High resolution magnetometer based on a high frequency magnetoelectric MEMS-CMOS oscillator. *J. Microelectromech. Syst.* **2015**, *24*, 134–143. [[CrossRef](#)]
33. Bowen, C.R.; Kim, H.A.; Weaver, P.M.; Dunn, S. Piezoelectric and ferroelectric materials and structures for energy harvesting applications. *Energy Environ. Sci.* **2014**, *7*, 25–44. [[CrossRef](#)]
34. Ramadan, K.S.; Sameoto, D.; Evoy, S. A review of piezoelectric polymers as functional materials for electromechanical transducers. *Smart Mater. Struct.* **2014**, *23*, 033001. [[CrossRef](#)]
35. Palneedi, H.; Annapureddy, V.; Priya, S.; Ryu, J. Status and perspectives of multiferroic magnetoelectric composite materials and applications. *Actuators* **2016**, *5*, 9. [[CrossRef](#)]
36. Chu, Z.; PourhosseiniAsl, M.; Dong, S. Review of multi-layered magnetoelectric composite materials and devices applications. *J. Phys. D Appl. Phys.* **2018**, *51*, 243001. [[CrossRef](#)]
37. Dufay, T.; Guiffard, B.; Thomas, J.C.; Seveno, R. Transverse piezoelectric coefficient measurement of flexible lead zirconate titanate thin films. *J. Appl. Phys.* **2015**, *117*, 204101. [[CrossRef](#)]
38. Conde, J.; Mural, P. Characterization of sol-gel $\text{Pb}(\text{Zr}_{0.53}\text{Ti}_{0.47}\text{O}_3)$ in thin film bulk acoustic resonators. *IEEE Trans. Ultrason. Ferr.* **2008**, *55*, 1373–1379. [[CrossRef](#)] [[PubMed](#)]
39. Iqbal, A.; Mohd-Yasin, F. Reactive sputtering of aluminum nitride (002) thin films for piezoelectric applications: A review. *Sensors* **2018**, *18*, 1797. [[CrossRef](#)]
40. Todaro, M.T.; Guido, F.; Algieri, L.; Mastronardi, V.M.; Desmaele, D.; Epifani, G.; De Vittorio, M. Biocompatible, flexible, and compliant energy harvesters based on piezoelectric thin films. *IEEE Trans. Nanotechnol.* **2018**, *17*, 220–230. [[CrossRef](#)]
41. Fei, C.; Liu, X.; Zhu, B.; Li, D.; Yang, X.; Yang, Y.; Zhou, Q. AlN piezoelectric thin films for energy harvesting and acoustic devices. *Nano. Energy* **2018**, *51*, 146–161. [[CrossRef](#)]
42. Kholkin, A.L.; Wüthrich, C.; Taylor, D.V.; Setter, N. Interferometric measurements of electric field-induced displacements in piezoelectric thin films. *Rev. Sci. Instrum.* **1996**, *67*, 1935–1941. [[CrossRef](#)]
43. Dubois, M.-A.; Mural, P. Measurement of the effective transverse piezoelectric coefficient $e_{31,f}$ of AlN and $\text{Pb}(\text{Zr}_x\text{Ti}_{1-x})\text{O}_3$ thin films. *Sensor. Actuat. A Phys.* **1999**, *77*, 106–112. [[CrossRef](#)]
44. Mural, P. Ferroelectric thin films for micro-sensors and actuators: A review. *J. Micromech. Microeng.* **2000**, *10*, 136–146. [[CrossRef](#)]
45. Dubois, M.-A.; Mural, P. Stress and piezoelectric properties of aluminum nitride thin films deposited onto metal electrodes by pulsed direct current reactive sputtering. *J. Appl. Phys.* **2001**, *89*, 6389–6395. [[CrossRef](#)]
46. Martin, F.; Mural, P.; Dubois, M.A.; Pezous, A. Thickness dependence of the properties of high- c -axis textured AlN thin films. *J. Vac. Sci. Technol. A* **2004**, *22*, 361–365. [[CrossRef](#)]
47. Sivaramakrishnan, S.; Mardilovich, P.; Schmitz-Kempen, T.; Tiedke, S. Concurrent wafer-level measurement of longitudinal and transverse effective piezoelectric coefficients ($d_{33,f}$ and $e_{31,f}$) by double beam laser interferometry. *J. Appl. Phys.* **2018**, *123*, 014103. [[CrossRef](#)]
48. Liu, J.M.; Pan, B.; Chan, H.L.W.; Zhu, S.N.; Zhu, Y.Y.; Liu, Z.G. Piezoelectric coefficient measurement of piezoelectric thin films: an overview. *Mater. Chem. Phys.* **2002**, *75*, 12–18. [[CrossRef](#)]
49. Sandlund, L.; Fahlander, M.; Cedell, T.; Clark, A.E.; Restorff, J.B.; Wun-Fogle, M. Magnetostriction, elastic moduli, and coupling factors of composite Terfenol-D. *J. Appl. Phys.* **1994**, *75*, 5656–5658. [[CrossRef](#)]
50. Dong, S.; Zhai, J.; Li, J.-F.; Viehland, D. Magnetoelectric effect in Terfenol-D/ $\text{Pb}(\text{Zr},\text{TiO})_3/\mu$ -metal laminate composites. *Appl. Phys. Lett.* **2006**, *89*, 122903. [[CrossRef](#)]

51. Butera, A.; Gómez, J.; Weston, J.L.; Barnard, J.A. Growth and magnetic characterization of epitaxial Fe₈₁Ga₁₉/MgO (100) thin films. *J. Appl. Phys.* **2005**, *98*, 033901. [[CrossRef](#)]
52. Lou, J.; Insignares, R.E.; Cai, Z.; Ziemer, K.S.; Liu, M.; Sun, N.X. Soft magnetism, magnetostriction, and microwave properties of FeGaB thin films. *Appl. Phys. Lett.* **2007**, *91*, 182504. [[CrossRef](#)]
53. Greve, H.; Woltermann, E.; Quenzer, H.-J.; Wagner, B.; Quandt, E. Giant magnetoelectric coefficients in (Fe₉₀Co₁₀)₇₈Si₁₂B₁₀-AlN thin film composites. *Appl. Phys. Lett.* **2010**, *96*, 182501. [[CrossRef](#)]
54. Lou, J.; Liu, M.; Reed, D.; Ren, Y.; Sun, N.X. Giant electric field tuning of magnetism in novel multiferroic FeGaB/Lead zinc niobate-lead titanate (PZN-PT) heterostructures. *Adv. Mater.* **2009**, *21*, 4711–4715. [[CrossRef](#)]
55. Kalarickal, S.S.; Krivosik, P.; Wu, M.; Patton, C.E.; Schneider, M.L.; Kabos, P.; Silva, T.J.; Nibarger, J.P. Ferromagnetic resonance linewidth in metallic thin films: Comparison of measurement methods. *J. Appl. Phys.* **2006**, *99*, 093909. [[CrossRef](#)]
56. Ekreem, N.B.; Olabi, A.G.; Prescott, T.; Rafferty, A.; Hashmi, M.S.J. An overview of magnetostriction, its use and methods to measure these properties. *J. Mater. Process. Tech.* **2007**, *191*, 96–101. [[CrossRef](#)]
57. Klokholm, E. The measurement of magnetostriction in ferromagnetic thin films. *IEEE Trans. Magn.* **1976**, *12*, 819–821. [[CrossRef](#)]
58. Tam, A.C.; Schroeder, H. A new high-precision optical technique to measure magnetostriction of a thin magnetic film deposited on a substrate. *IEEE Trans. Magn.* **1989**, *25*, 2629–2638. [[CrossRef](#)]
59. Shima, T.; Fujimori, H. An accurate measurement of magnetostriction of thin films by using nano-indentation system. *IEEE Trans. Magn.* **1999**, *35*, 3832–3834. [[CrossRef](#)]
60. Jahns, R.; Zabel, S.; Marauska, S.; Gojdka, B.; Wagner, B.; Knöchel, R.; Adelung, R.; Faupel, F. Microelectromechanical magnetic field sensor based on ΔE effect. *Appl. Phys. Lett.* **2014**, *105*, 052414. [[CrossRef](#)]
61. Nan, T.; Hui, Y.; Rinaldi, M.; Sun, N.X. Self-biased 215 MHz magnetoelectric NEMS resonator for ultra-sensitive DC magnetic field detection. *Sci. Rep.* **2013**, *3*, 1985. [[CrossRef](#)] [[PubMed](#)]
62. Berry, B.S.; Pritchett, W.C. Vibrating reed internal friction apparatus for films and foils. *IBM J. Res. Dev.* **1975**, *19*, 334–343. [[CrossRef](#)]
63. Dong, C.; Li, M.; Liang, X.; Chen, H.; Zhou, H.; Wang, X.; Gao, Y.; McConney, M.E.; Jones, J.G.; Brown, G.J.; et al. Characterization of magnetomechanical properties in FeGaB thin films. *Appl. Phys. Lett.* **2018**, *113*, 262401. [[CrossRef](#)]
64. McCord, J. Irregular domain patterns in structured magnetic thick films. *J. Appl. Phys.* **2004**, *95*, 6855–6857. [[CrossRef](#)]
65. Urs, N.O.; Teliban, I.; Piorra, A.; Knöchel, R.; Quandt, E.; McCord, J. Origin of hysteretic magnetoelastic behavior in magnetoelectric 2–2 composites. *Appl. Phys. Lett.* **2014**, *105*, 202406. [[CrossRef](#)]
66. Chung, T.-K.; Carman, G.P.; Mohanchandra, K.P. Reversible magnetic domain-wall motion under an electric field in a magnetoelectric thin film. *Appl. Phys. Lett.* **2008**, *92*, 112509. [[CrossRef](#)]
67. Unguris, J.; Bowden, S.R.; Pierce, D.T.; Trassin, M.; Ramesh, R.; Cheong, S.W.; Fackler, S.; Takeuchi, I. Simultaneous imaging of the ferromagnetic and ferroelectric structure in multiferroic heterostructures. *APL Mater.* **2014**, *2*, 076109. [[CrossRef](#)]
68. Chen, D.; Gao, X.; Liu, J.-M. Domain structures and magnetoelectric effects in multiferroic nanostructures. *MRS Commun.* **2016**, *6*, 330–340. [[CrossRef](#)]
69. McCord, J. Progress in magnetic domain observation by advanced magneto-optical microscopy. *J. Phys. D: Appl. Phys.* **2015**, *48*, 333001. [[CrossRef](#)]
70. Urs, N.O.; Mozooni, B.; Mazalski, P.; Kustov, M.; Hayes, P.; Deldar, S.; Quandt, E.; McCord, J. Advanced magneto-optical microscopy: Imaging from picoseconds to centimeters-imaging spin waves and temperature distributions (invited). *AIP Adv.* **2016**, *6*, 055605. [[CrossRef](#)]
71. Lage, E.; Urs, N.O.; Röbisch, V.; Teliban, I.; Knöchel, R.; Meyners, D.; McCord, J.; Quandt, E. Magnetic domain control and voltage response of exchange biased magnetoelectric composites. *Appl. Phys. Lett.* **2014**, *104*, 132405. [[CrossRef](#)]
72. Gao, Y.; Hu, J.M.; Wu, L.; Nan, C.W. Dynamic in situ visualization of voltage-driven magnetic domain evolution in multiferroic heterostructures. *J. Phys. Condens. Mat.* **2015**, *27*, 504005. [[CrossRef](#)] [[PubMed](#)]
73. Soldatov, I.V.; Schafer, R. Selective sensitivity in Kerr microscopy. *Rev. Sci. Instrum.* **2017**, *88*, 073701. [[CrossRef](#)] [[PubMed](#)]

74. Von Hofe, T.; Onur Urs, N.; Mozooni, B.; Jansen, T.; Kirchhof, C.; Bürgler, D.E.; Quandt, E.; McCord, J. Dual wavelength magneto-optical imaging of magnetic thin films. *Appl. Phys. Lett.* **2013**, *103*, 142410. [[CrossRef](#)]
75. Röbisch, V.; Yarar, E.; Urs, N.O.; Teliban, I.; Knöchel, R.; McCord, J.; Quandt, E.; Meyners, D. Exchange biased magnetolectric composites for magnetic field sensor application by frequency conversion. *J. Appl. Phys.* **2015**, *117*, 17B513. [[CrossRef](#)]
76. Jovičević Klug, M.; Thormählen, L.; Röbisch, V.; Toxværd, S.D.; Höft, M.; Knöchel, R.; Quandt, E.; Meyners, D.; McCord, J. Antiparallel exchange biased multilayers for low magnetic noise magnetic field sensors. *Appl. Phys. Lett.* **2019**, *114*, 192410. [[CrossRef](#)]
77. Schmelz, M.; Stolz, R.; Zakosarenko, V.; Schönau, T.; Anders, S.; Fritsch, L.; Mück, M.; Meyer, M.; Meyer, H.G. Sub-fT/Hz^{1/2} resolution and field-stable SQUID magnetometer based on low parasitic capacitance sub-micrometer cross-type Josephson tunnel junctions. *Physica C* **2012**, *482*, 27–32. [[CrossRef](#)]
78. Wang, Y.; Gray, D.; Berry, D.; Gao, J.; Li, M.; Li, J.; Viehland, D. An extremely low equivalent magnetic noise magnetolectric sensor. *Adv. Mater.* **2011**, *23*, 4111–4114. [[CrossRef](#)]
79. Röbisch, V.; Salzer, S.; Urs, N.O.; Reermann, J.; Yarar, E.; Piorra, A.; Kirchhof, C.; Lage, E.; Höft, M.; Schmidt, G.U.; et al. Pushing the detection limit of thin film magnetolectric heterostructures. *J. Mater. Res.* **2017**, *32*, 1009–1019. [[CrossRef](#)]
80. Zhao, P.; Zhao, Z.; Hunter, D.; Suchoski, R.; Gao, C.; Mathews, S.; Wuttig, M.; Takeuchi, I. Fabrication and characterization of all-thin-film magnetolectric sensors. *Appl. Phys. Lett.* **2009**, *94*, 243507. [[CrossRef](#)]
81. Kirchhof, C.; Krantz, M.; Teliban, I.; Jahns, R.; Marauska, S.; Wagner, B.; Knöchel, R.; Gerken, M.; Meyners, D.; Quandt, E. Giant magnetolectric effect in vacuum. *Appl. Phys. Lett.* **2013**, *102*, 232905. [[CrossRef](#)]
82. Dubois, M.-A.; Muralt, P. Properties of aluminum nitride thin films for piezoelectric transducers and microwave filter applications. *Appl. Phys. Lett.* **1999**, *74*, 3032–3034. [[CrossRef](#)]
83. Piorra, A.; Jahns, R.; Teliban, I.; Gugat, J.L.; Gerken, M.; Knöchel, R.; Quandt, E. Magnetolectric thin film composites with interdigital electrodes. *Appl. Phys. Lett.* **2013**, *103*, 032902. [[CrossRef](#)]
84. Yarar, E.; Salzer, S.; Hrkac, V.; Piorra, A.; Höft, M.; Knöchel, R.; Kienle, L.; Quandt, E. Inverse bilayer magnetolectric thin film sensor. *Appl. Phys. Lett.* **2016**, *109*, 022901. [[CrossRef](#)]
85. Yarar, E.; Hrkac, V.; Zamponi, C.; Piorra, A.; Kienle, L.; Quandt, E. Low temperature aluminum nitride thin films for sensory applications. *AIP Adv.* **2016**, *6*, 075115. [[CrossRef](#)]
86. Salzer, S.; Jahns, R.; Piorra, A.; Teliban, I.; Reermann, J.; Höft, M.; Quandt, E.; Knöchel, R. Tuning fork for noise suppression in magnetolectric sensors. *Sensor. Actuat. A Phys.* **2016**, *237*, 91–95. [[CrossRef](#)]
87. Jahns, R.; Greve, H.; Woltermann, E.; Quandt, E.; Knöchel, R. Sensitivity enhancement of magnetolectric sensors through frequency-conversion. *Sensor. Actuat. A Phys.* **2012**, *183*, 16–21. [[CrossRef](#)]
88. Salzer, S.; Durdaut, P.; Röbisch, V.; Meyners, D.; Quandt, E.; Höft, M.; Knöchel, R. Generalized magnetic frequency conversion for thin-film laminate magnetolectric sensors. *IEEE Sens. J.* **2017**, *17*, 1373–1383. [[CrossRef](#)]
89. Salzer, S.; Röbisch, V.; Klug, M.; Durdaut, P.; McCord, J.; Meyners, D.; Reermann, J.; Höft, M.; Knöchel, R. Noise limits in thin-film magnetolectric sensors with magnetic frequency conversion. *IEEE Sens. J.* **2018**, *18*, 596–604. [[CrossRef](#)]
90. Hayes, P.; Salzer, S.; Reermann, J.; Yarar, E.; Röbisch, V.; Piorra, A.; Meyners, D.; Höft, M.; Knöchel, R.; Schmidt, G.; et al. Electrically modulated magnetolectric sensors. *Appl. Phys. Lett.* **2016**, *108*, 182902. [[CrossRef](#)]
91. Hayes, P.; Schell, V.; Salzer, S.; Burdin, D.; Yarar, E.; Piorra, A.; Knöchel, R.; Fetisov, Y.K.; Quandt, E. Electrically modulated magnetolectric AlN/FeCoSiB film composites for DC magnetic field sensing. *J. Phys. D Appl. Phys.* **2018**, *51*, 354002. [[CrossRef](#)]
92. Akulov, N.; Kondorsky, E. Über einen magnetomechanischen Effekt. *Z. Phys.* **1932**, *78*, 801–807. [[CrossRef](#)]
93. Kersten, M. Über den temperaturkoeffizienten des elastizitätsmoduls ferromagnetischer stoffe. *Z. Phys.* **1933**, *85*, 708–716. [[CrossRef](#)]
94. Akulov, N.; Kondorsky, E. über Mechanostriktion und δ E-Effekt. *Z. Phys.* **1933**, *85*, 661–671. [[CrossRef](#)]
95. Lee, E.W. Magnetostriction and magnetomechanical effects. *Rep. Prog. Phys.* **1955**, *18*, 184–229. [[CrossRef](#)]
96. Becker, R.; Döring, W. *Ferromagnetismus*; Verlag von Julius Springer: Berlin, Germany, 1939.
97. Honda, K.; Terada, T. II. On the change of elastic constants of ferromagnetic substances by magnetization. *Lond. Edinb. Dubl. Phil. Mag.* **1907**, *13*, 36–83. [[CrossRef](#)]

98. Livingston, J.D. Magnetomechanical properties of amorphous metals. *Phys. Status Solidi A* **1982**, *70*, 591–596. [[CrossRef](#)]
99. Atalay, S.; Squire, P.T. Magnetomechanical damping in FeSiB amorphous wires. *J. Appl. Phys.* **1993**, *73*, 871–875. [[CrossRef](#)]
100. Gutiérrez, J.; García-Arribas, A.; Garitaonandia, J.S.; Barandiarán, J.M.; Squire, P.T. ΔE effect and anisotropy distribution in metallic glasses with oblique easy axis induced by field annealing. *J. Magn. Magn. Mater.* **1996**, *157–158*, 543–544. [[CrossRef](#)]
101. Squire, P.T.; Atalay, S.; Chiriac, H. ΔE effect in amorphous glass covered wires. *IEEE Trans. Magn.* **2000**, *36*, 3433–3435. [[CrossRef](#)]
102. Ludwig, A.; Quandt, E. Optimization of the ΔE effect in thin films and multilayers by magnetic field annealing. *IEEE Trans. Magn.* **2002**, *38*, 2829–2831. [[CrossRef](#)]
103. Charles, F. Development of the Shear Wave Magnetometer. Ph.D. Thesis, University of Bath, Bath, UK, 1992.
104. Gojdka, B.; Jahns, R.; Meurisch, K.; Greve, H.; Adelung, R.; Quandt, E.; Knöchel, R.; Faupel, F. Fully integrable magnetic field sensor based on delta-E effect. *Appl. Phys. Lett.* **2011**, *99*, 223502. [[CrossRef](#)]
105. Zabel, S.; Kirchhof, C.; Yarar, E.; Meyners, D.; Quandt, E.; Faupel, F. Phase modulated magnetoelectric delta-E effect sensor for sub-nano tesla magnetic fields. *Appl. Phys. Lett.* **2015**, *107*, 152402. [[CrossRef](#)]
106. Zabel, S.; Reermann, J.; Fichtner, S.; Kirchhof, C.; Quandt, E.; Wagner, B.; Schmidt, G.; Faupel, F. Multimode delta-E effect magnetic field sensors with adapted electrodes. *Appl. Phys. Lett.* **2016**, *108*, 222401. [[CrossRef](#)]
107. Reermann, J.; Zabel, S.; Kirchhof, C.; Quandt, E.; Faupel, F.; Schmidt, G. Adaptive readout schemes for thin-film magnetoelectric sensors based on the delta-E effect. *IEEE Sens. J.* **2016**, *16*, 4891–4900. [[CrossRef](#)]
108. Durdaut, P.; Salzer, S.; Reermann, J.; Röbbisch, V.; Hayes, P.; Piorra, A.; Meyners, D.; Quandt, E.; Schmidt, G.; Knöchel, R.; et al. Thermal-mechanical noise in resonant thin-film magnetoelectric sensors. *IEEE Sens. J.* **2017**, *17*, 2338–2348. [[CrossRef](#)]
109. Durdaut, P.; Reermann, J.; Zabel, S.; Kirchhof, C.; Quandt, E.; Faupel, F.; Schmidt, G.; Knöchel, R.; Höft, M. Modeling and analysis of noise sources for thin-film magnetoelectric sensors based on the delta-E Effect. *IEEE Trans. Instrum. Meas.* **2017**, *66*, 2771–2779. [[CrossRef](#)]
110. Spetzler, B.; Kirchhof, C.; Reermann, J.; Durdaut, P.; Höft, M.; Schmidt, G.; Quandt, E.; Faupel, F. Influence of the quality factor on the signal to noise ratio of magnetoelectric sensors based on the delta-E effect. *Appl. Phys. Lett.* **2019**, *114*, 183504. [[CrossRef](#)]
111. Lin, C.-M.; Yantchev, V.; Zou, J.; Chen, Y.-Y.; Pisano, A.P. Micromachined one-port aluminum nitride lamb wave resonators utilizing the lowest-order symmetric mode. *J. Microelectromech. Syst.* **2014**, *23*, 78–91. [[CrossRef](#)]
112. Tu, C.; Lee, J.E.Y. VHF-band biconvex AlN-on-silicon micromechanical resonators with enhanced quality factor and suppressed spurious modes. *J. Micromech. Microeng.* **2016**, *26*, 065012. [[CrossRef](#)]
113. Xing, X.; Liu, M.; Li, S.; Obi, O.; Lou, J.; Zhou, Z.; Chen, B.; Sun, N.X. RF magnetic properties of FeCoB/Al₂O₃/FeCoB structure with varied Al₂O₃ thickness. *IEEE Trans. Magn.* **2011**, *47*, 3104–3107. [[CrossRef](#)]
114. Webb, D.; Forester, D.; Ganguly, A.; Vittoria, C. Applications of amorphous magnetic-layers in surface-acoustic-wave devices. *IEEE Trans. Magn.* **1979**, *15*, 1410–1415. [[CrossRef](#)]
115. Kittmann, A.; Durdaut, P.; Zabel, S.; Reermann, J.; Schmalz, J.; Spetzler, B.; Meyners, D.; Sun, N.X.; McCord, J.; Gerken, M.; et al. Wide Band Low Noise Love Wave Magnetic Field Sensor System. *Sci. Rep.* **2018**, *8*, 278. [[CrossRef](#)] [[PubMed](#)]
116. Durdaut, P.; Kittmann, A.; Rubiola, E.; Friedt, J.-M.; Quandt, E.; Knöchel, R.; Höft, M. Noise analysis and comparison of phase-and frequency-detecting readout systems: Application to SAW delay line magnetic field sensor. *IEEE Sens. J.* **2019**, *1*. [[CrossRef](#)]
117. Reermann, J.; Durdaut, P.; Salzer, S.; Demming, T.; Piorra, A.; Quandt, E.; Frey, N.; Höft, M.; Schmidt, G. Evaluation of magnetoelectric sensor systems for cardiological applications. *Measurement* **2018**, *116*, 230–238. [[CrossRef](#)]
118. Friedrich, R.M.; Zabel, S.; Galka, A.; Lukat, N.; Wagner, J.M.; Kirchhof, C.; Quandt, E.; McCord, J.; Selhuber-Unkel, C.; Siniatchkin, M.; et al. Magnetic particle mapping using magnetoelectric sensors as an imaging modality. *Sci. Rep.* **2019**, *9*, 2086. [[CrossRef](#)] [[PubMed](#)]
119. Yao, Z.; Wang, Y.E.; Keller, S.; Carman, G.P. Bulk Acoustic wave-mediated multiferroic antennas: Architecture and performance bound. *IEEE Trans. Antenn. Propag.* **2015**, *63*, 3335–3344. [[CrossRef](#)]

120. Domann, J.P.; Carman, G.P. Strain powered antennas. *J. Appl. Phys.* **2017**, *121*, 044905. [[CrossRef](#)]
121. Nan, T.; Lin, H.; Gao, Y.; Matyushov, A.; Yu, G.; Chen, H.; Sun, N.; Wei, S.; Wang, Z.; Li, M.; et al. Acoustically actuated ultra-compact NEMS magnetoelectric antennas. *Nat. Commun.* **2017**, *8*, 296. [[CrossRef](#)]
122. Piazza, G.; Stephanou, P.J.; Pisano, A.P. Piezoelectric aluminum nitride vibrating contour-mode MEMS resonators. *J. Microelectromech. Syst.* **2006**, *15*, 1406–1418. [[CrossRef](#)]
123. Larson, J.D.; Bradley, P.D.; Wartenberg, S.; Ruby, R.C. Modified Butterworth-Van Dyke circuit for FBAR resonators and automated measurement system. In Proceedings of the 2000 IEEE Ultrasonics Symposium, San Juan, PR, USA, 22–25 October 2000; IEEE: Piscataway, NJ, USA, 2000; pp. 863–868.
124. Ruby, R. A snapshot in time: The future in filters for cell phones. *IEEE Microw. Mag.* **2015**, *16*, 46–59. [[CrossRef](#)]
125. Salahun, E.; Quéffélec, P.; Tanné, G.; Adenot, A.-L.; Acher, O. Correlation between magnetic properties of layered ferromagnetic/dielectric material and tunable microwave device applications. *J. Appl. Phys.* **2002**, *91*, 5449–5455. [[CrossRef](#)]
126. Kuanr, B.; Celinski, Z.; Camley, R.E. Tunable high-frequency band-stop magnetic filters. *Appl. Phys. Lett.* **2003**, *83*, 3969–3971. [[CrossRef](#)]
127. Kuanr, B.K.; Marvin, D.L.; Christensen, T.M.; Camley, R.E.; Celinski, Z. High-frequency magnetic microstrip local bandpass filters. *Appl. Phys. Lett.* **2005**, *87*, 222506. [[CrossRef](#)]
128. Fetisov, Y.K.; Srinivasan, G. Electric field tuning characteristics of a ferrite-piezoelectric microwave resonator. *Appl. Phys. Lett.* **2006**, *88*, 143503. [[CrossRef](#)]
129. Pettiford, C.; Dasgupta, S.; Jin, L.; Yoon, S.D.; Sun, N.X. Bias field effects on microwave frequency behavior of PZT/YIG magnetoelectric bilayer. *IEEE Trans. Magn.* **2007**, *43*, 3343–3345. [[CrossRef](#)]
130. Lou, J.; Reed, D.; Liu, M.; Sun, N.X. Electrostatically tunable magnetoelectric inductors with large inductance tunability. *Appl. Phys. Lett.* **2009**, *94*, 112508. [[CrossRef](#)]
131. Moffett, M.B.; Clark, A.E.; Wun-Fogle, M.; Linberg, J.; Teter, J.P.; McLaughlin, E.A. Characterization of Terfenol-D for magnetostrictive transducers. *J. Acoust. Soc. Am.* **1991**, *89*, 1448–1455. [[CrossRef](#)]
132. Clark, A.E.; Wun-Fogle, M.; Restorff, J.B.; Lograsso, T.A.; Cullen, J.R. Effect of quenching on the magnetostriction on $\text{Fe}_{1-x}\text{Ga}_x$ ($0.13x < 0.21$). *IEEE Trans. Magn.* **2001**, *37*, 2678–2680. [[CrossRef](#)]
133. Dong, S.; Zhai, J.; Li, J.; Viehland, D. Near-ideal magnetoelectricity in high-permeability magnetostrictive/piezofiber laminates with a (2-1) connectivity. *Appl. Phys. Lett.* **2006**, *89*, 252904. [[CrossRef](#)]
134. Rais-Zadeh, M.; Kohl, P.A.; Ayazi, F. A packaged micromachined switched tunable inductor. In Proceedings of the 2007 IEEE 20th International Conference on Micro Electro Mechanical Systems (MEMS), Hyogo, Japan, 21–25 January 2007; pp. 799–802.
135. Kim, J.; Peroulis, D. Tunable MEMS spiral inductors with optimized RF performance and integrated large-displacement electrothermal actuators. *IEEE Trans. Microw. Theory* **2009**, *57*, 2276–2283. [[CrossRef](#)]
136. Shim, Y.; Wu, Z.; Rais-Zadeh, M. A multimetal surface micromachining process for tunable RF MEMS passives. *J. Microelectromech. Syst.* **2012**, *21*, 867–874. [[CrossRef](#)]
137. Salvia, J.; Bain, J.A.; Yue, C.P. Tunable on-chip inductors up to 5 GHz using patterned permalloy laminations. In Proceedings of the IEEE International Electron Devices Meeting, 2005. IEDM Technical Digest, Washington, DC, USA, 5 December 2005; pp. 943–946.
138. Gao, Y.; Zardareh, S.Z.; Yang, X.; Nan, T.X.; Zhou, Z.Y.; Onabajo, M.; Liu, M.; Aronow, A.; Mahalingam, K.; Howe, B.M.; et al. Significantly enhanced inductance and quality factor of GHz integrated magnetic solenoid inductors with FeGaB/Al₂O₃ multilayer films. *IEEE Trans. Electron Dev.* **2014**, *61*, 1470–1476. [[CrossRef](#)]
139. Gao, Y.; Zare, S.; Onabajo, M.; Li, M.; Zhou, Z.; Nan, T.; Yang, X.; Liu, M.; Mahalingam, K.; Howe, B.M.; et al. Power-efficient voltage tunable RF integrated magnetoelectric inductors with FeGaB/Al₂O₃ multilayer films. In Proceedings of the 2014 IEEE MTT-S International Microwave Symposium (IMS2014), Tampa, FL, USA, 1–6 June 2014; IEEE: Piscataway, NJ, USA, 2014; pp. 1–4.
140. Ishak, W.S.; Kok-Wai, C. Tunable microwave resonators using magnetostatic wave in YIG films. *IEEE Trans. Microw. Theory* **1986**, *34*, 1383–1393. [[CrossRef](#)]
141. Murakami, Y.; Ohgihara, T.; Okamoto, T. A 0.5–4.0-GHz tunable bandpass filter using YIG film grown by LPE. *IEEE Trans. Microw. Theory* **1987**, *35*, 1192–1198. [[CrossRef](#)]

142. Tsai, C.S.; Qiu, G.; Gao, H.; Yang, L.W.; Li, G.P.; Nikitov, S.A.; Gulyaev, Y. Tunable wideband microwave band-stop and band-pass filters using YIG/GGG-GaAs layer structures. *IEEE Trans. Magn.* **2005**, *41*, 3568–3570. [[CrossRef](#)]
143. Uher, J.; Hofer, W.J.R. Tunable microwave and millimeter-wave band-pass filters. *IEEE Trans. Microw. Theory* **1991**, *39*, 643–653. [[CrossRef](#)]
144. Wu, J.; Yang, X.; Beguhn, S.; Lou, J.; Sun, N.X. Nonreciprocal tunable low-loss bandpass filters with ultra-wideband isolation based on magnetostatic surface wave. *IEEE Trans. Microw. Theory* **2012**, *60*, 3959–3968. [[CrossRef](#)]
145. Hunter, I.C.; Rhodes, J.D. Electronically tunable microwave bandpass filters. *IEEE Trans. Microw. Theory* **1982**, *30*, 1354–1360. [[CrossRef](#)]
146. Chandler, S.R.; Hunter, I.C.; Gardiner, J.G. Active varactor tunable bandpass filter. *IEEE Microw. Guided* **1993**, *3*, 70–71. [[CrossRef](#)]
147. Brown, A.R.; Rebeiz, G.M. A varactor-tuned RF filter. *IEEE Trans. Microw. Theory* **2000**, *48*, 1157–1160. [[CrossRef](#)]
148. Entesari, K.; Rebeiz, G.M. A differential 4-bit 6.5-10-GHz RF MEMS tunable filter. *IEEE Trans. Microw. Theory* **2005**, *53*, 1103–1110. [[CrossRef](#)]
149. Cheng, C.-C.; Rebeiz, G.M. High-Q 4–6-GHz suspended stripline RF MEMS tunable filter with bandwidth control. *IEEE Trans. Microw. Theory* **2011**, *59*, 2469–2476. [[CrossRef](#)]
150. Sekar, V.; Armendariz, M.; Entesari, K. A 1.2–1.6-GHz substrate-integrated-waveguide RF MEMS tunable filter. *IEEE Trans. Microw. Theory* **2011**, *59*, 866–876. [[CrossRef](#)]
151. Lin, H.; Jing, W.; Xi, Y.; Hu, Z.; Nan, T.; Emori, S.; Gao, Y.; Guo, R.; Wang, X.; Sun, N.X. Integrated non-reciprocal dual H- and E-Field tunable bandpass filter with ultra-wideband isolation. In Proceedings of the 2015 IEEE MTT-S International Microwave Symposium, Phoenix, AZ, USA, 17–22 May 2015; IEEE: Piscataway, NJ, USA, 2015; pp. 1–4.
152. Stancil, D.D. Propagation characteristics and excitation of magnetostatic waves. In *Theory of Magnetostatic Waves*; Stancil, D.D., Ed.; Springer: New York, NY, USA, 1993; pp. 119–153. [[CrossRef](#)]
153. Lin, H.; Nan, T.; Qian, Z.; Gao, Y.; Hui, Y.; Wang, X.; Guo, R.; Belkessam, A.; Wei, S.; Rinaldi, M.; et al. Tunable RF band-pass filters based on NEMS magnetoelectric resonators. In Proceedings of the 2016 IEEE MTT-S International Microwave Symposium (IMS), San Francisco, CA, USA, 22–27 May 2016; IEEE: Piscataway, NJ, USA, 2016; pp. 1–4.



© 2019 by the authors. Licensee MDPI, Basel, Switzerland. This article is an open access article distributed under the terms and conditions of the Creative Commons Attribution (CC BY) license (<http://creativecommons.org/licenses/by/4.0/>).

Summary of Own Contributions to the Publications

Publications as first/equally contributing author

First and equally contributing authors are underlined.

- 1 B. Spetzler, P. Wiegand, P. Durdaut, M. Höft, A. Bahr, R. Rieger, and F. Faupel, "Modeling and parallel operation of exchange-biased delta-E effect magnetometers for sensor arrays", *Sensors*, vol. 21, no. 22, 2021, doi: [10.3390/s21227594](https://doi.org/10.3390/s21227594).

Major contribution to this publication. Conceptualization, writing of original manuscript, modeling and simulations (shared), analysis and interpretation, and visualization.

- 2 A. D. Matyushov, B. Spetzler, M. Zaeimbashi, J. Zhou, Z. Qian, E. V. Golubeva, C. Tu, Y. Guo, B. F. Chen, D. Wang, A. Will-Cole, H. Chen, M. Rinaldi, J. McCord, F. Faupel, and N. X. Sun, "Curvature and stress effects on the performance of contour-mode resonant ΔE effect magnetometers", *Advanced Materials Technologies*, vol. 6, no. 9, 2021, doi: [10.1002/admt.202100294](https://doi.org/10.1002/admt.202100294).

Major contribution to this publication shared with A. D. Matyushov. Conceptualization (shared), writing of original manuscript (shared), modeling and simulation, analysis and interpretation (shared), and visualization (shared).

- 3 B. Spetzler, C. Bald, P. Durdaut, J. Reermann, C. Kirchhof, A. Teplyuk, D. Meyners, E. Quandt, M. Höft, G. Schmidt, and F. Faupel, "Exchange biased delta-E effect enables the detection of low frequency pT magnetic fields with simultaneous localization", *Scientific Reports*, vol. 11, 2021, doi: [10.1038/s41598-021-84415-2](https://doi.org/10.1038/s41598-021-84415-2).

Major contribution to this publication. Conceptualization (shared), writing of original manuscript (shared), modeling and simulations (shared), analysis and interpretation (shared), and visualization (shared).

- 4 B. Spetzler, J. Su, R.-M. Friedrich, F. Nickiel, S. Fichtner, F. Lofink, and F. Faupel, "Influence of the piezoelectric material on the signal and noise of magnetoelectric magnetic field sensors based on the delta-E effect", *Applied Physics Letters Materials*, vol. 9, no. 3, 2021, doi: [10.1063/5.0042448](https://doi.org/10.1063/5.0042448).

Major contribution to this publication. Conceptualization, writing of original manuscript, modeling and simulations, analysis and interpretation, and visualization.

- 5 **B. Spetzler**, E. V. Golubeva, R.-M. Friedrich, S. Zabel, C. Kirchhof, D. Meyners, J. McCord, and F. Faupel, "Magnetoelastic coupling and delta-E effect in magnetoelectric torsion mode resonators", *Sensors*, vol. 21, no. 6, 2021, doi: [10.3390/s21062022](https://doi.org/10.3390/s21062022).

Major contribution to this publication. Conceptualization, writing of original manuscript, modeling and simulations, measurements (shared), analysis and interpretation, and visualization.

- 6 **B. Spetzler**, C. Kirchhof, E. Quandt, J. McCord, and F. Faupel, "Magnetic sensitivity of bending-mode delta-E-effect sensors", *Physical Review Applied*, vol. 12, no. 16, 2019, doi: [10.1103/PhysRevApplied.12.064036](https://doi.org/10.1103/PhysRevApplied.12.064036).

Major contribution to this publication. Conceptualization, writing of original manuscript, modeling and simulations, measurements (shared), analysis and interpretation, and visualization.

- 7 **B. Spetzler**, E. V. Golubeva, C. Müller, J. McCord, and F. Faupel, "Frequency dependency of the delta-E effect and the sensitivity of delta-E effect magnetic field sensors", *Sensors*, vol. 19, no. 21, 2019, doi: [10.3390/s19214769](https://doi.org/10.3390/s19214769).

Major contribution to this publication. Conceptualization, writing of original manuscript, modeling and simulations (shared), analysis and interpretation (shared), and visualization.

- 8 **B. Spetzler**, C. Kirchhof, J. Reermann, P. Durdaut, M. Höft, G. Schmidt, E. Quandt, and F. Faupel, "Influence of the quality factor on the signal to noise ratio of magnetoelectric sensors based on the delta-E effect", *Applied Physics Letters*, vol. 114, no. 18, 2019, doi: [10.1063/1.5096001](https://doi.org/10.1063/1.5096001). Editor's Pick.

Major contribution to this publication shared with C. Kirchhof. Conceptualization (shared), writing of original manuscript, modeling and simulations (shared), analysis and interpretation (shared), and visualization.

- 9 A. Kittmann, P. Durdaut, S. Zabel, J. Reermann, J. Schmalz, **B. Spetzler**, D. Meyners, N. X. Sun, J. McCord, M. Gerken, G. Schmidt, M. Höft, R. Knöchel, F. Faupel, and E. Quandt, "Wide band low noise Love wave magnetic field sensor system", *Scientific Reports*, vol. 8, 2018, doi: [10.1038/s41598-017-18441-4](https://doi.org/10.1038/s41598-017-18441-4). Top 100 Articles 2018.

Major contribution to this publication together with A. Kittmann, P. Durdaut, S. Zabel, J. Reermann, J. Schmalz. Conceptualization (shared), writing of original manuscript (shared), modeling and simulations (shared), analysis and interpretation (shared), and visualization (shared).

Publications as Coauthor

Additional publications related to the ΔE effect and ΔE -effect magnetometers are listed in the following. First and equally contributing authors are underlined.

- 1 J. Schmalz, A. Kittmann, P. Durdaut, **B. Spetzler**, F. Faupel, M. Höft, E. Quandt, and M. Gerken, "Multi-mode Love-wave SAW magnetic-field sensors", *Sensors*, vol. 20, no. 12, 2020, doi: [10.3390/s20123421](https://doi.org/10.3390/s20123421).

Partial contribution to this publication. Modeling and simulations (shared).

- 2 P. Durdaut, E. Rubiola, J.-M. Friedt, C. Müller, **B. Spetzler**, C. Kirchhof, D. Meyners, E. Quandt, F. Faupel, J. McCord, R. Knöchel, and M. Höft, "Fundamental noise limits and sensitivity of piezoelectrically driven magnetoelastic cantilevers", *Journal of Microelectromechanical Systems*, vol. 29, no. 5, 2020, doi: [10.1109/JMEMS.2020.3014402](https://doi.org/10.1109/JMEMS.2020.3014402).

Partial contribution to this publication. Conceptualization (shared), modeling and simulations (shared).

- 3 N. Lukat, R.-M. Friedrich, **B. Spetzler**, C. Kirchhof, C. Arndt, L. Thormählen, F. Faupel, and C. Selhuber-Unkel, "Mapping of magnetic nanoparticles and cells using thin film magnetoelectric sensors based on the delta-E effect", *Sensors and Actuators A: Physical*, vol. 309, 2020, doi: [10.1016/j.sna.2020.112023](https://doi.org/10.1016/j.sna.2020.112023).

Partial contribution to this publication. Measurements and methodology (shared).

- 4 C. Tu, Z.-Q. Chu, **B. Spetzler**, P. Hayes, C.-Z. Dong, X.-F. Liang, H.-H. Chen, Y.-F. He, Y.-Y. Wei, I. Lisenkov, H. Lin, Y.-H. Lin, J. McCord, F. Faupel, E. Quandt, and N. X. Sun, "Mechanical-resonance-enhanced thin-film magnetoelectric heterostructures for magnetometers, mechanical antennas, tunable RF inductors, and filters", *Materials*, vol. 12, no. 14, 2019, doi: [10.3390/ma12142259](https://doi.org/10.3390/ma12142259).

Partial contribution to this publication. Writing of original manuscript (shared).

- 5 J. Schmalz, **B. Spetzler**, F. Faupel, and M. Gerken, "Love wave magnetic field sensor modeling - from 1D to 3D model", *Proceedings of the International Conference on Electromagnetics in Advanced Applications (ICEAA)*; IEEE: Granada, Spain, 2019, doi: [10.1109/ICEAA.2019.8879389](https://doi.org/10.1109/ICEAA.2019.8879389).

Partial contribution to this publication. Modeling and simulations (shared).

Declaration of Authorship

I herewith declare that this thesis and the corresponding research were composed and authored by myself. The work complies with the DFG guidelines for safeguarding good scientific practice. All content and ideas drawn directly or indirectly from external sources are clearly indicated. This thesis has not been published or been submitted to any other institution and all related research items that have been published in peer-review journals are indicated as such. I declare that no academic degree has been withdrawn from me.

Kiel, October 21, 2021